Universidade do Porto

Faculdade de Engenharia

FEUP

# LIGHTWEIGHT STIFFENED PANELS: MECHANICAL CHARACTERIZATION OF EMERGING FABRICATION TECHNOLOGIES

by

Pedro Miguel Guimarães Pires Moreira

A thesis submitted in conformity with the requirements for the Doctoral Degree in Mechanical Engineering,
Departamento de Engenharia Mecânica e Gestão Industrial,
Faculdade de Engenharia da Universidade do Porto, Portugal

January 2008

*I dedicate this work to my parents and sister, and also to Filipa*

# Abstract

The increasing use of aluminium alloys in the transportation industry, *e.g.* in aeronautics, creates the need for research on more efficient and reliable welding processes to be used. In order to allow the industry to use novel manufacturing techniques as Laser Beam Welding and Friction Stir Welding, which promise high efficiency but still lack dedicated research, there is a need for further experimental and numerical work. The present dissertation, with a predominant experimental focus, aims to contribute:

- to the assessment of the mechanical behaviour of structural connections manufactured using these new processes, and
- to fundamental knowledge and to damage tolerance criteria of modern lightweight monolithic stiffened panels.

Since heat generation is a fundamental aspect of any welding technique, an effective temperature measurement procedure that could be applied to any welding process was developed. Gas Metal Arc Welding, an aggressive and well known welding method, was used as a basis for the development of an accurate temperature measurement procedure. Fibre Bragg grating sensors proved to be a convenient, novel means of temperature field acquisition, validated in this thesis using other techniques. Also, a comparison of temperature fields of Metal Inert Gas welding, Laser Beam and Friction Stir Welding was carried out.

Residual stresses are locked-in stresses which exist in a structural part in the absence of any service or other external loads. Residual stresses may be detrimental, *e.g.* in fatigue, and promote structural failures. They are caused by mechanically induced plasticity or by thermal effects which arise from a production process as welding. A comparative study of several residual stress measuring techniques is presented, since quantitative estimation of residual stresses is important for the safe performance of structural components.

The mechanical behaviour of Friction Stir Welded and Laser Beam Welded joints was the object of three separate but complementary studies.
Due to design constraints, friction stir welded components may include notches in the weldment and so far there is no available information on the fatigue behaviour of such structural details. Therefore, in a first study the effect of notches on friction stir weldments was investigated.
In the second study an experimental characterization and computational modelling analysis of dissimilar friction stir welded butt joints performed between aluminium alloys 6061-T6 and 6082-T6 was carried out. Bending tests were performed to characterize this example of multimaterial joint, a type of connection made possible by Friction Stir Welding. An approximate finite element

modelling of a bending test of a weldment, taking into account the spatial dependence of the tensile strength properties, was made.
Notwithstanding the widespread interest in the possibilities offered by Friction Stir and Laser Beam Welding, data concerning the fatigue behaviour of joints obtained using these processes is still needed. Research work on S-N and fatigue crack growth data concerning the weld zone is required to provide tools to assess fatigue behaviour. The third study is a contribution to this effort, contrasting the fatigue behaviour of joints made using a traditional process, Metal Inert Gas welding, with those made with Laser Beam and Friction Stir Welding.

An aircraft fuselage structure includes, among other parts, the external skin and longitudinal stiffeners. Most commonly stiffeners are connected to the skin by means of fasteners (rivets). Stiffeners improve the strength and stability of the structure and provide means of slowing down or arresting the growth of cracks in a panel. Riveted stiffeners remain intact as a crack propagates under them, providing an alternative path for the panel load to pass. The continuous need for lower costs and the emergence of new welding technologies as Laser Beam and Friction Stir Welding has brought interest on large integral metallic structures for aircraft applications. However, studies show that a crack approaching a stiffener propagates simultaneously in the skin and into the stiffener and breaks it.
Damage tolerance analysis for these structures is performed using linear elastic fracture mechanics concepts where the stress intensity factor plays a fundamental role. Fracture mechanics in conjunction with the Paris and other propagation laws are widely used to analyze and predict crack growth and fracture behaviour of aircraft panels. To study crack growth, and predict remaining life of stiffened panels, rigorous numerical analyses have to be performed to compute stress intensity factors. A study on three-dimensional stress intensity factor solutions for a cracked stiffened plate using the Finite Element Method was carried out.
The European Union DaToN project aims to provide missing fundamental knowledge and assessment tools for the damage tolerance of integrally stiffened structures produced by means of three novel production methods: Laser Beam and Friction Stir Welding and High Speed Cutting or High Speed Machining. A testing programme which included fatigue crack growth rate of High Speed Machining, Laser Beam and Friction Stir welded stiffened panels was performed. This test programme was complemented by a Scanning Electron Microscopy analysis of the fractured specimens.

# Resumo

O aumento do uso de ligas de alumínio nas indústrias de transporte, como por exemplo na aeronáutica, fomenta a necessidade de investigação relativa a técnicas de soldadura eficientes e aplicáveis nesse contexto. Esta tese pretende ser um contributo, com enfoque predominantemente experimental, para o estudo do comportamento mecânico de juntas realizadas por técnicas de soldadura inovadoras com elevado potencial mas que, porém, necessitam ainda de um maior conhecimento. Entre estas encontram-se a soldadura laser (*Laser Beam Welding*) e a soldadura por fricção linear (*Friction Stir Welding*). O trabalho agora apresentado pretende dar um contributo para uma melhor compreensão:

- do comportamento mecânico de juntas soldadas por estes processos, e
- do comportamento à fadiga e da tolerância ao dano de estruturas fabricadas utilizando estas novas técnicas de soldadura.

Tendo em conta que a geração de calor é um aspecto fundamental em qualquer tipo de soldadura, foi desenvolvida uma técnica eficiente para a medição de temperatura durante a sua execução. Este estudo, visando o desenvolvimento de um método capaz de medições precisas de temperatura, foi realizado para um ambiente agressivo como o existente na soldadura por arco eléctrico. Foi desenvolvido um processo conveniente para medir campos de temperatura usando sensores de Bragg, e esta aplicação inovadora destes sensores foi validada usando outros processos mais usuais de medição de temperatura. Foram ainda comparados os campos de temperatura desenvolvidos em soldadura *Metal Inert Gas*, por *Friction Stir Welding* e por laser.

As tensões residuais são tensões existentes numa estrutura sobre a qual não actua nenhuma carga externa. Este tipo de tensões pode contribuir negativamente para falhas estruturais. As tensões residuais podem ser criadas por plasticidade mecanicamente induzida ou por efeitos térmicos resultantes do processo de fabrico, como por exemplo durante o processo de soldadura. O conhecimento do campo de tensões residuais existente é portanto muito importante para o correcto funcionamento de uma estrutura. Assim sendo, foi realizado um estudo comparativo de diferentes técnicas para medição do campo dessas tensões.

Nesta tese é apresentado um estudo, composto por três trabalhos complementares, sobre o comportamento mecânico de soldaduras laser e soldadura por *Friction Stir Welding*.
Devido a restrições de *design*, os componentes soldados por *Friction Stir Welding* podem incluir entalhes no próprio cordão, e até ao momento ainda não existe informação disponível sobre o comportamento de estruturas com estas particularidades. Assim, no primeiro trabalho é realizado um estudo sobre o

comportamento de estruturas contendo entalhes em cordões criados por *Friction Stir Welding*.
No segundo trabalho é apresentado um estudo sobre a caracterização experimental de juntas dissimilares, compostas pelos alumínios 6082-T6 e 6061-T6 soldados por *Friction Stir Welding*. Para caracterizar este tipo de juntas multimaterial foram realizados ensaios de dobragem, um tipo de ensaio ainda não documentado na literatura, neste contexto. O ensaio de dobragem foi modelado através de um modelo simplificado de elementos finitos, tendo em conta a variação das propriedades mecânicas do material nas diferentes zonas de um provete soldado.
Apesar do elevado interesse nas técnicas de soldadura laser e *Friction Stir Welding*, ainda existe a necessidade de mais informação sobre o comportamento à fadiga das respectivas juntas, nomeadamente através de ensaios S-N e de propagação de fendas. Assim, o terceiro trabalho é uma contribuição neste sentido, contrastando o comportamento à fadiga de juntas soldadas por um processo tradicional, soldadura por arco eléctrico com gás inerte, e juntas obtidas por soldadura laser e *Friction Stir Welding*.

Na indústria aeronáutica a fuselagem de um avião inclui, entre outros componentes, o painel externo e reforços longitudinais. Presentemente os reforços são ligados ao painel da fuselagem por meio de rebites. Estes reforços melhoram a resistência e estabilidade da estrutura e são um meio para desacelerar ou mesmo deter o crescimento de fendas. Os reforços rebitados podem permanecer intactos quando uma fenda se propaga no painel, e funcionam como um caminho alternativo para a distribuição de forças. No caso de uma estrutura integral, que pode ser obtida por exemplo por *Friction Stir Welding*, uma fenda irá propagar simultaneamente no painel e no reforço, causando a fractura do mesmo.
O estudo da tolerância ao dano pode ser efectuado usando conceitos de mecânica da fractura linear elástica, sendo o factor de intensidade de tensão um dos principais. A mecânica da fractura pode ser usada em conjunto com a lei de Paris ou outra lei de propagação para prever a vida à fadiga de fuselagens aeronáuticas. De modo a estudar a propagação de fendas e prever a vida residual à fadiga de painéis aeronáuticos reforçados é necessário realizar simulações numéricas complexas, e nesta tese é apresentado um estudo numérico tridimensional do factor de intensidade de tensão em painéis fissurados contendo reforços.
O projecto da DaToN, da União Europeia, tem como objectivo estudar e desenvolver ferramentas que permitam o conhecimento da tolerância ao dano de estruturas integrais que contenham reforços. As estruturas integrais estudadas neste projecto (painéis com dois reforços) foram produzidas através de três diferentes processos: maquinagem de alta velocidade, soldadura laser e *Friction Stir Welding*.
Foi realizado um programa de ensaios que inclui o estudo da velocidade de propagação de fendas em cada tipo de painel. Este estudo foi completado pela análise das diferentes superfícies de fractura usando microscopia electrónica de varrimento.

# Resumé

L'usage croissant de l'aluminium dans les industries des transports, comme par exemple dans l'aéronautique, a entrainé au développement de techniques de jonction structurale plus efficaces et applicables dans ce contexte d'utilisation. Ce travaille de thèse de doctorat, avec un accent prédominant expérimentale, vise contribuer à l'étude du comportement mécanique des joints produits avec des technologies de soudage émergentes, mais pas encore suffisamment établies dans le contexte aéronautique. Parmi celles-ci, le soudage par friction malaxage (en Anglais, *friction stir welding*) et le soudage laser (en Anglais, *laser beam welding*) sont l'objet du présent travail, que vise à

- étudier le comportement mécanique des joints soudés par ces procédés,
- contribuer à la connaissance relative à la tolérance au dommage mécanique (en Anglais: *damage tolerant behaviour*) de structures fabriquées avec ces techniques.

Vu que la génération de chaleur est un aspect fondamental de tous les procédés de soudage, une technique pour mesurer des champs de température a été développée. Un environnement particulièrement agressif a été choisi pour cette étude, qui a été conduite sur la soudure MIG. Une utilisation innovatrice des senseurs de fibre de Bragg a été développée et validée, utilisant des procédés classiques alternatifs, comme la thermographie et les thermocouples. Une étude comparative des champs de température générée par MIG, soudage par friction malaxage et soudage laser a aussi été conduite.

Les contraintes résiduelles sont des contraintes qui existent dans un solide en l'absence de chargement externe. Ce type de contraintes peut avoir des conséquences négatives sur l'intégrité structurale, particulièrement en ce qui concerne la résistance à la fatigue. Elles peuvent être le résultat soit d'effets thermiques, soit de déformations plastiques générées pendant des procédés de soudage. Alors, la connaissance des champs de contraintes résiduelles est importante, et des procédés pour les mesurer ont été étudiés en détail, avec le but de comparer leur performance.

Une étude du soudage par friction malaxage est présentée dans cette thèse. Trois aspects complémentaires ont été abordés:
Le problème des entailles qui existe dans les joints obtenus par friction malaxage, problème pas encore traité dans la littérature technique et scientifique, est étudié avec un programme d'essais de fatigue réalisés en control de force.
Le second aspect est la possibilité de réaliser des joints avec des matériaux différents. Des joints de ce type ont été réalisés et testés particulièrement avec des essais de flexion et modelées par la méthode des éléments finis, une application pas encore documentée dans la littérature.

Le troisième aspect est une comparaison systématique du comportement en fatigue des joints obtenus par friction malaxage, soudage laser et MIG. Le principal objectif de ce travail est le comportement du type SN, mais des essais de caractérisation de la propagation ont aussi été aussi réalisés, pour étudier l'influence des altérations des matériaux dus au soudage.

Dans l'industrie aéronautique, le fuselage d'un avion comprend, parmi d'autres composants, le panneau externe (peau, ou en Anglais *skin*) et des renforcements. Typiquement les renforcements sont liés à la peau par des rivets. Ces renforcements contribuent à la résistance de la structure, dans la mesure où ils ralentissent la propagation des fissures. Néanmoins, dans une structure monolithique, comme les structures produites par soudage, une fissure peut se propager dans la peau et peut aussi se propager dans le renforcement, conduisant ainsi à la rupture.

L'étude de *damage tolerance* est conduite avec des notions de la mécanique de la rupture, particulièrement la notion de facteur d'intensité de contrainte. Avec la loi de Paris ou d'autres lois de propagation, la mécanique de la rupture permet de modeler la vie en fatigue de structures, comme les panneaux renforcées en aéronautique. L'étude du comportement de ces structures impose des solutions 3D pour l'état de contrainte. Ainsi, les effets 3D dans la détermination du facteur d'intensité de contrainte ont été particulièrement étudiés, dans un cas simple (panneau avec une fissure centrale) et dans le cas d'un panneau renforcé.

Le projet de recherche DaToN, de l'Union Européenne, a comme objectif étudier et développer des outils qui permettent comprendre le comportement mécanique et de tolérance au dommage de structures réalisées avec les procédés de soudage para friction malaxage, soudage laser et usinage de haute vitesse (en Anglais, *high speed machining or cutting*). Un programme d'essais de panneaux renforcés et une analyse des surfaces de rupture par microscopie électronique de balayage sont présentés dans la partie finale de ce travail de thèse de doctorat.

# Acknowledgements

I want to express my sincere appreciation and gratitude to Paulo M S T de Castro, Professor of the Universidade do Porto and my supervisor, for his permanent assistance and patience.

In particular I would like to thank Artur Portela (University da Madeira, Portugal), Fernando M F de Oliveira and Miguel A V de Figueiredo (both of FEUP, Portugal), and Stefan D Pastrama (University Politehnica of Bucharest, Romania) for their guidance and valuable information during this research. Without their technical advice and support this work could not have been done. I want to thank the great help of Rui A M da Silva (FEUP, Portugal) in the experimental work.

I want to acknowledge my colleagues Valentin Ritcher-Trummer and Sérgio M O Tavares for their collaboration during this work.

The work presented in this thesis was financially supported by PhD scholarship FCT SFRH/BD/19281/2004 and FP6 project DaToN (contract AST3-CT-2004–516053 of the European Union). The research group where this work took place also benefited of FCT contract PTDC/EME-TME/66362/2006 starting July 2007.

Specimens for the experimental work were obtained in collaboration with EADS (Ottobrunn, Germany, and Suresnes, France), ISQ (Oeiras, Portugal), and AIMEN (Porriño, Spain). The specimens machining operations were performed with the fruitful cooperation of the staff of the mechanical workshop of DEMEGI, FEUP.

The present work benefited from the cooperation of many other individuals, in Portugal and abroad. Great or small, their contribution is acknowledged, and included, among others, access to experimental equipment, advice on adhesives, benchmarking of stiffened panels testing, coordination of DATON project, electrical discharge machining, fibre Bragg sensors, friction stir welding, FSW bi-material samples, FSW CT testing, FSW samples, FSW stiffened panel specimens, high speed machined stiffened panels, instrumentation, laser beam welding, LBW stiffened panel specimens, microstructures examination, preliminary thesis planning, scanning electron microscopy, machining of specimens and testing rigs, supply of Al alloy 6056, testing, X-ray diffraction studies.

Further to those already mentioned, other individuals contributed to this work, including participation in its initial design of A Morão Dias (University de

Coimbra, Portugal; presently Director-General for Higher Education, Ministry for Science, Technology and Higher Education, Lisbon). Among others, the following are acknowledged: Abílio M P de Jesus (UTAD, Vila Real, Portugal), Albino Calisto Dias (Oficinas do DEMEGI, FEUP, Porto, Portugal), Alfredo S Ribeiro (UTAD, Vila Real, Portugal), Altino Loureiro (FCTUC, Coimbra, Portugal), Daniela Silva (Universidade do Porto, CEMUP, Portugal), Delphine Allehaux (EADS Corporate Research Center, Suresnes, France), Emília Soares (DEMEGI, FEUP, Porto, Portugal), Frank Palm (EADS Corporate Research Center, Ottobrunn, Germany), J C Prata Pina (FCTUC, Coimbra, Portugal), Jean Christophe Ehrström (ALCAN, CRV, Voreppe, France), João Ribeiro (Instituto Politécnico de Bragança, Bragança, Portugal), Joaquin Vazquez (AIMEN, Porriño, Spain), José F Rocha Almeida (Oficinas do DEMEGI, FEUP, Porto, Portugal), José Luís Santos (INESC and FCUP, Porto, Portugal), José Marafona (DEMEGI, FEUP, Porto, Portugal), Lucas F M da Silva (DEMEGI, FEUP, Porto, Portugal), Luigi Lazzeri (Dipartimento di Ingegneria Aerospaziale, Università di Pisa, Italy), Luís A Ferreira (DEMEGI, FEUP, Porto, Portugal), Maria Teresa Restivo (DEMEGI, FEUP, Porto, Portugal), Orlando Frazão (INESC and FCUP, Porto, Portugal), Pedro Vilaça (IST, Lisbon, Portugal), Peter Horst (Technische Universität Braunschweig, Germany), Rui Louro (ISQ, Oeiras, Portugal), Rui Neto (INEGI and DEMEGI, FEUP, Porto, Portugal), Telmo Santos (IST, Lisbon, Portugal), Ventura Belinho (EDAETECH, Esposende, Portugal), Zdenek Horák (VKV HORÁK s.r.o, Brno, Czech Republic).

# Contents


Abstract i
Resumo iii
Resumé v
Acknowledgements vii
Contents ix
List of Figures xiii
List of Tables xxv
Nomenclature xxix
Acronyms xxxi
1. Introduction and state of the art 3
1.1 Stiffened panels 6
1.2 LBW and FSW: A literature review 7
1.2.1 Laser Beam Welding 8
1.2.2 Friction Stir Welding 27
2. Temperature field acquisition during a welding process 55
2.1 Development of a feasible technique using fibre Bragg sensors to acquire the temperature field during GMAW 55
2.1.1. Welding process 56
2.1.2 Thermocouples 57
2.1.3 Thermography 58
2.1.4 Temperature measurements, plate surface opposite to weldments 58
2.1.5 Fibre Bragg grating sensors 62
2.1.6 Temperature measurements in the plate welded surface 65
2.1.7 Temperature profile, direction perpendicular to the weld line 67
2.1.8 Concluding remarks 69
2.2 Temperature field in GMAW, LBW and FSW 70
2.2.1 MIG welding – temperature profiles 71
2.2.2 FSW welding – temperature profiles 80
2.2.3 LBW welding – temperature profiles 82
2.2.4 Results comparison and concluding remarks 84
2.3 Conclusions 85
3. Residual stress evaluation 89
3.1 Sectioning method 90
3.2 Hole drilling method 91
3.3 X-ray diffraction method 96
3.4 Results 97
3.4.1 Sectioning method 98
3.4.2 X-ray diffraction method 101
3.4.3 Hole drilling method 103
3.4.4 Results comparison 117
3.5 Contour method, results comparison 118

3.6 Conclusions 119
4. Studies on FS welded joints 123
4.1 Fatigue behaviour of notched specimens of FS welded AA6063-T6 123
4.1.1 Material and welding process 124
4.1.2 Friction stir weld visual analysis 126
4.1.3 Metallographic analysis 127
4.1.4 Hardness tests 129
4.1.5 Tensile tests 130
4.1.6 S-N fatigue data 133
4.1.7 Scanning electron microscopy analysis 134
4.1.8 Stress analysis of welded and un-welded specimens 137
4.1.9 Strain-life 141
4.1.10 Concluding remarks 149
4.2 Mechanical and metallurgical characterization of FS welded dissimilar joints of AA6061-T6 with AA6082-T6 150
4.2.1 Material and welding process 151
4.2.2 Tensile tests 151
4.2.3 Residual stresses 153
4.2.4 Microhardness measurements 155
4.2.5 Metallographic analysis 158
4.2.6 Bending tests 162
4.2.7 Concluding remarks 169
4.3 Fatigue behaviour of FS welds, LB welds and MIG welds of AA6061-T6 and AA6082-T6 170
4.3.1 Material and welding processes 171
4.3.2 Tensile tests 171
4.3.3 Microhardness profiles 177
4.3.4 S-N fatigue data 181
4.3.5 Fatigue crack propagation 187
4.3.6 Metallographic analysis 199
4.3.7 SEM analysis 207
4.3.8 Concluding remarks 218
4.4 Conclusions 219
5. Stress intensity factor calculation using 3D finite element models 223
5.1 Plate with a central crack 226
5.1.1 Case 1 - Plate with a central crack h/b=0,5, c/b=0,5 229
5.1.2 Case 2 - Plate with a central crack h/b=2, c/b=1/3 and t/c=1/5 239
5.1.3 Case 3 - Plate with a central crack h/b=0,875, c/b=0,5 243
5.1.4 Concluding remarks 259
5.2 Finite element analysis of a stiffened cracked plate 260
5.2.1 Mesh 261
5.2.2 SIF evaluation for the case of an unbroken stiffener 262
5.2.3 SIF evaluation for the case of a broken stiffener 269
5.2.4 Concluding remarks 274
5.3 Conclusions 275
6. Stiffened cracked panel (DaToN specimen) 279
6.1 Finite element analysis of DaToN specimen 280
6.1.1 Specimen geometry 281

6.1.2 Preliminary specimen geometry 300
6.1.3 Concluding remarks 307
6.2 DaToN stiffened panels fatigue life; experimental measurements 308
6.2.1 Base material tensile and crack growth tests 309
6.2.2 High Speed Machining AA6056 panels 313
6.2.3 Laser Beam Welded AA6056 2-stiffener panels 322
6.2.4 Friction Stir Welding AA6056 2-stiffener panels 353
6.2.5 Results discussion 367
6.2.6 Crack growth prediction 370
6.2.7 Concluding remarks 374
6.3 SEM analysis 376
6.3.1 HSM 6056-T6 R=0,5 specimen (HSM02) 377
6.3.2 HSM 6056-T6 R=0,1 specimen (HSM01) 384
6.3.3 LBW1 6056 PWHT-T6 R=0,1 specimen (LBW03) 387
6.3.4 LBW2 6056-T6 as-welded R=0,1 specimen (LBW07) 396
6.3.5 FSW 6056-T4 PWHT-T6 R=0,1 specimen (FSW09) 402
6.3.6 Concluding remarks 409
6.4 Conclusions 410
7. Conclusions and future work 415
7.1 Conclusions 415
7.2 Suggestions for future work 419
References 421
Appendix A - Temperature field in GMAW, LBW and FSW; measurement details 435
MIG welding – temperature profiles 435
Aluminium 6061-T6 435
FSW welding – temperature profiles 439
LBW welding – temperature profiles 441
Aluminium 6082-T6 441
Aluminium 6061-T6 443

# List of Figures


Figure 1 - Deep penetration effect in LBW, [29]. 9
Figure 2 - Principle of LBW, [34]. 10
Figure 3 - Hardness profile of the LBW joint, [51]. 19
Figure 4 - Plot of the distributed microhardness profile, [36]. 20
Figure 5 - LBW tensile strength, [34]. 21
Figure 6 - Fatigue strength of LBW butt joints on aluminium, [34]. 22
Figure 7 - Fatigue properties of LBW seams on aluminium, [34]. 22
Figure 8 - Nominal stress *vs.* nominal strain curves obtained from micro-flat tensile specimens taken from different zones of the weld joint, [51]. 24
Figure 9 - Load *vs.* deformation (CMOD) curves of compact tension specimen for BM, FZ and HAZ, [51]. 24
Figure 10 - Schematic diagram of the FSW process, [61] 28
Figure 11 - FSW tools examples, [26]. 32
Figure 12 - Schematic drawing of marker insert placement, [73]. 34
Figure 13 - Comparison of predicted (black squares) and experimentally (red and blue marker) observed flow pattern in FSW. The markers of advancing (blue) and retreating (red) side are displayed in the undeformed and deformed stage. [73] 35
Figure 14 - Distinct regions of the weld zone, [77]. 36
Figure 15 - FS welded AA2195, [79]. 37
Figure 16 - Hardness profiles: a- AA5083; b- AA6082. [78] 41
Figure 17 - Vickers hardness profiles across the stir zone in the FS welds of the ARB and starting materials, [89]. 42
Figure 18 - (a) Vickers hardness of AA6082, FSW, MIG-pulse and TIG welded. Advancing side to the left for FSW specimens. (b) Hardness below maximum level of AA6082 T6 FS welded with high, low, and extra low welding speed. [90] 43
Figure 19 - Residual stresses distribution along the weld of a FS welded 6013-T4 sheet determined with different measurement methods. Welding parameters: rotational speed $2500 min^{-1}$; welding speed $1000 mm\ s^{-1}$; shoulder diameter $15 mm$. [91] 44
Figure 20 - Crack front positions in the SCT samples, showing location with respect to the FSW macrostructure [99]. 49
Figure 21 - Robot for MIG welding. 56
Figure 22 - Rig setup for the MIG welds. 57
Figure 23 - Conditioning circuit for thermocouples. 58
Figure 24 - Points of temperature acquisition in the plate surface opposite to weldments. 59
Figure 25 - Thermographic temperature distribution in three welding moments. 60
Figure 26 - 3D temperature distributions at different welding times. 60
Figure 27 - Temperature time function measured with thermocouples, incorrect measurements. 61
Figure 28 – Temperature time function measured with thermocouples. 62
Figure 29 - Locations where FBG sensors were placed in the first study (from left, cases 1 to 4). 63
Figure 30 - Example of a fibre placed at $10 mm$ parallel to the weld line and a fibre placed as case 4 (Figure 29). 63

Figure 31 - Welding test using epoxy glue and aluminium sheet stripes to protect the FBG sensors. 64
Figure 32 - Sensors protected with aluminium sheet stripes after welding. 64
Figure 33 - Sensors protected with cyanoacrylate glue after welding. 65
Figure 34 - Welding test protecting FBG sensors with silicon based compound. 65
Figure 35 - Thermocouple of 0,08$mm$ diameter covered with a silicone based compound. 66
Figure 36 - Temperature measured at 15$mm$ in a perpendicular direction of the welding line using thermocouples and FBG sensors. 67
Figure 37 - Schematic representation of thermocouples and FBG sensors location. 67
Figure 38 - Measured temperature profiles with thermocouples and FBG sensors. 68
Figure 39 - Peak (maximum) temperatures acquired with thermocouples and FBG sensors. 69
Figure 40 - Thermocouples and thermographic temperature acquisition sites at the plate top surface. 71
Figure 41 - Thermocouple measurement sites at the plate back surface. 72
Figure 42 - Temperature distribution in the plate top surface. 73
Figure 43 - Temperature distribution in the plate top surface, results compilation. 73
Figure 44 - Temperature profiles in thermocouples placed parallel to the weld line. 74
Figure 45 - Temperature profiles in thermocouples placed perpendicular to the weld line. 75
Figure 46 - Temperature distribution in welding deposition 4, plate back side. 76
Figure 47 - Temperature profiles in thermocouples placed parallel to the weld line in the plate back surface. 77
Figure 48 - Temperature profiles in thermocouples placed perpendicular to the weld line in the plate back surface. 78
Figure 49 - Temperature distribution in the plate top and back surface 78
Figure 50 - Temperature distribution in the plate back surface. 79
Figure 51- Temperature distribution in the plate top surface. 79
Figure 52 - Temperature distribution in the plate top and back surface. 80
Figure 53 - Thermocouples temperature acquisition sites 80
Figure 54 - 1000$mm$ long instrumented plate. 81
Figure 55 - Temperature distribution in the plate top surface. 81
Figure 56 - Temperature distribution in line 3 and 5 of the top surface. 82
Figure 57 - LBW process instrumentation. 83
Figure 58 - Temperature distribution during welding of the AA6082-T6 plate. 83
Figure 59 - Temperature distribution in welding of the AA6061-T6 plate. 84
Figure 60 - Temperature profile for the MIG, FSW and LBW processes in a line containing thermocouples 6, 7 and 8. 85
Figure 61- Strain rosette arrangement for determining residual stresses, [127]. 92
Figure 62 - Percent strain versus normalized hole depth for uniform stress with depth, [126]. 94
Figure 63 - Comparisons of the results from four stress calculation methods [131]. 96
Figure 64 - Instrumented plate before the sectioning method. 98
Figure 65 - Sectioning method experimental setup. 98
Figure 66 - Sectioning method, band saw sectioning procedures. 99
Figure 67 - Plate after the cuts for the sectioning method. 99
Figure 68 - Sectioned surface after the second cut. 99
Figure 69 - Residual stresses measured in the second cut at 5$mm$ from the strain gages. 100
Figure 70 - Stresses obtained by the sectioning method. 101
Figure 71 - X-ray diffraction residual stress values in the full plate width. 102
Figure 72 - X-ray diffraction residual stress values near the weld bead using the full plate and two small specimens. 102
Figure 73 - X-ray diffraction residual stress values through the thickness. 103

Figure 74 - Milling machine used for the hole drilling process. 104
Figure 75 - Hole drilling procedure. 104
Figure 76 - Nearest hole to the weldment. 105
Figure 77 - X and Y stress for the integral method, 7,4$mm$ distance. 106
Figure 78 - X and Y stress for the integral method, 15$mm$ distance. 107
Figure 79 - X and Y stress for the integral method, 20$mm$ distance. 109
Figure 80 - X and Y stress for the integral method, 30$mm$ distance. 110
Figure 81 - X and Y stress for the integral method, 45$mm$ distance. 111
Figure 82 - X and Y stress for the integral method, 115$mm$ distance. 112
Figure 83 - X and Y stress for the power method, 150$mm$ distance. 113
Figure 84 - Residual stress profiles obtained with the hole drilling process. 114
Figure 85 - Hole drilling, residual stress profile for different depths. 115
Figure 86 - Schematic representation of the contour plots location. 115
Figure 87 - Residual stress field for depths lower than 0,4$mm$. 116
Figure 88 - Residual stress field for depths lower than 0,9$mm$. 116
Figure 89 - Residual stress values: sectioning method, X-ray diffraction and hole drilling method. 117
Figure 90 - Residual stress values measured with the contour method. 118
Figure 91 - Tensile and fatigue specimens. 124
Figure 92 - Identification of specimen orientation [139]. 125
Figure 93 - Notch surface finishing details. 125
Figure 94 - Specimens surface definition. 126
Figure 95 - Visual inspection of FSW joints, top and back surfaces. 126
Figure 96 - Side surface cut by guillotine. 127
Figure 97 - Scheme of microstructural analysis. 127
Figure 98 - Welded specimen microstructures, surface perpendicular to the top surface. 128
Figure 99 - Welded specimen microstructures, top surface. 129
Figure 100 - Microhardness profile. 130
Figure 101 - Complete test assembly. 131
Figure 102 - Tensile specimen after test (base material). 131
Figure 103 - Tensile tested FSW specimen. 132
Figure 104 - Tensile test results. TUW – un-welded specimens; TFW - welded specimens (reference x.6 strain corresponds to 6$mm$ gage length). 132
Figure 105 - Notched specimens fatigue life results. 134
Figure 106 - SEM analysis of a crack surface on a FS welded specimen. 135
Figure 107 - SEM analysis of an un-welded specimen. 136
Figure 108 - SEM analysis of crack surfaces, fatigue striations identification. 137
Figure 109 - Mesh detail. 138
Figure 110 - Detail of stress $\sigma_{22}$ distribution in the notched area. 139
Figure 111 - Stress distribution in the top surface of specimen mid plane close to the notch. Remote stresses of: 79,1$MPa$ (70% of reference $\sigma_{yield}$); 90,4$MPa$ (80% of reference $\sigma_{yield}$), 101,7$MPa$ (90% of reference $\sigma_{yield}$), 158,2$MPa$ (140% of reference $\sigma_{yield}$). 140
Figure 112 - Maximum strain values for specimen of base material. 141
Figure 113 - Maximum strain values for FS welded specimens using two different material behaviours. 141
Figure 114 - Total strain-life plot for AA6063-T6. 143
Figure 115 - Total strain life plot for welded specimens when c=-0,5. 145
Figure 116 - Strain life plot using the uniform materials method and the median method. 147
Figure 117 - Comparison of total strain life plots for welded specimens, JSMS equation (uniform materials method), and FS material equation. 148
Figure 118 - Comparison of total strain life plots for welded specimens, new parameters estimation. 149

Figure 119 - Tensile tests curves. 152
Figure 120 - Tensile tests of the TMAZ for welded material specimens (6*mm* gage). 153
Figure 121 - Strain gages near the weldment. 154
Figure 122 - Measured plate after being sectioned. 154
Figure 123 - Residual stress in a FS welded AA6082-T6 plate, advancing side. 155
Figure 124 - Microhardness profile of the FS welded specimens. 156
Figure 125 - Hardness profile thorough the joint thickness. 157
Figure 126 - Macrostructure of the dissimilar weld and each base material. 159
Figure 127 - Microstructure details of the dissimilar joint, TMAZ. 160
Figure 128 - Dissimilar joint base material microstructure. 160
Figure 129 - FS welded 6082-T6 joint microstructure. 161
Figure 130 - FS welded 6061-T6 joint microstructure. 162
Figure 131 - 4 point bending test assemblage. 163
Figure 132 - Schematic representation of the 4 point bending test. 163
Figure 133 - Force displacement in 4 point bending tests. 164
Figure 134 - Elastic behaviour of the welded specimens in the 4 point bending tests. 164
Figure 135 - AA6082-T6 base material and FS welded specimen configuration for different roller displacement. 165
Figure 136 - 3 point bending device test. 165
Figure 137 - Specimens after bending. 167
Figure 138 - Bending test results. 167
Figure 139 - Deformed specimen and rigid surfaces model 168
Figure 140 - Comparison between experimental results and FEM results. 169
Figure 141 - Tensile tests of MIG, LB and FS welded specimens. 172
Figure 142 - Fracture surface of an AA6082-T6 base material specimen. 173
Figure 143 - Fracture surface of a MIG welded specimen of AA6061-T6. 175
Figure 144 - Fracture surface of AA6082-T6 FS welded specimen. 175
Figure 145 - Fracture surface of AA6061-T6 FS welded specimen. 175
Figure 146 - AA6061-T6 LB weld fracture surface. 176
Figure 147 - Tensile tests of the TMAZ, FS welded specimens, and HAZ, MIG welded specimens (6*mm* gage). 177
Figure 148 - Microhardness profiles of the MIG welded 6061-T6 and 6082-T6 specimens. 178
Figure 149 - Microhardness profile of the FS welded specimens. 178
Figure 150 - Microhardness profile of the FS welded 6082-T6 and 6061-T6 (6062-T6: 6*mm* diameter pin, shoulder 15mm; 6061-T6: 4mm diameter pin, shoulder 10*mm*). 179
Figure 151 - Microhardness profile of the LB welded AA6061-T6. 180
Figure 152 - Microhardness profile of the LB, MIG and FS welded AA6061-T6. 181
Figure 153 - MIG welding specimens with the overfill milled. 182
Figure 154 - Fracture location of MIG specimens in the as-welded configuration. 182
Figure 155 - Fracture surface for the fatigue tested MIG specimens. 182
Figure 156 - Fractograph of a MIG welding specimen containing entrapped pores 183
Figure 157 - S-N fatigue data of the MIG welded specimens. 184
Figure 158 - Fracture location of FS welded specimens. 185
Figure 159 - Fracture surface for the fatigue tested FS welded specimens. 185
Figure 160 - S-N fatigue data of the FS welded specimens. 185
Figure 161 - AA6061-T6 LB welded specimen weld bead overfill. 186
Figure 162 - S-N fatigue data of the LB welded AA6061-T6 specimens. 186
Figure 163 - S-N data of base material and welded specimens. 187
Figure 164 - Specimen orientation tested. 188
Figure 165 - Fractured AA6082-T6 base material specimen. (for the sake of uniformity all CT specimens are represented with the crack on the right side) 188
Figure 166 - Fractured specimens, crack in the HAZ configuration. 188
Figure 167 - Fractured specimens, WM configuration. 189

Figure 168 - Fractured specimens, crack transverse to the weld line configuration. 189
Figure 169 - Fatigue crack propagation data for AA6082-T6 base material specimens. 190
Figure 170 - Fatigue crack propagation data for AA6082-T6 FS welded specimens. 191
Figure 171 - Fatigue crack propagation data for AA6061-T6 base material specimens. 192
Figure 172 - Base material, WM with notch orientated transverse to the weldment, AA6061-T6 specimens. 193
Figure 173 - FCP R=0,1 for both base materials in the longitudinal and transverse orientation. 194
Figure 174 - FCP R=0,1 for both stirred specimens of both base materials. Crack in the weldment at crack transverse to the weldment. 194
Figure 175 - Fractured CT specimens analyzed using SEM. 195
Figure 176 - Fracture surface of different CT specimens. 195
Figure 177 - Fracture surface details for different crack lengths. 196
Figure 178 - Fracture surface particular features. 196
Figure 179 - Fracture surface details near the initial notch. 197
Figure 180 - Fracture surface particular features. 197
Figure 181 - Fracture surface particular features in the striations created by the material flow. 198
Figure 182 - Fracture surface details near the initial notch. 198
Figure 183 - Fracture surface at the weld nugget. 199
Figure 184 - Sites for microstructural analysis of MIG and FS welds. 199
Figure 185 - Macrostructure of the MIG welded AA6082-T6. 200
Figure 186 - MIG welded AA6082-T6 microstructures. 200
Figure 187 - Macrostructure of the MIG welded AA6061-T6. 201
Figure 188 - MIG welded AA6061-T6 microstructures. 201
Figure 189 - Macrostructure of the FS welded AA6082-T6 containing defects. 202
Figure 190 - Welded nugget detail of the defected joint. 202
Figure 191 - FS welded AA6082-T6 containing defects 203
Figure 192 - Macrostructure of the FS welded AA6082-T6. 203
Figure 193 - Welded nugget detail of the FS welded AA6082-T6. 203
Figure 194 - FS welded AA6082-T6 microstructures. 204
Figure 195 - Macrostructure of the FS welded AA6061-T6. 205
Figure 196 - FS welded AA6061-T6. 205
Figure 197 - Macrostructure of the LBW welded AA6061-T6. 206
Figure 198 - LBW welded AA6061-T6 microstructures. 207
Figure 199 - Fatigue crack of base material specimens, striation measurements sites. 208
Figure 200 - Fatigue striations for different crack lengths. 209
Figure 201 - Fatigue striation spacing *vs.* crack length for specimen of AA6082-T6. 209
Figure 202 - Fatigue striation spacing *vs.* crack length for specimen of AA6061-T6. 210
Figure 203 - Fatigue crack of MIG welded specimens, striation measurements sites. 211
Figure 204 - Fatigue striations for two crack lengths, AA6082-T6 MIG welded specimen. 211
Figure 205 - SEM analysis of the AA6082-T6 MIG welded specimen. 212
Figure 206 - Fatigue striations for two crack lengths, AA6061-T6 MIG welded specimen. 212
Figure 207 - SEM analysis of the AA6061-T6 MIG welded specimen. 213
Figure 208 - Fatigue striation spacing *vs.* crack length AA6082-T6 MIG welded specimen. 213
Figure 209 - Fatigue striation spacing *vs.* crack length AA6061-T6 MIG welded specimen. 214
Figure 210 – Fractured surface of the MIG welded specimens. 214
Figure 211 - Fatigue crack of FS welded specimens, striation measurements sites. 216
Figure 212 - Fatigue crack initiation site, AA6082-T6 FS welded specimen. 216
Figure 213 - Fatigue crack structure and striations, AA6082-T6 FS welded specimen. 217

Figure 214 - Fatigue striations for two crack lengths, AA6061-T6 MIG welded specimen. 217
Figure 215 - Fatigue striation spacing *vs.* crack length AA6061- T6 FS welded specimen. 218
Figure 216 - Contour used for the determination of J integral. 224
Figure 217 - Tractions at a point. 225
Figure 218 - Stress $\sigma_p$ in a point p at a distance $\varepsilon$ of the crack tip. 226
Figure 219 - Average SIF for an element (crack front is line $\overline{AC}$). 227
Figure 220 - Plate with a central crack. 228
Figure 221 - 3D 19440 elements $\sigma_y$ mesh detail (1/4 of the plate is represented). 230
Figure 222 - Comparative plot of the % differences between Tada [191] and FEM as a function of the coordinate z/t for both meshes. 231
Figure 223 - Non-dimensional SIF along thickness. 232
Figure 224 - Comparative plot of the % differences between Tada [191] and FEM as a function of z/t for both meshes. 234
Figure 225 - Non-dimensional SIF along thickness. 235
Figure 226 - 3D 19440 elements $\sigma_y$ (S22) mesh detail (1/8 of the plate is represented). 236
Figure 227 - Comparative plot of the % differences between Tada [191] and FEM as a function of z/t for both meshes. 237
Figure 228 - Non-dimensional SIF along thickness. 237
Figure 229 - Non-dimensional SIF for each studied plate thickness. 238
Figure 230 - Difference between the 3D FEM SIF for each plate thickness and the 2D DBEM J integral result. 239
Figure 231 - Detail of a 2D mesh used in [192]. Because of symmetry, only ¼ of the plate was modelled. 240
Figure 232 - 3D mesh detail, von Mises stress for 120 units of remote stress. 241
Figure 233 - Non-dimensional SIF along thickness. 242
Figure 234 - Comparative plot of the % differences between Tada [191] and FEM as a function of the coordinate z/t for both meshes. 243
Figure 235 - Non-dimensional SIF along thickness. 245
Figure 236 - Comparative plot of the % differences between Tada [191] and FEM as a function of z/t for both meshes. 246
Figure 237 - Non-dimensional SIF along thickness. 248
Figure 238 - Comparative plot of the % differences between Tada [191] and FEM as a function of z/t for both meshes. 249
Figure 239 - Non-dimensional SIF along thickness. 250
Figure 240 - Comparative plot of the % differences between Tada [191] and FEM as a function of z/t for both meshes. 251
Figure 241 - Non-dimensional SIF along thickness. 252
Figure 242 - Non dimensional SIF for each studied plate thickness. 253
Figure 243 - Difference between 3D FEM results for each studied thickness and 2D DBEM J integral result. 254
Figure 244 - Degree of plane strain in the x direction. 256
Figure 245 - Degree of plane strain in the z direction for different x location. 257
Figure 246 - Stress distribution in the y direction near the crack front. 258
Figure 247 - Stress distribution in the z direction near the crack front. 259
Figure 248 - Cross section through the stiffened plate with a crack crossing a stiffener. 261
Figure 249 - Deformed mesh detail in the less refined mesh for 2c=195$mm$, case of an unbroken stiffener. 261
Figure 250 - SIF along the thickness for several crack lengths, crack tip A and crack tip B obtained with the 21356 elements mesh, unbroken stiffener. 263
Figure 251 - SIF along the thickness for several crack lengths, crack tip A and crack tip B obtained with the 57759 elements mesh, unbroken stiffener. 264
Figure 252 - Non-dimensional SIF for the crack crossing an unbroken stiffener, compound and 21356 elements mesh results. 265

Figure 253 - Mesh detail and element layer through thickness order. 266
Figure 254 - Results of SIFs for crack tip A for several crack lengths using the compounding technique and the FEM (results for each layer of elements), unbroken stiffener. 267
Figure 255 - Results of SIFs for crack tip B for several crack lengths using the compounding technique and the FEM (results for each layer of elements), unbroken stiffener. 268
Figure 256 - SIF along the thickness for several crack lengths for a broken stiffener, crack tip A and crack tip B obtained with the 129651 elements mesh. 270
Figure 257 - Results of SIFs for crack tip A for several crack lengths using the compounding technique and the FEM (results for each layer of elements), broken stiffener. 271
Figure 258 - Results of SIFs for crack tip B for several crack lengths using the compounding technique and the FEM (results for each layer of elements), broken stiffener. 272
Figure 259 - Stress $\sigma_y$ in the stiffener side (top layer) and in the opposite side (back layer) for c=32,5$mm$. 272
Figure 260 - Stress $\sigma_y$ and FEM mesh for the 2D analysis of plate with broken stiffener (c=32,5$mm$) 273
Figure 261 - Specimen geometry of specimens to be used in the experimental component of the DaToN project, [195]. 280
Figure 262 - Schematic representation of the specimen middle plane cross section identifying the centre of gravity (section A-A of Figure 261). 280
Figure 263 - Finite element mesh used in the global stress analysis: a) mesh of half specimen; b) end of the stiffener, mesh detail. 281
Figure 264 - Stress distribution on the stiffened plate, stress in the load direction. 282
Figure 265 - Deformed model (deformation scale factor of 20) and stress distribution on the stiffened plate, stress in the load direction. 282
Figure 266 - Detail of specimen middle cross section. 283
Figure 267 - Stress distribution along the nodes that lay on the arrow shown in Figure 266. 283
Figure 268 - Specimen middle cross section. 284
Figure 269 - $\sigma_y$ distribution in the specimen middle cross section in the front and back layer nodes. 285
Figure 270 - Displacement x in the specimen middle cross section in the front and back layer nodes 285
Figure 271 - $\sigma_y$ distribution along the specimen longitudinal direction. 286
Figure 272 - $\sigma_y$ distribution through the specimen longitudinal direction in three lines: a) stiffener top surface; b) plate's lateral layer; c) plate's centre layer. 286
Figure 273 - Displacement in the x direction through the specimen longitudinal direction in three lines: a) stiffener top surface; b) plate's lateral layer; c) plate's centre layer. 287
Figure 274 - Stress concentration factor at the end of the stiffener. 288
Figure 275 - Identification of zones with compressive stresses 288
Figure 276 - Stress $\sigma_y$ distribution and deformed model of a stiffened panel with a crack (deformation scale factor of 20), stress in the load direction. 289
Figure 277 - Detail of specimen middle cross section, stiffened panel with a crack. 289
Figure 278 - Stress distribution along the nodes that lay on the arrow a) presented in Figure 277. Stiffened panel with a crack. 290
Figure 279 - $\sigma_y$ distribution in the specimen middle cross section in the front and back layer nodes. 291
Figure 280 - Displacement x in the specimen middle cross section, with and without a crack, in the front layer nodes. 291

Figure 281 - $\sigma_y$ distribution through the specimen longitudinal direction in stiffener top surface a), lateral surface b) and centre layer c), as presented in Figure 271. Stiffened panel with and without a crack. 292
Figure 282 - Displacement in the x direction through the specimen principal dimension in three lines: a) stiffener top surface; b) plate's lateral layer; c) plate's centre layer. Stiffened panel with and without a crack. 293
Figure 283 - Stress $\sigma_y$ distribution and deformed model (deformation scale factor of 20). Model with a crack and an anti-bending device. 294
Figure 284 - Detail of specimen middle cross section. Model with a crack and an anti-bending device. 294
Figure 285 - Stress distribution along the nodes that lay on the arrow a) presented in Figure 284. 295
Figure 286 - $\sigma_y$ distribution in the specimen middle cross section in the front and back layer nodes. Stiffened cracked panel, with and without an anti-bending device. 296
Figure 287 - Displacement x in the specimen middle cross section, with and without a crack, in the front layer nodes. 296
Figure 288 - $\sigma_y$ distribution along the specimen longitudinal direction. Data for lines b) and c) corresponds to the plate front side. Model with a crack and an anti-bending device. 297
Figure 289 - $\sigma_y$ distribution through the specimen longitudinal direction in three lines: a) stiffener top surface; b) plate's lateral layer; c) plate's centre layer. 298
Figure 290 - Displacement in the x direction through the specimen longitudinal direction in three lines: a) stiffener top surface; b) plate's lateral layer; c) plate's centre layer. Stiffened panel with a crack and an anti-bending device. 299
Figure 291 - Stress concentration factor at the end of the stiffener in the presence of an anti-bending device. 299
Figure 292 - Identification of zones with compressive stresses 300
Figure 293 - Preliminary specimen geometry of specimens proposed for use in the experimental component of the DaToN project [195]. 300
Figure 294 - Stress distribution on the stiffened plate preliminary geometry (deformation scale factor of 20), stress in the load direction. 301
Figure 295 - Detail of preliminary geometry specimen middle cross section, $\sigma_y$ stress distribution. 301
Figure 296 - Stress distribution along the nodes that lay on the arrow presented in Figure 295. 302
Figure 297 - $\sigma_y$ distribution in the specimen middle cross section in the front and back layer nodes. 303
Figure 298 - Displacement x in the specimen middle cross section in the front and back layer nodes. 304
Figure 299 - $\sigma_y$ distribution along the specimen longitudinal direction. Data for lines b) and c) was obtained in the front side. 304
Figure 300 - $\sigma_y$ distribution through the preliminary and current specimen geometry principal dimension in three lines: a) stiffener top surface; b) plate's lateral layer; c) plate's centre layer. 305
Figure 301 - Displacement in the x direction through the preliminary and current specimen geometry longitudinal direction along three lines: a) stiffener top surface; b) plate's lateral layer; c) plate's centre layer. 306
Figure 302 - Stress concentration factor at the end of the stiffener. 307
Figure 303 - Identification of zones with compressive stresses in the preliminary specimen geometry. 307
Figure 304 - Fatigue crack measurement scheme. 309
Figure 305 - Tensile test specimen geometry. 309
Figure 306 - Stress/strain plot of base material tensile tests. 310

Figure 307 - Fracture surface of CT specimens. 311
Figure 308 - Compact tension (CT) specimen (dimensions in *mm*). 311
Figure 309 - Crack propagation data obtained with CT specimens from the HSM AA6056-T651 and from the LBW AA6056-T6 panels. 312
Figure 310 - DaToN panel strain gages location (front gages in brackets, see Figure 304). 314
Figure 311 - Stress distribution for different applied remote stress, specimen HSM01. 315
Figure 312 - Stress distribution for different applied remote stress, specimen HSM02. 315
Figure 313 - Stress distribution during the fatigue crack growth test, HSM01. 316
Figure 314 - Stress distribution during the fatigue crack growth test, HSM02. 317
Figure 315 - Fatigue crack growth test, specimen HSM01. 318
Figure 316 - Fatigue crack growth test, specimen HSM02. 319
Figure 317 - Test setup. 320
Figure 318 - Crack propagating in specimen HSM01. 320
Figure 319 - Cracks at the stiffeners (113700 cycles), specimen HSM01. 321
Figure 320 - Crack in the stiffeners, specimen HSM02. 321
Figure 321 - Fatigue crack surface for HSM01. 322
Figure 322 - Welding configurations for the LBW specimens. 322
Figure 323 - Stress distribution for different remote stress, specimen LBW03. 323
Figure 324 - Stress distribution for different remote stress, specimen LBW04. 324
Figure 325 - Stress distribution for different remote stress, specimen LBW05. 325
Figure 326 - Stress distribution for different remote stress, specimen LBW06. 326
Figure 327 - Stress distribution for different remote stress, specimen LBW07. 327
Figure 328 - Stress distribution for different remote stress, specimen LBW08. 328
Figure 329 - Comparison of static loading of HSM and LBW specimens. 329
Figure 330 - Details of beginning and end site of weldments. 330
Figure 331 - Visual detail of a polished stiffener end. 330
Figure 332 - Secondary crack at 17500 cycles. 331
Figure 333 - Patches used to control the fatigue crack growth of secondary cracks. 331
Figure 334 - Secondary cracks in all stiffeners ends at 100000 cycles. 332
Figure 335 - Down side cracks function of the number of cycles. 333
Figure 336 - Up side cracks function of the number of cycles. 333
Figure 337 - Riveting procedure in the down left side crack. 333
Figure 338 - Stress distribution during the fatigue crack growth test, LBW1 6056 PWHT-T6 $\sigma_{max}$=80*MPa* R=0,1. 334
Figure 339 - Fatigue crack growth test, LBW1 6056 PWHT-T6 $\sigma_{max}$=80*MPa* R=0,1. 335
Figure 340 - Stress distribution during the fatigue crack growth test, LBW1 6056 PWHT-T6 $\sigma_{max}$=110*MPa* R=0,5. 336
Figure 341 - Fatigue crack growth test, LBW1 6056 PWHT-T6 $\sigma_{max}$=110*MPa* R=0,5. 337
Figure 342 - Stiffener ends smoothing procedures. 338
Figure 343 - Patch comprehending both stiffeners. 338
Figure 344 - Riveting process of the LBW2 6056 PWHT-T6 $\sigma_{max}$=80*MPa* R=0,1 at 105000 cycles. 339
Figure 345 - Longitudinal crack. 339
Figure 346 - Stress distribution during the fatigue crack growth test, LBW2 6056 PWHT-T6 $\sigma_{max}$=80*MPa* R=0,1. 340
Figure 347 - Fatigue crack growth test, LBW2 6056 PWHT-T6 $\sigma_{max}$=80*MPa* R=0,1. 341
Figure 348 - Comparison of a-N LBW1 6056 PWHT-T6 *vs.* LBW2 6056 PWHT-T6, R=0,1. 342
Figure 349 - Stress distribution during the fatigue crack growth test, LBW2 6056 PWHT-T6 $\sigma_{max}$=110*MPa* R=0,5. 343
Figure 350 - Fatigue crack growth test, LBW2 6056 PWHT-T6 $\sigma_{max}$=110*MPa* R=0,5. 344
Figure 351 - Stiffener smoothing procedures. 345
Figure 352 - Stiffener after hand polishing. 345
Figure 353 - Fatigue cracked specimen. 346

Figure 354 - Detail of an adhesive patch. 346
Figure 355 - Fatigue crack just outside the stiffeners. 347
Figure 356 - Fatigue crack propagating at the stiffener. 347
Figure 357 - Fatigue crack crossing the strain gage opposite to the stiffener. 347
Figure 358 - Stress distribution during the fatigue crack growth test, LBW2 6056 as-welded $\sigma_{max}$=80*MPa* R=0,1. 348
Figure 359 - Fatigue crack growth test, LBW2 6056-T6 as-welded $\sigma_{max}$=80*MPa* R=0,1. 349
Figure 360 - Comparison of a-N LBW1 6056 PWHT-T6/LBW2 6056 PWHT-T6/LBW2 6056-T6 as-welded, R=0,1. 350
Figure 361 - Smoothed stiffener. 351
Figure 362 - Fatigue crack just outside the stiffeners. 351
Figure 363 - Stress distribution during the fatigue crack growth test, LBW2 6056 as-welded $\sigma_{max}$=110*MPa* R=0,5. 352
Figure 364 - Fatigue crack growth test, LBW2 6056-T6 as-welded $\sigma_{max}$=110*MPa* R=0,5. 353
Figure 365 - FSW panels geometry and correspondent clamping extensions. 354
Figure 366 - Distortion detail of the HSM, LBW and FSW panels. 354
Figure 367 - Testing machine FSW panel assemblage. 355
Figure 368 - Details of specimen and extension assemblage. 355
Figure 369 - Detail of specimen FSW09 instrumentation. 356
Figure 370 - Stress distribution for different remote stress, specimen FSW09. 357
Figure 371 - Stress distribution for different remote stress, specimen FSW10. 358
Figure 372 - Comparison of static loading of HSM, LBW and FSW specimens. 359
Figure 373 - Fatigue FSW specimen detail. 360
Figure 374 - Fatigue crack, specimen front surface at approximately 135000 cycles. 360
Figure 375 - Crack growing in a FSW specimen. 361
Figure 376 - Cracked specimen back surface. 361
Figure 377 - FSW T-joint crack surface detail. 362
Figure 378 - Stress distribution during the fatigue crack growth test, FSW 6056 PWHT-T6 $\sigma_{max}$=80*MPa* R=0,1. 362
Figure 379 - Fatigue crack growth test, FSW 6056 PWHT-T6 $\sigma_{max}$=80*MPa* R=0,1. 363
Figure 380 - FSW10 specimen. 364
Figure 381 - Grip system details. 364
Figure 382 - Crack reaching the TMAZ. 364
Figure 383 - Fatigue crack crossing a stiffener, different stages. 365
Figure 384 - Fatigue crack details, central notch and root of broken stiffener. 365
Figure 385 - Stress distribution during the fatigue crack growth test, FSW10 6056 PWHT-T6 $\sigma_{max}$=110*MPa* R=0,5. 366
Figure 386 - Fatigue crack growth test, FSW 6056 PWHT-T6 as-welded $\sigma_{max}$=110*MPa* R=0,5. 367
Figure 387 - Residual stress profile in the surface opposite to the stiffeners for a LBW2 PWHT-T6 specimen (stiffeners located at 150*mm* and 300*mm*). 368
Figure 388 - Comparison of a-N for all specimens tested at R=0,1. 369
Figure 389 - Comparison of a-N for all specimens tested at R=0,5. 369
Figure 390 - Stress intensity factor calibration for the DaToN panels' geometry. 370
Figure 391 - Comparison between predicted and experimental fatigue life for HSM panels. 371
Figure 392 - Unstiffened and stiffened panel areas for fatigue life comparison. 372
Figure 393 - Crack growth for panels with and without stiffeners. 373
Figure 394 - Comparison between the predicted and the experimental fatigue life of a LBW1 PWHT-T6 panel. 374
Figure 395 - Macrographs of welded specimens. 377
Figure 396 - Sample location for SEM analysis of the HSM 6056 PWHT-T6 R=0,5 specimen. 377
Figure 397 - Initial site of the fatigue crack. 378
Figure 398 - Fissure in sample A. 378

Figure 399 - Sample B fractograph showing Manganese particles as light particles (back scatted electron detector). 379
Figure 400 - Sample C, features before reaching the stiffener. 379
Figure 401 - Sample C features near the stiffener. 380
Figure 402 - Features observed after the stiffener. 380
Figure 403 - Crack surface along the stiffener (load direction) 381
Figure 404 - Sample D fractographs. 381
Figure 405 - Fractographs showing striations in sample C. 382
Figure 406 - Fractograph showing the stiffener root. 382
Figure 407 - Fractographs showing striations before the stiffener. 383
Figure 408 - Fractographs showing striations in and after the stiffener. 383
Figure 409 - Fatigue striation spacing along the base plate. 384
Figure 410 - Fatigue striation spacing along the stiffener. 384
Figure 411 - Sample location for SEM analysis of the HSM 6056 PWHT-T6 R=0,1 specimen. 385
Figure 412 - Fissure in sample A. 385
Figure 413 - Features observed after the stiffener. 386
Figure 414 - Fatigue striation spacing along the base plate. 387
Figure 415 - Fatigue striation spacing along the stiffener. 387
Figure 416 - Sample location for SEM analysis of the LBW1 6056 PWHT-T6 R=0,1 specimen. 388
Figure 417 - Initial site of the fatigue crack. 388
Figure 418 - Pores disperse along the fatigue crack. 389
Figure 419 - Sample B fractograph showing different striations sets and some pores. 389
Figure 420 - T-joint LBW1 PWHT-T6 R=0,1. 390
Figure 421 - Cracks just outside the weld bead. 390
Figure 422 - Striations at both sides of the weld line (weld bead and parent material). 391
Figure 423 - Stiffener root analysis. 392
Figure 424 - Sample D ductile fracture surface. 392
Figure 425 - Pores identification. 392
Figure 426 - Sample D fracture surface particular features. 393
Figure 427 - Fractographs showing striations in sample C. 393
Figure 428 - Fractographs sites near the stiffener root. 394
Figure 429 - Fractographs showing striations in different positions around the stiffener. 395
Figure 430 - Fatigue striation spacing in the stiffener. 395
Figure 431 - Fatigue striation spacing in the specimen base plate. 396
Figure 432 - Sample location for SEM analysis of the LBW2 6056-T6 as-welded R=0,1 specimen. 396
Figure 433 - Initial site of the fatigue crack. 397
Figure 434 - Pores disperse along the fatigue crack. 397
Figure 435 - Sample B, fatigue crack surface. 397
Figure 436 - T-joint LBW2-T6 as-welded R=0,1. 398
Figure 437 - Details of the stiffened area. 398
Figure 438 - Weld bead limit near the specimen plate. 399
Figure 439 - Weld bead limit located at the stiffener. 400
Figure 440 - Sample E fracture surface, fractograph 12. 400
Figure 441 - Fractographs showing striations in samples A and B. 401
Figure 442 - Fractographs showing striations in different positions around the stiffener. 401
Figure 443 - Fatigue striation spacing along the stiffener. 402
Figure 444 - Fatigue striation spacing along the specimen base plate. 402
Figure 445 - Sample location for SEM analysis of the FSW 6056 PWHT-T6 R=0,1 specimen. 403
Figure 446 - Initial site of the fatigue crack, sample A. 403

Figure 447 - T-joint FSW 6056 PWHT-T6 R=0,1. 404
Figure 448 - Details of the stiffened area, TMAZ. 404
Figure 449 - Fracture surface outside the TMAZ, fractograph 34. 405
Figure 450 - Stiffener surface, fractograph 35. 405
Figure 451 - Stiffener surface detail, fractograph 40. 406
Figure 452 - Fractographs showing striations in sample A. 406
Figure 453 - Fractographs showing striations on the skin before (fractograph 2) and after (fractograph 27) the stiffener. 407
Figure 454 - Fractograph showing striations in the weld affected area, x=75,74 y=0,65, s=2,11μm. 407
Figure 455 - Fractographs showing striations before (fractograph 38) and after (fractograph 43) the weld affected zone in the stiffener. 408
Figure 456 - Fatigue striation spacing along the stiffener. 408
Figure 457 - Fatigue striation spacing along the specimen base plate. 409
Figure 458 - Temperature distribution the plate back surface. 435
Figure 459 - Temperature profiles in thermocouples placed parallel to the weld line. 436
Figure 460 - Temperature profiles in thermocouples placed perpendicular to the weld line. 437
Figure 461 - Temperature profiles in thermocouples placed parallel to the weld line in the top surface. 438
Figure 462 - Temperature profiles in thermocouples placed perpendicular to the weld line in the plate top surface. 439
Figure 463 - Temperature distribution in welding deposition 1. 439
Figure 464 - Temperature profiles in thermocouples placed parallel to the weld line. 440
Figure 465 - Temperature profiles in thermocouples placed perpendicular to the weld line. 441
Figure 466 - Temperature profiles in thermocouples placed parallel to the weld line. 442
Figure 467 - Temperature profiles in thermocouples placed perpendicular to the weld line. 443
Figure 468 - Temperature profiles in thermocouples placed parallel to the weld line. 444
Figure 469 - Temperature profiles in thermocouples placed perpendicular to the weld line. 445

# List of Tables


Table 1 - Measured temperatures 62
Table 2 - Rosettes characteristics [$mm$] 104
Table 3 - Power method and integral method results, 7,4$mm$ distance 106
Table 4 - Power method and integral method results, 15$mm$ distance 107
Table 5 - Power method and integral method results, 20$mm$ distance 108
Table 6 - Power method and integral method results, 30$mm$ distance 109
Table 7 - Power method and integral method results, 45$mm$ distance 111
Table 8 - Power method and integral method results, 115$mm$ distance 112
Table 9 - Power method and integral method results, 150$mm$ distance 113
Table 10 - Chemical composition AA6063-T6 125
Table 11 - Material properties AA6063-T6 126
Table 12 - Etchant used in the microscopic examination 127
Table 13 - Grain size in microstructure WM3 128
Table 14 - Material properties, data acquired in tensile tests (average values) 132
Table 15 - Fatigue tests parameters 133
Table 16 - Average results of fatigue life for un-welded specimens 133
Table 17 - Average results of fatigue life for FS welded specimens 133
Table 18 - Strain-life fatigue properties 143
Table 19 - Total strain for each stress level 143
Table 20 - Engineering/true stress [$MPa$]/strain properties from tensile tests where a 25$mm$ region was measured 144
Table 21 - Engineering/true stress [$MPa$]/strain properties from tensile tests where a 6$mm$ region was measured 144
Table 22 - Strain-life fatigue properties for the welded material 144
Table 23 - $\sigma_b$ converted from hardness results 146
Table 24 - Chemical composition of the AA6061-T6 and AA6082-T6 151
Table 25 - Data acquired in tensile tests 151
Table 26 - Material properties for FS welded TMAZ [6$mm$ gage] 153
Table 27 - Maximum mid plane displacements until plastic behaviour 164
Table 28 - Maximum force values for each bending test 166
Table 29 - Material properties for base materials, data from materials suppliers 173
Table 30 - Material properties for base material 6082-T6 and 6061-T6, tensile tests 173
Table 31 - Material properties for MIG welded specimens, tensile tests 174
Table 32 - Material properties for FS welded specimens, tensile tests 174
Table 33 - Material properties for LB welded specimens, tensile tests 174
Table 34 - Material properties for FS welded TMAZ and MIG welded HAZ 176
Table 35 - Chemical composition of the of the MIG welded 6082-T6 [%] 215
Table 36 - Chemical composition of the of the MIG welded 6061-T6 [%] 215
Table 37 - The studied geometries of the plate 228
Table 38 - 2D results, FEM and DBEM 229
Table 39 - Geometry, [units of length] 230
Table 40 - Non-dimensional 3D FEM SIF along the thickness, 19440 elements mesh 230
Table 41 - Non-dimensional 3D FEM SIF along the thickness, 67200 elements mesh 231
Table 42 - 3D FEM $K\Big/\left(\sigma\sqrt{\pi c}\right)$, 19440 elements mesh 232
Table 43 - Geometry, [units of length] 233
Table 44 - Non-dimensional 3D FEM SIF along thickness, 19440 elements mesh 233

Table 45 - Non-dimensional 3D FEM SIF along thickness, 67200 elements mesh 233
Table 46 - 3D FEM $K/\left(\sigma\sqrt{\pi c}\right)$, 19440 elements mesh 235
Table 47 - Geometry, [units of length] 235
Table 48 - Non-dimensional 3D FEM SIF along thickness, 19440 elements mesh 236
Table 49 - Non-dimensional 3D FEM SIF along thickness, 67200 elements mesh 236
Table 50 - 3D FEM $K/\left(\sigma\sqrt{\pi c}\right)$, 19440 elements mesh 238
Table 51- Geometry, [units of length] 239
Table 52 - Non-dimensional SIF obtained in the 2D analysis [192] 240
Table 53 - Non-dimensional 3D FEM SIF along thickness, 2700 elements mesh 241
Table 54 - Non-dimensional 3D FEM SIF along thickness, 36480 elements mesh 241
Table 55 - 2D results, FEM and DBEM 242
Table 56 - 3D FEM $K/\left(\sigma\sqrt{\pi c}\right)$, 2700 elements mesh 242
Table 57 - 3D FEM $K/\left(\sigma\sqrt{\pi c}\right)$, 36480 elements mesh 243
Table 58 - 2D results, FEM and DBEM 244
Table 59 - Geometry, [units of length] 244
Table 60 - Non-dimensional 3D FEM SIF along thickness 245
Table 61 - 3D FEM $K/\left(\sigma\sqrt{\pi c}\right)$, 51072 elements mesh 246
Table 62 - Geometry, [units of length] 247
Table 63 - Non-dimensional 3D FEM SIF along thickness 247
Table 64 - 3D FEM $K/\left(\sigma\sqrt{\pi c}\right)$, 51072 elements mesh 248
Table 65 - Geometry, [units of length] 249
Table 66 - Non-dimensional 3D FEM SIF along thickness 250
Table 67 - 3D FEM $K/\left(\sigma\sqrt{\pi c}\right)$, 51072 elements mesh 251
Table 68 - Geometry, [units of length] 252
Table 69 - Non-dimensional 3D FEM SIF along thickness (67200 elements mesh) 252
Table 70 - Difference [%] between the estimated $K_{3D}$ and the FEM calculated $K_{3D}$ at the plate mid thickness 255
Table 71 - Size of the plane strain zone 257
Table 72 - Unbroken stiffener, non-dimensional SIF compounding results [194] 262
Table 73 - Average $K/\sigma\sqrt{\pi c}$ for crack tip A and crack tip B, unbroken stiffener 265
Table 74 - Average $K/\sigma\sqrt{\pi c}$ for crack tip A, unbroken stiffener 266
Table 75 - Average $K/\sigma\sqrt{\pi c}$ for crack tip B, unbroken stiffener 267
Table 76 - Difference between SIFs of FEM of elements layer 7 and the compounding results, unbroken stiffener 268
Table 77- Broken stiffener, non-dimensional SIF compounding results [194] 269
Table 78 - Average $K/\sigma\sqrt{\pi c}$ for crack tip A, broken stiffener 270
Table 79 - Average $K/\sigma\sqrt{\pi c}$ for crack tip B, broken stiffener 271
Table 80 - Difference between FEM SIFs of elements layer 4 and the compounding results, broken stiffener 273
Table 81 - Comparison between 3D and 2D FEM results, case of broken stiffener 274
Table 82 - Tensile test results of DaToN specimens base material 310
Table 83 - C and m Paris law parameters for the AA6056 material from the HSM and LBW panels 312
Table 84 - Strain gages measurements function of the remote stress applied [*MPa*] 314

Table 85 - Strain gages measurements function of the remote stress applied, specimen LBW03 [*MPa*] 323
Table 86 - Strain gages measurements function of the remote stress applied, specimen LBW04 [*MPa*] 324
Table 87 - Strain gages measurements function of the remote stress applied, specimen LBW05 [*MPa*] 325
Table 88 - Strain gages measurements function of the remote stress applied, specimen LBW06 [*MPa*] 325
Table 89 - Strain gages measurements function of the remote stress applied, specimen LBW07 [*MPa*] 326
Table 90 - Strain gages measurements function of the remote stress applied, specimen LBW08 [*MPa*] 327
Table 91 - Strain gages measurements function of the remote stress applied, specimen FSW09 6056 PWHT-T6 [*MPa*] 356
Table 92 - Strain gages measurements function of the remote stress applied, specimen FSW10 6056-T6 [*MPa*] 357
Table 93 - C and m Paris law parameters for the AA6056 material from the HSM panels 371

# Nomenclature

| | |
|---|---|
| A | Final section after rupture |
| $A_0$ | Initial section |
| *b* | Fatigue strength exponent or Basquin exponent |
| *c* | Fatigue ductility exponent |
| E | Young modulus or modulus of elasticity |
| f | Frequency |
| G | Energy release rate |
| K, $K_I$, $K_{II}$, $K_{III}$ | Stress intensity factor |
| $K_{max}$, $K_{min}$ | Maximum and minimum stress intensity factors |
| $N_f$ | Number of cycles to failure |
| X stress | Stress in the longitudinal direction |
| Y stress | Stress in the transversal direction |
| $\Delta K$ | Stress intensity factor range |
| $\Delta K_{th}$ | Stress intensity factor threshold |
| $\varepsilon'_f$ | Fatigue ductility coefficient |
| $\varepsilon_e$ | Elastic strain |
| $\varepsilon_p$ | Plastic strain amplitude |
| $\nu$ | Poisson's ratio |
| $\mu_s$ | Standard deviation |
| $\sigma$ | Stress |
| $\sigma'_f$ | Fatigue strength coefficient |
| $\sigma_{22}$ | Stress in the yy direction |
| $\sigma_a$ | Stress amplitude |
| $\sigma_b$ | Tensile strength |
| $\sigma_m$ | Mean stress |
| $\sigma_{max}$ | Maximum remote stress |
| $\sigma_{max}$ | Maximum remote stress |
| $\sigma_{rupt}$ | Rupture stress |
| $\sigma_s$ | Average value |
| $\sigma_y$ | Stress in the yy direction |
| $\sigma_{yield}$ | Yield stress |

# Acronyms

| | |
|---|---|
| 2D | Two-dimensional |
| 3D | Three-dimensional |
| AA | Aluminium alloy |
| AE | Acoustic Emission |
| AIMEN | Asociación de Investigación Metalúrgica del Noroeste |
| ASME | American Society of Mechanical Engineers |
| ASTM | American Society for Testing and Materials |
| ARB | Accumulative Roll-Bonding |
| BM | Base material |
| BoP | Bead-on-plate |
| CCP | Continuous cooling precipitation |
| CDRX | Continuous dynamic recrystallization |
| CMM | Coordinate measuring machine |
| CNC | Computerized Numerical Control |
| COD | Crack opening displacement |
| CT | Compact tension |
| cw | Continuous wave |
| DBEM | Dual Boundary Element Method |
| DEMEGI | Departamento de Engenharia Mecânica e Gestão Industrial |
| DXZ | Dynamically Recrystallized Zone |
| EADS | European Aeronautic Defence and Space Company |
| EDM | electro discharge machining |
| EDS | Energy Dispersive Spectrometer |
| F | Force |
| FBG | Fibre Bragg Grating |
| FCP | Fatigue crack propagation |
| FCT | Fundação para a Ciência e a Tecnologia |
| FE | Finite Element |
| FEM | Finite Element Method |
| FP6 | 6th Framework Programme for Research of the European Union |
| FS | Friction stir |
| FSW | Friction stir welding |

| | |
|---|---|
| FEUP | Faculdade de Engenharia da Universidade do Porto |
| FZ | Fusion Zone |
| GMAW | Gas metal arc welding |
| GTA | Gas Tungsten Arc |
| HAZ | Heat affected zone |
| HSLA | High-strength low alloy |
| HSM | High speed Machining |
| ISQ | Instituto de Soldadura e Qualidade |
| JSMS | Japanese Society of Materials Science |
| LB | Laser Beam |
| LBW | Laser beam welding |
| LEFM | Linear Elastic Fracture Mechanics |
| LPB | Low Plasticity Burnishing |
| MIG | Metal inert gas |
| NC | Numerical Control |
| NDT | Non-destructive testing |
| NZ | Nugget zone |
| ORNL | Oak Ridge National Laboratory |
| pw | Pulsed wave |
| PWHT | Post welded heat treated |
| qnp | Quarter node point |
| SCT | Surface Crack Tension |
| SEM | Scanning Electron Microscopy, or Society for Experimental Mechanics |
| SIF | Stress intensity factor |
| S-N | Stress-life (in fatigue tests) |
| SST | Singularity Subtraction Technique |
| TEM | Transmission Electron Microscopy |
| TIG | Tungsten Inert Gas |
| TMAZ | Thermo-mechanically affected zone |
| TWI | The Welding Institute |
| VCCT | Virtual crack closure technique |
| WM | Welded metal |

# Chapter 1

# Introduction and state of the art

The increasing use of aluminium alloys in the transportation industry, not only in aeronautics but also in the automotive, railways and shipbuilding sectors, creates the need for research on the more efficient and reliable welding processes to be used. In order to allow the industry to use novel manufacturing techniques as Laser Beam and Friction Stir Welding, research on the mechanical behaviour of joints manufactured using such new tools should be performed.
This Chapter introduces the work carried out for this thesis and presents a detailed review of the relevant topics, concentrating on stiffened panels, Laser Beam Welding and Friction Stir Welding.

The present thesis is concerned with the novel use of integral structures in aeronautical industry. Although no specific open literature publication is derived of the present Chapter, the following paper gives a survey of some aspects of fatigue of aeronautical structures of traditional, riveted, design: P M S T de Castro, P F P de Matos, P M G P Moreira and L F M da Silva, An overview on fatigue analysis of aeronautical structural details: open hole, single rivet lap-joint, and lap-joint panel, *Materials Science and Engineering A*, 468-470, 2007, p. 144-157

# 1. Introduction and state of the art

The increasing use of aluminium alloys in the transportation industry, not only in aeronautics but also in the automotive, railways and shipbuilding sectors, creates the need for research on the more efficient and reliable welding processes to be used.
In order to allow the industry to use novel manufacturing techniques as Laser Beam Welding (LBW) and Friction Stir Welding (FSW), which promise high efficiency, research on the mechanical behaviour of joints manufactured using such new tools should be performed. This thesis aims to provide contributions to fundamental knowledge and to damage tolerance assessment of such modern structures.
Notwithstanding the widespread interest in the possibilities offered by Friction Stir Welding and Laser Beam Welding, data concerning their mechanical behaviour is still scarce. These emerging techniques lead to a type of structure which is close to an integral structural design offering benefits, *e.g.* from the cost point of view, but quite some concerns from the damage tolerance behaviour, crucial point in their application which today limits their application.

This thesis is divided in seven Chapters.
The first Chapter introduces the work developed and presents a detailed review of the relevant literature, concentrating on stiffened panels, Laser Beam Welding and Friction Stir Welding.

Since heat generation is a fundamental aspect of any welding technique, Chapter two presents the development of an effective temperature measurement procedure that could be applied to any welding process. As a basis for the development of an accurate temperature measurement procedure, an aggressive and well known welding method - Gas Metal Arc Welding (GMAW) - was used. A feasible technique for the use of fibre Bragg grating (FBG) sensors was introduced, developed, and validated using thermocouple and thermographic readings. Also, in this Chapter a comparative study of temperature fields acquired during Metal Inert Gas (MIG) welding, Friction Stir Welding and Laser Beam Welding is described.

Residual stresses are locked-in stresses which exist in a structural part without the application of any service or other external loads. Residual stresses may be

detrimental with a predominant contribution to fatigue and other structural failures. Residual stresses are created due to mechanically induced plasticity or by thermal effects which arise from a production process, *e.g.* welding. Quantitative estimation of such residual stresses is important for the safe performance of structural components.
Chapter three is dedicated to a comparative study of several residual stress measuring techniques. Since the arc welding process MIG introduces high residual stresses which can be of the order of the material yield stress, it was used to perform such a study.

In Chapter four the mechanical behaviour of Laser Beam Welded and Friction Stir Welded joints was studied. This Chapter is composed of three different and complementary parts.
In a first study the effect of notches on friction stir weldments was analyzed. Due to design constraints, friction stir welded components may include notches in the weldment. So, the influence of Friction Stir Welding on the fatigue life of specimens of an aluminium alloy, containing notches in the thermo-mechanically affected zone (TMAZ) was investigated. For this purpose, welded and un-welded notched specimens were fatigue tested at different stress levels under load control. The notch-strain analysis was used for the approximate modelling of the observed fatigue behaviour.
In the second study presented in this Chapter, an experimental characterization and computational modelling analysis of dissimilar friction stir welded butt joints performed between two aluminium alloys of the series 6xxx was carried out. For comparison, similar single material joints made from each one of the two alloys were used. Bending tests, not yet reported on the literature in the present context, were performed. An approximate finite element model of the joint, taking into account the spatial dependence of the tensile strength properties, was made, modelling a bending test of the weldments. Following a procedure presented in Chapter three, the residual stresses generated during the Friction Stir Welding process were estimated.
Data concerning the fatigue behaviour of joints obtained using Friction Stir and Laser Beam Welding is still needed. Research work on S-N and fatigue crack growth data for the weld zone is required to provide tools to assess the damage tolerance issues. The third study of Chapter four is a contribution to this effort, contrasting the fatigue behaviour of joints made using a traditional process (Metal Inert Gas welding), and two emerging ones, Friction Stir and Laser Beam Welding. A particular effort is made to relate the macroscopic mechanical behaviour to the microstructural features of the weldments.

An aircraft fuselage structure includes, among other parts, the external skin and longitudinal stiffeners. Investigations on the strength and behaviour of aluminium alloy stiffened sheet specimens used in aircraft construction have been carried out for several decades. Stiffeners improve the strength and stability of the structure and may provide a means of slowing down or arresting the growth of cracks in a panel. Most commonly stiffeners are connected to the skin by means of fasteners. Riveted stiffeners may remain intact as a crack propagates under them, providing an alternative path for the panel load to pass. The

continuous need for low cost and the emergence of new technologies has brought interest for large integral metallic structures for aircraft applications. However, studies show that in an integral stiffened plate a crack propagates simultaneously in the stiffener and in the skin, breaking the stiffener.
Damage tolerance analyses can be performed using linear elastic fracture mechanics (LEFM) concepts where the stress intensity factor (SIF) plays a fundamental role. Fracture mechanics in conjunction with the Paris law [1] are widely used to analyze and predict crack growth and fracture behaviour of aircraft panels. To study crack growth and to evaluate remaining life of stiffened panels, rigorous numerical methods analysis have to be performed to compute stress intensity factors. In such structures having complex shapes, it is important to take into account the effect of nearby boundaries. In the literature there is still a lack of stress intensity factor solutions for the emerging integrally stiffened cracked panels. A study on three-dimensional (3D) stress intensity factor solutions for a cracked stiffened plate using the Finite Element Method (FEM) is presented in Chapter five.

Chapter six is a contribution to the European Union FP6 DaToN project. Its aim is to provide missing fundamental knowledge and assessment tools for the damage tolerance of integrally stiffened structures, produced by means of three modern production methods: Laser Beam Welding, Friction Stir Welding and High Speed Cutting or High Speed Machining (HSM). There is an urgent pressure from the manufacturing side in the aerospace industry to apply these advanced structural concepts, since they promise considerable cost and production time benefits. In addition, a smaller number of fatigue and corrosion critical locations are produced. The main drawback of integrally stiffened structures is the damage tolerance behaviour. Such an integrally stiffened design behaves totally different from the differential designs, which are usually created by using riveted stiffeners. The prime problem is the crack-arresting capability of the stiffeners both in crack growth as well as in residual strength. Fatigue and damage tolerance is therefore one of the main drivers in innovative aerospace structural designs as well as one of the main concerns on the safety of aging aircraft.
The first task in this study was the Finite Element Method analysis of the stiffened panel that was used in the DaToN project. A testing programme including fatigue crack growth of High Speed Machining, Laser Beam Welding, and Friction Stir Welding stiffened panels was performed. This test programme was complemented by a Scanning Electron Microscopy analysis of the fractured specimens. This work helped to increase the knowledge on the behaviour of integrally stiffened structures manufactured with these innovatively methods.

The seventh and final Chapter of this thesis presents the major achievements and suggestions for future and complementary work.

## 1.1 Stiffened panels

Minimum weight is a major concern in aircraft design, [2]. Since the early 1950's, experience has shown that the ability to tolerate a substantial amount of damage is a requirement for modern aircraft. It has become increasingly important to develop methodologies to predict failure in fatigue damaged fuselage structures, [3]. The damage tolerant philosophy must ensure the continued safe operation of the aging aircraft. The fuselage is supposed to sustain cracks safely until it is repaired or its economic service life has expired. Strength assessment of the structures is necessary for their in-service inspection, planning, repair, retrofitting, rehabilitation, requalification and health monitoring, [4]. Therefore, damage tolerance analysis should provide information about the effect of cracks on the strength of the structure. The author of the present thesis was involved in several studies of mechanical behaviour of riveted fuselages; a concise review of some of that work and of his contributions is included in [5]. The way forward for those earlier studies is to investigate integral monolithic structures, topic chosen for the present doctoral thesis. Recently, studies are being conducted to validate designs with equal or better performance than conventional designs with regard to weight and structural integrity, while achieving a significant reduction in manufacturing cost, [6].

The skin structure of a pressurized fuselage for transport aircraft is fatigue sensitive which is a problem often requiring frequent repairs. Under cyclic loading, a flaw can develop into a fatigue crack and propagate until fracture occurs. The residual strength concept permits the determination of the maximum crack length that can be safely sustained. With this information and the characterization of the crack growth behaviour of the material, the number of loading cycles that will be necessary for the crack to grow up to its critical length can be estimated in order to ensure safe operation, [7]. The development of numerical methodologies with the help of small laboratory coupon test results should be used to predict the residual strength of complex built-up aircraft fuselage structures, [8].

An aircraft fuselage structure includes, among other parts, the external skin and longitudinal stiffeners (stringers and longerons) [9]. Already in the 1920's and 1940's investigations on the strength and behaviour of aluminium alloy stiffened sheet specimens used in aircraft construction were carried out, [10, 11]. Stiffened panels are light and highly resistant metal sheets reinforced by stringers structures designed to cope with a variety of loading conditions. Stiffeners improve the strength and stability of the structure and provide a mean of slowing down or arresting the growth of cracks in the panel. Most common stiffener cross-sections are bulb, flat bar or T- and L-sections, that can be bonded, extruded, connected by means of fasteners, machined or welded to form a panel. When experimentally testing stiffened panels attention should be given to the loading and boundary conditions to ensure that the behaviour of the panel in the complete structure is reproduced, [12].

Riveted and bolted stiffeners tend to remain intact as the crack propagates under them providing an alternative path for the panel load to pass. Also, riveted stiffeners continue to limit crack growth after the crack propagates past the stiffener since a crack cannot propagate directly into the stiffener. The permanent need for low cost and the emergence of new technologies has brought interest in large integral metallic structures for aircraft applications. Evaluative programs for replacement of traditional fastening with these new emerging technologies have been carried out all over the aircraft sector, *e.g.* [13]. Studies show that in an integral stiffener (machined, extruded or welded) a crack propagates simultaneously in the stiffener and in the skin beyond the stiffener at approximately the same rate. In this case the crack may propagate into and break the stiffener, [14], although in [15] it was observed that the rate of crack growth is significantly reduced in the presence of stiffeners.

Damage tolerance analysis can be performed using linear elastic fracture mechanics concepts where the stress intensity factor plays a fundamental role. Fracture mechanics concepts in conjunction with the Paris and other crack propagation laws are widely used to analyze and predict crack growth and fracture behaviour of aircraft panels. During the past decades, several studies have been conducted to the calculate stress intensity factors in cracked stiffened panels. Configurations involving cracks in infinite and semi-infinite plates with integral or discretely attached stiffeners have been studied by several authors, *e.g.* [16]. A compilation of results is presented in a parametric form in [17]. It is noticed that the SIF decreases as the crack approaches a stiffener, indicating that the stiffener aided in restraining the crack or slowing down the propagation. Experiments on box girders with welded stiffeners to study crack growth and remaining life concluded that rigorous finite element analysis has to be performed to compute stress intensity factor for a structural component having a complex geometry, [18]. Therefore, in engineering structures with complex shapes it is important to take the effect of nearby boundaries into account using numerical methods of structural analysis. The Finite Element Method has been extensively used for the solution of crack problems in fracture mechanics. Stress intensity factors for riveted stiffened cracked panels were calculated using the FEM in conjunction with strain energy release rate and the crack tip opening displacement in [19, 20]. The use of special crack tip enriched elements to solve problems involving edge cracks in stiffened panels is reported in [21]. In a work using the boundary collocation method [22], a technique using complex variable combined with compatible deformations was applied to finite stiffened panels.

### 1.2 LBW and FSW: A literature review

Welding can be defined as the joining of two components by a coalescence of the surfaces in contact with each other, [23]. Two emerging processes to join

aluminium are of particular interest in the present thesis: Laser Beam Welding (LBW) and Friction Stir Welding (FSW).
Aluminium alloys are the principal materials for light-weight constructions especially in the transportation industry due to their good mechanical properties and low density. Currently, the preferred manufacturing process for aircraft fuselage structures is riveting and in some cases adhesive bonding. Appropriate alternatives technologies to join aluminium are the LBW and FSW, due to their low distortion, high strength of the joint and high processing speeds.

Laser Beam Welding is a promising joining technique being considered for use in aircraft structures to replace the riveted and bolted joints currently used in aircraft structures. The laser welding of aircraft parts is regarded as a pioneering technology for the efficient manufacturing of weight-reduced, metal fuselage structures. LBW has already been in use at AIRBUS for the serial production of the A318. Recent analyses indicate that a move from riveted to welded airframe structures could result in manufacturing costs savings of 30% [24]. Advances in LBW have been significant in recent years. It is a field of growing importance in industry. Because its low heat input, high welding speed and productivity as well as its flexibility, low distortion and good weld quality, LBW is used with success in industrial production.

Friction Stir Welding is a solid-state process, more similar to forging and extruding than to fusion welding, developed and patented by the The Welding Institute (TWI) in 1991 [25]. It emerged as a commercial joining technique to weld high strength alloys that were difficult to join with the existing techniques. The process was developed initially for aluminium alloys, but since then a large number of materials were found suitable for joining by FSW. In the past decade, FSW has been developed for many diverse industries, like aerospace, automotive, marine, and nuclear assemblies. Aircraft structures, where cost and weight can be reduced by using new joining techniques instead of riveting [26], are a potential field of application.
A FSW system used by Eclipse Aviation has completed part of a aircraft Eclipse 500 cabin skin, [27]. The company says it also uses the process on the fuselage and wing skin, and each aircraft has a total 136 meters of welds. At Eclipse, FSW eliminated 60 percent of the rivets that the plane would have otherwise required. In side-by-side tests, friction stir welded joints had two or more times the static strength of a comparable yet conservatively designed riveted joint, and fatigue properties were found to be at least as good as those of riveted joints.
FSW makes possible joining speeds six times faster than automated riveting or 60 times faster than manual riveting, with improved quality.

### *1.2.1 Laser Beam Welding*

Advances in Laser Beam Welding have been significant in recent years. For example, Joining Technologies [28] has invested in the newest and most precise laser technologies available for industrial welding and joining applications. LBW

is a field of growing importance in industry. It is a natural transition from Electron Beam Welding.

Aluminium alloys are potential materials for light-weight constructions especially in the transportation industry due to their good mechanical properties and low density. An appropriate joining technology is the LBW process due to its because low heat input, high welding speed and productivity as well as its flexibility, low distortion and good weld quality. The concentrated heat input permits a deep penetration effect, leading to small but deep weld seam, Figure 1.

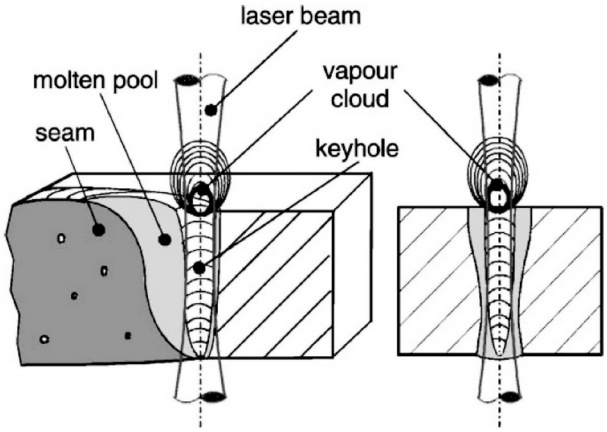


**Figure 1 - Deep penetration effect in LBW, [29].**

LBW offers the possibility of manufacturing joints of all light metals and their combinations. Currently, the preferred manufacturing process for aircraft fuselage structures is riveting and the principal material for these structures is aluminium. LBW is a promising joining technique to replace riveted and bolted joints currently used in aircraft structures.
Recent analyzes indicate that a move from riveted to welded airframe structures could lead to manufacturing costs saving of 30%, [24]. Laser welding is one of the techniques currently considered to use in aircraft structures, [30].

*1.2.1.1 The process*

LBW is a fusion joining process that uses the energy from a laser beam to melt and subsequently solidify a metal, resulting in a bond between parts, [31]. LBW can be successfully used to join many metals to themselves as well as dissimilar metals. The LBW is a thermal effecting melting process, which causes metallurgical changes in the weld metal as well as in the heat affected area beside the weld seam.

Laser radiation can be used as the thermal source for welding, cutting and surface treatment of metals [32]. The excitation source drives the atoms, ions or molecules of the laser medium to a situation where there is an excess of those at high energy level over those at a low level. The transition from high to low energy will emit a photon, which in turn stimulates further emission, perfectly in phase, and at the same wavelength, from the other excited members of the medium: the

radiation is thus rapidly amplified. An optical resonator directs and controls the radiation by allowing an appropriate fraction to be bled off as a near-parallel beam, whilst the remainder is circulated within the cavity to maintain laser action. The output is monochromatic, usually with high spatial and temporal coherence. The wavelength depends on the laser medium used for generation: 1,06 $\mu m$ in the neodymium YAG (Nd:YAG) laser with beam power up to 4 $kW$ and 10,6 $\mu m$ in the carbon dioxide ($CO_2$) laser with beam power up to 40 $kW$.
The welding processes are affected by numerous parameters, such as the shape of the component, the temperature-dependent material properties (thermal conductivity, specific heat capacity, density) as well as the process parameters, such as the laser power rating, welding speed, temperature of the component at the beginning of the process, ambient temperature, and environmental conditions (type and quantity of process gas and type of gas feed).
There are two major laser types: continuous-wave laser welding process and the pulsed laser welding. Pulsed laser welding refers to the low repetition rate regime in which significant re-solidification of the workpiece occurs between laser pulses, [33]. As the laser beam intermittently interacts with the workpiece over very short time intervals, very rapid heating and cooling cycles result. The weld bead is the product of a number of overlapping spot welds, and every point in the weld area experiences a complex series of thermal cycles during the passage of the laser beam. This complexity implies that numerical modelling techniques are the best choice.
The $CO_2$ laser gives potential to weld material with thickness up to 15$mm$ or to use high welding speed, in the case of the Nd:YAG laser optical fibbers can be used to guide the laser beam to the focusing optic, [34]. The principle of the welding process is shown in Figure 2.

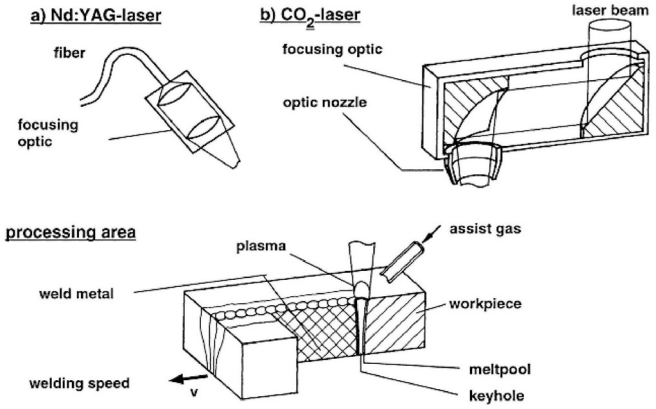


**Figure 2 - Principle of LBW, [34].**

The laser beam is focused onto the surface of the workpiece. Above a certain intensity the material starts to evaporate, a keyhole is formed which leads to a strong increase in beam absorption. The threshold intensity to ignite this process depends on the material and the normal absorvity. As a consequence of these influences in the threshold intensity and the weld depth which can be reached in dependence on beam power or intensity are affected by the type of laser, *i.e.* the wavelength.

The beam energy is absorbed by the material and converted into heat, [35]. A very concentrated energy source provides a high power density that results in producing a narrow and deep hole (known as keyhole) during welding, the same as in plasma arc or electron beam welding. The keyhole provides the deep penetration that gives the weld a high depth-to-width ratio, [36]. In metals the beam energy is transformed into kinetic energy of the electrons as well as lattice oscillations. The temperature of the joint depends on the physical properties of the material as well as on the geometry of the joint. During the laser welding process, a very narrow zone under the laser beam is suddenly heated with respect to the surrounding area, and, consequently, vaporized and locally fused, [37]. The elevated temperature gradients present in this area both during the heating and the cooling phases, along with the sharp decreasing of mechanical properties during heating, cause the appearance of non-homogeneous permanent strains and residual stresses after the process. The effect of welding residual stresses in the neighbourhood of the seam has a great influence on brittle fractures, fatigue crack propagation and structural strength. The power of an industrial laser designed for material processing can be $10^8 Wcm^{-2}$. When focusing the beam to give a power density below approximately $10^6 Wcm^{-2}$ welds can be made, [30]. The beam energy is deposited on the material surface, transferred into the material by conduction, and a hemispherical weld bead is formed in a similar manner to conventional fusion welding processes. In contrast, a higher power density causes local vaporization, and a narrow, deeply penetrating vapour cavity is formed by a multiple internal reflection of the beam. The process of laser deep penetration welding is characterized by the existence of plasma and a keyhole. As stated by Carmignani *et al.* [37], if the power density of the laser welding source is sufficiently high (greater than $5x10^5 Wcm^{-2}$) vaporization of the weld pool occurs, and the moving source can penetrate deeply inside the material. In this case the metallic vapour at high temperatures and pressure apart the surrounding melted metal allowing the formation of a narrow and deep hole (keyhole). Temperatures inside the hole can reach $20x10^3 °C$. Although the laser beam affects only small parts of the workpiece, there are transformation processes in the heat affected zone (HAZ), which have an influence on the mechanical properties of the workpiece. During the execution of a deep penetration laser welding, equilibrium between the metal vapour pressure, which tends to widen the hole, and the hydrostatic pressure of the surrounding liquid metal, which tends to close the hole, occurs. As a matter of fact the heat is transferred principally from the keyhole walls to the exterior, rather than from top to down, and with the progress of the keyhole at a prescribed velocity of the laser source, the melted metal moves round the sides of the hole and solidifies at the rear. Part of the metal vapour, rather than contributing to the energy transfer within the workpiece, can leave the surface causing the desfocalization and partial absorption of the incident laser beam and a consequent widening of the fusion zone near the surface: typical is the nail head shape of the seam along the thickness of the plate.

In order to evaluate the thermal cycle one has to assume the quasi stationary state of heat dissipation. This is true if the weld seam is long enough. Usually laser welding is done without filler material. This requires, however, a minimal weld gap width and hence an intensive seam preparation. To avoid an additional seam preparation one can also use fillers. The additional material fills the gap

but it also can enhance the mechanical properties of the seam due to the alloying elements in the filler material. Numerous experiments have demonstrated that laser welding permits the manufacture of precision welded joints with a high depth-to-width ratio and a high welding speed. Owing to these advantages, laser beam welding is widely applied in industrial production. It has also been reported that laser beam welding can produce welds of a similar quality to electron beam welds.
Recently Joining Technologies [28] introduced the new Trumpf multi-kilowatt continuous YAG laser; it rivals electron beam welding speeds but does not requires the same costly cycle times.

Fawzi *et al.* [38] introduced a technique to achieve deep and efficient Nd:YAG pulsed LBW of stainless steel with constant energy, while applying a variable vertical or horizontal electric field to the specimen. It was found that pulsed LBW is greatly affected by the electric field, the weld depth increases with increase in electric field intensity. Also, proper arrangement and shielding gas could enhance the weld together with the electric filed.

Zhang *et al.* [39] presented a study concerning the relationship between weld quality and optical emissions in underwater Nd:YAG laser welding. It was found that the weld quality is dependent on the shielding conditions of the local dry cavity when other welding parameters are fixed. Although the laser beam can be transmitted through a certain water depth, the interaction between the laser beam and the water may induce plasma which has strong shielding effect on the laser beam. The results show that the detected signal well reflects the shielding conditions variations on the local dry cavity.

In order to achieve reliable laser welds with minimal distortion for the fabrication of components for the aerospace industry, Li *et al.* [40] studied several techniques on titanium alloy sheets using the $CO_2$ and the Nd:YAG pulsed laser. It was found that welding with filler wire has a relaxed tolerance to face fit up, but the porosity needs to be controlled. It was found that shaping the edges with a special relief defined as built-in filler before welding enables avoiding using the classical filler wire. A cosmetic butt weld without filler was done re-melting the surface of the outside of the components. An autogenous butt joint with regular bead profiles was made using high power Nd:YAG pulsed laser, the undercut and slump being controlled by the pulsed energy, pulse duration, frequency, waveform and overlapping rate. This study demonstrates that LBW techniques of titanium alloy sheet are very suitable for the fabrication of light-weight structures with precise dimensions for the aerospace industry.

#### *1.2.1.2 Joint design*

It is possible to use several joint types with the LBW technique. When welding thick plates and high speed materials, the butt joint is an ideal geometry for keyhole welding. To obtain good results, part fit up must be good in order to maintain the alignment of the beam and the joint, and to avoid bead concavity

caused by air gaps. Lap joints are a type of joints where LBW can be used with success, [30]. In the aeronautical industry, the T-joint configuration is commonly used to fabricate stiffeners by joining a vertical web to a horizontal flange. In LBW joint design gaps of greater than 10% of the plate thickness could lead to insufficient weld metal, resulting in concavity or undercut. Penetration in square butt welding was reported to be 10% greater than with melt runs. The tolerance of fit up can be increased using wire feeding.

*1.2.1.3 Advantages and disadvantages*

In recent years high power density welding technologies, like laser welding, have been increasingly utilized in industrial manufacturing with respect to traditional welding methodologies due to lower dimension of the affected area and shape distortion of pieces, and greater processing velocity, [37].
LBW has the capacity to weld pre-machined precision components with restricted heat input and minimal distortion. Advantages of the LBW technique are single-sided access, reduced flange widths and mass, smaller HAZ, less thermal distortion, increased structural strength, high speed automated processing and good design flexibility, high heating rates, slight thermal effect on the material and high automation potential, high welding speed, low distortion and ease of automation, [41]. In addition to advanced motion control, LBW offer high-speed beam deflection capability which can often perform welds that are not possible with conventional motion systems. Pulsed laser welding offers the advantage of very low heat input to the weld, resulting in low distortion and the ability to weld heat sensitive components.

Due to high energy density, LBW is attractive for heat treatable aluminium alloys, because of the narrow width of the fusion zone and HAZ. LBW is suitable for welding aluminium alloys with the characteristic of high welding speeds, high flexibility of laser beam tool, high energy density of the beam and low distortion. In particular, there is an advantage in applying LBW to age-hardened aluminium alloys since its low overall heat input minimizes the size of the weld fusion zone and HAZ. Although possible, the laser welding of aluminium is generally perceived to be difficult because of the initial high surface reflectivity and the high thermal conductivity of aluminium, both of which contribute to the risk of weld imperfections such as lack of penetration or cracking, in certain alloys, [24]. Weld metal porosity is also frequently associated with the laser welding of aluminium. Surface contamination and the natural oxide layer on aluminium alloys, both which contain moisture are potential sources of hydrogen, which is released during welding when the coating melts. Hydrogen as a solubility in molten aluminium about 20 times grater than that in solid aluminium, and is rejected on solidification as fine porosity. The condition of the surface also determines the fraction of incident light absorbed and the threshold power density at which keyholing may be achieved. Due to low heat input, easy to transfer energy and control adaptability, underwater Nd:YAG LBW has been researched as a repairing technology in nuclear facilities. The low heat input is important for reducing the sensitivity of stainless steels to stress corrosion cracking.

Disadvantages, as in other fusion welding processes, are porosity, solidification cracking, poor weld bead geometry, loss of alloying elements, and grain boundary melting in the HAZ [30]. These defects can be controlled by a proper selection of the filler metals, process gases, material preparation, and in some instances, adaptive control systems. Laser welding is a well established process, but in certain situations loss of focus of the beam causes problems, as already mentioned in section 1.2.1.1. Despite of the numerous advantages, LBW still suffers from statistically occurring seam imperfections like notches or holes in the seam which reduces the mechanical properties of the joint. The reason for this process instabilities is a resonant reaction in the system laser-beam, vapour cloud and keyhole, [29].

In LBW the thermal influence on the material structure beside the weld seam is very small, [34]. If an alloy is welded which is sensitive to hot cracking additional wire can be used to overcome this problem as in conventional welding. In the transition area between the weld seam and the heat effected zone some defects occur but with near molecular dimensions. So, there is no negative influence on the properties of the weld component.
The seam surfaces are characterized by a structure which is defined by the high welding speed and rapid solidification. Effects such as oxidation reactions are comparable to other thermal treatments in the case of aluminium; but because of the short cycle time oxidation of the weld seam is very low. Welding an alloy which does not require additional wire because of metallurgical effects shows that there is no change in chemical composition compared to the base material. If the base material is characterized by relatively strong fluctuations of the local chemical composition the laser beam welding process homogenizes and refines the composition and the structure of the material. This gives positive effects on mechanical and corrosion properties of the welded component.

#### *1.2.1.4 Monitoring*

LBW is a well established process, but, as mentioned before, a loss of focus of the delivered beam onto the workpiece can cause problems. To solve these problems several focus control techniques were developed. Mueller *et al.* [42] presented a technique based on the measurement of capacitance between an electrode and the workpiece, which is a function of their separation. It is a commercially available technique but it has some restrictions. It must be used between pulses and the best results are obtained with flat surfaces being the results unreliable in sharp curvatures.
Other focus measurements techniques are based on vision systems, based in triangulations. These techniques have the disadvantage of requiring an off axis measurement which implies good optical access to the workpiece that can function as an intrusion in the process.
Hand *et al.* [43], introduced a technique for focus measurements that is optical, unaffected by electromagnetic interference, and results in no intrusion. The technique is based on detection of the process generated radiation, conveniently

collected by the effector optics whose main purpose is to deliver the laser beam to the workpiece. The technique can be used with all types of laser, but is especially convenient with fibre-delivered Nd:YAG radiation.

#### *1.2.1.5 Applications*

Demands for improved production quality, productivity, and flexibility are constantly enlarging the field of laser welding applications. LBW is now a common production line manufacturing process in many areas of industry like automotive, domestic goods, and electronic sectors, [30]. Laser welded components used every day include automobile body parts, transmission components, and chassis members, pipes and tubing, housings for white goods, razors, and electronic packages. Continued growth in the use of LBW can be attributed to its high productivity, high weld quality, low distortion, manufacturing flexibility, ease of automation, and the opportunity to design products and process in a novel manner. Main applications are related to welding steels, titanium, nickel alloys and aluminium alloys. More recently it has been used in such diverse fields as medical instruments manufacturing, where heart pacemakers and dental instruments are laser welded, and nuclear and naval equipment, where containers and sheet metal are also laser welded. Medical devices and sensor components can now be welded by precision high speed welding.
LBW applications in the automotive industry include welding the roof to the side panels. Advantages over spot welding were the formation of a continuous watertight weld, no post treatment required, and less displaced material resulting in better accuracy. In addition, the problem of welding the zinc-coated material was overcome by carefully selecting weld parameters. Other car manufacturers use a layer system to assemble gear transmission shafts, and a particular company laser welds automobile roofs using 5-axis $CO_2$ $5kW$ laser equipment.
Costa *et al.* [44] studied the process of LBW hard metals to steel. Due to its great hardness and good wear properties they have been used mostly as cutting tools, where high strength at high temperatures is required. Since hard metals are brittle and expensive only the active part of the tool is usually made of hard metal. Laser beam weldability was examined with high power (cw) $CO_2$ laser, (cw) Nd:YAG laser and (pw) Nd:YAG laser. It was found that continuous laser leads to full penetration, high resistant and low cracking weld joints. Continuous Nd:YAG laser was found to present best results. The results show that LBW is an alternative joining technique for hard metals.

#### *1.2.1.6 Metallurgy*

The LBW process is similar to other welding techniques, a thermal effecting melting process which causes metallurgical changes in the weld metal as well as in the HAZ beside the weld seam.

Generally, welded aluminium alloys are characterized by lower strength in the weld zone compared to the base material. This type of strength mismatch, defined by the ratio of yield stress of weld material (WM) and base material (BM) $M = \sigma_{yieldWM}/\sigma_{yieldBM} < 1$, is known as under matching. The whole weld is characterized by three zones with different microstructures and mechanical properties. The fusion zone (FZ) along the fusion line can contain porosity due to hydrogen gas entrapment. A transition zone known as HAZ, which contains recrystallized grains, experiences a degradation of the material due to the input heat generated during welding. This transition zone passes over in the unaffected original material, called base material. Global fracture properties of test specimens as well as of welded structures are therefore dependent on the location of the initial crack within the weld. Reduction of maximal load and load at fracture as well as lower ductility is observed when crack initiates and grows within the lower strength FZ, which is typical for aluminium alloy joints.

In a work by Behler *et al.* [34] an alloy of the 6000-series has been welded applying a 5% Si additional wire. Because of the rapid cooling and in the transition area a fine grained solidification structure was formed with a nearly linear orientation to the centre of the weld seam. In the central area of the weld seam a fine disperse globular structure of the solidified material appeared. Because of the large temperature region between melting and solidification solidus/liquidus interval in the HAZ the material is partially molten in the solid aluminium matrix. On the weld seam side there is a region of some microns where small defects (solidification cracks) occur during the solidification process. These defects are typical in the transition area of weld seam on hot cracking sensitive material. Due to their size it is not possible to detect them by using non-destructive methods such as X-ray transmission photography. Because of the 'molecular' size of these defects, length $<3\mu m$ and width $<1\mu m$, there is no special negative influence on the mechanical properties of the weld seam. In a typical micrograph of the surface of a laser beam welded seam the structure and the direction of the solidification lines are a result of the relative high welding speed. Especially in the centre line of the seam a slight oxidation occurs. At the side of the weld seam small pores as well as a recondensed layer occur. This area is located in the transfer area between weld seam and HAZ. So it can be assumed that this is caused by melting or evaporating material with low transfer. Additionally some small solidification cracks occur at the surface. This is also an effect of the rapid welding process in combination with the solidification characteristics of the used alloy. In general there is no negative influence of the pores as well as of the small cracks on the mechanical properties. Another main aspect in welding is the possible influence of the process energy on the chemical composition and the grain structure in the weld zone. Conventional welding processes which generate a melt pool, as arc welding methods, partially require additional material to reach a chemical composition in the weld area which is similar to the base material. In addition to that, the heat input of the welding process often lead to a coarse grain structure in the weld zone. Refining elements in additional materials are used to homogenize the solidification structure and to reduce the typical dimensions of the grains.

Braun *et al.* [45] studied the microstructure of butt welds of 1,6$mm$ thick 6013-T6 sheets produced by LBW. LBW was performed using a 3$kW$ Nd:YAG laser helium shielding gas and filler powders of the alloys Al-5%Mg and Al-12%Si were employed. Metallographic and fractographic examinations revealed pores in the fusion zone, occurring in higher number when using the filler alloy Al-5%Mg. Metallographic sections revealed a dendritic microstructure in the fusion zone.

In a study to increase de productivity of an automotive plant Quintino *et al.* [41] evaluated the use of the $CO_2$ laser welding process. Two types of shielding gas were tested: argon and helium. With both gases a good weld appearance was obtained, the helium being the one that gives the best result in terms of superficial finishing. Porosity occurred when using the argon gas and lower welding speeds due to hydrogen induced porosity and unstable evaporation of the metal over the front wall of the keyhole. When using helium gas the porosity occurred due to keyhole instability. It was concluded that small centreline porosity located near the toe of the weld bead corresponds to cases of incomplete penetration. With helium shielding and slightly higher welding speeds, macro and aligned porosity were almost eliminated, being this reduction due to stabilization effect on the keyhole caused by increased welding speeds.
Full penetration levels were accomplished only with helium. With argon, incomplete penetration was encountered, despite the use of lower welding speeds. Maximum penetration occurred when the beam was focused slightly below the top surface. One of the main characteristics of overall weld quality is the width and nature of the crystalline structure formed in the HAZ.

Haboudou *et al.* [46] studied the porosity formation on (cw) YAG laser with helium shielding welds on two aluminium alloys: a AA5083-O wrought alloy with Mg content (4,5%) and a A356 cast alloy with 7% Si and a cast oxide layer. It was verified that porosity formation is greatly influenced in aluminium alloys by the low vaporization point element (Mg, Zn) content, or by process instability such as key-hole closures that tend to entrap occluded gases during welding, and the very high solubility of hydrogen in molten aluminium favours microporosity generation. Surface preparation reduced the hydrogen sources responsible for microporosity generation, and produced a nearly total suppression of pores in A356. Also, dual beam welding are adequate methods for reducing porosity formation tendency assemblies. Metallurgical and mechanical modifications were rather identical for all the welding conditions investigated.

Verhaeghe *et al.* [24] conducted a research project to reduce the fine and coarse porosity in laser welded 3,2$mm$ thickness 2024 aerospace aluminium alloy. It was found that despite the little difference visually, whether the parent material cleaned or not prior to welding produced an obvious distinction in the resulting level of porosity. In a filler wire cleaning versus porosity study it was found that all welds produced with a chemietched filler wire good results were obtained. Trials with twin spot laser energy profile showed that the levels of coarse porosity were lower when compared with a single spot laser profile. With the twin spot technique, the laser power is shared between both spots, creating a lower power density in each of the spots, necessitating a lower travel speed. To examine how

moisture in the shielding gas contributes to the presence of fine weld metal porosity, welds were produced using a high purity, low density research grade helium shielding gas and a modified shielding gas delivery system. Welds produced using the modified delivery system and a research grad (low moisture content) helium shielding gas demonstrated a considerable reduction in pore numbers compared with welds made under exactly the same conditions but using industrial grade helium.

In a study by Zhao *et al.* [47] the mechanism of pore formation and a solution for this problem during (cw) Nd:YAG LBW of magnesium alloys was studied. It was found that the pre-existing pores in the base metal coalesced and expanded during welding resulting in large pores formation. The porosity in the fusion zone increased with the increase in heat input. It was also found that the stability of the keyhole was not a major factor in fusion zone pore formation, and that the controlled re-melting of the fusion zone resulted in the elimination of some pores.

In a work by Wu *et al.* [48] LBW of Ti-24Al-17Nb alloy was conducted to investigate the effects of the welding parameters on the microstructure. The LBW was performed with a $CO_2$ laser with helium shielding. It was found that the microstructure became coarser as the heat input of the LBW increased. The microstructure examination results suggested that the structures of the weld metal made with the welding conditions employed in this work were predominantly metastable β(B2). The weld parameters had no effect on the phase constitution but the microstructure size and orientation.

Caiazzo *et al.* [49] analyzed lap and butt laser welding processes by a $CO_2$ laser system using two covering gases (helium and argon) with different welding covering gas nozzles, gas pressure and flow rates. This study was conducted in titanium alloy $Ti_6Al_4V$. It was found that the thickness of superficial oxide layers is greater using argon indicating an increased contamination level. It was concluded that the use of argon produces a higher percentage of faulty specimens. Examination of the trends of the morphological weld bead measurements highlighted that there is no great difference in the results obtained compared to those obtained using other materials.

Heo *et al.* [50] studied the metallurgical and mechanical properties of laser weldment using YAG laser for low activation $V_4Cr_4Ti$ alloy. $V_4Cr_4Ti$ alloys are attractive candidate low activation structural materials for fusion reactors, due to their low induced radioactivity, good resistance to neutron radiation damage and good elevated temperature strength. Increasing the average power and decreasing the travelling speed was possible to obtain a wide range of full penetration. Due to the increase in the impurity level induced by the resolution of precipitates an increase in the material hardness was verified. It was also verified that the width of the weld metal and the HAZ increased with increasing the input energy per unit bead length.

*1.2.1.7 Joint properties*

*1.2.1.7.1 Hardness profiles*

Hardness profiles have been made across laser beam welds. The profiles are extremely useful, as they can assist in the interpretation of the weld microstructure and mechanical properties. The exact shape of the weld profile depends on the alloy type being welded, and the processing conditions.

In a work already mentioned, Braun *et al.* [45] studied the hardness profile of butt welds of 1,6*mm* thick 6013-T6 sheets produced by LBW. The hardness in the weld zone was lower compared to that of the base material in the peak-aged temper. The hardness decreased from the level of the parent material to reduced values in the weld zone. A hardness minimum was measured in the fusion zone.

Caiazzo *et al.* [49] analyzed lap and butt laser welding processes, in a titanium alloy $Ti_6Al_4V$, using a $CO_2$ laser system with different welding covering gas nozzles, gas pressure and flow rates. The cross sections of the beads were subjected to micro hardness tests. Examination showed that hardness values increase when proceeding from the base material across the HAZ towards the melted zone. This behaviour is due to the very high cooling rates to which the melted zone is subjected following the laser welding process. The micro hardness values found on the weld bead cross section underline an appreciable increase beginning at the base metal up to the fused zone.

Nègre *et al.* [51] presented a work where the fracture behaviour of different zones of a laser beam weld is investigated by means of numerical work and experimental work to verify the accuracy of the simulations. Microhardness tests were carried out to identify different zones of the weld: fusion zone with low hardness, the HAZ having an elevated hardness and the base material showing the highest values, Figure 3.

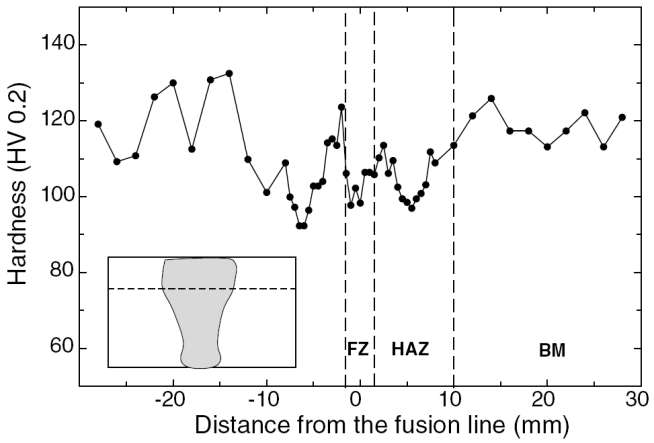


**Figure 3 - Hardness profile of the LBW joint, [51].**

In a work by Wang *et al.* [36] the tensile properties of laser beam welds in Ti6Al-4V alloy were evaluated at temperatures below 450*°C*. Microhardness tests

indicate that the hardness of the fusion zone is higher than both the HAZ and parent material, Figure 4.

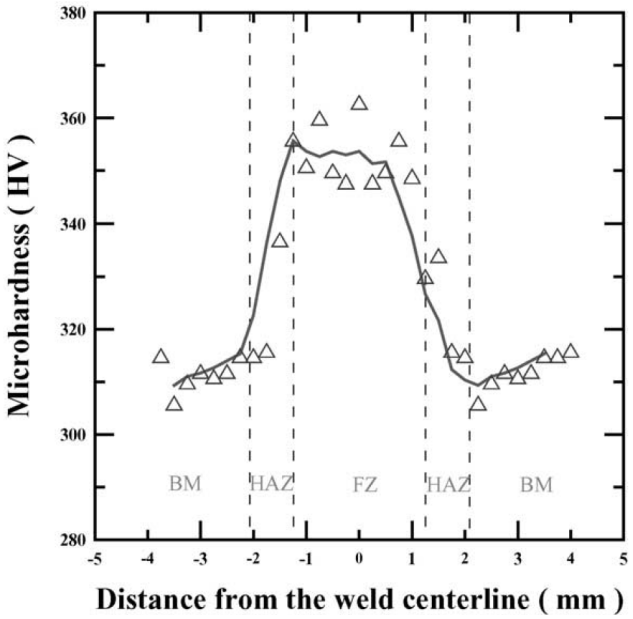


**Figure 4 - Plot of the distributed microhardness profile, [36].**

*1.2.1.7.2 Tensile, fatigue and fracture mechanics properties*

Tensile, fatigue and fracture mechanics tests were performed in several alloys. In this section several studies and their main conclusions are presented.
Braun *et al.* [45] have also studied through tensile testes the tensile properties of butt welds of 1,6*mm* thick 6013-T6 sheets produced by LBW. It was found that joint efficiencies (ratio between the welded and base correspondent base material tensile strength) of laser beam welds were 60 and 78% using the filler powders Al-5%Mg and Al-12%Si, respectively. Tensile specimens of LBW sheet failed in the fusion zone or along the fusion boundary. The specimens failed in a ductile dimple like fracture mode. Pores were observed in the fracture surface.

Quintino *et al.* [41] in the already mentioned study to increase de productivity of an automotive plant evaluated the $CO_2$ laser welding process and also performed mechanical tests. A tear-down test was performed to evaluate the strength of the joint. A flexion test was conducted to assess the door flexion resistance. A fatigue test involving the opening and closing a car door was performed. The performance of the doors mechanically tested was limited by plastic deformation in the welded parts and was not limited by the mechanical strength of the joint.

In a work by Behler *et al.* [34] tensile strength tests on base material as well as on laser beam welded seams on AlMgSi where analyzed, Figure 5.

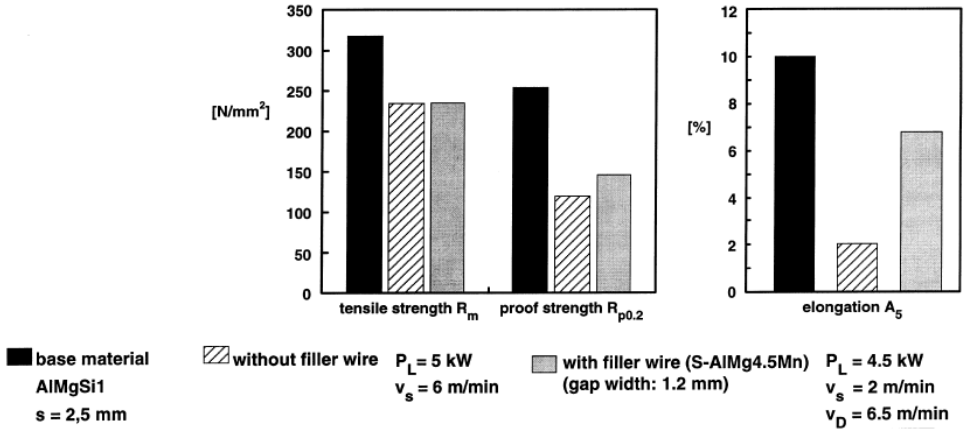


**Figure 5 - LBW tensile strength, [34].**

The weld seams were obtained with and without additional material. Because of the heat input during welding, the tensile strength in the weld seam area is reduced because of the annealing effect of the precipitated material. This occurs in both cases, welding with or without additional material. The proof strength is also reduced if the results of the weld seams to the base material are compared. The reason for this is also the annealing in the weld zone area. It can be seen in the elongation results that when welding without additional wire there is only 2% elongation of the whole specimen. By using additional wire the elongation can be increased to 7%, typical level of arc welding methods. The low level of the elongation in the case of welding without additional wire is caused by the annealing effect in the weld zone as well as by the small width of laser beam welded seams. During the strength test the complete elongation is concentrated in the weld seam area because of its reduced strength. Because of this concentration the local elongation of the weld seam area is very much more than the elongation level of the complete specimen. If additional material is used the seam width is enlarged so the local elongation potential will increase. This results in an increase of the specimen elongation.
In this work results of fatigue tests on laser beam welded specimens, butt weld, on different materials ($AlMg_{0,4}Si_{1,2}$, $AlMg_3$ and $AlFe_{1,5}Mn$) are presented, Figure 6. It can be seen in that there is a typical drop down of the fatigue strength to approximately 60% of the base material. The reasons for this change in the properties are the reduced strength capabilities in the weld metal and heat affected zone as it has been shown in the static strength tests. There is also a strong influence of geometrical defects.

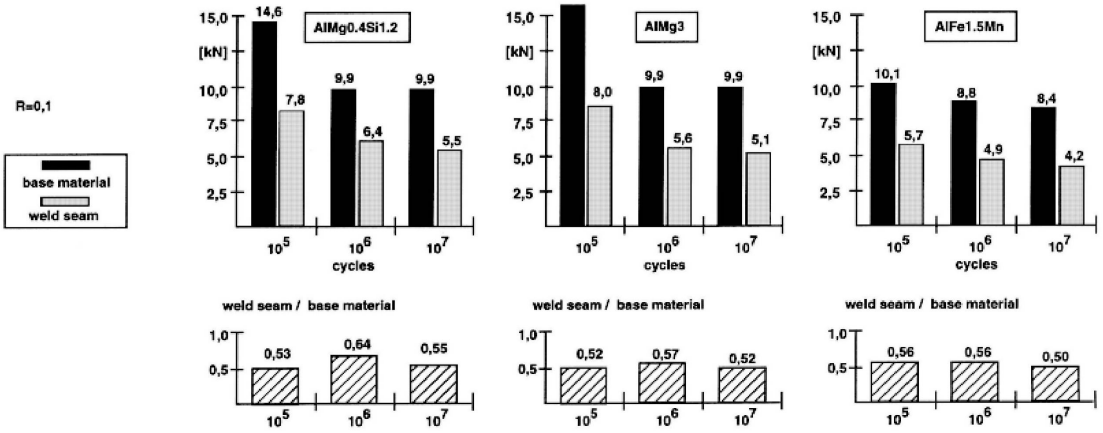


**Figure 6 - Fatigue strength of LBW butt joints on aluminium, [34].**

This can be seen from the results in Figure 7. Here the results of fatigue tests on welded specimens with two different surface conditions are shown. The results in the lower level curves are examined with specimen in the as-welded condition. Because the welds were carried out using additional wire there was a seam overfill of $0{,}9mm$ at the top and the bottom of the weld seam. FEM calculations show that the geometrical function of the transition curve from the weld seam to the original surface of the base material can be interpreted as a geometrical defect which, because of stress concentration, enhances the initiation of a first crack during the fatigue load. If the weld seam surfaces were post-machined so that there is a plane surface at top and bottom of the specimen the fatigue load level will increase by nearly 50% compared to the condition as-welded.

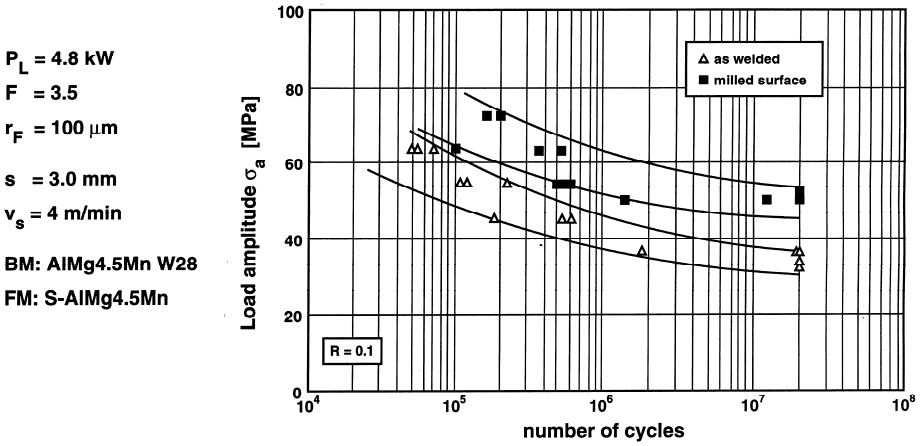


**Figure 7 - Fatigue properties of LBW seams on aluminium, [34].**

In the work by Wang *et al.* [36], further to the hardness tests, the tensile properties of laser beam welds in Ti-6Al-4V alloy were evaluated at temperatures below $450°C$. The ultimate tensile strength was found to be slightly higher than that of the parent metal. The yield stress of the weldment is slightly inferior to that of the parent metal, especially in the 150-$450°C$ range.

Liu *et al.* [52] studied the tensile fracture behaviour in $CO_2$ laser beam welds of 7075-T6 aluminium alloy. The welds were conducted at two different speeds and

compared with gas tungsten arc (GTA) welding. Results indicated that both the hardness and the tensile strength of the laser beam welds are higher than those of GTA welds. It was found that in laser beam welds the tensile fracture occurs in the fusion zone where as the fracture position of GTA welds was in the HAZ. The tensile strength of laser beam welds subjected to the artificial aging treatment is still lower than that of the base metal.

The fatigue behaviour of laser welds by $CO_2$ of high-strength low alloy (HSLA) steels was studied in a work by Onoro *et al.* [32]. LBW was tested on this type of steels in order to improve the productivity, increase the process reliability and avoid the deformation. Good fatigue life results were achieved and it was found that cracks started in the fusion zone, near the borderline between the fusion zone and the HAZ, and the presence of undercuts and surface rugosity have an accelerating effect on the generation of cracks.

In the already mentioned work by Wu *et al.* [48], LBW of Ti-24Al-17Nb alloy was conducted to investigate the effects of the LBW parameters also on the bend ductility and tensile strength of the joints. In three point bend tests the inducing crack strain and the fracturing strain decreased with the heat input increasing, revealing that the ductility of the joint was dependent on the heat input of the LBW. The transverse tensile strength of the LBW joints was independent of the welding parameters.

In the analysis of lap and butt laser welding processes by a $CO_2$ laser system Caiazzo *et al.* [49] performed tensile tests. In order to test the possible strong influence of the preparation of the edges and coupling conditions on laser welded zones two types of tensile specimens, bead-on-plate (BoP) and butt welds, were used. The tensile tests carried out on the base material demonstrated an ultimate strength of $1150 MPa$. As regards the BoP specimens, the diagram of stress-strain showed a similar trend to that of the base metal, while for butt joints, the failure almost always occurred at the beginning of the plastic field, reaching values equal to 75% of $1150 MPa$.

Nègre *et al.* [51] presented a work where the fracture behaviour of different zones of a laser beam weld is investigated by means of numerical work and experimental work to verify the accuracy of the simulations. Tensile tests for the several weld zones were performed, Figure 8. The tests showed different behaviour of the FZ, HAZ and BM in both, yield strength and elongation at fracture, whereas the strain hardening seems to be similar in all zones. Fracture toughness tests to determine the crack resistance curves for the three zones were conducted using compact tension specimens. These tests show a similar trend, Figure 9.

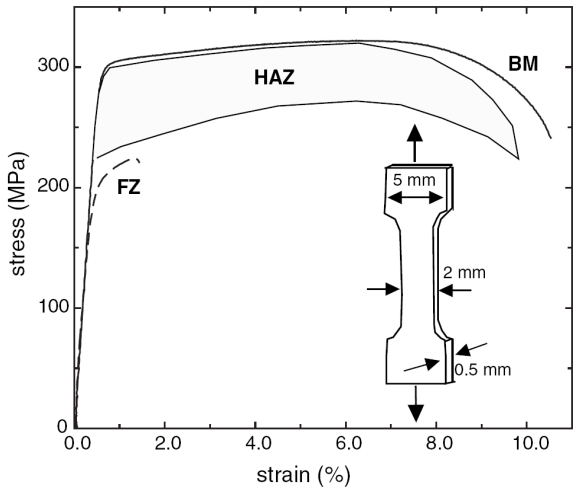


**Figure 8 - Nominal stress *vs.* nominal strain curves obtained from micro-flat tensile specimens taken from different zones of the weld joint, [51].**

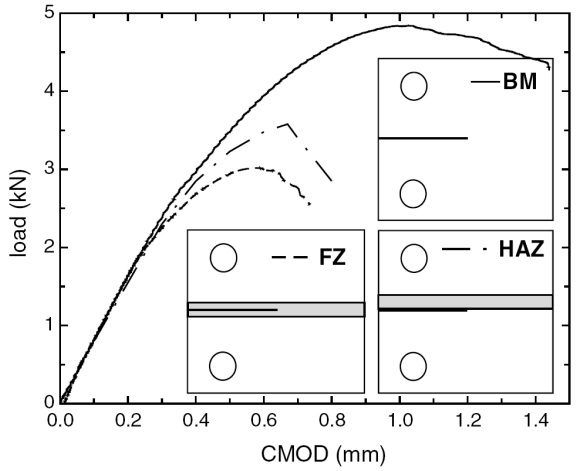


**Figure 9 - Load *vs.* deformation (CMOD) curves of compact tension specimen for BM, FZ and HAZ, [51].**

Eibl *et al.* [53] studied the fatigue properties of laser beam welded thin sheet aluminium. Three types of single lap joints with a full penetration slot weld and butt welds were tested. It was found that for butt weld configuration, the cyclic properties were governed by porosity. If pores are present, the fatigue strength was limited to about one half of the base material. In the case of laser welded overlap joints, the crack like notch overrides the effect of porosity. Modelling the hydrogen pores as three-dimensional globular defects showed that their effect on fatigue strength exceeds the effect of the moderate weld toe curvature at butt welds. It was concluded that the welding process optimization should focus on maintaining cross section and achieving no or finely dispersed hydrogen porosity.

As fatigue testing is a lengthy and costly process, there is a need for predictive methods that estimate the fatigue properties of the weld. Wang [54] studied the correlation between the fatigue life of a laser weld and its J integral values. It can be used to predict the effects of geometric variables on the fatigue resistance of laser welds. The lap-shear configuration was used in this study. The methodology is based upon the fact that the fatigue behaviour is governed by fatigue crack

propagation. It was also concluded that the mechanism of crack growth of HAZ is striation growth.

#### *1.2.1.7.3 Corrosion and stress corrosion cracking resistance*

Very little work as been reported on the corrosion properties of laser welded aluminium alloys. Nevertheless, Braun *et al.* [45] studied the corrosion behaviour of butt welds of 1,6*mm* thick 6013-T6 sheets produced by LBW. The heat input during welding did not cause a degradation of the corrosion behaviour of the welds, as found in continuous immersion tests in an aqueous chloride-peroxide solution. In contrast to the 6013-T6 parent material, the weld zone was not sensitive to intergranular corrosion. Alternate immersion tests in 3,5% NaCl solution indicated high stress corrosion cracking resistance of the joints. For laser beam welded sheet, the weld zone of alternately immersed specimens suffered severe degradation by pitting and intergranular corrosion, which may be associated with galvanic coupling of filler metal and parent material.

### *1.2.1.8 Modelling*

Studies have shown that the laser welding process is very complex, including such phenomena as thermal conduction in a multi-phase system, fluid flow, gas dynamics, and plasma effects.

Residual stress measurement techniques have experimental and practical limitations: using non-destructive procedures, usually only the stress state on the surface of the structure can be determined, and even using destructive procedures, the whole three-dimensional stress field is difficult to evaluate accurately. Carmignani *et al.* [37] presented a work where the laser welding residual stresses and strains in a rectangular thick steel plate were investigated by means of a three-dimensional finite element analysis. The constitutive equations formulated are implemented by a fully implicit time-integration procedure. The resulting algorithm seems to be promising for the mechanical response simulation of the material subjected to high thermal transient loads.

Draugelates *et al.* [55] conducted heat transfer simulations and thermodynamic equilibrium calculations to study the laser welding of magnesium alloys. Theoretical studies for modelling LBW of magnesium alloys facilitate the development of model concepts which supplies a better understanding of the process involved. The analytical implementation of the models in simulation programmes allows a determination and quantification of the effect of process and material parameters on the welding result by means of parameter studies. A comparison of the numerical heat transfer simulations with thermodynamic equilibrium calculations revealed a good agreement. As a conclusion of this work it is possible to state that numerical simulations can give a considerable benefit for a better understanding of the LBW of magnesium alloys.

In a work by Bruggemann *et al.* [35] a comparison between thermographic process monitoring at LBW of metal materials and numerical simulated temperature distributions was carried out. In this work, essential process parameters like workpiece feed and beam power have been optimized by means of an analysis of numerical simulated and experimental determined temperature fields.

Dattoma *et al.* [56] evaluated by numerical simulation the residual stress state relaxation of a laser welded component subjected to cyclic external load. A numerical procedure, implemented by the ABAQUS code, carries out the residual stress field originated by a welding process and it is taken as a pre-stress condition in the simulations. The numerical model has been first implemented by a thermal and a subsequent structural analysis. The numerical results show a significant reduction in the initial residual stress level, even after the first load cycle. The subsequent cycles are not able to change the stress distribution.

Frewin *et al.* [33] presented a model of pulsed laser welding where the heat transfer and parametric design capabilities of the finite element code ANSYS were employed. While there are several models to describe the continuous wave laser welding process, due to the complexity of the laser material interaction process few models of pulsed laser welding exist. The model is capable to predict the transient temperature profiles and the dimensions of fusion and HAZ. With this work it was possible to conclude that temperature profiles and weld dimensions are strong functions of the absorvity and energy distribution of the laser beam.

Du *et al.* [57] presented a mathematical model for the flow simulation of full penetration LBW of titanium alloy. Until this model, all previous models were mainly focused on the study on the steel materials or aluminium alloys. In this model, the heat source comprises a plane heat source on the top surface and a cylindrical heat source along the z-direction, which takes into account the plasma effect and the keyhole absorption. A good agreement between the model and the experimental results for the geometry profile was found. The calculated results indicate that the metal flow is the main reason for forming the typical hourglass cross section profile. The used methodology for modelling of mushy region provided a simple way to deal with the pressure and velocity boundary conditions on the interface of phase transformation.

In a work by Chan *et al.* [58] the results of calculation using various heat source equations that have been proposed by other authors were compared to a prediction of a new model. The model developed treats the problem of predicting, by numerical means, the thermo-mechanical behaviour of laser spot welding for thin stainless steel plates. The presented model was designed to extend the capabilities of numerical analysis using the heat source equation over a wide range of process conditions. A three-dimensional model was used for the heat transfer analysis, this model was validated with experimental work. It was found that the finite element model using the proposed heat source equation can estimate the laser spot weld bead shape of the stainless steel sheets more

precisely than the precious models. Also, precise thermal analysis using the proposed heat source equation can be effectively used to analyze the thermal distortion and residual stresses.

Nègre *et al.* [51] presented a work where the fracture behaviour of different zones of a laser beam weld is investigated by means of numerical work and experimental work to verify the accuracy of the simulations. A micromechanical constitutive relation based on damage mechanics was applied to simulate crack growth in welded joints. All simulations were performed using the finite element code ABAQUS, including the Gurson-Tvergaard-Needlman model as a subroutine. The results obtained with this model were defined by the authors as encouraging.

Mahrle *et al.* [59] studied the influence of the fluid flow phenomena on LBW. They developed a mathematical three-dimensional model for the simulation of characteristic weld pool phenomena during deep penetration LBW based on a numerical solution of the conservation equations of energy, momentum and mass. This model in combination with the implemented solution enabled the computation of the local temperature on the fusion zone in agreement with experimental results.

### *1.2.2 Friction Stir Welding*

Friction Stir Welding (FSW), one of the major advances in welding technology in recent years, is a solid-state welding process developed and patented by the The Welding Institute (TWI) in 1991 [25]. It emerged as a commercial joining technique to weld high strength alloys that were difficult to join with the existing techniques. The process was developed initially for aluminium alloys, but since then FSW was found suitable for joining a large number of materials. It produces nearly defect-free welds for such demanding applications as space hardware at lower cost than conventional fusion welds. A potential field of application is aircraft structures where cost and weight can be reduced by using new joining techniques instead of riveting [26].
In March 2002, 67 non-exclusive licenses were held by organizations to use the process. Most of them are industrial companies, and several of them exploit the process in commercial production, [60]. They have filed more than 440 patent applications related to FSW up to that date, a number that is steadily increasing since then.
The FSW process will be presented in several sections. First an overview of the process is carried out, with references to advantages and disadvantages, type of materials that can be joined and applications.

#### *1.2.2.1 The process*

In the FSW process a non-consumable rotating tool, consisting of a shoulder and profiled probe or pin, is forced down into the joint line under conditions where the

frictional heating is sufficient to raise the temperature of the material to the range where it is plastically deformed, Figure 10.

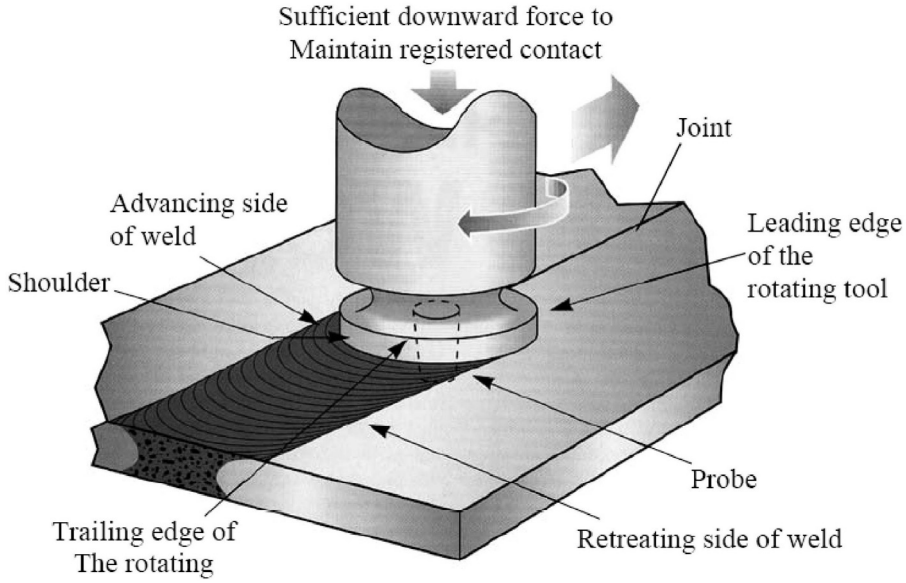


**Figure 10 - Schematic diagram of the FSW process, [61]**

The pin is typically slightly shorter than the thickness of the workpiece and its diameter is approximately the thickness of the workpiece. As the tool moves along the joint between the two components, the material is forced to flow from the leading edge to the trailing edge of the tool, and the material that flows around the tool undergoes extreme levels of plastic deformation. The shape of the tool promotes high hydrostatic pressure along the joint line, causing consolidation of the material plasticized due to heat generation. The workpiece has to be firmly clamped onto a backing bar and secured against vertical, longitudinal and lateral forces, which will try to lift them and push them apart. It is established that a gap of up to 10% of the sheet thickness can be tolerated. The probe height is generally slightly smaller than the workpiece thickness, and its vertical penetration into the workpiece is halted when the shoulder makes contact with the workpiece surface. A downward forging pressure from the shoulder helps to prevent the expulsion of softened material, in addition to providing supplementary frictional heating. Optimized welding parameters and clamping requirements were assessed by a large number of studies.
In this text, the different sides of the friction stir weld will be referred to as the advancing side when the rotational motion of the pin and its translation motion are in the same direction; the retreating side is the side in which the rotational motion is in the opposite direction to that of the translation motion.

*1.2.2.2 Advantages and disadvantages*

In general, FSW is claimed to produce stronger, lighter and more efficient welds than other joining processes, with the ability to join dissimilar materials, and materials previously thought to be un-weldable, or not recommended for fusion welding. As presented in [61], the major advantages of the FSW process are: the

absence of melting resulting in less weld contamination; no consumables; minimal edge preparation required; very controllable process with high productivity; high integrity welds with low shrinkage and little porosity; relatively simple process, with low running costs; fine grained microstructure in the weld region, leading to improved mechanical properties; low distortion and residual stress levels, compared to arc welding processes; environmentally friendly and relatively quiet process, with absence of fumes and spatter; no gas shielding required; able to join wrought to cast products; repeatable, resulting in less structural conservatism and possible over-design.
The current limitations of the FSW process are: welding speeds slower than those of some fusion welding processes; workpiece requires rigid clamping; backing bar required; keyhole at the end of each weld.
Mechanical properties of friction stir welds in aluminium alloys typically exceed those of arc welding, [62, 63]. Among the advantages of FSW is a decreased heat input relative to arc welds, which provides better mechanical properties as well as a decrease in distortion and residual stresses. The lower heat inputs also minimizes grain growth in the HAZ, [64]. Problems with hydrogen cracking and softening of the HAZ are eliminated since FSW is a solid-state process.

#### *1.2.2.3 Materials joined*

A wear resistant rotating tool is used to join sheet and plate materials using FSW. Although the process was initially developed for joining aluminium alloys, it is now used on a wide variety of materials, including: aluminium and its alloys; aluminium-based metal matrix composites; copper and its alloys; titanium and its alloys; magnesium alloys; lead; zinc; steels; plastics. As it is a solid phase process, FSW permits joining of materials that cannot be welded with conventional fusion welding process, such as aluminium-lithium alloys [60]. Dissimilar aluminium alloys can also be joined (5000 to 6000 or even 2000 to 7000). Aluminium alloys in the thickness range of 1,2 to 75$mm$ can be joined by FSW without shielding gas or filler material.

Recent developments in tool materials and design now make possible FSW of steel alloy, [63, 64]. In a study by Lienert *et al.* [64] a DH-36 steel was friction stir welded. Acceptable tensile properties with no measurable tool wear were found. The inadequate tool design lead to the existence of lack of bonding defects. Although with an optimized tool design FSW of DH-36 steel appears feasible.
In another study Lienert *et al.* [63] demonstrate the feasibility of FSW of a mild steel (hot-rolled AISI 1018 mild steel).

Preliminary investigations have established that the FSW technique can be applied to titanium and its alloys being capable of producing rapid, a cost-effective and technically simple method capable of producing rapid, high quality welds in titanium alloys. FSW of titanium alloys is still under development and the process is not optimized for high performance aerospace welds, John *et al.* [65].

A current TWI project aims to develop the process to a point where it can be considered for industrial use. Initial studies have been carried out on Ti-6Al-4V, but they intend to investigate other alloys in due course. Although the main interest in these alloys stems from the aerospace industry, producers of oil pipelines and offshore platforms would like to use friction stir welded titanium alloys for applications where extreme corrosion resistance is required, [61].

#### *1.2.2.4 Types of machines*

The first friction stir weld was manufactured in a conventional milling machine with automatic feed. To ensure weld quality a constant download force of the tool and over-loading due to unexpectedly high process forces lead to the development of special FSW machines, [66].

The Institute for Machine Tools and Industrial Management of the TU München is pursuing the approach of using a cost-favourable Computerized Numerical Control (NC) milling machine. To use milling machines for the manufacture of high-quality welds, it is necessary to have tool cooling, force measurement and display as well as force-controlled welding. The greatest downward force arises when the tool is immersed into the still cold joining members; this observation provides the basis for the sensible utilization of modern milling machines in FSW. The rapid increase in force can be moderated using a shorter plunging advance and the pre-drilling of the plunging point. This makes it possible to use a milling machine with smaller dimensions for carrying out the joining process with the same welding parameters and workpiece thickness as in the case of a special machine. The risk of damaging the machine tool as a result of impermissibly high advance forces is practically ruled out with NC milling machines since any overloading of the drives is monitored by the machine controller. Building upon capabilities of the NC milling machines, it was possible within a relatively short time to implement the force display and force measurements functions.

ESAB has developed the SuperStir machine. The equipment has a gantry type design with a welding area of 8x5$m$ and two heads of different sizes. The first head is used for welding thin sheets with high rotation speeds. The second head can be used for thick sheets while applying high downward forces. Until 2001, up to 16$m$ long SuperStir machines have been designed, built and commissioned by ESAB since 1996. A PowerStir machine was developed by Crawford Swift and is used for fabricating prototype aluminium wings and fuselage skins for aircraft.

#### *1.2.2.5 Joint design*

In addition to relatively straightforward butt and lap welds, it is also reported that annular or circumferential joints can be produced by rotation of the workpiece underneath the probe [67, 68]. A number of friction based technologies have been developed that enable the friction processes to be applied to a range of components shapes and products. For example non-rotary, orbital, linear and

angular reciprocating motions have enabled the friction process to be applied to a variety of non-round components. CNC (Computerized Numerical Control) and robots can be used for both non-linear and three-dimensional joints. An obvious advantage of a solid state welding process is the absence of gravitation effects, thereby facilitating its use in all positions, namely, horizontal, vertical, overhead, and orbital [66-68]. The FSW process can also be used to weld materials of different thickness, dissimilar materials, and can be used to join cast or extruded products to sheet material. FSW can also be used to make repair welds, with robotic systems offering the opportunity to effect repairs off-line to avoid disruption to the production process.

#### *1.2.2.6 Applications*

In the work of Harris *et al.* [61] a list, compiled by TWI, of industries to whom the FSW process is attractive is presented. Most of these industries have the process already implemented. The various sectors identified are shipbuilding and marine, aerospace and aeronautical, land transportation - road and rail; construction, electrical, and others. For each sector a list of possible applications of the FSW process is also presented. The first commercial application of FSW concerned the manufacture of hollow aluminium panels for deep freezing of fish boats.

Among these sectors, the aeronautical will be emphasized in this dissertation. Possible applications for FSW in this sector are wings, fuselages, empennages, cryogenic fuel tanks for space vehicles, aviation fuel tanks, external throw-away tanks for military aircraft, military and scientific rockets, repair of faulty MIG welds.
FSW would appear to be the ideal process to replace bolted and riveted joints in aircraft construction, with obvious advantages in terms of weight saving and lower production costs. FSW is used in the fabrication of the structural wing and fuselage members of the Eclipse 500 jet aircraft [69]. With this technique approximately 65% of the previously riveted joints could be replaced, representing a weight saving of over 23$kg$, or equivalent to an extra 50 nautical miles in flight. The speed of fabrication is also greatly enhanced, with the FSW joints being made an order of magnitude faster than a manual riveting procedure. The projected savings from adopting FSW are estimated to be between $\$$50000 and $\$$100000 per plane [70].
FSW is the most recent upgrade to the Space Shuttle's external tank, [71]. In 1993, NASA challenged Lockheed Martin Laboratories to develop a high-strength, low-density, lighter-weight replacement for aluminium alloy 2219 used on the original Space Shuttle External Tank. A new alloy known as Aluminium Lithium Al-Li 2195 was developed, which reduced the weight of the External Tank by 3402$kg$. The FSW process produces a joint stronger than the fusion arc welded joint, obtained in the earlier Light Weight Tank program.

*1.2.2.7 Tool design*

At the heart of the FSW process is the design of the welding tool. Early in the development of FSW it was realized that the form of the welding tool was critical in achieving sound welds with good mechanical properties. Although there is still much proprietary information on the design of tools, the fundamentals of tool design and the functions of each part of the tool are now well established.
The FSW tool, which moves along the joint between two components, is generally made with a profiled pin, which is contained in a shoulder with a larger diameter than that of the pin (Figure 11). Tools with specially profiled pins and optimized shoulder designs have been developed at TWI and are now being used in industrial applications [26].
The FSW tools are manufactured from a wear resistant material with good static and dynamic properties at elevated temperature. They are designed to permit up to $1000m$ of weld in $5mm$ thick aluminium extrusions without being changed.
In the early days of the FSW process, the tools were very simple and usually consisted of left or right handed threads based on. As an example of new tools, TWI developed tools like the Whorl and Triflute [26, 61, 67]. These new tools aim to improve the welding process and extending of the weldable thickness range for aluminium alloys, Figure 11.

Prototype Whorl tool

Prototype Triflute tool with three flutes and a helical ridge around the flutes' lands

**Figure 11 - FSW tools examples, [26].**

In these tools, instead of using a cylindrical pin, a probe can be used (the more generic term probe includes for example truncated cones, non-round cross sections, conical spirals and whisks). The shoulder profile of these tools is designed to provide better coupling between the tools shoulder and the workpiece. The aim is to prevent plasticized material from being expelled.

The Whorl concept provides for non-circular probe cross-sections. In this way, the probe displacement volume is less than its volume of rotation, to enable the easier flow of plasticized material.
The Triflute family is constituted of the MxTriflute for butt welding and the Flared-Triflute with tip profiled for lap welding.
The MxTriflute are multi-helix tolls. They have an odd number of relatively steeply angled flutes and incorporate a coarse helical ridge around the flutes land.

These reduce the tool volume further and therefore aid material flow and to break-up and disperse surface oxides. This tool is even more complex in appearance, being frustum-shaped, with surface triflutes enveloped by an outer, coarser helical ridge or thread, which, it is claimed, ensures adequate working of the weld line material, and facilitates a better control of the material flow. For lap welding, the Flared-Triflute has been developed to provide a wider region and also to help avoid problems associated with upper plate thinning at the lap weld interface. In this welds the width of the weld interface and the angle at which the notch meets the edge of the weld is of major importance, especially for those application that are subjected to fatigue.

#### *1.2.2.8 Heat flow into tools*

Dickerson *et al.* [72] calculated the transient heat losses into FSW using experimental welding data and thermal modelling. In FSW the welding efficiency is reduced by the heat that is conducted into the welding tool. Constant temperature boundary conditions based on experimental observations were used in the weld tool models. The comparison of these results with experimental results obtained by the tempering colours observed showed good agreement. It was found that for FSW of light alloys using a solid steel tool, in the steady state welding, 10% of the heat generated is lost through the tool. In short welds the loss can be 20% or higher. They concluded that using tools with grooves cut into the shank the heat loss decreases, increasing the process stability.

#### *1.2.2.9 Material flow*

Although significant effort has been expended in putting FSW to use in full scale production the material flow during the process is not fully characterized. To improve the knowledge of this technology several studies on material flow have been published, some of them being discussed here.
Experimental techniques have been developed to allow the investigation of metal flows during FSW. The techniques are based on the use of a marker material that is re-distributed during welding.
In the work published by Seidel *et al.* [73] the material flow is visualized using a Marker Insert Technique. This technique consists in placing marker inserts in the weld path in a manner that the marker can be detected after welding. This marker needs to have similar mechanical properties as the base material and should have significant different metallographic etching characteristics. A scheme of the technique is shown in Figure 12.

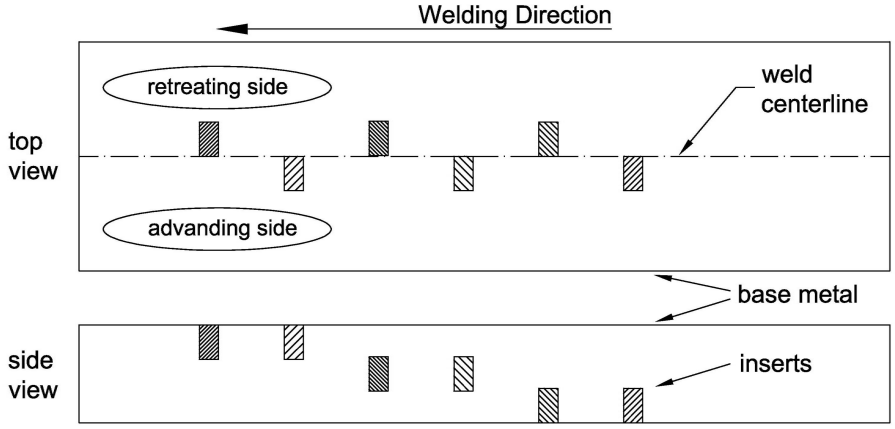


**Figure 12 - Schematic drawing of marker insert placement, [73].**

The inserts were placed on the advancing and retreating side at three different heights. From the final position of the markers it was concluded that the bulk marker material was moved to a final position behind its original position and only a small amount of the material on the advancing side was moved to a final position in front of its original position. No material was transported further backwards than one pin diameter behind its original position. It was verified that material from the retreating side was transported along with the rotating tool to the advancing side and parts of it even to a position in front of its original position. From the analysis along the height it was found that the material inside the pin diameter is pushed downwards on the advancing side and moved upwards in the retreating side. This phenomenon is referred as a vertical circular motion. Three-dimensional plots of the deformed marker provide a good qualitative characterization of the material flaw of friction stir welds.

To validate this experimental work, in a work by Seidel *et al.* [73] the FSW process was simulated with the commercial software Computational Fluid Dynamics FLUENT. The process was modelled as a two-dimensional, steady state, and laminar fluid flow past a rotating cylinder. The base material was treated as a fluid at elevated temperatures. A non-Newtonian power law viscosity function, which is calculated on experimental flow stress data, describe the material flow properties. This two-dimensional simulation was able to predict the material flow in a cold weld at middle heights. Since the amount of vertical mixing is very small in a cold weld, the material flow is nearly two-dimensional in a sufficient vertical distance to the tool shoulder. Figure 13 shows the comparison between the predicted and experimental results. Since the two-dimensional model was unable to predict the influence of the shoulder on the flow, a three-dimensional model has to be developed to simulate the influence to the real tool geometry.

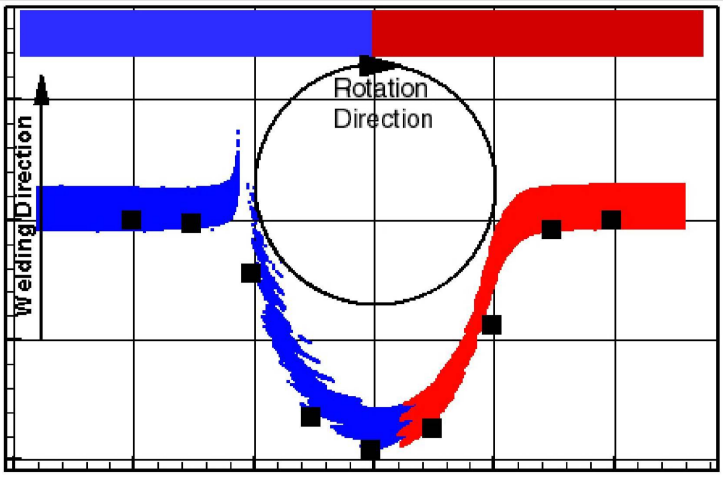


**Figure 13 - Comparison of predicted (black squares) and experimentally (red and blue marker) observed flow pattern in FSW. The markers of advancing (blue) and retreating (red) side are displayed in the undeformed and deformed stage. [73]**

In another work, Dickerson *et al.* [74] used copper strips (0,1$mm$ thick) as markers. The aim was to investigate the marker movement using various techniques: radiography, tomography and metallurgical sectioning. It was found that the copper did influence some of the welds. The analysis techniques tested could easily detect the copper markers. It was also concluded that if the markers are placed in the top third of the joint line it is possible to get information about the through thickness flow.

Guerra *et al.* [75] investigated the flow of metal during FSW using a faying surface tracer and a pin frozen in place during welding. His work shows that the material is transported by two processes. The first is a wiping of material from the advancing front side of the pin onto a zone of material that rotates and advances with the pin. The material undergoes a helical motion within the rotational zone that rotates, advances, and descends in the wash of the threads on the pin and rises on the outer part of the rotational zone. After one or more rotations, this material is sloughed off in its wake of the pin, primarily on the advancing side. The second process is an entrainment of material from the front retreating side of the pin that fills in between the sloughed off pieces from the advancing side. It was found that the material transported by these two processes has very different thermo-mechanical histories and properties.
This work concludes that there is a large vertical or vortex movement of material within the rotational zone caused by the wash and backwash of the threads. Material entering this zone thus follows an unwound helical trajectory formed by the rotational motion, the vortex flow, and the translational motion of the pin.

### *1.2.2.10 Metallurgy*

The FSW process is now being commercially used in a wide range of applications despite the fact that for many alloys the metallurgy of the welded joint is still not fully understood. The first attempt at classifying microstructures in aluminium alloys was made by Threadgill [76], and subsequently revised [77] when it became

apparent that the microstructural changes in aluminium alloys were not replicated in most other metallic materials. A cross section of a friction stir welded joint can be divided into several distinct regions (Figure 14): Unaffected Material - A; Heat Affected Zone (HAZ) - B; Thermo-Mechanically Affected Zone (TMAZ) - C; Weld Nugget - D.

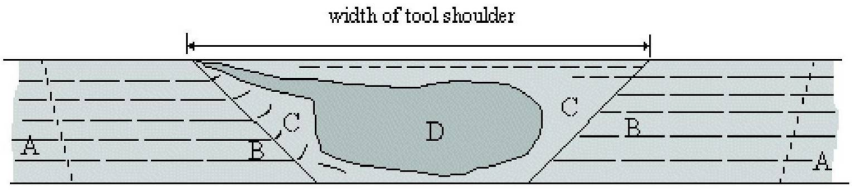


**Figure 14 - Distinct regions of the weld zone, [77].**

Unaffected material

This is material remote from the weld, which has not been deformed, and which, although it may have experienced a thermal cycle from the weld, is not affected by the heat in terms of microstructural or mechanical properties.

Heat Affected Zone

In this region, which lies closer to the weld centre, the material has experienced a thermal cycle that modified the microstructure. There is no plastic deformation in this area. In aluminium alloy friction stir welds, this zone is susceptible to corrosion problems.

Thermo-Mechanically Affected Zone

In this region, the material has been plastically deformed by the FSW tool, and the heat of the process also influences the material. In aluminium alloys this leads to a region of partially recrystallized grains in which many of the fibrous grains, which are normally aligned in the rolling direction, are rotated. This can be very dangerous as the newly aligned high angle grain boundaries can be susceptible to stress corrosion cracking. In other materials, the distinct recrystallized region (weld nugget) is absent and the whole of the TMAZ appears to be recrystallized. This appears in materials such as pure titanium, b titanium alloys, austenitic stainless steels and copper which have no thermally induced phase transformation, which would induce transformation in the absence of strain. In materials such as ferritic steels, the understanding the microstructure is made more difficult by the thermally induced phase transformation, and this can also make the HAZ/TMAZ boundary difficult to identify.

Weld Nugget

The centre of the weld, commonly referred to as the 'nugget zone', consists of a very fine grained, 1-10$\mu m$, microstructure. The majority of the grain boundaries within the nugget zone are high angle (misorientation between grains being greater than $15^{o}$), and are believed to be formed through dynamic

recrystallization during the stirring process. The width of the nugget zone depends on the combination of tool design, welding parameters, and alloy composition. It is suggested that this area is treated as a separate sub-zone of the TMAZ.

Svensson *et al.* [78] presented a detailed assessment of the microstructure of friction stir welds in two aluminium alloys: 5083 (a non-hardenable alloy) and 6082 (a precipitation hardening alloy), using electron microscopy. These alloys are mostly used in the marine sector and usually welded in a process called "friction super stir welding" developed by ESAB AB.
It was found that there is a large difference in the welding speed attainable with the two alloys. Alloy 6082 could be welded much more rapidly than 5083 for the same plate thickness. Alloy 5083 had relatively uniform grain size, slightly elongated in the rolling direction, alloy 6082 contained two sizes of grains, owing to partial recrystallization. The general microstructure of the welds was in good agreement with previously published investigations: the grain size of the nugget zone was ~10$\mu m$ in both alloys. The welding affected the particles appearing in the material. Very fine particles, which to a large extent control the hardness of 6082 alloys, dissolved in the nugget and transformed to a non-hardening type of particle where the minimum hardness was observed.

Oertelt *et al.* [79] investigated the microstructure in a friction stir welded aluminium alloy 2195. The microstructure was analyzed in the as-welded and post-weld thermal cycle conditions. As-welded microstructure the macrograph indicates three distinct regions of the weld: Dynamically Recrystallized Zone (DXZ), TMAZ and HAZ, Figure 15.

**Figure 15 - FS welded AA2195, [79].**

The macrographs shows the lack of symmetry along the centreline of the weld, which is attributed to the nature of the plasticized metal movement around the tool. Recovered and heavily dislocated grains coexist next to each other. There is the presence of small precipitates within the grain and long grain boundaries that are either rich in copper alone or in both copper and iron. With post-weld thermal cycling, hardness in the DXZ decrease. The average dislocation density in these regions is qualitatively less than that in the as-welded condition. There are small precipitates containing silver, as well as composite copper-rich precipitates containing a silver-rich phase, along the grain boundaries. The precipitates fractions increased with thermal cycling.

Jata *et al.* [80] tried to develop a basic understanding of the evolution of microstructure in the DXZ region and relate it to the deformation process variables of strain, strain rate and temperature. The material used consisted of a friction stir welded plate of an Al-Li-Cu alloy. In this analysis was found that

FSW gave rise to noticeable microstructural changes. The deformation in the TMAZ resulted in severe bending of the grain structure. In contrast, the microstructure within the weld nugget in which DXZ occurred consisted of grains which where much smaller and equiaxed when compared to the severe-elongated and pancake shaped parent metal microstructure. In the DXZ microstructure of the weld nugget some grains were left with dislocation tangles at the boundaries suggesting that recovery or/and recrystallization may not been completed.
During FSW, the original grain and subgrain boundaries appear to be replaced with fine, equiaxed recrystallized grains in the weld nugget. It is unlikely that dynamic recrystallization occurred via a discontinuous process; it appears that a continuous dynamic recrystallization (CDRX) process was operative. The process that appears to explain the present observations is the dislocation-glide-assisted-subgrain-rotation model. In this model, dislocation glide gives rise to a gradual relative rotation of adjacent subgrains.

Rhodes *et al.* [81] have conducted a study to evaluate the microstructural changes by FSW of a 7075 aluminium alloy. The parent 7075-T6 plate exhibits elongated matrix grain morphology. There are two populations of strengthening precipitates: the larger tend to be oriented in the rolling direction of the plate; the smaller were too small for diffraction analysis. The weld nugget is characterized by concentric flow lines which represent plastic deformation increments that develop as the rotating tool pin moves through the joint. Unlike the parent metal, the weld nugget has a recrystallized, fine equiaxed grain structure. In contrast to the parent metal, the dislocation density of the weld nugget is quite low. The recrystallization of the weld nugget grains and the redistribution of the precipitates indicate that the temperature excursion during joining as above the solution temperature for the hardening precipitates, but below the melting point of the alloy. The transition between the parent and the weld nugget is characterized by a highly deformed structure. The elongated grains of the parent metal have been deformed in a flowing pattern around the nugget. These grains have not recrystallized, as occurs in the weld nugget. This 7075 alloy is difficult to weld with typical welding techniques; nevertheless FSW provides a method for joining without introducing a cast microstructure.

Benavides *et al.* [82] published a study comparing the residual grain size and microstructure in a 2024 aluminium alloy friction stir welded at room temperature ($30^{o}C$) and low temperature ($-30^{o}C$). It was found that the weld efficiency declines appreciably at low temperature, and also that the actual weld zone shape and size decreases with temperature. This narrowing of the weld zone was reflected on microhardness tests. Comparing the recrystallized grain structure near the top and the bottom of the weld centre line it was found that there is an increase in the weld zone equiaxed grain size from the bottom to the top, but in the low temperature the difference is smaller from bottom to top. The grain size is considerably smaller in the low temperature weld.

Sutton *et al.* [83] presented a detailed study of the variations in microstructure in a 2024-T3 aluminium friction stir welded joint. It was observed that the nugget has a refined microstructure. At the edge of the welding tool pin an abrupt

transition from highly refined, equiaxed, grains comprising the nugget to deformed base metal grains occur. At a location corresponding to approximately the tool shoulder radius on the advancing side relatively coarse, recrystallized grain structure is observed. Banded structure appears most pronounced near the mid-thickness of the weld. These banding results from the alternating regions of high and low particle density, the band spacing corresponds to the welding tool advance per revolution. This implies that homogeneity of the microstructure can be modified by changing the welding parameters. It was found that the fracture path is strongly influenced by the microstructure. During the early stages of crack growth under mixed-mode loading, fracture propagates along particle-rich bands. As the cracks growth along the bands and the direction of the band changes, it is conjectured that the reduction in tensile stress perpendicular to the bands eventually becomes inconsistent with crack growth in the bands under the applied loading. At that point, the fracture path transitions and the fracture occurs along a path that stays within the FSW and near the advancing side of the FSW.

Liu *et al.* [84] used light metallography (microscopy) and Transmission Electron Microscopy (TEM) to characterize the microstructure of a friction stir welded 6061-T6 aluminium alloy. It was found that the frictional heating is greater near the top surface (250$^{o}C$). This effect is shown by hardness measurements as a slight softening relative to the weld zone base. There was also softening throughout the weld zone compared to the workpiece hardness even though the average grain size is reduced by a factor of 10 (characteristic of dynamic recrystallization). The TEM analysis suggests that although there was a reduction in the grain size by dynamic recrystallization, there is a reduction in dislocation density. Complex precipitation phenomena associated with transition zone extending between the workpiece and the actual weld zone was found.

Flores *et al.* [85] investigated a compositionally modified 1100 aluminium alloy forming a stable microdendritic (second-phase), equiaxed cell structure that was friction stir welded. Friction stir welds in as-cast and as-cast-and-50% cold-rolled alloy plates produced a DXZ weld zone with homogeneously re-distributed precipitates or second phase particles due to the severe plastic flow. Results indicate that the workpiece microstructure has an insignificant effect on the FSW process in contrast to the tool rotational speed.

Lienert *et al.* [63] studied the microstructure of a stir welded mild steel. The weld area displayed several microstructurally distinct regions including the stir zone along the weld centreline, the HAZ surrounding the stir zone, and the base metal. Unlike welds on aluminium alloys no distinct TMAZ was identified in the steel welds. Comparison of metallographic from the weld stir area and the remainder of the weld show a greater number of composite structures of Mo formed in early stages of mechanical alloying in the weld start are, suggesting high transfer and mechanical mixing of tool material with material from the workpiece. Extrapolation of measured temperatures of the stir zone exceed 1100$^{o}C$.

Yang *et al.* [86] carried out a metallurgical analysis on banded microstructure in aluminium 2024-T351 and aluminium 2524-T351 aluminium friction stir welds. In both alloys FSW zones was identified a band structure. These bands indicates the presence of periodic variations in the size of equiaxed grains, microhardness and concentration of base metal impurity particles that correlate with the observed band spacing. Even though particle segregation is less evident in 2524, the microhardness measurements show variation across the bands in both alloys, suggesting that refinement and redistribution of secondary particles are not the primary source of bond to bond variation in microhardness.

#### *1.2.2.11 Monitoring*

Monitoring the FSW process has become important since this joining technique rapidly expanded its application. Chen *et al.* [87] carried out a research to find an in-process sensing technique that allows for real-time monitoring of the tool condition and product quality. They conducted the first study on the use of Acoustic Emission (AE) technique to monitor FSW process. Wavelets with an order six are used to decompose the signals. Due to the fast response and high signal-noise-ratio, the AE signals can play an important role in the on-line monitoring of the FSW process. There are significant sudden changes in the band energy at the moment when the probe penetrates into and pulls out of the weld joint, as well as when the shoulder makes contact with or detaches from the plates. The band energy variation during the traversing of the tool over the defected region reflects the existence, location, and size of the weld defects. A three-dimensional representation of band energy *vs.* time and scale gives valuable information on the potential weld defects during friction stir welding.

#### *1.2.2.12 Joint properties*

##### *1.2.2.12.1 Hardness profiles*

Hardness profiles have been made across friction stir welds for several aluminium alloys. As already mentioned, the profiles are extremely useful, as they can assist in the interpretation of the weld microstructure and mechanical properties. The exact shape of the weld profile depends on the alloy type being welded, and the processing conditions.

Leal *et al.* [88] studied the effect of the weld travel speed on the defects formation and on changes in the hardness profiles of the friction stir welds in alloys 5083-O, 2024-T3 and 6063-T6. In the 6063-T6 alloy hardness drastically decrease in the weld-deformed zone, but alloys 2024-T3 and 5083-O have hardness respectively identical and superior to that of the parent material. The increase of travel speed increases the plastic flow speed and the grade of dynamic recrystallization is lower than for lower travel speeds. The increase in welding speed produces the strain hardening of the material which causes reduces the in plastic capacity. The heat developed by friction may not be enough to compensate this hardening and

the plastic deformation happens in the grain boundary occasioning the appearing of cracks in the zone. Defects tend to form only in alloys 5083-O and 2024-T3. These defects tend to form on the advancing side. The increase of the weld travel speed augments the frequency of defects formation and the increase of the axial force changes its position from the surface to the centre of the weld.

A study of a non-heat treatable alloy such as the 5083 was conducted by Svensson *et al.* [78]. The hardness profile was found to be practically constant across the weld (Figure 16a)). For this type of alloy, the main strengthening mechanism is through deformation hardening and the build up of high dislocation densities in the deformed microstructure. Analysis of the microstructure confirmed that the dislocation density of the base material was low. Although the nugget zone had undergone a considerable amount of deformation, the final microstructure was recrystallized, and so the dislocation density in the weld nugget was also low, leading to the uniform hardness profile.
In the same study, it was found that for heat treatable aluminium alloys such as 6082, the microstructure of the base alloy and weld zone are very different, leading to variations in hardness across the weld, Figure 16b). For this alloy, the average hardness of the nugget zone is significantly lower than the base alloy. Furthermore, there is a region either side of the nugget zone corresponding to the HAZ which has an even lower hardness. For alloys such as 6082, the main strengthening precipitate is ($Mg_5Si_6$) which is stable at temperatures >200*ºC*. In the friction stir weld, the peak temperature in the HAZ is expected to be approximately 350ºC, and so on heating, the ($Mg_5Si_6$) precipitates dissolve. The small $Mg_{1,7}Si$ precipitate are formed on cooling. They have less of a strengthening effect which gives a much smaller contribution to strength and hardness. It has also been suggested that the difference in grain size between the weld nugget and the HAZ could account for the difference in hardness between the two zones, although this has yet to be confirmed.

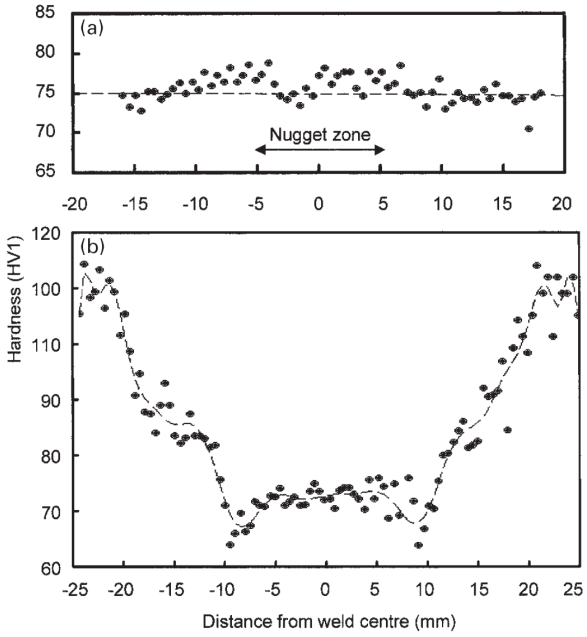


**Figure 16 - Hardness profiles: a- AA5083; b- AA6082. [78]**

Sato *et al.* [89] have conducted a study to confirm the use of FSW for ultrafine grained materials by using the aluminium alloy 1100 produced by Accumulative Roll-Bonding (ARB). Due to grain refinement induced by ARB the hardness of the material increased from 30*HV* to 85*HV*. Figure 17 shows the Vickers hardness profile across the stir zone of the friction stir weld of the ARB material and the starting material. It should be noticed that only the stir zone of the starting material and the ARB material have the same hardness. FSW results in a decrease of hardness in the ARB material and an increase in the starting material. Gas tungsten arc welding of the ARB material was attempted and resulted in a hardness of 30*HV*. This suggests that FSW is a much more favourable process for retention of high hardness in ARB material than a conventional fusion welding.

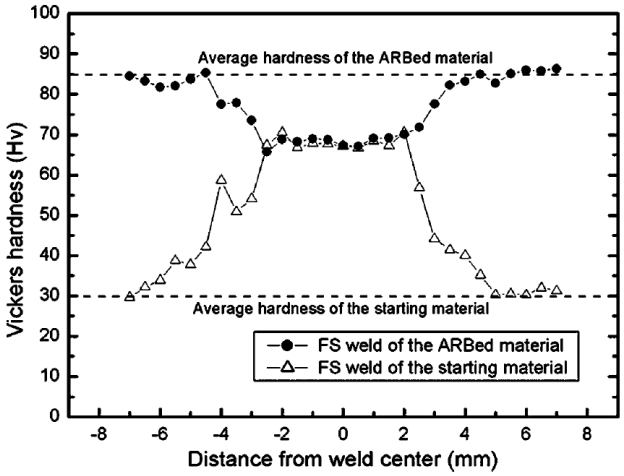


**Figure 17 - Vickers hardness profiles across the stir zone in the FS welds of the ARB and starting materials, [89].**

Lienert *et al.* [63] studied the hardness of a friction stir welded mild steel. The hardness of the parent material was 135*HV*, while the hardness of the stir zone ranges from 155*HV* to 175*HV*. Hardness decreases with increasing distance from the stir zone from approximately 150*HV* to 160*HV* in the grain coarsened region to between 135*HV* and 140*HV* in the base metal.

Ericsson *et al.* [90] compared the hardness profile of joints welded by FSW, Metal Inert Gas (MIG) and Tungsten Inert Gas (TIG). Joints of aluminium alloy 6082 welded at two different weld speeds were investigated. The results are presented in Figure 18. For FSW, T6 hardness drops in the HAZ due to distortion and growth of precipitates, being the minimum 70*HV* reached around the weld/HAZ border for the high speed specimens. It was verified that the width and depth of the HAZ are larger for the low speed specimens. The MIG pulse welded specimens have a higher hardness decrease in the weld than the FSW specimens; occurring the minimum value of 60*HV* in the centre of the weld. The hardness decreases at the beginning of the HAZ followed by a small increase and after that another decrease appears in the area closest to the joint line. In the TIG welded specimens a HAZ with a slightly larger width than that of MIG was produced because it has a higher heat input per unit length.

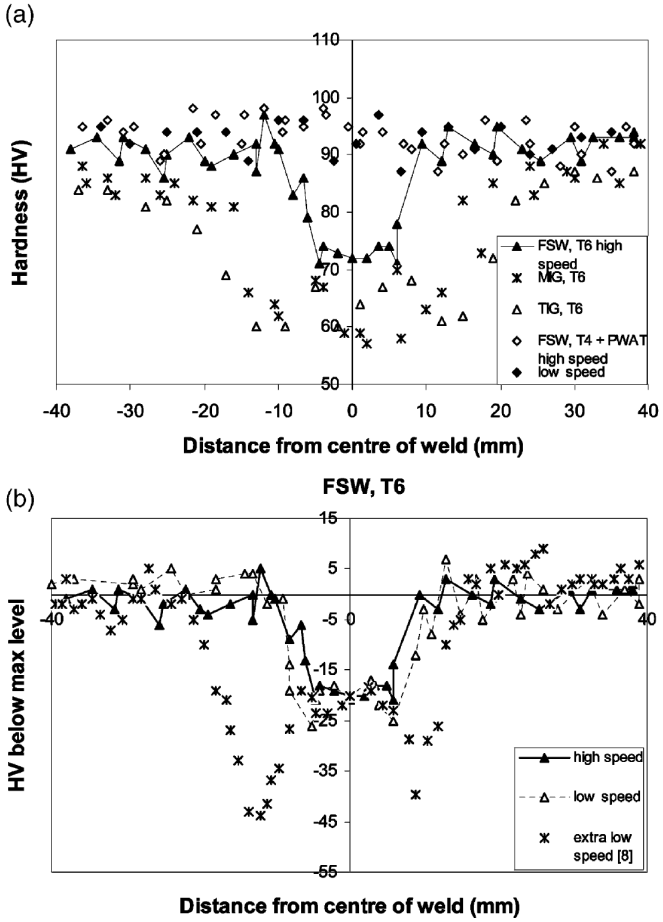


**Figure 18 - (a) Vickers hardness of AA6082, FSW, MIG-pulse and TIG welded. Advancing side to the left for FSW specimens. (b) Hardness below maximum level of AA6082 T6 FS welded with high, low, and extra low welding speed. [90]**

*1.2.2.12.2 Residual stress measurements*

Since FSW is a low temperature welding process compared with other techniques, it is believe that residual stresses are low in these weldments.
In a comprehensive study of the development of residual stresses by Donne *et al.* [91], 4$mm$ thick aluminium alloy sheets 2024-T3 and 6013-T6 friction stir welded, X-rays (10$\mu m$ penetration depth in aluminium) were used to determine the residual stresses within the weld surfaces, while high energy synchrotron radiation and neutrons (10$\mu m$ penetration depth in aluminium) measured the stresses developed within the bulk of the weld. The SIF due to residual stresses was determined directly with the so called "cut compliance method" (strain change due to the progression saw cut measured by a strain gage). The cut compliance method delivers the residual stress as a SIF, suitable for direct use in fracture mechanics studies. The results of the investigations show an inhomogeneity in the residual stress distribution in the three principal directions. In longitudinal and transverse direction, diffraction methods yield an "M" form stress distribution, with a small compressive residual stress measured in the weld seam, and tensile residual stresses in the TMAZ and HAZ regions.

The maximum values of the tensile residual stresses are located in the HAZ, but then they fall quite quickly, with small compressive stresses observed in the parent plate adjacent to the HAZ. It was found that the maximum residual stresses, independent on the pin diameter, welding speed and rotational speed of the tool, were higher in longitudinal direction than in transverse direction. Residual stress levels were found to be dependant upon the probe diameter and rotational speed, and the welding speed. Larger probes inevitably produce an increased TMAZ, with a consequent movement of the peak tensile residual stresses away from the weld, whilst the stresses decrease with decreasing probe rotation speed and welding speed due to lower levels of frictional heat, and an increased time for heat transfer into the adjacent parent material. In addition to a reduction in the tensile residual stresses, a widening of the HAZ was also observed. For all test conditions the residual stresses were found to be higher in the longitudinal direction rather than the transverse direction. An example of the results obtained by Donne *et al.* [91], Figure 19 shows the residual stress distribution in the longitudinal direction function of various welding parameters.

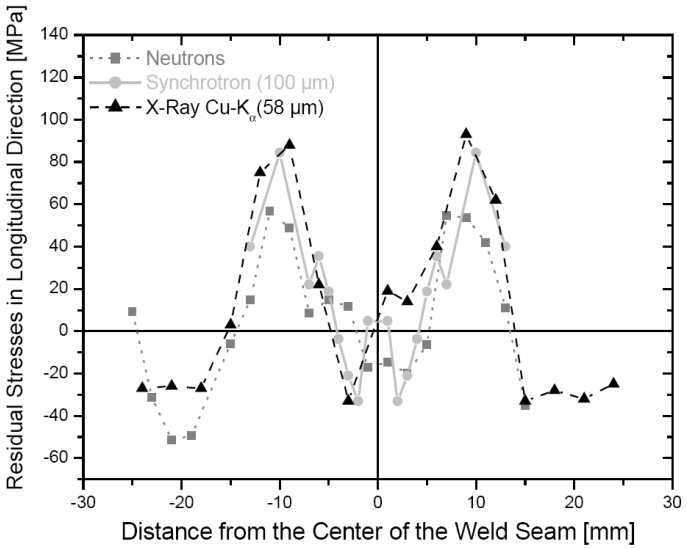


**Figure 19 - Residual stresses distribution along the weld of a FS welded 6013-T4 sheet determined with different measurement methods. Welding parameters: rotational speed 2500*min*$^{-1}$; welding speed *1000mm* $s^{-1}$; shoulder diameter 15*mm*. [91]**

Staron *et al.* [92] presented a study of the influence of a coolant applied during welding of aluminium sheets on the residual state of the FSW joint. Liquid $CO_2$ coolant was applied near the weld seam for rapid cooling of the weld zone, which introduces a thermal tensioning effect counteracting the forces which lead to residual stresses and distortion. The residual stresses across the weld were measured by neutron diffraction. This technique decreased significantly the magnitude of the tensile residual stress in the centre of the weld and produce beneficial compressive stresses. This beneficial effect does not extend into the HAZ, where tensile stresses were still present.

John *et al.* [65], present a comprehensive study conducted on near-threshold fatigue crack growth in friction stir welded aluminium alloy 7050-T7451 and a titanium alloy Ti-6Al-4V. Tests were conducted on weld coupons as a function of

specimen geometry (compact tension, eccentrically loaded single edge and centre-crack tension) and stress ratio to understand the effects of residual stresses in the HAZ of the alloy. Crack growth rates in the weld regions were characterized using edge crack (compact tension and eccentrically loaded single edge) and centre-crack configuration. The crack growth results show that residual stresses play a key role in the crack growth parallel to the weld path in the HAZ. Although FSW introduces low residual stresses, this study shows that near-threshold fatigue crack growth along the weld can still be significantly affected by residual stresses. In general, the magnitude of the shift in the fatigue threshold in the friction stir welded coupons is a function of microstructure, residual stresses and specimen geometry. However, for a constant microstructure, fatigue thresholds at low stress ratios, were specimen geometry dependent. The thresholds were either higher or lower than those of the parent material. At high stress ratio, the differences due to the specimen geometry vanish. Stress ratio studies show that the centre crack tension geometry is less sensitive to the residual stress effects compared to the compact tension geometry.

*1.2.2.12.3 Tensile Properties*

Aluminium alloys

Cross sample tensile tests have been performed on several aluminium alloy friction stir welds.
For aluminium alloy 5083 welds, the tensile strength varied between 303$MPa$ and 344$MPa$ depending on plate thickness and welding speed. In this alloy, fracture was found close to the centre of the weld. The fracture surface in general was inclined at 45°. At the root side the fracture surface was very close to the original joint line, [78]. For aluminium alloy 6082, the tensile strength varied between 226$MPa$ and 254$MPa$. In this alloy fracture never occurred close to the original joint line. Instead it occurred mostly close to the line where the shoulder of the tool had touched the top side of the weld.

In a work on root flaws in friction stir welds carried out by Dickerson *et al.* [93] it was found that flaws in friction stir welds did not influence the tensile properties compared to flaw-free welds of aluminium alloys 5083-O and 6082-T6. It suggest that in these alloys root flaws welds can be considered insignificant when compared to unflawed welds. But testing aluminium alloy 5083-H321 showed that root flaws influenced the ultimate tensile strength.

Liu *et al.* [94] have conducted the first study on FSW of the heat-treatable 2017-T351 aluminium alloy. It was found that for every revolutionary pitch tested the tensile properties are lower than those of the base material. When the revolutionary pitch is greater than 0,13$mm/rev$, all the tensile properties dramatically decrease to considerably low levels. This indicates that, also in this alloy a softening effect has occurred, and the softening level is affected by the welding parameters. Studying the fracture location was found that as the revolutionary pitch increases, the fracture location of the joint gradually

approaches the weld centre. It was also found that the fracture never occurred on the retreating side, so the tensile properties are better on this side.

Steel

In tensile tests performed on a mild steel by Lienert *et al.* [63], welded samples failed in regions corresponding to the base metal and demonstrated yield and ultimate tensile strengths comparable to those of the base metal. These results suggest the stir zone and HAZ have greater yield and tensile strengths than the base metal.

#### *1.2.2.12.4 Corrosion and stress corrosion cracking resistance*

The corrosion of friction stir welds was investigated by Davenport *et al.* [95]. The mechanism of corrosion in FSW of aluminium alloys 2024 and 7010, and how this is affected by the processing parameters, were analyzed. It was found that the tool rotation speed is an important parameter to the corrosion susceptibility of welds. At higher rotation speeds, anodic attack is concentrated in the HAZ, and the nugget of the weld act as a local cathode owing to the presence of a large number of fine precipitates. In contrast, for a slow rotation speed, the reactivity of the nugget is greater than the HAZ. In all cases, anodic attack is predominantly intergranular. It was found that the laser surface treatment shows great promise as a method for protecting friction stir welds from corrosion. It produces a high homogeneous layer without sensitized grain boundaries or cathodic active intermetallic particles.

In [96, 97] the applicability of Low Plasticity Burnishing (LPB) as a post-weld surface treatment to improve the corrosion fatigue performance of a friction stir welded aluminium alloy 2219 plate is studied. LPB is a new surface enhancement technology which can provide compression with minimum cold work in the surface layer of sufficient depth (maximum of $4mm$) to effectively eliminate the degradation in corrosion/fatigue life attributed to salt pit corrosion. This salt corrosion pitting occurs during exposure to a marine atmosphere and results in intergranular corrosion; the fatigue strength reduction caused by salt pit corrosion is well established and typically reduces the endurance limit to nominally half of the uncorred value.
Residual stress distributions mapped by X-ray diffraction through the thickness of the weld indicates zones of tension parallel to the weld line at the interface of the weld and parent metal on both advancing and retreating sides. Pitting and stress corrosion cracking tend to follow these regions of tension. Residual stresses vary as a function of distance from the weld centreline reaching minimums in the HAZ region on the advancing and the retreating side. This is likely due to the LPB procedure. Residual stresses perpendicular to the weld direction are essentially zero. LPB induced in the weld region high compressive stresses. High cycle fatigue test were performed at R=0,1 in four-point specimens. LPB provided nearly complete mitigation of the pitting corrosion damage, with comparable fatigue performance regardless of salt fog exposure. LPB appears to provide a

practical weld post-treatment for improved corrosion fatigue performance by 60% in salt corroded friction stir welded specimens.

#### *1.2.2.12.5 Fatigue and fracture mechanics*

Aluminium alloys 5083 and 6082 were fatigue tested by Svensson *et al.* [78]. In most specimens, fracture was initiated in the base material or in the centre of the weld. In only a few specimens the fracture initiated in the weld-base transition. The fatigue stresses were in general well above the design curve requirement. There are some indications that lower speed resulted in a higher fatigue resistance of the weld. Welds in aluminium alloy 5083 exhibited higher fatigue properties, compared with welds in aluminium alloy 6082.

Dickerson *et al.* [93] studied the fatigue behaviour of friction stir welds in aluminium alloys that contain root flaws. If FSW optimized parameters are used defect free welds are produced, but by using parameters outside tolerance welds can contain flaws. If parameters outside tolerance are used costs with tests to assure flaw-free welds can be decreased and higher productivity can be achieved. Hence the properties of welds with flaws are needed to enhance confidence in the design and application of FSW. In this study, monotonic strength and fatigue behaviour of single sided but welds, in aluminium alloys 5083-O, 5083-H321 and 6082-T6, with and without root flaws was investigated.
It was found that large changes of the optimum welding parameters are needed to produce welds with root flaws, FSW is relatively insensitive to many welding parameters. An exception is when the plate is too thick for the tool being used.
Root flaws were not detected using non-destructive testing (NDT) methods. This detection was improved by tension loading the weld while carrying out NDT. It was found that only bend tests with the root in tension were found to be reliable to detect flaws. An alternative to NDT is to process control set and maintain welding conditions where flaws will not be produced, but until now there are no standards relating specifically to the quality of friction stir welds.
By fatigue tests it was found that root flaws have a significant influence on the fatigue life of the 5083-H321 welds, but in the other two alloys fatigue tests gave lives on or above the upper bound live predictions (suggests that the bonding across the root flaws was sufficient to prevent immediate initiation of fatigue crack growth).

Lanciotti *et al.* [98] have conducted a test programme to characterize the damage tolerance of a friction stir welded 2195-T8 aluminium alloy. Parameters as fatigue behaviour, crack propagation and residual stresses were analyzed.
In tensile tests was found that friction stir welded specimens have values of tensile stress and rupture stress respectively 50% and 70% of the base material. The rupture stress of the weld is lower than the tensile stress of the parent material.
From microhardness tests it was found that FSW decreased the hardness in 37% in the limit of the HAZ. Fatigue testing showed a high scatter in specimens of base material and in specimens friction stir welded in only one step. Results in

welds performed in two steps were homogeneous. In both welds the fatigue life decreased, but fatigue lives remained with high values. Cracks always initiate in the limit of the HAZ, indifferent in the advancing and retreating side.
Residual stress measurements showed a maximum (130*MPa*) at the centre of the weld. Outside the weld affected zone the residual stress changes rapidly to a negative value (-20*MPa*) that remains almost constant throughout the remaining plate.
If a crack parallel to the weld direction is present the crack growth rate was found to be higher than in the base material, when tested at R=0,1. When tested with R=0,5, the results of crack growth rate in both type of specimens are similar.
If a crack perpendicular to the welding direction is present, a high increase in the crack growth rate takes place when compared with the base material. An agreement between experimental and predicted fatigue life was found taking into account the value of the residual stress intensity factor.

Bussu *et al.* [99] investigated the effect of weld residual stress and HAZ on the fatigue propagation of cracks parallel and orthogonal to the weld direction in friction stir welded 2024-T351 joints. Surface Crack Tension (SCT) specimens and compact tension specimens were tested. In SCT specimens, semicircular flaws of 1*mm* nominal radius were introduced by Electric Discharge Machining (EDM). Residual stresses were measured using the hole-drilling method.
It was found that cracks propagated almost immediately from the EDM defects and maintained their approximately semicircular shape until becoming through cracks. Figure 20 shows the crack propagation for both specimen types. It was verified that the relief of the residual stresses by applying 2% of plastic strain, originated crack growth rates almost identical to those of the parent plate. The mechanical stress relief drastically reducing the differences in crack growth rate and $\Delta K_{th}$ did not influence joint hardness or microstructure, which indicates that weld residual stress is responsible for the differences in fatigue crack growth rate and $\Delta K_{th}$ values.

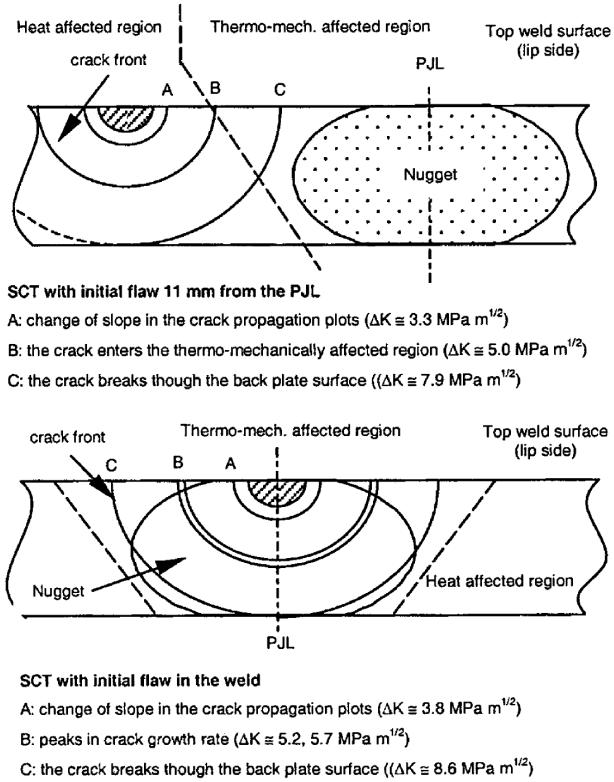


**Figure 20 - Crack front positions in the SCT samples, showing location with respect to the FSW macrostructure [99].**

Sutton *et al.* [100] performed a detailed microstructural study and mode I fracture tests on three families of friction stir welds of 2024-T3 aluminium plate designated hot, medium and cold. These families have different levels of nominal heat input during the FSW process. It was found that the nugget grain structure is relatively uniform in all welds, with a banded microstructure in which the spatial wavelength corresponds to the tool advance per revolution. From the hardness point of view it was found that the hot welds presents the lowest overall value and the lower values of hardness occur in the HAZ. Results from mode I fracture tests indicate that the measured critical Crack Opening Displacement (COD) at a fixed distance behind the crack tip is a viable fracture parameter for FSW joints. Fracture tests revealed that all of the welds have lower COD values than the base material. Measured critical COD values indicate that 2024-T3 FSW's with higher heat input typically have lower measured fracture toughness. They concluded that differences in fracture resistance could not be correlated with observed microstructural features.

Sutton *et al.* [101] performed the first mixed mode I/II fracture experiments on a friction stir weld. They used 2024-T351 aluminium plates welded with three different energy inputs levels per unit weld length designated: hot, medium and cold. In the tests a loss in fracture toughness due to the microstructural changes produced during the FSW process was verified. Crack paths in the hot weld closely mirror the base metal crack paths, but the cold and medium welds resulted in different crack paths. Fractographic observations indicate that the particle bands serve for initiation of low energy fracture, and that they will

separate in the presence of sufficiently high local stress normal to the particle band. It was observed that the initial crack path is along the particle band and the microstructural features alter this path within the highly non-homogeneous FSW joint. So, the overall stable growing crack path can be different for different welding parameters. The COD values indicate that transition from mode I to mode II dominant crack growth occurs at lower loading angles for FSW joints having higher specific weld energy input, with truly mixed mode I/II COD measured during crack growth in the medium FSW joint.

In the study by Ericsson *et al.* [90], already mentioned in the hardness section of this report, the fatigue strength of FSW, MIG and TIG welds was also compared. TIG welds showed better fatigue performance than the MIG pulse welds, but the best performance was achieved by the friction stir welds. From fatigue tests it was found that the scatter is generally small in the friction stir welded specimens. The results show that the fatigue performance does not decline with increased welding speeds, being the low welding speed beneficial only at high stresses.

#### *1.2.2.13 Modelling*

Considerable experimental work has been reported in the published literature, but numerical modelling of the process is still very scarce. Numerical modelling is necessary to improve to understand the physics of FSW.

Chen *et al.* [102] developed a three-dimensional model based on finite element analysis to study the thermal history and thermomechanical process in the butt-welding of aluminium alloy 6061-T6. The model incorporates the mechanical reaction of the tool and thermomechanical process of the welded material. It consists of a parametric study varying the traverse speed of the tool. Experimental values validated the accuracy of the model. Both predictions and measurements revealed that maximum temperature gradients occur beyond the shoulder edge. It was also found that the longitudinal residual stress is greater than the lateral residual stress at the top surface of the weld. Both experimental and numerical analyses of FSW results show that a higher traverse speed induces a larger high longitudinal stress zone and a narrower lateral stress zone. The good agreement obtained between the numerical model and the experimental results validate the work carried out.

Ulysse [103] presented an attempt to model the FSW process using three-dimensional visco-plastic modelling. Due to model simplifications, the temperature predictions tend to be high when compared to experimental data. However, it was found that both numerical and measured maximum temperatures tend to decrease as the translation speed increases. While increasing the welding speed tends to decrease the maximum temperature, increasing the rotational speed has the opposite effect. With the three-dimensional model created it was possible to predict the stresses that actuate in the pin for several welding parameters. It was found that increasing the welding speed, regardless of rotational speed, has the effect of increasing the axial thrust

and shear force on the pin. Also, for a fixed welding speed, increasing the rotational speed has the effect of decreasing the forces acting on the pin.

Song *et al.* [104] introduced a moving coordinate to model the transient three-dimensional heat transfer in the FSW process. The coordinate was chosen stationary with the moving tool; this simplifies the stir process modelling making the model more accurate. The finite difference method was applied in solving the control equations. With this model was reduced the difficulty of determining the temperature distribution near the moving tool pin. It was concluded that preheat is beneficial to increase the temperature of the workpiece in front of the pin, making the material easier to weld.

Zhu *et al.* [105] conducted three-dimensional non-linear thermal and thermomechanical simulations for the FSW process using the finite elements method. Two welding rotational speeds, 300*rpm* and 500*rpm*, on FSW of 304L stainless steel were analyzed. Based on the experimental data of transient temperature an inverse analysis method was developed and conducted to an effective calculation of the temperature field. For both rotational speeds a good temperature agreement between experimental and numerical results was found. Using the numerically calculated temperature field, the residual stress was obtained in a subsequent three-dimensional elastic-plastic mechanical simulation. It was also found that nearly 50% of the total mechanical energy measured from the FSW machine is transformed to increase the temperature of the workpiece. The other 50% energy may be dissipated in the large plastic deformation of the weld material, the clamped fixture strips, and the support plates, and the heat transferred to the tool and the machine head.

Vilaça *et al.* [106] proposed a thermal analytical model for FSW called *i*STIR. The model allows simulation of asymmetric heat field developed below the tool shoulder due to the composition of the rotation and linear speeds, and the hot-to-cold welding conditions, considered in the establishment of the thermal field generated resulting from all the energy sources.

# Chapter 2

# Temperature field acquisition during a welding process

Since heat generation is a fundamental aspect of any welding technique, this Chapter presents the development of an effective temperature measurement procedure that could be applied to any welding process. As a basis for the development of an accurate temperature measurement procedure, an aggressive and well known welding method - Gas Metal Arc Welding - was used. A feasible technique for the use of fibre Bragg grating sensors was introduced, developed, and validated using thermocouple and thermographic readings.
A comparative study of temperature fields acquired during Metal Inert Gas welding, Friction Stir Welding and Laser Beam Welding was performed.

The work presented in Section 2.1 was published by the Institute of Physics (UK) as: P M G P Moreira, O Frazão, S M O Tavares, M A V de Figueiredo, M T Restivo, J L Santos and P M S T de Castro, Temperature field acquisition during gas metal arc welding using thermocouples, thermography and fibre Bragg grating sensors, *Measurement Science and Technology*, 18, p. 877-883, 2007.

# 2. Temperature field acquisition during a welding process

## 2.1 Development of a feasible technique using fibre Bragg sensors to acquire the temperature field during GMAW

This study was performed in order to develop effective systems of temperature acquisition during an aggressively high heat flux welding process such as Gas Metal Arc Welding (GMAW), MIG (Metal Inert Gas) welding type [107]. It is expected that a system providing good results with MIG welding will certainly also perform well with lower heat input welding processes as LBW and FSW.

The arc welding process, invented in Russia in 1888, is currently the most widely used welding process. The arc and the weld are protected from atmospheric contamination by a gas shield. An electric potential is established between the electrode and the workpiece causing a current flow, which generates thermal energy in the partially ionised gas [108].
Three different temperature acquisition systems were analysed, involving thermocouples, thermographic equipment and fibre Bragg grating (FBG) sensors. Two different sets of tests were carried out. In the first tests temperature was acquired in the plate surface opposite to the weldments using thermocouples and a thermographic camera. In the second set of tests temperature was acquired using thermocouples and FBG sensors in the arc weld side of the plate.
An effective technique to use FBG sensors during welding was developed, and two different types of thermocouples and techniques for their connection to the plates was tested.

Literature on welding process monitoring includes the synergic use of different thermographic methods by Meola *et al.* in [109]. Camilleri *et al.* [110] studied the alternative simulation techniques for distortion of a thin plate due to fillet-welded stiffeners, where temperature gradients were measured with thermocouples and a thermographic camera. Another example of the applicability of thermographic techniques in welding is presented by Doong *et al.* [111], investigating the feasibility of using infrared sensing devices to measure the surface temperature variation near the molten pool and to correlate this temperature variation with the changes in welding parameters.

### *2.1.1. Welding process*

Weldments were deposited on $10mm$ thick $500\times300mm$ aluminium alloy 6082-T6 plates. The MIG welding parameters used were: $170A$, $26V$, $60cm/min$ and Argon at a $22l/min$ flow rate. A filler wire with the designation ESAB OK Autrod 18.15 with a diameter of $1mm$, [112], was used. Welds were performed using an automated welding robot, GMF ROBOTICS – Arc Mat Sr., shown in Figure 21.

The rig setup for the studies involving MIG welding presented in Chapters 2 and 3 is shown in Figure 22. The plate was supported in its back surface near its edges; dashed lines identify the clamping area. The centre area is free in both surfaces making possible the temperature measurements.

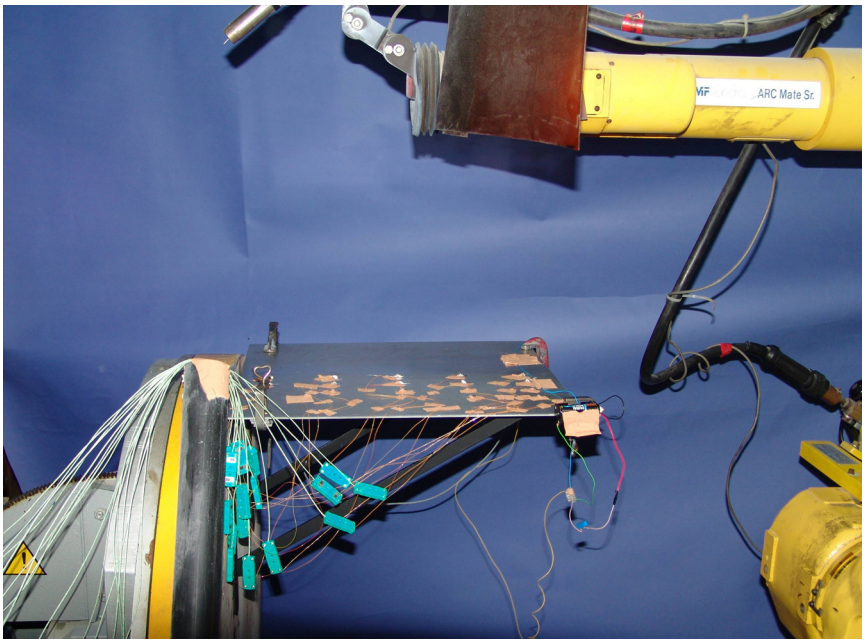


**Figure 21 - Robot for MIG welding.**

Different sets of tests were performed to acquire temperatures on the plate top and back surface. The top surface is defined as the surface where weldments were deposited, and back surface is the opposite surface. Temperatures were only acquired at the surfaces in order to use these welded plates in future mechanical tests.

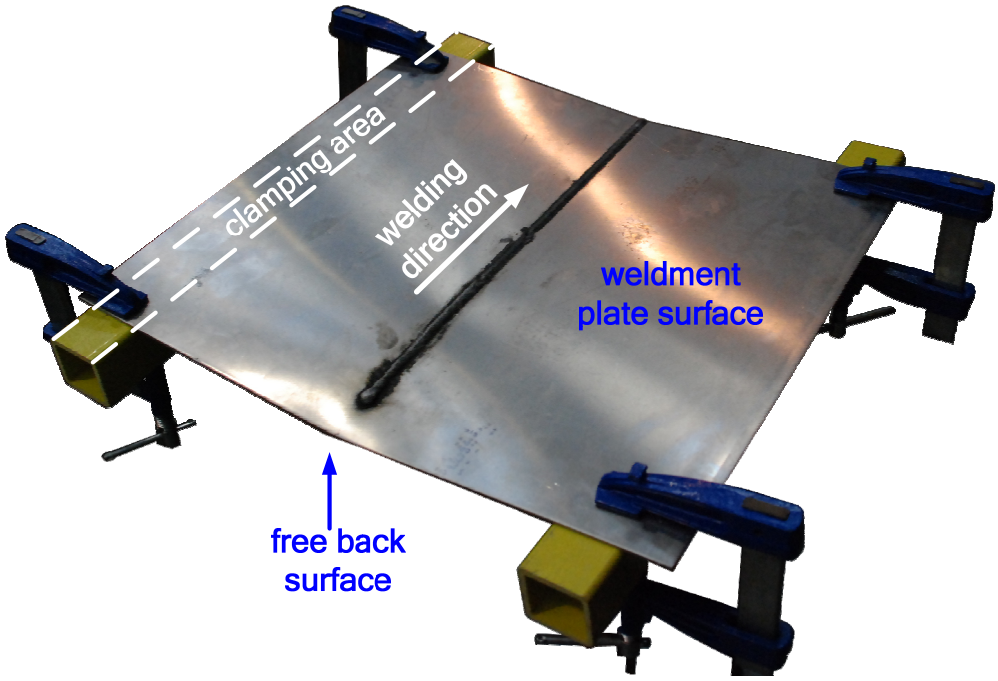


**Figure 22 - Rig setup for the MIG welds.**

### *2.1.2 Thermocouples*

Thermocouples are popular transducers used for temperature measurement due to their large temperature range, stability and low cost. Using thermocouples a large number of points can be monitored.
Thermocouples are often welded to a metal part or clamped under a screw. They can be manufactured, for example, by silver-soldering or welding. When the thermocouple wires are soldered together, third metal can be introduced into the thermocouple circuit, but as long as the temperature of the junction is uniform an error is not introduced, [113]. To reach a higher measurement temperature, the joint must be welded. Since commercial thermocouples are high cost sensors, they are welded on expensive machinery using a capacitive-discharge technique to insure uniformity; the thermocouples used in these tests were manufactured in our laboratory. To weld the thermocouples wires a capacitive-discharge was built and several manufacturing techniques, including oxyacetylene flame, were tested. Type K thermocouples (chromel alumel) were used in all tests. They are the most commonly used thermocouples and support oxidizing atmospheres. Their working range is from -200°*C* up to 1100°*C*, although above 800°*C* oxidation causes drift and de-calibration. Thermocouples of K type have a sensitivity of 40,44$\mu V/°C$. Thermocouples with 0,2$mm$ and 0,08$mm$ diameter were tested.
The response time for a thermocouple is defined as the time taken for the thermal voltage to reach 63% of its maximum for the temperature at that moment [114]. It is dependent on the thermocouples diameter and length, and tip configuration. Thermocouples with grounded junctions display response times some 20% to 30% faster than those with insulated junctions. Very good sensitivity is provided by fine gage unsheathed thermocouples. With conductor diameter in the range

0,025$mm$ to 0,81$mm$, response times in the region of 0,05 to 0,40 seconds can be realized.

In this work AD 594's IC's from Analog Devices are used as complete instrumentation amplifiers for K type thermocouple with cold junction compensation and a gain of 247,3 (10$mV/°C$ divided by 40,44$\mu V/°C$) for measuring and amplifying the thermocouple f.e.m. [115]. The signal from each thermocouple conditioning circuit is then the input signal in a PC using a HBM Spider 8 system. The circuit that makes the interface between the thermocouples and the Spider 8 was built in our laboratory, Figure 23.

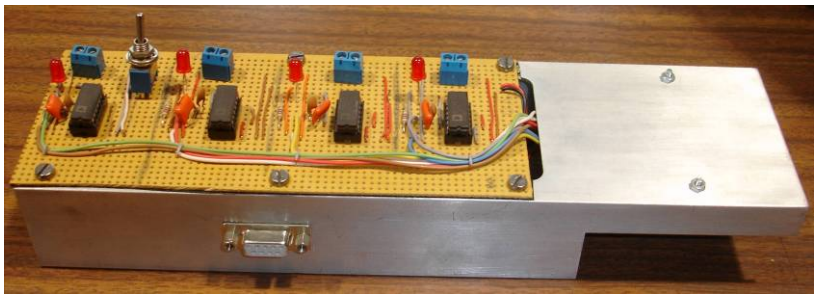

**Figure 23 - Conditioning circuit for thermocouples.**

### *2.1.3 Thermography*

Thermography gives an overall full field thermal picture of the welded plate providing a remote observation of surface temperature distribution [116]. The thermographic working principle is based on capturing infrared emission from the part under study [117]. It involves determining the spatial distribution of thermal energy emitted from the surface of an object. This technique allows mapping of the temperature distribution and can be used in conjunction with software analysis to provide quantitative information. Thermography is a non-intrusive technique that can show reasonably fine detail where the pattern of radiant energy from a prescribed area of the object in question is scanned continuously. The radiant energy is converted to an electrical voltage with a suitable detector and this voltage is then available for further processing. It can, however, be expensive and the uncertainty is a function of the knowledge of surface emissivity and the transmission path. The temperature range covered by thermal imaging systems is of the order of -40°$C$ to 2000°$C$.

The aluminium plate surface were spray painted black mat prior to welding in order to have a radiating surface with a black body emissivity near unity (perfect absorber). For measurements a FLIR ThermaCam PM575 was used.

### *2.1.4 Temperature measurements, plate surface opposite to weldments*

Temperatures were acquired in three points at the plate surface opposite to weldments using thermocouples and a thermographic camera as shown in Figure 24. These points were positioned just under the weldment line. Thermocouples

were place at the plate surface. For their connection to the plate a spring effect capable of preventing any displacement throughout the measuring process was created. Thermocouple 2 was placed at the middle length of the welding line and the other thermocouples (1 and 3) were placed at a distance of 15*mm* before and after thermocouple 2.

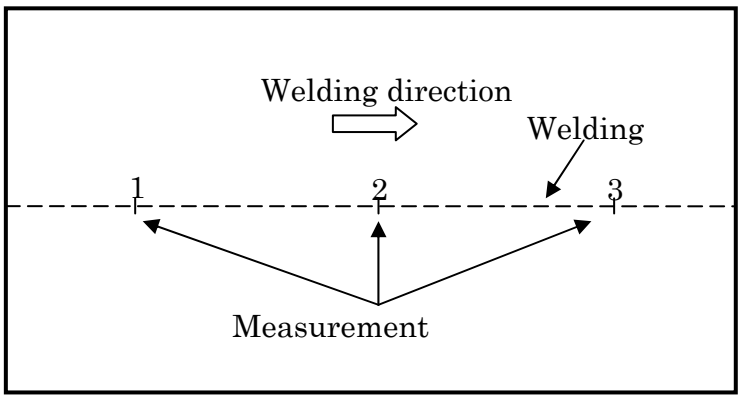


**Figure 24 - Points of temperature acquisition in the plate surface opposite to weldments.**

A thermographic camera was positioned behind the plate with three spots located in the same place as the thermocouples. The result obtained with the thermographic camera when the heat source is under each point is presented in Figure 25. The interpretation of the temperature distribution is achieved by post-processing and conversion to three-dimensional (3D) plots presented in Figure 26. These three-dimensional plots show how temperature is distributed in the plate in different welding times.

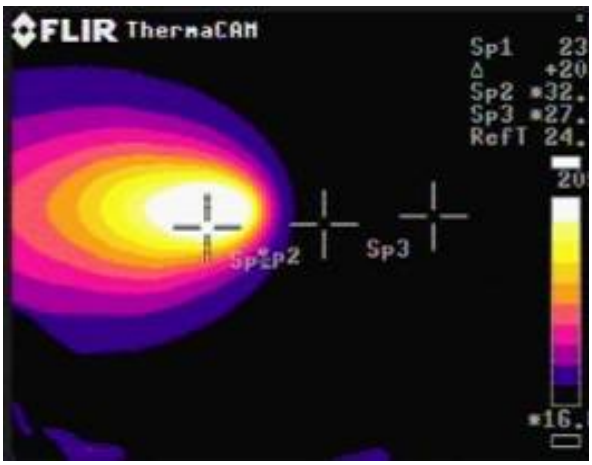


a) maximum temperature in the first point, 231*°C*

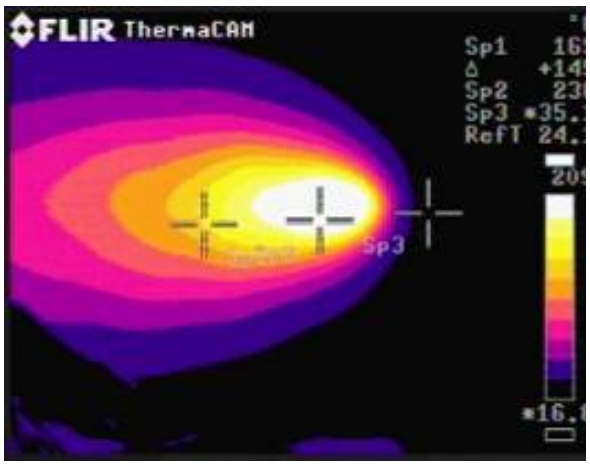


b) maximum temperature in the second point, 238*°C*

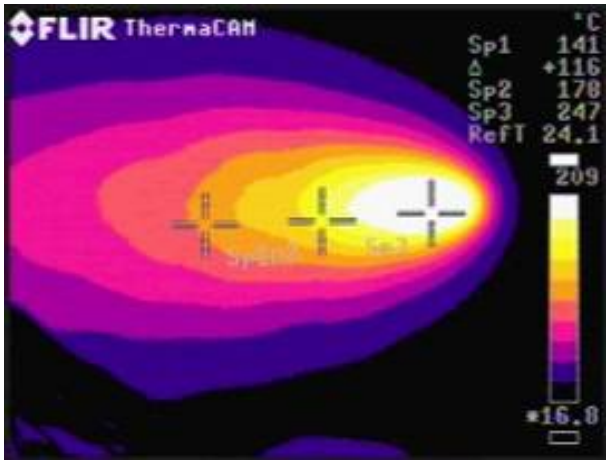


c) maximum temperature in the third point, $247°C$

**Figure 25 - Thermographic temperature distribution in three welding moments.**

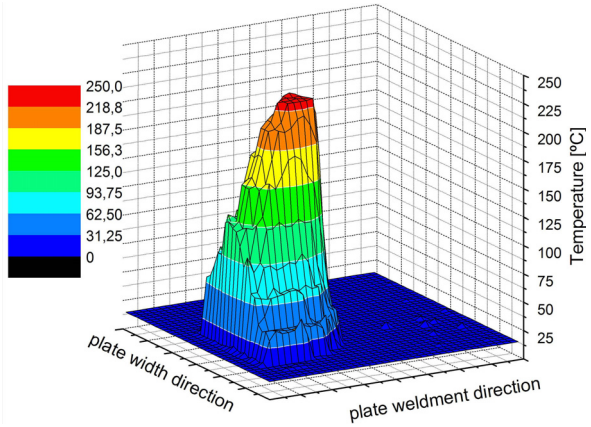


a) 3D temperature distribution when the heat source is under point 1

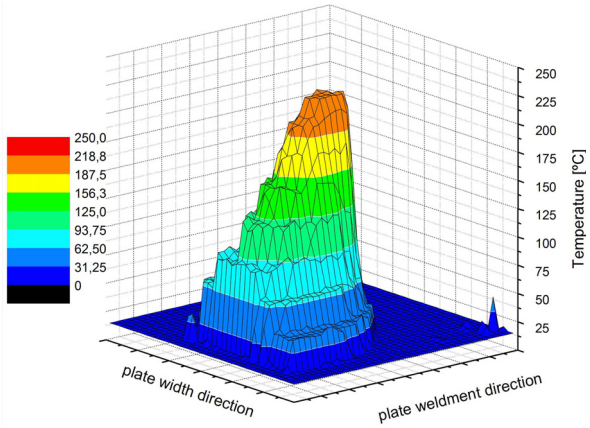


b) 3D temperature distribution when the heat source is under point 2

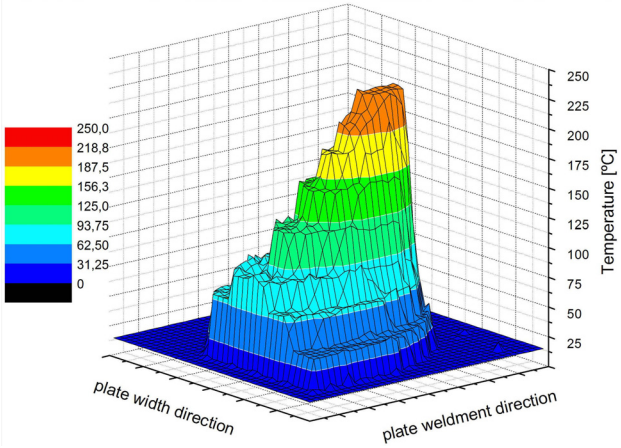


c) 3D temperature distribution when the heat source is under point 3

**Figure 26 - 3D temperature distributions at different welding times.**

Thermocouples with two different diameters, $0{,}2mm$ and $0{,}08mm$, were also used in this test. Thermocouples were manufactured in-house testing different techniques to fuse the thermocouples junction: oxyacetylene flame, and electrical discharge using different contact materials. Also, different solutions to connect the thermocouples to the plates were tested.

Firstly, thermocouples of $0{,}2mm$ diameter were tested. With this type of thermocouples and testing several techniques to fuse the thermocouple junction the difference between maximum values obtained with the thermographic camera and the thermocouples was of the order of $30°C$ to $60°C$. This result can be explained by the high response time of these thermocouples. Their response time is too slow to follow the high rate temperature changes due to the welding process speed and to the high thermal conductivity of aluminium ($170 W/m\ K$).

Thermocouples with the $0{,}08mm$ diameter gave better results. Electrical insulation of the thermocouple was achieved by protecting its measuring part with a thin clad of cyanoacrylate glue. Since measurements were made at the plate surface and to compensate a measuring delay due to the cyanoacrylate glue, thermocouple junction that was in connection with the plate were covered by silver based compound (silver, zinc oxide, aluminium oxide and boron nitride particles) with a reasonable conductivity ($8{,}89 W/m\ K$). The technique to fuse (weld) the thermocouples junction that gave the best results was to weld the junction wires in a Mercury bath by an electrical discharge.

Temperatures obtained in points 1, 2 and 3 using thermocouples of $0{,}2mm$ diameter insulated with cyanoacrylate glue and covered with a silicon based compound are shown in Figure 27. Temperatures were found to be lower than expected due to the slow response time of these thermocouples; furthermore, problems concerning inducted electromagnetic fields noise were present.

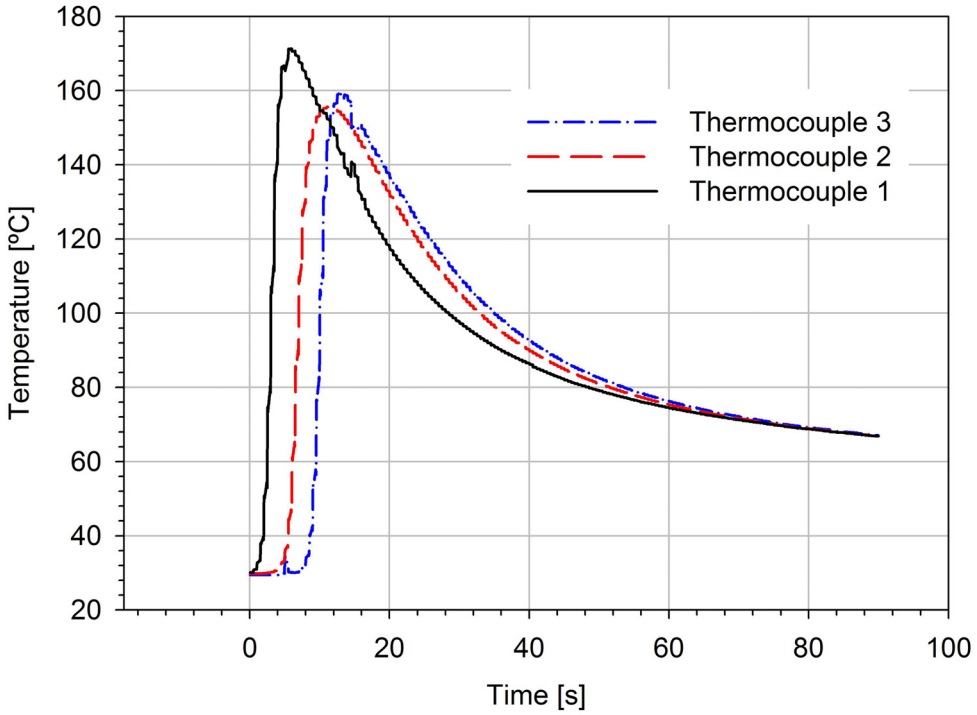


**Figure 27 - Temperature time function measured with thermocouples, incorrect measurements.**

The best results were obtained with thermocouples of $0{,}08mm$ diameter covered with a silver based compound. Temperature distributions in points 1 and 3 are

presented in Figure 28. The result of thermocouple placed under point 2 was disregarded in this test due to lack of electrical insulation.

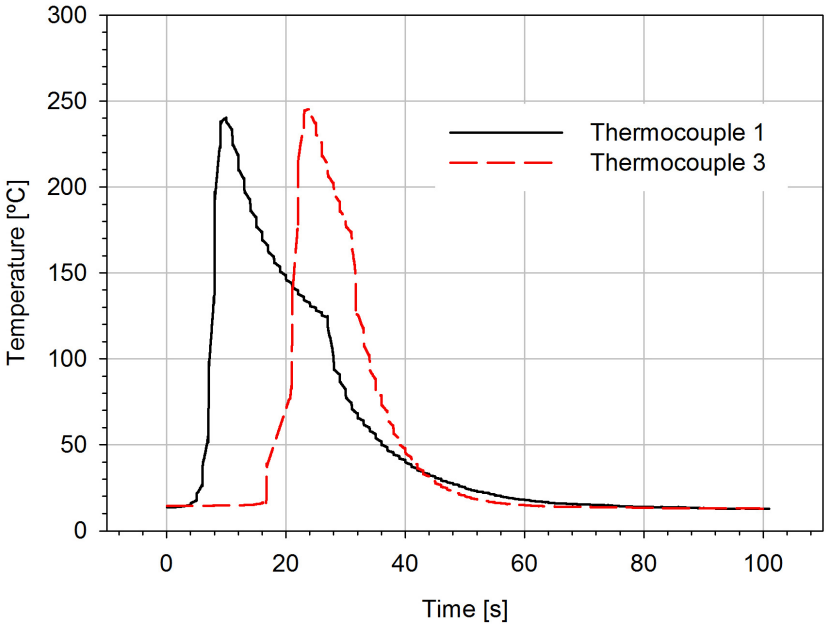


**Figure 28 – Temperature time function measured with thermocouples.**

A comparison between maximum temperatures in each point acquired with thermography and thermocouples of 0,08*mm* diameter is presented in Table 1. A good agreement between both techniques was found.

**Table 1 - Measured temperatures**

| | Acquisition system (temperatures) | |
|---|---|---|
| Point | Thermography [*ºC*] | Thermocouples [*ºC*] |
| 1 | 231 | 240 |
| 2 | 238 | disregarded |
| 3 | 247 | 245,2 |

### *2.1.5 Fibre Bragg grating sensors*

FBG is a periodic modulation of the refractive index of the core of a single mode optical fibre [118]. Many FBGs with different resonance wavelengths can be inscribed in a single optical fibre, its number being only dependent on the spectral width of the optical source used. Current technology allows this number to be larger than 50. One major advantage of using fibre optic sensors in welding processes where electrical currents are present is their immunity to electromagnetic interference.

In a work by Suaréz *et al.* [119] a FBG sensor and a thermocouple were used to monitor a TIG arc welding process. In that work the FBG sensor was placed in the side of the plate opposite to the welding line and some difficulties due to the connection of the sensor to the plate are described.

A first study to develop feasible techniques to use FBG sensors to acquire temperatures in welding procedures was carried out. In a first study FBG sensors

were placed in four different locations, schematically represented in Figure 29 (two details presented in Figure 30). It was found that all lead to unsatisfactory results, since the fibres became damaged in the cases 1 and 4, and the location was found unsuitable in cases 2 and 3.

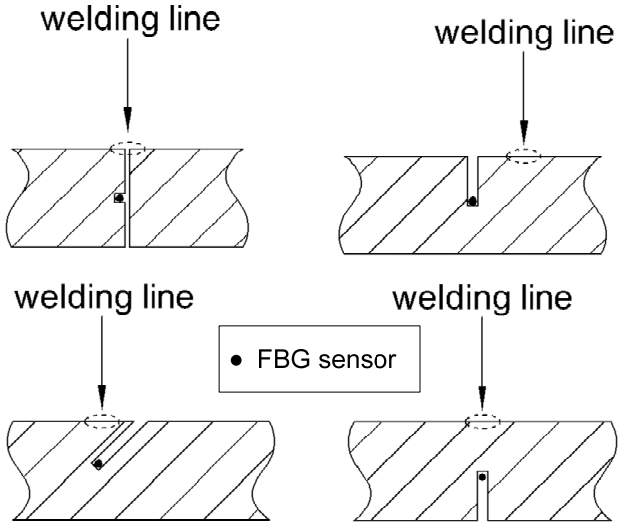


**Figure 29 - Locations where FBG sensors were placed in the first study (from left, cases 1 to 4).**

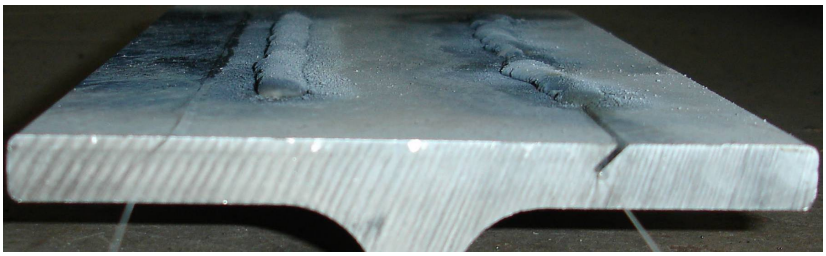

**Figure 30 - Example of a fibre placed at 10*mm* parallel to the weld line and a fibre placed as case 4 (Figure 29).**

In a second study, placing the sensors in the weldment plate side, the minimum distance to the welding line from which temperatures could be acquired was evaluated. In these tests sensors were placed parallel to the weld line at distances multiple of 5*mm*. Since MIG is an arc welding process involving an aggressively high heat flux, unprotected and protected sensors, using three different techniques, were tested. The protection techniques were: a cyanoacrylate glue, stripes of aluminium foil covering each sensor, and silicon based compound. The silicon based compound gave the best result. A result of a test using cyanoacrylate glue and stripes of aluminium foil is presented in Figure 31.

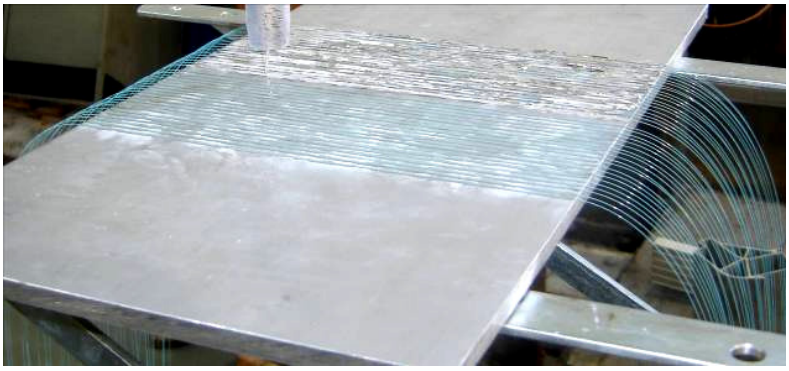

a) FBG sensors setup prior to welding

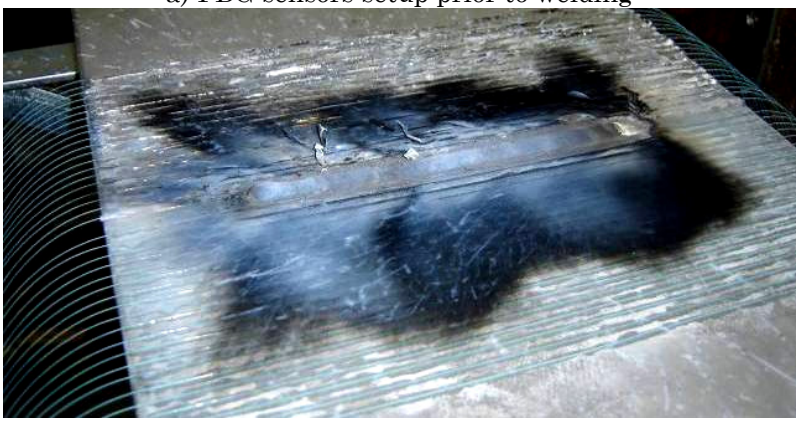

b) FBG sensors setup after welding

**Figure 31 - Welding test using epoxy glue and aluminium sheet stripes to protect the FBG sensors.**

When covered with cyanoacrylate glue and aluminium stripes, sensors were able to maintain integrity of measurement at a distance of 15$mm$ in the perpendicular direction to the weld line. Sensors placed near the weld line lost their measuring capabilities. A damaged (broken) and an undamaged sensor protected with aluminium stripes are shown in Figure 32. A damaged and an undamaged sensor protected with cyanoacrylate glue are shown in Figure 33.

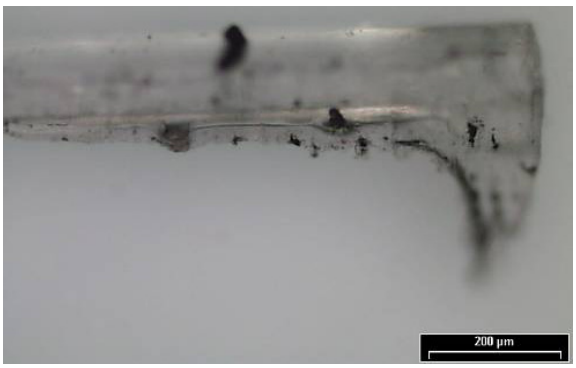


a) damaged sensor (15$mm$ from welding line)

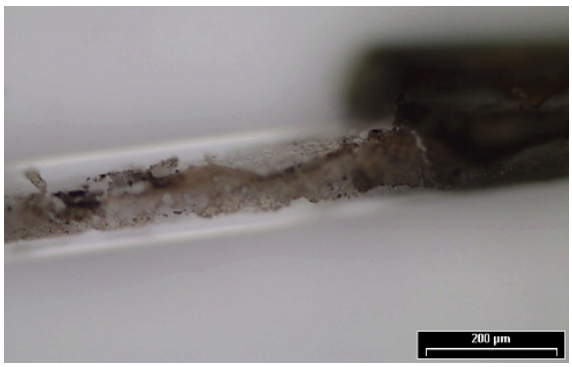


b) resistant sensor (15$mm$ from welding line)

**Figure 32 - Sensors protected with aluminium sheet stripes after welding.**

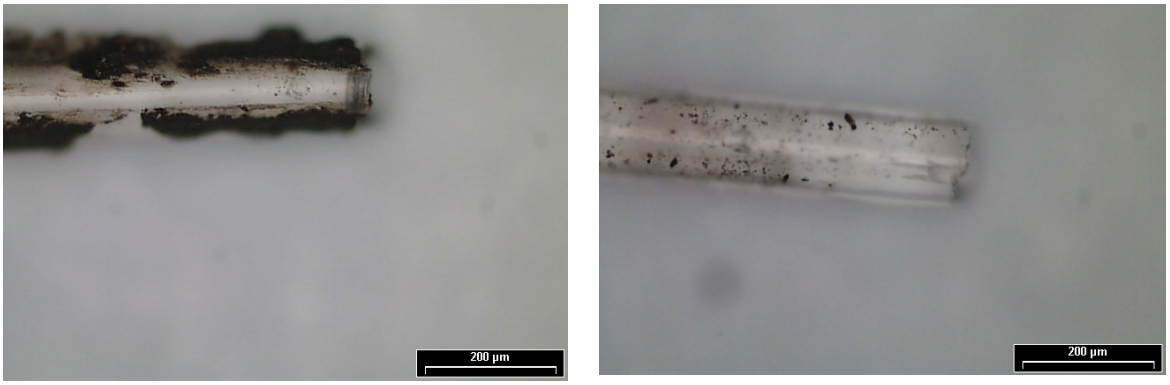


a) damaged sensor (10$mm$ from welding line) b) resistant sensor (15$mm$ from welding line)

**Figure 33 - Sensors protected with cyanoacrylate glue after welding.**

Using silicon based compound, to protect the FBG sensors during welding, a faster and easier test setup is achieved. A test setup using a silicon based compound to protect the FBG sensors is shown in Figure 34. With this technique sensors could be placed at 10$mm$ in a perpendicular direction to the weld line.

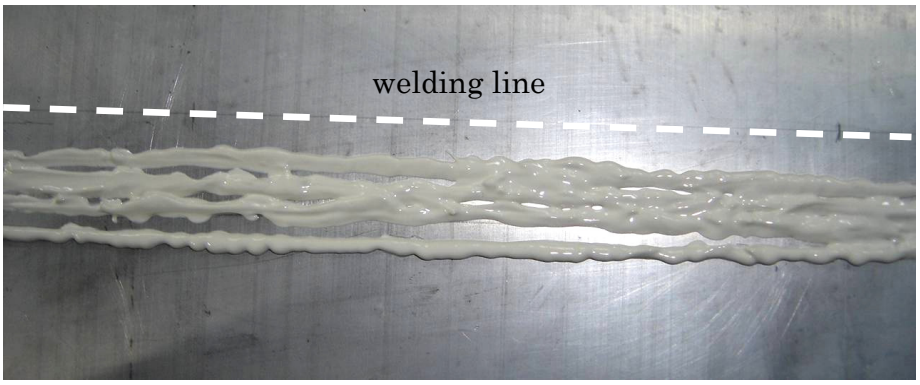


a) FBG sensors setup prior to welding

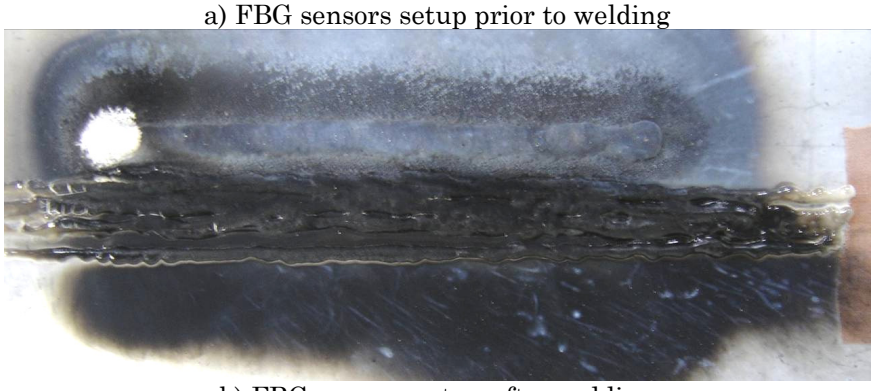

b) FBG sensors setup after welding

**Figure 34 - Welding test protecting FBG sensors with silicon based compound.**

### *2.1.6 Temperature measurements in the plate welded surface*

After defining the best protecting technique for the FBG sensors, a benchmark exercise involving thermocouples and FBG sensors was performed. A weldment was deposited on a 500×300$mm$ and 10$mm$ thick aluminium alloy 6082-T6 plate and measurements were performed in a site at half of the welding line length. Temperature measurements in the welded plate side (called top surface) were

performed at 15$mm$ in the perpendicular direction to the weldments. Thermocouples of type K with 0,08$mm$ of diameter protected by a silver based compound were used. A protective covering layer of silicon based compound was also used since temperatures were acquired at 15$mm$ from the weld line, as shown in Figure 35. In this figure the brown stripes are used to create a spring effect which results in a permanent contact between the thermocouples and the aluminium plate.

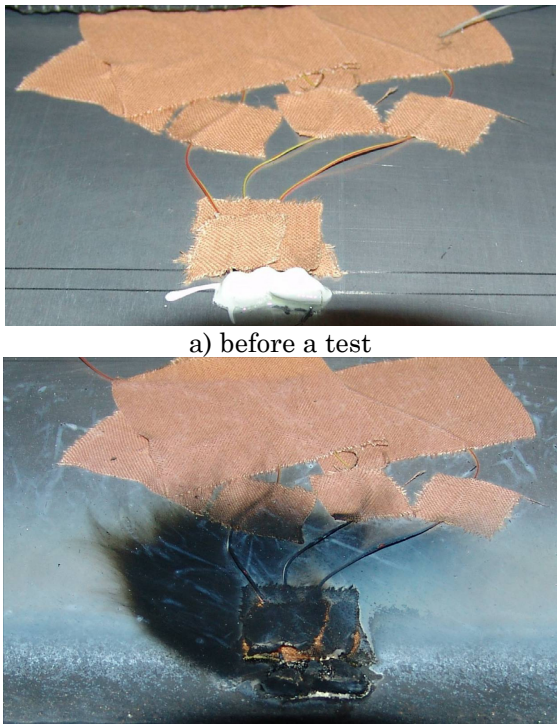

a) before a test

b) after a test

**Figure 35 - Thermocouple of 0,08$mm$ diameter covered with a silicone based compound.**

The FBG sensors with a length of 30$mm$, were written in a hydrogen loaded standard optical communication fibre (SMF 28) using an excimer laser. The Bragg wavelength peak at room temperature was at 1545$nm$ with reflectivity and spectral bandwidth at half maximum of ~ 98% and ~ 0,1$nm$, respectively. FBG sensors were protected with the silicon based compound.
A comparison of the results obtained with both techniques is presented in Figure 36.
Results obtained with both measuring techniques present good agreement, particularly as concerns the maximum value. FBG results plotted in Figure 36 correspond to one value per second, whereas thermocouple acquisition plots twenty values per second. Also, the FBG sensor grating was 30$mm$ long, implying that the presented result takes into account the difference in temperature along the 30$mm$ grating, which may justify the delay in the beginning of the acquisition. The results obtained suggest the possibility to use this new type of sensors to acquire temperature values in the aggressive conditions found in arc welding processes.

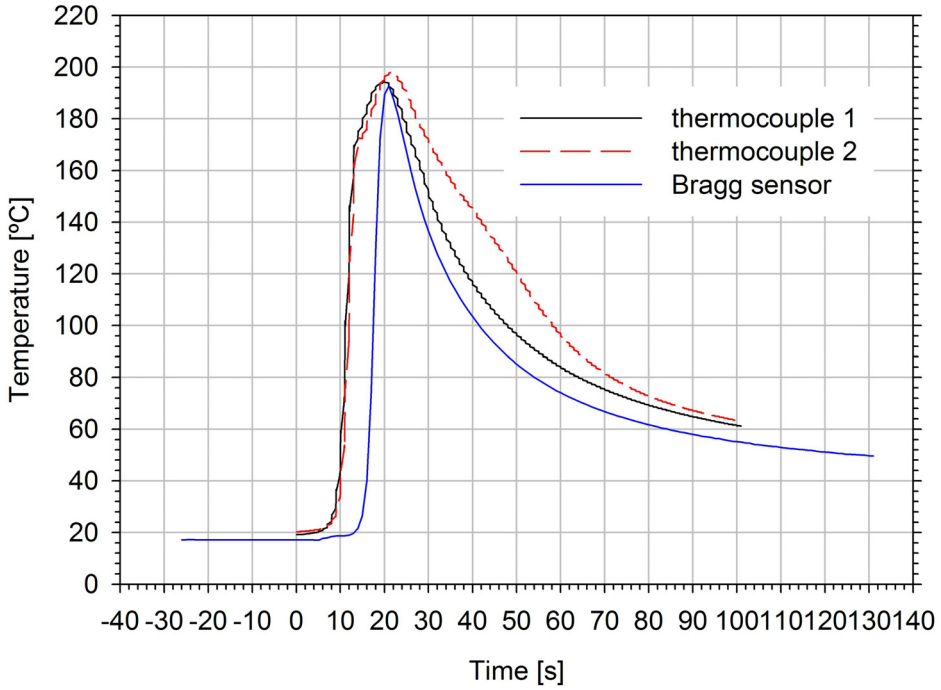


**Figure 36 - Temperature measured at 15*mm* in a perpendicular direction of the welding line using thermocouples and FBG sensors.**

### *2.1.7 Temperature profile, direction perpendicular to the weld line*

Temperature measurements in the perpendicular direction to the weldment were performed using thermocouples and FBG sensors with a 10*mm* length (grating) according to the scheme presented in Figure 37. The sensors were placed at the weldment middle length.

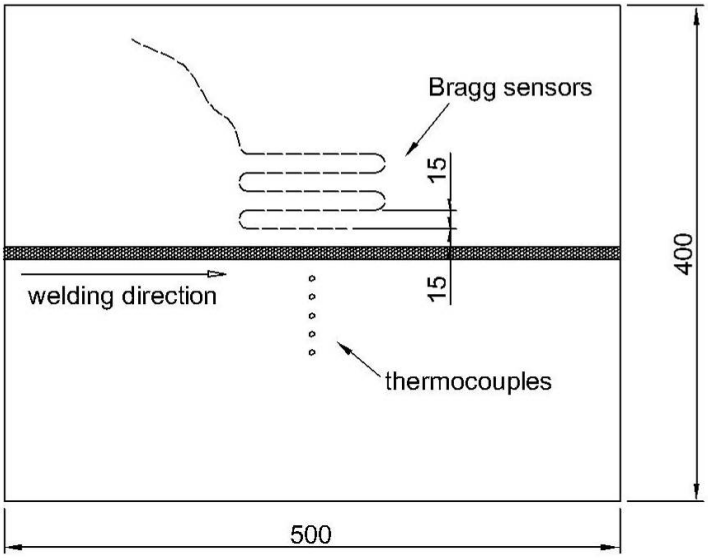


**Figure 37 - Schematic representation of thermocouples and FBG sensors location.**

The different temperature profiles obtained with the thermocouples and the FBG sensors are presented in Figure 38. A direct comparison of the temperature peaks

acquired with each type of sensor at different distances from the weld centre is presented in Figure 39. A good agreement was found between both techniques, and shows a high temperature gradient near the weldment.

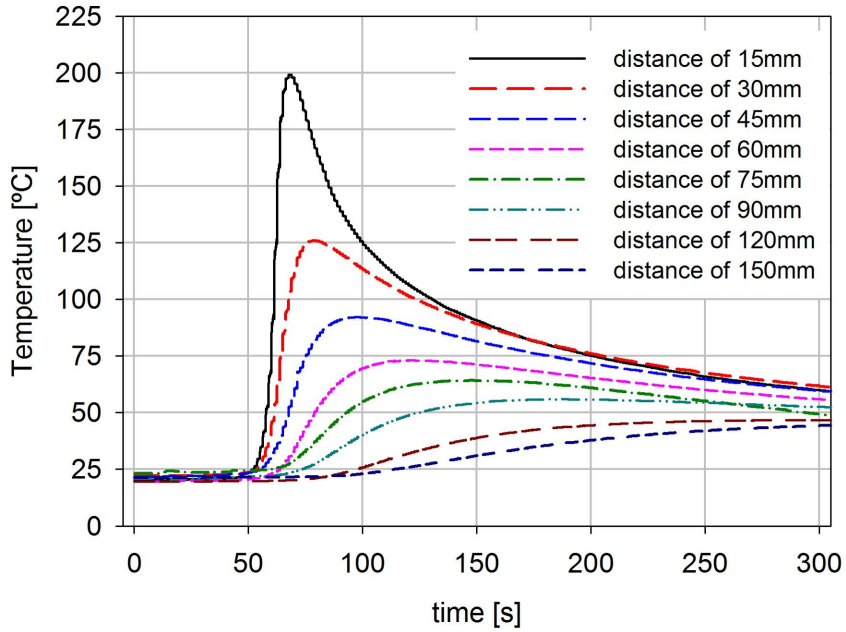


a) thermocouples at different distances from the weld centre

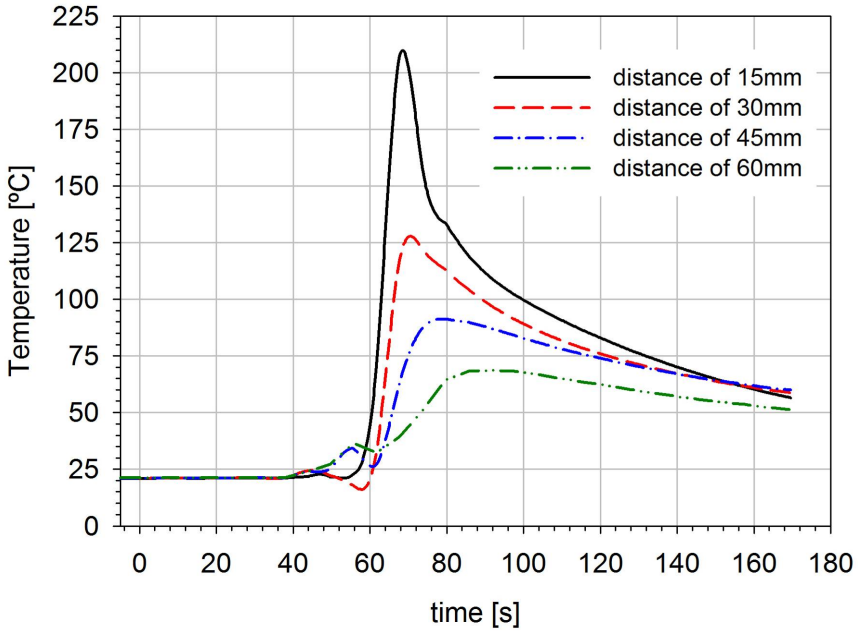


b) FBG sensors at different distances from the weld centre

**Figure 38 - Measured temperature profiles with thermocouples and FBG sensors.**

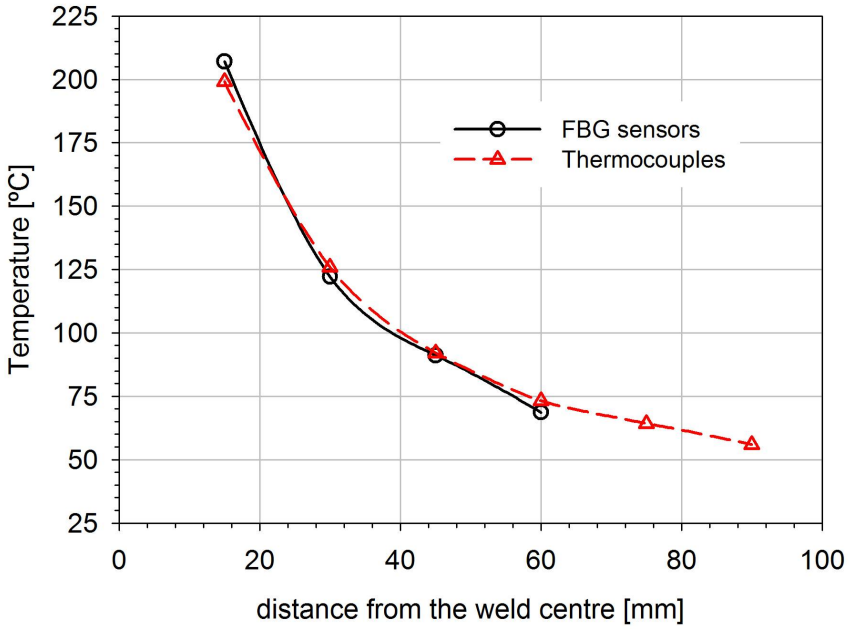


**Figure 39 - Peak (maximum) temperatures acquired with thermocouples and FBG sensors.**

### *2.1.8 Concluding remarks*

Three different temperature acquisition systems during GMAW welding, involving thermocouples, a thermographic camera and fibre Bragg grating sensors, were analysed. Weldments were deposited on 500×300$mm$ and 10$mm$ thick aluminium alloy 6082-T6 plates.

Two different set of tests were carried out. In the first tests temperature was acquired in the plate surface opposite to the weldments using thermocouples and a thermographic camera. Thermocouples with 0,2$mm$ diameter and thermocouples with 0,08$mm$ were tested. Thermocouples with a diameter of 0,2$mm$ presented some 30$ºC$ to 60$ºC$ of difference with reference temperatures at around 250$ºC$. The best results were achieved with the 0,08$mm$ diameter thermocouples with their junction covered by thin cyanoacrylate glue clad to insulate electrically the thermocouples from the plate. In this set of tests a comparison between maximum temperatures in each point acquired with thermography and thermocouples shows a good agreement between both techniques.

In the second set of tests temperatures were acquired using thermocouples and FBG sensors in the weldments side (top side) of the plate. A feasible technique to use FBG sensors to acquire temperatures in welding procedures was developed. Sensors protected with cyanoacrylate glue, stripes of aluminium foil covering each sensor, and a silicon based compound were able to maintain integrity of measurement at a distance of 15$mm$ in the perpendicular direction to the weld line. With the silicon based compound this distance can reach 10$mm$. The silicon based compound gave the best result and also permits a faster and easier test setup. Thermocouples were also used in these tests with effective measurements

at 15*mm* from the weld line. Results obtained with FBG sensor and thermocouples present good agreement, particularly as concerns the maximum value. The results obtained suggest the possibility to use this new type of sensors to acquire temperature values in the aggressive conditions found in the arc weld side of the plate.

## 2.2 Temperature field in GMAW, LBW and FSW

As lower heat input processes, LBW and FSW are expected to generate lower temperatures than MIG. It was decided to measure the temperature fields generated by these processes, to quantify these differences. In this study the temperature fields generated during three different welding techniques are analyzed: MIG (Metal Inert Gas), LBW (Laser Beam Welding) and FSW (Friction Stir Welding). MIG welding was performed at FEUP, LBW at AIMEN (Porriño, Spain) and FSW was carried out at Estaleiros Navais do Mondego/ISQ (Figueira da Foz, Portugal).
The welding temperature profiles during welding were acquired and analyzed using two different techniques: thermocouples and thermography (only for the MIG welding). Weldments were deposited in 3*mm* thickness plates (450x500*mm*) of two different aluminium alloys: 6082-T6 and 6061-T6.

Sixteen thermocouples were used in each plate and temperatures were acquired during welding. Type K thermocouples (chromel alumel) with a diameter of 0,08*mm* manufactured in our laboratory were used in all tests. They were place in the plate surface using the technique already described in this Chapter (junction covered by thin cyanoacrylate glue clad to insulate electrically the thermocouples from the plate). The signal from each thermocouple conditioning circuit is then the input signal in a PC using a HBM Spider 8 system.
In order to have an overall thermal picture of the welded plate during MIG welding using thermography, the aluminium plate surface were spray painted black mat prior to welding in order to have a radiating surface with a black body emissivity near unity (perfect absorber).

Different sets of tests were performed to acquire temperatures on the plate top and back surface. The top surface is defined as the surface where weldments were deposited, and back surface is the opposite surface. Temperatures were only acquired at both surfaces, and not through the thickness, in order to use these welded plates in future mechanical tests.

### *2.2.1 MIG welding – temperature profiles*

#### *2.2.1.1 Introduction*

Different sets of tests were performed to acquire temperatures on the plate top and back surfaces. A weld bead was deposited in four plates of aluminium 6082-T6 and four plates of aluminium 6061-T6, all with 450x500x3$mm$. The temperature distribution was measured using thermocouples on both sides of the plate, and a thermographic camera was also used in the plate opposite side to weldments. Temperatures measured using thermocouples were acquired with a frequency of 14$Hz$. The welding parameters used for all tests were: 20l/min of Argon flow rate, 70$cm/min$ weld travelling speed, 128$A$ and 17,1$V$; and a stick-out of 15$mm$ was used.
To calibrate the welding time a fuse wire was placed at 43$mm$ from the plate final edge and another one was placed at 423$mm$ from the previous. The weldments had a length of about 438$mm$, and ended at 32$mm$ from each plate edge. Thermocouples, in a total of sixteen, were distributed along the plate surface according to Figure 40, along 4 columns and 5 lines. As an example, the first column was placed at 15$mm$ from the welding line and contained thermocouples 1, 3, 6, 9 and 13 and the second line contained thermocouples 3, 4 and 5. Each welding trial lasted for approximately 38$s$.

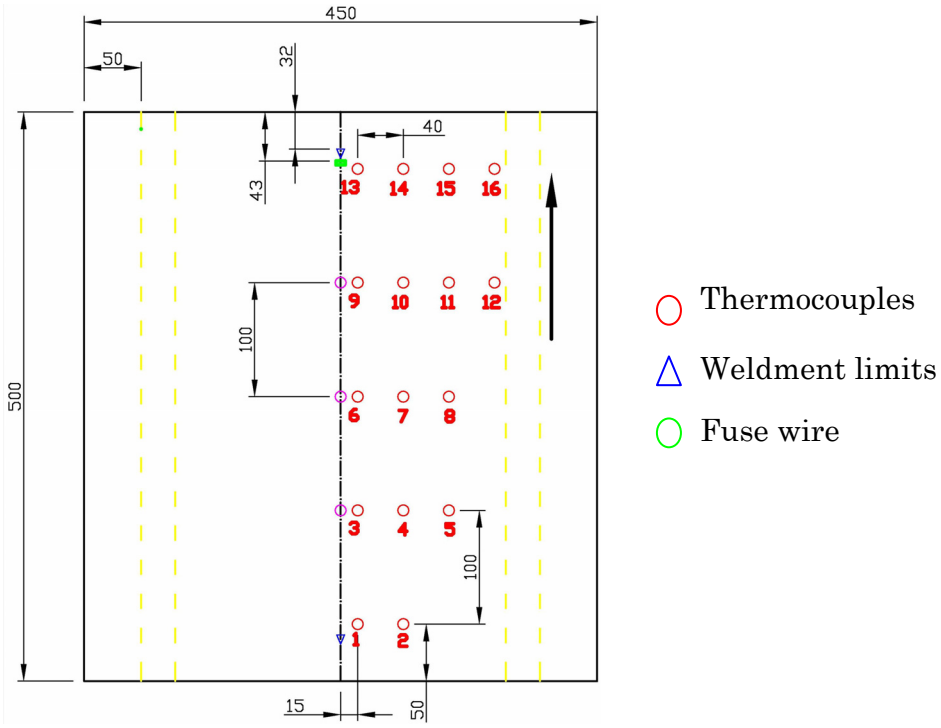


**Figure 40 - Thermocouples and thermographic temperature acquisition sites at the plate top surface.**

In the plate back surface thermocouples were placed according to Figure 41. The first column of thermocouples is now placed at 5$mm$ from the welding line and 16 thermocouples were again used.

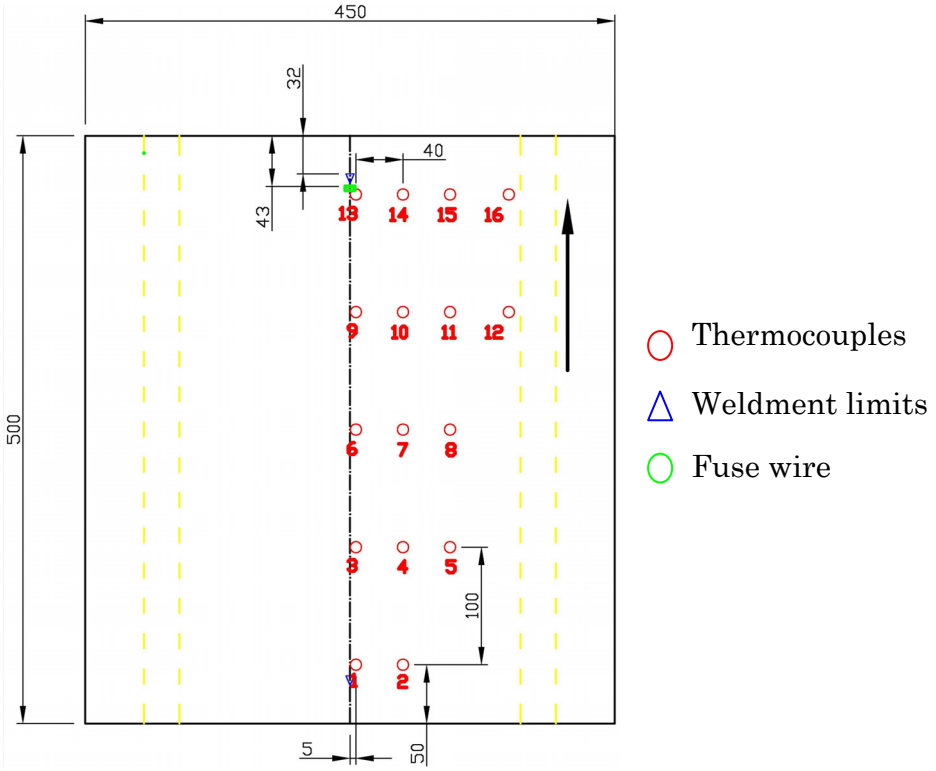


**Figure 41 - Thermocouple measurement sites at the plate back surface.**

*2.2.1.2 Aluminium 6082-T6*

In the first, second and third temperature acquisition the thermocouples were placed in the plate top surface, and simultaneously temperatures were acquired by a thermographic camera in the plate back surface.
In the first deposition when the torch was at 55*mm* from the plate edge instability occurred in the electric arc, and thermocouples 10, 11 and 14 suffered from an insulation problem, so their result was not considered. The temperature distributions during welding are presented in Figure 42 a), b) and c).

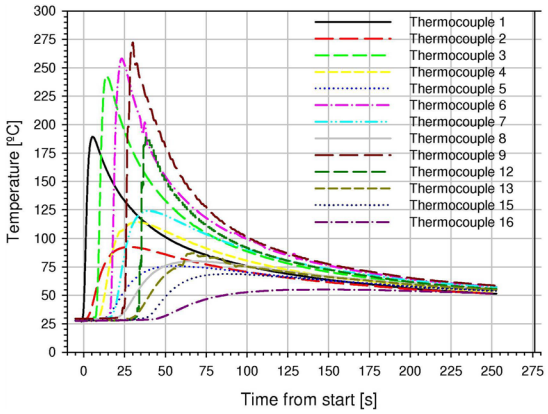


a) deposition 1

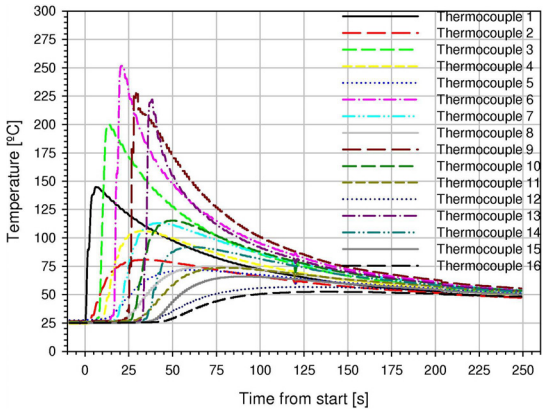


b) deposition 2

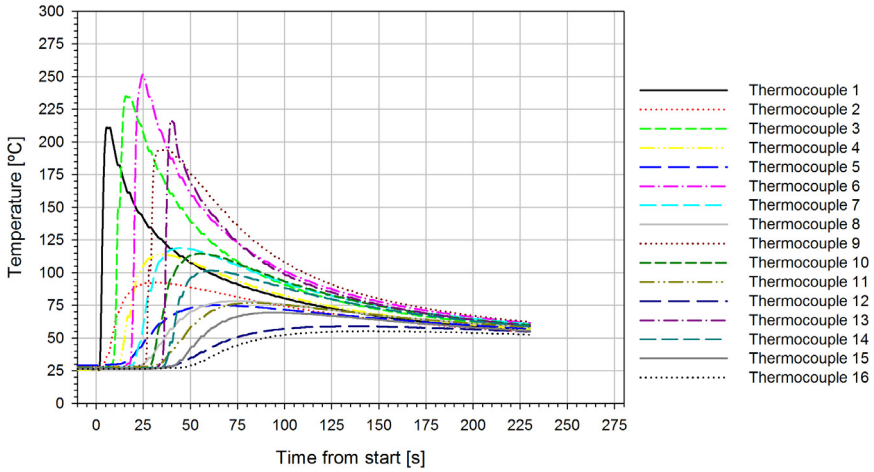


c) deposition 3.

**Figure 42 - Temperature distribution in the plate top surface.**

Since three measurements were performed on the top surface, and to account for experimental variability, judgement was applied to identify the best temperature profile obtained with each thermocouple location, and the result is plotted in Figure 43.

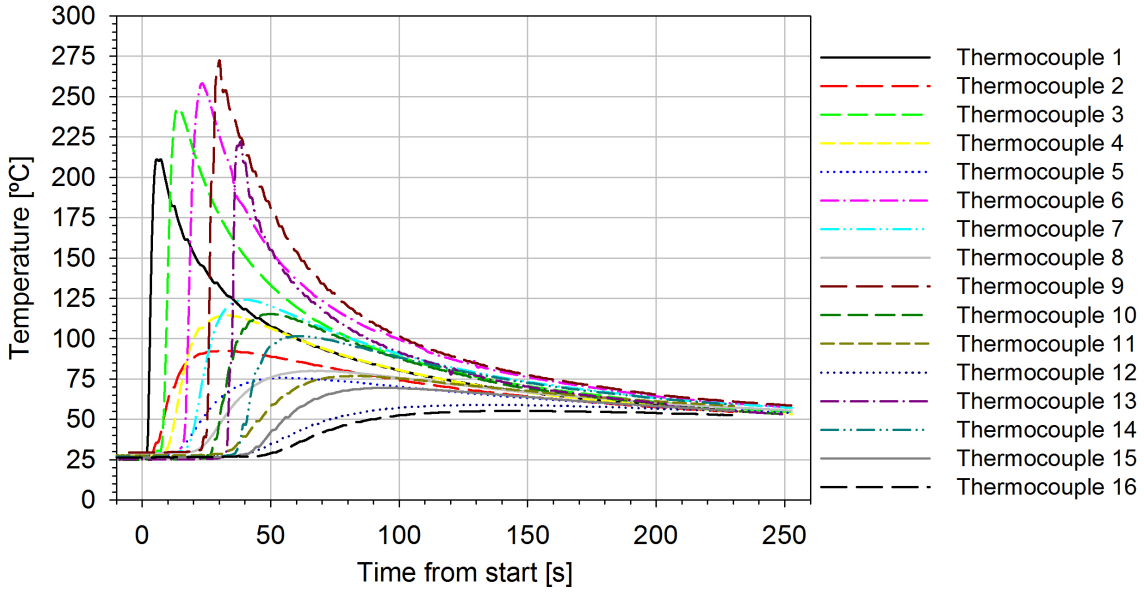


**Figure 43 - Temperature distribution in the plate top surface, results compilation.**

In order to understand the temperature distributions along the plate a comparative plot of the 5 lines and 4 columns of thermocouples temperature profiles are presented. The temperature distributions in column 1, 2, 3 and 4 are presented in Figure 44. Column 1 represents the thermocouples nearest to the weld line. They are positioned at $15mm$ from the weld line and separated by $100mm$ from each other. As the welding advances in the plate, at the same distance from the weld line, thermocouples acquire higher temperatures. This trend is identified comparing the maximum temperatures of thermocouples 1, 3, 6 and 9. Since thermocouple 13 is almost coincident with the end of the weldment it has a lower temperature than thermocouple 9.

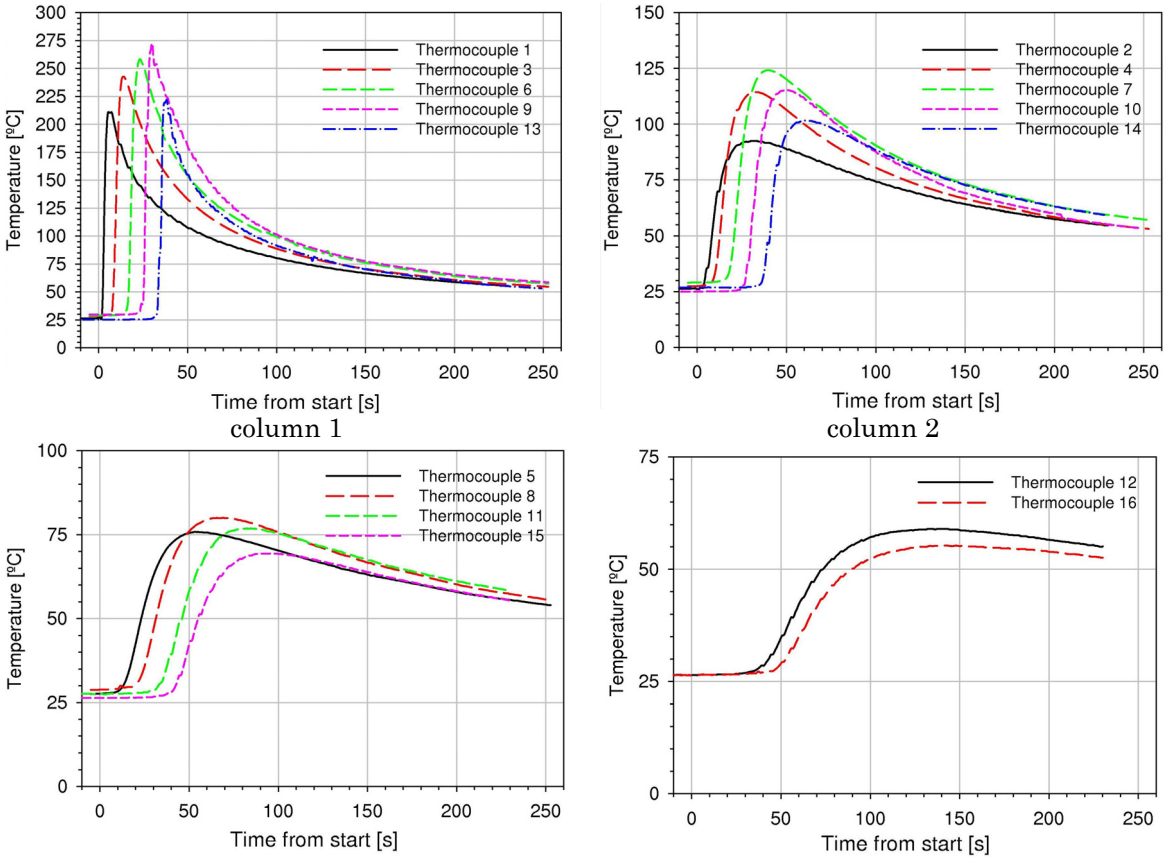


**Figure 44 - Temperature profiles in thermocouples placed parallel to the weld line.**

The temperature distributions in lines 1, 2, 3, 4 and 5 are presented in Figure 45. These lines represent the perpendicular direction to the weld line and are placed $100mm$ between each other. As expected, a temperature decrease in the perpendicular direction to the weld line is present in all plots.

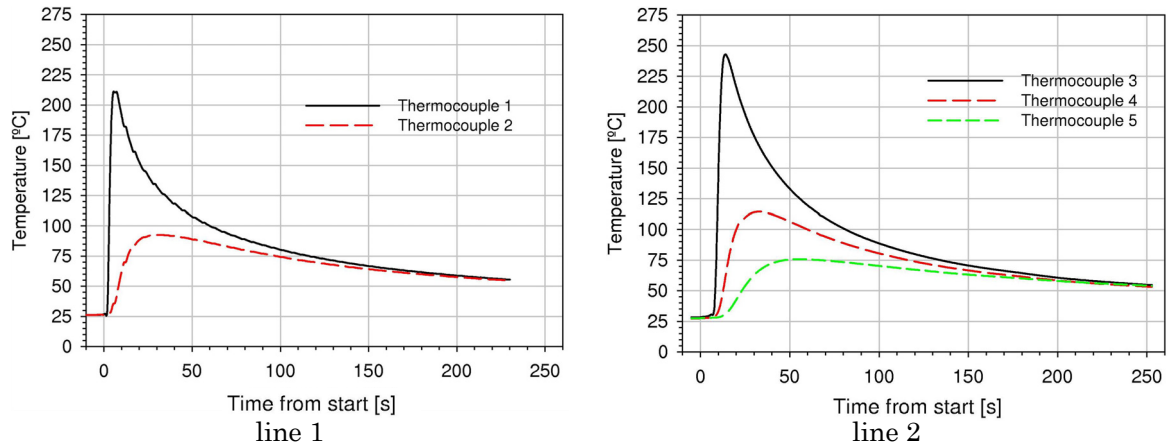

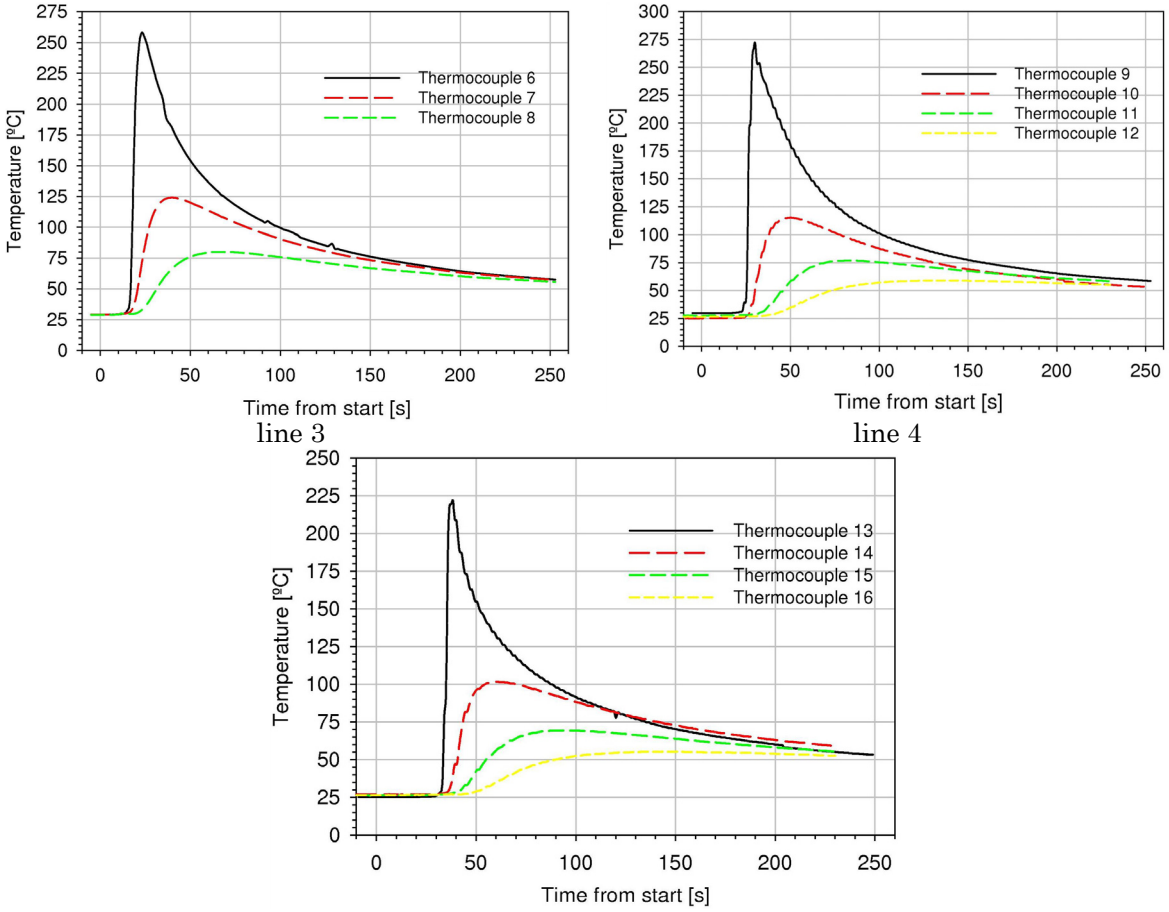


**Figure 45 - Temperature profiles in thermocouples placed perpendicular to the weld line.**

In the fourth weld deposition the temperatures were measured in the plate back side using thermocouples (thermocouple 9 was not considered). In this deposition, measurements with the thermographic camera were not performed. The temperatures measured are presented in Figure 46.

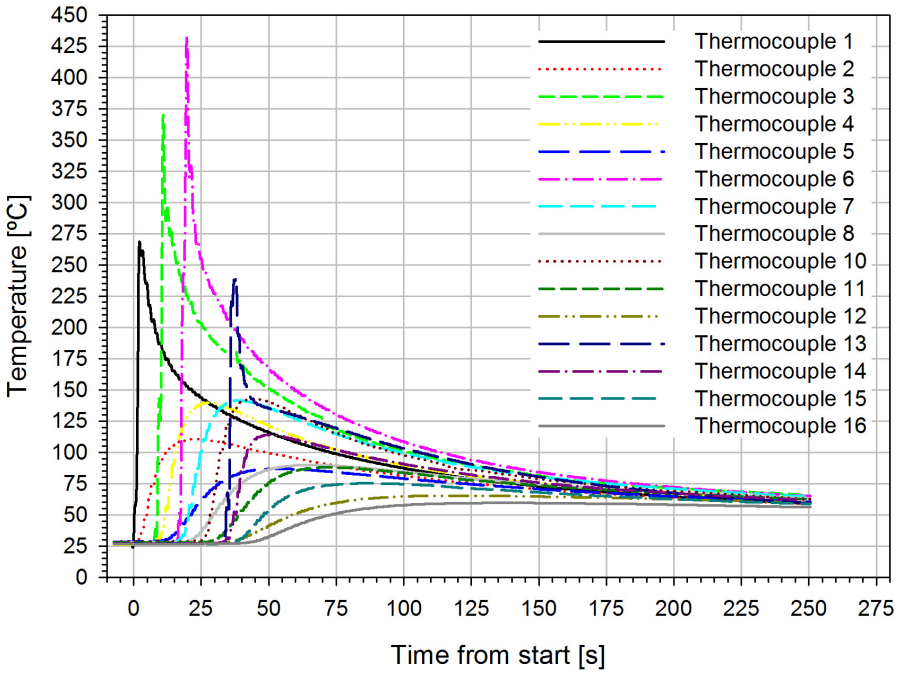


**Figure 46 - Temperature distribution in welding deposition 4, plate back side.**

To understand the temperature distributions along the plate back surface a comparative plot of the 5 lines and 4 columns of thermocouples temperature profiles are presented. The temperature distribution in column 1, 2, 3 and 4 are presented in Figure 47. Column 1 represents the thermocouples nearest to the weld line. In this case, they are positioned at $5mm$ from the weld line and separated by $100mm$ from each other. Again, as the welding advance in the plate, at the same distance from the weld line thermocouples acquire higher temperatures.

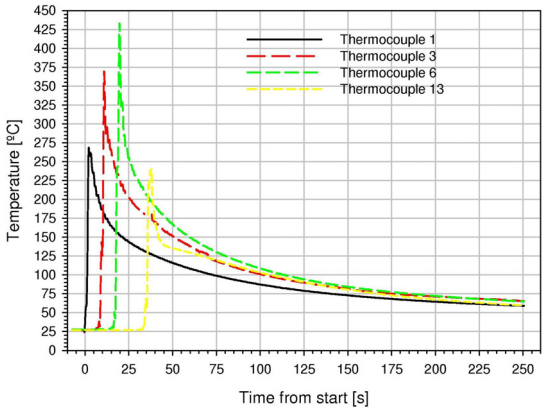


column 1

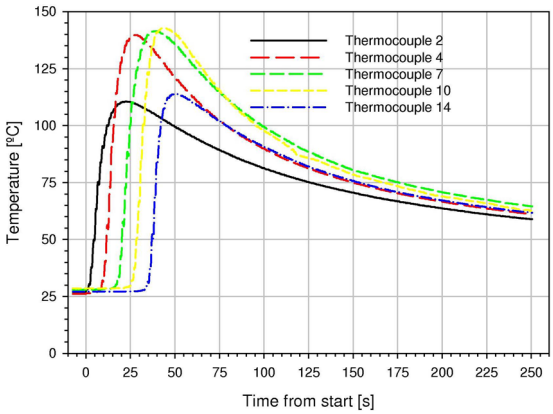


column 2

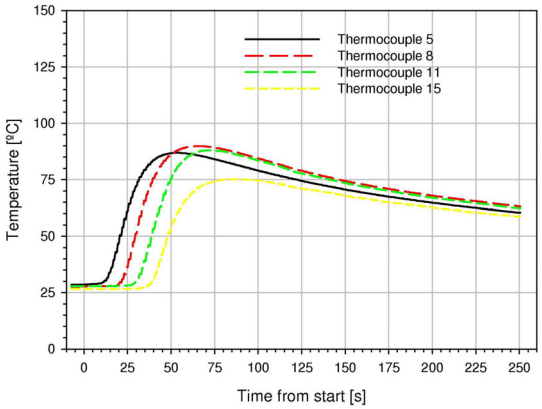


column 3

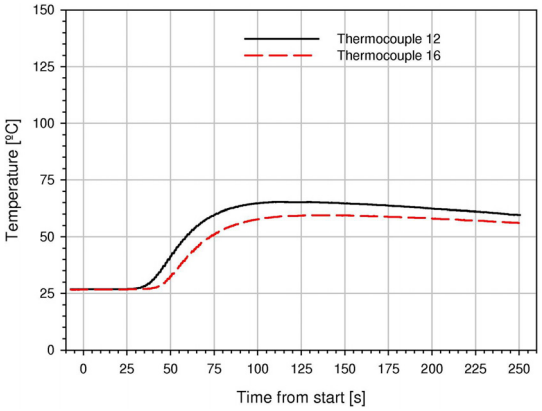


column 4

**Figure 47 - Temperature profiles in thermocouples placed parallel to the weld line in the plate back surface.**

The temperature distributions in lines 1, 2, 3, 4 and 5 are presented in Figure 48, showing the expected temperature decrease in the perpendicular direction to the weld line.

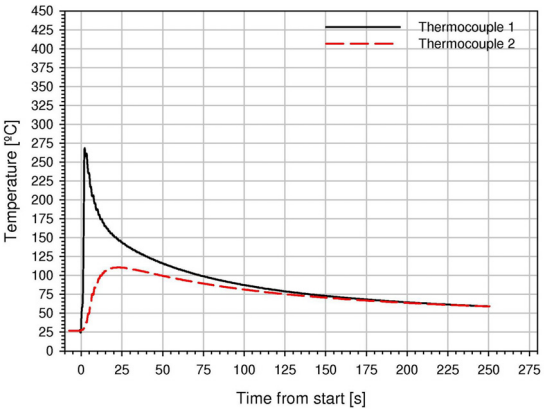


line 1

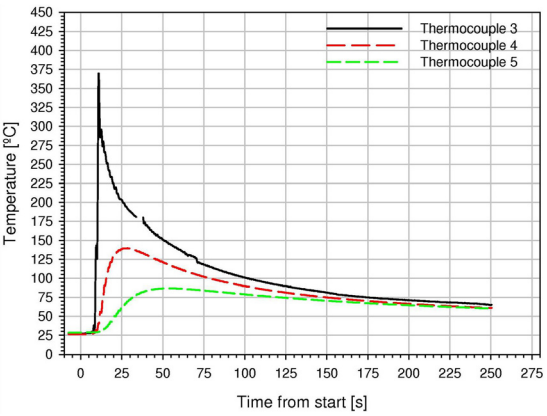


line 2

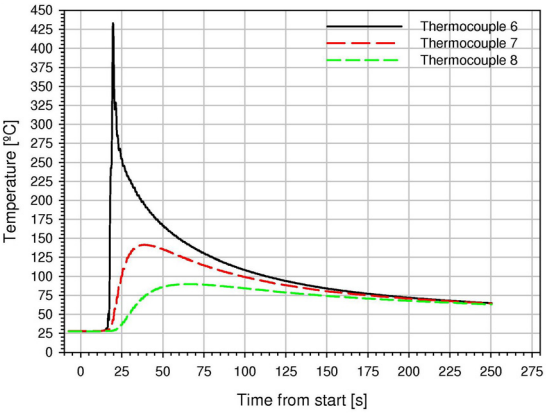


line 3

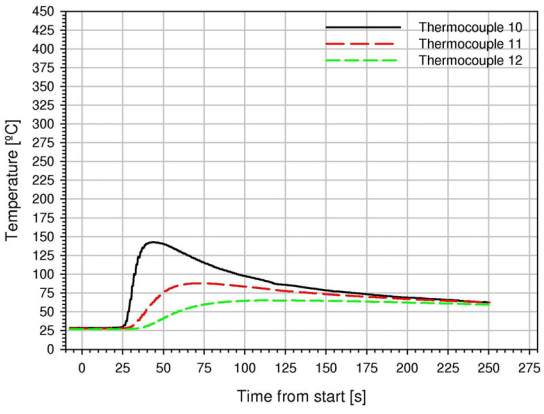


line 4

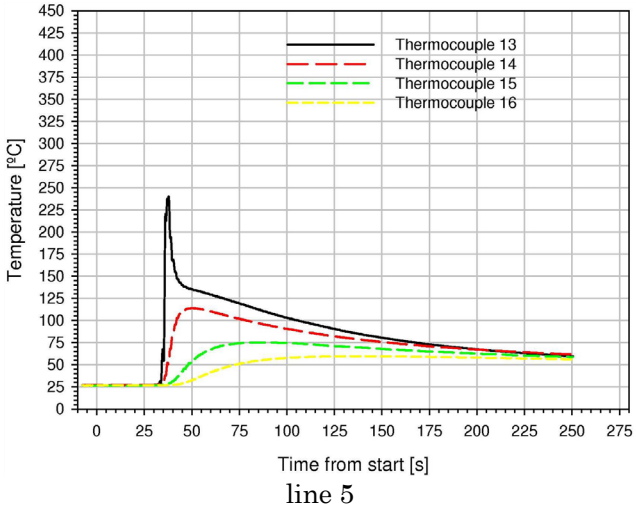


**Figure 48 - Temperature profiles in thermocouples placed perpendicular to the weld line in the plate back surface.**

A direct comparison between two lines of thermocouples, line 3 (thermocouples 6, 6 and 8) and line 5 (thermocouples 13, 14 and 15), placed in the top and back surface is presented in Figure 49. All lines of temperature distribution were successfully fitted with a power equation. As expected, for the same line, the temperature is higher in the top surface.

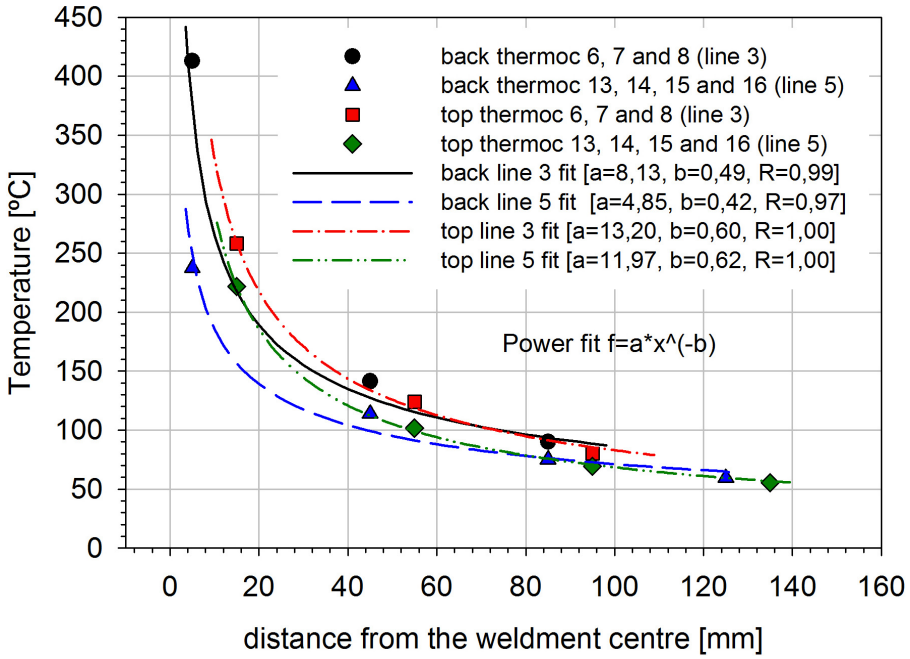


**Figure 49 - Temperature distribution in the plate top and back surface**

*2.2.1.3 Aluminium 6061-T6*

Since two measurements were performed on the back surface, and to account for experimental variability, judgement was applied to identify the best temperature profile obtained with each thermocouple, and the result is plotted in Figure 50.

Detail information of the measurements performed in each deposition can be found in the Appendix A.

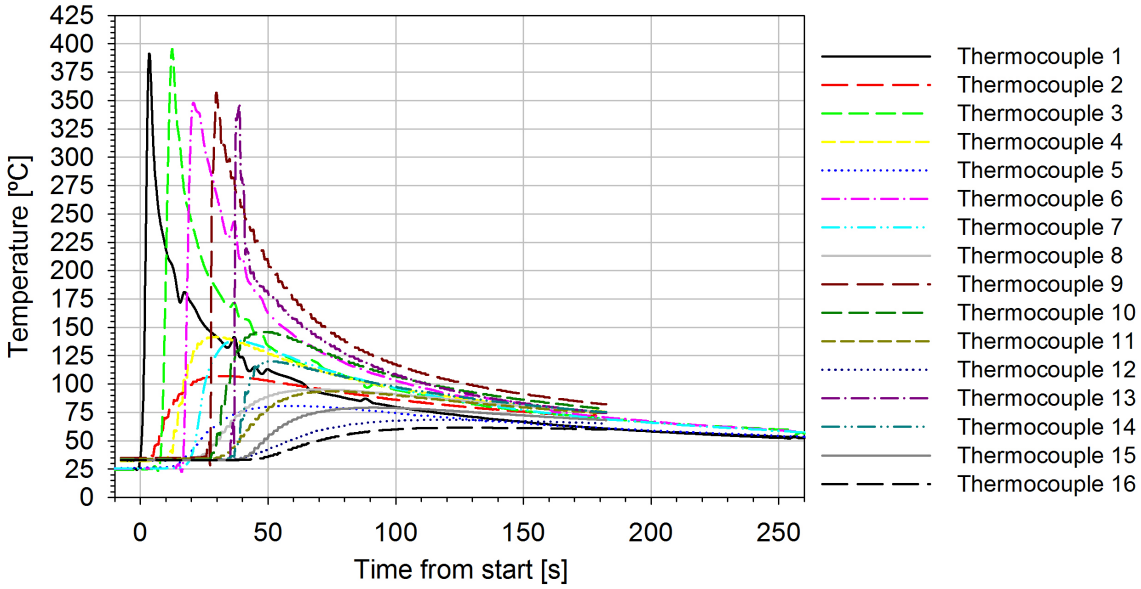


**Figure 50 - Temperature distribution in the plate back surface.**

In the third and fourth depositions temperatures were acquired by thermocouples in the plate top surface. The best temperature profiles obtained with each thermocouple are plotted together in Figure 51. Detail information of the temperature distribution along the plate top surface can be found in the Appendix A.

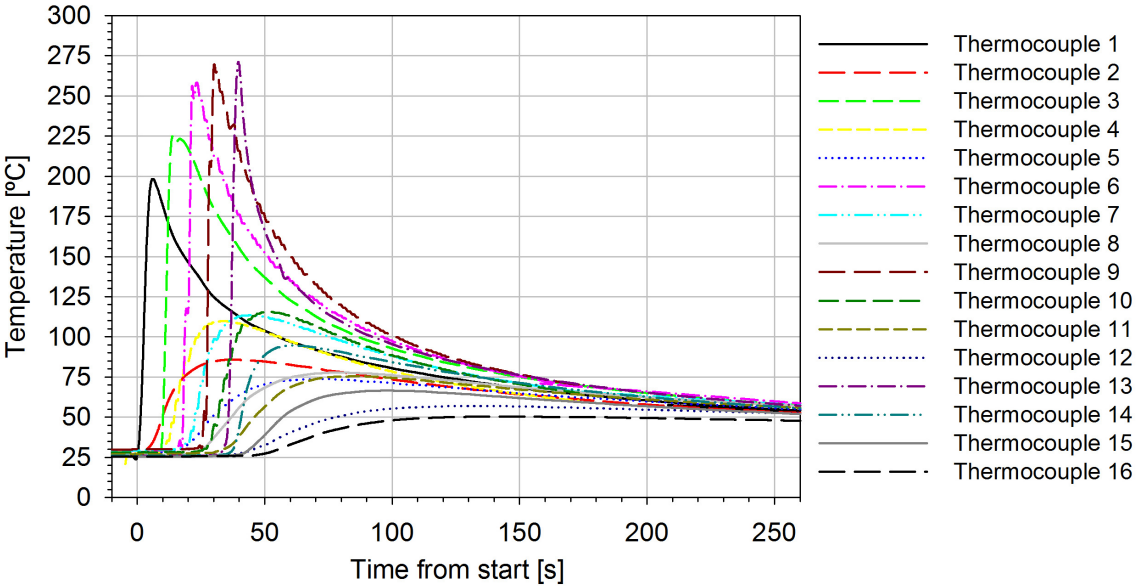


**Figure 51- Temperature distribution in the plate top surface.**

A direct comparison between two lines of thermocouples, line 3 and 5, placed in the plate top and back surface is presented in Figure 52. All lines were

successfully fitted with a power equation. As expected, for the same line, the temperature is higher in the top surface.

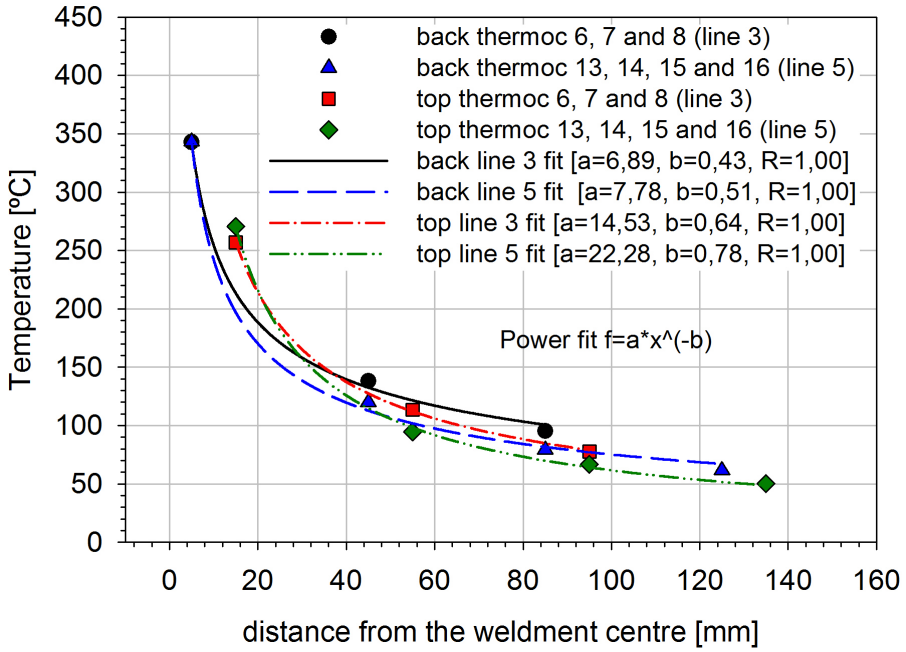


**Figure 52 - Temperature distribution in the plate top and back surface.**

### *2.2.2 FSW welding – temperature profiles*

To acquire the temperature profile during FSW, welds on aluminium 6082-T6 plates were performed using the parameters: welding speed of $800 mm/min$; pitch angle of 2º; rotating speed of $1500 rpm$. The FSW process was performed using a tool with a $4 mm$ diameter threaded pin and a shoulder of $10 mm$ diameter. The penetration depth was adapted to produce a fully penetration butt joint in a material of $3 mm$ thickness. Thermocouples were placed in the plate top surface as presented in Figure 53.

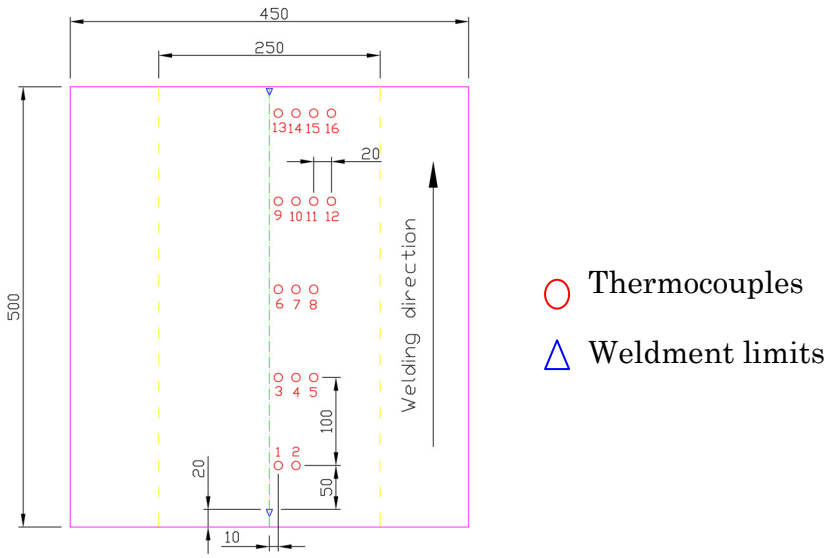


**Figure 53 - Thermocouples temperature acquisition sites**

A 1000*mm* long instrumented plate used for the two different trials of temperature acquisition is presented in Figure 54.

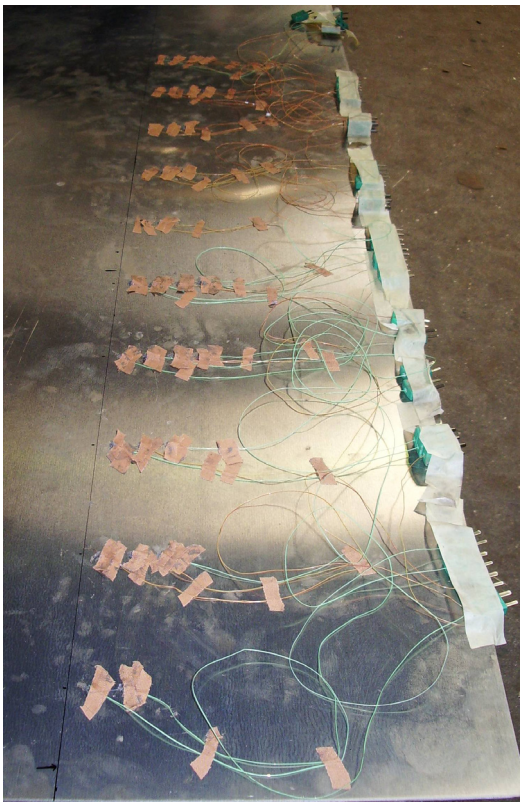

**Figure 54 - 1000*mm* long instrumented plate.**

Since two measurements were performed in the top surface, the best temperature profiles obtained with each thermocouple are plotted together in Figure 55. Detail information of the measurements performed in each deposition can be found in the Appendix A.

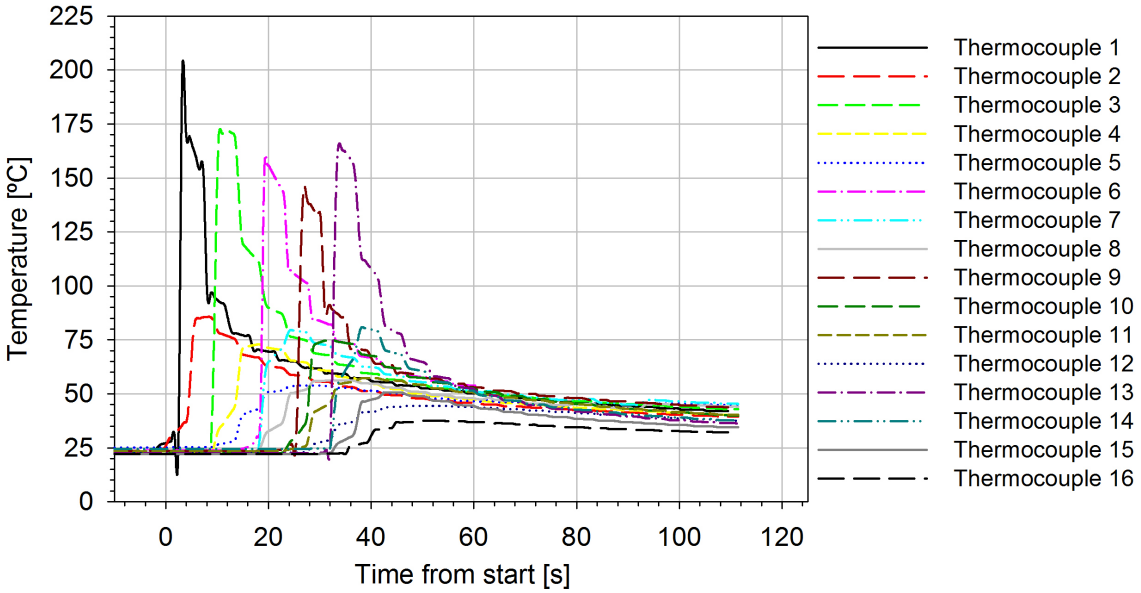


**Figure 55 - Temperature distribution in the plate top surface.**

A direct comparison between 2 lines of thermocouples, line 3 and 5, placed in the top surface is presented in Figure 56. All lines temperature distributions were successfully fitted with a power equation.

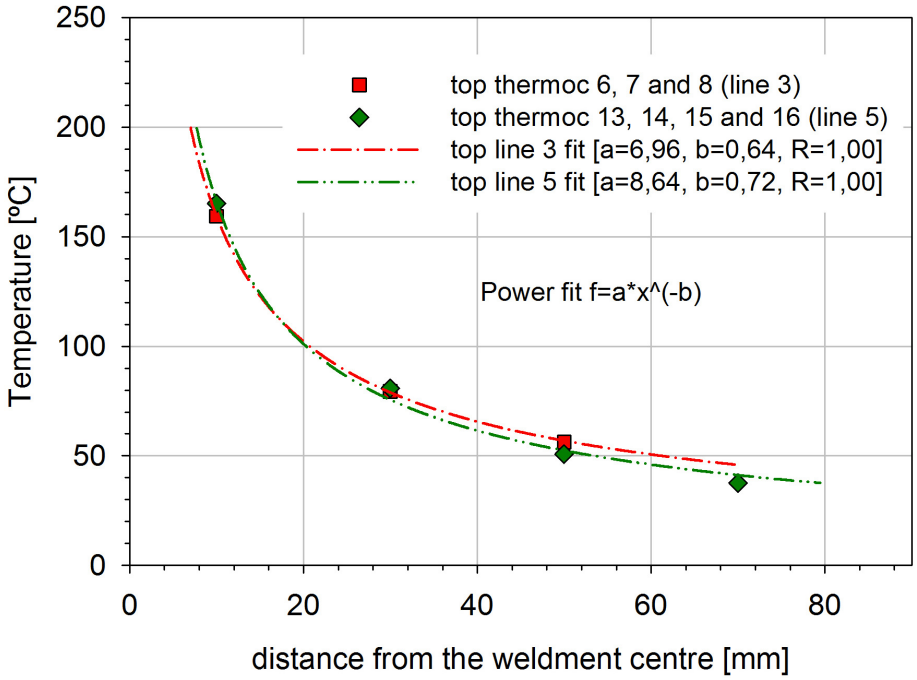


**Figure 56 - Temperature distribution in line 3 and 5 of the top surface.**

In a work by Chen *et al.* [102] measurements of the temperature distribution in an aluminium 6061-T6 friction stir welded at $350 mm/min$ are presented. Lower temperatures are found in the present study, which can be justified by the much higher welding speed used ($800 mm/min$).

### *2.2.3 LBW welding – temperature profiles*

A weldment was deposited in an aluminium 6082-T6 plate and another weldment in an aluminium 6061-T6 plate using a Nd:YAG laser, and the temperature profiles during these laser beam welding processes were studied. Preliminary tests were performed in order to obtain welds with no visually detected defects, as lack of penetration or unstable weldment. Different parameters were used for the aluminium 6082-T6 and the aluminium 6061-T6. For the aluminium 6082-T6 the parameters used were: power $4 kW$; travelling speed $50 mm/s$; gap $0{,}2 mm$; focal length $200 mm$; gas flow $40 l/min$ He; gap $0{,}2 mm$; wire diameter $1{,}2 mm$; wire speed $6{,}7 m/min$; wire typeER4043. For the aluminium 6061-T6 the parameters used were: power $4 kW$; travelling speed $50 mm/s$; focal length $200 mm$; gas flow $40 l/min$ He; gap $0{,}2 mm$; wire diameter $1{,}2 mm$; wire speed $5{,}5 m/min$; wire type ER4043. Each weldment deposition lasted approximately $9 s$ and temperatures where acquired at a frequency of $15 Hz$.
Plates of $500 \times 500 mm$ were instrumented in the plate top surface according to the scheme presented in Figure 53, with the first line of thermocouples placed at

5*mm* from the weld line. An instrumented plate, during and after the welding procedure, is presented in Figure 57.

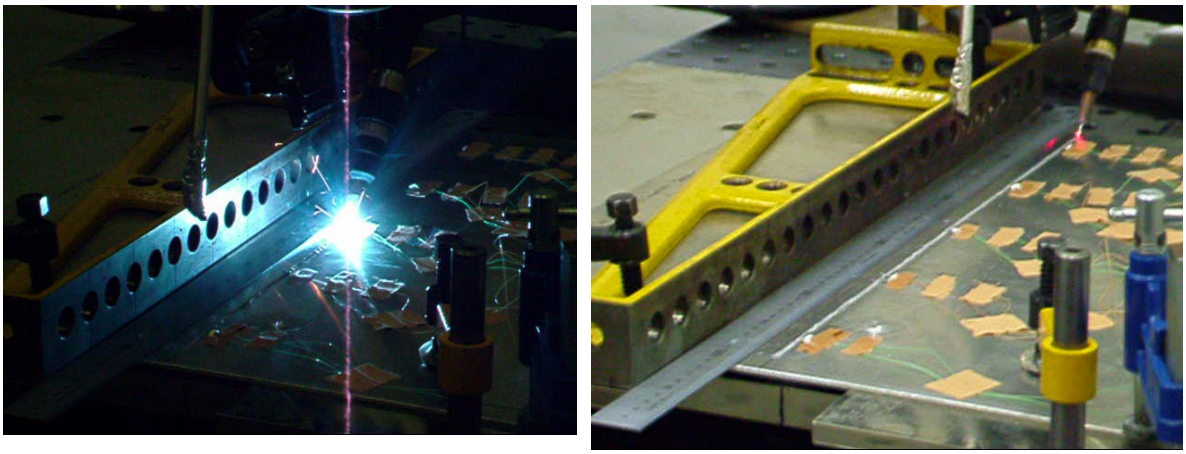

a) during welding b) after welding

**Figure 57 - LBW process instrumentation.**

*2.2.3.1 Aluminium 6082-T6*

In the aluminium 6082-T6 plate a weldment of 460*mm* length was deposited. Thermocouples 2, 11, 14 and 15 failed due to an error in their setup. The temperature distribution during welding is presented in Figure 58. Detail information of the measurements performed can be found in the Appendix A.

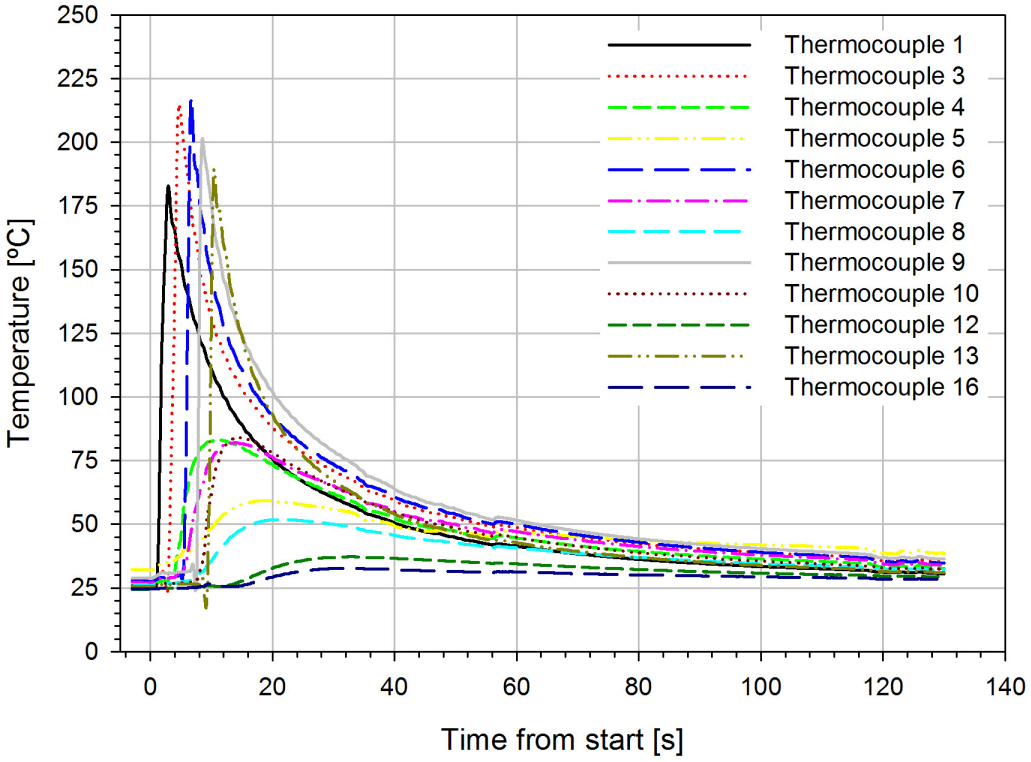


**Figure 58 - Temperature distribution during welding of the AA6082-T6 plate.**

*2.2.3.2 Aluminium 6061-T6*

In the aluminium 6061-T6 plate a weldment of 460$mm$ length was deposited. Thermocouples 11 and 14 failed due to an error in their setup. The temperature distribution during welding is presented in Figure 59. Detail information of the measurements performed can be found in the Appendix A.

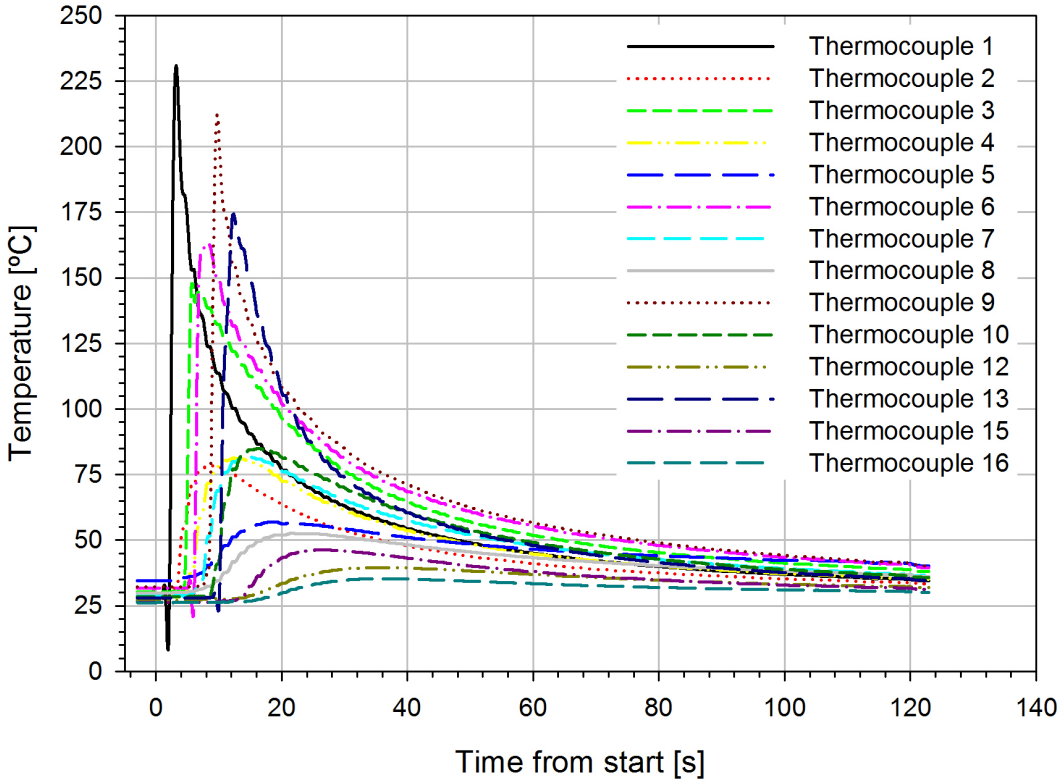


**Figure 59 - Temperature distribution in welding of the AA6061-T6 plate.**

### *2.2.4 Results comparison and concluding remarks*

The difference of temperature distribution in LBW process when compared with the MIG and FSW processes plot is presented in Figure 60. This figure shows a direct comparison of the temperature profile obtained in the perpendicular direction to the weldment in a line containing thermocouples 6, 7 and 8 (see Figure 53).

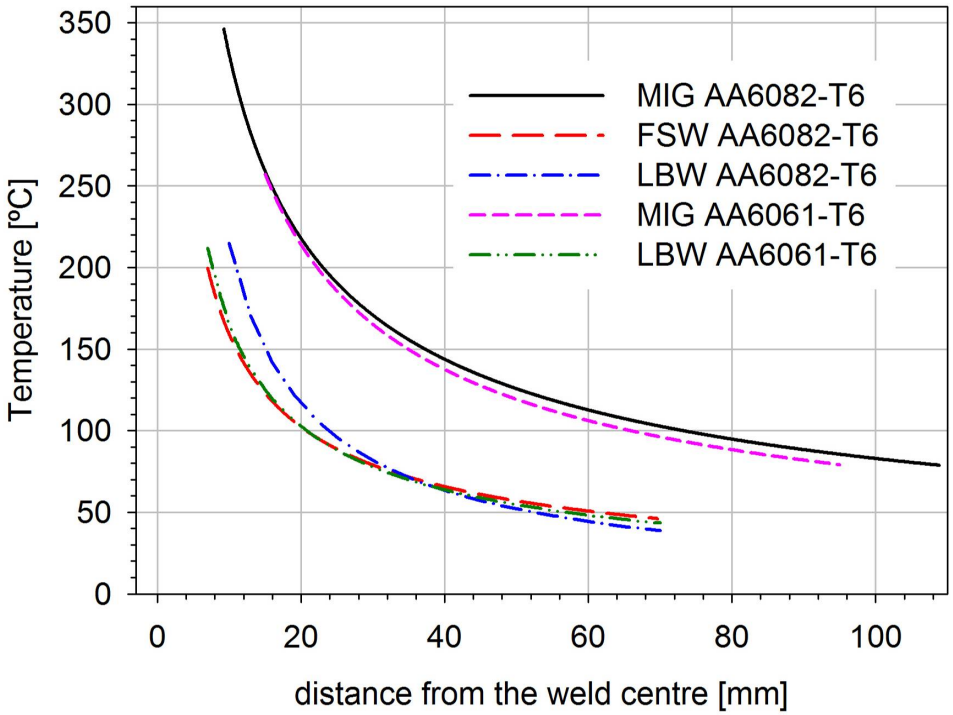


**Figure 60 - Temperature profile for the MIG, FSW and LBW processes in a line containing thermocouples 6, 7 and 8.**

Despite the differences in the boundary constraints the MIG welding presented the higher temperature profile for both materials. The LBW and FSW welds present approximately similar temperature profiles at the distances being compared.

## 2.3 Conclusions

As a result of this work, the following conclusions may be reached:

- Three different temperature acquisition systems during GMAW welding were analysed: thermocouples, a thermographic camera and fibre Bragg grating sensors, and it was concluded that:
    - The best results were achieved with the $0{,}08mm$ diameter thermocouples with their junction covered by thin cyanoacrylate glue clad to insulate electrically the thermocouples from the plate. In this set of tests a comparison between maximum temperatures in each point acquired with thermography and thermocouples shows a good agreement between both techniques.
    - A feasible technique to use FBG sensors to acquire temperatures in welding procedures was developed. Sensors protected with cyanoacrylate glue, stripes of aluminium foil covering each sensor, and a silicon based compound were able to maintain integrity of

measurement at a distance of 15$mm$ in the perpendicular direction to the weld line. Results obtained with FBG sensor and thermocouples present good agreement, particularly as concerns the maximum value. The results obtained suggest the possibility to use this new type of sensors to acquire temperature values in the aggressive conditions found in the arc weld side of the plate.

- Using thermocouples, and despite the differences in the boundary constraints, the MIG welding presented the higher temperature profile for both materials. The LBW and FSW welds present approximately similar temperature profiles at the distances being compared.
    - A comparison of temperature profiles for MIG, FSW and LBW revealed that in identical locations MIG temperatures are approximately twice as great as those found in FSW and LBW;
    - For the welding parameters used, FSW and LBW presented rather similar temperature measurements in identical locations.

# Chapter 3

# Residual stress evaluation

Residual stresses are locked-in stresses which exist in a structural part in the absence of any service or other external loads. Residual stresses may be detrimental with a predominant contribution to fatigue and other structural failures. Quantitative estimation of such residual stresses is important for safe performance of structural components.
Chapter three is dedicated to a comparative study of several residual stress measuring techniques.

The work presented in Section 3.4 was presented as: P M G P Moreira, V Richter-Trummer, R A M da Silva, M A V de Figueiredo, P M S T de Castro, Residual stress evaluation of a MIG welded plate using the sectioning method and the hole drilling method, 7º Congresso Nacional de Mecânica Experimental - CNME 2008, Vila Real, Portugal, January 23–25, 2008.

The work mentioned in Section 3.5 was presented at the Residual Stress Summit 2007: V Richter-Trummer, S M O Tavares, P M G P Moreira, P M S T de Castro, Residual stress measurement using the contour and the sectioning methods: Application to MIG and FSW joints, in Proceedings of the 3rd Residual Stress Summit, ORNL, USA, October 1-4, 2007 (cd available from the Society for Experimental Mechanics - SEM).

# 3. Residual stress evaluation

Residual stresses are locked-in stresses which exist in a structural part without the application of any service or other external loads. The effects of residual stress may be either beneficial or detrimental, depending upon the magnitude, sign (tensile or compressive), and distribution of the stress with respect to the in service applied loads. Residual stresses added to the applied stresses act in mechanical components during its service life. Usually, residual stresses are detrimental with a predominant contribution to fatigue and other structural failures.
Residual stresses are created due to mechanically induced plasticity or by thermal effects [120]. In most cases, residual stresses arise from the production process. Virtually all manufacturing and fabricating processes (casting, welding, machining, molding, heat treatment, etc.) introduce residual stresses and reduce the damage tolerance of those mechanical equipments because of their tensile nature. As the manufacturing process introduces residual stresses in the component, quantitative estimation of residual stress is important for safe performance of structural components, [121].
Arc welding processes introduce high residual stresses which can be in the order of the material yield stress. Nevertheless, some surface treatment techniques introduce superficial compressive residual stresses which retard crack initiation.

Residual stress may be divided into three categories:

- residual stresses of first kind (type I), acting over several grains;
- residual stresses of second kind (type II), acting over one grain;
- residual stresses of third kind (type III), acting within one grain.

The residual stresses type II and III, microscopic stresses, were not evaluated in this study. Type I residual stresses are macroscopic stresses acting over a group of grains, which were evaluated in this work.

To measure residual stress, usually the locked-in stress must be relieved so that a sensor can register the change in strain caused by removal of the stress. This is usually done destructively or semi-destructively by sectioning or by removal of successive surface layers.
Destructive methods are mechanical methods based on the relaxation of residual stresses when portions of the analyzed specimen are removed by some kind of

machining or other material removing procedure. This may include the sectioning method, the contour method, and the X-ray measurement with which, following adequate material removal procedures, through the thickness results can be obtained.
In some structures, if a small hole is drilled to measure the strain relief (hole-drilling method), this can be considered almost non-destructive. The structure may stay usable as long as the created holes do not introduce significant stress concentration points, detrimental to its strength. Such methods are known as semi-destructive methods.
Diffraction is the most efficient non-destructive technique available. X-ray and neutron diffraction strain measurement techniques do not require stress relaxation and offer a non-destructive alternative, but also have limitations. They allow studying and separating all three kinds of residual stress. Unfortunately they need complex and expensive equipment, which can limit field application, and usually are limited to strain measurements in a limited depth.

Welding is one of the most significant causes of residual stresses and typically produces large tensile stresses whose maximum value can be approximately equal to the yield strength of the materials being joined, balanced by lower compressive residual stresses elsewhere in the component. These large tensile stresses are often responsible for premature component failure. In the affected areas, due to the elastic superposition principle, high tensile stresses may appear which can easily exceed the yield strength of the material during service life.
During the welding process, a localized expansion may occur in the heat affected zone. While the metal is still in its fusion state, this space may be taken up either by molten metal (filler material) or by repositioned base material. The cooling process down to operating temperature may not occur in a homogeneous way throughout the whole plate. Some parts of the material may cool and therefore contract faster than others, leading to the creation of deformations and residual stresses, [122]. The high initial stress level at some locations (like near the welding joint for example) strongly influences the fatigue life of components. As the stresses induced by welding may be as high as the yield strength of the material, when external loads of some kind are applied to the structure, plasticity may occur.

In this study residual stresses in an aluminium alloy 6082-T6 (yield stress of 276$MPa$ and rupture stress of 323$MPa$) MIG butt welded 3$mm$ thick plate were evaluated using the sectioning, the X-ray diffraction and the hole drilling methods (destructive, semi-destructive and non-destructive methods, respectively). Fusion welding (MIG) normally introduces very high residual stresses because of the large thermal gradient near the welded joint.

### 3.1 Sectioning method

The sectioning method, an expensive and somehow time-consuming method, consists in making a cut on an instrumented solid in order to release the residual stresses that were present on the cutting line. Typically it is applied to plates.

The cutting process used shall not introduce plasticity or heat, so that the original residual stress can be measured without the influence of plasticity effects on the cutting planes' surface. Strain gages have to be applied to the section that should be measured, and then a cut is made near this section. The maximum possible resolution of this method depends on the number of strain gages used. The main relaxation of residual stresses due to the cut can be related to the residual stresses using equation (1).

$$\sigma = -\varepsilon \cdot E \quad \textbf{(1)}$$

Since the stresses to be determined are the residual stresses that were present before the cut was made, signs of the measured stresses have to be inverted. This procedure was previously applied with success as reported by other authors, *e.g.* [123, 124].

### 3.2 Hole drilling method

The introduction of a hole into a solid containing residual stresses relaxes those at that location. The hole drilling method for residual stress measurements was first proposed by Mathar [125]. Presently, this method is a widely accepted technique for measuring residual stresses. It is a semi-destructive technique where a tolerable small volume of material is removed.
The method is very versatile and can be performed in either the laboratory or the field, on different materials components ranging widely in size and shape. The hole is typically $0{,}8mm$ to $4{,}8mm$ in both diameter and depth. Nevertheless, achieving accurate results is not trivial; a meticulous measurement practice and the choice of data analysis method are crucial to obtaining good results.

The basic hole drilling procedure, standardized in ASTM E837 [126], involves drilling a small hole into the surface of a component at the centre of a special strain gage rosette and measuring the relieved strains. The theoretical background for the hole drilling method was first developed on the basis of a small hole drilled completely through a thin, wide, flat plate subjected to uniform plane stress. Such a configuration is far from typical applications since ordinary components requiring residual stress analysis may be of any size or shape, and are rarely thin or flat. In reality, in most practical applications of the method, a blind hole is drilled with a depth equal to its diameter, and small compared to the thickness of the component. The residual stresses originally at the hole location are then calculated from the measured strain values acquired with a special strain rosette, Figure 61.

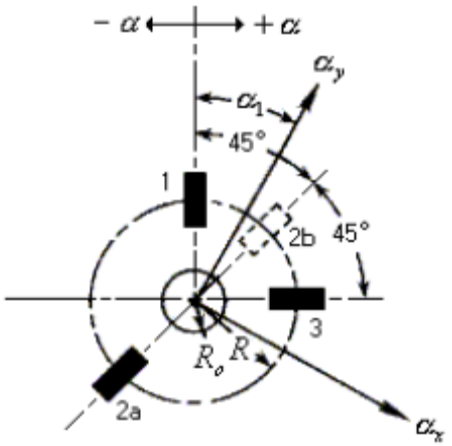


**Figure 61- Strain rosette arrangement for determining residual stresses, [127].**

The objective of the hole drilling measurements is to evaluate in-plane residual stresses that can be assumed to be uniform with depth either from the surface of a thick specimen, or through the thickness of a thin specimen. ASTM E837 [126] refers to these cases. However, in many practical cases, the residual stresses are not uniform with depth. In such cases, the assumption of uniform stress with depth may give a misleading solution.
A blind hole produces a very complex local stress state which implies the use of empirical techniques for calculation of the residual stresses from the measured strains. Incremental hole drilling, which involves carrying out the drilling in a series of small steps, improves the versatility of the method and enables stress profiles and gradients to be measured.

The data-reduction relationships, equation (2), are applicable to the blind-hole when appropriate coefficients are available. Compared to the through-hole procedure, blind-hole analysis involves one additional independent variable; namely, the dimensionless hole depth, Figure 62.

$$\sigma_{\max} = \frac{\varepsilon_1 + \varepsilon_3}{4\overline{A}} \pm \frac{1}{4\overline{B}} \sqrt{\left(\varepsilon_3 - \varepsilon_1\right) + \left(\varepsilon_3 + \varepsilon_1 - 2\varepsilon_2\right)^2}$$

$$\tan 2\alpha = \frac{\varepsilon_1 - 2\varepsilon_2 + \varepsilon_3}{\varepsilon_1 - \varepsilon_3} \qquad \textbf{(2)}$$

Thus, in a generalized functional form, the coefficients can be expressed as:

$$\overline{A} = f_A\left(E, \nu, r, Z/D\right)$$
$$\overline{B} = f_B\left(E, \nu, r, Z/D\right)$$

where r is the ratio between the hole diameter and an arbitrary radius from hole centre. For any given initial state of residual stress and a fixed hole diameter the relieved

strains generally increase (at a decreasing rate) as the hole depth is increased. Therefore, in order to maximize the strain signals, the hole is normally drilled to a depth corresponding to at least Z/D=0,4 (ratio of the hole depth to the mean diameter of the strain gage circle).
For any given set of material properties, Young modulus E and Poisson's ratio ν, the coefficients $\overline{A}$ and $\overline{B}$ are simply geometric functions, and thus constants for all geometrically similar cases.

Whether the residual stress analysis application involves through hole or blind-hole drilling, the coefficients $\overline{A}$ and $\overline{B}$ must be determined to calculate the stresses from the relieved strains. In the case of the through hole, the coefficients $\overline{A}$ and $\overline{B}$ can be accurate values obtained by analytical calculation. This is done by integrating, over the area of the gage grid, the component of strain parallel to the primary strain-sensing axis of the gage.
Nevertheless, the needed coefficients for either through-hole or blind-hole analysis can always be determined by experimental calibration. This procedure automatically accounts for the mechanical properties of the test material, strain gage rosette geometry, hole depth and diameter, and the strain-averaging effect of the strain gage grid. Its principal disadvantage is that the calibration must be repeated each time a different set of geometric parameters is involved.
As an example the $\overline{A}$ and $\overline{B}$ coefficients for the rosettes used in this study are provided graphically in [127] for the blind holes and through holes assuming, in both cases, that the initial residual stress is uniform with depth. Special strain gage rosettes for residual stress analysis, among other features, incorporate centring patterns for positioning the boring tool precisely at the centre of the gage circle.

A fundamental test should be made to check that the residual stresses are uniform within the hole depth. This test indicates what type of analysis should be performed, uniform stress data or non-uniform stress data. As recommended in ASTM E837 [126], it is always preferable to drill the hole in small increments of depth, recording the observed strains and measured hole depth at each increment. This procedure allows the judgment whether the residual stress is essentially uniform with depth, thus validating the use of the standard full-depth coefficients and for calculating the stress magnitudes. If incremental measurements are not taken, there are no means for making references about stress uniformity, and the calculated residual stress may be in error.
The incremental data, consisting of relieved strain versus hole depth, can be used to detect if a non-uniform stress distribution is present. The Standard outlines the graphical procedure, Figure 62, for determining stress uniformity based on combination strains. The sums and differences of the measured strain data $\varepsilon_3+\varepsilon_1$ and $\varepsilon_3-\varepsilon_1$ or $\varepsilon_3+\varepsilon_1-2\varepsilon_2$ should be calculated for each depth increment [126]. The data should be expressed as fractions of their values when the hole depth equals 0,4 times the mean diameter of the strain gage circle. The data points indicate the percentage values of the specified strains and the curves show the limits of the two largest computed combination strains. This approach may be extended further by calculating the strain values for the theoretical case where the residual

stresses are uniform with depth. The graph should yield data points very close to the curves presented in [126]. Data points that deviate by more than 3% from the curves presented in the standard indicate either substantial stress non-uniformity through the material thickness, or strain measurement errors. In either case, this indicates that analysing the data assuming a uniform stress distribution through the thickness will yield false results.

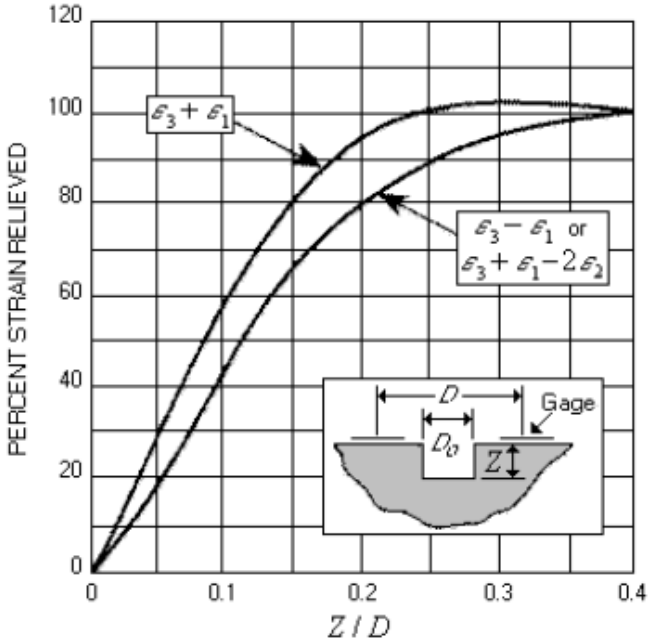


**Figure 62 - Percent strain versus normalized hole depth for uniform stress with depth, [126].**

Four techniques for analysing residual strain data are available in the literature: Uniform Stress, Equivalent Uniform Stress, Power Series and Integral methods. The four methods are as follows [128]:

- Uniform Stress Method – This is the method specified in ASTM E837 [126]. It assumes that the residual stresses are uniform with depth from the specimen surface. Thus, the method has no spatial resolution. However, when the measured residual stresses are truly uniform, this is the method of choice because it is the least sensitive to the effects of experimental error;

- Equivalent Uniform Stress Method– This method of data analysis is described in the Measurements Group Technical Note MG TN 503-5 [127]. The Equivalent Uniform Stress is defined as that stress magnitude, which, if uniformly distributed through the thickness would produce the same total relieved strain, at any depth, as measured during hole drilling. If the residual stress varies with depth, the stresses at incremental depths do not represent the actual residual stress, but the equivalent uniform stress that would produce the same relieved strain at that depth. The results from this technique can be difficult to interpret but can provide qualitative

information about the stress variation with depth. Also known as the average stress method, it is useful only when experimental calibration is available. This method was not used in this study.

- Power Series Method– This method was introduced by Schajer [129] as an approximate technique of calculating non-uniform stress fields from incremental strain data. It assumes a linear variation of residual stress with depth. Finite element calculations are used to relate the removed stresses to the measured strains by computing a series of coefficients corresponding to the strain responses measured during hole drilling. An advantage of the Power Series method is that the least-squares procedure forms a best fit curve through the measured strain data. A limitation of the method is that it is suitable only for smoothly varying stress fields with depth and it is sensitive to measurement errors.

- Integral Method– Initial developments of this method where introduced by Niku-Lari *et al.* [130] among others, where finite element calculations were used as a calibration procedure. In the integral method, the contributions of the total measured strain relaxations of the stresses at all depths are considered simultaneously [131]. This provides a separate evaluation of residual stress within each increment of depth. Thus, the spatial resolution is the highest of all the calculation methods and is the method of choice when measuring rapidly varying residual stresses. However, the sensitivity of the calculated stresses to small experimental errors is also the most severe. The problem rapidly deteriorates if an attempt is made to increase spatial resolution by using many small hole depth increments. In practice, five or six increments yield a satisfactory level of detail for many stress distributions. If this number is significantly increased, residual stresses between successive calculation increments are seen to oscillate about the true stress level. Any additional 'smoothing' of the strain data to reduce oscillation and permit the use of smaller stress calculation increments is unlikely to reveal a significant increase in the detail of the 'true' stress distribution.

A future ASTM standard for the application of the hole drilling technique to uniform and non-uniform stress along the thickness is presently under consideration, [132].

Figure 63 shows a comparison of the results of four stress calculation methods for a non-uniform stress field [131]. The integral method gives a good stepped approximation to the actual stress variation with depth, and the power series method gives a close straight-line fit. The other methods give much less satisfactory results because they are essentially 'calibrated' using uniform stress field data.

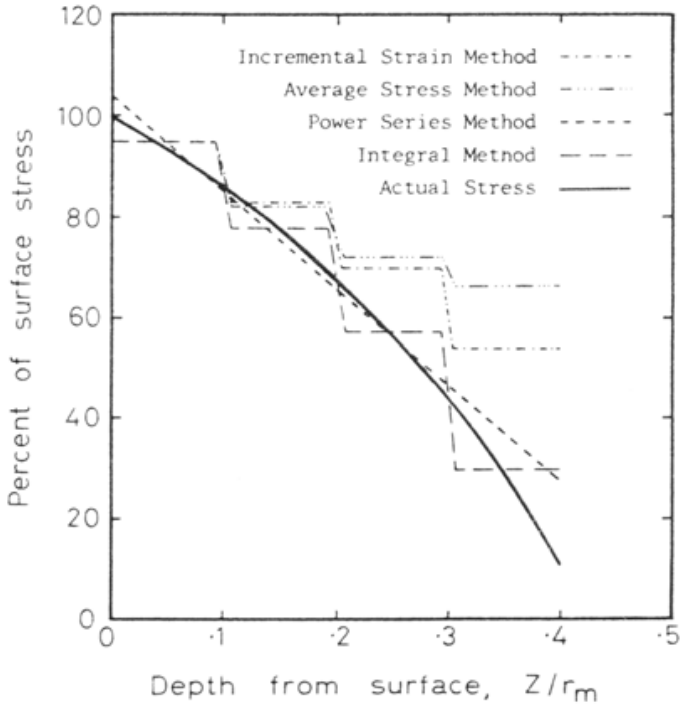


**Figure 63 - Comparisons of the results from four stress calculation methods [131].**

Previous studies have shown that the Integral method usually permits best results for non-uniform stress fields, in particular those where the stress varies rapidly with depth, *e.g.* [128].

### 3.3 X-ray diffraction method

X-ray diffraction is a non-destructive and well-established technique which can be applied for the residual stress evaluation in the near surface region of crystalline solids. Aluminium alloys can exhibit rolling and crystallization textures which, generally, make it difficult to use the technique [133]. In such a situation, the possible reflection directions are restricted to small angular ranges near the intensity poles of the texture and the influences of elastic anisotropy and grain interactions on the X-ray strain measurements may have to be taken into account. The crystallographic texture effects are considered at two steps of the X-ray diffraction stress analysis: the data collection and the stress calculation.

In this study, using Cu-Kα radiation the different alloy components were studied in a small specimen taken from the plate. With this experimental procedure it was observed that aluminium is the major element in the alloy composition, being the only one identified by this method. Nevertheless the diffracted intensities indicate the existence of a metallographic texture.
The texture was studied acquiring the 111, 200, 220, and 311 incomplete pole figures. The background was subtracted, and correction factors were applied for absorption and desfocalization. It was observed that the texture has a weak intensity and the planes 100 are parallel to the surface. Due to this weak texture which generates scattered data, the rolling direction was not possible to identify.

In the deposited weldment a component study was also performed in order to confirm that the aluminium was the major element. This study was performed after the residual stress analysis because it implies the cutting of a segment of the plate (due to the goniometry maximum specimen size). As expected the aluminium was the major element in the weldment.

In a first task measurements were performed in the plate width at the weldment middle length using the entire plate. The residual stress measurements were performed at the plate middle length in the direction perpendicular to the deposited weldment and stresses were measured in the weldment longitudinal direction. Measurements were performed using the Kα-Cr radiation to study the 222 aluminium planes, which have a Bragg angle of approximately 156,6º. For each measurement 17 different angles were used to obtain the stress value. The experimental parameters used indicate that the measurements were performed at a penetration depth of 11,5$\mu m$. The measurements were only performed at the plate top surface.

In a second task the stresses were again evaluated near the weldment with more detail using 50x50$mm^2$ segments cut from the plate. The X-ray diffraction measurements were performed on a four-circle goniometer, provided with a germanium detector. Cu-Kα radiation was used for the data collection studying the 311 aluminium planes, which have a Bragg angle of approximately 139,3º. For each measurement 17 different angles were used to obtain the stress value. The experimental parameters used indicate that the measurements were performed at a penetration depth of 11,5$\mu m$. This plane family is not so influenced by the crystalline anisotropy and is more representative of the macroscopic deformation. Data was acquired for diffraction angles between 136,5º and 142,5º, with steps of 0,15º. The experimental parameters used indicate that the measurements were performed at a penetration depth of 11$\mu m$. In this analysis, besides measuring the stress at the plate surface, the residual stress profile was measured at different depths electro polishing the surface until depths of 5$\mu m$, 100$\mu m$, 300$\mu m$ and 1000$\mu m$. The electro polishing process is expected to have a marginal influence in the residual stresses.

### 3.4 Results

A MIG weld bead was deposited in aluminium alloy 6082-T6 plates with 450x500x3$mm$. The welding parameters used for all tests were: 20$l/min$ of Argon flow rate, 70$cm/min$ weld travelling speed, 128$A$ e 17,1$V$; a stick-out of 15$mm$. The deposited weldment has a width of approximately 8$mm$. The plates, welding parameters and fixing rig is the same used in temperature measurements presented in Figure 22.

### *3.4.1 Sectioning method*

For the acquisition of the longitudinal (weld bead direction) stress relieved during the cut twenty strain gages were used, ten in each side of the plate (back and top side), Figure 64. Strain gages were distributed by both sides of the weld bead to confirm symmetry, and were concentrated in sites where a high stress gradient was expected.

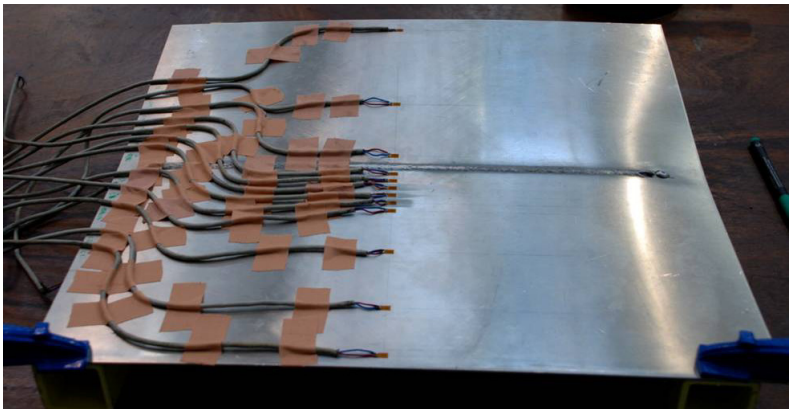

**Figure 64 - Instrumented plate before the sectioning method.**

The gages were connected to three 8-channel Spider8 data acquisition systems manufactured by HBM, and one 4-channel strain gage recorder "P3 indicator and recorder" from Vishay was also used. A personal computer was used to store the measured data from the data acquisition system. Strain gages with the reference Vishay CEA-13-125UN-120 were used; their resistance is 120,0$\Omega$±0,3% and have a gage factor of 2,110±5%. The cut was made on a band saw as presented in Figure 65.

**Figure 65 - Sectioning method experimental setup.**

Two cuts at different distances from the strain gages were performed. The first cut was made at a distance of 10$mm$ from the strain gage line, Figure 66a). The second cut verified that the distance used in the previous one was able to describe the real stress state, Figure 66b). The plate after both cuts is presented in Figure 67. A detail of the sectioned surface after the second cut is presented in Figure 68.

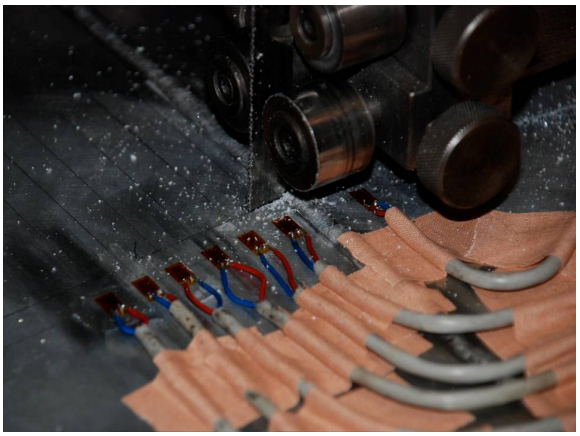

a) first cut

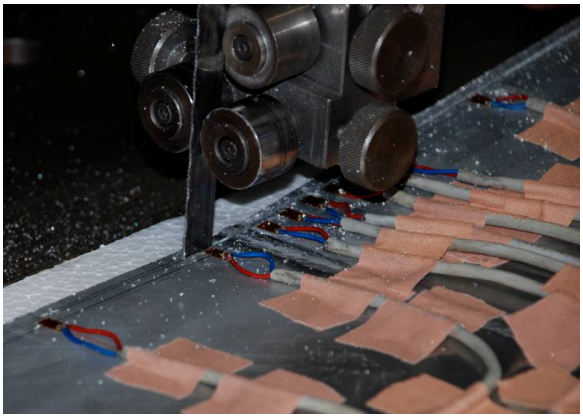

b) second cut

**Figure 66 - Sectioning method, band saw sectioning procedures.**

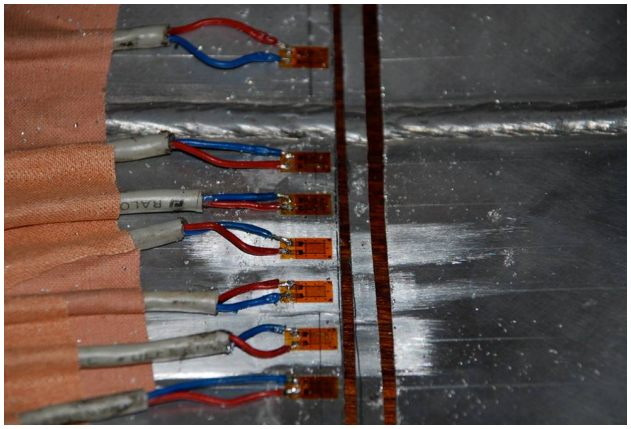

**Figure 67 - Plate after the cuts for the sectioning method.**

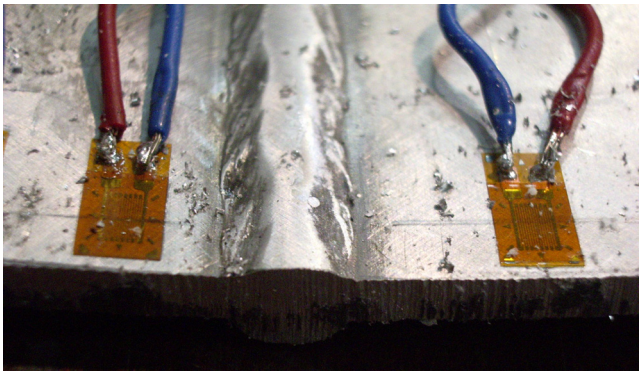

**Figure 68 - Sectioned surface after the second cut.**

The stresses relieved by the second cut are all below 10*MPa* and in most cases below 5*MPa*, see Figure 69, which is almost negligible when compared to the stresses obtained with the first cut, Figure 70.

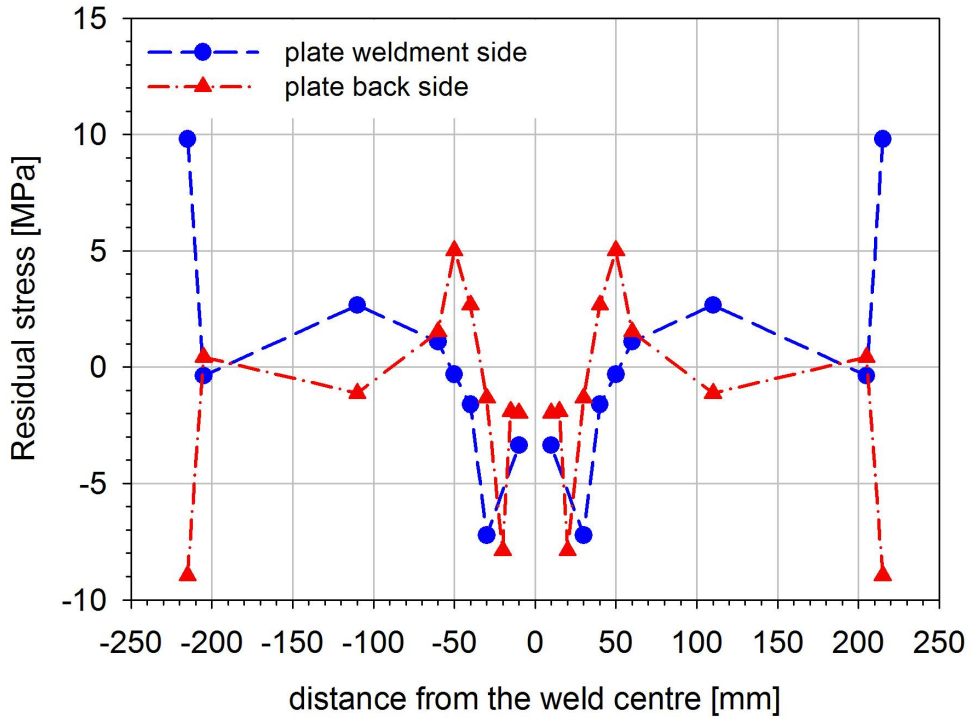


**Figure 69 - Residual stresses measured in the second cut at 5*mm* from the strain gages.**

The residual stress profile measured is presented in Figure 70. A symmetric profile was verified which enabled the representation of the profile in the complete plate width. The residual stress is always higher in the plate top surface (side of the weldment). It was verified that for distances, from the weld centre, higher than 25*mm* that the residual stresses in the back surface have negative values. In the plate top surface, between 35*mm* and 90*mm*, the residual stress has negative values, but for distances higher than 90*mm* they become positive. For distances lower than 25*mm*, the residual stress profile presents positive values increasing towards the weld bead limit.

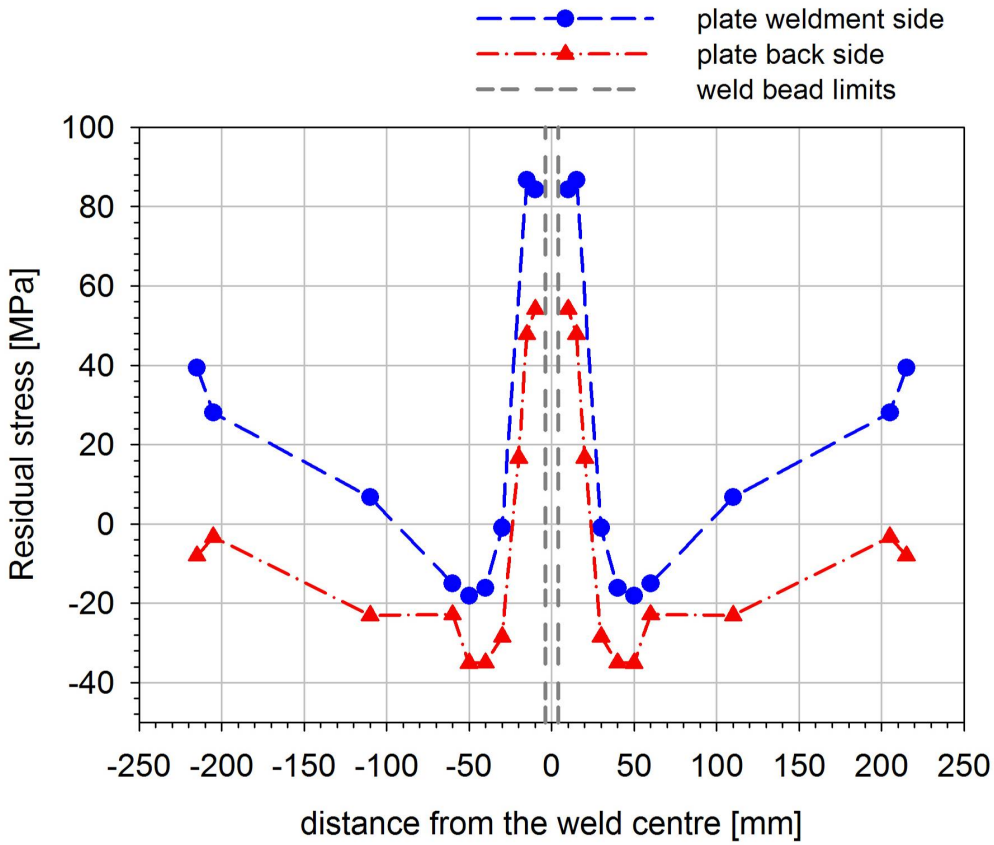


**Figure 70 - Stresses obtained by the sectioning method.**

### *3.4.2 X-ray diffraction method*

The X-ray measurements were performed at Universidade de Coimbra. The first X-ray residual stress measurements were performed without sectioning the plate. Measurements were performed at the plate top surface in the direction perpendicular the weldment near the weldment half length plane. Stresses were acquires in the longitudinal direction of the weldment. The results obtained are presented in Figure 71. The dashed lines are a polynomial fit of data obtained outside the central area, near de weldment. Measurements were difficult to perform and a careful analysis had to be carried out. At points near the weldment a larger scatter was found, but it was observed that the residual stresses tend to have compressive values.

In a second study two 50x50$mm^2$ specimens were cut from the plate and more detailed measurements were performed near the weldment. The results obtained are presented in Figure 72. Near and inside the weldment, in all analysis, compressive stresses were measured.

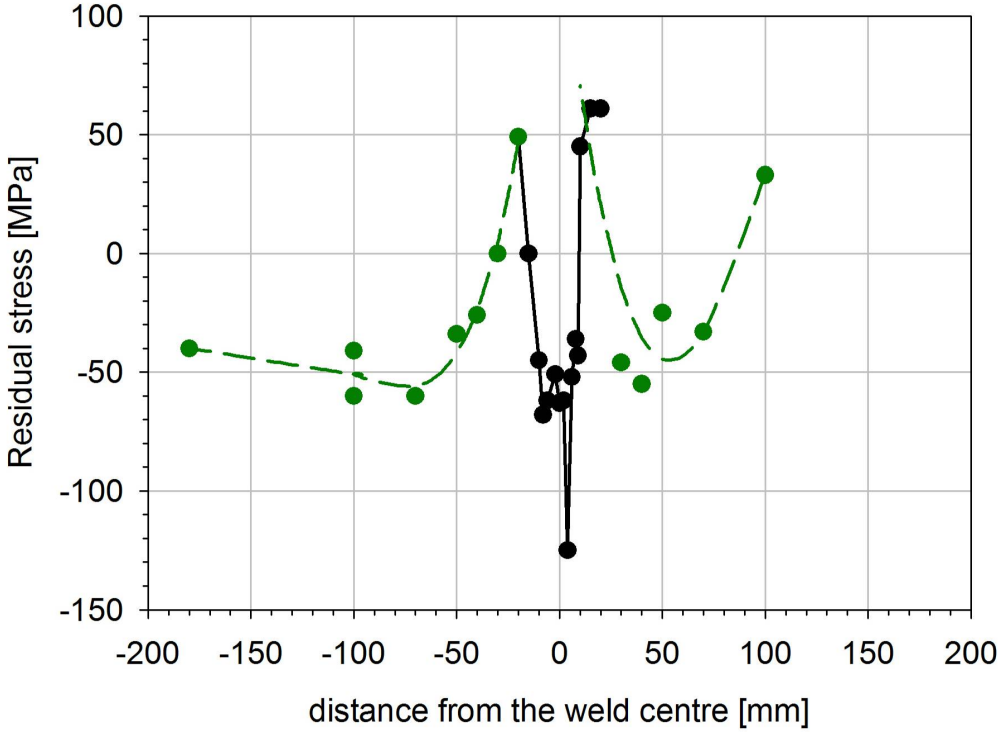


**Figure 71 - X-ray diffraction residual stress values in the full plate width.**

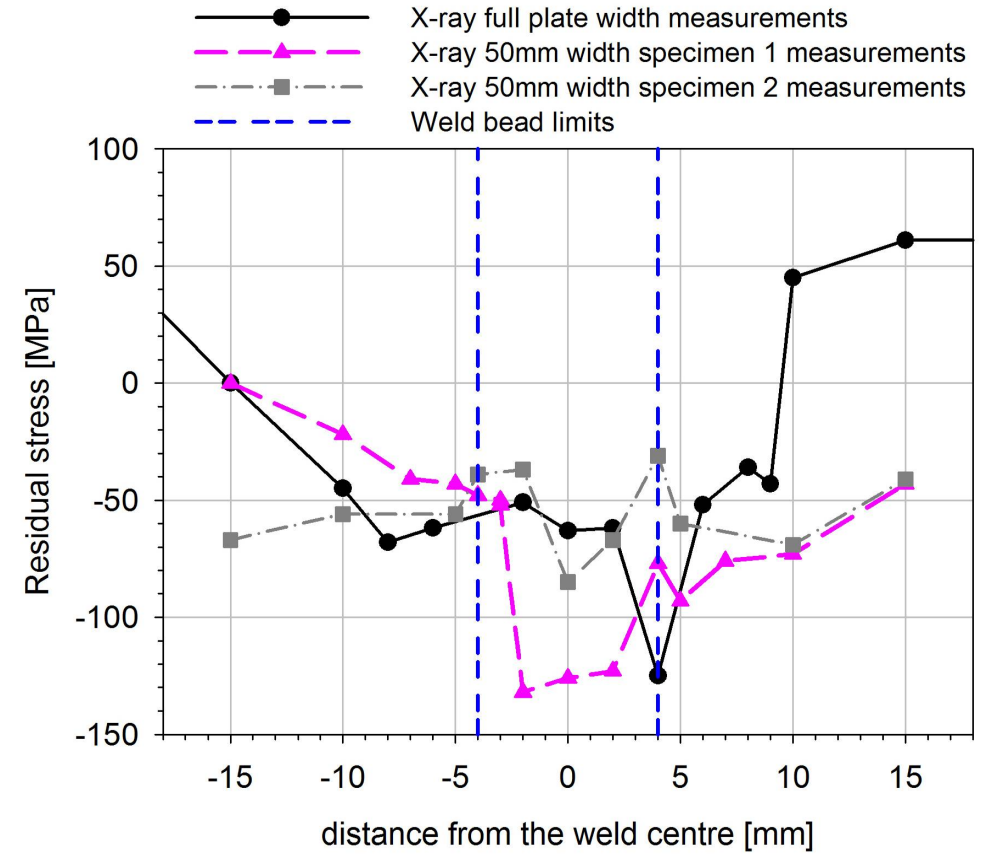


**Figure 72 - X-ray diffraction residual stress values near the weld bead using the full plate and two small specimens.**

In a third study, residual stresses were analysed until a depth of 1000$\mu m$, Figure 73. This analysis was achieved using one of the small 50x50$mm^2$ specimens, and removing layers of material by electro polishing. Measurement performed at a higher depths, revealed that the residual stresses present less compressive values; residual stresses at 1000$\mu m$ depth are near zero.

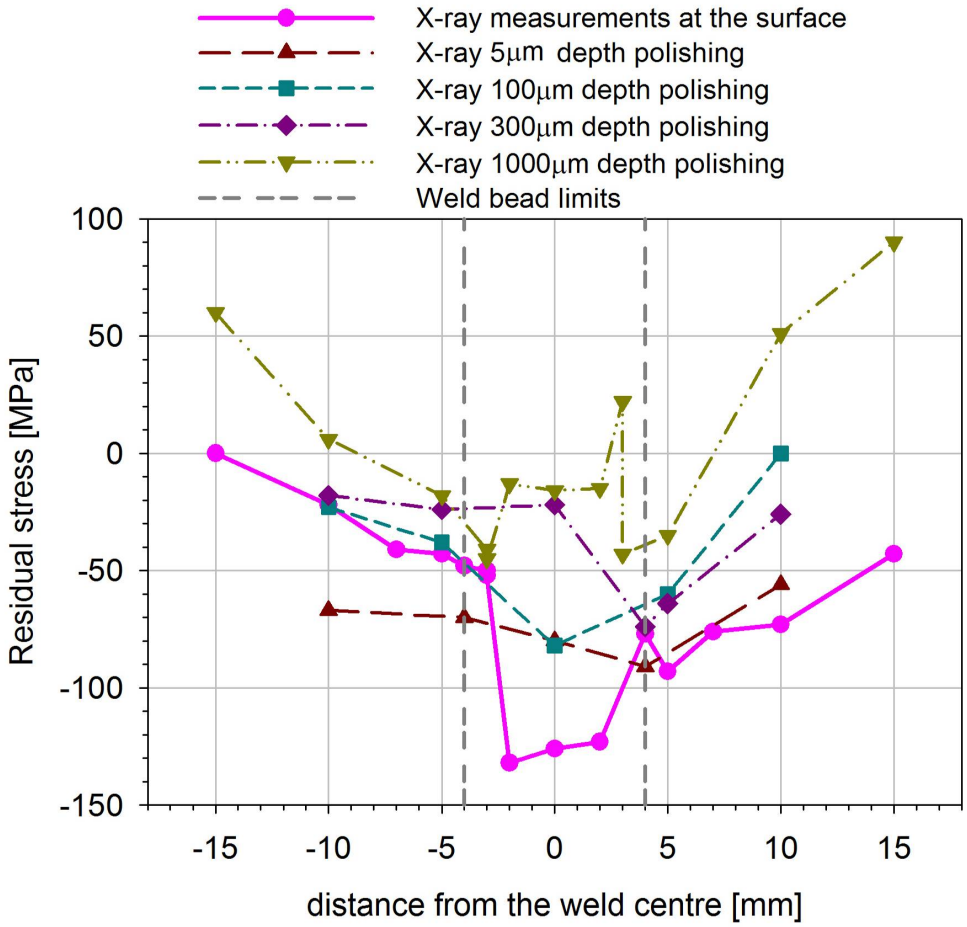


**Figure 73 - X-ray diffraction residual stress values through the thickness.**

### *3.4.3 Hole drilling method*

Special three-element strain gage rosettes were installed on the test plate at the point where residual stresses were to be determined. Seven 120Ω rosettes were used for measurements: five rosettes CEA-13-062UM-120 and two rosettes CEA-13-062UL-120. The UL designs have the gage-circle diameter equal to 3,25 times the active gage length. The 062UM rosette configuration has the same ratio of gage circle to grid length, but the grids are narrower to permit their close grouping on one side of the hole. As a result, the sensitivity of the gage to the relieved strains is slightly greater. The rosettes main characteristics are presented in Table 2.

**Table 2 - Rosettes characteristics [*mm*]**

| | CEA-13-062UL-120 | CEA-13-062UM-120 |
|---|---|---|
| Gage length (per section) | 1,57 | 1,57 |
| Grid centreline diameter | 5,13 | 5,13 |
| Hole diameter | 1,5 to 2,0 | 1,5 to 2,0 |
| Matrix length | 12,7 | 9,6 |
| Matrix width | 15,7 | 12,2 |
| Rosette configuration | 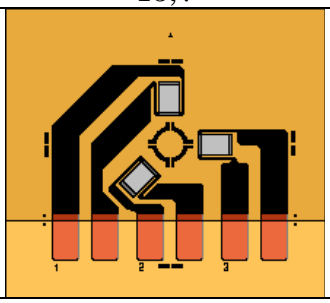 | 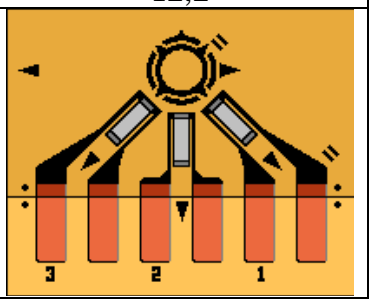 |

A precision milling guide was attached to the test part and accurately centred over a drilling target on the rosette. A detail of the milling equipment used is presented in Figure 74. Also details of a hole being drilled are presented in Figure 75. The hole has to be shallow and align through the centre of the rosette.

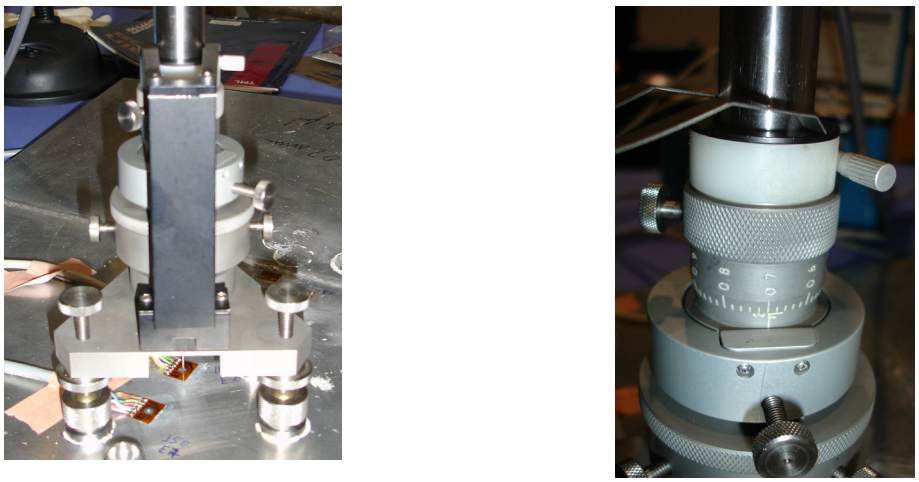

**Figure 74 - Milling machine used for the hole drilling process.**

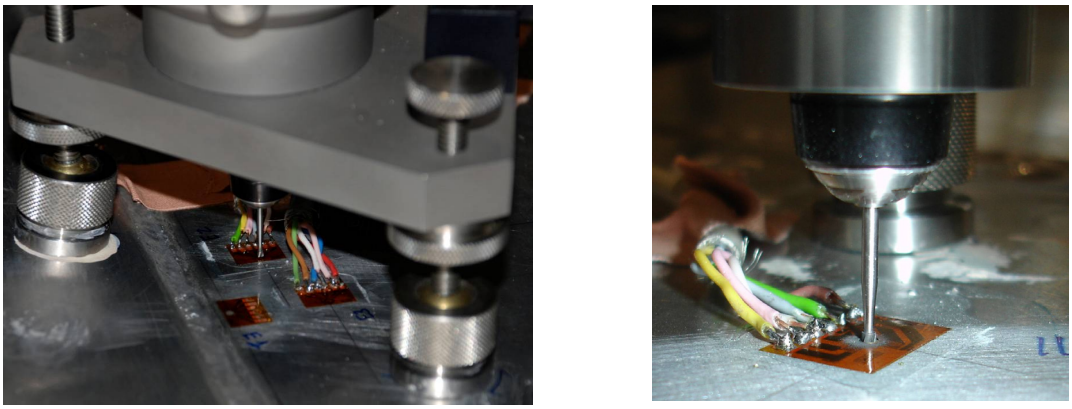

**Figure 75 - Hole drilling procedure.**

The holes were drilled with a carbide-tipped cutter with 1,6*mm* of diameter. The seven holes were positioned relatively to the centre of the weldment, in its perpendicular direction, at locations of: 7,4*mm*, 15*mm*, 20*mm*, 30,4*mm*, 45*mm* 115*mm* and 150*mm*. The minimum distance from the weldment centre that was possible to place a rosette was 7,4*mm*. As an example, details of the hole drilled nearest to the weldment (7,4*mm*) are presented in Figure 76. Because of the weldment bead irregular geometry and surface it was not possible to place any rosettes at the top of the weldment.

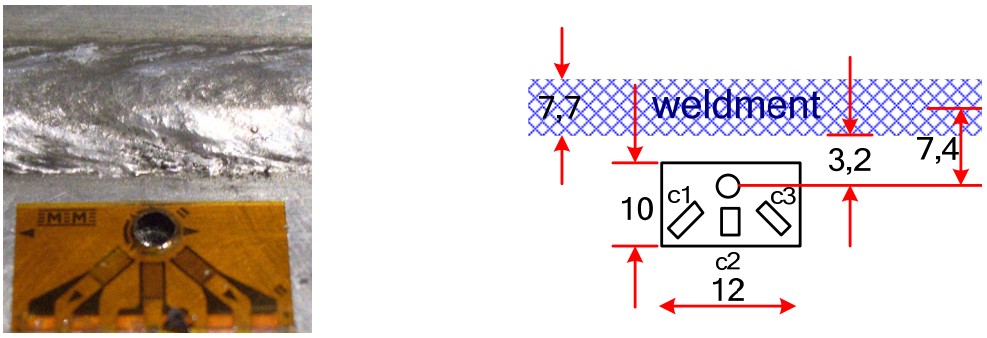


**Figure 76 - Nearest hole to the weldment.**

Measured strain data was analyzed using the commercial software H-Drill [134]. Using special data-reduction relationships the principal residual stresses and their angular orientation are calculated from the measured strains.

The choice of which stress calculation method to use depends on which one gives the most satisfactory balance between a realistic result and a stable solution. Since the nature of the residual stresses being measured is generally not known in advance, the strategy was to try all three methods (Integral, Power Series, and Uniform Stress). An engineering judgment combined with knowledge of the stresses expected were used to choose the most appropriate stress calculation method.
The difference between the strains corresponding to the stress solution and the actual measured strains is called the "misfit". A modest misfit is acceptable providing that it is of similar size to the uncertainty (experimental error) in the strain measurements. Also, the simple test which compares the experimental data with the percent strain *vs.* normalized hole depth for uniform stress helped to defined what type of data was being analyzed, uniform stress data or non-uniform stress data.
In all the seven sets of measured strain data, the uniform method could not be applied due to the variation of the residual stress field through the thickness. In this analysis the X stress is the stress in the weldment longitudinal direction and the Y stress is align perpendicular to the weldment.

### *3.4.3.1 Hole drilled at 7,4mm from the weldment*

The results obtained with the integral and power method are presented in Table 3. Analyzing the data for the hole drilled at 7,4*mm* from the centre of the

weldment it was observed that the integral method gave the best result, Figure 77. Nevertheless results were only valid until a depth of approximately 0,25*mm*. At the surface a compressive residual stress field occurs and as the depth increases the stress value became positive.

**Table 3 - Power method and integral method results, 7,4*mm* distance**

| Power method | | | | | |
|---|---|---|---|---|---|
| Depth [*mm*] | Max stress [*MPa*] | Min stress [*MPa*] | X stress [*MPa*] | Y stress [*MPa*] | XY shear [*MPa*] |
| 0,0 | -147 | -196 | -147 | -196 | -6 |
| 0,1 | 20 | -35 | -35 | 20 | -2 |
| 0,2 | 236 | 77 | 77 | 235 | 2 |
| 0,3 | 451 | 190 | 190 | 451 | 5 |
| Integral method | | | | | |
| 0,033 | -37 | -62 | -62 | -37 | -2 |
| 0,150 | 96 | 2 | 2 | 96 | -1 |
| 0,250 | 248 | 77 | 77 | 248 | 1 |

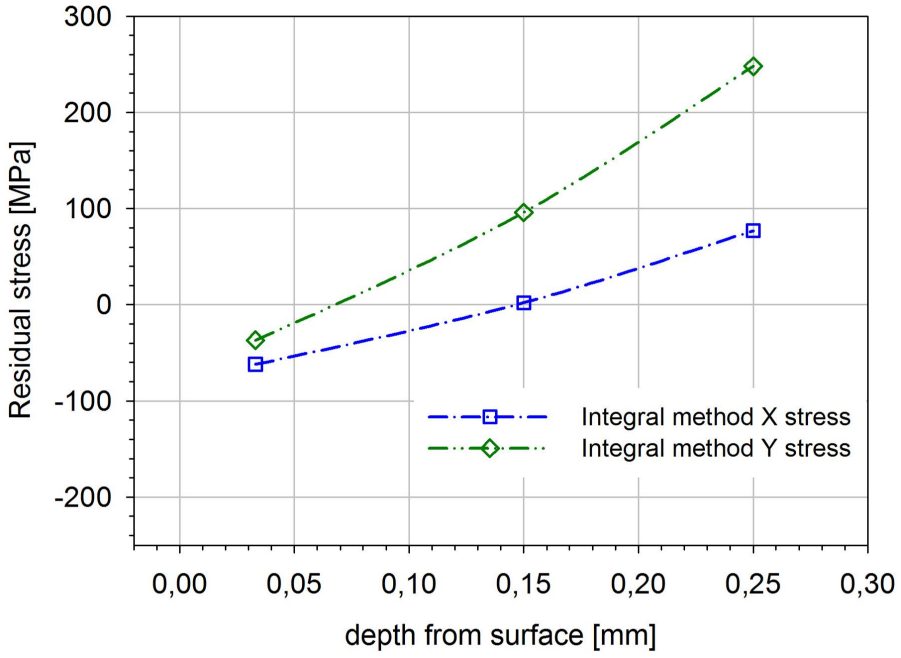


**Figure 77 - X and Y stress for the integral method, 7,4*mm* distance.**

*3.4.3.2 Hole drilled at 15mm from the weldment*

The results obtained with the integral and power method are presented in Table 4. Analyzing the data for the hole drilled at 15*mm* from the centre of the weldment it was observed that the integral method gives the best approximation, Figure 78. The longitudinal stress has strong compressive values near the surface but from 0,2*mm* to 0,5*mm* it acquires tensile values. It should be noticed that from 0,3*mm* to 0,7*mm* the principal stress gives higher values than the material yield stress. So, for this depth interval the values were disregarded but it can be concluded that a strong tensile stress field is present.

**Table 4 - Power method and integral method results, 15*mm* distance**

| Power method | | | | | |
|---|---|---|---|---|---|
| Depth [*mm*] | Max stress [*MPa*] | Min stress [*MPa*] | X stress [*MPa*] | Y stress [*MPa*] | XY shear [*MPa*] |
| 0,0 | 66 | -66 | -57 | 57 | -33 |
| 0,1 | 103 | -48 | -41 | 96 | -30 |
| 0,2 | 140 | -30 | -26 | 136 | -27 |
| 0,3 | 178 | -13 | -11 | 176 | -24 |
| 0,4 | 217 | 3 | 5 | 215 | -21 |
| 0,6 | 295 | 35 | 36 | 294 | -14 |
| 0,7 | 334 | 51 | 51 | 334 | -11 |
| 0,8 | 373 | 66 | 67 | 373 | -8 |
| 0,9 | 413 | 82 | 82 | 413 | -5 |
| 1,0 | 452 | 97 | 97 | 452 | -1 |
| Integral method | | | | | |
| 0,033 | -1 | -208 | -164 | -44 | -85 |
| 0,150 | 120 | -23 | -22 | 119 | -12 |
| 0,250 | 240 | 74 | 75 | 240 | 11 |
| 0,350 | 311 | 118 | 118 | 311 | 3 |
| 0,500 | 280 | 13 | 15 | 279 | -22 |
| 0,650 | 265 | -19 | -18 | 264 | -17 |
| 0,750 | 249 | -33 | -32 | 249 | -16 |
| 0,850 | 239 | -37 | -35 | 237 | -23 |
| 0,967 | 235 | -39 | -34 | 230 | -37 |

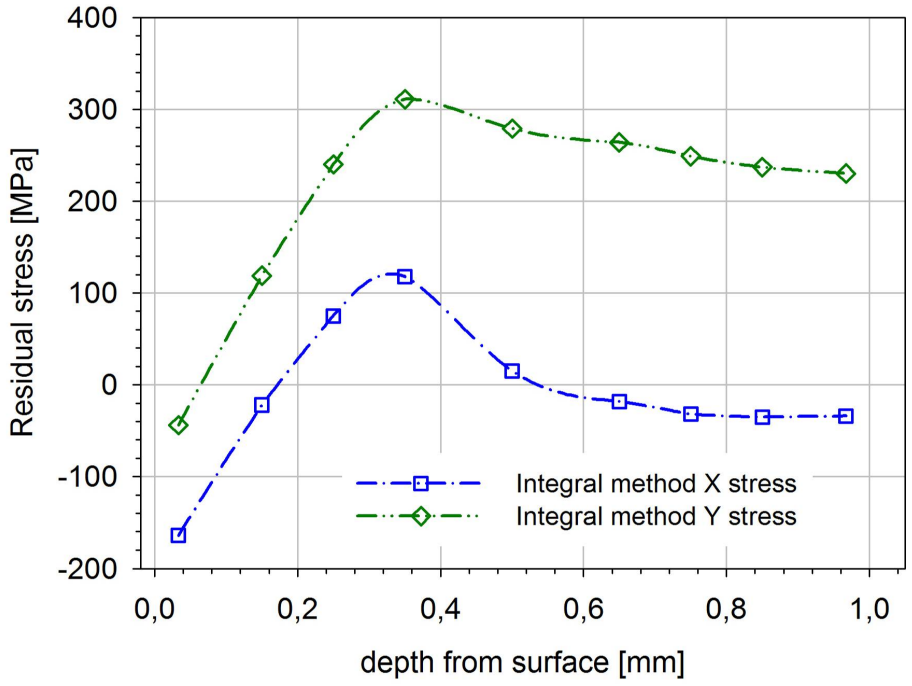


**Figure 78 - X and Y stress for the integral method, 15*mm* distance.**

*3.4.3.3 Hole drilled at 20mm from the weldment*

The results obtained with the integral and power method are presented in Table 5. Analyzing the data for the hole drilled at 20*mm* from the centre of the weldment it was observed that the integral method gave the best result, Figure 79. In this case results were valid until a depth of approximately 0,9*mm*. At the surface the longitudinal stresses still have compressive values that with depth became tensile from 0,35*mm* to 0,55*mm*.

**Table 5 - Power method and integral method results, 20*mm* distance**

| Power method | | | | | |
|---|---|---|---|---|---|
| Depth [*mm*] | Max stress [*MPa*] | Min stress [*MPa*] | X stress [*MPa*] | Y stress [*MPa*] | XY shear [*MPa*] |
| 0,0 | 70 | -46 | -45 | 70 | -9 |
| 0,2 | 78 | -27 | -26 | 77 | -9 |
| 0,3 | 82 | -18 | -17 | 81 | -10 |
| 0,4 | 86 | -9 | -8 | 85 | -10 |
| 0,5 | 91 | 0 | 2 | 89 | -11 |
| 0,6 | 95 | 10 | 11 | 93 | -11 |
| 0,7 | 99 | 19 | 21 | 97 | -12 |
| 0,8 | 103 | 28 | 30 | 101 | -12 |
| 0,9 | 107 | 37 | 39 | 105 | -13 |
| Integral method | | | | | |
| 0,067 | 47 | -58 | -57 | 46 | -10 |
| 0,250 | 99 | -6 | -5 | 98 | -9 |
| 0,350 | 132 | 27 | 28 | 131 | -9 |
| 0,450 | 135 | 33 | 34 | 134 | -9 |
| 0,550 | 111 | 16 | 17 | 110 | -11 |
| 0,650 | 63 | -15 | -13 | 61 | -12 |
| 0,750 | 9 | -55 | -52 | 6 | -14 |
| 0,867 | -45 | -99 | -94 | -49 | -15 |

*3.4.3.4 Hole drilled at 30mm from the weldment*

The results obtained with the integral and power method are presented in Table 6. Analyzing the data for the hole drilled at 30*mm* from the centre of the weldment it was observed that both methods gave similar results, but the integral method describes better the stress profile, Figure 80. In this case results were valid until a depth of approximately 1,0*mm*. The longitudinal stress is almost zero near the surface acquiring compressive values through depth stabilizing near 0,8*mm*.

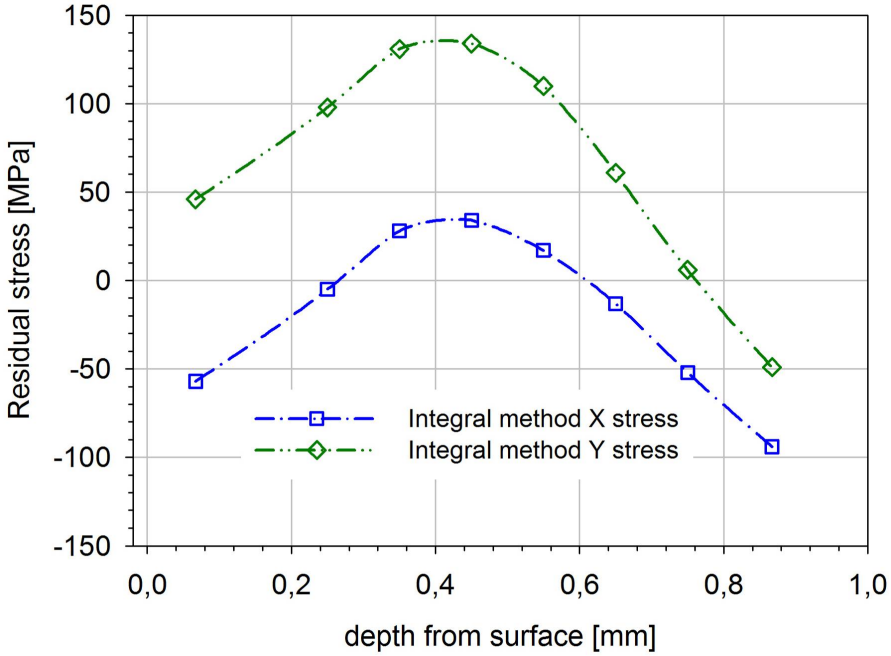


**Figure 79 - X and Y stress for the integral method, 20*mm* distance.**

**Table 6 - Power method and integral method results, 30*mm* distance**

| Power method | | | | | |
|---|---|---|---|---|---|
| Depth [*mm*] | Max stress [*MPa*] | Min stress [*MPa*] | X stress [*MPa*] | Y stress [*MPa*] | XY shear [*MPa*] |
| 0,0 | 33 | 10 | 13 | 30 | 7 |
| 0,1 | 19 | 6 | 8 | 17 | 5 |
| 0,2 | 6 | 1 | 2 | 5 | 3 |
| 0,3 | -3 | -8 | -3 | -8 | 0 |
| 0,4 | -8 | -21 | -9 | -21 | -2 |
| 0,6 | -18 | -48 | -20 | -46 | -7 |
| 0,7 | -23 | -61 | -25 | -59 | -9 |
| 0,8 | -28 | -74 | -30 | -72 | -11 |
| 1,0 | -37 | -101 | -41 | -97 | -16 |
| Integral method | | | | | |
| 0,033 | 36 | -2 | -1 | 34 | 7 |
| 0,150 | 17 | 3 | 4 | 15 | 4 |
| 0,250 | 7 | -4 | 7 | -4 | 1 |
| 0,350 | 5 | -23 | 5 | -22 | -2 |
| 0,500 | -14 | -48 | -15 | -47 | -6 |
| 0,650 | -21 | -55 | -23 | -53 | -8 |
| 0,750 | -27 | -57 | -30 | -55 | -9 |
| 0,933 | -28 | -49 | -34 | -43 | -9 |

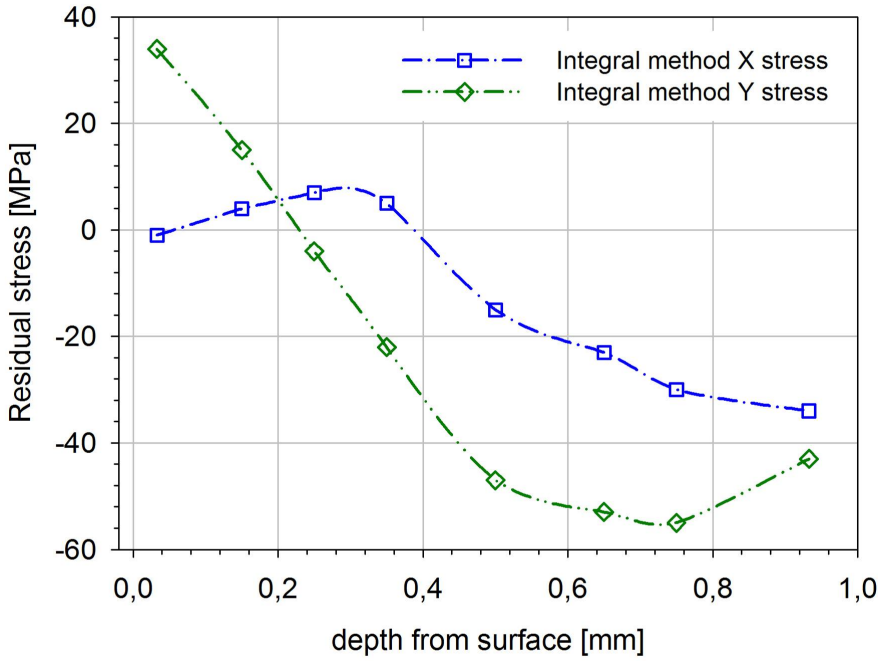


**Figure 80 - X and Y stress for the integral method, 30*mm* distance.**

*3.4.3.5 Hole drilled at 45mm from the weldment*

The results obtained with the integral and power method are presented in Table 7. Analyzing the data for the hole drilled at 45*mm* from the centre of the weldment it was observed that the integral method gives the best approximation to the stress profile, Figure 81. In this case results were valid until a depth of approximately 1,0*mm*. The longitudinal stresses are almost zero until a depth of 0,6*mm* is reached and than acquire tensile values.

*3.4.3.6 Hole drilled at 115mm from the weldment*

The results obtained with the integral and power method are presented in Table 8. Analyzing the data for the hole drilled at 115*mm* from the centre of the weldment it was observed that integral method gives the best approximation to the stress profile, Figure 82. Nevertheless, for the longitudinal stress (X stress) since the result is almost constant trough the dept (around 10*MPa*) the power method also gives a good approximation.

**Table 7 - Power method and integral method results, 45*mm* distance**

| Power method | | | | | |
|---|---|---|---|---|---|
| Depth [*mm*] | Max stress [*MPa*] | Min stress [*MPa*] | X stress [*MPa*] | Y stress [*MPa*] | XY shear [*MPa*] |
| 0,0 | 1 | -25 | 0 | -25 | 3 |
| 0,1 | 1 | -26 | 1 | -26 | 2 |
| 0,2 | 2 | -27 | 1 | -27 | 2 |
| 0,3 | 2 | -28 | 2 | -27 | 2 |
| 0,4 | 2 | -28 | 2 | -28 | 1 |
| 0,5 | 3 | -29 | 3 | -29 | 1 |
| 0,6 | 3 | -30 | 3 | -30 | 1 |
| 0,7 | 4 | -31 | 4 | -31 | 0 |
| 0,9 | 5 | -33 | 5 | -33 | 0 |
| 1,0 | 6 | -34 | 6 | -34 | 0 |
| Integral method | | | | | |
| 0,033 | 8 | -17 | 8 | -17 | 3 |
| 0,150 | 3 | -25 | 3 | -25 | 2 |
| 0,250 | -2 | -31 | -2 | -31 | 2 |
| 0,350 | -5 | -35 | -5 | -35 | 2 |
| 0,450 | -5 | -36 | -5 | -36 | 1 |
| 0,550 | -2 | -34 | -2 | -34 | 1 |
| 0,650 | 4 | -31 | 4 | -31 | 1 |
| 0,800 | 21 | -16 | 21 | -16 | 0 |
| 0,967 | 28 | -8 | 28 | -8 | 0 |

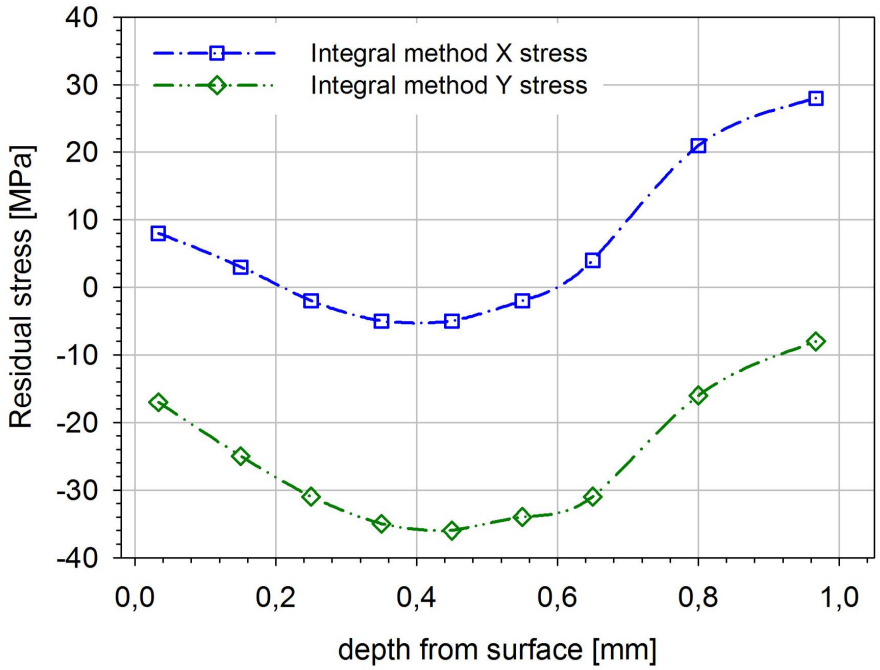


**Figure 81 - X and Y stress for the integral method, 45*mm* distance.**

**Table 8 - Power method and integral method results, 115*mm* distance**

| Power method | | | | | |
|---|---|---|---|---|---|
| Depth [*mm*] | Max stress [*MPa*] | Min stress [*MPa*] | X stress [*MPa*] | Y stress [*MPa*] | XY shear [*MPa*] |
| 0,0 | 13 | 6 | 9,5 | 9 | 3 |
| 0,2 | 12 | 8 | 9,7 | 10 | 2 |
| 0,3 | 11 | 9 | 9,7 | 11 | 1 |
| 0,5 | 12 | 10 | 9,9 | 12 | -1 |
| 0,6 | 13 | 9 | 9,9 | 12 | -1 |
| 0,9 | 16 | 8 | 10,1 | 14 | -4 |
| 1,0 | 17 | 7 | 10,2 | 15 | -5 |
| Integral method | | | | | |
| 0,067 | 12 | 6 | 10 | 8 | 3 |
| 0,250 | 11 | 7 | 8 | 9 | 2 |
| 0,400 | 15 | 10 | 10 | 15 | -1 |
| 0,550 | 17 | 10 | 11 | 17 | -2 |
| 0,750 | 11 | 8 | 9 | 10 | -2 |
| 0,967 | 9 | 6 | 8 | 7 | -2 |

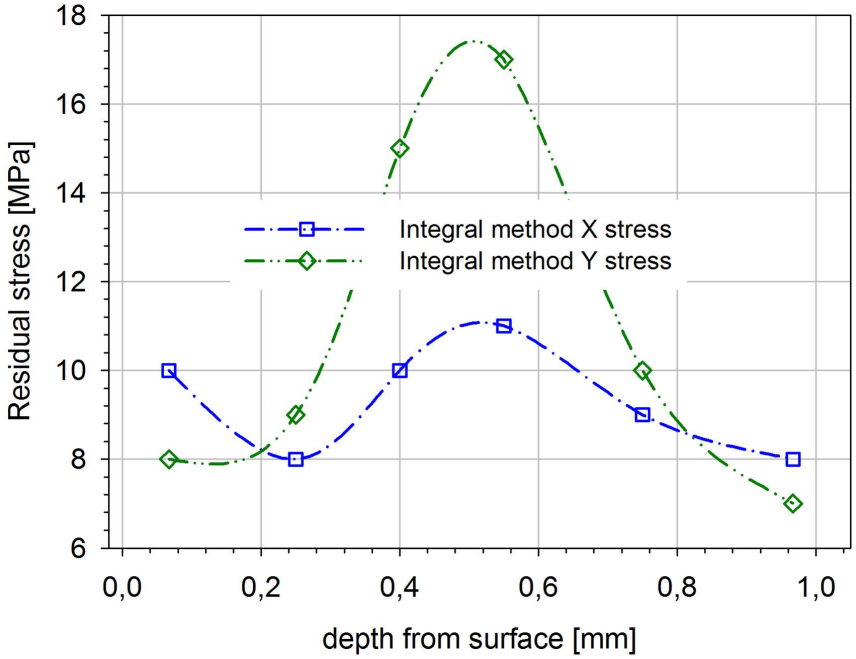


**Figure 82 - X and Y stress for the integral method, 115*mm* distance.**

*3.4.3.7 Hole drilled at 150mm from the weldment*

The results obtained with the integral and power method are presented in Table 9. Analyzing the data for the hole drilled at 150*mm* from the centre of the weldment it was observed that power method gives the best approximation to the stress profile, Figure 83. The longitudinal stress has tensile values through the valid measured depth (1*mm* maximum).

**Table 9 - Power method and integral method results, 150*mm* distance**

| Power method | | | | | |
|---|---|---|---|---|---|
| Depth [*mm*] | Max stress [*MPa*] | Min stress [*MPa*] | X stress [*MPa*] | Y stress [*MPa*] | XY shear [*MPa*] |
| 0,0 | 15 | 5 | 15 | 5 | 0 |
| 0,1 | 14 | 4 | 14 | 4 | -1 |
| 0,2 | 13 | 2 | 13 | 3 | -2 |
| 0,3 | 12 | 1 | 12 | 2 | -3 |
| 0,4 | 11 | -1 | 10 | 0 | -3 |
| 0,6 | 10 | -4 | 8 | -2 | -5 |
| 0,7 | 9 | -6 | 7 | -3 | -5 |
| 0,8 | 9 | -7 | 6 | -4 | -6 |
| 0,9 | 8 | -9 | 4 | -5 | -7 |
| 1,0 | 7 | -11 | 3 | -7 | -8 |
| Integral method | | | | | |
| 0,033 | 13 | 5 | 13 | 6 | -2 |
| 0,150 | 15 | 2 | 15 | 2 | -1 |
| 0,250 | 15 | 0 | 15 | 0 | -2 |
| 0,350 | 13 | 1 | 13 | 1 | -2 |
| 0,500 | 9 | -1 | 7 | 2 | -4 |
| 0,650 | 9 | -4 | 7 | -1 | -5 |
| 0,750 | 9 | -8 | 7 | -6 | -5 |
| 0,850 | 9 | -11 | 7 | -9 | -7 |
| 0,967 | 10 | -16 | 5 | -11 | -10 |

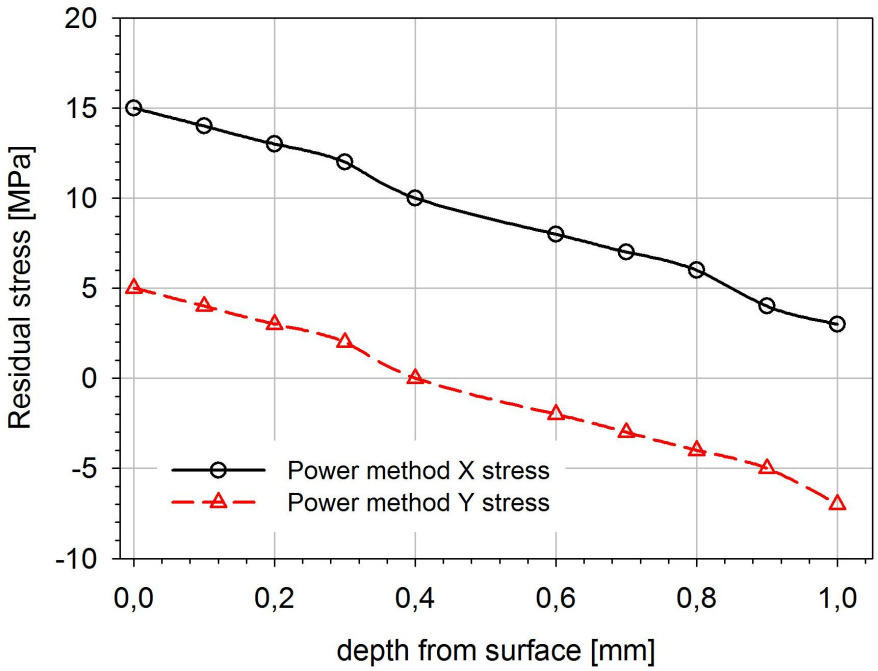


**Figure 83 - X and Y stress for the power method, 150*mm* distance.**

*3.4.3.8 Results analysis*

The residual stress profile, obtained with the hole drilling process, for different depths at each distance where a hole was drilled is plotted in Figure 84. For a distance from the weld centre of 30$mm$ measurements at different depths present values between -10$MPa$ and 10$MPa$. After this distance, the residual stress profile for all depths have a linear variation with a positive slope. After 90$mm$ the residual stress at all depths acquire similar values, which increase towards 20$MPa$ at a distance of 160$mm$ from the weld centre. Near the weldment, measurements for depths lower than 0,1$mm$ present high compressive stresses. These conclusions are also verified plotting the residual stress profile as function of the distance from the weld centre until a depth of 0,4$mm$, as presented in Figure 85. As the depth increases, the residual stress values become positive, and for a depth of 0,3$mm$ they are in agreement with the results obtained with the sectioning method, Figure 85.

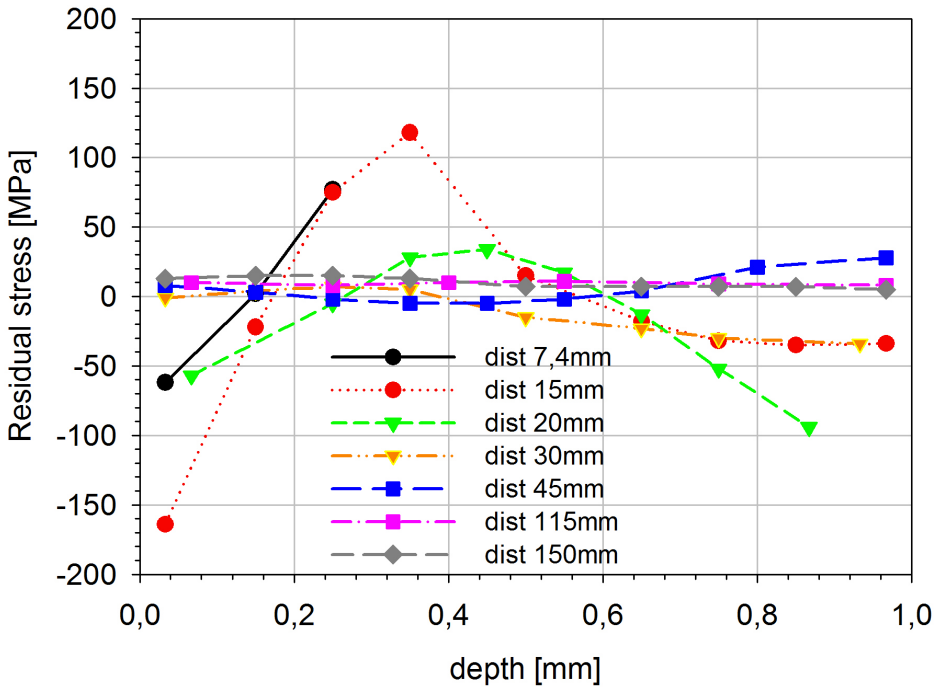


**Figure 84 - Residual stress profiles obtained with the hole drilling process.**

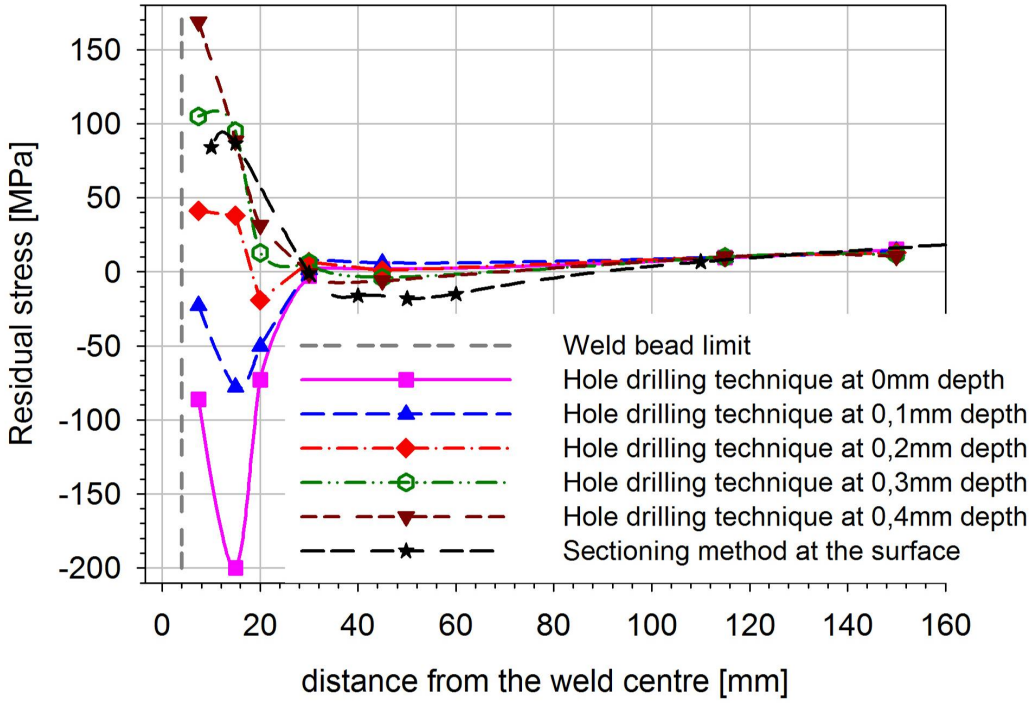


**Figure 85 - Hole drilling, residual stress profile for different depths.**

With the data collected from the hole drilling procedure a contour plot analysis of the residual stresses through the thickness as a function of the distance from the weld centre was performed. This analysis resulted in two contour plots as schematically represented in Figure 86.

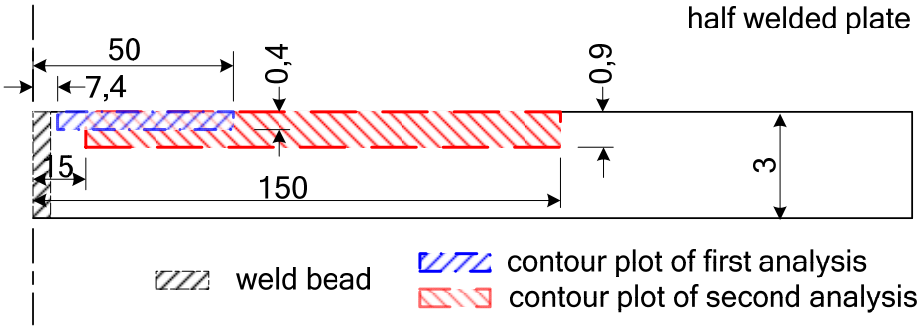


**Figure 86 - Schematic representation of the contour plots location.**

A first step was to analyse the residual stress field until a depth of $0{,}4mm$ and at distances from the weld centre between $7{,}4mm$ and $50mm$, Figure 87. For this analysis the whole seven sets of data could be used.
In a second analysis, the residual stress profile was analyzed until a depth of $0{,}9mm$ and at distances from the weld centre between $15mm$ and $150mm$, Figure 88. For this analysis the rosette nearest to the weldment could not be considered because the data was only valid for depths below $0{,}4mm$.
Near the weldment, at the surface and around $0{,}9mm$ of depth a compressive stress field occurs. Between these areas, around $0{,}4mm$, the stress becomes positive. As the distance from the weld centre increases, at all depths, the residual stress field acquire low tensile stress values.

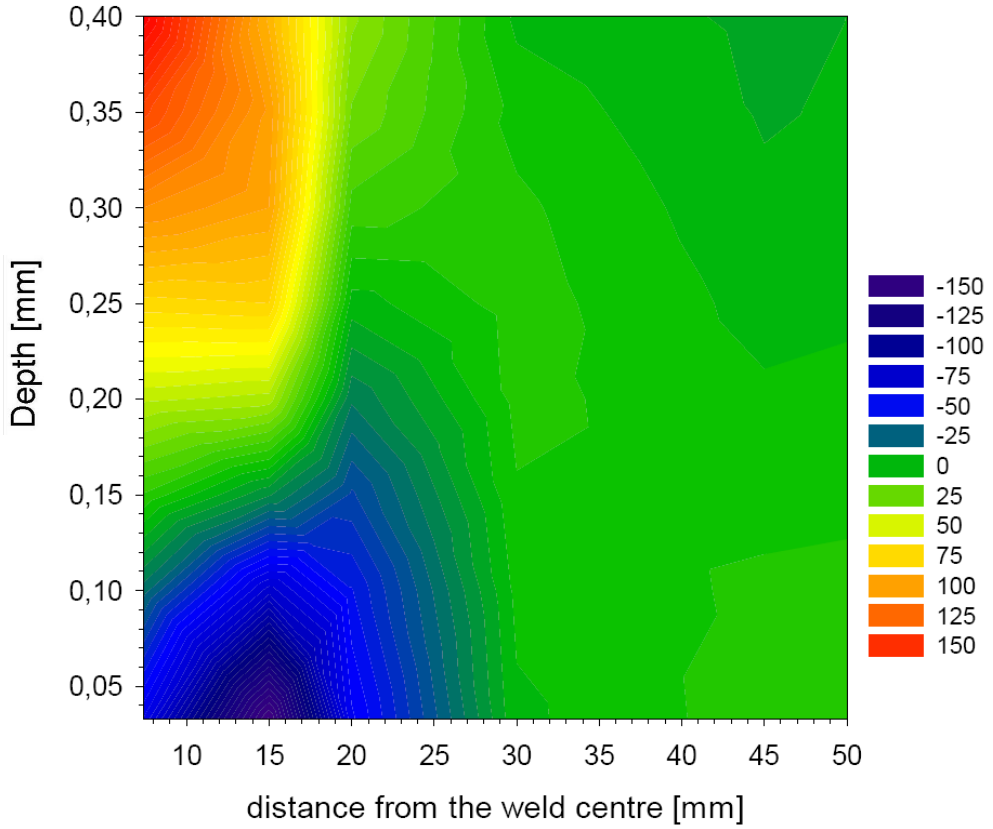


**Figure 87 - Residual stress field for depths up to 0,4*mm*.**

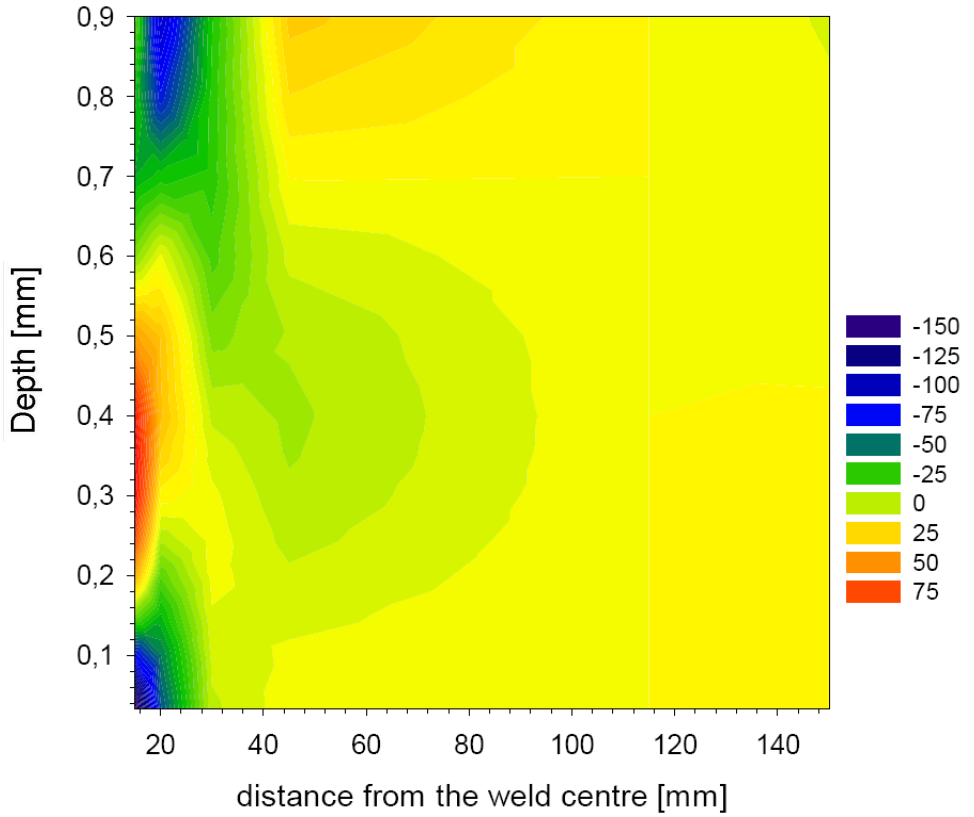


**Figure 88 - Residual stress field for depths up to 0,9*mm*.**

### *3.4.4 Results comparison*

Figure 89 presents a direct comparison between the data obtained with the sectioning method, X-ray diffraction method and hole drilling technique. For the hole drilling technique the values plotted correspond to measurements at 0,3$mm$ depth. As previously shown, these measurements are in agreement with the values measured using the sectioning method.
It was verified that the sectioning method does not give the residual stress values just at the surface, but it gives a measurement of an average thin layer of material. If so, this method and the hole drilling method are in good agreement.
The X-ray diffraction revealed to be a procedure not easily applied in welded aluminium plates. A high scatter was found making difficult the evaluation of the true residual stress profile. When comparing the three methods it is verified that the X-ray diffraction is not in good agreement with the other methods. Nevertheless, the results present a similar trend in all measuring methods. The main advantage of the X-ray method was the capability of measuring the residual stress profile inside the weldment. This fact was not verified with the sectioning and hole drilling methods.

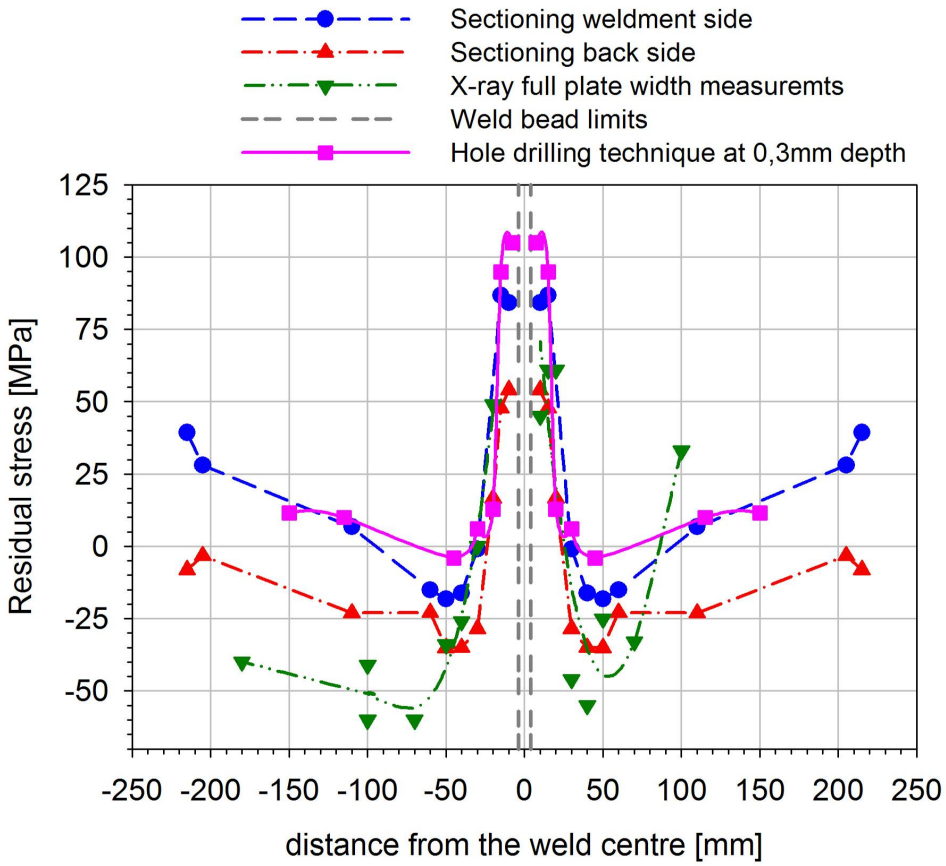


**Figure 89 - Residual stress values: sectioning method, X-ray diffraction and hole drilling method.**

### 3.5 Contour method, results comparison

For the same plate geometry (450x500x3$mm$) and welding parameters, results of residual stress measurements using an alternative destructive method, contour method, are presented in [135, 136].
Most of the destructive residual stress measurement methods are based on the analysis of a structure new equilibrium state after removing part of it in the area of interest. The contour method has been introduced by Prime [137], and consists in the measurement and analysis of a cut-surface (usually by EDM) in the plane where residual stress is to be measured. The relaxation due to the cut creates a deformation field which can be measured and then used to infer the residual stresses that were present at the plane of interest before the cut was made. This method can be applied to the measurement of through-the-thickness residual stresses in complex structures. Since the measurement procedure requires physical measuring of a few thousand points, it is a quite time-consuming method. The precision and accuracy of the best current touch probes (CMM - coordinate measuring machine) is around 3$\mu m$. In the present case, depths of up to 600$\mu m$ were measured.
Measurements obtained with the contour method, at two different depths, 0,25$mm$ and 1,5$mm$, are presented in Figure 90. Outside the weldment area, the results obtained with all methods are in good agreement. It was also verified that the stress profile (measured with the contour method) at 1,5$mm$ depth, half the thickness, is in between of results obtained with the sectioning method for each plate surface.

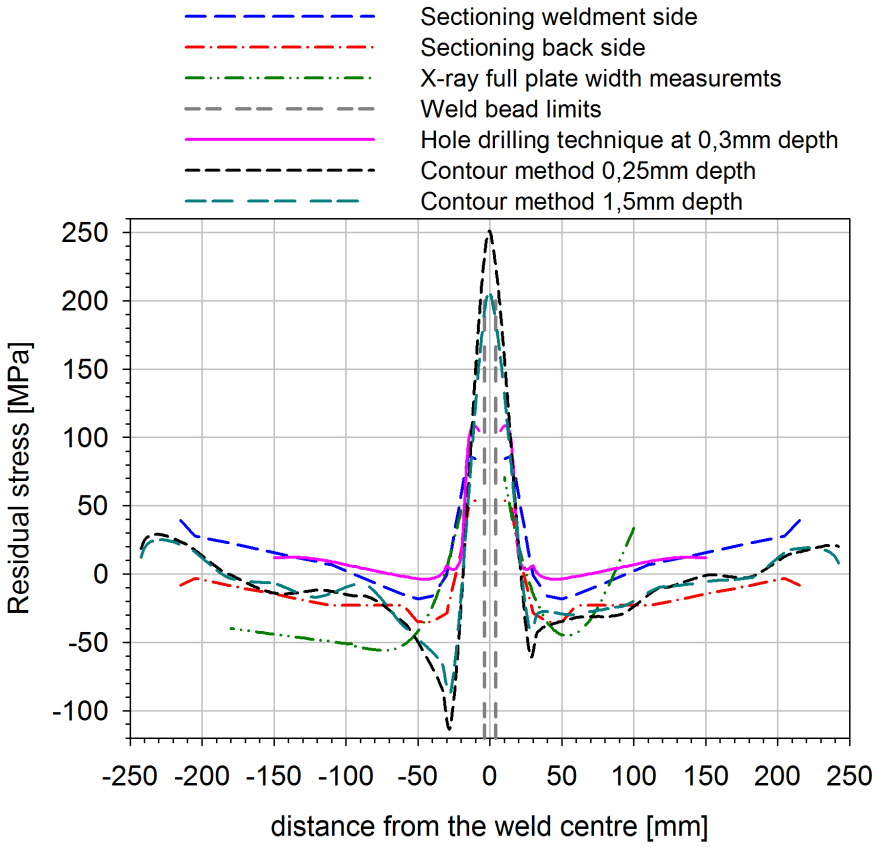


**Figure 90 - Residual stress values measured with the contour method.**

### 3.6 Conclusions

As a result of this work, the following conclusions may be reached:

- In this study the applicability of the sectioning, hole drilling, and X-ray methods in MIG welded aluminium plate was verified;
- Using the hole drilling technique, it was verified that measurements at $0{,}3mm$ depth are in agreement with the values measured using the sectioning method. It was verified that the sectioning method does not give the residual stress values just at the surface, but instead it gives a measurement of an average thin layer of material.;
- The X-ray diffraction revealed to be a procedure not easily applied in welded aluminium plates. A high scatter was found making it difficult the evaluation of the true residual stress profile;
- Measurements obtained with the contour method outside the weldment area are in good agreement with the other methods used in this study.

Further studies of residual stresses will be presented in section 4.2.3 for FSW joints using the sectioning method, and in section 6.2.5 for LBW panels using X-ray.

# Chapter 4

# Studies on FS welded joints

Chapter four is composed of three different and complementary parts. Due to design constraints, friction stir welded components may include notches in the weldment. So, the influence of Friction Stir Welding on the fatigue life of specimens of an aluminium alloy containing notches in the thermo-mechanically affected zone was investigated.
In the second study, an experimental characterization and computational modelling analysis of dissimilar friction stir welded butt joints performed between two aluminium alloys was carried out.
Notwithstanding the widespread interest in the possibilities offered by Friction Stir and Laser Beam Welding, data concerning the fatigue behaviour of joints obtained using these processes is still needed. The third study of Chapter four is a contribution to this effort, contrasting the fatigue behaviour of joints made using a traditional process, Friction Stir and Laser Beam Welding.

The work presented in Section 4.1 was published as:

- P M G P Moreira, F M F de Oliveira, P M S T de Castro, Fatigue behaviour of notched specimens of friction stir welded aluminium alloy 6063-T6, *Journal of Materials Processing and Technology*, in press.

The work presented in Section 4.2 was presented as:

- P M G P Moreira, Telmo Santos, Sérgio M O Tavares, Valentin Richter-Trummer, Pedro Vilaça, P M S T de Castro, Friction stir welds of dissimilar aluminium alloys AA6061-T6 and AA6082-T6, mechanical characterization, 13th Conference of Sociedade Portuguesa de Materiais, Porto, Portugal, April 1-4, 2007.

The work presented in Section 4.3 was published as:

- P M G P Moreira, M A V de Figueiredo, P M S T de Castro, Fatigue behaviour of FSW and MIG weldments for two aluminium alloys, *Theoretical and Applied Fracture Mechanics*, 48, (2), 2007, p. 169-177
- P M G P Moreira, V Richter-Trummer and P M S T de Castro, Fatigue behaviour of FS, LB and MIG welds of AA6061-T6 and AA6082-T6, invited chapter, in: George C Sih, ed, *Multiscale Fatigue Crack Initiation and Propagation of Engineering Materials - Structural Integrity and Microstructural Worthiness*, Springer Science + Business Media BV, in press
- P M G P Moreira, A M P de Jesus, A S Ribeiro and P M S T de Castro, Assessment of the fatigue behaviour of friction stir welded joints: Aluminium alloy 6082-T6, *Key Engineering Materials*, 348-349, 2007, p. 209-212

# 4. Studies on FS welded joints

In this Chapter three different and complementary studies on the characterization of friction stir welded joints are presented. For comparison, laser beam welded joints and traditional MIG joints data is also presented. The mechanical characterization includes hardness, tensile and fatigue tests, microstructure examination and scanning electron microscopy analysis.
In a first study the effect of notches on friction stir (FS) weldments is presented. Due to design constraints, friction stir welded components may include notches in the weldment, and for this reason, the influence of friction stir welding on the fatigue life of specimens of an aluminium alloy (6063-T6), containing notches in the thermo-mechanically affected zone was studied.
An experimental characterization and computational modelling analysis of dissimilar friction stir welded butt joints performed between aluminium alloys 6061-T6 and 6082-T6 was carried out in a second study. Bending tests, not yet reported in the literature in this context, were performed and an approximate finite element modelling of the test is presented.
Notwithstanding the widespread interest in the possibilities offered by friction stir and laser beam welding, data comparing the fatigue behaviour of joints obtained using these processes is still needed. In the third study the fatigue behaviour of joints made using a traditional process (metal inert gas welding), laser beam welding (LBW) and friction stir welding (FSW) was contrasted.

## 4.1 Fatigue behaviour of notched specimens of FS welded AA6063-T6

Friction stir welding [138], a solid-state joining process developed and patented by the The Welding Institute, emerged as a welding technique to be used in high strength alloys that were difficult to join with conventional techniques. The process was developed initially for aluminium alloys, but since then FSW was found suitable for joining a large number of materials. In aeronautics, for instance, riveting is the preferred manufacturing process for aircraft fuselage structures; nevertheless, FSW is emerging as an appropriate alternative technology due to low distortion, high strength of the joint and high processing speeds. Design of friction stir welded components may include notches in the weldment (friction stirred material), and there is a lack of information on the fatigue behaviour of the weldment in those conditions.

The purpose of this first study was to quantify the influence of the FSW technique on the fatigue life of notched specimens of the aluminium alloy 6063-T6. Welded and un-welded specimens were fatigue tested at several stress levels. Welding was performed parallel to the rolling direction, and the specimens were loaded perpendicular to this direction. Fatigue life was measured as the number of cycles to failure. Hardness tests were performed, and yield stress ($\sigma_{yield}$), rupture stress ($\sigma_{rupt}$) and Young's modulus ($E$) of the aluminium alloy were measured with tensile tests of welded and un-welded specimens. An approximate strain based modelling of the observed fatigue behaviour was carried out using a non-linear finite element method (FEM) analysis of the fatigue test specimen. Scanning electron microscopy (SEM) analysis was performed in order to identify welding defects and features of crack surfaces.

### *4.1.1 Material and welding process*

Aluminium 6063-T6 plates ($300x100x3mm$) were friction stir welded with the process parameters:$1000rpm$ pin-tool rotation speed; $9{,}17mm/s$ welding speed; $4{,}5kN$ axial force. A tool with a $15mm$ diameter shoulder and a $6mm$ threaded pin was used. From this sheet, 13 fatigue specimens and 5 tensile test specimens were machined, Figure 91. Two semi circular notches ($0{,}5mm$ radius) were machined in the welded and base material fatigue specimen creating an elastic stress concentration factor of 2,82. The specimen's dimensions are not standard; they were also chosen as a function of the welded material availability and welded plate dimension The geometry chosen for the specimens, although not standard, is adequate to answer the question of whether or not a possible circular notch in the stir welded material of a FSW joint of this material has better or worse fatigue performance than an equal notch in base material. The diameter chosen seeks to ensure that the notch directly affects friction stir welded material only.

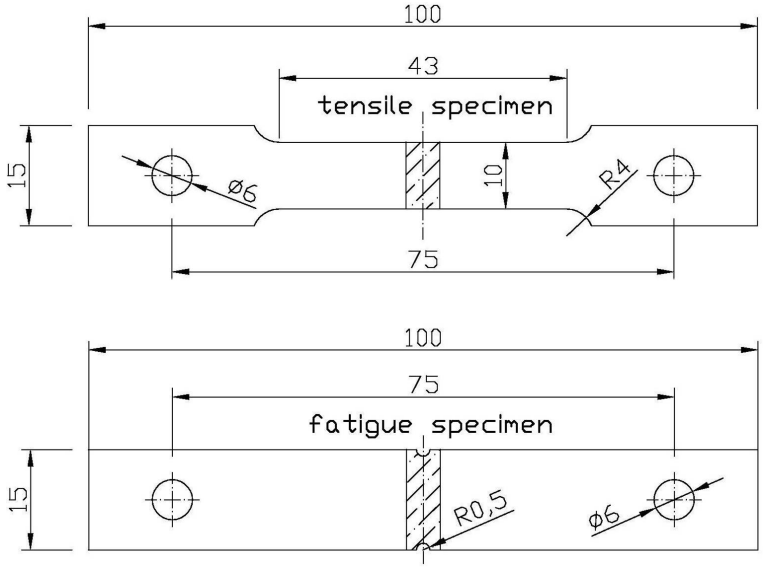


**Figure 91 - Tensile and fatigue specimens.**

According to [139], identifying the specimen orientation with a two letter code system which is based on an arrangement of three reference axes related to the material grain flow, as presented in Figure 92, these tests can be identified as T-L (the weldment was deposited parallel to the material rolling direction).

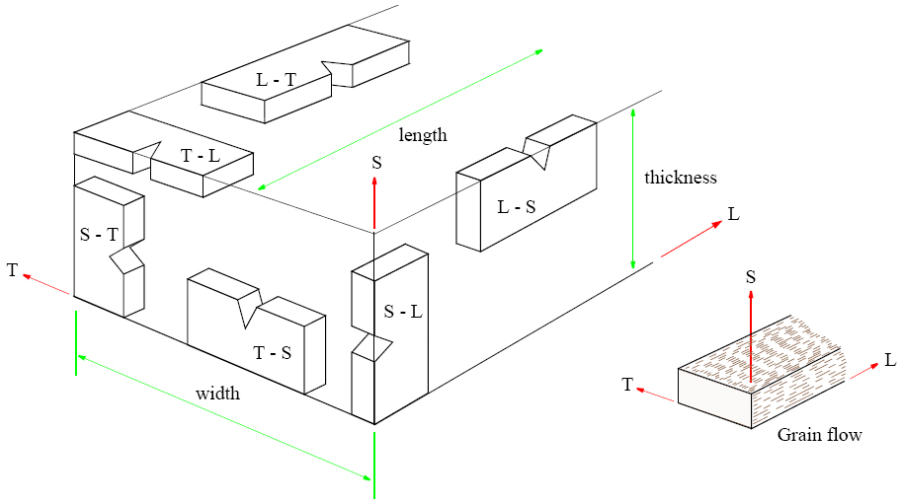


**Figure 92 - Identification of specimen orientation [139].**

Three images of the notch, created in the fatigue specimens, in two different perspectives which show the surface finishing are presented in Figure 93.

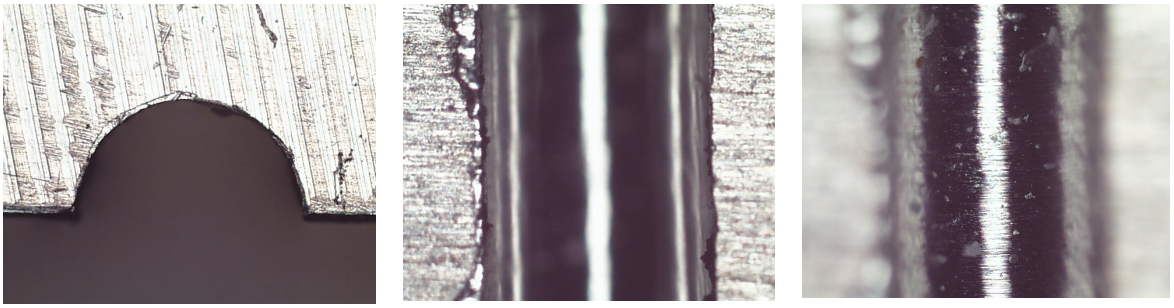

a) magnified notch geometry b) notch external border c) notch internal surface

**Figure 93 - Notch surface finishing details.**

Aluminium alloy 6063-T6 contains Mg and Si as major alloying elements. This alloy was subjected to temper with the designation T6 where T stands for products that had an increase in strength due to thermal treatments, with or without supplementary strain-hardening operations, and the digit 6 after the T means that it is solution heat-treated and artificially aged, [140].
The mechanical properties, chemical composition and thermal properties of the aluminium alloy 6063-T6 given from [141] are shown in Table 10, and Table 11.

**Table 10 - Chemical composition AA6063-T6**

| Component | Wt. % | Component | Wt. % | Component | Wt. % |
|---|---|---|---|---|---|
| Al | Max 97,5 | Mg | 0,45-0.9 | Si | 0,2-0,6 |
| Cr | Max 0,1 | Mn | Max 0,1 | Ti | Max 0,1 |
| Cu | Max 0,1 | Other, each | Max 0,05 | Zn | Max 0,1 |
| Fe | Max 0,35 | Other, total | Max 0,15 | | |

**Table 11 - Material properties AA6063-T6**

| | | | |
|---|---|---|---|
| Rupture stress [*MPa*] | 241 | Elongation (%) | 12 |
| Yield stress [*MPa*] | 214 | Machinability (%) | 50 |
| Young modulus [*GPa*] | 68,9 | Poisson's ratio | 0,33 |
| Hardness Vickers | 80 | Hardness Brinell | 75 |

### *4.1.2 Friction stir weld visual analysis*

The nomenclature shown in Figure 94 was used to identify the different surfaces of specimens; top surface corresponds to the crown side of the weldment, and side surface corresponds to a plane perpendicular to the weldment (cross section of the specimen).

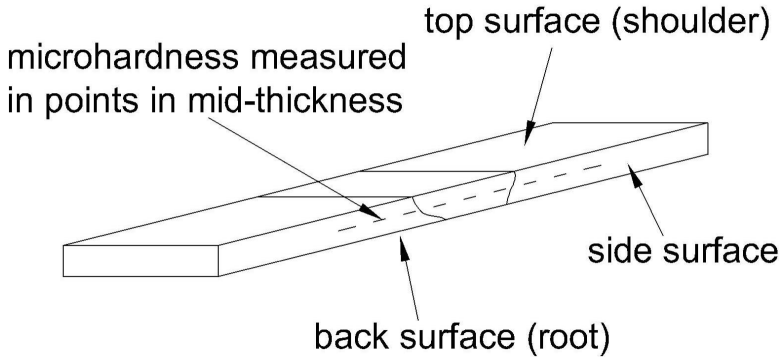


**Figure 94 - Specimens surface definition.**

In the visual analysis of the friction stir weld neither flaws nor defects were detected on the top and back surfaces of the weld, as shown in Figure 95.

a) specimen welding shoulder side

b) specimen root side

**Figure 95 - Visual inspection of FSW joints, top and back surfaces.**

The side surfaces (perpendicular to the weld line) were cut by guillotine, and it was possible to visually identify zones with different hardness, Figure 96. In this type of examination, well documented by several authors, *e.g.* [78, 90], the darker zone, in the centre of the image, indicates the material that was affected by the welding process. The increase in the darker area is a characteristic of lower values of hardness which leads to higher plastic deformation during the cut.

**Figure 96 - Side surface cut by guillotine.**

### *4.1.3 Metallographic analysis*

The aim of the metallographic analysis was the identification of microstructural changes due to the FSW process. Microstructures of the welded and base material were acquired according to the scheme presented in Figure 97.

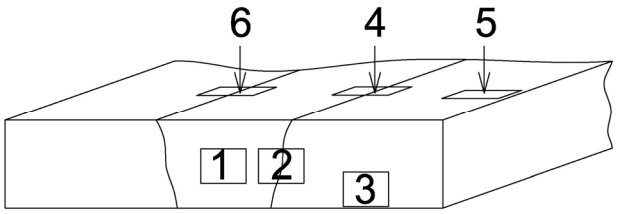


**Figure 97 - Scheme of microstructural analysis.**

According to reference [142] there are several etchants that can be used to identify and differentiate the microstructure of aluminium alloys. The etchant used in this work is presented in Table 12.

**Table 12 - Etchant used in the microscopic examination**

| Etchant | Composition |
|---|---|
| HF etch | $1mL$ HF (48%), $200mL$ $H_2O$ |

In microstructure WM2 it was possible to identify the transition between the zone affected by the welding process and the base material, Figure 98. The material affected by the welding process presents a fine stirred grain structure and the material near the heat affected zone (HAZ) presents regular grains. In the friction stir welded zone very fine recrystallized grains are present due to the high deformation and high temperature during the process. The microstructure within the weld nugget shows dynamic recrystallized grains much smaller and equiaxed when compared to the elongated base metal microstructure, as already shown in [84].
Microstructure WM3, base material, shows larger grains near the plate free surface and smaller grains outside this layer, Figure 98.

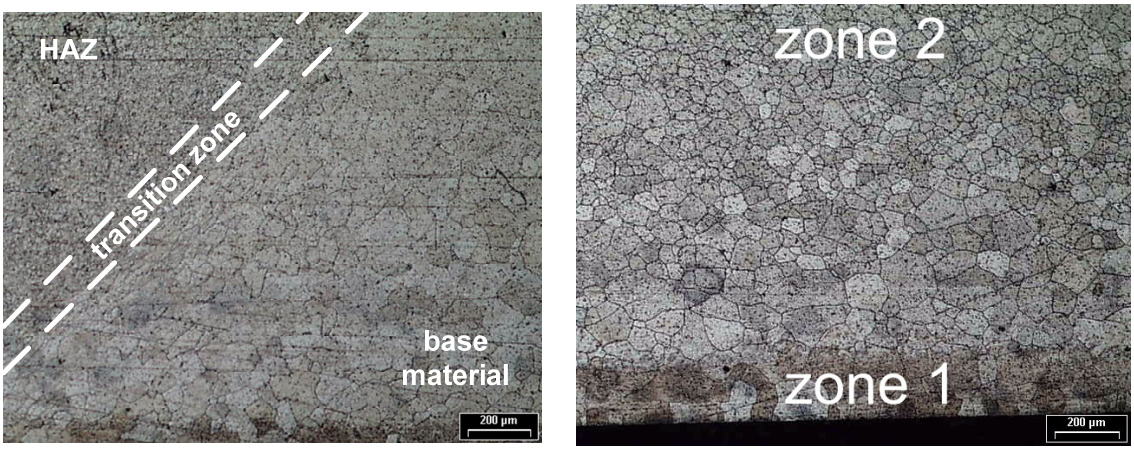


a) microstructure WM2 b) microstructure WM3

**Figure 98 - Welded specimen microstructures, surface perpendicular to the top surface.**

To determine the grain size diameter, microstructure 3 was divided in two zones, zone 1 near the plate edge and zone 2 outside the plate edge. In each zone the grain diameter was measured in 5 grains. The grains on middle thickness have an average diameter of 70,2$\mu m$ and near the plate surface present a diameter of 144,0$\mu m$, Table 13. This difference was due to the fabrication process; grains at the surface have recrystallized due to heat and working [142].

**Table 13 - Grain size in microstructure WM3**

| zone 1 | Diameter [$\mu m$] | | | |
|---|---|---|---|---|
| grain | 1 | 2 | 3 | average |
| 1 | 125,4 | 187,4 | 167,6 | 160,1 |
| 2 | 94,8 | 103,4 | 132,8 | 110,3 |
| 3 | 107,2 | 174,7 | 125,8 | 135,9 |
| 4 | 262,3 | 193,7 | 109,6 | 188,6 |
| 5 | 124,0 | 136,1 | 114,4 | 124,8 |
| average | | | | 144,0 |
| zone 2 | Diameter [$\mu m$] | | | |
| grain | 1 | 2 | 3 | average |
| 1 | 67,2 | 82,7 | 72,8 | 74,2 |
| 2 | 66,6 | 77,2 | 84,0 | 76,0 |
| 3 | 50,4 | 60,2 | 57,5 | 56,0 |
| 4 | 71,0 | 79,1 | 68,8 | 72,9 |
| 5 | 77,1 | 73,1 | 65,5 | 71,9 |
| average | | | | 70,2 |

Microstructures WM5 and WM6 are shown in Figure 99. In microstructure WM6 it is possible to identify the transition between the zone affected by the welding process and the base material, delimited by the dashed line.

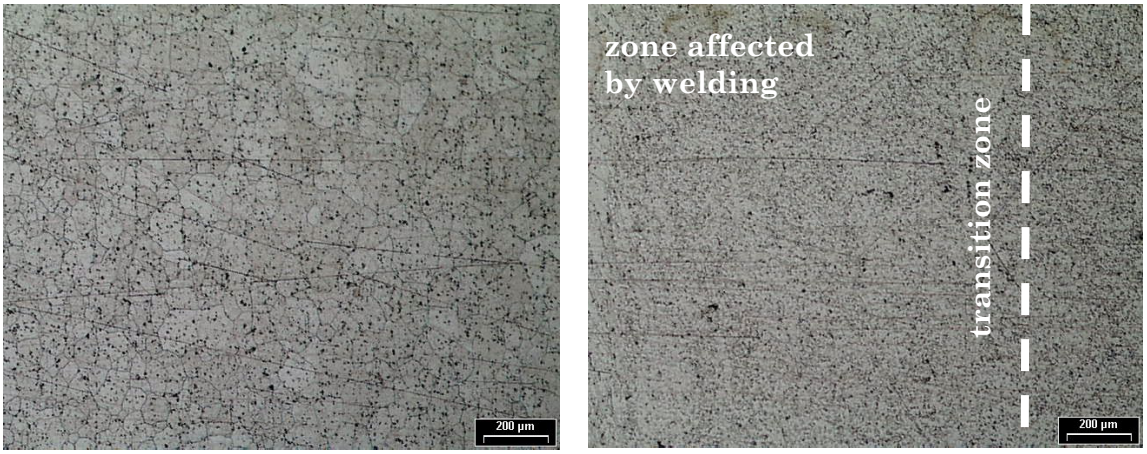


a) microstructure WM5 (base material) b) microstructure WM6

**Figure 99 - Welded specimen microstructures, top surface.**

### *4.1.4 Hardness tests*

The microhardness tests (200*gf* load) were performed in the top and side surfaces in mid thickness of the specimen. The *HV* microhardness results are presented in Figure 100. Hardness drastically decreases in the weld thermo-mechanically affected zone (TMAZ). The average hardness of the nugget zone was found to be significantly lower than the hardness of the base alloy. It was also possible to identify higher hardness values when measuring the hardness at the side surface. Measurements at the side surface show a zone with lower hardness values just outside the nugget (transition between the TMAZ and the HAZ). As suggested in [61] this hardness variation was due to the different microstructures of the base material (BM) and welded material (WM). Hardness decrease of 27% and 32% were found in the top surface and side surface, respectively. Similar results are shown by Scialpi et al. [143]. In the TMAZ, the top surface presents lower hardness values than the side surface due to the additional heat generated by the contact with the shoulder which leads to a more pronounced recrystallization process.

In the zone not affected by the welding process (base material), hardness values at the side surface are higher than those measured at the top surface. This difference was due to the different grain size of the side and top surfaces. The grain at the middle thickness plane has average diameters between 70,2$\mu m$, whereas grains near the plate surface have an average diameter of 144,0$\mu m$.

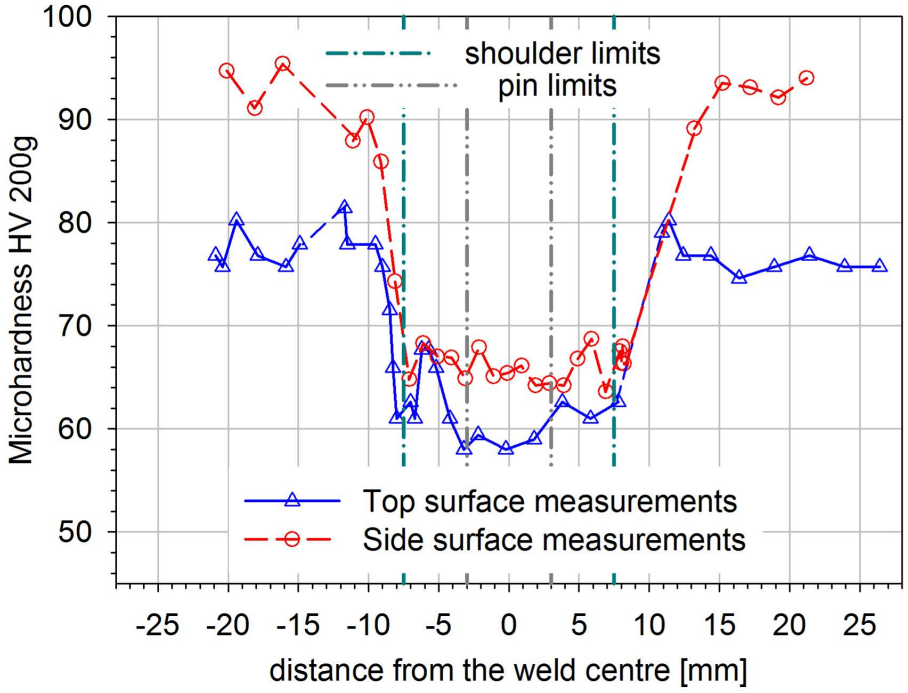


**Figure 100 - Microhardness profile.**

### *4.1.5 Tensile tests*

Tensile tests were performed to determine the mechanical properties of the material ($\sigma_{yield}$, $\sigma_{rupt}$ and E). Five $3mm$ thick tensile specimens of the welded material were tested. Two different tests were performed in the welded specimens. In the first three specimens, strain was measured in an area which includes welded and un-welded material ($25mm$ gage length). Since the welded zone was approximately $14mm$ wide, in the other two specimens strain values were acquired with a $6mm$ gage length, included in the welded material area only. This procedure was carried out to evaluate the material behaviour of only the welded material.

The machine used was an MTS 312.31 with a load cell of $10kN$. The both testing, tensile and fatigue, the set up used is shown in Figure 101. Its components are:
A - bottom fork connected to the actuator;
B - grip;
C - top fork connected to the load cell;
D - fork shaft;
E - grip shaft.

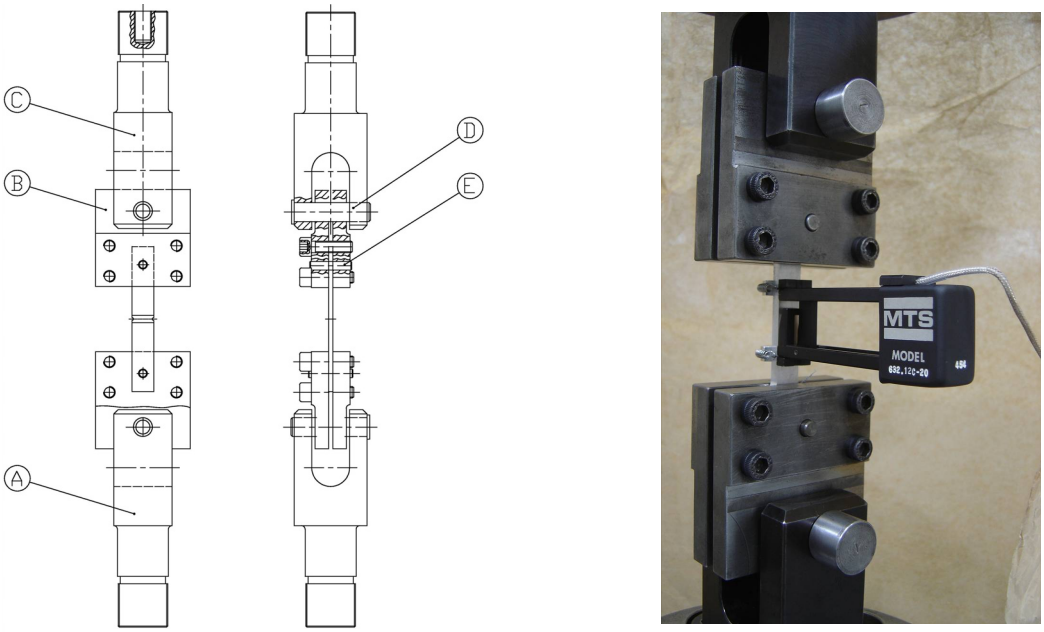


**Figure 101 - Complete test assembly.**

The tensile test specimens were identified with three letters. The first letter is a T which indicates that it is a tensile test specimen. The other two letters, UW for the un-welded specimens and FW for the friction stir welded specimens, indicate the specimen type. In the case where strain values were acquired with 6$mm$ gage length, the reference '.6' was included at the end of the numbering (TFW.6). Specimens TUW and TFW all failed in the same manner, 45º shear plane. An example is presented in Figure 102.

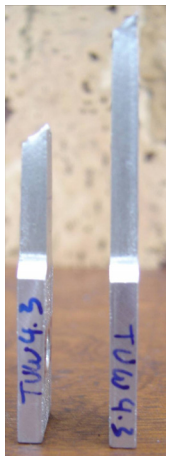

**Figure 102 - Tensile specimen after test (base material).**

In friction stir welded specimens the rupture occurred in the external part of the weld line, in a transition between welded and un-welded material zone. This site corresponds to the zone where minimum values of hardness occur, Figure 103. Also, a decrease in resistant area in the other side of the weld line was noticed.

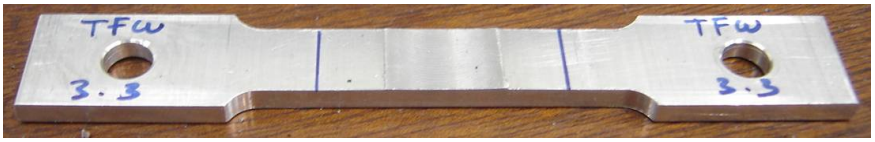


a) specimen TFW3.3 before tensile test

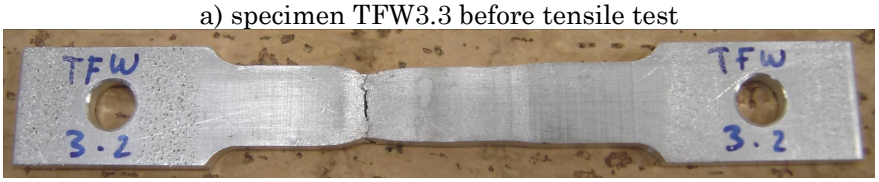


b) specimen TFW3.2 after tensile test

**Figure 103 - Tensile tested FSW specimen.**

To identify the influence of FSW on the specimen tensile properties, the stress/strain (σ/ε) records of all tensile tests are plotted in Figure 104.

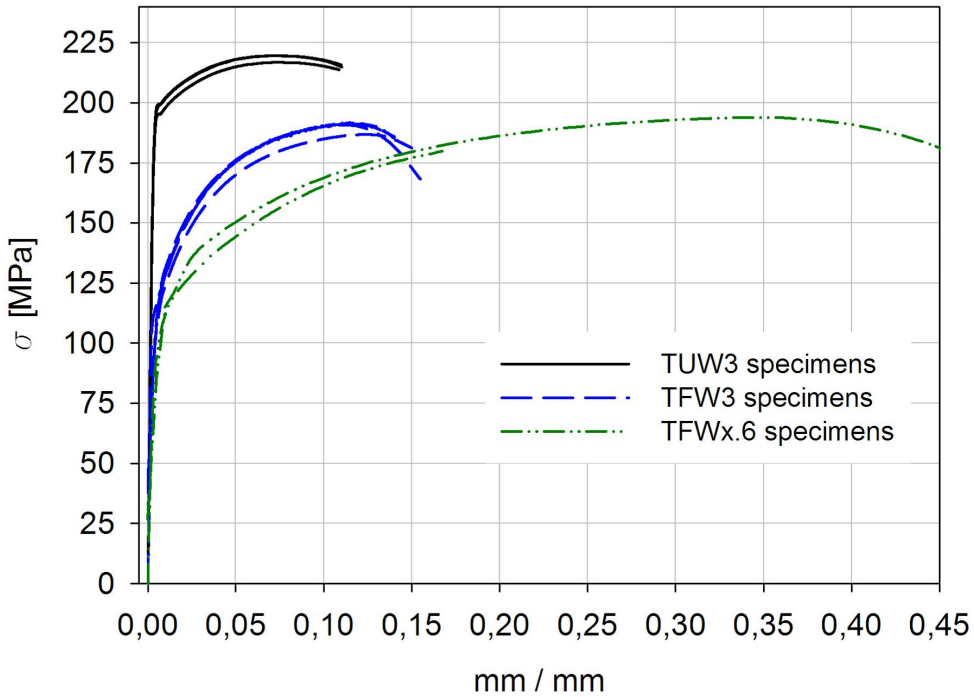


**Figure 104 - Tensile test results. TUW – un-welded specimens; TFW - welded specimens (reference x.6 strain corresponds to 6*mm* gage length).**

When using the 6*mm* gage length it was not possible to measure the elongation values, because of the location of rupture mentioned above. The average value of yield stress, rupture stress and Young's modulus ($\sigma_{yield}$, $\sigma_{rupt}$ and E, respectively) of all sets specimens tested are presented in Table 14. The yield stress was determined specifying and offset of 0,2% [144].

**Table 14 - Material properties, data acquired in tensile tests (average values)**

| Specimen | $\sigma_{yield}$ [*MPa*] | $\sigma_{rupt}$ [*MPa*] | E [*GPa*] | Elongation [%] |
|---|---|---|---|---|
| Literature [141] | 214 | 241 | 68,9 | 12 |
| TUW | 191,7 | 218,0 | 60,6 | 16,8 |
| TFW | 113,0 | 190,2 | 69,5 | 16,1 |
| TFWx.6 | 111,3 | 194,7 | 31,9 | - |

Yield stress and rupture stress of friction stir welded specimens have lower values than un-welded specimens. Considering the joint efficiency as the ratio between the rupture stress of the welded joint and base material, a value of 87,3% was obtained.
The lower value of Young modulus found for the TFWx.6 specimens can be justified by the lower material density due to defects (as pores), and by the thickness reduction imposed by the shoulder downward force during the welding process.

### *4.1.6 S-N fatigue data*

Studies on fatigue life of friction stir welded specimens can be found in the literature, as documented in the review published by Mishra *et al.* [145] but data concerning notched specimens is still not available. The fatigue tests, carried out in a MTS servo-hydraulic machine of 250$kN$ capacity, were performed at several stress levels with $\sigma_{min}/\sigma_{max}=R=0,1$ and $f=8Hz$. A total of 25 tests of welded an un-welded material were carried out in order to obtain the S-N plot. The parameters used for each level are presented in Table 15 [% $\sigma_y$ refers to material properties of welded material tensile tests ($\sigma_{yield}=113MPa$)].

**Table 15 - Fatigue tests parameters**

| $\sigma_{yield}$ TFW | 140% | 100% | 90% | 80% | 75% | 70% | 60% |
|---|---|---|---|---|---|---|---|
| $\sigma_{max}$ [$MPa$] | 158,2 | 113,0 | 101,7 | 90,4 | 84,8 | 79,1 | 67,8 |

Results of average fatigue life for un-welded and welded specimens are presented in Table 16 and Table 17, respectively.

**Table 16 - Average results of fatigue life for un-welded specimens**

| Stress [%] | Max stress [$MPa$] | Fatigue life [cycles] |
|---|---|---|
| 70 | 79,1 | 1662514 |
| 80 | 90,4 | 455471 |
| 90 | 101,7 | 259435 |
| 100 | 113 | 172187 |
| 140 | 158,2 | 17846 |

**Table 17 - Average results of fatigue life for FS welded specimens**

| Stress [%] | Max stress [$MPa$] | Fatigue life [cycles] |
|---|---|---|
| 70 | 79,1 | 28420655 |
| 80 | 90,4 | 2303303 |
| 90 | 101,7 | 544904 |
| 140 | 158,2 | 40788 |

It was found that FSW specimens display longer fatigue lives than similar un-welded specimens tested under the same loading conditions, , although generally of the same order of magnitude Figure 105. Even at 158,2$MPa$ maximum stress level, *i.e.* 140% of the yield stress of the friction stir welded specimens, welded specimens presented longer fatigue lives, whereas for the lower stress level

tested, the fatigue life of welded specimens, is one order of magnitude greater than the fatigue life of base material specimens. Biallas *et al.* [146] found in their study for another aluminium alloy that using high welding speeds similar fatigue lives were obtained testing both friction stir welded and base material of un-notched specimens.

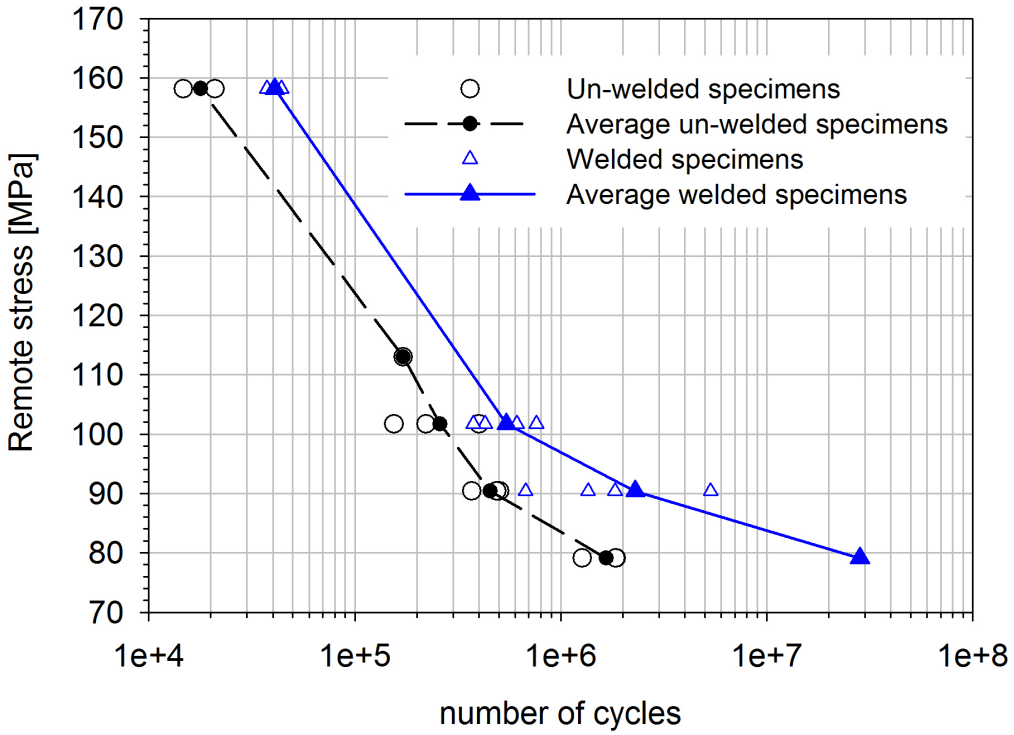


**Figure 105 - Notched specimens fatigue life results.**

### *4.1.7 Scanning electron microscopy analysis*

Scanning electron microscopy was used to identify microscopic features, such as welding defects and fatigue striations. Two welded specimens and two un-welded specimens were analysed. Notwithstanding the good properties obtained in the fatigue tests of the welded specimens, some defects were identified. Inner defects, such as cavities, cannot be seen on the surface, however by SEM inspection it was revealed that a defect linearly existed along the joint line, Figure 106. The defects were regularly spaced in a distance similar to the advance per revolution. The present study was not intended to optimize process parameters; the parameters used were in the range of those found in the literature, see for example [90]. It can be speculated that the pin shape was not optimum for such a high advance per revolution, leading to a cavity or groove-like defect caused by insufficient heat input. These defects were situated at mid thickness so they were not root flaws or lack of penetration and are likely to be due to use of non optimal FSW process parameters.

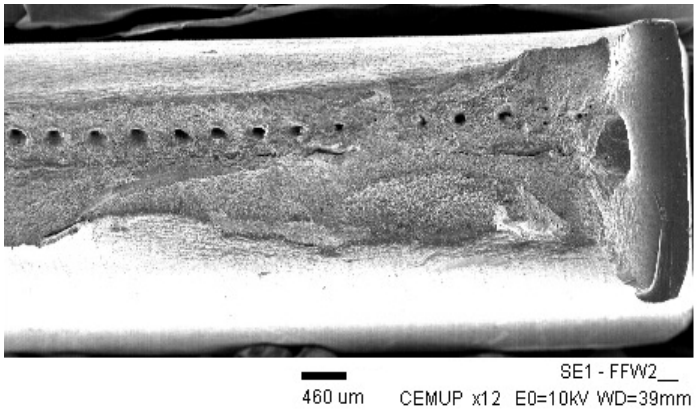


a) crack surface

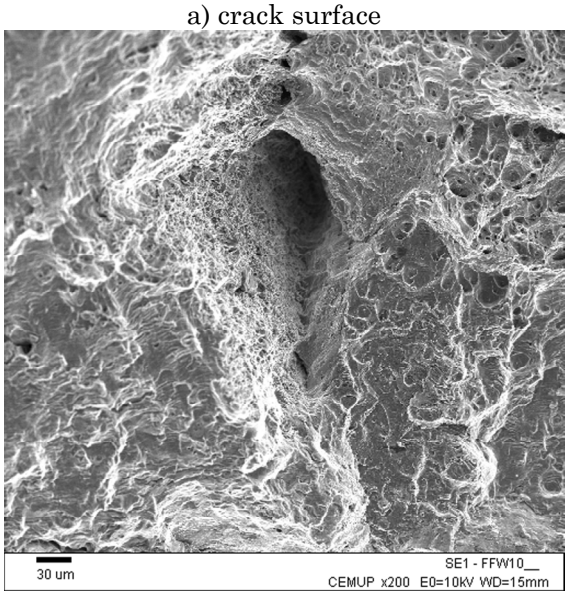


b) inner welding defect

**Figure 106 - SEM analysis of a crack surface on a FS welded specimen.**

Studying friction stir welded butt joint specimens of aluminium 2024-T6, Biallas *et al.* [146] concluded that the presence of pores was negligible for the tensile strength as well as for high cycle fatigue performance.

The fatigue crack growth area of an un-welded specimen is presented in Figure 107. In the friction stir welded specimens the crack propagation area was harder to identify. This difficulty is created by the stirring process that leads to a heterogeneous volume of material. Experimental and numerical techniques have been developed to allow the investigation of the stirring effect, metal flow, during FSW. Experimental and numerical techniques have been developed to allow the investigation of the stirring effect, metal flow, during FSW. In a work by Seidel *et al.* [73] it was verified that the material is moved to a final position behind its original location and only a small amount of the material on the advancing side moves to a final position in front of its original position. Also, the material from the retreating side is transported along with the rotating tool to the advancing side and parts of it even to a position in front of its original position. From the analysis along the height it was found that the material inside the pin diameter is

pushed downwards on the advancing side and moved upwards in the retreating side.
In another study Guerra *et al.* [75] showed that the material is transported by two processes. The first is a wiping of material from the advancing front side of the pin onto a zone of material that rotates and advances with the pin. The material undergoes a helical motion within the rotational zone that rotates, advances, and descends in the wash of the threads on the pin and rises on the outer part of the rotational zone. The second process is an entrainment of material from the front retreating side of the pin that fills in between the sloughed off pieces from the advancing side.

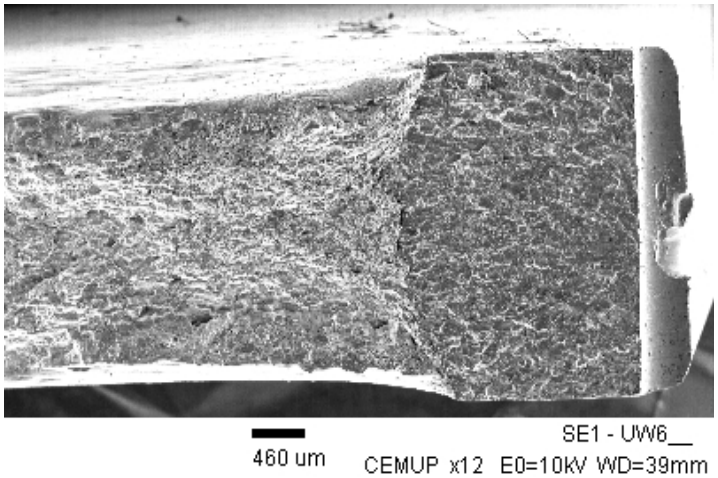


**Figure 107 - SEM analysis of an un-welded specimen.**

In the SEM analysis of the fatigue cracks, fatigue striations were identified in both welded and un-welded specimens, Figure 108. However, due to the more heterogeneous fracture surface, it was more difficult to identify fatigue striations on the welded specimens.

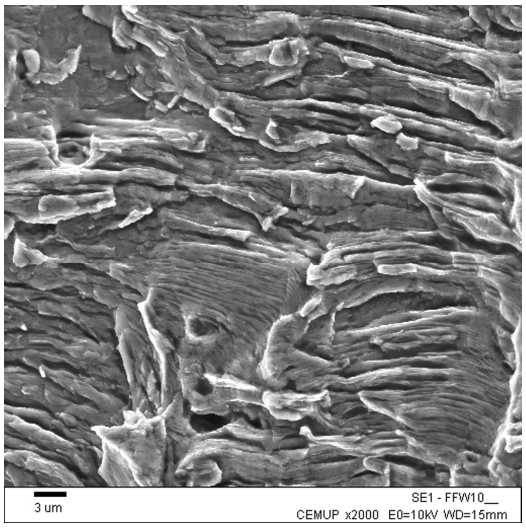


a) fatigue striations, welded specimen

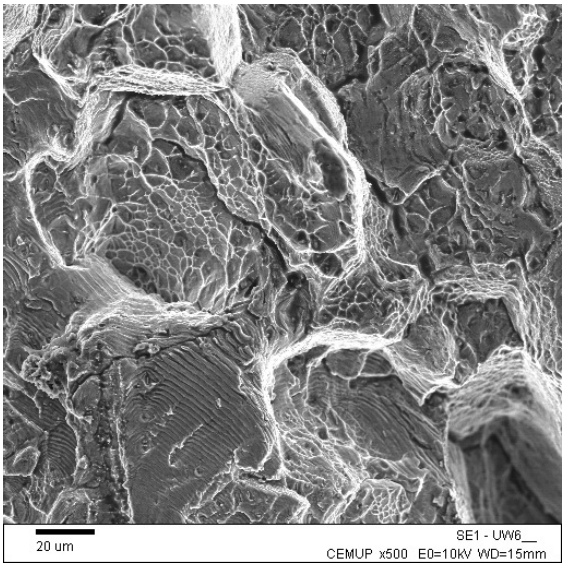


b) fatigue striations, un-welded specimen

**Figure 108 - SEM analysis of crack surfaces, fatigue striations identification.**

### *4.1.8 Stress analysis of welded and un-welded specimens*

As a contribution to understanding why the fatigue lives of friction stir welded specimens were found to be higher than those of un-welded material, and since the elongation obtained in tensile tests of base material (TUW) and welded material (TFW) specimens presented similar results, a non-linear stress analysis using the finite elements software ABAQUS [147] was carried out. Since the notch introduces a stress concentration, the mesh was refined in its vicinity. For each stress level experimentally used three analyses were carried out.

In a first analysis the tensile test data obtained for the un-welded material was introduced as material properties.
In the second analysis, the material properties data obtained in tensile tests of friction stir welded specimens (25$mm$ gage length) were used in the mesh in a zone of 14$mm$ length physically affected by the FSW process. In this case the specimen behaviour depends upon the combination of base and friction stir welded materials (these results are identified as 'mix material behaviour'). The remaining specimen length has the properties of the base material.
In the third analysis, in a zone of 14$mm$ length physically affected by the FSW process, the material properties obtained in tensile tests with 6$mm$ gage length were used.

The second and third analysis above are approximations that model the welded joints as a two material solid, not taking into account the very complex distribution of properties.
Firstly a coarser mesh was used to identify the areas where strong stress gradients were present. Then a finer mesh was developed containing 4254 elements (C3D8 and C3D6 type) and 5916 nodes. A mesh detail is presented in Figure 109.

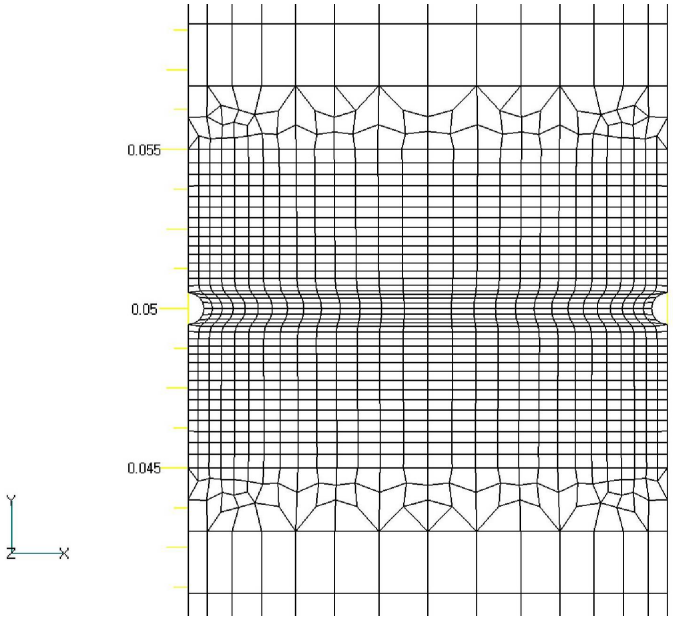


**Figure 109 - Mesh detail.**

The stress distribution in the load direction ($\sigma_{22}$) near the notched area using base material properties and $25mm$ length measurement properties, for some stress levels used in fatigue tests, is presented in Figure 110.

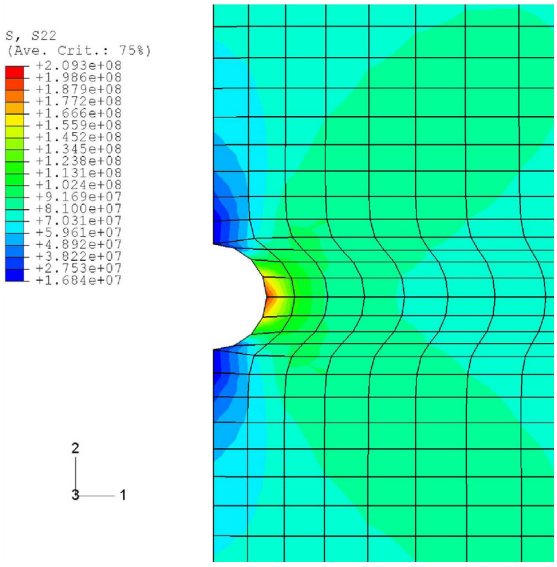


a) 70% σ fatigue test of un-welded specimen

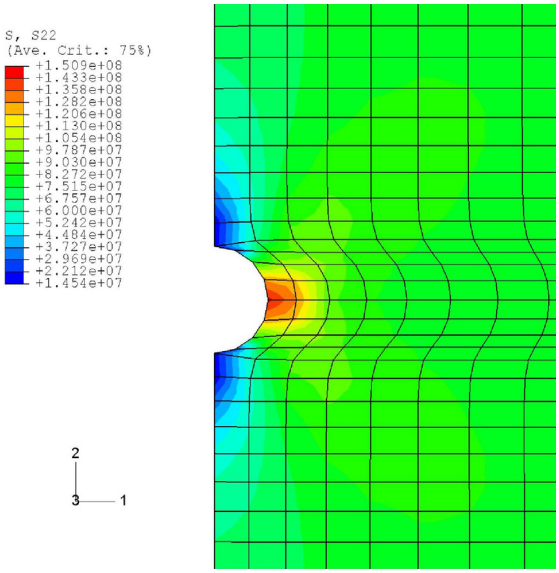


b) 70% σ fatigue test of welded specimen

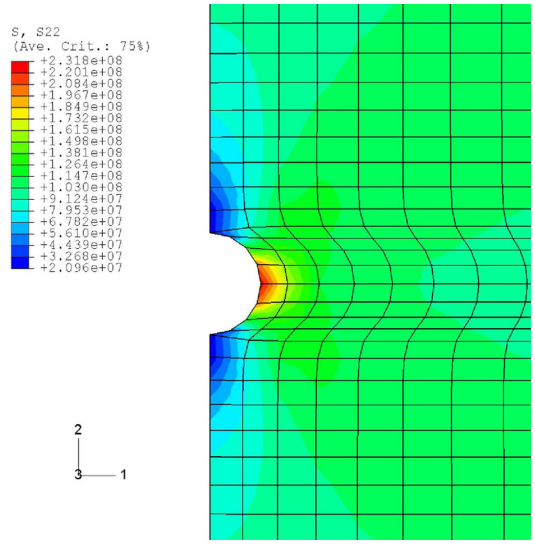


c) 90% σ fatigue test of un-welded specimen

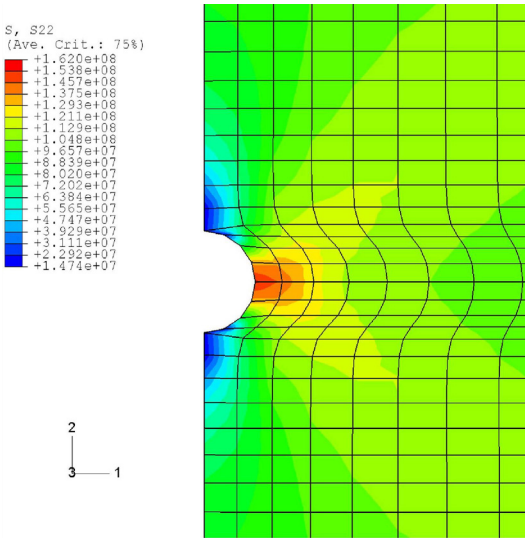


d) 90% σ fatigue test of welded specimen

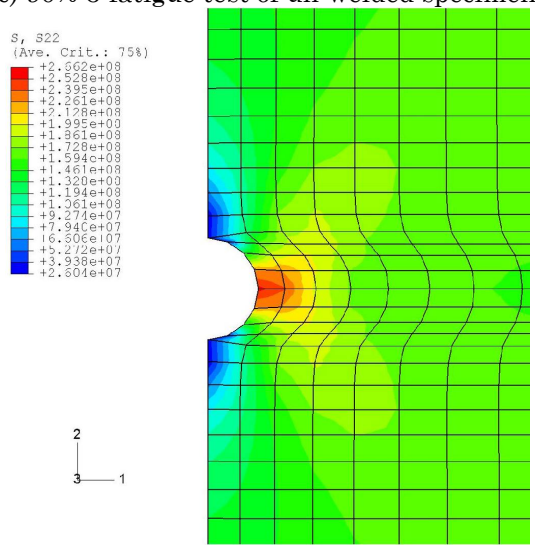


e) 140% σ fatigue test of un-welded specimen

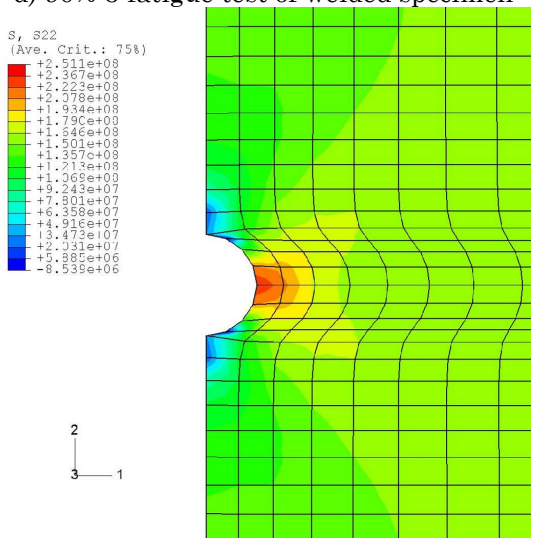


f) 140% σ fatigue test of welded specimen

**Figure 110 - Detail of stress $\sigma_{22}$ distribution in the notched area.**

Figure 111 presents the stress distribution in the loading direction ($\sigma_{22}$) in the top surface of specimen mid plane when tested at 70%, 80%, 90% and 140% of yield stress of the welded specimen (79,1; 90,4; 101,7; and 158,2*MPa* respectively). This shows that for all remote stress levels the notch stress concentration effect is more intense in the un-welded specimens, a fact due to the earlier plastification of the area surrounding the notch in the friction stir welded specimen. Furthermore it was verified that there is a small influence in maximum stress values of the type of approach to model the 14*mm* thermo-mechanically affected zone: *i* - stress/strain behaviour obtained with gage length 25*mm*; *ii* - stress/strain behaviour obtained with 6*mm* gage length. Figure 111 only includes the curves of type *i*, since both models gave very similar results.

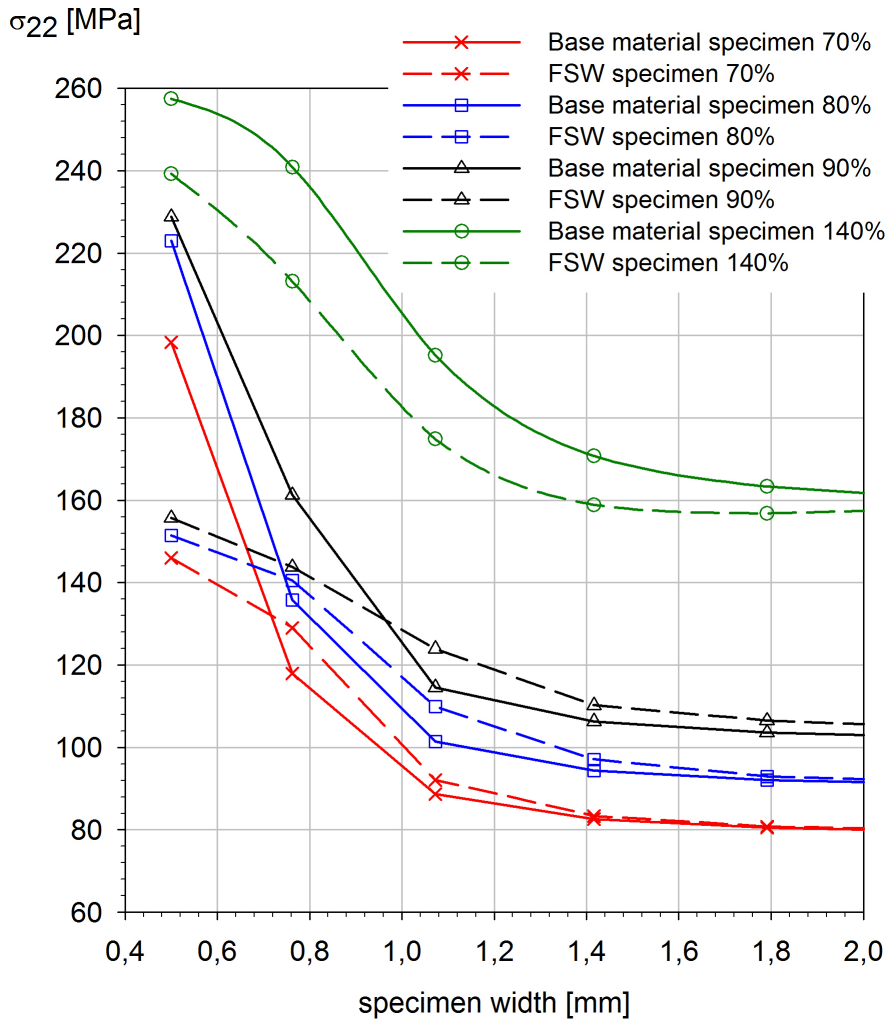


**Figure 111 - Stress distribution in the top surface of specimen mid plane close to the notch. Remote stresses of: 79,1*MPa* (70% of reference $\sigma_{yield}$); 90,4*MPa* (80% of reference $\sigma_{yield}$), 101,7*MPa* (90% of reference $\sigma_{yield}$), 158,2*MPa* (140% of reference $\sigma_{yield}$).**

Maximum values of total, plastic and elastic strain obtained when loading a base material specimen at several remote stresses are presented in Figure 112. Figure 113 presents values of total, plastic and elastic strain obtained for several remote stresses when loading a FS welded specimen, using mix material properties, and FS welded material properties only. At lower stress levels, below FS welded material $\sigma_{yield}$, elastic and plastic strain are of the same order of magnitude.

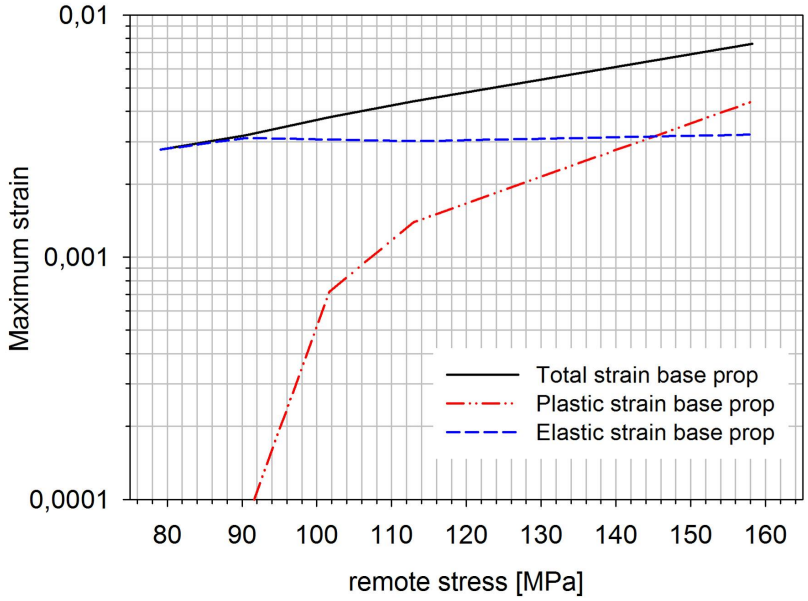


**Figure 112 - Maximum strain values for specimen of base material.**

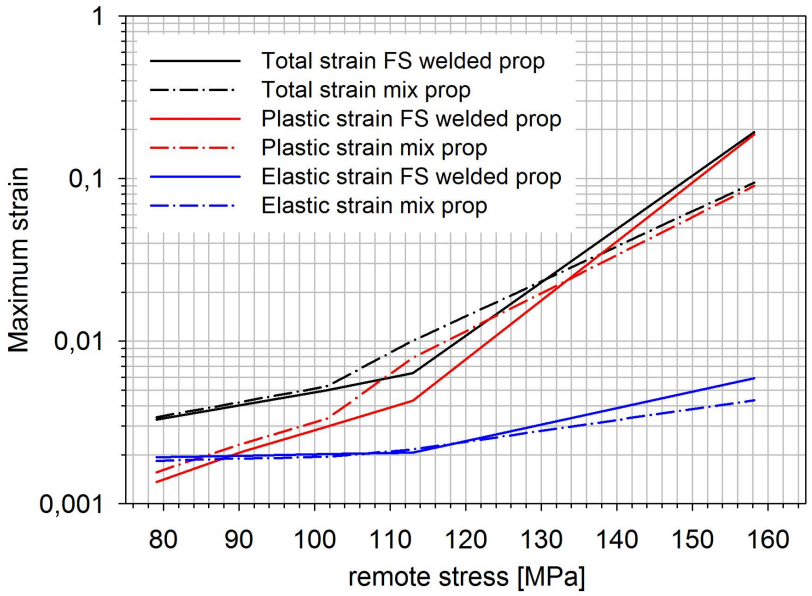


**Figure 113 - Maximum strain values for FS welded specimens using two different material behaviours.**

For the lower stress tested the elastic strain is the dominant strain. As the stress level increases plastic strain has the major role. Approximately similar values of strain (total, plastic and elastic) were obtained modelling friction stir welded specimens using mix material properties and only friction stir welded material properties.

### *4.1.9 Strain-life*

The strain based approach to fatigue [148-152] was used for life prediction, given the plastic deformation of the specimens. Stresses and strains in notch regions

were analyzed and used as a basis for life estimates. Coffin and Manson proposed a characterization of fatigue life based on the plastic strain amplitude. For short lives, for a series of completely reversed tests at different strain ranges, it was found for ductile metals that a log-log plot of the fatigue life versus the stable plastic strain amplitude gives a band of points that can be approximated by a straight line [153]. The plastic component of strain was described by Manson-Coffin as equation (3) where $\Delta\varepsilon_p/2$ is the plastic strain amplitude; $\varepsilon'_f$ the fatigue ductility coefficient; and $c$ the fatigue ductility exponent. For ductile metals the fatigue ductility exponent is nearly a universal constant, and the fatigue ductility coefficient can be approximated as a true fracture ductility $\varepsilon_f$ from a monotonic tension test.
For long lives the elastic component is used, equation (4). In this equation, $\Delta\varepsilon_e/2$ is the elastic strain amplitude; $\sigma_a$ is the stress amplitude; $E$ the modulus of elasticity; $\sigma'_f$ is the fatigue strength coefficient, defined by the stress intercept at one load reversal ($2N_f=1$); $2N_f$ number of reversals to failure or twice the number of cycles; $b$ the fatigue strength exponent or Basquin exponent.
Data for strain life curves are obtained from cyclic tension-compression tests of smooth specimens. The curve takes into account elastic and inelastic strain contributions. Equation (5) defines this methodology, and it is applied in intermediate lives where the resistance to total strain is dependent on the combined ductility and strength of the material. The influence of a mean stress $\sigma_m$ in fatigue may be accounted as an increase or decrease of the fatigue strength coefficient (elastic component) [153]. Using this concept in equation (5) we have the Morrow equation, equation (6).

$$\frac{\Delta\varepsilon_p}{2} = \varepsilon'_f \left(2N_f\right)^c \quad \textbf{(3)}$$

$$\frac{\Delta\varepsilon_e E}{2} = \sigma_a = \sigma'_f \left(2N_f\right)^b \quad \textbf{(4)}$$

$$\frac{\Delta\varepsilon}{2} = \frac{\sigma'_f}{E}\left(2N_f\right)^b + \varepsilon'_f \left(2N_f\right)^c \quad \textbf{(5)}$$

$$\frac{\Delta\varepsilon}{2} = \frac{\sigma'_f - \sigma_m}{E}\left(2N_f\right)^b + \varepsilon'_f \left(2N_f\right)^c \quad \textbf{(6)}$$

*4.1.9.1 Un-welded specimens*

Coefficients for aluminium 6063-T6 are presented in Table 18, [149]. For the approximate modelling of these fatigue results, strain for each load level was obtained from FEM analysis, Table 19. It is recognized that the present load controlled tests differ from the strain controlled tests upon which the methods of this section are based; therefore the following considerations should be taken as

an empirical description of the tests, based on stress and strain estimates corresponding to the first cycles of loading. The strain values obtained by the FEM simulation and the fatigue life values of each test are plotted in conjunction with the curves given by equations (3), (4) and (5) in Figure 114.

**Table 18 - Strain-life fatigue properties**

| Product form | $\sigma'_f$ [*MPa*] | b | $\varepsilon'_f$ | c |
|---|---|---|---|---|
| Sheet | 544 | -0,1008 | 0,691 | -0,811 |

**Table 19 - Total strain for each stress level**

| Stress [*MPa*] | 79,1 | 90,4 | 101,7 | 113,0 | 158,2 |
|---|---|---|---|---|---|
| Maximum ε | 0,002778 | 0,00318 | 0,00378 | 0,00401 | 0,00704 |

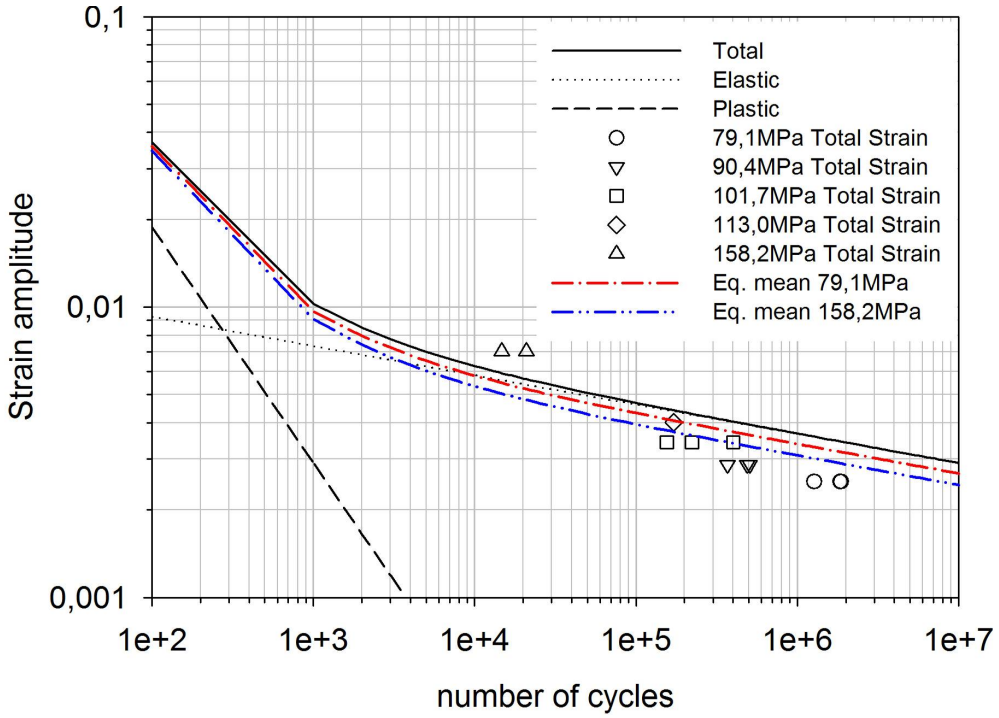


**Figure 114 - Total strain-life plot for AA6063-T6.**

A good agreement between the predicted and experimental fatigue lives was found. The influence of the mean stress in the strain life approach, equation (6), for the maximum and minimum mean stress applied in all tests of the present programme is shown in Figure 114. For tests performed with maximum stresses up to 113,0*MPa* (90% of the friction stir welded material yield stress), the elastic strain have a higher influence in the total strain. In this case, the fatigue life prediction is controlled by the elastic strain component of equation (6).

*4.1.9.2 FS welded specimens*

*4.1.9.2.1 First approach*

For the friction stir welded material there are no parameters published in the available literature; therefore an estimation of their values based on prediction of

fatigue from static properties was carried out [153]. Taking into account the basic concepts of engineering stress/strain and true stress/strain the parameters were estimated ($A$ the final section after rupture and $A_0$ the initial section of the specimen).

- In a log $\Delta\sigma/2$ versus $2Nf$ plot the fatigue strength coefficient $\sigma'_f$ is the intercept at one reversal and the fatigue strength exponent $b$ is the slope of the line [148, 153];
- The fatigue strength coefficient $\varepsilon'_f$ can be approximated by $\varepsilon'_f \approx \varepsilon_f = \ln(A_0/A)$, [153];
- The fatigue ductility exponent $c$ has a nearly constant value for metals between -0,5 and -0,7 [153].

The stress/strain properties obtained in tensile tests using $25mm$ and $6mm$ gage length are presented respectively in Table 20 and Table 21.

**Table 20 - Engineering/true stress [*MPa*]/strain properties from tensile tests where a 25*mm* region was measured**

| Specimen | A $mm^2$ | $A_0$ $mm^2$ | $F_{max}$ [N] | True strain ε | True stress σ | Su |
|---|---|---|---|---|---|---|
| TFW1 | 17,64 | 30 | 5790,61 | 0,5308 | 328,20 | 193,02 |
| TFW2 | 18,13 | 30 | 5810,43 | 0,5034 | 320,43 | 193,68 |
| TFW3 | 17,71 | 30 | 5811,29 | 0,5271 | 328,14 | 193,71 |
| $\mu_s$ | 0,266 | 0,00 | 11,698 | 0,015 | 4,470 | 0,390 |
| $\sigma_s$ | 17,829 | 30,00 | 5804,11 | 0,520 | 325,589 | 193,470 |

**Table 21 - Engineering/true stress [*MPa*]/strain properties from tensile tests where a 6*mm* region was measured**

| Specimen | A $mm^2$ | $A_0$ $mm^2$ | $F_{max}$ [N] | True strain ε | True stress σ | Su |
|---|---|---|---|---|---|---|
| TFW1 | 16,30 | 30 | 5844,39 | 0,6103 | 358,63 | 194,81 |
| TFW2 | 16,10 | 30 | 5836,26 | 0,6224 | 362,50 | 194,54 |
| $\mu_s$ | 0,139 | 0,00 | 5,745 | 0,009 | 2,737 | 0,191 |
| $\sigma_s$ | 16,198 | 30,00 | 5840,32 | 0,616 | 360,566 | 194,677 |

With these values and the considerations presented above, the values of the welded material to be used in equations (5) and (6) were determined and presented in Table 22.

**Table 22 - Strain-life fatigue properties for the welded material**

| | $\sigma'_f$ [*MPa*] | b | $\varepsilon'_f$ | c |
|---|---|---|---|---|
| mix material behaviour | 189,2 | -0,1076 | 0,5205 | -0,7 to -0,5 |
| only FS welded material | | | 0,6163 | |

Using the parameters presented in Table 22 a comparison between results based on material properties acquired in a $25mm$ length (mix material behaviour) and material properties acquired in a $6mm$ length (only friction stir welded material) was carried out. The strain values obtained by the FEM simulation and the fatigue life values of each test are plotted in conjunction with equation (5) in Figure 115.

The Young's modulus values used in equation (5) were taken from Table 14, 69,5$GPa$ for the case of the mix material behaviour and 31,9$GPa$ for the measurement performed on friction stir welded material only. In this figure the results represented with a continuous line and filled symbols correspond to values obtained using the 25$mm$ gage length (mix material behaviour); the results represented with a dashed line and open symbols correspond to values obtained using the 6$mm$ gage length (friction stir welded material behaviour).

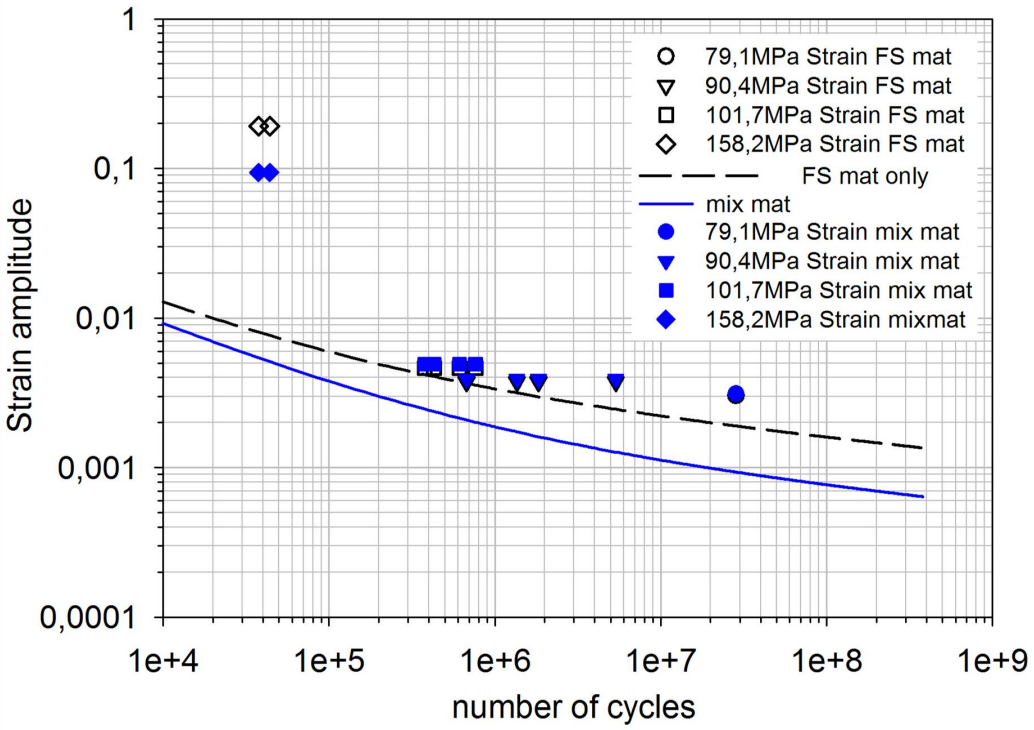


**Figure 115 - Total strain life plot for welded specimens when c=-0,5.**

For both approaches, mix material behaviour and friction stir welded material, the value of $c$ that best fit the experimental results is -0,5. This parameter only influences the plastic part of equation (5). A considerable difference between the predicted values and the experimental values combined with FEM results was found. Nevertheless the parameters estimation based on the mechanical properties acquired with the 6$mm$ length clip gage (dashed line and open symbols) lead to a best fit of the measured fatigue life.

*4.1.9.2.2 Second approach*

In order to have a best fit of the experimental data an analysis based on approximations available in the literature was carried out. A comprehensive discussion of several methods for estimating fatigue life from hardness is presented by Lee *et al.* [154].
From the correlations between hardness and ultimate tensile strength ($\sigma_b$) that could be found in the literature the only one that is dedicated to aluminium is proposed by the Japanese Society of Materials Science (JSMS), equation (7) [154].

$$\sigma_b = \frac{(HV - 21.9)}{0.242}\ (MPa) \tag{7}$$

Since the JSMS is the only method for estimating $\sigma_b$ from hardness for aluminium alloys, Lee *et al.* made an attempt to apply to aluminium other estimation methods proposed for steels. These methods are the Mitchell equation, equation (8); Roessle-Fatemi's equation, equation (9); and the Kloos-Velten's equation, equation (10).

$$\sigma_b = 3.45 \cdot HB\ (MPa) \tag{8}$$

$$\sigma_b = 0.0012 \cdot HB^2 + 3.3 \cdot HB\ (MPa) \tag{9}$$

$$\begin{aligned} \sigma_b &= 3.29HV - 47\ (MPa)\ \ HV \le 445 \\ \sigma_b &= 4.02HV - 374\ (MPa)\ \ HV > 445 \end{aligned} \tag{10}$$

From their study Lee *et al.* [154] concluded that all methods provide similar results. For comparison, all methods will be used in this work.
Since the microhardness profiles were measured in *HV* units, for the sake of using all methods the conversion of *HV* to *HB* proposed by ASTM [155] was used, equation (11). As presented in Figure 100 an average value of 62,6*HV* was experimentally measured.

$$HB = \frac{HV + 2.9744}{1.2005}\ \ for\ 40 \le HB \le 160 \tag{11}$$

Using equation (11) a value of 54,7*HB* is obtained. The estimation of $\sigma_b$ using the methods presented in equations (7)-(10) is presented in Table 23.

**Table 23 - $\sigma_b$ converted from hardness results**

| | Mitchell equation | Roessle-Fatemi's equation | Kloos-Velten's equation | JSMS equation |
|---|---|---|---|---|
| $\sigma_b$ [*MPa*] | 188,5 | 183,9 | 159,1 | 168,3 |

From the approximations for aluminium alloys presented in [154] the uniform materials method (equation (12)), and the medians method (equation (13)) are applied in this study.

$$\frac{\Delta\varepsilon}{2} = 1.67\frac{\sigma_b}{E}\left(2N_f\right)^{-0.095} + 0.35\left(2N_f\right)^{-0.69} \tag{12}$$

$$\frac{\Delta\varepsilon}{2} = 1.9\frac{\sigma_b}{E}\left(2N_f\right)^{-0.11} + 0.28\left(2N_f\right)^{-0.66} \tag{13}$$

The result obtained with the combination each value presented in Table 23 with the methods present in equation (12) and (13) is presented in Figure 116.

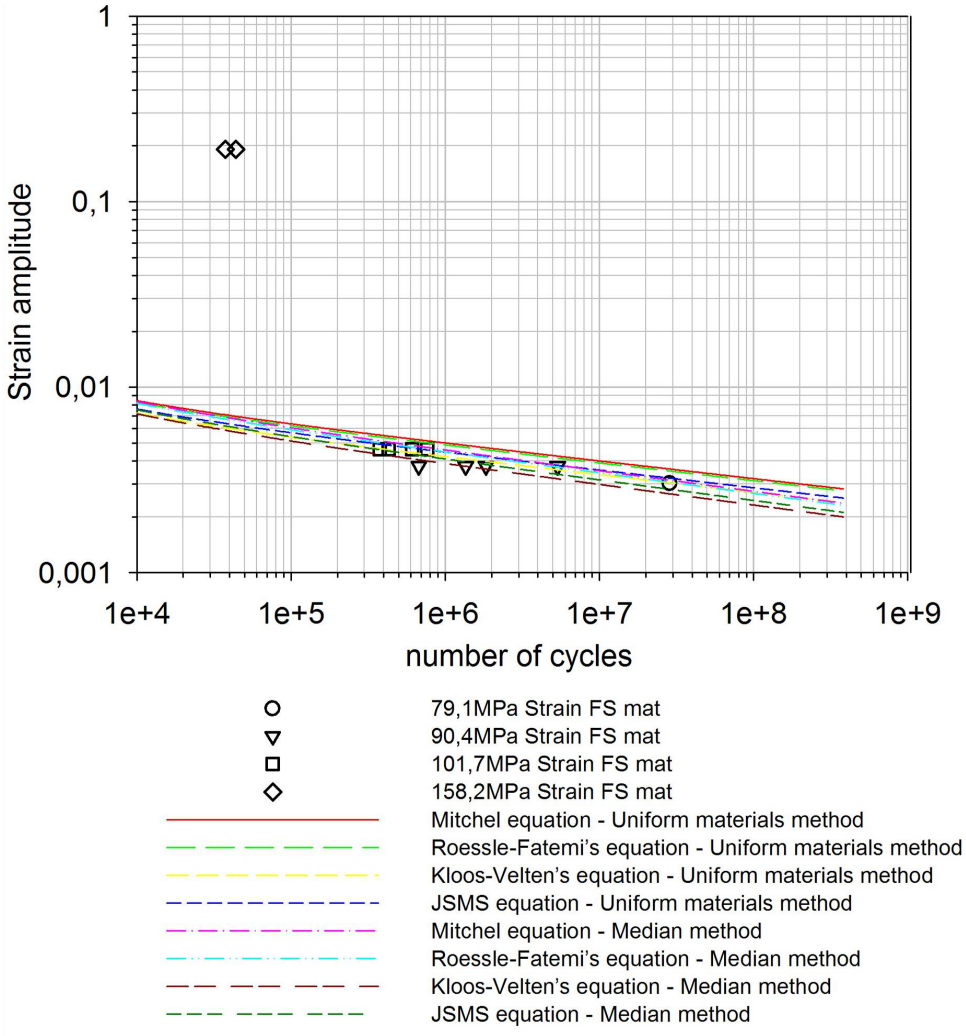


**Figure 116 - Strain life plot using the uniform materials method and the median method.**

With the methods used in Figure 116 a good agreement was found between the experimental fatigue lives and the predicted lives when the stress level used is under the friction stir welded yield stress (79,1*MPa* to 101,7*MPa* results). Nevertheless when testing over the friction stir welded material yield stress a large discrepancy was found.

Since all methods presented in Figure 116 present a similar agreement with the experimental data, the JSMS equation combined with the uniform materials method will be used in subsequent analyses.
A comparison study between the JSMS equation combined with the uniform materials method with the friction stirred material equation (presented in Figure 115) is presented in Figure 117. It was found that the JSMS equation combined with the uniform materials method shows a better agreement with the

experimental data. Nevertheless in the plastic regime this equation lacks accuracy.

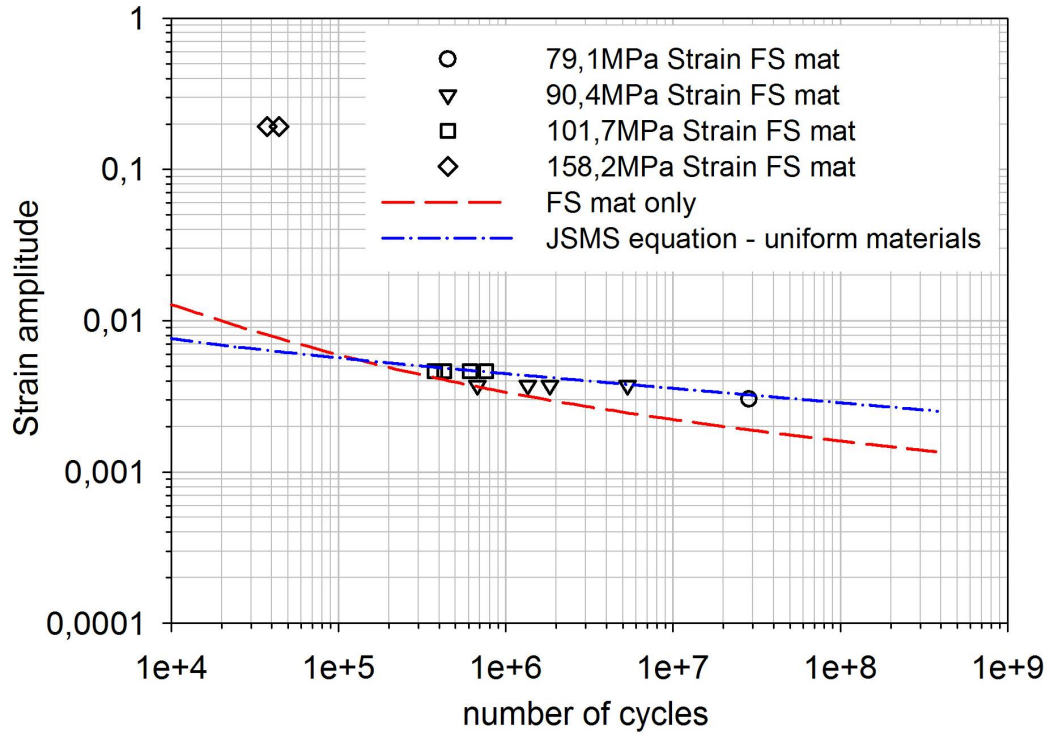


**Figure 117 - Comparison of total strain life plots for welded specimens, JSMS equation (uniform materials method), and FS material equation.**

*4.1.9.2.3 Third approach*

Because of the difficulty in dealing with the heterogeneous nature of the material, a fitting procedure was used to estimate parameters to be used in equation (5). The elastic regime of the JSMS equation for hardness conversion to $\sigma_b$ combined with the uniform materials method presented a good agreement with the experimental data. So, the elastic part of this approximation was not changed, and new parameters e and f for the plastic part were calculated (equation (14)). These parameters were estimated by a fit exercise with the data available from the experimental tests.

$$\frac{\Delta\varepsilon}{2} = 1.67\frac{\sigma_b}{E}\left(2N_f\right)^{-0.095} + e\left(2N_f\right)^{f} \qquad \textbf{(14)}$$

The parameters that gave a good fit were e=3E6 and f=-1,666. Equation (15) presents the new equation which is plotted in Figure 118.

$$\frac{\Delta\varepsilon}{2} = 1.67\frac{\sigma_b}{E}\left(2N_f\right)^{-0.095} + 3\cdot10^{6}\left(2N_f\right)^{-1.666} \qquad \textbf{(15)}$$

Equation (15) gives reasonable agreement with the experimental data. In the elastic region the accuracy is preserved, and an improvement was achieved in the

plastic region, overcoming the difficulties of applying the strain life approach to model the fatigue behaviour of the very heterogeneous FSW specimens in the large strain regime.

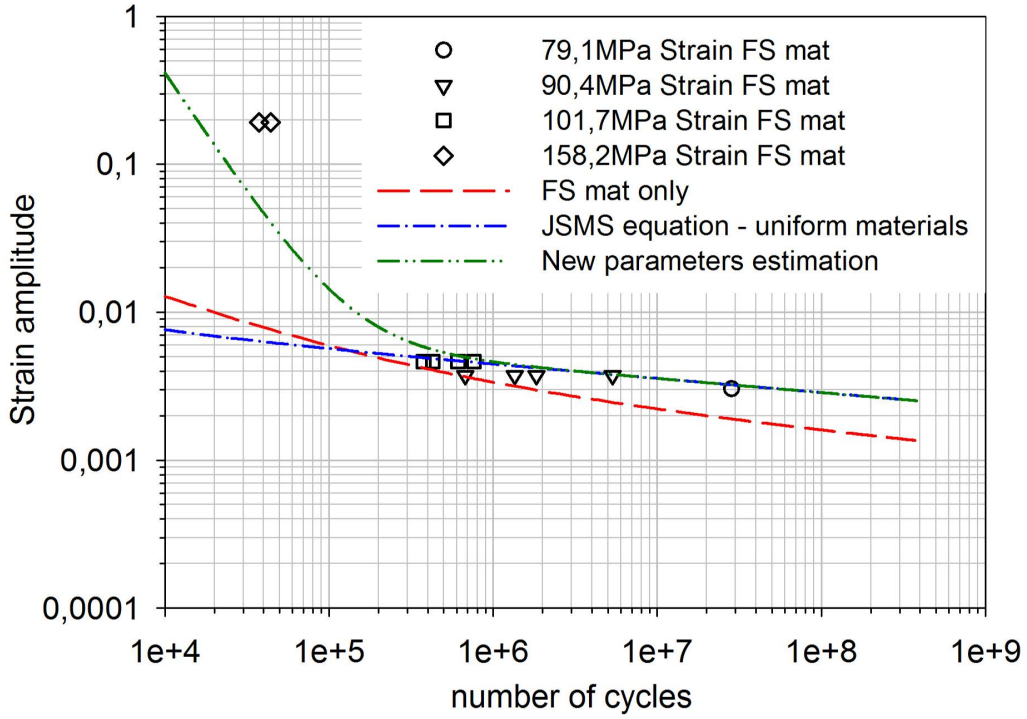


**Figure 118 - Comparison of total strain life plots for welded specimens, new parameters estimation.**

### *4.1.10 Concluding remarks*

This study quantifies the influence of the FSW process on the fatigue life of the aluminium alloy 6063-T6 notched specimens. Notched specimens with and without welding were fatigue tested under load control at several stress levels.

Hardness drastically decreases in the thermo-mechanically affected zone; the average hardness of the nugget zone is significantly lower than the base alloy.
Yield stress and rupture stress of friction stir welded specimens have lower values than un-welded specimens.
Welded specimens presented longer fatigue lives than un-welded specimens for all stress levels; even at 158,2*MPa* maximum stress level, 140% of the yield stress of the friction stir welded specimens, friction stir welded specimens present longer fatigue lives. It should be emphasised that this increase in fatigue life was obtained using specimens that contain a notch machined only in material directly affected by the stirring process.
As a result of the FEM analysis of the fatigue specimens it was found that that for all remote stress levels the notch stress concentration effect is more intense in the un-welded specimens, due to an earlier plastification of the area surrounding the notch. It was verified that at lower stress levels, below the friction stir welded material yield stress, elastic and plastic strain are of the same order of magnitude. For the lower stress level tested elastic strain is the dominant strain.

As the stress level increases plastic strain has the major role. As a result of the fatigue specimens finite element analysis it was found that for all remote stress levels the notch stress concentration effect is more pronounced in the un-welded specimens, due to an earlier plastification of the area surrounding the notch. It was verified that for stress levels below the friction stir welded material yield stress, elastic and plastic strain are of the same order of magnitude. For analyses of friction stir welded specimens using material properties acquired with the $6mm$ or the $25mm$ length gages, similar strain values are obtained for low stress levels, but for the maximum stress different strain results are verified.
In the SEM examination features as welding defects were identified; nevertheless good fatigue properties were obtained.
The strain based approach to fatigue was used for life prediction. For un-welded specimens a reasonable fit with present data was found. For the friction stir welded specimens with heterogeneous materials properties three different approaches were attempted. In a first attempt strain life parameters were estimated from the tensile tests results. In a second approach several methods available in the literature for estimation of the fatigue life from hardness data were used. In these two first attempts the results lack accuracy for higher loading but revealed a good agreement in the elastic region, particularly the methods based on the estimation of the fatigue life from hardness. In the third attempt a fit of new parameters was performed. With this fitting, the accuracy of results in the elastic region is similar to previous results, and an improvement was achieved in the plastic region.

### 4.2 Mechanical and metallurgical characterization of FS welded dissimilar joints of AA6061-T6 with AA6082-T6

Further to joining parts of the same alloy, friction stir welding is being studied for welding dissimilar alloys which can be of particular interest in some industrial applications. Presently some works can be found in the literature, *e.g.* [156-160], but data is still scarce on the characterisation of this joint type. In this study the ability to join dissimilar alloys (multimaterial) by friction stir welding was studied using butt welded plates. The mechanical characterization of friction stir welds between aluminium alloys 6061-T6 and 6082-T6 was carried out. For comparison, similar joints made from each of the two alloys were also performed. The work included microstructure examination, microhardness, tensile and bending tests of all joint types. An approximate finite element model of the joint, taking into account the spatial dependence of the tensile strength properties, was made, modelling a bending test of a welded specimen. The residual stresses generated during the friction stir welding process were estimated using strain gage measurements.

### *4.2.1 Material and welding process*

The aluminium alloys 6082-T6 and 6061-T6 are high strength Al–Mg–Si alloys that contain manganese to increase ductility and toughness. The chemical composition was determined before welding by spectrometry using a SPECTROLAB M7, Table 24. For both aluminium alloys a good agreement was found between our measurements and the supplier values. If the material is stored at room temperature natural ageing takes place (T4 condition). The T6 condition is obtained through artificial ageing at a temperature of approximately 180°C [90]. The friction stir welds of $3mm$ thick plates were performed along the rolling direction. The process parameters implemented in this study resulted from a development process based on visual analysis of top and bottom surfaces of the joint and preliminary bending tests with the root under tensile stresses enabling to minimize the level of root defect. The selected parameters were: travel speed of $224mm/min$; tilt angle of $2{,}5^{o}$; rotating speed of $1120rpm$. In all trials, a modular tool was used with the following geometry: M5 threaded pin; shoulder was smooth and $7^{o}$ concave with $17mm$ diameter.

**Table 24 - Chemical composition of the AA6061-T6 and AA6082-T6**

| Element | AA6082-T6 [%] | | AA6061-T6 [%] | |
|---|---|---|---|---|
| | SPECTRO LAB M7 | Supplier 6082-T6 | SPECTRO LAB M7 | Supplier 6061-T6 |
| Mg | 0,69 | 0,6-1,2 | 0,84 | 0,9 |
| Al | 97,4 | remaining | 97,7 | remaining |
| Si | 0,91 | 0,7-1,3 | 0,54 | 0,59-0,62 |
| Mn | 0,56 | 0,4-1 | 0,01 | 0,01 |
| Fe | 0,23 | 0,5 | 0,40 | 0,5 |
| Cu | 0,062 | 0,1 | 0,24 | 0,24-0,26 |
| Cr | 0,035 | 0,25 | 0,18 | 0,18-0,19 |
| Zn | 0,098 | 0,2 | 0,006 | 0,01-0,02 |
| Ti | 0,019 | 0,1 | 0,031 | 0,02-0,03 |

### *4.2.2 Tensile tests*

Tensile tests of specimens drawn transversal to weld line were performed to determine the mechanical properties of the welded and un-welded material, using a $25mm$ gage length, [144]. The stress/strain records of welded specimens are presented in Table 25 and Figure 119.

**Table 25 - Data acquired in tensile tests**

| FSW | $\sigma_{yield}$ $[MPa]$ | $\sigma_{rupt}$ $[MPa]$ | Elongation % | Joint efficiency % |
|---|---|---|---|---|
| base AA6082-T6 | 276,2 | 322,9 | 17,5 | - |
| base AA6061-T6 | 306,3 | 342,0 | 17,1 | - |
| FSW 6082-T6 | 134,3 | 221,3 | 6,5 | 68,5% |
| FSW 6082-T6 + 6061-T6 | 140,5 | 218,6 | 5,5 | 67,7 (6082-T6)<br>63,9 (6061-T6) |
| FSW 6061-T6 | 148,3 | 231,6 | 5,9 | 64,2% |

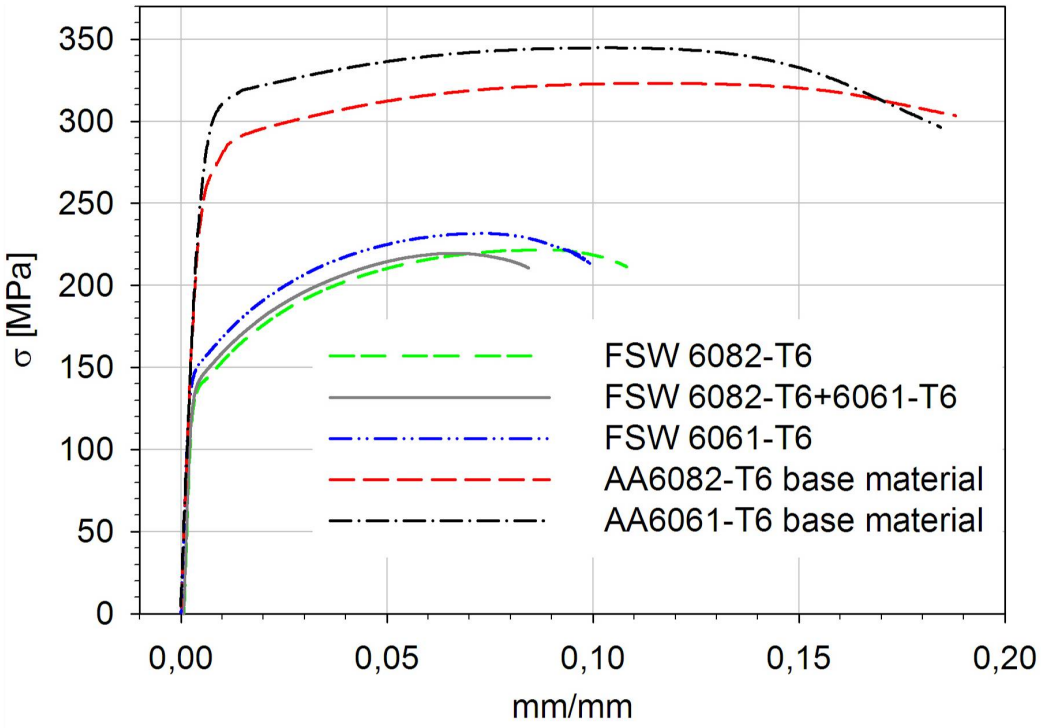


**Figure 119 - Tensile tests curves.**

The friction stir welded and base material 6061-T6 specimens present the higher yield and rupture stresses. The dissimilar weld specimens presented an intermediate behaviour, although the smallest elongation value and the ultimate stress very close to the welded aluminium 6082-T6 should be emphasized. In the friction stir welded specimens, fracture occurred near the weld edge line, corresponding to the transition between the thermo-mechanically affected zone (TMAZ) and the heat affected zone (HAZ) and characterised by the lowest hardness, as demonstrated in Figure 124 and also documented in [143]. The fracture occurred according to 45º shear planes which is also documented in [78]. Considering joint efficiency as the ratio of the rupture stress of the base material divided by the rupture stress of the welded joint an analysis of all joints was performed, Table 25. All joints presented approximately the same efficiency; their values are similar to those presented by others authors for single material joints, *e.g.* [61, 90, 93].

To obtain the material behaviour of the TMAZ in a second set of tests strain values were acquired with a $6mm$ gage length. The results obtained in conjunction with the results obtained with the $25mm$ gage length are presented in Figure 120. Stress/strain records show that the TMAZ presents higher strain values than in an area composed by the base material, the TMAZ and the HAZ. An estimation of the yield stress in the TMAZ is presented in Table 26. The yield stress in the TMAZ is always lower than that obtained using larger gage lengths ($25mm$). The higher ductility of the TMAZ was also reflected in the microhardness profiles presented in Figure 124.

**Table 26 - Material properties for FS welded TMAZ [6*mm* gage]**

| FSW [TMAZ] | $\sigma_{yield}$ [*MPa*] |
|---|---|
| FSW 6082-T6 | 129,1 |
| FSW 6082-T6 + 6061-T6 | 128,3 |
| FSW 6061-T6 | 133,0 |

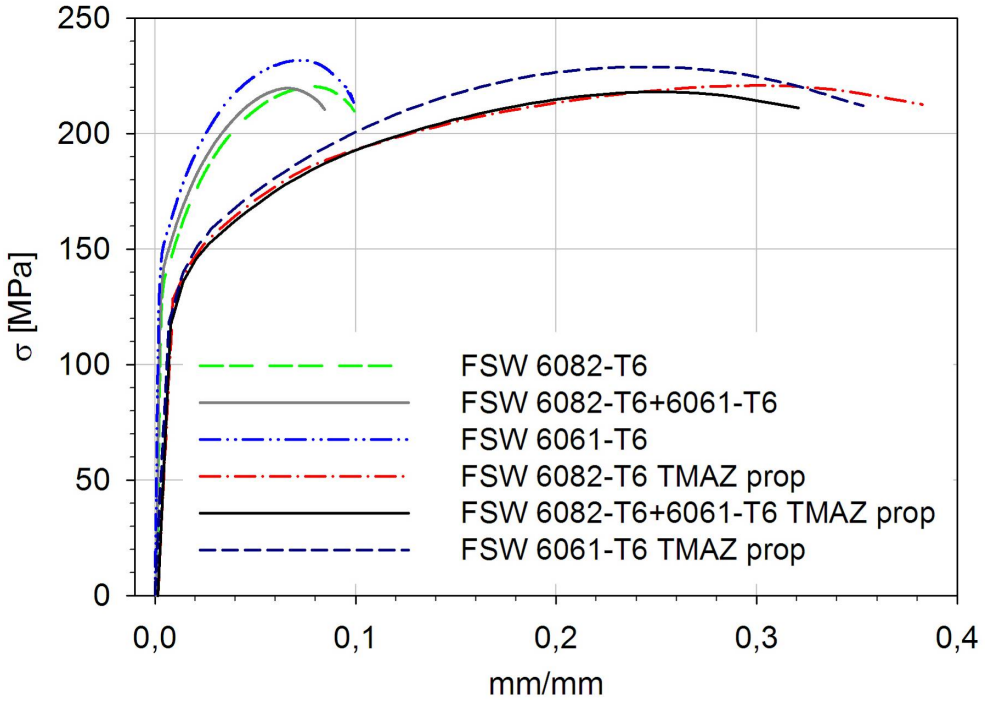


**Figure 120 - Tensile tests of the TMAZ for welded material specimens (6*mm* gage).**

### *4.2.3 Residual stresses*

Despite being a solid state process with low heat input supplied to the plate, residual stresses are created mainly due to the rigid clamping system needed to perform sound welds. Residual stresses were estimated using a method – already discussed in Chapter 3 - which consists of cutting a welded plate, previously instrumented with strain gages, along a line perpendicular to the weldments. This sectioning method relieves the residual stresses and gives a reasonable estimation of the stress profile; care should be taken to avoid introducing plastic deformations during the cut. This procedure was previously applied with success as reported by other authors, *e.g.* [123, 124].

Both plate surfaces were instrumented with eight strain gages placed at the side of the plate correspondent to the tool advancing side. The residual stress profile is expected to be similar in the plate side correspondent to the tool retreating side, as documented by other authors *e.g.* [161]. An aluminium 6082-T6 friction stir welded plate was analyzed; it is expected that the residual stress field for the butt joint with the two materials should not be substantially different, because the tensile properties of both are approximately similar.

In Figure 121 are presented the strain gages placed nearest to the weldment in the top and root surface. In the top surface of the weld bead it was not possible to measure stresses in the area affected by the shoulder since the surface

irregularity does not permit the instrumentation with a strain gage. Nevertheless in the root of the weld bead a strain gage was placed at the initial joint line. The sectioned plate is presented in Figure 122.

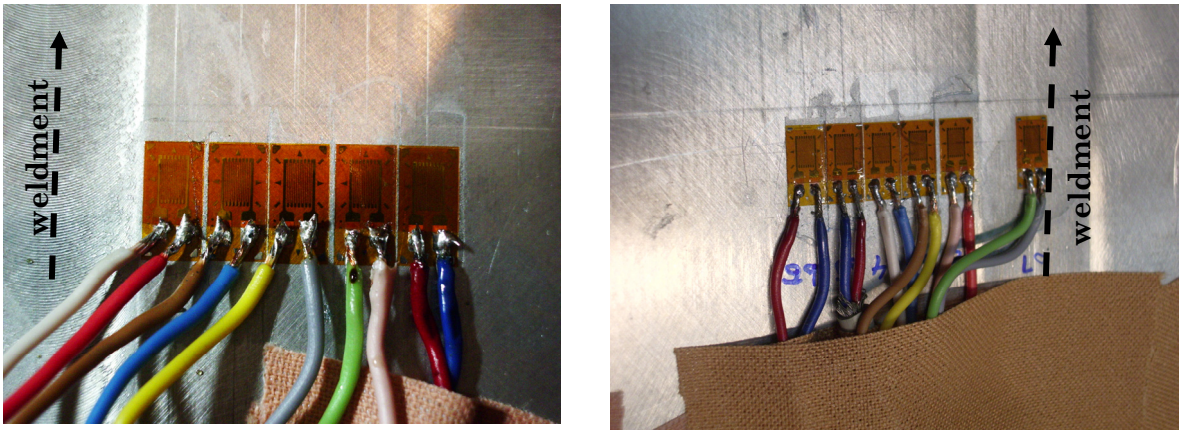


**a) weldment top side** **b) weldment root side**

**Figure 121 - Strain gages near the weldment.**

**Figure 122 - Measured plate after being sectioned.**

In the top surface of the weld bead (plate side where the shoulder contacted the plate) compressive residual stresses were obtained almost along all the plate width. Nevertheless near the TMAZ the stresses increase their values towards positive values, Figure 123. This profile was also observed in the plate root surface where the residual stresses are always positive. At the nugget zone a decrease of the stress value was observed. A maximum residual stress value of 91,7*MPa* was found in the root surface at the limit of the tool shoulder, whereas in the same site but at the top surface of the weld bead the stress reaches 36,4*MPa*.

Observations of compressive residual stresses are also reported by Fratini *et al.* [162] when analysing friction stir welded joints of aluminium 6082-T6. Also, for a similar alloy the studies [102, 163] presented values of the same order from the ones presented in this study.

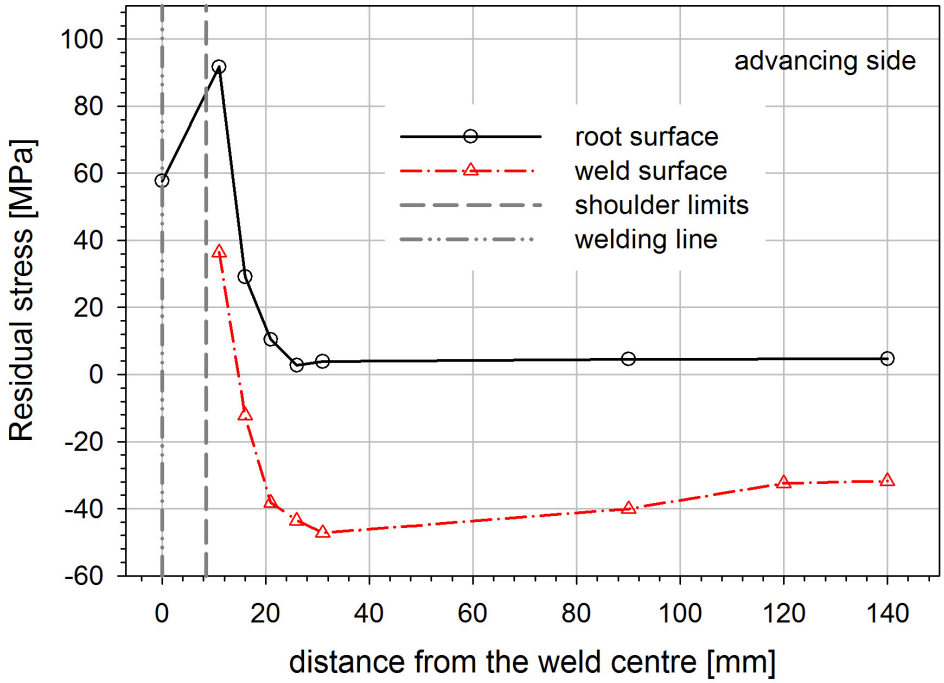


**Figure 123 - Residual stress in a FS welded AA6082-T6 plate, advancing side.**

### *4.2.4 Microhardness measurements*

The hardness profiles can assist the interpretation of the weld microstructures and mechanical properties. Microhardness tests were performed in order to characterize the hardness profile in the vicinity of the weld affected area. The microhardness tests were performed at the specimen's middle thickness across the weld zone and into the parent material, using a 100*gf* load. The Vickers hardness profiles for all welded specimens are presented in Figure 124.

A hardness decrease is verified along the TMAZ. The average hardness of the nugget zone (NZ) was found to be significantly lower than the hardness of the base alloy. The hardness increases in the HAZ towards the base material. There is a zone outside the nugget zone which has the lower hardness value (transition between TMAZ and HAZ). In [61] it is suggested that the variation of the microhardness values in the welded area and parent material is due to the difference between the microstructures of the base alloy and weld zone. Hardness in the dissimilar joint presented the lower values of all joints. The lower values occur in the aluminium 6082-T6 alloy plate side. In the tensile tests of the dissimilar specimens it was observed that the fracture surface is coincident with this zone of lower values of hardness. The hardness in the nugget area is similar for all joints and it is always higher than the values in the transition between the TMAZ and the HAZ.

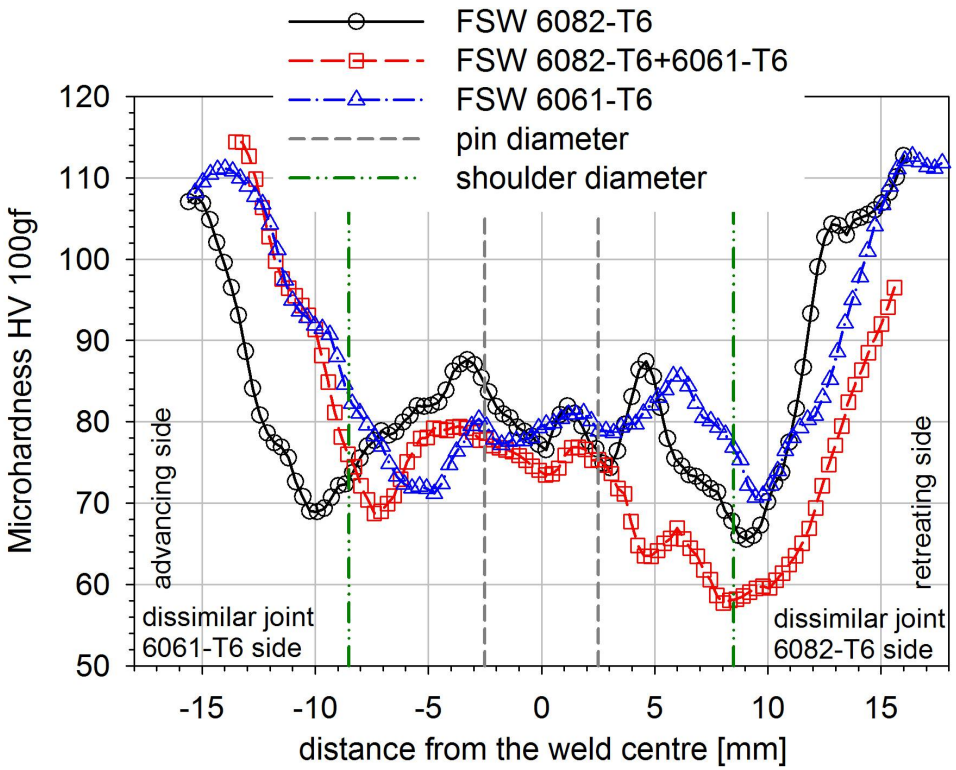


**Figure 124 - Microhardness profile of the FS welded specimens.**

A second hardness profile examination was carried out measuring the hardness through the specimen thickness, between the shoulder limits, for the three different joint types, Figure 125.

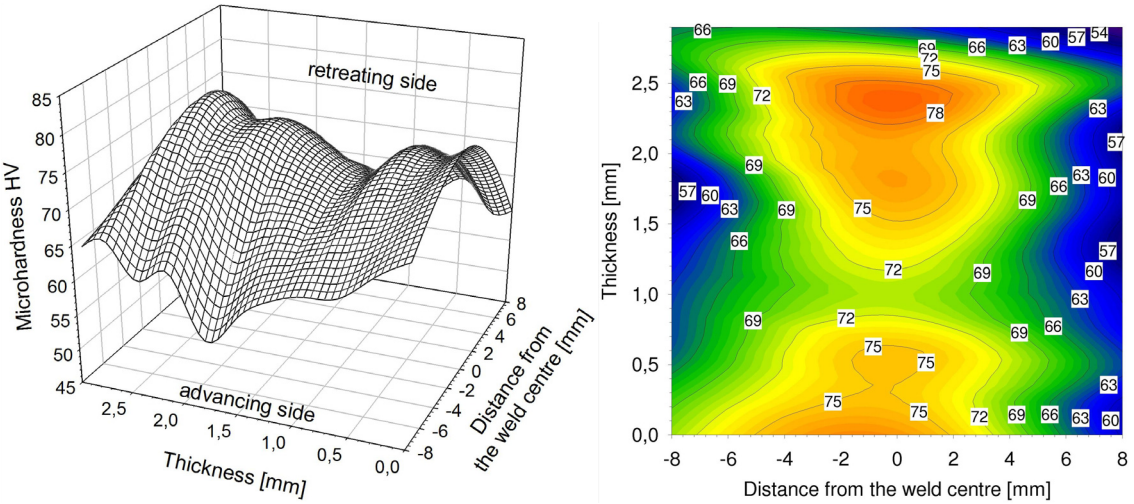


a) FS AA6082-T6

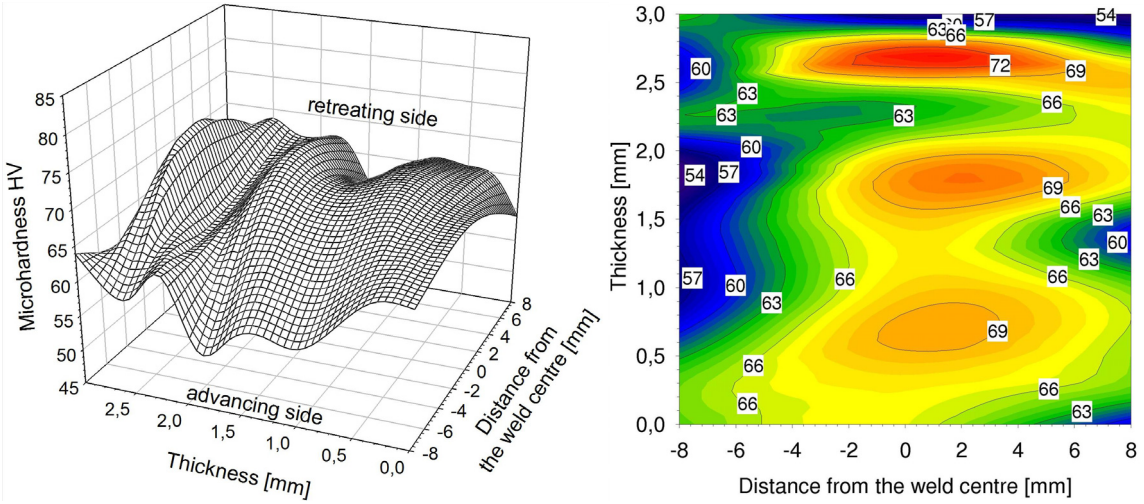


b) FS AA6061-T6

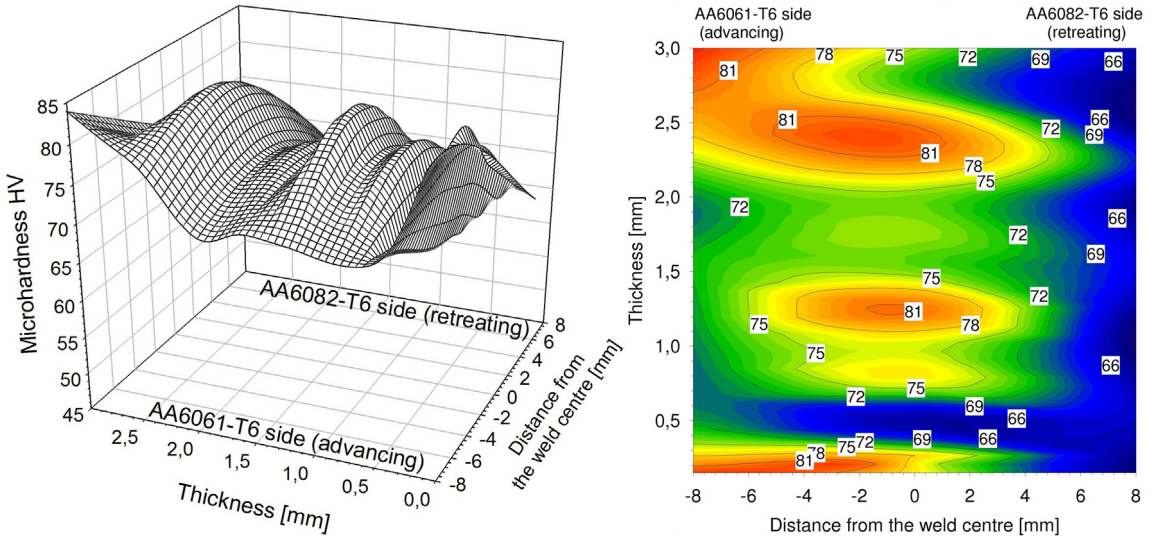


c) FS AA6082-T6 + AA6061-T6

**Figure 125 - Hardness profile thorough the joint thickness.**

It was verified in all joints that the minimum hardness values are coincident with the limits of the shoulder.

It should be noticed that Figure 125 is based upon data obtained along three lines of measurement perpendicular to the plate surface: two lines coinciding with shoulder limits and one with the weld centre. In Figure 125, root corresponds to the coordinate $3mm$ along the thickness axis. For the dissimilar joint, through the thickness measurements show a pronounced variation of hardness in the specimen middle plane (plane perpendicular to the plate surface, along the middle of the weld). This feature is attributed to the presence of either aluminium 6061-T6 material or aluminium 6082-T6 material in this area.

The lowest hardness value is usually present at the joint retreating side. The hardness at the root and top surfaces of the weld bead are similar in all joints, compare 0 and $3mm$ data in the thickness axis of Figure 125.

The loss of T6 condition, which occurs during welding, is expected to decrease the mechanical strength reflected in the drop of hardness. As described in the literature, in aluminium alloys such as 6082 and 6061 the main strengthening precipitate is ß″-Mg5Si6 which is stable at temperatures lower than 200°*C* [164]. This β″ precipitate is the main responsible for hardening. This precipitate exists in the unaffected base material but is absent in the nugget and in the HAZ. In the friction stir weld temperatures are expected to be over 200-250°*C*, during heating, and the β″ is easily dissolved [78]. Svensson [78] reported that no other fine scale precipitation was found in the nugget, while in the HAZ precipitation of β'-Mg1,7Si occurred on the AlMnSi dispersoids. On cooling, precipitation of β′ is favourable to β″, and since the β′ precipitates have less of a strengthening effect compared to β″, a lower hardness is obtained. The β' will act as a nucleation sites for the precipitates. Following the diagram of continuous cooling precipitation (CCP) presented by Grong [164], in the HAZ where temperatures are near or less than 300ºC the precipitation of β' is very high, so occurs the transition from β" to β' by dissolution. In the weld nugget, the temperature is expected to be higher, therefore the MgSi precipitates go into solution. On cooling, the time for precipitation is limited, therefore only a small volume fraction of the ß′ precipitates are formed in the weld nugget. The nugget hardness recovery is due to recrystallization of a very fine grain structure.

### *4.2.5 Metallographic analysis*

For the analysis of microstructural changes due to the FSW process, the joints were cross-sectioned perpendicularly to the welding direction and etched with HF reagent [142]. Aluminium 6061-T6 has similar silicon and magnesium contents to aluminium 6082-T6, but higher copper content and lower manganese content. Aluminium alloys always contain some impurities, mainly iron and silicon, [78]. For example, iron, silicon, manganese, copper, and chromium form fairly coarse intermetallic compounds. In the age hardenable alloys, hardening occurs through precipitation of very fine scale precipitates.

Microstructures were acquired in different zones: transition between welded and base material; welded material; and base material. In Figure 126 the macrostructure of the friction stir weld of the dissimilar specimen aluminium 6082-T6+6061-T6 and of each base material are presented. In each macrostructure the different zones (NZ, TMAZ, and HAZ) are identified. The retreating side, at the left side of each macrostructure, presents more flash and is also the location of the lower values of hardness.

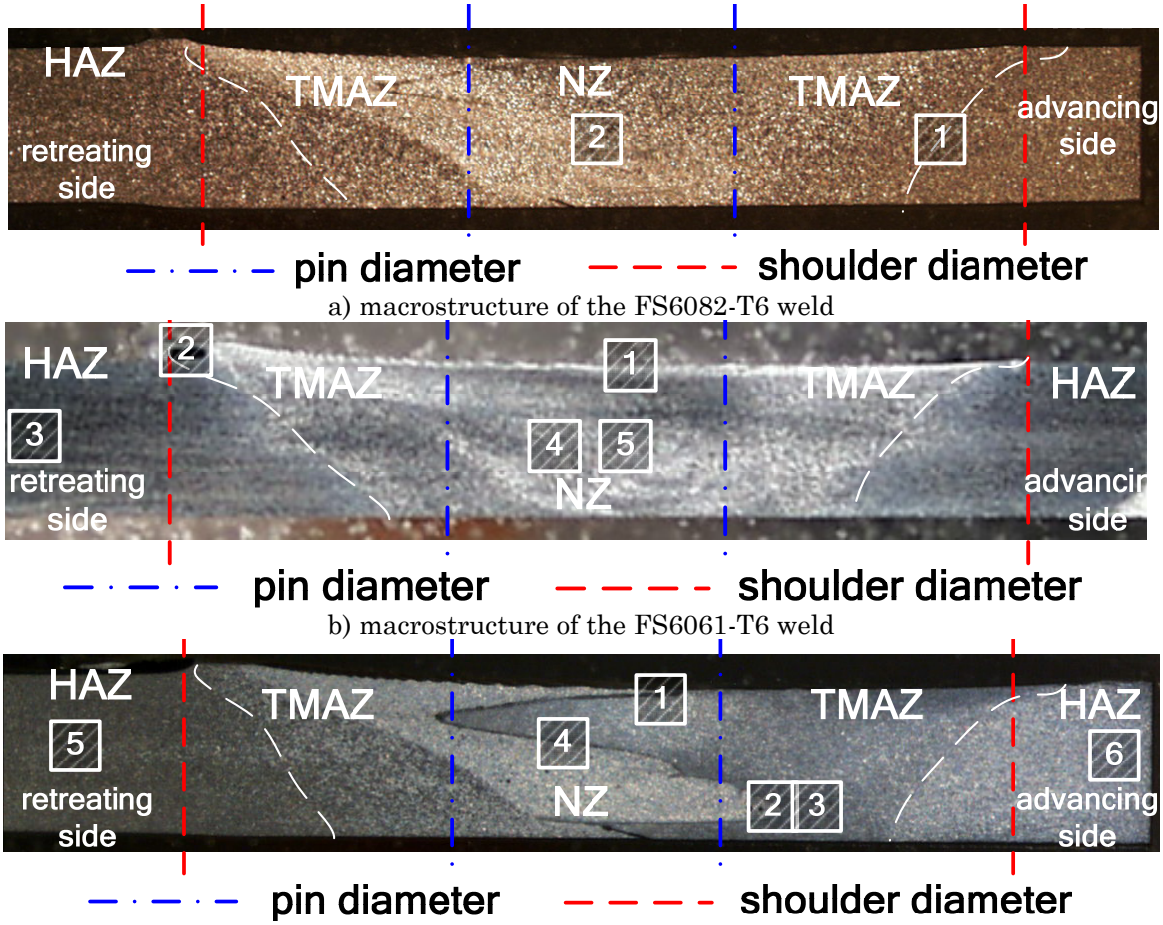


a) macrostructure of the FS6082-T6 weld

b) macrostructure of the FS6061-T6 weld

c) macrostructure of the dissimilar weld

**Figure 126 - Macrostructure of the dissimilar weld and each base material.**

FSW originates microstructure changes. At the centre, nugget zone, the mixture of the two different alloys is easily identified. The nugget zone experiences high strain and is prone to recrystallization. Immediately at its side is the TMAZ which ends at the tool shoulder delimited by the dashed lines. After the TMAZ appears a zone affected only by the heat generated during the welding process, *e.g.* [143, 165].

#### *4.2.5.1 Dissimilar joint microstructure*

Microstructural details of the dissimilar joint TMAZ are presented in Figure 127. The location of each microstructure is presented in Figure 126c).
In the transition between the two alloys the lighter colour represents the aluminium 6061-T6. The different structure of the two alloys is easily identified; the aluminium 6061-T6 is characterized by larger grains and the aluminium 6082-T6 by precipitates dispersed in a finer matrix.

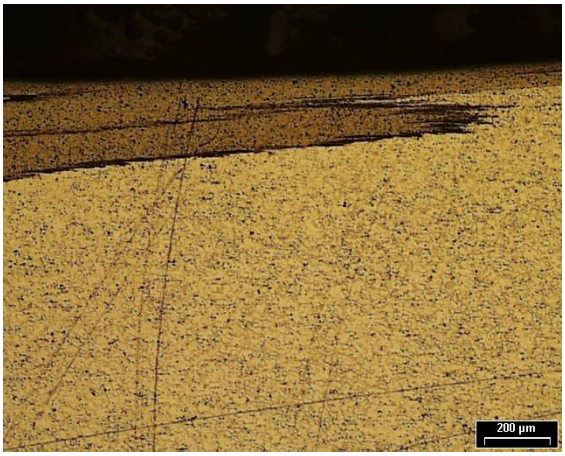


a) detail of the mixture of the two alloys at the shoulder side, microstructure 1

b) three different zones in the mixture of the two alloys, microstructure 2

c) striations formed due to the pin rotation, microstructure 3

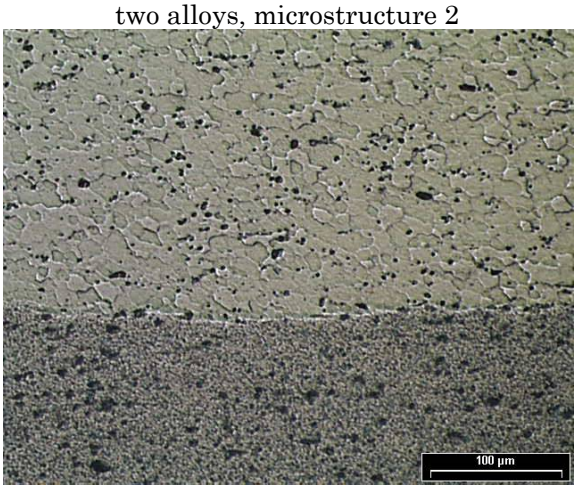


d) nugget zone, microstructure 4

**Figure 127 - Microstructure details of the dissimilar joint, TMAZ.**

It is possible to notice a trace of particles concentration at the root of the weld bead, typical from the materials processing with conventional FSW. This feature is more visible in the macrostructure of the dissimilar weld. Also, the analysis of both base materials microstructure is presented in Figure 128.

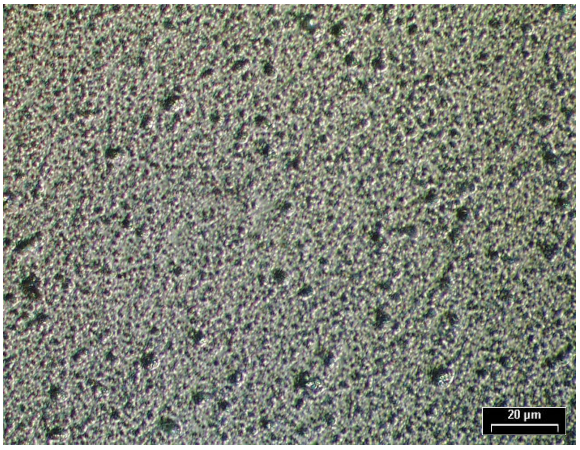


a) 6082-T6 base material, microstructure 5

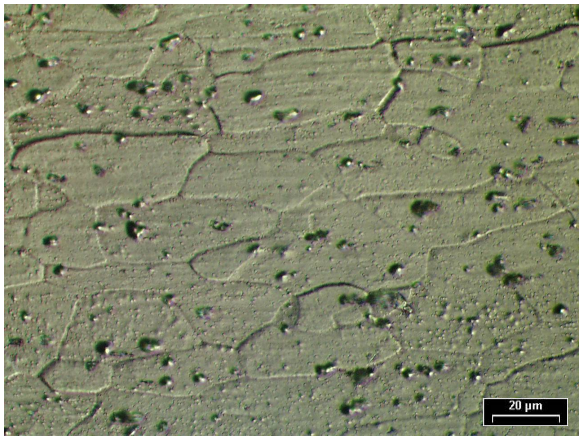


b) 6061-T6 base material, microstructure 6

**Figure 128 - Dissimilar joint base material microstructure.**

*4.2.5.2 FS AA6082-T6 joint microstructure*

Microstructural details of the friction stir welded 6082-T6 joint TMAZ are presented in Figure 129. The location of each microstructure is presented in Figure 126. Since Figure 129a) represents the transition of the stirred material to non stirred material, the flow patterns can be easily identified at the left side of the microstructure. Figure 129b), nugget microstructure detail, can be directly compared with Figure 128a) which represents its base material.

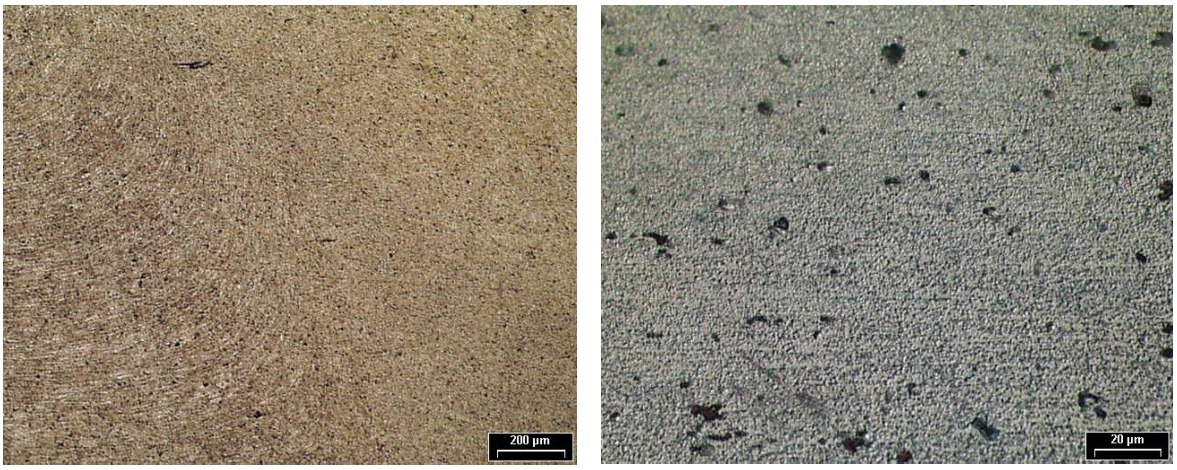


a) stirred material limit, microstructure 1 b) nugget structure detail, microstructure 2

**Figure 129 - FS welded 6082-T6 joint microstructure.**

*4.2.5.3 FS AA6061-T6 joint microstructure*

Microstructural details of the friction stir welded 6061-T6 joint are presented in Figure 130. The location of each microstructure is presented in Figure 126. Figure 130a) presents a material flow layer near the shoulder contacting surface. Figure 130b) shows the microstructure in the flash created at the retreating side during welding. Figure 130 c) and d) show the weld nugget microstructure and when compared with the base material microstructure, Figure 130e); the smaller recrystallized grains of the nugget are identified.

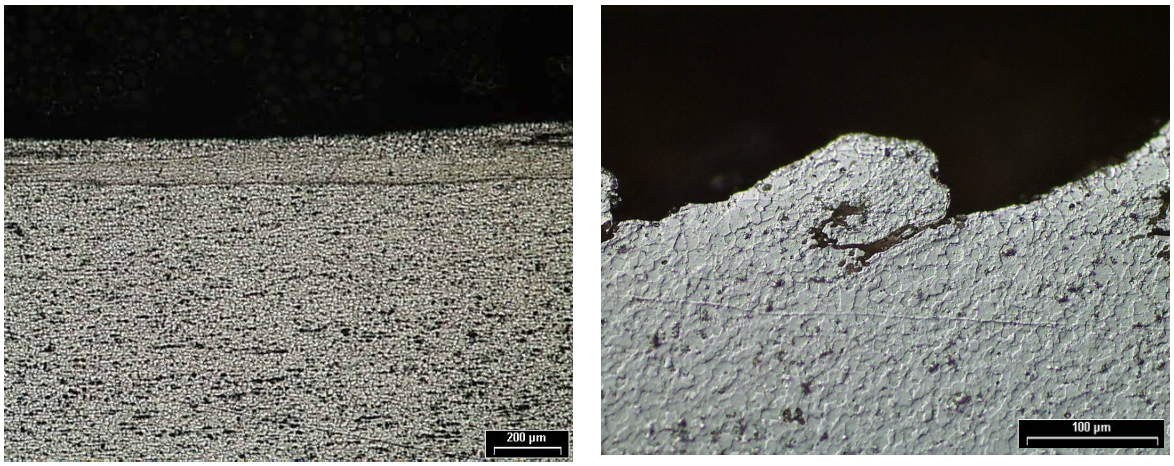


a) material flow layer near the shoulder contacting surface, microstructure 1

b) flash microstructural detail in the retreating side, microstructure 2

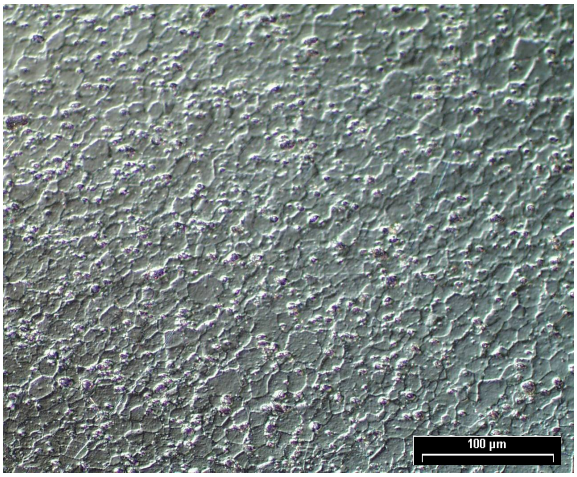


c) nugget microstructural detail, microstructure 4

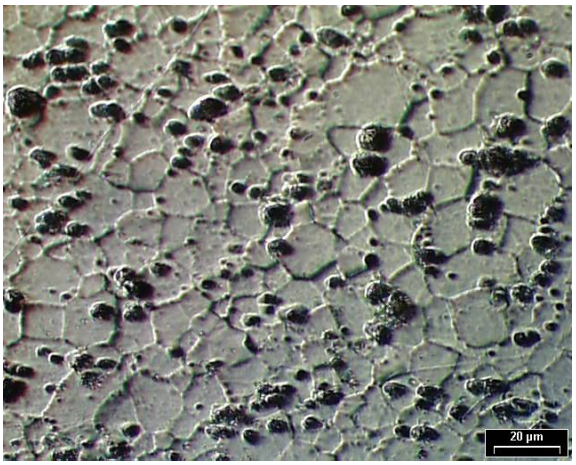


d) nugget microstructural detail microstructure 5

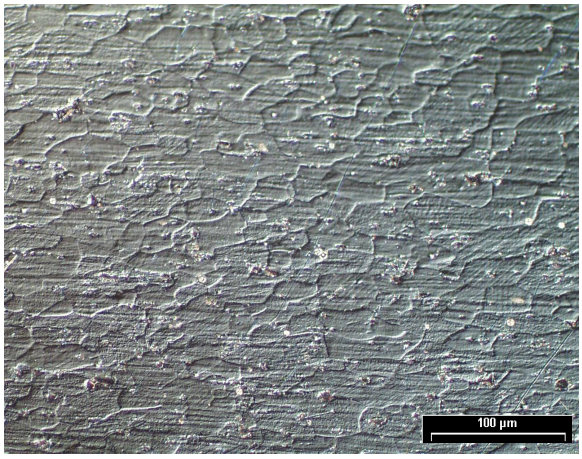


e) base material microstructure, microstructure 3

**Figure 130 - FS welded 6061-T6 joint microstructure.**

### *4.2.6 Bending tests*

The mechanical resistance of all joint types and base material specimens was also addressed via bending tests which is a test very sensitive to defects near the surfaces of the weld bead, such as root flaws. Two different types of bending tests were performed: 4 point bending tests and 3 point bending tests. In all tests the specimens had 150$mm$ length and 20$mm$ width.

#### *4.2.6.1 Four point bending tests*

In the four points bending test the specimen is supported on two outer fixed rollers and deformed by driving two concentrated loads by two rollers. The maximum stresses are located at the loads. The 4 point bending tests assemblage is presented in Figure 131. Also, in order to show the setup configuration a schematic representation is presented in Figure 132.

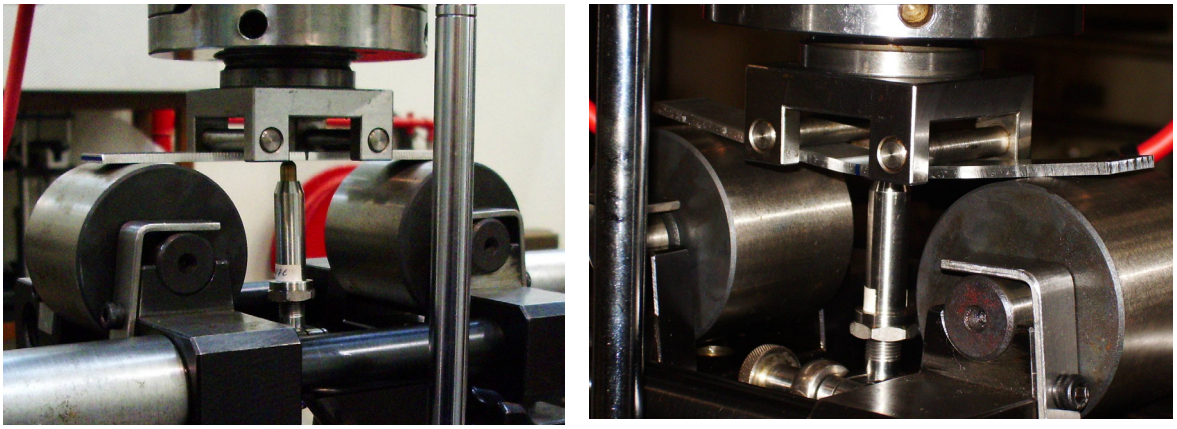

**Figure 131 - 4 point bending test assemblage.**

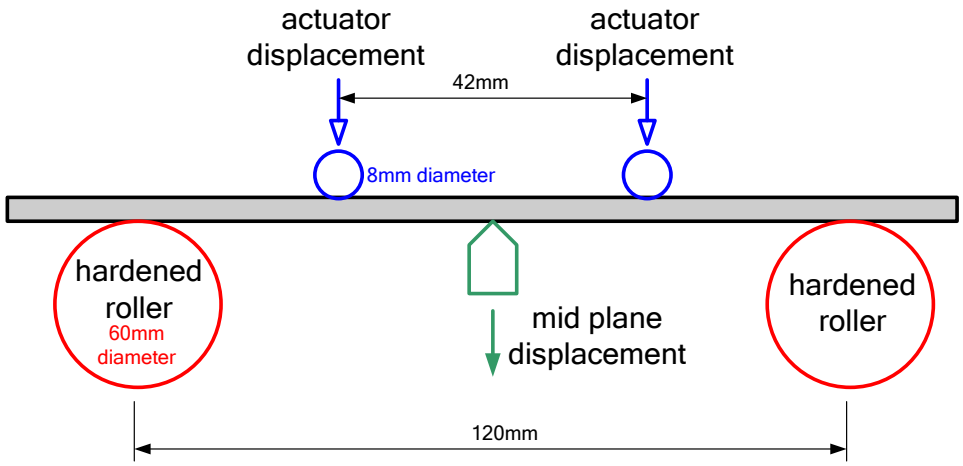


**Figure 132 - Schematic representation of the 4 point bending test.**

For each specimen was applied to the upper rollers an incremental displacement until a value of $5mm$ was reached. The force displacement data for each specimen is presented In Figure 133. For the maximum displacement at the rollers the base materials specimens present the maximum loads. For the friction stir welded specimens the 6061-T6 presents the higher load and the 6082-T6 the lowest load. It is easily identified the site where each specimen enters the plastic regime.

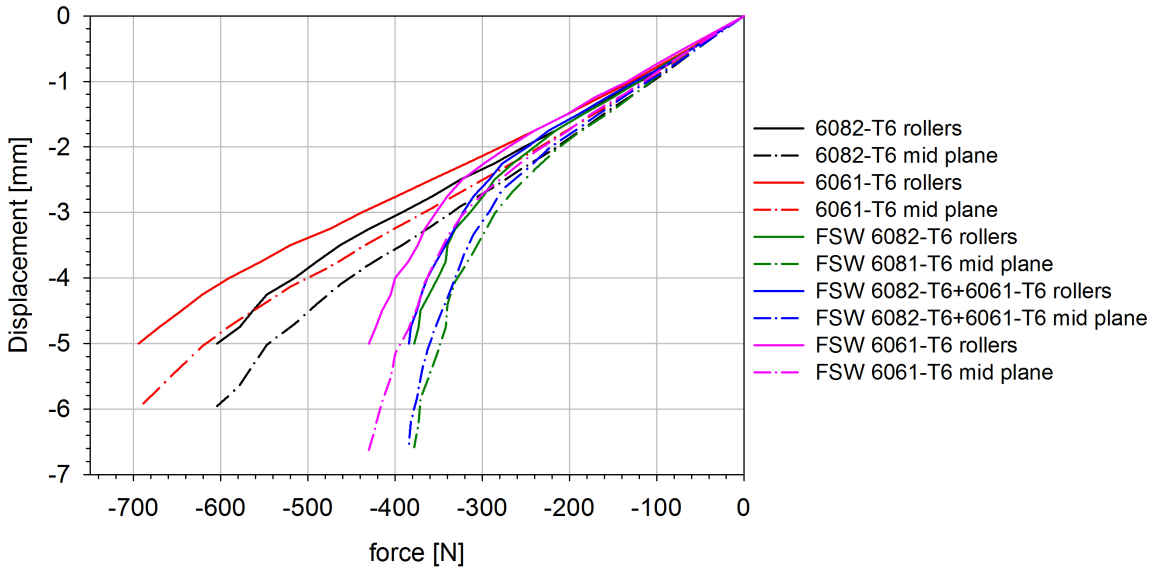


**Figure 133 - Force displacement in 4 point bending tests.**

The maximum displacement in the rollers that corresponds to the elastic behaviour limit is presented in Table 27. The elastic behaviour of the welded specimens is documented in Figure 134.

**Table 27 - Maximum mid plane displacements until plastic behaviour**

| Specimen | Displacement [$mm$] |
|---|---|
| 6082-T6 | -3 |
| 6061-T6 | -3,25 |
| FSW 6082-T6 | -1,5 |
| FSW 6082-T6+6061-T6 | -1,5 |
| FSW 6061-T6 | -1,75 |

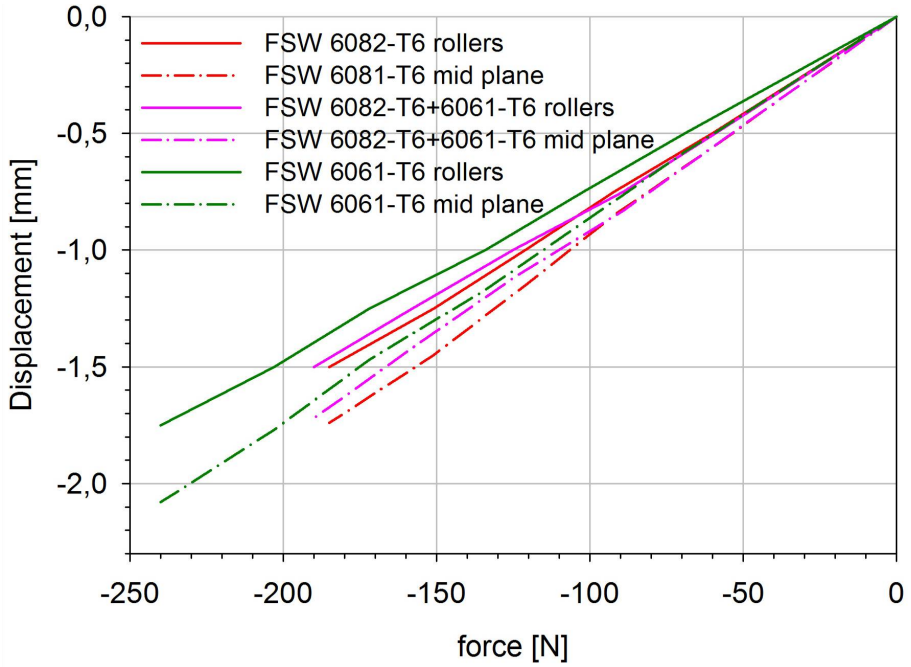


**Figure 134 - Elastic behaviour of the welded specimens in the 4 point bending tests.**

With the dimensions presented in the schematic configuration presented in Figure 132 and the displacement data acquired during the test, it was possible to plot the specimen configuration for different displacements of the roller. As an example, the result for the aluminium 6082-T6 base material and friction stir welded specimen are presented in Figure 135. As the roller's displacement increases the difference between the base material and welded specimens' displacement also increases.

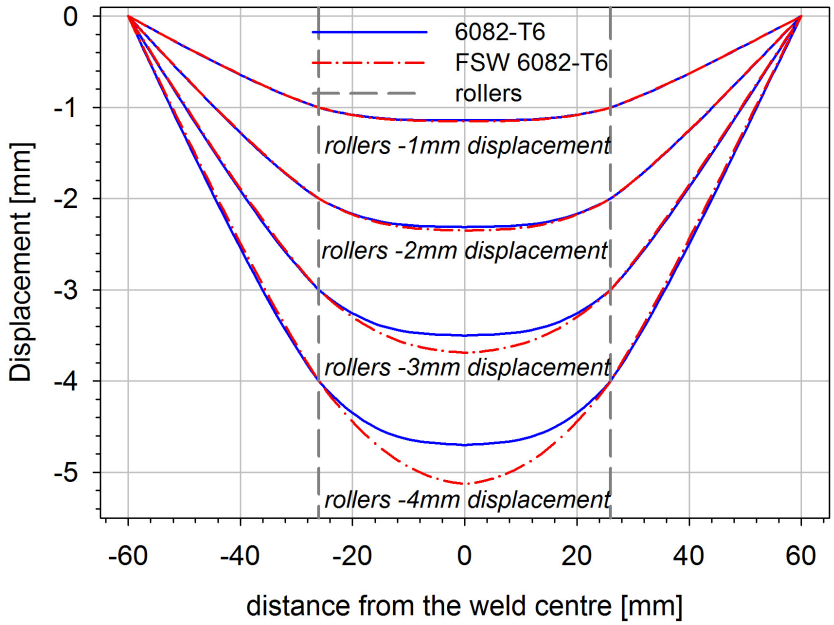


**Figure 135 - AA6082-T6 base material and FS welded specimen configuration for different roller displacement.**

*4.2.6.2 Three point bending tests*

The 3 point bending tests assemblage and schematic geometry is presented in Figure 136. These tests were performed in accordance with standards [166, 167].

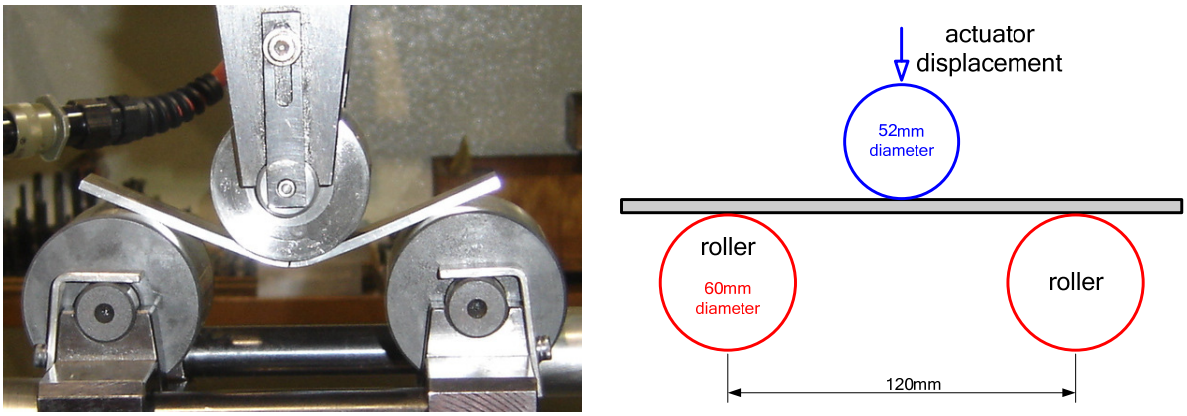


a) test assemblage b) schematic representation

**Figure 136 - 3 point bending device test.**

For each type of specimen, two bending tests were performed, one with the root in the actuator side and another one with the root in the side opposite to the actuator. It was interesting to notice that no difference was identified between these test configurations. The force/displacement data and final geometry configurations are quite similar.
The maximum force values obtained in each test are presented in Table 28. Test 1 corresponds to tests where the welding shoulder surface was faced to the actuator and test 2 corresponds to tests where the root was faced to the actuator. Considering the joint efficiency as the ratio of the maximum force of a test by the maximum force of its base material, efficiencies of 97,0% and 103,6% are obtained for the FSW 6082-T6 and FSW 6061-T6, respectively.

**Table 28 - Maximum force values for each bending test**

| | Test 1 F [*N*] | Test 2 F [*N*] | Average F [*N*] |
|---|---|---|---|
| base material 6082-T6 | 833 | 845 | 839 |
| base material 6061-T6 | 962 | 936 | 949 |
| FSW 6082-T6 | 807 | 821 | 814 |
| FSW 6082-T6 + 6061-T6 | 884 | 854 | 869 |
| FSW 6061-T6 | 965 | 970 | 968 |

No root flaws or other defects were detected in all joints. Each specimen configuration after testing is presented in Figure 137. It is clear the different geometry after testing of the base material and welded specimens. Also the multimaterial specimen shows an unsymmetrical configuration due to the different materials properties and the marginal different thickness.

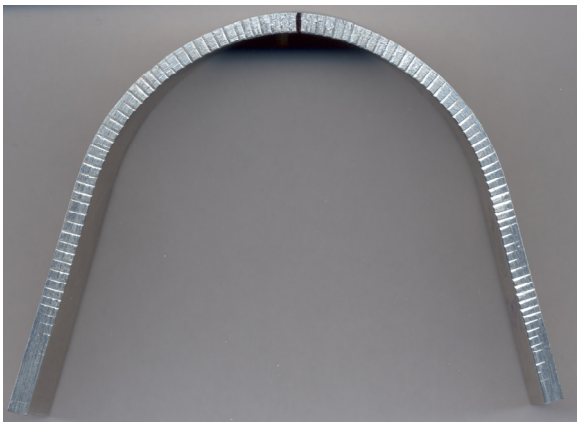

a) base material 6082-T6

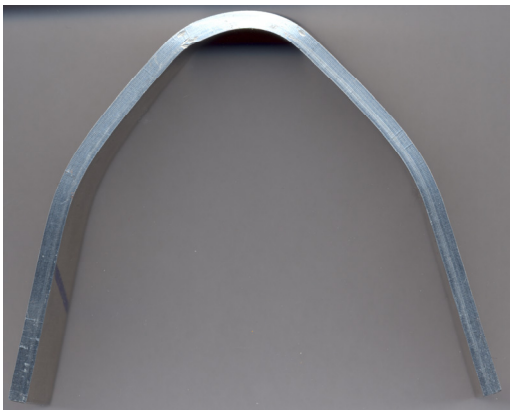

b) FSW 6082-T6

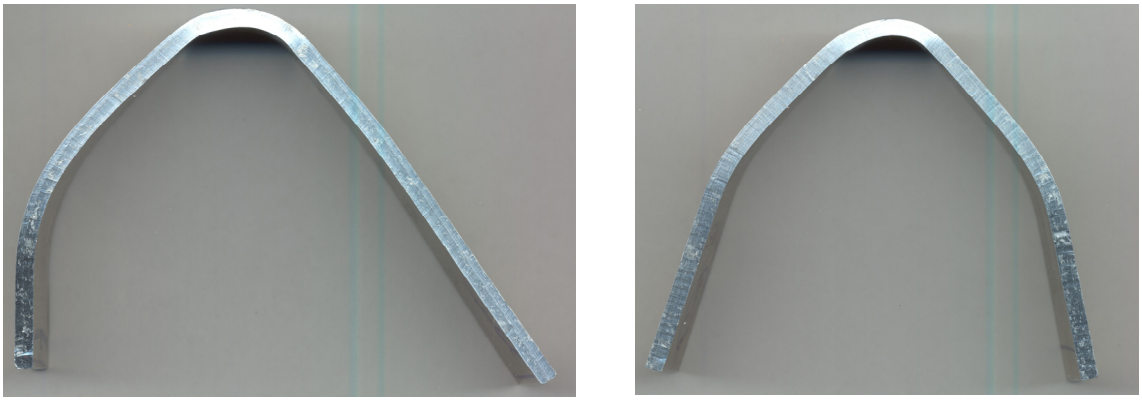

c) FSW 6082-T6+6061-T6 d) FSW 6061-T6

**Figure 137 - Specimens after bending.**

The force/displacement record was acquired during testing to identify the behaviour of each specimen, as shown in Figure 138.

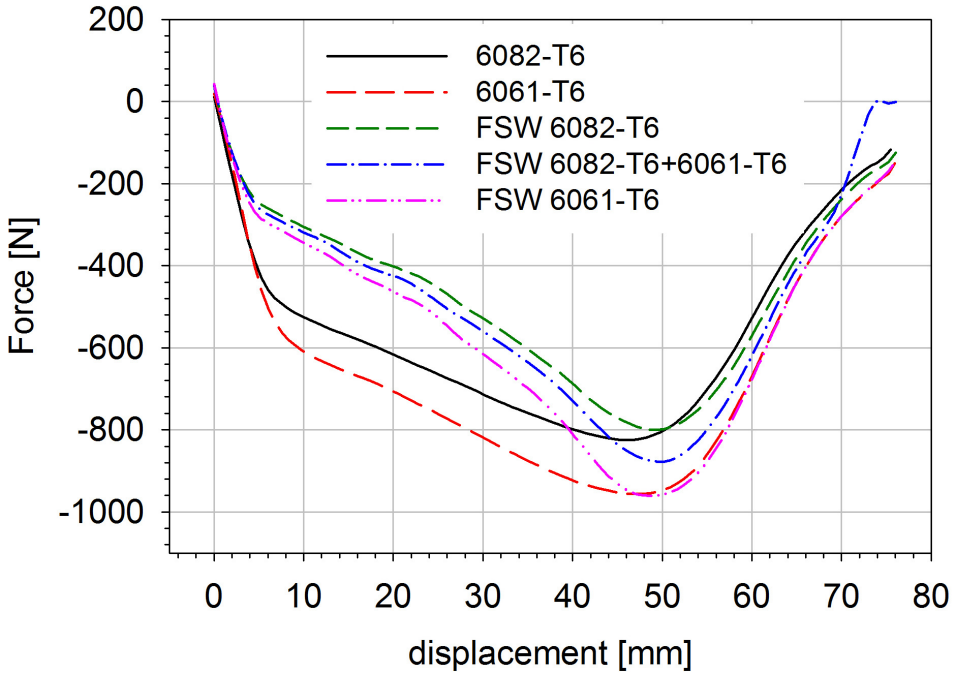


**Figure 138 - Bending test results.**

Both base material specimens have a linear behaviour until a load of approximately 420*N* is reached. For loads higher than 420*N*, for the same displacement the aluminium 6061-T6 presents higher mechanical resistance. The three welded joints present a linear behaviour until a load of approximately 220*N*. The friction stir welded aluminium 6061-T6 joint supports higher loads than the friction stir welded 6082-T6. The dissimilar weld joint show an intermediate behaviour.

Numerical simulations of bending tests were performed using a finite element model. As an approximation stress-strain curves of base material and welded joints were used in relevant parts of the specimen. These two-dimensional plane

strain simulations may give relevant information about these tests and about the mechanical properties of the welded material.
ABAQUS [168] using material and geometrical nonlinearity was used in order to model the load *vs.* displacement curves. In these models the stress-strain curves used were obtained from tensile tests of base material and welded zone. The rollers of the test device were defined by analytical rigid surfaces and the frictionless contact between these surfaces and the specimen was modelled. This is a complex problem because large displacement theory and multiple stress-plastic strain data were used.
An advanced step of the analysis is shown in Figure 139, where the mesh and the rigid analytical surfaces are plotted.

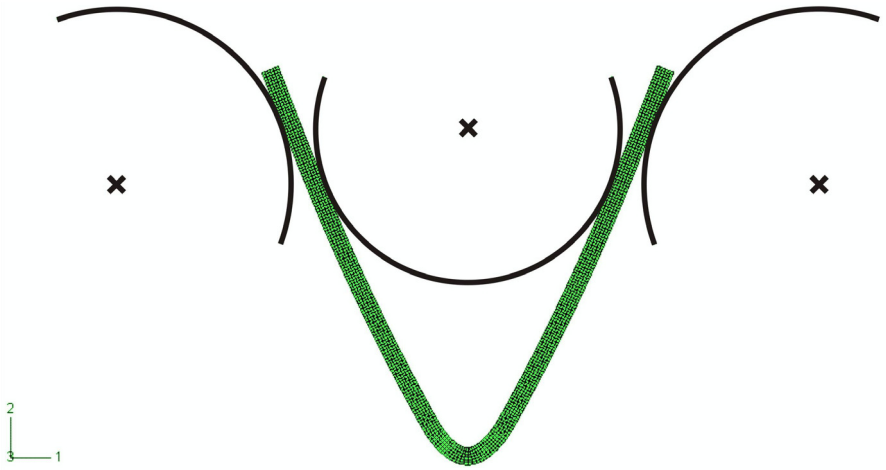


**Figure 139 - Deformed specimen and rigid surfaces model**

The load *vs.* displacement behaviour was calculated and compared with experimental values for friction stir welded aluminium 6082-T6, friction stir welded aluminium 6061-T6 and friction stir welded aluminium 6082-T6+6061-T6, Figure 140, where a good agreement was found.

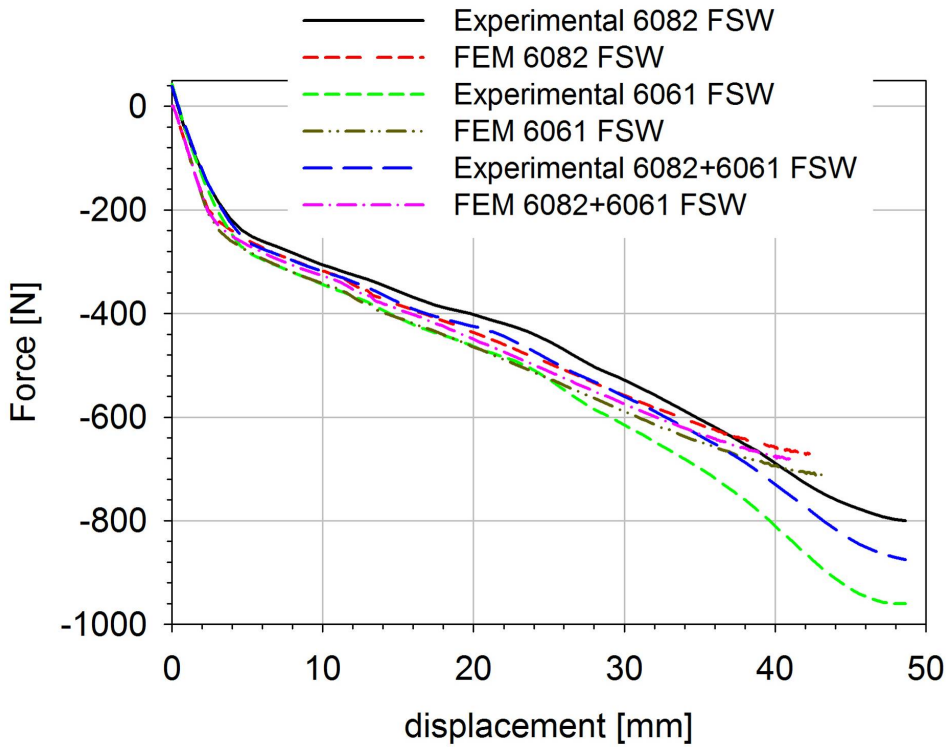


**Figure 140 - Comparison between experimental results and FEM results.**

### *4.2.7 Concluding remarks*

Friction stir butt welded plates of single material 6082-T6 and 6061-T6, and dissimilar joints of both alloys were performed.

The friction stir welded aluminium 6082-T6 material revealed lower yield and ultimate stresses, and the dissimilar joints displayed intermediate properties. In the tensile tests failures occurred near the weld edge line.
The hardness profile of the dissimilar joint presents the lowest values of all joints in the aluminium 6082-T6 alloy plate side where rupture occurred. Nevertheless in the nugget all three joints present similar values.
In the microstructure analysis of the dissimilar joint the mixture of the two alloys is easily identified by the different etching response of both alloys.
The approximate finite element model of the bending test successfully simulated the tests carried out, up to approximately maximum load.
Residual stress profile was measured by a destructive process and compressive values were found in the plate weld surface. Maximum residual stress values reached 91,7*MPa* at the root surface.

### 4.3 Fatigue behaviour of FS welds, LB welds and MIG welds of AA6061-T6 and AA6082-T6

Conventional fusion welding of aluminium alloys produces a weld prone to defects such as porosity, as a consequence of entrapped hydrogen gas not being able to escape from the weld pool during solidification. An example of a fusion process is the Gas Metal Arc Welding (GMAW) process, MIG (Metal Inert Gas) welding process [107]. In the MIG welding process the arc and the weld are protected from atmospheric contamination by a gas shield, and an electric potential is established between the electrode and the workpiece causing a current flow, which generates thermal energy in the partially ionized inert gas [108].

The Laser Beam Welding (LBW) process is also a thermal effecting melting process which causes metallurgical changes in the weld metal as well as in the heat affected area beside the weld seam. Effects such as oxidation reactions are comparable to other thermal treatments in the case of aluminium; but because of the short cycle time oxidation of the weld seam is very low [34].
Because of the large temperature interval between melting and solidification in the heat affected zone the material is partially molten in the solid aluminium matrix. In the transition area between the weld seam and heat effected zone small defects (solidification micro cracks and pores) occur during the solidification process. Because of their size there is no special negative influence on the mechanical properties. The thermal influence on the material structure beside the weld seam itself is very small. Welding an alloy which does not require additional wire shows that there is no change in chemical composition compared to the base material. The main reasons for this feature are: the high welding speed; the short cycle time of the melting and solidification process; the deep penetration effect of the keyhole with a very large ratio of depth to width; and the turbulent melt pool dynamic.

In Friction Stir Welding (FSW) the interaction of a non consumable and rotating tool with the workpieces being welded creates a welded joint trough frictional heating and plastic deformation at temperatures below the melting temperature of the alloys being joined.

In this study an analysis of the fatigue behaviour of friction stir and laser beam butt welds of two $3mm$ thickness age hardenable aluminium, 6082-T6 and 6061-T6 alloys, is presented. For comparison, MIG butt welds of the same alloys were also performed and tested. Tensile tests and microhardness measurements of weld joints and base materials were performed in order to determine the influence of each welding process in the mechanical properties. The fatigue behaviour (S-N curves) of specimens of all welding process was analyzed. Microstructure was examined and correlated with the macroscopic mechanical behaviour. Scanning electron microscopy was carried out and the fractographic features of friction stir welds and MIG welds compared.

### *4.3.1 Material and welding processes*

The alloys 6082-T6 and 6061-T6 are high strength Al–Mg–Si alloys that contain manganese to increase ductility and toughness. The alloy was solution heat treated at ≈540°C, followed by quenching to room temperature which leads to a supersaturated solution. If the material is stored at room temperature natural ageing takes place (T4 condition). The T6 condition is obtained through artificial ageing at a temperature of approximately 180°C [90].

The MIG welding parameters used were: $128A$, $17{,}1V$, $700mm/min$ and Argon at a $20l/min$ flow rate. A filler wire AWS ER5356 (with the designation ESAB OK Autrod 18.15) with a diameter of $1mm$ [169] was used. Welds were performed using an automated welding robot, GMF ROBOTICS – Arc Mat Sr..

The laser beam welds were performed using an ABB IRB6600 robot in conjunction with a Nd:YAG laser, with a power source of $4kW$. The following parameters were used to weld the aluminium 6061-T6: welding speed $50mm/seg$; focal distance $200mm$; $40l/min$ He flow; gap between plates $0{,}2mm$; filler wire of $1{,}2mm$ diameter with a feeding speed of $5{,}5m/min$ ER4043. For the aluminium 6082-T6 were used the parameters: welding speed $45mm/seg$; focal distance $200mm$; $40l/min$ He flow; gap between plates $0{,}2mm$; filler wire of $1{,}2mm$ diameter with a feeding speed of $6{,}7m/min$ ER4043.

The friction stir welds were performed in a prototype machine with a capability of $6m$ weld length developed by ISQ to be used in a Portuguese shipyard (Estaleiros Navais do Mondego). For both aluminium alloys the same parameters: welding speed of $800mm/min$; pitch angle of $2^{o}$; rotating speed of $1500rpm$ were used. The FSW process of the aluminium 6082-T6 was performed using a tool with a $6mm$ diameter threaded pin and the shoulder had $15mm$ diameter. For the aluminium 6061-T6 a tool with a $4mm$ diameter threaded pin and a shoulder of $10mm$ diameter were used. Since the optimal welding speed depends on several factors: alloy type, penetration depth and joint type being the most important these parameters were chosen by trial and error attempts until no visually detected defects could be identified. The penetration depth was adapted to fully penetrated butt joint in a material of $3mm$ thickness.

### *4.3.2 Tensile tests*

Tensile tests were performed to determine the mechanical properties of the welded and un-welded material (yield stress $\sigma_{yield}$, rupture stress $\sigma_{rupt}$ and Young modulus $E$), [144]. The stress/strain records of all tensile tests are plotted in Figure 141. For the base material and each welding processes three specimens were tested to avoid measurements errors.

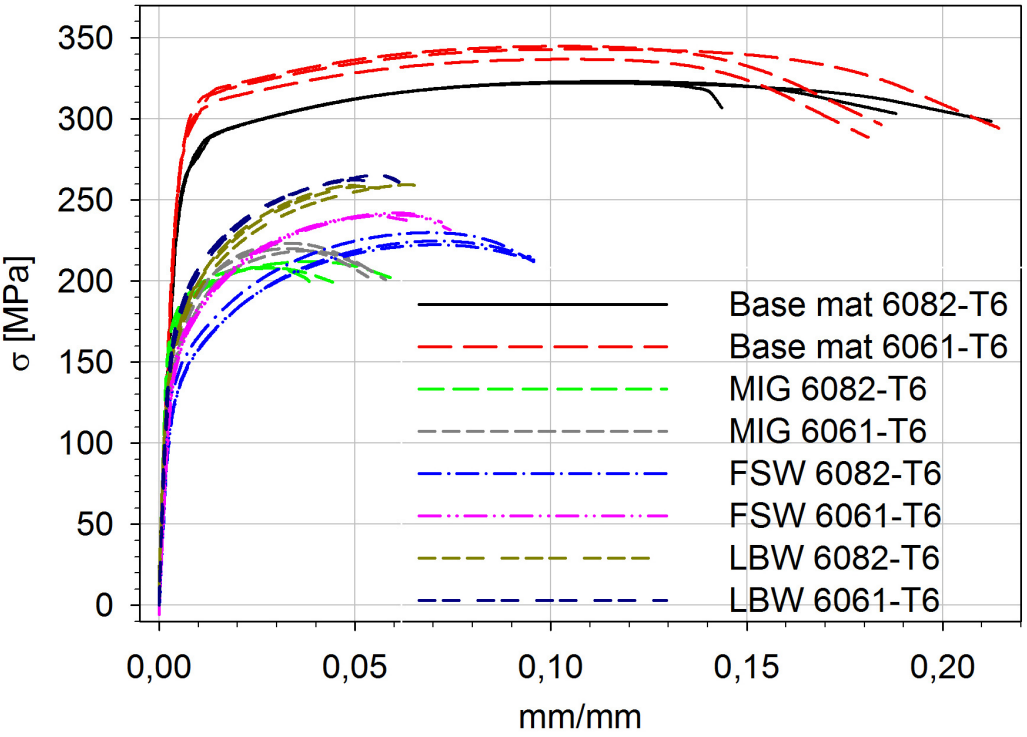


a) tensile test curves of base material and welded specimens

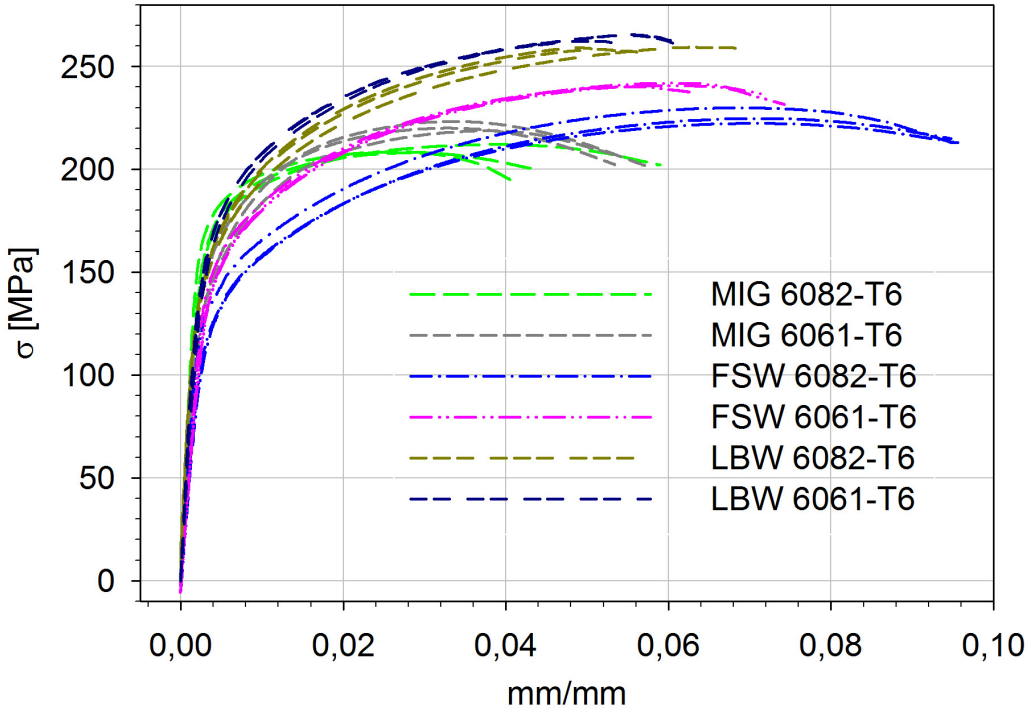


b) tensile test curves of welded specimens only

**Figure 141 - Tensile tests of MIG, LB and FS welded specimens.**

According to the material suppliers, the base material properties expected for both alloys are presented in Table 29. The average values of $\sigma_{yield}$, $\sigma_{rupt}$ and E of tests performed in base material specimens of both aluminium 6082-T6 and aluminium 6061-T6 alloy are presented in Table 30.

**Table 29 - Material properties for base materials, data from materials suppliers**

| Material type | $\sigma_{yield}$ [*MPa*] | $\sigma_{rupt}$ [*MPa*] | E [*GPa*] | Elongation [%] |
|---|---|---|---|---|
| 6082-T6 | >260 | 310 | 69 | 10 |
| 6061-T6 | 276 | 310 | 68,9 | 12 |

**Table 30 - Material properties for base material 6082-T6 and 6061-T6, tensile tests**

| Material | Specimen | $\sigma_{yield}$ [*MPa*] | $\sigma_{rupt}$ [*MPa*] | E [*GPa*] | Elongation [%] |
|---|---|---|---|---|---|
| 6082-T6 | 1 | 276,0 | 322,6 | 65,9 | 18,9 |
| | 2 | 276,0 | 323,4 | 64,7 | 16,4 |
| | 3 | 276,5 | 322,7 | 70,7 | 17,2 |
| | average | 276,2 | 322,9 | 67,1 | 17,5 |
| 6061-T6 | 1 | 307,0 | 343,5 | 67,2 | 17,7 |
| | 2 | 301,0 | 337,3 | 73,7 | 16,9 |
| | 3 | 311,0 | 345,2 | 64,4 | 16,9 |
| | average | 306,3 | 342,0 | 68,5 | 17,1 |

For each batch of specimens' of the same material the tests present similar results which are higher than the values predicted by the material suppliers. The aluminium 6061-T6 has an ultimate tensile stress about 6% higher than the aluminium 6082-T6. All base material (BM) specimens failed in the same manner, 45º shear plane. As an example the fracture surface of aluminium 6082-T6 base material specimen is presented in Figure 142.

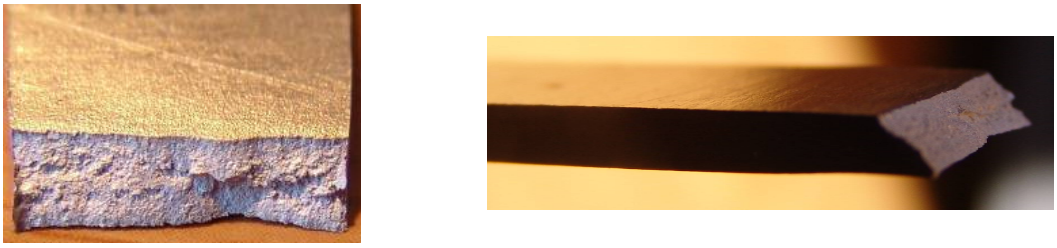

**Figure 142 - Fracture surface of an AA6082-T6 base material specimen.**

The average values of $\sigma_{yield}$, $\sigma_{rupt}$ and E of tests performed in base material specimens of both aluminium 6082-T6 and aluminium 6061-T6 alloy welded by MIG, LBW and FSW technique are presented in Table 31, Table 32 and Table 33 respectively.

In MIG tests the Young modulus has higher values than the base material. This increase is 'virtual' since the welded specimen includes both welded and parent material. In the welded area was added material which causes an over thickness profile that acted as a stiffener detail during the tensile test. Since the rupture stress of the MIG welded specimens is lower than the yield stress of the parent material the elongation measured in the fractured surface will only reflect the measurement of the material affected by the welding process. This resulted in lower values of elongation when compared with the base material.

**Table 31 - Material properties for MIG welded specimens, tensile tests**

| Material | Specimen | $\sigma_{yield}$ [*MPa*] | $\sigma_{rupt}$ [*MPa*] | E [*GPa*] | Elongation [%] |
|---|---|---|---|---|---|
| 6082-T6 | 1 | 177,5 | 208,5 | 70,3 | 4,6 |
| | 2 | 180,5 | 209,0 | 92,5 | 3,1 |
| | 3 | 172,5 | 212,5 | 78,5 | 4,4 |
| | average | 176,8 | 210,0 | 80,5 | 4,0 |
| 6061-T6 | 1 | 151,0 | 219,2 | 91,4 | 3,5 |
| | 2 | 161,0 | 220,6 | 83,2 | 4,7 |
| | 3 | 157,0 | 223,9 | 60,0 | 4,5 |
| | average | 156,3 | 221,2 | 78,2 | 4,2 |

**Table 32 - Material properties for FS welded specimens, tensile tests**

| Material | Specimen | $\sigma_{yield}$ [*MPa*] | $\sigma_{rupt}$ [*MPa*] | E [*GPa*] | Elongation [%] |
|---|---|---|---|---|---|
| 6082-T6 | 1 | 138,5 | 225,1 | 46,3 | 5,9 |
| | 2 | 137,5 | 222,9 | 40,7 | 5,3 |
| | 3 | 145,5 | 230,4 | 61,3 | 5,4 |
| | average | 140,5 | 226,1 | 49,4 | 5,5 |
| 6061-T6 | 1 | 161,0 | 240,8 | 53,0 | 3,4 |
| | 2 | 158,0 | 241,2 | 48,6 | 4,0 |
| | 3 | 157,0 | 242,4 | 48,8 | 4,6 |
| | average | 158,7 | 241,5 | 50,1 | 4,0 |

**Table 33 - Material properties for LB welded specimens, tensile tests**

| Material | Specimen | $\sigma_{yield}$ [*MPa*] | $\sigma_{rupt}$ [*MPa*] | E [*GPa*] | Elongation [%] |
|---|---|---|---|---|---|
| 6082-T6 | 1 | 163,8 | 258,8 | 69,8 | 4,5 |
| | 2 | 164,3 | 259,8 | 73,7 | 4,5 |
| | 3 | 159,1 | 260,0 | 71,0 | 4,5 |
| | average | 162,4 | 259,5 | 71,5 | 4,5 |
| 6061-T6 | 1 | 169,0 | 266,0 | 64,4 | 4,5 |
| | 2 | 172,0 | 263,4 | 70,2 | 2,7 |
| | 3 | 172,0 | 266,7 | 67,8 | 3,9 |
| | average | 171,0 | 265,4 | 67,5 | 3,7 |

It was found that the friction stir welded specimens have similar yield stress values to the MIG specimens but higher values of the rupture stress. Also the elongation of the friction stir welded specimens presented higher values.

For the case of MIG welded specimens rupture occurred outside the welding seam in the HAZ (heat affected zone) as presented in Figure 143. Similar observations are presented by Ericsson *et al.* [90] where a 45º fractured surface was also found. The aluminium 6082-T6 MIG welded specimens present a yield stress and a rupture stress of 65% of the base material. The yield stress obtained in this work is 20% higher than the results presented by [90]. The aluminium 6061-T6 MIG welded specimens has a yield stress of 51% of the base material and a rupture stress of 65% of the base material. Comparing MIG weldments of both alloys it was found that the yield stress of the 6082-T6 is higher but the rupture stress is higher for the 6061-T6 MIG welded specimens.

**Figure 143 - Fracture surface of a MIG welded specimen of AA6061-T6.**

In the case of the 6082-T6 friction stir welded specimens fracture occurred near the weld edge, Figure 144, where a decrease of hardness occurs [143]. The fracture surface presents a 45º angle, as presented by Svensson *et al.* [78]. In the case of the aluminium 6061-T6 the fracture started at the weld root indicating that a lack of penetration occurred during welding (root flaw), Figure 145. Since the fracture surface occurred at the weld middle line it is possible to identify the different layers of material that were formed by each rotation of the welding tool. Dickerson *et al.* [93] suggested that root flaws up to 0,35*mm* deep do not cause degradation in mechanical performance when compared to flaw-free welds. The elongation of all friction stir welded specimens (4% to 5%) is approximately 25% of the base material (17%).

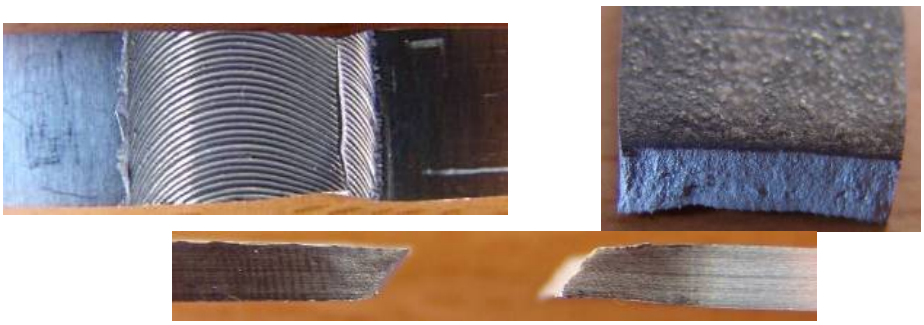

**Figure 144 - Fracture surface of AA6082-T6 FS welded specimen.**

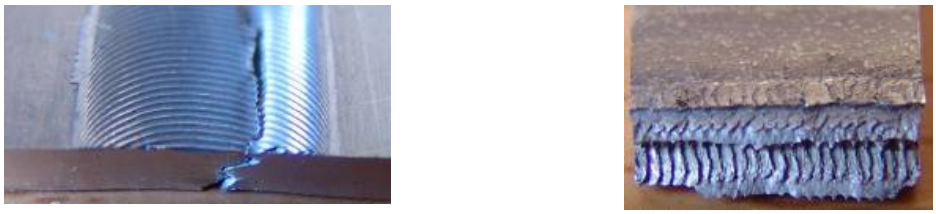

**Figure 145 - Fracture surface of AA6061-T6 FS welded specimen.**

The aluminium 6082-T6 friction stir welded specimens present a yield stress of 51% and a rupture stress of 70% of the base material. Scialpi *et al.* [143] obtained also a relation of rupture stress of 76% between the base material and friction stir welded specimens. Values of the same magnitude are also reported by Ericsson [90], Harris [61], and Nicholas [26] in their literature review.
The aluminium 6061-T6 friction stir welded specimens have a yield stress of 52% and a rupture stress of 71% of the base material. Hong *et al.* [170] performed

friction stir weld of 4*mm* thick aluminium 6061-T651 plates and found lower values for the yield stress and rupture stress when compared with those obtained in this study.

From all type of welded specimens, laser beam welded specimens present the higher yield and rupture stress. The aluminium 6082-T6 laser beam welded specimens have a yield stress of 59% and a rupture stress of 80% of the base material, and the 6061-T6 laser beam welded specimens have a yield stress of 56% and a rupture stress of 78% of the base material. These results are higher than the ones presented in [34, 171]. Nevertheless, the elongation present the lowest values.
In laser beam welds of both alloys the fracture occurred near the weld bead edge with a 45º angle, Figure 146.

**Figure 146 - AA6061-T6 LB weld fracture surface.**

To obtain the material behaviour of the TMAZ of friction stir welded specimens and of the HAZ in the MIG welded specimens, in a second set of tests strain values were acquired with a 6*mm* gage length. The results obtained are presented in Figure 147. Stress/strain records show that the TMAZ of FSW specimens and HAZ of the MIG welded specimens present higher strain values than in an area composed by the BM, the TMAZ and the HAZ. An estimation of the yield stress in the TMAZ or HAZ is presented in Table 34. Yield stress in the TMAZ or HAZ is always lower than that obtained using larger gage lengths (25*mm*). For the MIG welded specimens of both base materials similar yield stress values are found in the HAZ.

**Table 34 - Material properties for FS welded TMAZ and MIG welded HAZ**

| | $\sigma_{yield}$ [*MPa*] | |
|---|---|---|
| | 6082-T6 | 6061-T6 |
| FSW | 144,5 | 167,5 |
| MIG | 137,0 | 169 |

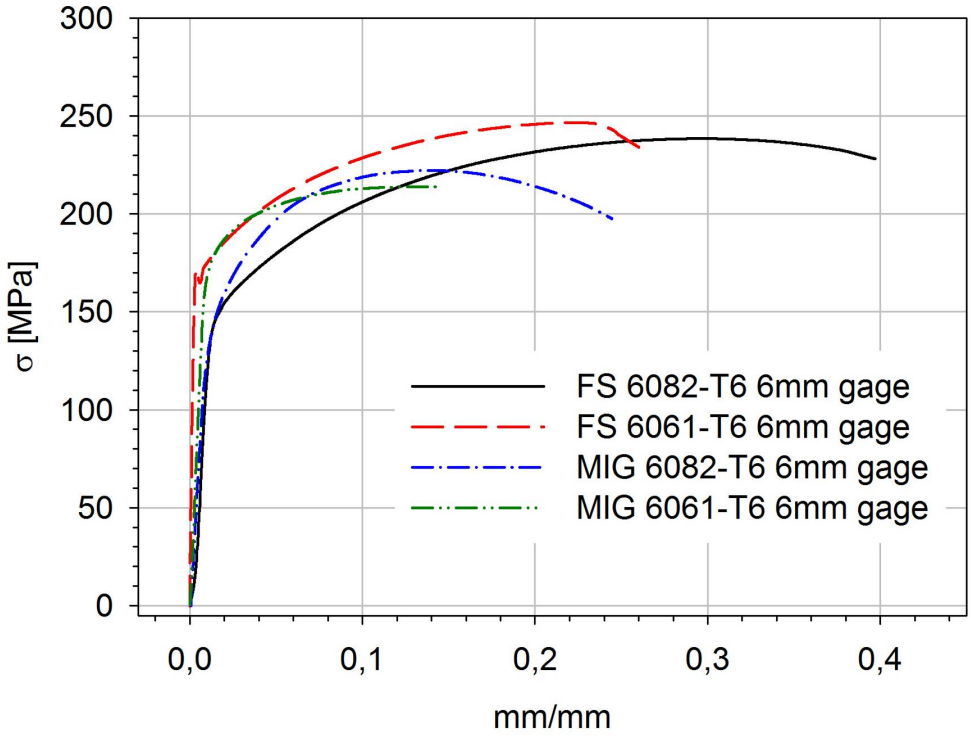


**Figure 147 - Tensile tests of the TMAZ, FS welded specimens, and HAZ, MIG welded specimens (6*mm* gage).**

### *4.3.3 Microhardness profiles*

The hardness profiles can assist in the interpretation of the weld microstructure and mechanical properties. Microhardness tests were performed to characterize the Vickers hardness profile in the vicinity of the weld area. Measurements were performed at the specimens' middle thickness using a 100*gf* load. Figure 148 illustrates the hardness profiles of the MIG welded aluminium 6061-T6 and 6082-T6 specimens. The major softened areas are the weld centre line, and the two transitions zones just at the limit of the HAZ. In these areas the hardness reaches a minimum value near 50*HV* and the base material has values over 90*HV*. Minimum average values are found in the aluminium 6082-T6 specimen.

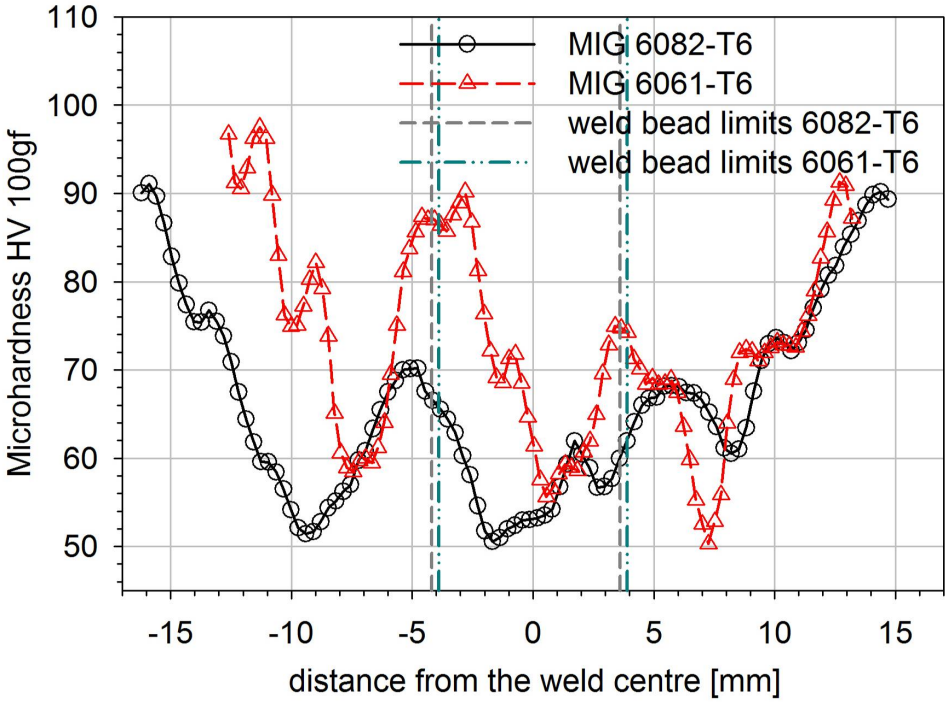


**Figure 148 - Microhardness profiles of the MIG welded 6061-T6 and 6082-T6 specimens.**

Figure 149 illustrates the microhardness profiles of the friction stir welded aluminium 6082-T6 and 6061-T6. A hardness decrease is identified in the TMAZ (thermo-mechanically affected zone). The average hardness of the nugget zone was found to be significantly lower than the hardness of the base alloy. There is a zone outside the nugget zone which has the lower hardness value. The welding process softened the material reducing the hardness to 33% of the parent material, as shown in [143].

The hardness minimum values are obtained in the welding retreating side, *e.g.* [78]. As it also suggested in [61] the variation of the microhardness values in the welded area and parent material is due to the difference between the microstructure of the base alloy and weld zone.

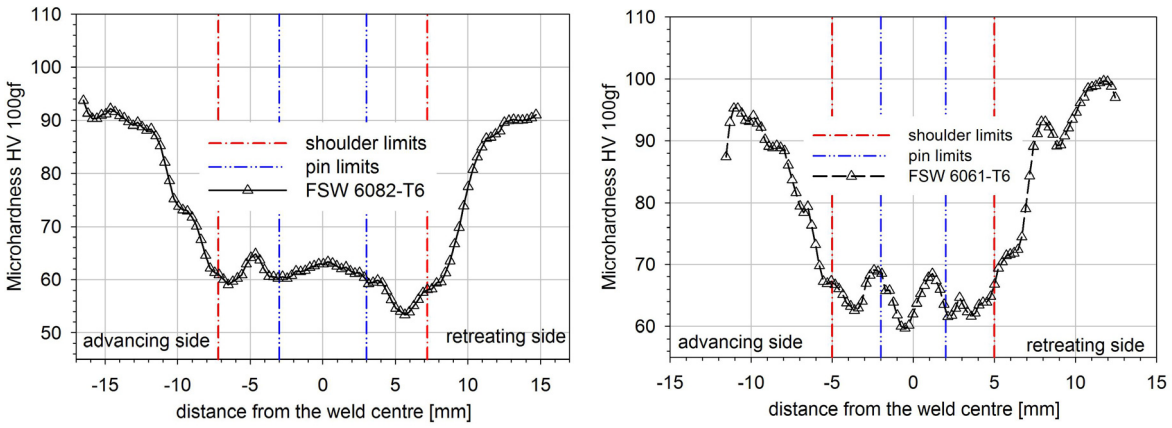


a) FS welded AA6082-T6 b) FS welded AA6061-T6

**Figure 149 - Microhardness profile of the FS welded specimens.**

A direct comparison of measurements of both friction stir welded alloys is presented in Figure 150.

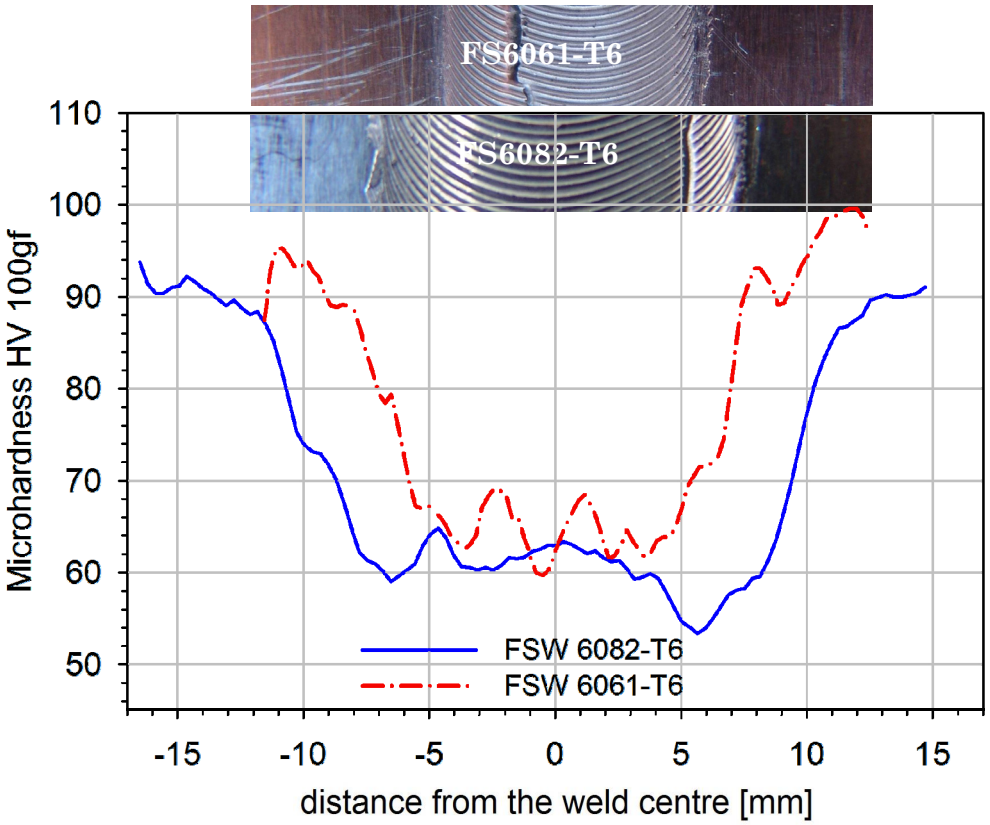


**Figure 150 - Microhardness profile of the FS welded 6082-T6 and 6061-T6 (6062-T6: 6*mm* diameter pin, shoulder 15mm; 6061-T6: 4mm diameter pin, shoulder 10*mm*).**

As described in the literature, in alloys such as 6082 and 6061 the main strengthening precipitate is ß″-Mg5Si6 which is stable at temperatures < 200°C [164]. This precipitate exists in the unaffected base material but is absent in the nugget and in the HAZ. In the friction stir weld temperatures are expected to be over 200-250°C, during heating, the ß″ is easily dissolved [78]. This ß″ precipitate is the mainly responsible for hardening. Svensson [78] reported that no other fine scale precipitation was found in the nugget, while in the HAZ precipitation of ß'-Mg1,7Si occurred on the Al–Mn–Si dispersoids. On cooling, precipitation of ß′ is favourable to ß″, and since the ß′ precipitates have less of a strengthening effect compared to ß″, a lower hardness is obtained. The ß' will act as a nucleation sites for the precipitates. Following the diagram of continuous cooling precipitation (CCP) presented by Grong [164], in the HAZ where temperatures are near or less than 300ºC the precipitation of ß' is very high, it occurs the transition from ß" to ß' by dissolution. In the weld nugget, where the temperature is expected to be higher and so the MgSi precipitates go into solution. On cooling, the time for precipitation is limited, and so only a small volume fraction of the ß′ precipitates form in the weld nugget. The nugget hardness recovery is due to recrystallization of a very fine grain structure when compared with the transition from the TMAZ to the HAZ.

The microhardness profile, at mid thickness, of the aluminium 6061-T6 laser beam weld is presented in Figure 151. The minimum hardness value found was obtained inside the weld bead, near its limit, and has a value of approximately $60HV$. The bead limit presented a width of $2{,}5mm$ and the HAZ, which corresponds to hardness values lower than the base material, has a width of approximately $4{,}5mm$ from each side of the bead limit.

As presented in Figure 152, when compared with the friction stir welds and MIG welds, the laser beam welds presented the smaller area (width) affected by the welding process, approximately $12mm$. For the friction stir welds the width of the welding affected area was approximately $15mm$, and in the MIG welding process $24mm$.

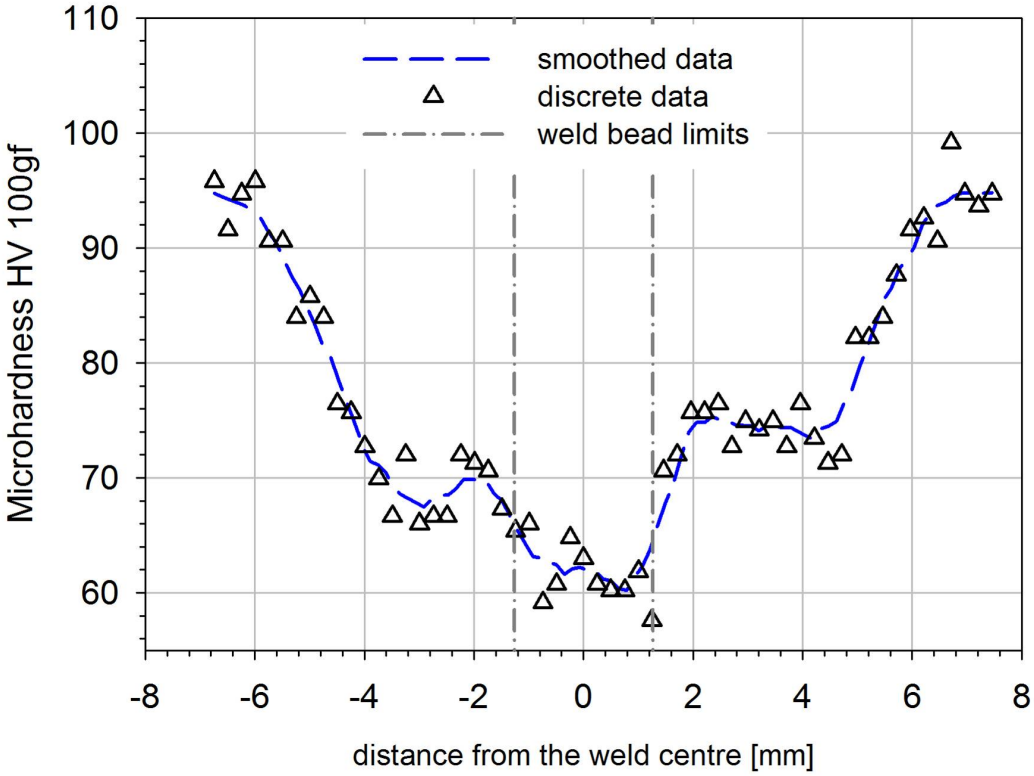


**Figure 151 - Microhardness profile of the LB welded AA6061-T6.**

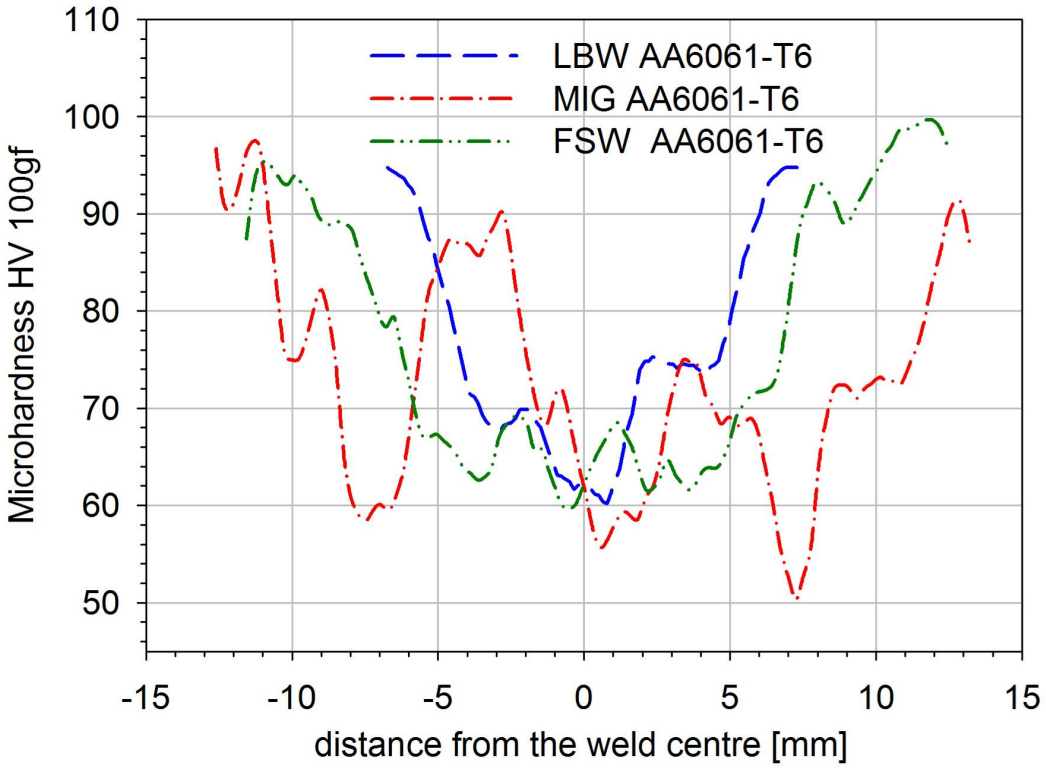


**Figure 152 - Microhardness profile of the LB, MIG and FS welded AA6061-T6.**

### *4.3.4 S-N fatigue data*

Fatigue tests were carried out in a servo-hydraulic MTS testing machine and specimens' dimensions were chosen according to the ASTM standard E466 [172]. The weld was perpendicular to the load direction in the S-N tests and to the material rolling direction. The maximum stress levels used were selected as a function of the yield stress for each type of joint. Values of 120% to 40% of the yield stress were chosen. A stress ratio of R=0,1 was used and the frequency was in the interval of 7–26*Hz* depending upon the stress level. Life was defined as the number of cycles to failure and the number of cycles considered as a threshold for infinite life was $10^7$ cycles. An extensive program, with a total of 147 specimens, was performed analysing all type of specimens of aluminium 6082-T6 and 6061-T6: base material specimens, MIG welded specimens with two surface conditions (as-welded configuration and milled weld overfill due to the additional filler wire), friction stir welded specimens and laser beam welded specimens (of aluminium 6061-T6 only).

For the MIG welding, specimens in the as-welded configuration and specimens with weld overfill milled (grinded) were tested, Figure 153. The geometrical detail of the transition from the weld seam to the plate surface of the base material can be interpreted as a geometrical defect that enhances the initiation of a first crack. The weld seam surfaces were machined to create a flat surface at the top and bottom of the specimen For both types of MIG weld specimens fracture occurred in the HAZ near the notch created during the deposition of filler material (as-welded configuration), Figure 154. Figure 155 presents examples of the fracture surface of all types of MIG specimens. In this figure, the effect of the grinding

procedure is easily identified noticing the removal of the material that was deposited during welding.

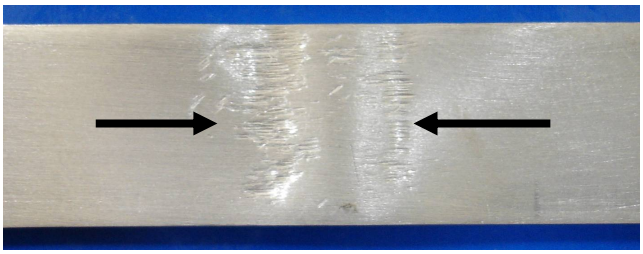

**Figure 153 - MIG welding specimens with the overfill milled.**

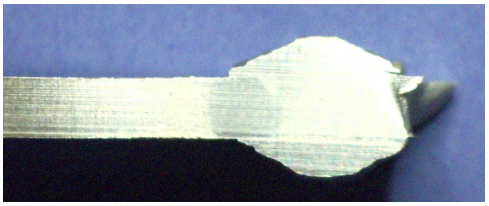

a) AA6082-T6 MIG welded fatigue tested specimen, fracture location

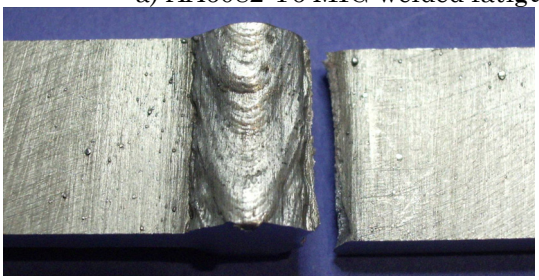

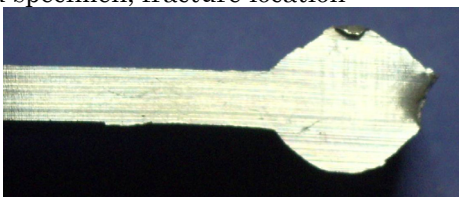

b) AA6061-T6 MIG welded fatigue tested specimen, fracture location

**Figure 154 - Fracture location of MIG specimens in the as-welded configuration.**

a) AA6082-T6 MIG specimen in the as-welded configuration, fracture surface

b) AA6061-T6 MIG specimen in the as-welded configuration, fracture surface

c) AA6082-T6 MIG specimen in grinded weldment configuration, fracture surface

d) AA6061-T6 MIG specimen in grinded weldment configuration, fracture surface

**Figure 155 - Fracture surface for the fatigue tested MIG specimens.**

Some MIG welded specimens presented defects due to the welding process. Due to the fusion nature of this process, during the welding the materials entrapped pores appear which influences the specimen mechanical behaviour. An example of this phenomenon is identified in the fractograph presented in Figure 156. This fractograph corresponds to a MIG welded 6061-T6 specimens tested at 75% of its yield stress and had a fatigue life of 16492 cycles (six times lower than the average fatigue life for this remote load).

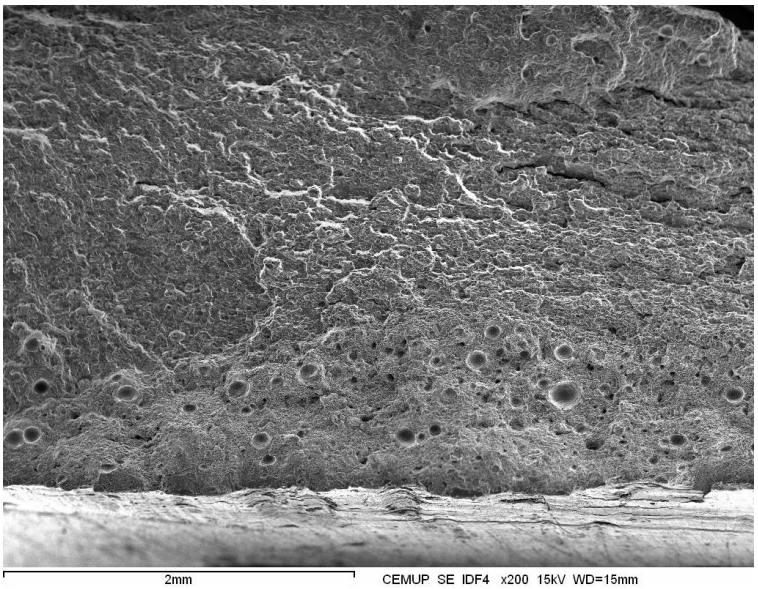


**Figure 156 - Fractograph of a MIG welding specimen containing entrapped pores**

Results for the fatigue tests are presented in Figure 157.

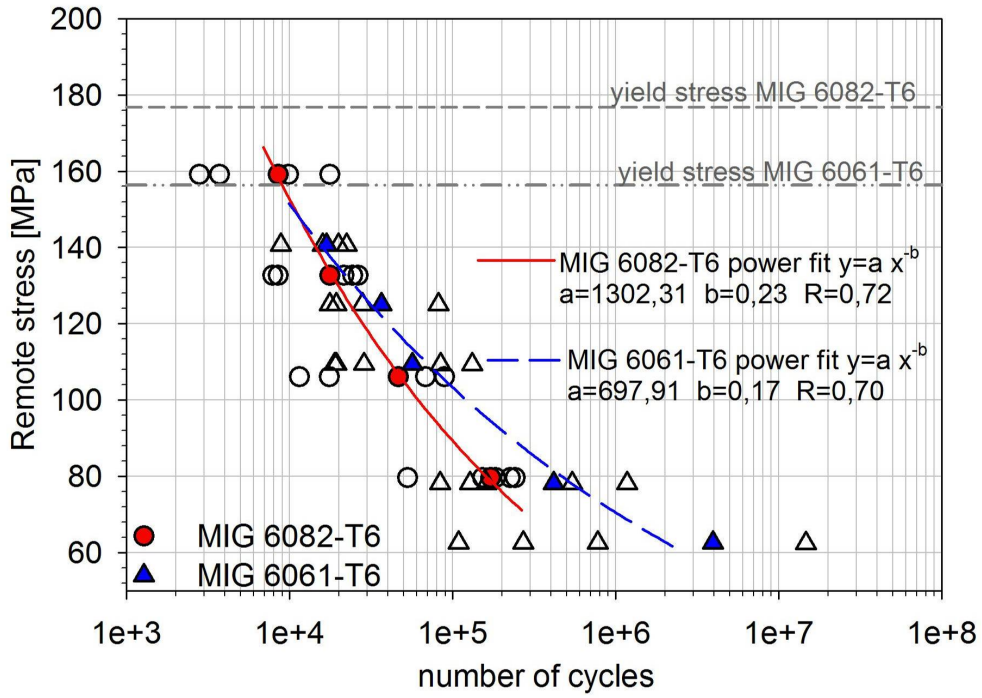


a) as-welded MIG specimens

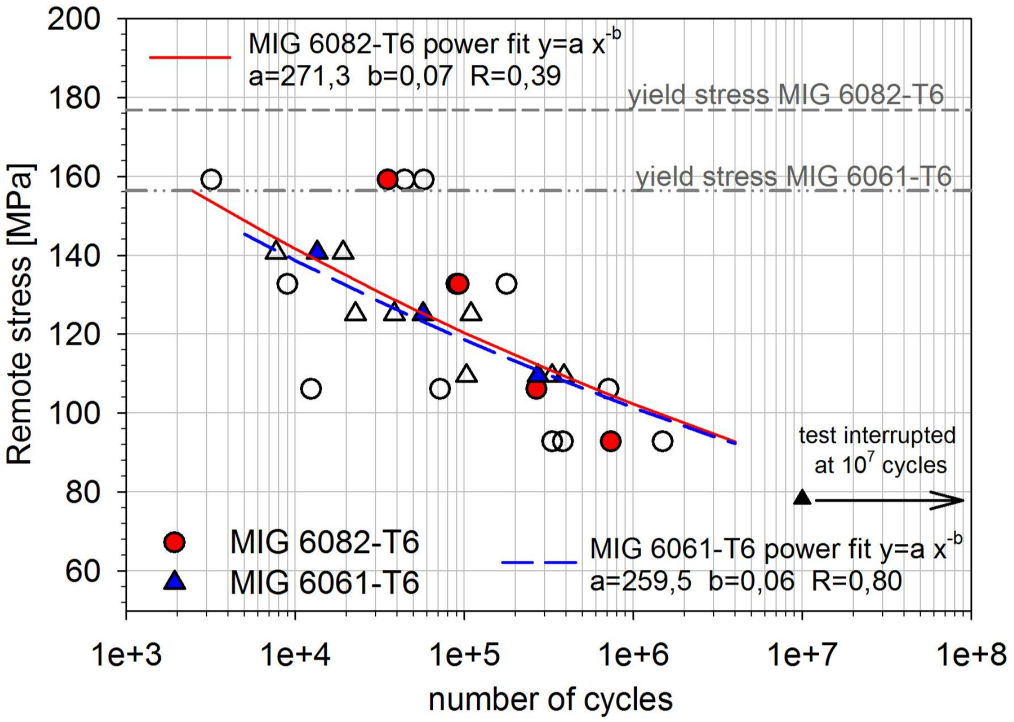


b) MIG specimens with milled overfill filler wire (grinded)

**Figure 157 - S-N fatigue data of the MIG welded specimens.**

Data was fitted using a power equation. Some fatigue scatter was found in the as-welded MIG specimens, being higher in the grinded specimens. In the as-welded configuration, the 6061-T6 MIG welded specimens presented higher fatigue lives than the MIG 6082-T6 specimens. In the grinded configuration both type of specimens present similar fatigue lives, but the aluminium 6082-T6 specimens have higher scatter. With the grinding procedure, the fatigue life improved mainly for low remote stress levels.

Friction stir welded specimens of both base materials were fatigue tested. The fracture location of the frictions stir welded specimens is shown in Figure 158. In the friction stir welded aluminium 6082-T6 specimens fracture propagated at the centre of the weld and in the aluminium 6061-T6 near the shoulder limit. These fracture locations were also identified in the tensile tests. Figure 159 presents examples of the fracture surface for all types of friction stir welded specimens where a more irregular surface is identified in the aluminium 6082-T6. Results of fatigue life obtained for the friction stir welded specimens are presented in Figure 160.

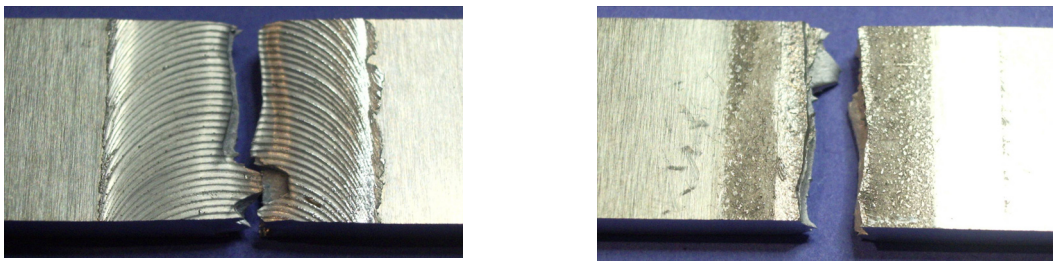

a) AA6082-T6 FS welded fatigue tested specimen, fracture location

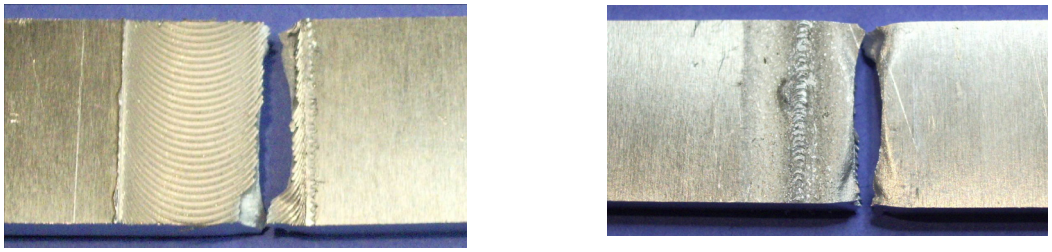

b) AA6061-T6 FS welded fatigue tested specimen, fracture location

**Figure 158 - Fracture location of FS welded specimens.**

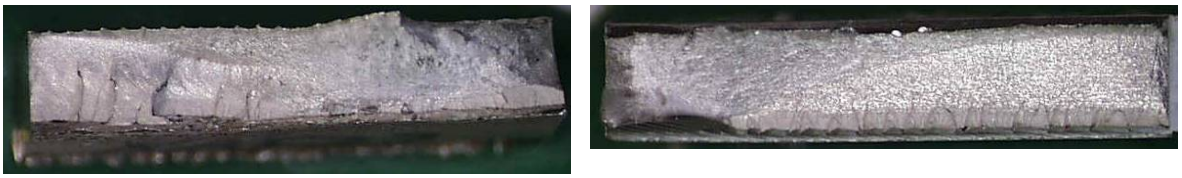

a) AA6082-T6 FS welded specimen, fracture surface

b) AA6061-T6 FS welded specimen, fracture surface

**Figure 159 - Fracture surface for the fatigue tested FS welded specimens.**

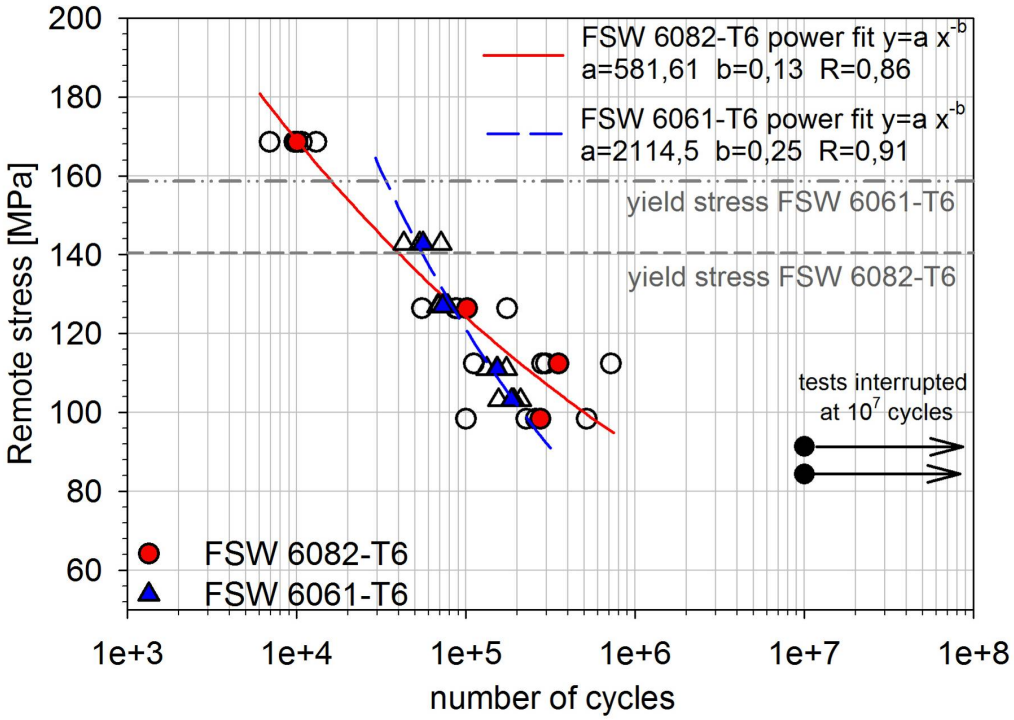


**Figure 160 - S-N fatigue data of the FS welded specimens.**

In tests of friction stir welded specimens, data shows a narrow scatter and was fitted using a power equation. For the friction stir welded 6082-T6 it was found that for 65% and 60% of the yield stress the fatigue life is considered infinite. In friction stir welded specimens fatigue cracks have propagated at the centre of the weld, as verified in [78] when studying friction stir welded $5mm$ and $10mm$ thick 6082-T6 specimens. Also, Ericsson *et al.* [90] in their study on the fatigue life assessment of the same alloy obtained a fatigue life of $5\times10^5$ cycles to failure with a stress range of about $90MPa$, at a stress ratio, R=0,5. In the present study, the fatigue life of $5\times10^5$ cycles is obtained at a stress range of $105MPa$. The friction

stir welded 6061-T6 specimens presented lower lives than the friction stir 6082-T6 specimens when tested at stresses lower than 130*MPa*. For the friction stir welded 6061-T6 specimens' cracks have propagated near the limit of the tool shoulder.

Laser beam welded specimens of aluminium 6061-T6 and 6082-T6 were fatigue tested. The laser beam welds were carried out using filler wire and there was a seam overfill of approximately 1*mm* at the top of the weld seam, Figure 161. The fracture location of the laser beam welded specimens occurred at the end of the overfill. Results of fatigue life obtained for the laser beam welded specimens are presented in Figure 162.

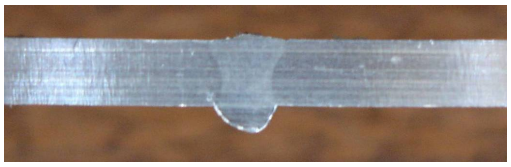

**Figure 161 - AA6061-T6 LB welded specimen weld bead overfill.**

Results of fatigue tests obtained in this study are significantly higher than those ones presented on [34]. When compared to its base material, there is a decrease of approximately 60% of the fatigue strength. The reasons for this change in the properties are the reduced strength capabilities in the weld metal and heat affected, and also a strong influence of geometrical discontinuities (especially in fatigue). Comparing both laser beam welded alloys the aluminium 6061-T6 performed better than the 6082-T6. Also, it was verified that for 94,1*MPa* the aluminium 6061-T6 presented a fatigue life higher than $10^7$cycles.

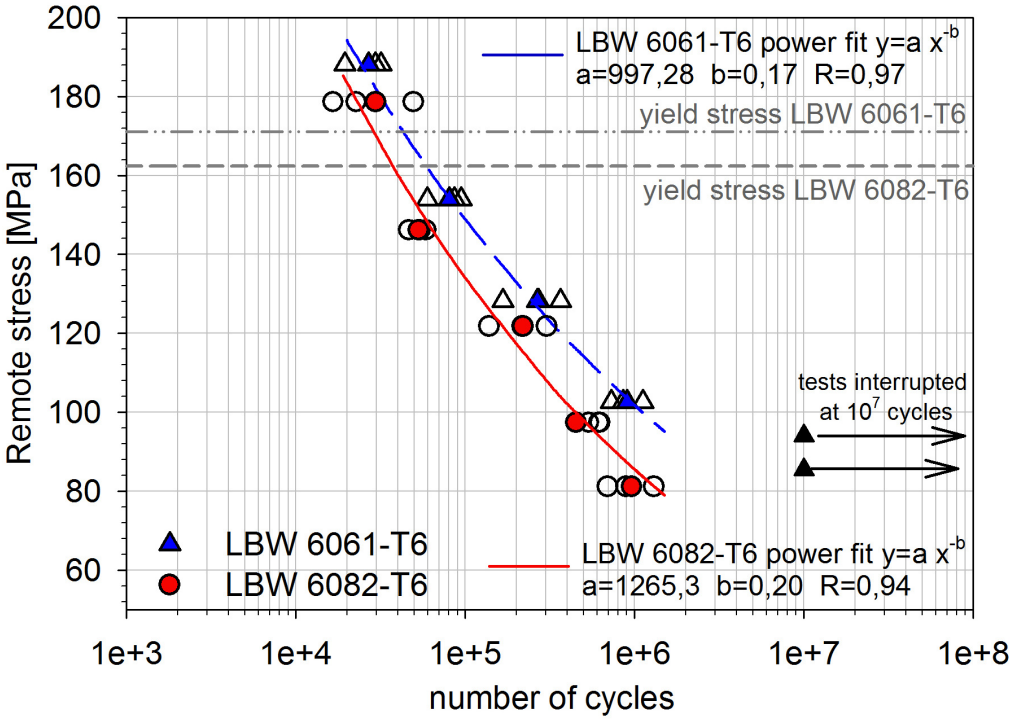


**Figure 162 - S-N fatigue data of the LB welded AA6061-T6 specimens.**

Base materials specimens were also fatigue tested at stresses between 90% and 65% of their yield stress. A comparison between the data from the base materials tests and all welded specimens is presented in Figure 163. The base materials specimens presented much higher fatigue live than any type of welded specimens, being the aluminium 6061-T6 the one that performed better.

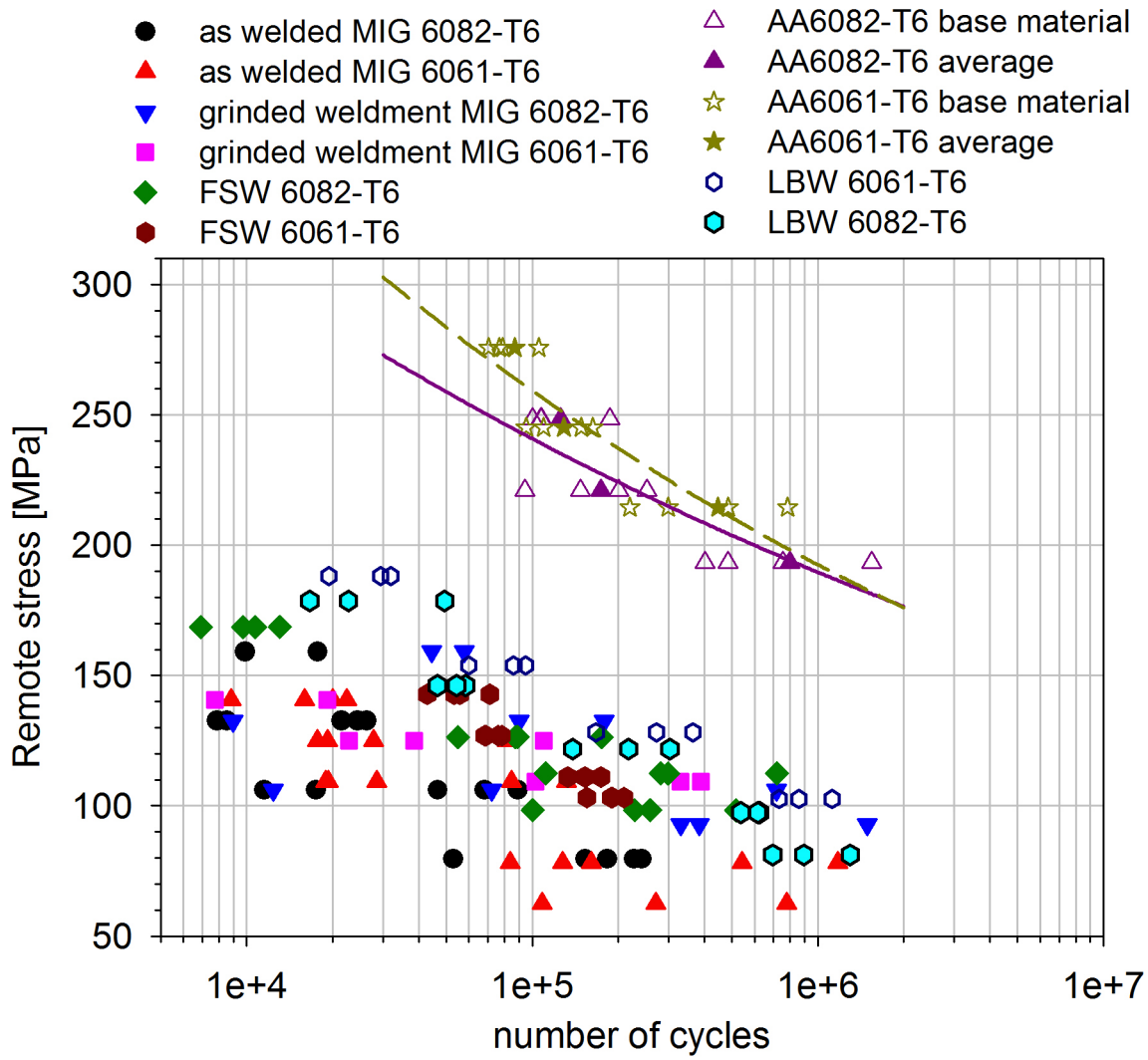


**Figure 163 - S-N data of base material and welded specimens.**

### *4.3.5 Fatigue crack propagation*

Since currently a very limited amount of data on fatigue crack propagation (FCP) in friction stir welded joints is available in the literature, this study presents a comprehensive study on fatigue crack propagation tests. Both base material specimens and friction stir welded specimens of aluminium 6082-T6 and 6061-T6 were investigated. All fatigue experiments were carried out under constant load amplitude, at room temperature and in laboratory air on a computer controlled servo-hydraulic INSTRON testing machine following ASTM E647 [173] standard. Crack propagation was monitored through visual measurements using a travelling microscope. As-welded $40mm$ wide compact tension specimens (CT)

were tested under R=0,1 for a 20*Hz* load frequency. The crack paths orientation in relation to the weld location are presented in Figure 164.

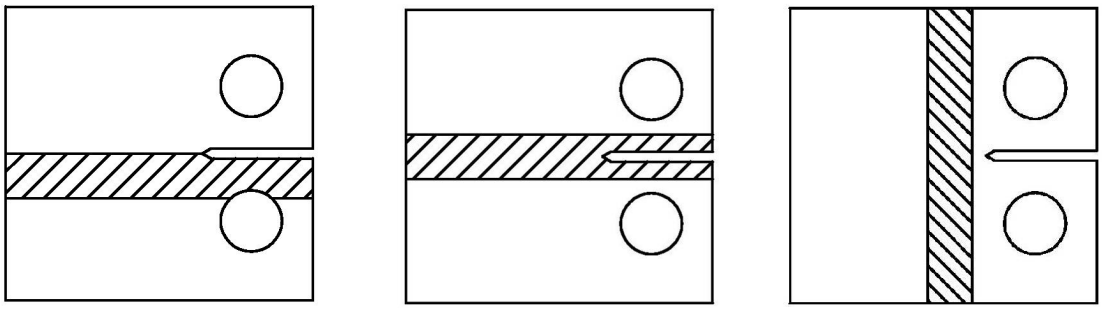

a) HAZ b) WM (welded material) c) transverse

**Figure 164 - Specimen orientation tested.**

An example of a fractured aluminium 6082-T6 base material specimen is presented in Figure 165.

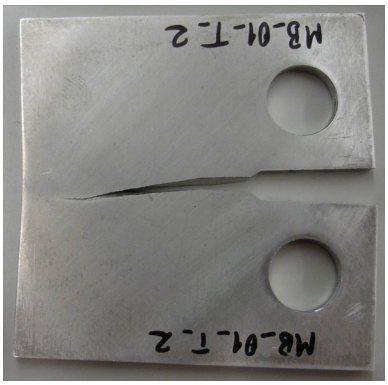


**Figure 165 - Fractured AA6082-T6 base material specimen. (for the sake of uniformity all CT specimens are represented with the crack on the right side)**

For the case of a notch created on the HAZ two examples of cracked specimens are presented in Figure 166. For this configuration generally the crack propagated in the HAZ, as presented in Figure 166a). In some specimens the crack deviated in the direction of the TMAZ.

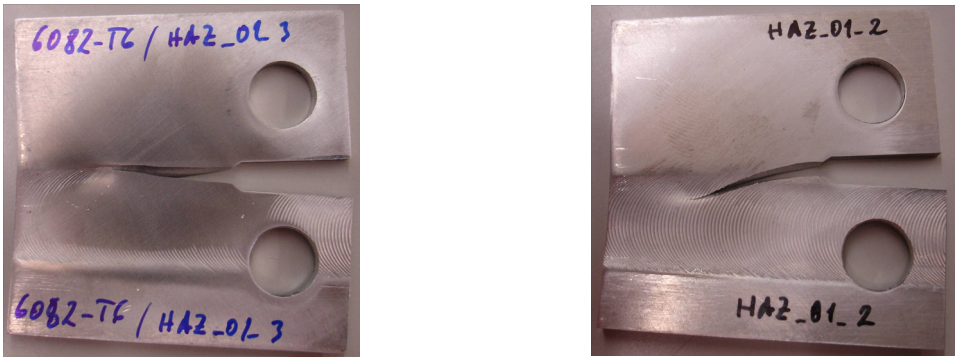


**Figure 166 - Fractured specimens, crack in the HAZ configuration.**

For the case of a notch created on the welded material two examples of cracked specimens are presented in Figure 167. For this configuration cracks generally

stayed inside the TMAZ (shoulder limits) as presented in Figure 167a). Nevertheless in some cases the crack deviated from the specimen middle line during the tests.

a) AA6082-T6 specimen b) AA6061-T6 specimen

**Figure 167 - Fractured specimens, WM configuration.**

For the case of a notch created transverse to the weld line two examples of cracked specimens are presented in Figure 168. For this configuration cracks generally present a deviation in their path just outside the TMAZ.

**Figure 168 - Fractured specimens, crack transverse to the weld line configuration.**

Figure 169 summarizes the main results obtained for the aluminium 6082-T6 base material tested with R=0,1 and R=0,5. An example of a fractured aluminium 6082-T6 base material specimen is presented in Figure 165.

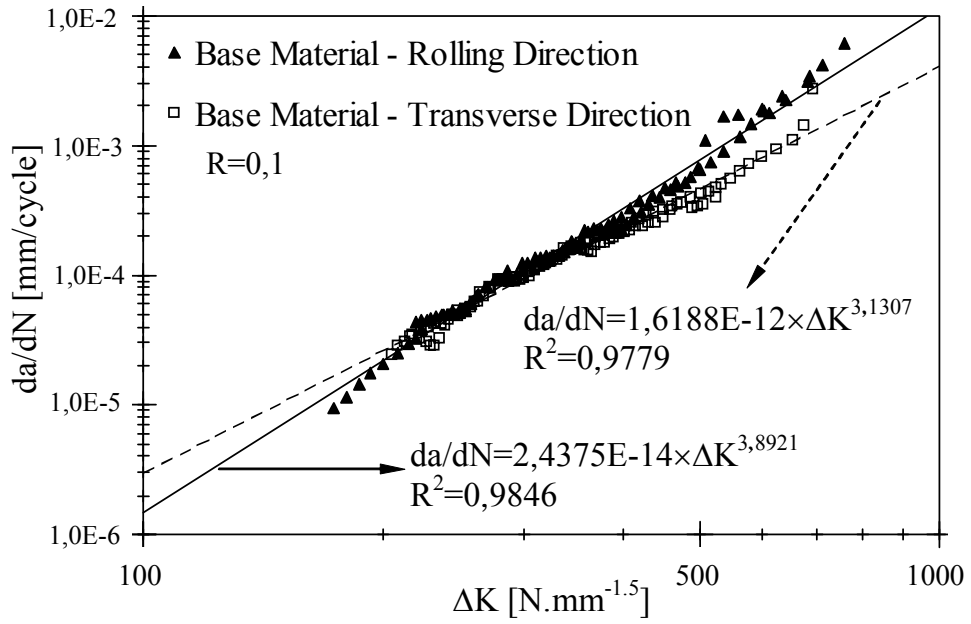


a) base material transverse and rolling direction, R=0,1

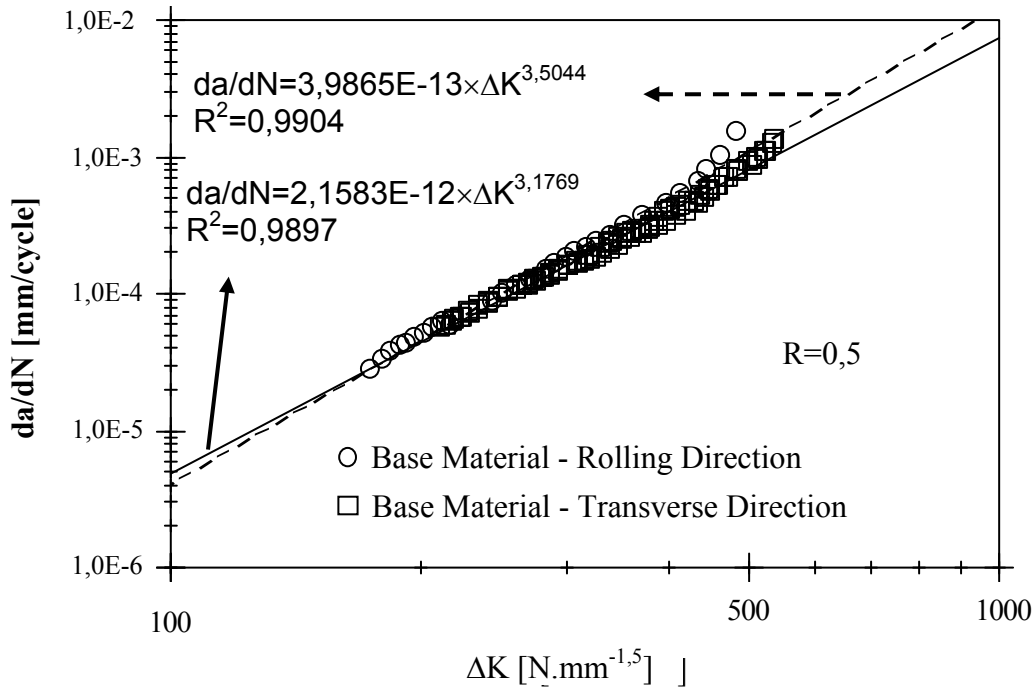


b) base material transverse and rolling direction, R=0,5

**Figure 169 - Fatigue crack propagation data for AA6082-T6 base material specimens.**

Figure 170 presents results of the aluminium 6082-T6 friction stir welded specimens.

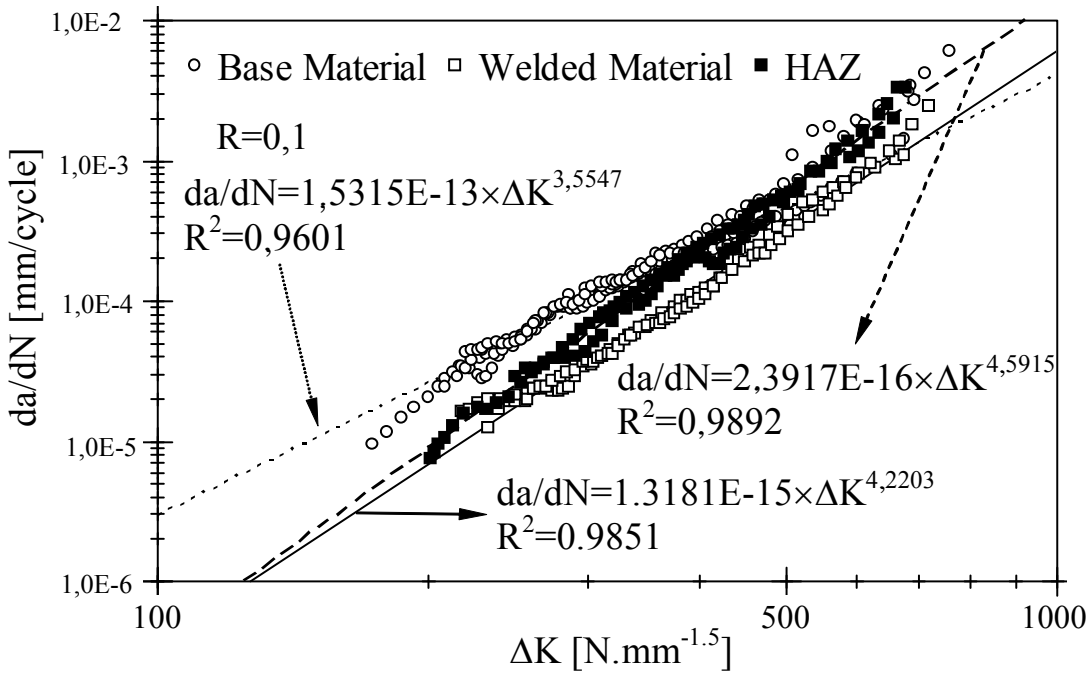


a) base material, WM and HAZ notch location specimens

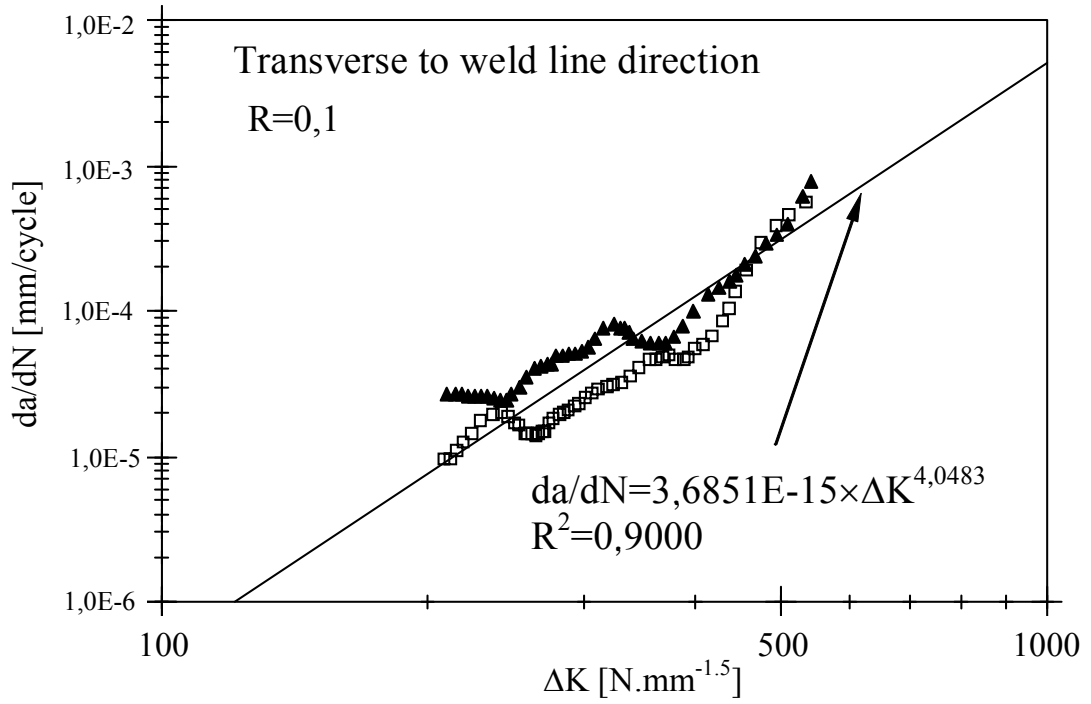


b) specimens with notch orientated transverse to the weldment

**Figure 170 - Fatigue crack propagation data for AA6082-T6 FS welded specimens.**

It is verified that for lower/intermediate stress intensity factor ranges (ΔK) the crack propagation rates of the base material in the rolling and transverse directions are very close; for higher ΔK some deviation is encountered – the crack growth rates in the rolling direction are greater than in transverse direction. It is interesting to note that the friction stirred material has markedly lower crack

propagation rates than the HAZ and the base material. The graphs include the Paris's law correlation which is achieved for very high correlation coefficients.

Figure 171 summarizes the main results obtained for the aluminium 6061-T6 base material tested with R=0,1 and R=0,5. Figure 172 presents results of the aluminium 6061-T6 friction stir welded specimens for R=0,1.

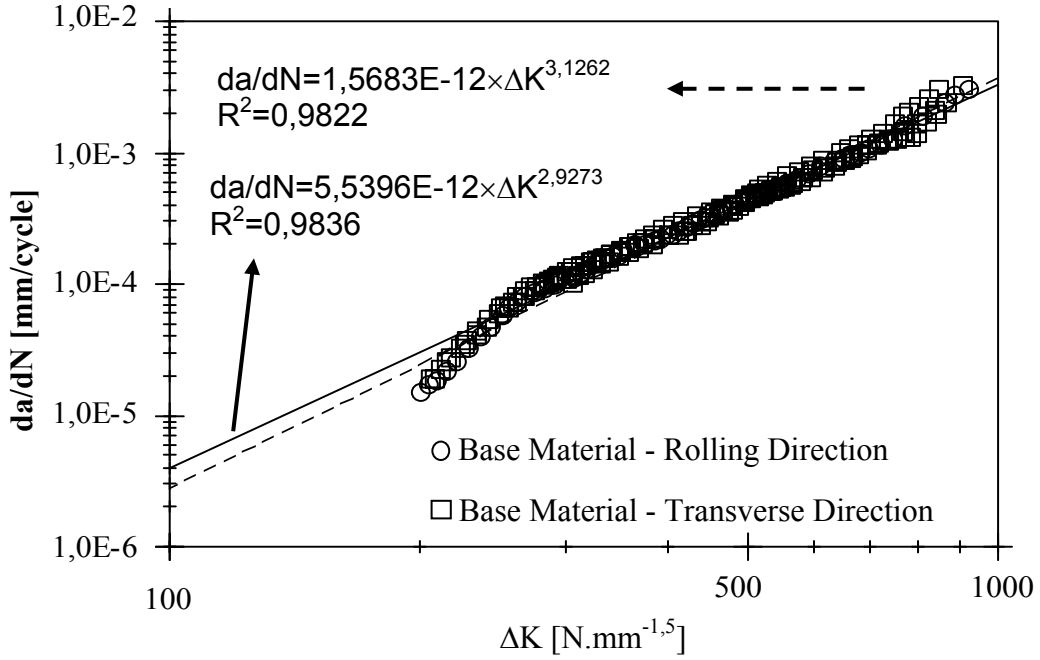


a) base material transverse and rolling direction, R=0,1

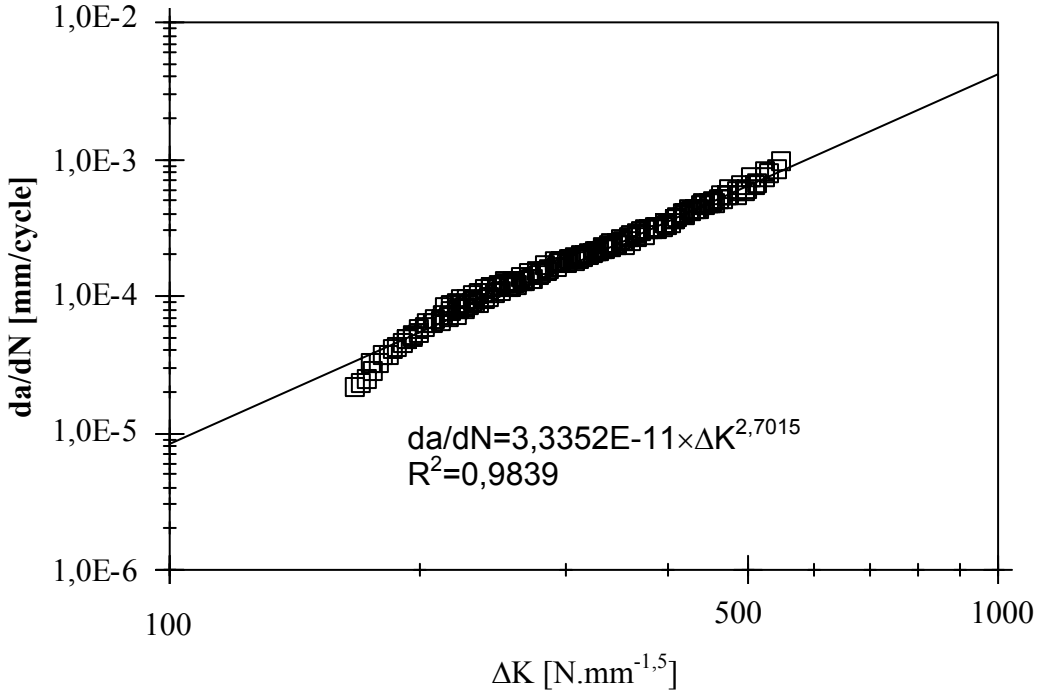


b) base material rolling direction, R=0,5

**Figure 171 - Fatigue crack propagation data for AA6061-T6 base material specimens.**

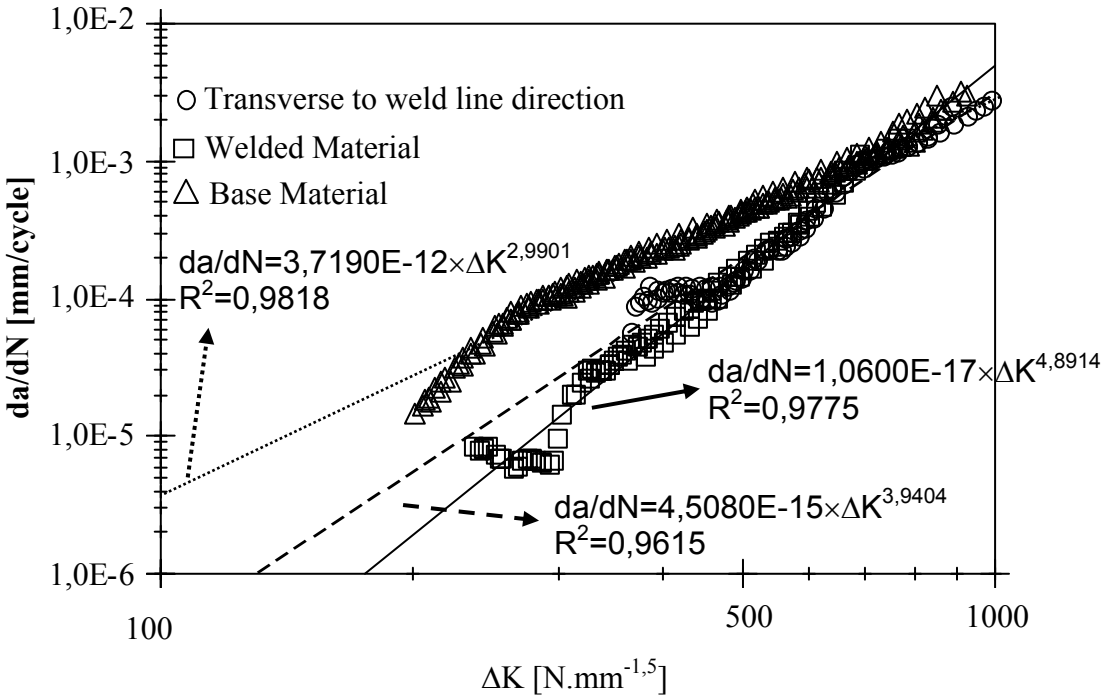


**Figure 172 - Base material, WM with notch orientated transverse to the weldment, AA6061-T6 specimens.**

As in the aluminium 6082-T6, for lower/intermediate stress intensity factor ranges the crack propagation rates of the base material in the rolling and transverse directions are very close. Also, the friction stirred material has lower crack propagation rates than the base material.

A plot of the direct comparison of fatigue crack propagation tests of specimens of both base materials tested with R=0,1 is presented in Figure 173. With the exception of aluminium 6082-T6 specimens tested in the longitudinal direction, all specimens' present similar fatigue crack growth rates.
A comparison of the crack growth rate (R=0,1) of friction stir welded specimens of both base materials with a crack growing in two different configurations is presented in Figure 174. It was found that for a crack growing in the weld bead and a crack growing transverse to the weldment the friction stir welded aluminium 6061-T6 materials has lower crack growth rates. Also, in both friction stir welded aluminium the welded material presents the lower propagation rates.

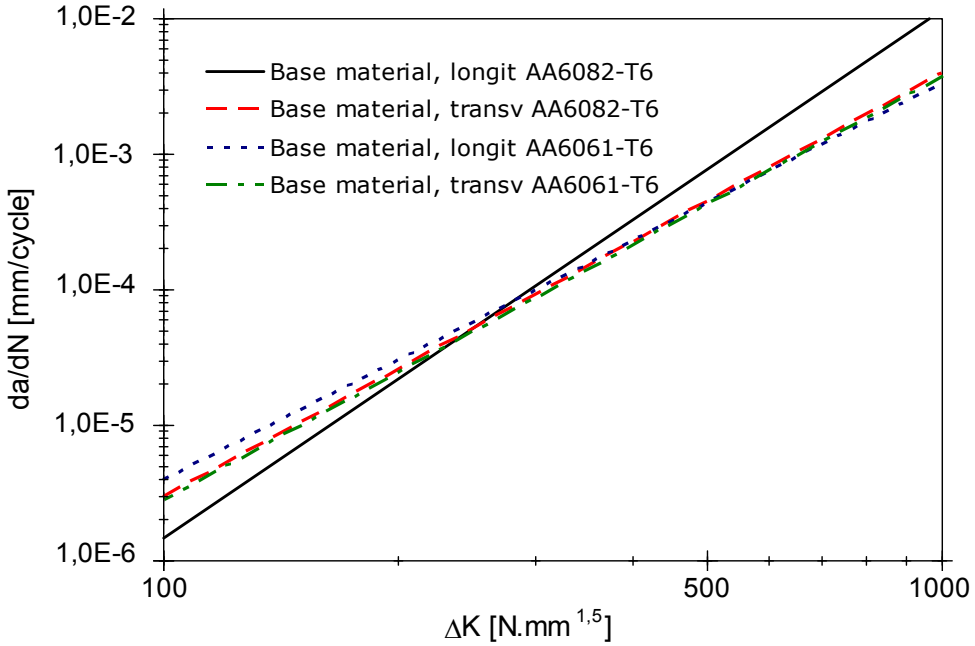


**Figure 173 - FCP R=0,1 for both base materials in the longitudinal and transverse orientation.**

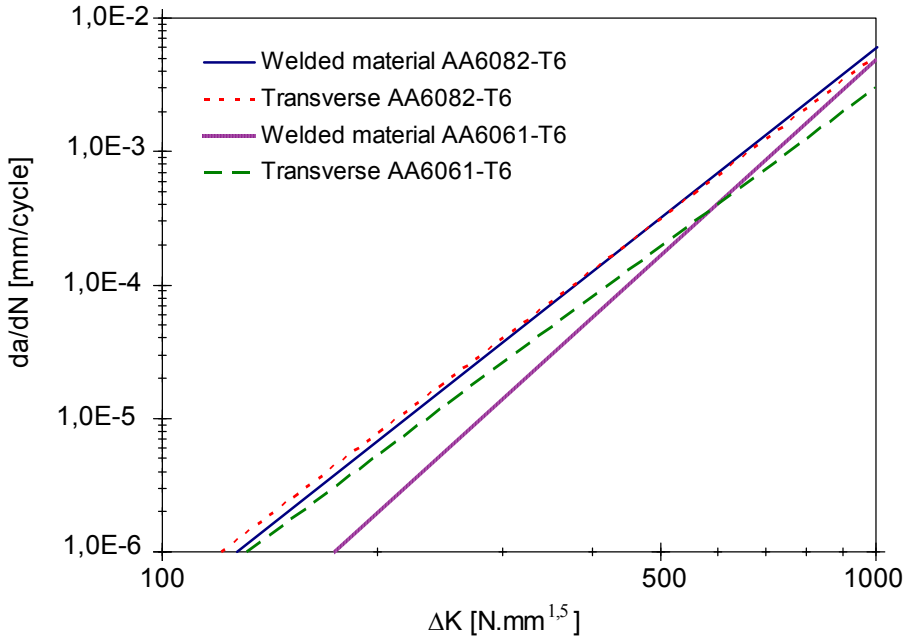


**Figure 174 - FCP R=0,1 for both stirred specimens of both base materials. Crack in the weldment at crack transverse to the weldment.**

*4.3.5.1 SEM analysis of AA6082-T6 CT specimens*

Three different friction stir welded aluminium 6082-T6 compact tension specimens were analysed using Scanning Electron Microscopy (SEM). Each crack configuration: crack in the HAZ, crack at the middle of the weldment, and crack transverse to the weldment were studied, Figure 175. For all specimens configuration measurable fatigue striations were difficult to identify. The

macrographs of the different crack surfaces that were found in each specimen are presented in Figure 176.

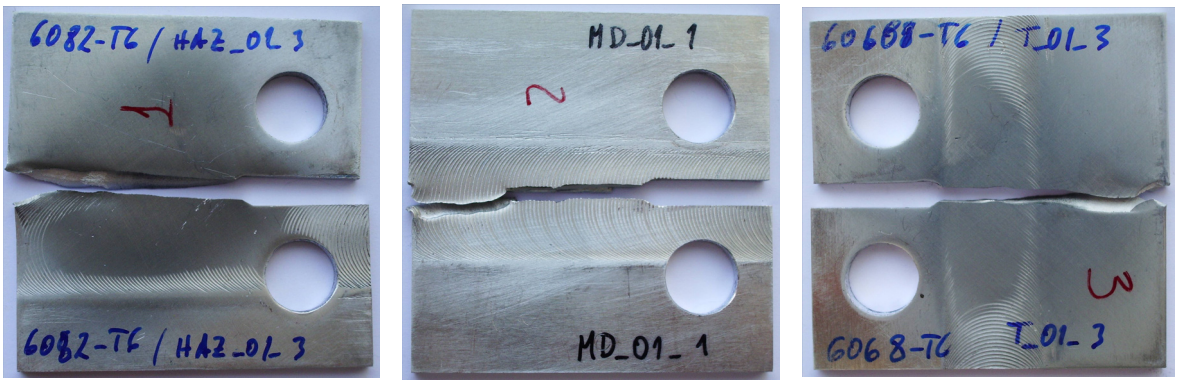


a) HAZ configuration b) welded configuration c) transverse configuration

**Figure 175 - Fractured CT specimens analyzed using SEM.**

When the crack grows on the HAZ there are no visually identifiable particular features, Figure 176a), but if the crack grows at the middle of the weld bead striations related with the tool advance per revolution are a characteristic of the surface, Figure 176b). For a crack growing transverse to the weldment different zones are identified, Figure 176c). First a regular surface corresponding to the HAZ is present, but when the crack reaches the TMAZ layers of stirred material, frequently called as onion rings, as marked on the surface.

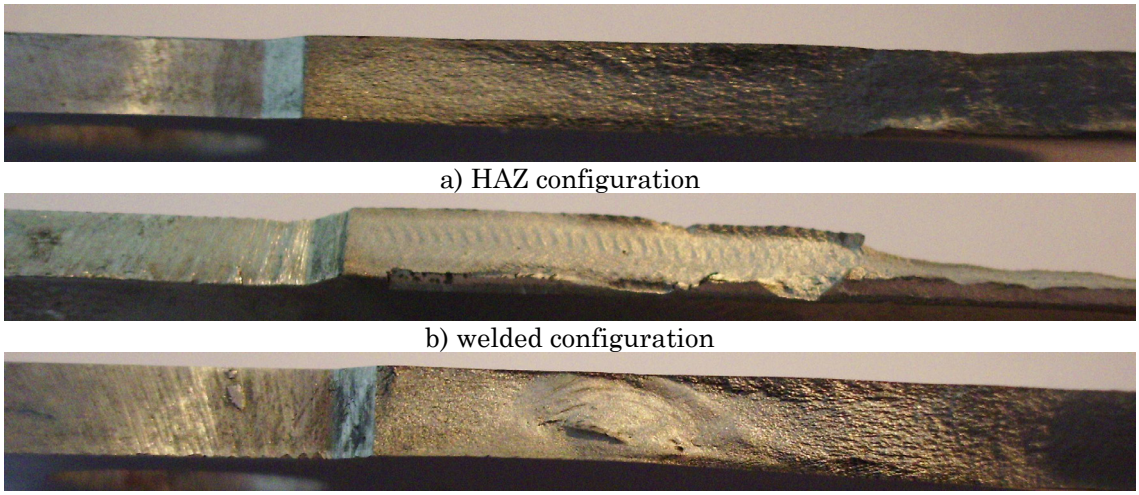

a) HAZ configuration

b) welded configuration

c) transverse configuration

**Figure 176 - Fracture surface of different CT specimens.**

CT specimen with a crack in the HAZ

The first specimen analyzed with SEM has a crack that grew in the HAZ. Details of the crack surface are presented in Figure 177. This figure, shows that the crack surface becomes rougher for higher crack lengths. High magnifications fractographs of particular details, as faded fatigue striations and voids, are presented in Figure 178.

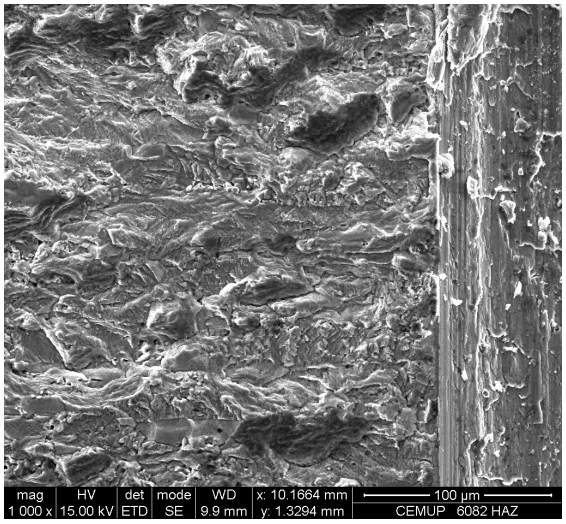


a) fracture surface at 0$mm$

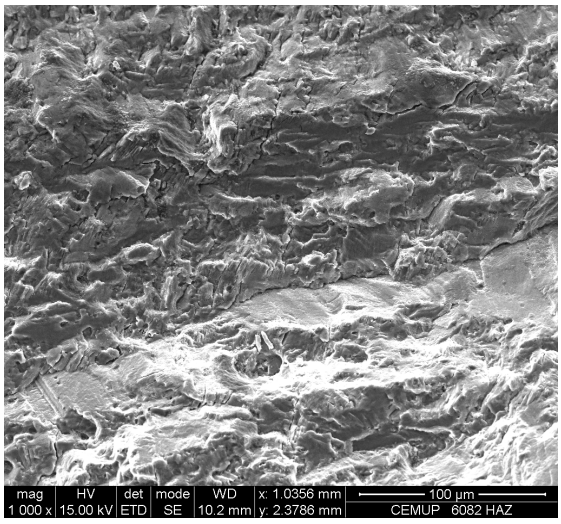


e) fracture surface at 9,16$mm$

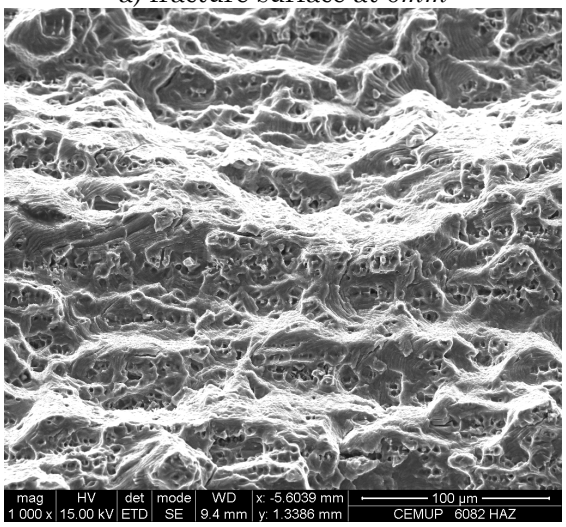


g) fracture surface at 15,76$mm$

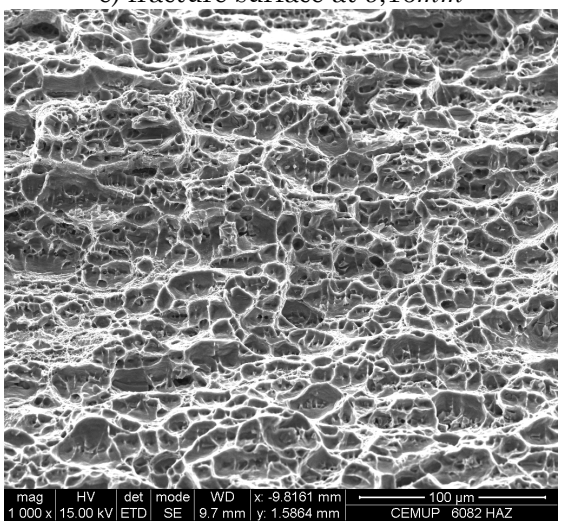


h) surface outside the crack growth area

**Figure 177 - Fracture surface details for different crack lengths.**

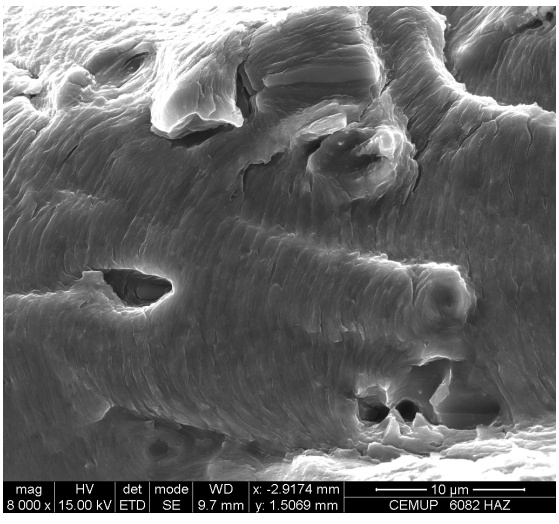


a) detail at 13$mm$

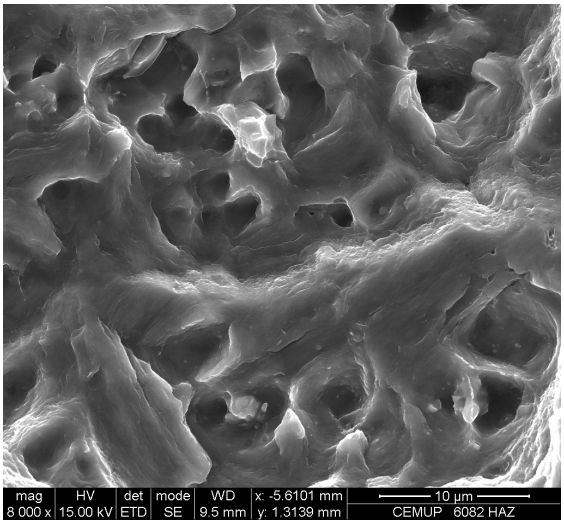


b) detail at 15,77$mm$

**Figure 178 - Fracture surface particular features.**

CT specimen with a crack at the middle of the weldment

The second specimen analyzed has a crack that grew at the middle of the weldment. The fatigue crack surface was similar in all its length, presenting striations which correspond to the tool advancing per revolution, as already presented in the Figure 176b) (macrograph). The fatigue crack surface near the initial notch and a detail of its heterogeneous structure is presented in Figure 179. The striations, which correspond to the tool advance per revolution, are presented in Figure 180. The crack surface is found to be different in the two different zones of each striation mark, as presented in Figure 181.

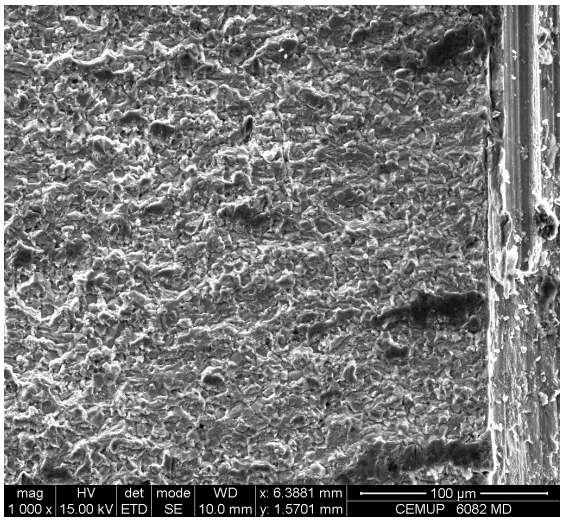


a) fracture surface at 0*mm*

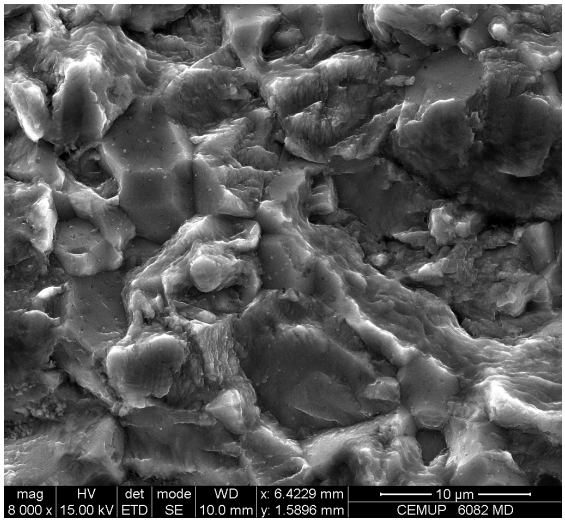


b) detail of the initial fatigue crack surface

**Figure 179 - Fracture surface details near the initial notch.**

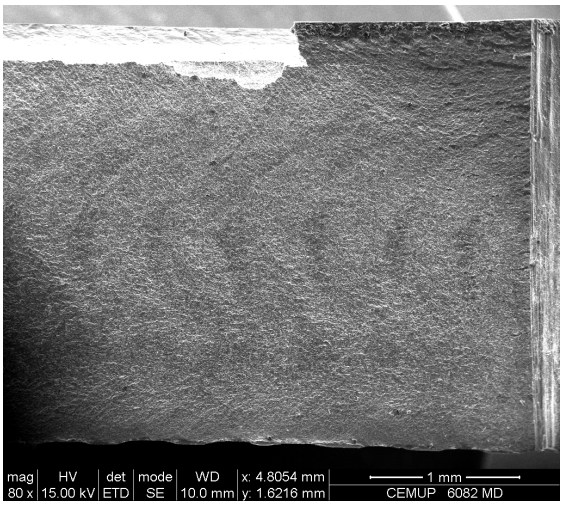


a) striations of the tool advance per revolution

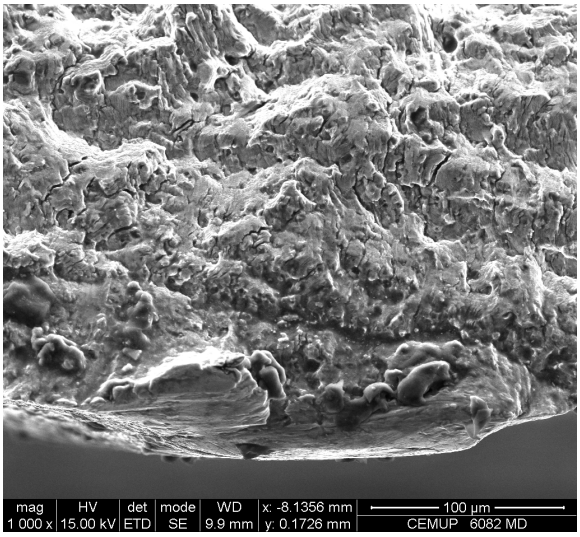


c) detail of the shoulder stir effect

**Figure 180 - Fracture surface particular features.**

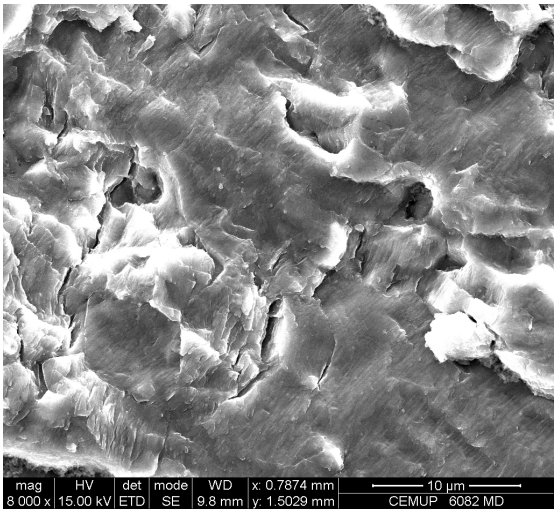


a) structure in the darker zone of the striations

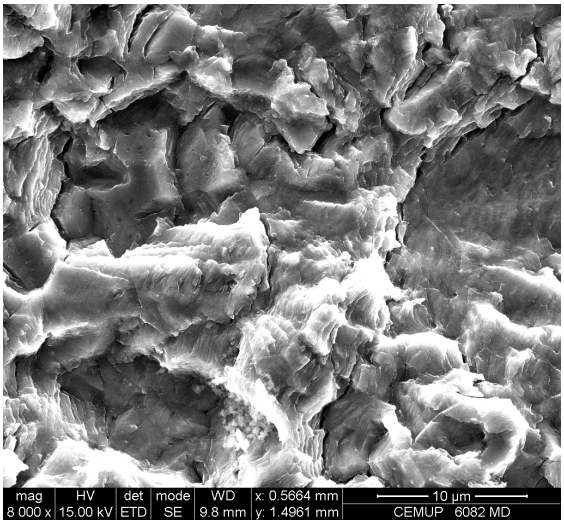


b) structure in the lighter zone of the striations

**Figure 181 - Fracture surface particular features in the striations created by the material flow.**

CT specimen with a crack transverse to the weld bead

The last specimen analyzed has a crack that grew transversal to the weldment, crossing the HAZ and then the TMAZ. In the HAZ the crack surface, as presented in Figure 182, is similar to the one found in the first specimen analyzed. The zone where the fatigue crack crossed the stirred material zone, TMAZ, has a topography which corresponds to the material flow during the friction stir welding process, Figure 183. The layers of material flow at the weld nugget can now be easily identified.

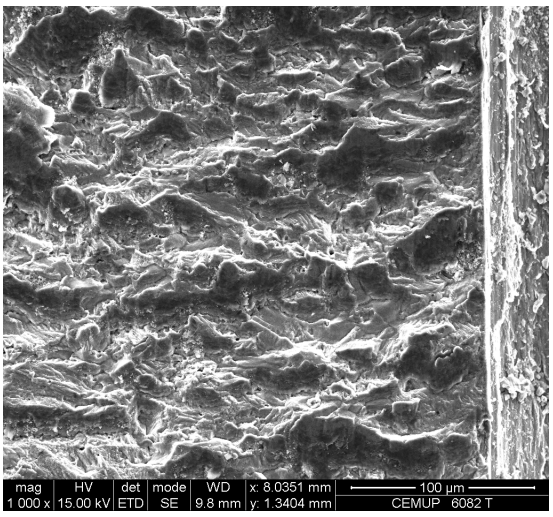


a) fracture surface at 0*mm*

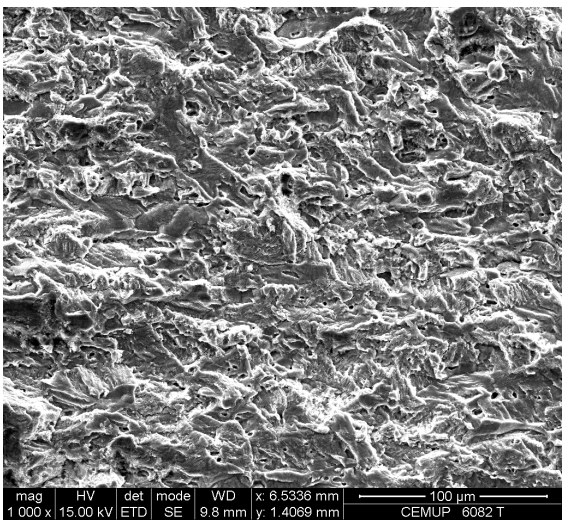


b) fracture surface at 1,6*mm*

**Figure 182 - Fracture surface details near the initial notch.**

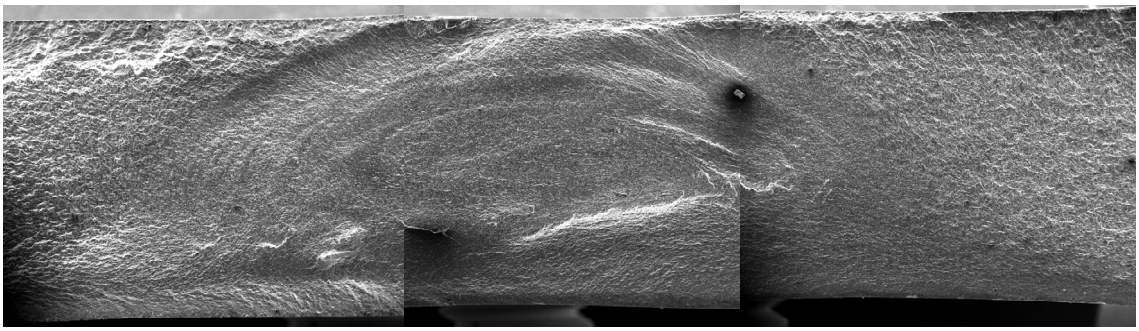

**Figure 183 - Fracture surface at the weld nugget.**

### *4.3.6 Metallographic analysis*

For the analysis of microstructural changes due to the MIG, FSW and LBW processes, the joints were cross-sectioned perpendicularly to the welding direction and etched with HF reagent [142]. A 40*mm* long sample of each specimen was assembled in resin. For the MIG welded and friction stir welded specimens microstructures are acquired according to the locations presented in Figure 184. Three different types of zones were analysed: zones of transition between welded and base material, zones of welded material and zones of only base material. Each microstructure has a reference identifying the site where it was acquired.

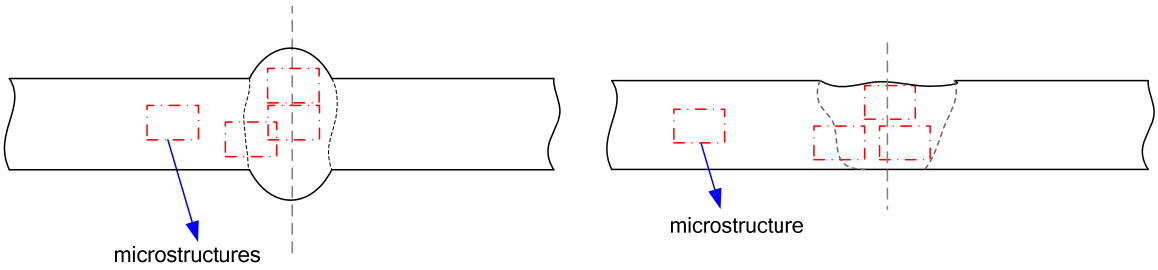


a) MIG weld b) FS weld

**Figure 184 - Sites for microstructural analysis of MIG and FS welds.**

Aluminium 6061-T6 has similar silicon and magnesium contents to aluminium 6082-T6, but higher copper content and lower manganese content. Aluminium alloys always contain some impurities, mainly iron and silicon, [78]. For example, iron, silicon, manganese, copper, and chromium form fairly coarse intermetallic compounds. In the age hardenable alloys, hardening occurs through precipitation of very fine scale precipitates.
The different types of specimens analyzed were: aluminium 6061-T6 MIG welded; aluminium 6082-T6 MIG welded; aluminium 6061-T6 FSW welded; aluminium 6082-T6 FSW welded; aluminium 6061-T6 LBW.

#### *4.3.6.1 MIG welded specimens*

##### *4.3.6.1.1 MIG welded AA6082-T6*

The macrostructure of the aluminium 6082-T6 MIG weld is presented in Figure 185. The identification of the two weld beads is straightforward, and the

transition between the HAZ and base material is also identified. Examples of microstructures are shown in Figure 186.

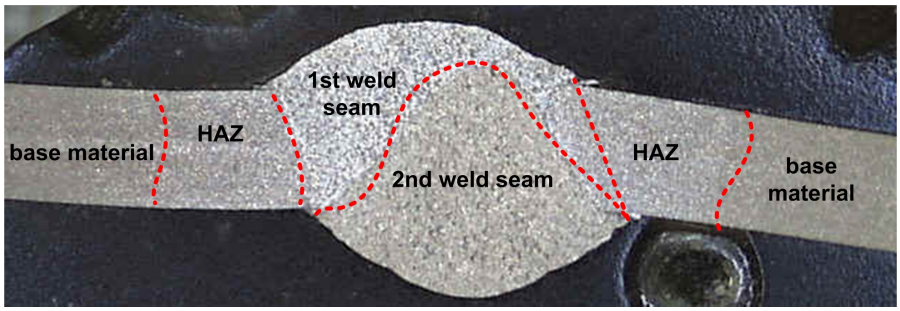


**Figure 185 - Macrostructure of the MIG welded AA6082-T6.**

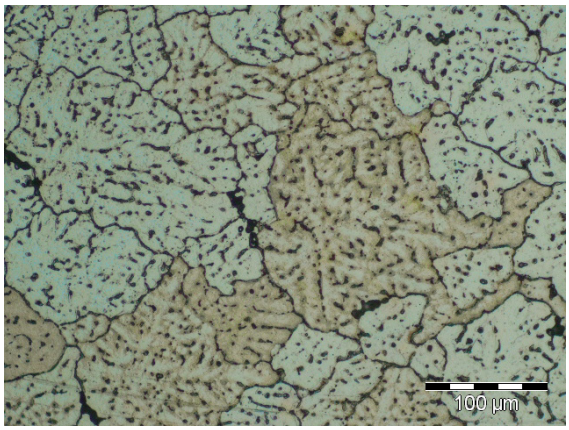


a) microstructure 1, weld (solidification)

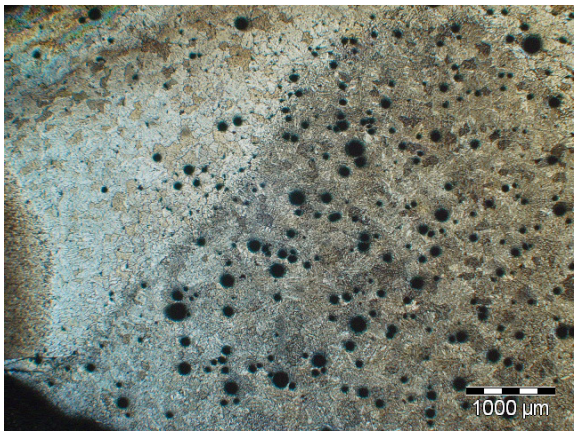


b) microstructure 2, weld

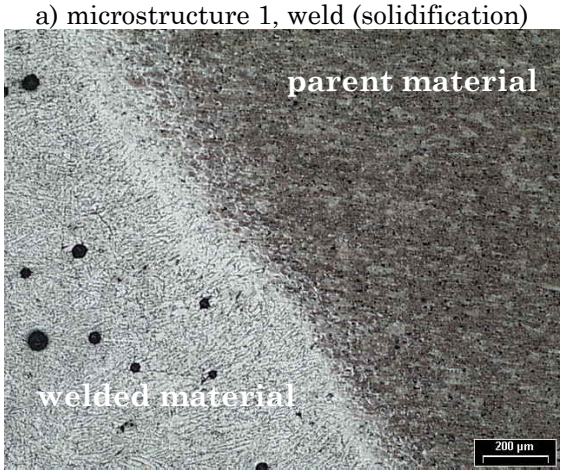


c) microstructure 3, weld

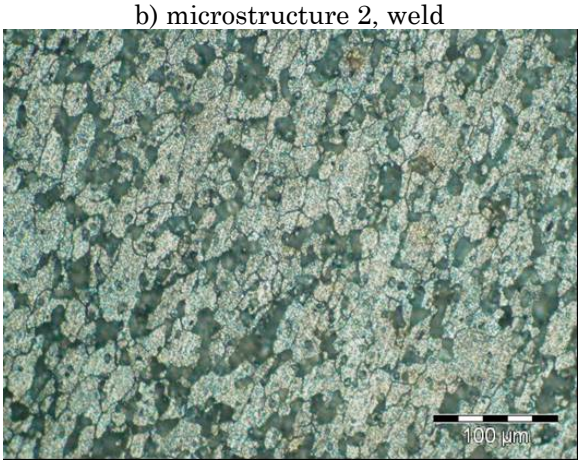


d) microstructure 4, base material

**Figure 186 - MIG welded AA6082-T6 microstructures.**

Microstructure 1 shows the solidification structure in the centre of the weld. Micropores with a diameter no larger than 100$\mu m$, dispersed in the matrix are identified in microstructures 2 and 3. These pores are due to the fusion nature of the MIG welding technique. The transition between the material that suffered fusion to the material only affected by the heat generated during welding is shown in microstructure 2. A structure of larger grains is identified in the left side of microstructure 3 which corresponds to material that suffered fusion. The HAZ material has a structure similar to the base material, fine grains with

dispersed precipitates. Microstructure 4 shows the base material. Similar conclusions were derived from the MIG 6061-T6 microstructural analysis.

#### *4.3.6.1.2 MIG welded AA6061-T6*

The macrostructure of the aluminium 6061-T6 MIG weld is presented in Figure 187. Also, the identification of the two weld beads is straightforward, and the transition between the HAZ and base material is also identified. Examples of microstructures are shown in Figure 188.

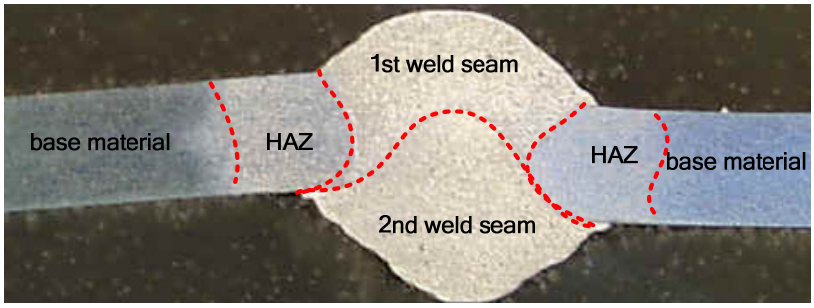


**Figure 187 - Macrostructure of the MIG welded AA6061-T6.**

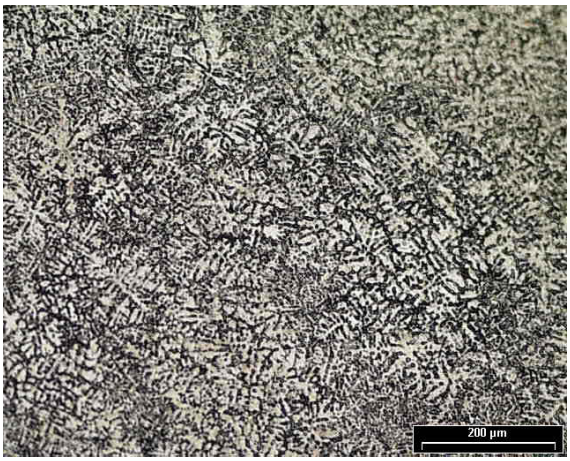


a) microstructure 1, weld (solidification)

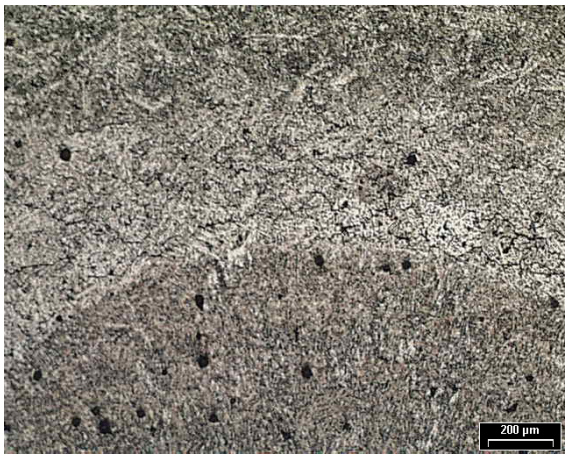


b) microstructure 2, centre of the weld

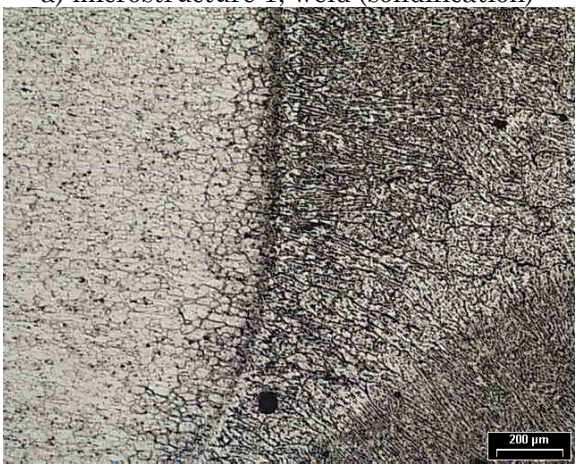


c) microstructure 3, limit of the weld bead

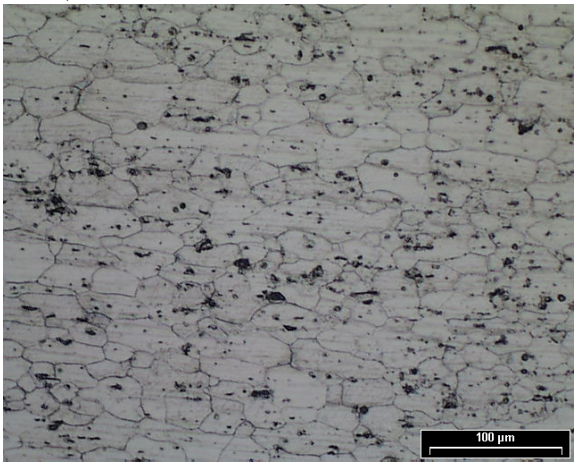


d) microstructure 4, base material

**Figure 188 - MIG welded AA6061-T6 microstructures.**

In microstructures 1 and 2, solidification structure, centre of the weld are identified micropores with approximately a maximum of 100$\mu m$ of diameter disperse in the matrix. In microstructure 3 is identified the transition between the material that suffered fusion (right side) to the material only affected by the heat generated during welding (left side). In the virtual line that defines the transition between the HAZ material and the fused material it is possible to identify a structure containing grains formed due recrystallization. Microstructure 4 shows the base material matrix where grains of approximately 80$\mu m$ and some precipitates are present.

*4.3.6.2 FSW specimens*

*4.3.6.2.1 Analysis of a preliminary weld containing defects*

A first analysis was performed in a aluminium 6082-T6 joint containing defects. This analysis makes possible the identification of friction stir welded defects such as lack of penetration. In Figure 189 the macrostructure of the weld containing defects formed during welding is presented. At the weld root the lack of penetration is observed. In the weld sample analysed, particularly at the advancing side, a high penetration of the shoulder is identified creating a notch effect that could affect mainly the fatigue lives.

**Figure 189 - Macrostructure of the FS welded AA6082-T6 containing defects.**

A detail of the weld nugget is presented in Figure 190. The nugget has flash lines in the direction of the advancing side of the tool and it is typically similar in diameter to the pin.

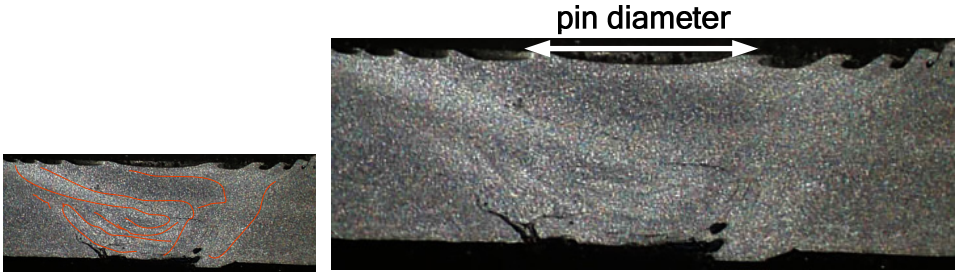


**Figure 190 - Welded nugget detail of the defected joint.**

Some microstructures obtained in different locations are shown in Figure 191. Material from the backing bar was identified in the weld nugget.

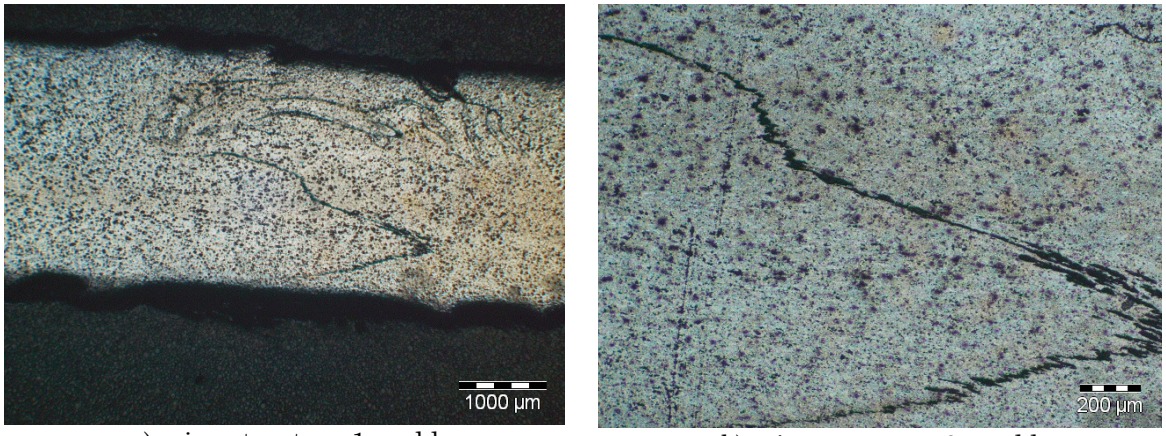


a) microstructure 1, weld b) microstructure 2 , weld

**Figure 191 - FS welded AA6082-T6 containing defects**

*4.3.6.2.2 FS welded AA6082-T6 specimens*

In Figure 192 the macrostructure of the friction stir weld of the aluminium 6082-T6 alloy is presented. At the centre is possible to identify the weld nugget (NZ) with its typical shape of onion rings. The weld nugget experiences high strain and is prone to recrystallization. Immediately at its side is the TMAZ which ends at the tool shoulder delimited by the dashed lines. After the TMAZ appears a zone affected only by the heat generated during the welding process, *e.g.* [143, 165].

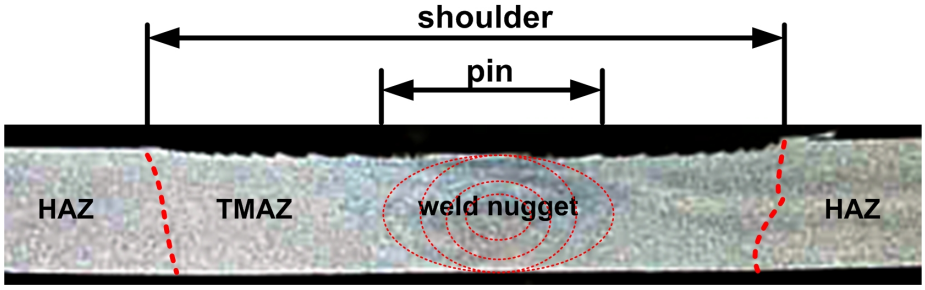


**Figure 192 - Macrostructure of the FS welded AA6082-T6.**

A detail of the weld nugget is presented in Figure 193. In this figure the onion ring structure is well defined consisting of ellipses of material distribution centred at the weld pin.

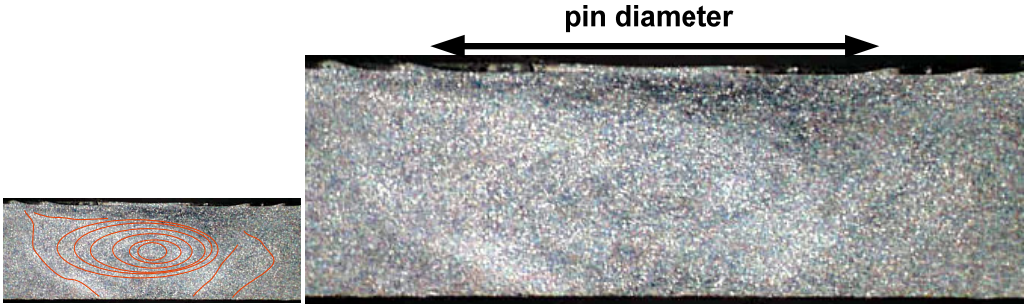


**Figure 193 - Welded nugget detail of the FS welded AA6082-T6.**

Microstructures obtained in the different locations are shown in Figure 194.

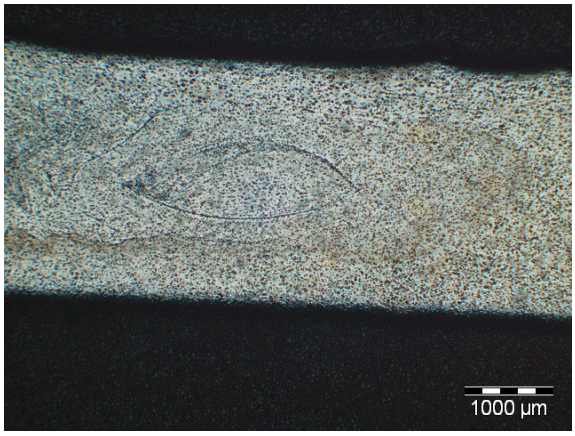


a) microstructure 1, weld

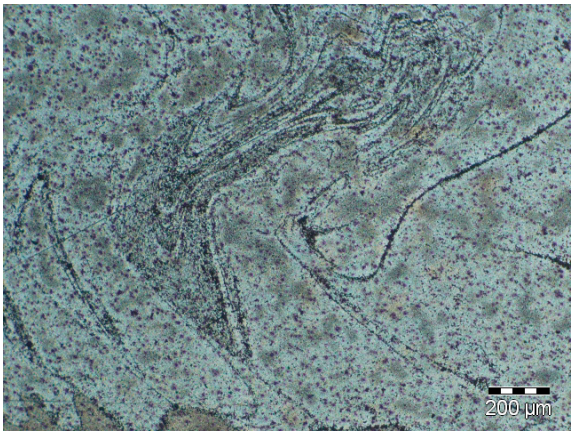


b) microstructure 2, weld

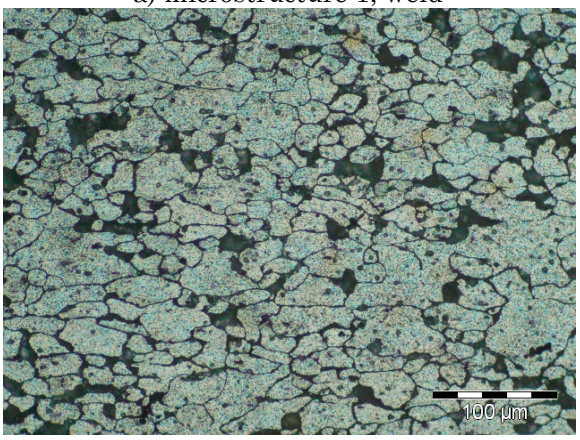


c) microstructure 3, weld nugget

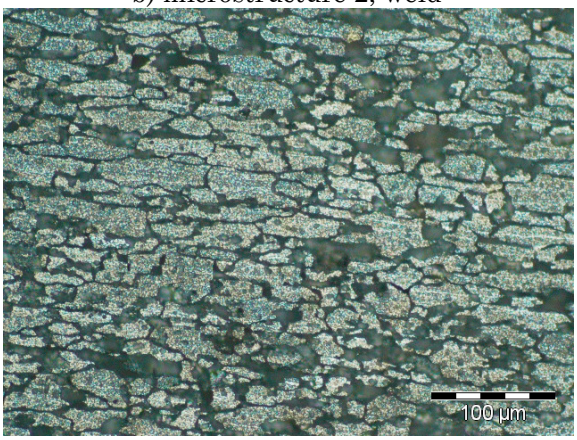


d) microstructure 4, base material

**Figure 194 - FS welded AA6082-T6 microstructures.**

Friction stir welding gives rise to microstructure changes. As observed in [78] the base material contains two sizes of grains owing to partial recrystallization. The recrystallized grains are approximately 20$\mu m$ in size while the non-recrystallized grains can be larger than 100$\mu m$. Microstructure 3, structure at the weld nugget, shows dynamic recrystallized grains much smaller and equiaxed when compared to the elongated base metal microstructure. The grain evolution between the base material and the welded affected material is evident comparing microstructures 3 and 4. The grains in the nugget zone are equiaxed [78]. In the HAZ the grain size is similar to the base metal. Similar observations are presented in [143]. The dynamic continuous recrystallization microstructure which characterizes the friction stir welding process of this alloy is well documented by Liu *et al.* [84].

#### *4.3.6.2.3 FS welded AA6061-T6 specimens*

In Figure 195 the macrostructure of the friction stir weld of the aluminium 6061-T6 alloy is presented. At the centre is possible to identify the weld nugget. The thermo-mechanically affected zone ends at the tool shoulder delimited by the dashed lines. After the thermo-mechanically affected zone appears the heat affected zone. In this weld sample, particularly at the advancing side, a high

penetration of the shoulder is identified creating a small notch effect that could affect mainly the fatigue lives.

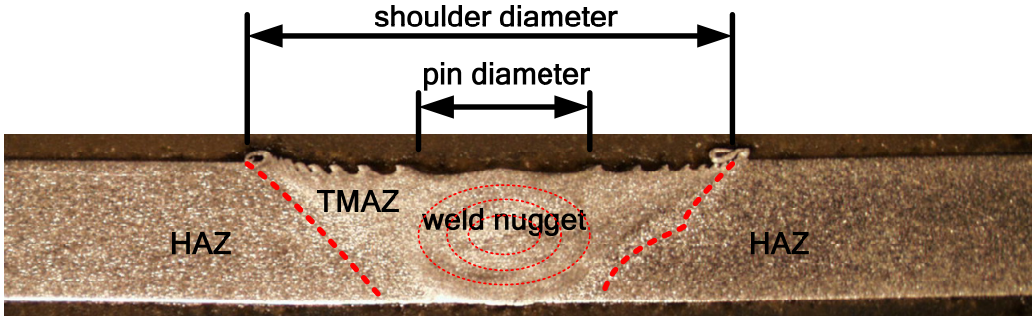


**Figure 195 - Macrostructure of the FS welded AA6061-T6.**

For the case of the friction stir welded aluminium 6061-T6 the microstructures obtained in the different locations are shown in Figure 196.

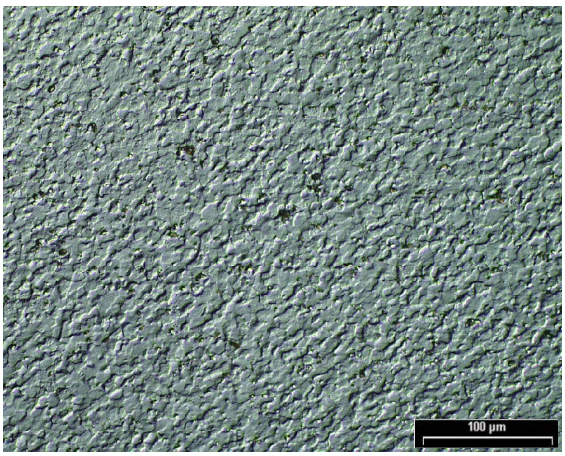


a) microstructure 1, weld nugget

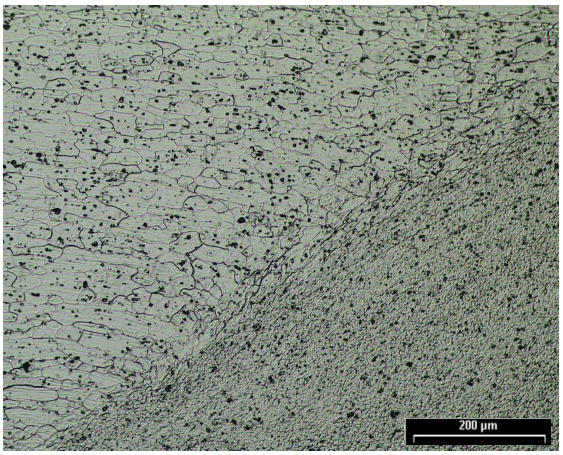


b) microstructure 2, limit of TMAZ to HAZ

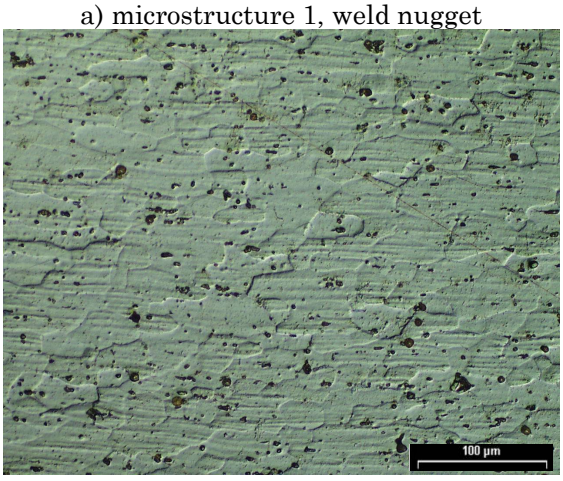


c) microstructure 3, base material

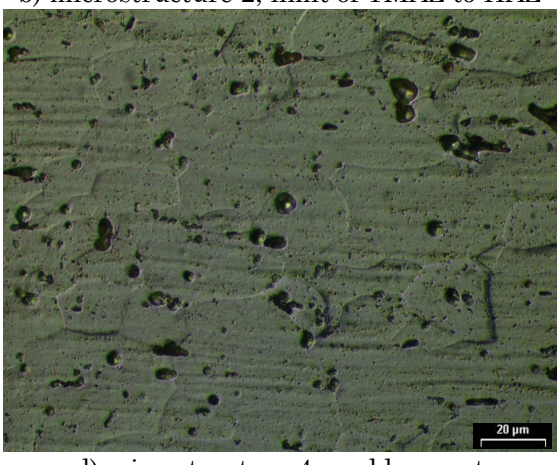


d) microstructure 4 , weld nugget

**Figure 196 - FS welded AA6061-T6.**

In the welded zone grain shape and dimensions evolution is quite evident. In the heat affected zone the grain size is similar to the base metal. Second-phase particles in the workpiece are essentially stirred into the weld zone. Similar observations are presented in [143]. The dynamic continuous recrystallization

microstructure which characterizes the friction stir welding process of this alloy is well documented by Liu *et al.* [84]. As in the aluminium 6082-T6, the grains in the nugget zone have an approximate equiaxed shape and a large difference between the base material and the nugget zone is easily identified as already shown by Liu *et al.* [84].

*4.3.6.3 LBW welded specimens*

The macrostructure of the aluminium 6061-T6 LBW weld is presented in Figure 197. The identification of the weld bead is straightforward, and the transition between the HAZ and base material is also identified (different colours at the macrograph). Examples of microstructures are shown in Figure 198.

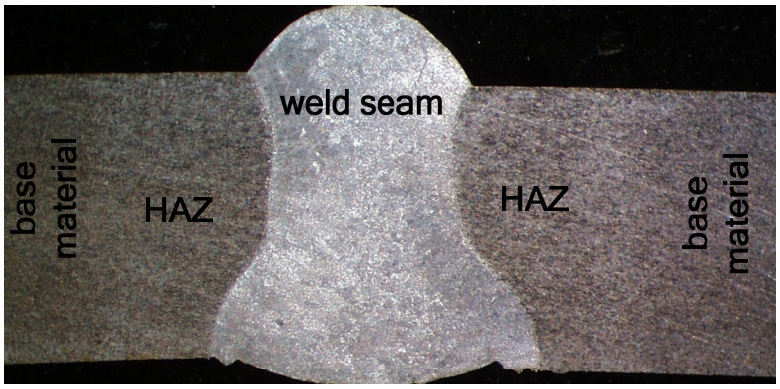


**Figure 197 - Macrostructure of the LBW welded AA6061-T6.**

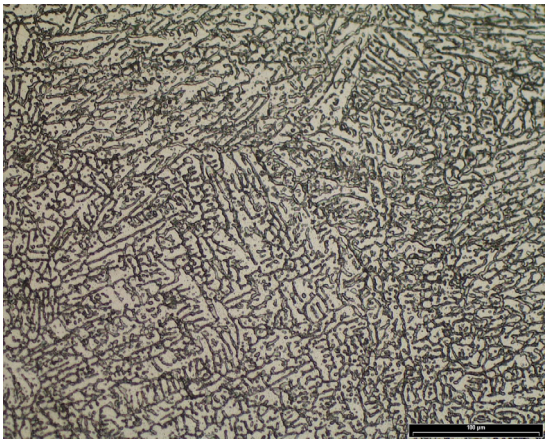

a) microstructure 1, centre of the weld

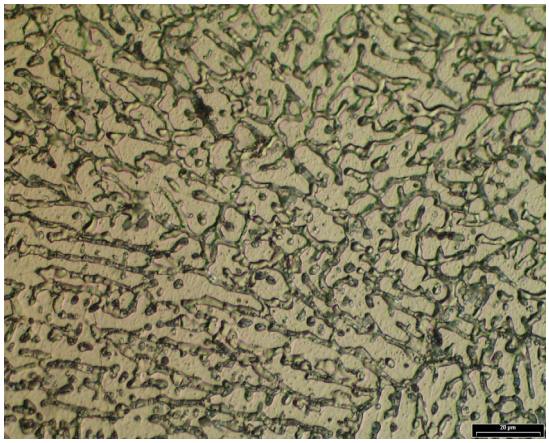

b) microstructure 2, centre of the weld detail

c) microstructure 3, limit of the weld bead

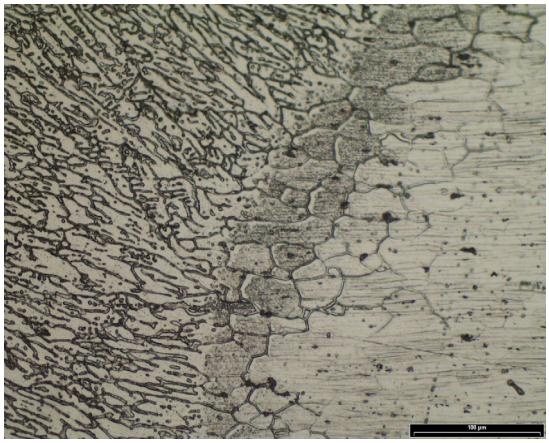

d) microstructure 4, limit of the weld bead detail

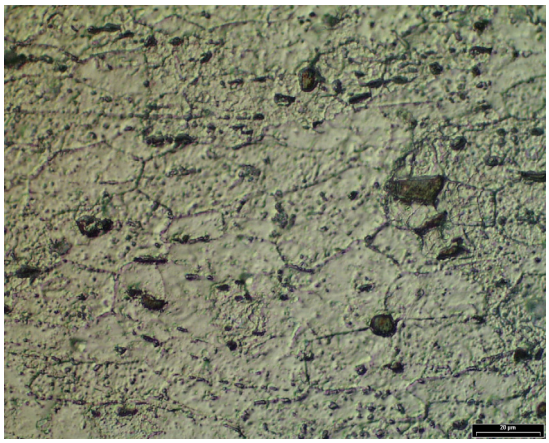

e) microstructure 5, HAZ

**Figure 198 - LBW welded AA6061-T6 microstructures.**

The microstructural analysis revealed a structure similar to the one found for MIG welding, but since the heat was very localized the area that experienced microstructural changes is much smaller in LBW. In microstructures 1 and 2, solidification structure, centre of the weld is almost absent of pores. In microstructure 3 is identified the transition between the material that suffered fusion to the material only affected by the heat generated during welding (HAZ). Microstructure 5 shows grain structure in the HAZ.

### *4.3.7 SEM analysis*

Fractured fatigue test specimens were analysed by SEM. Measurements were performed considering the crack initiation site as the origin and measurements were obtained through the crack length. The result in the coordinate is the average of four measurements of the number of striations in a perpendicular line to their orientation.

*4.3.7.1 Base material striations spacing*

A fatigue test specimen of aluminium 6082-T6 and another of aluminium 6061-T6 subjected to fatigue tests with a maximum stress of 70% of the yield stress (193,3*MPa* for the aluminium 6082-T6 and 214,4*MPa* for the aluminium 6061-T6) and R=0,1 were analysed. The 6082-T6 base material specimen analyzed had a fatigue life of 485858 cycles and the 6061-T6 a fatigue life of 783586 cycles.
A low magnification of both fatigue cracks are presented in Figure 199. In this figure, besides the fatigue crack growth area which presents a darker colour are also identified the several sites were measurements of fatigue striations spacing were measured. For the aluminium 6082-T6 the fatigue area has 12,6$mm^2$ and a crack length of 4,38*mm*. For the aluminium 6061-T6 the fatigue area has 13,4$mm^2$ and a crack length of 4,60*mm*.

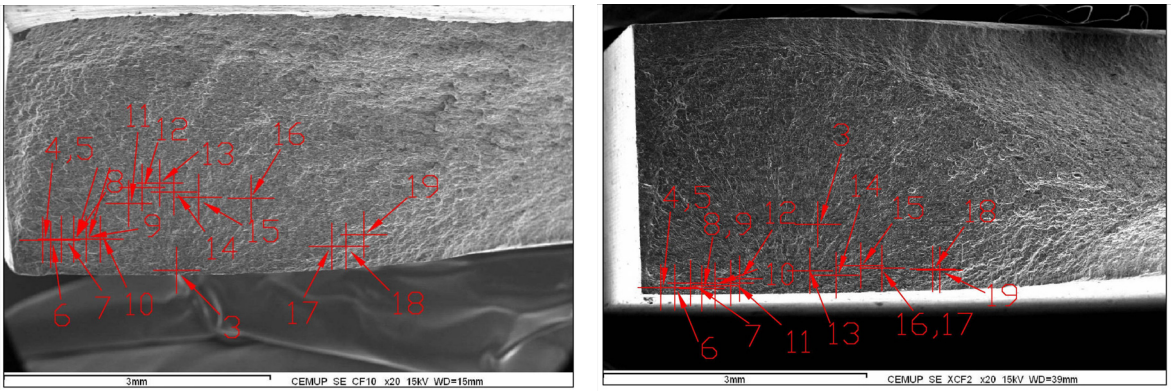


a) AA6082-T6 b) AA6061-T6

**Figure 199 - Fatigue crack of base material specimens, striation measurements sites.**

Figure 200 shows fatigue striations at different crack lengths.

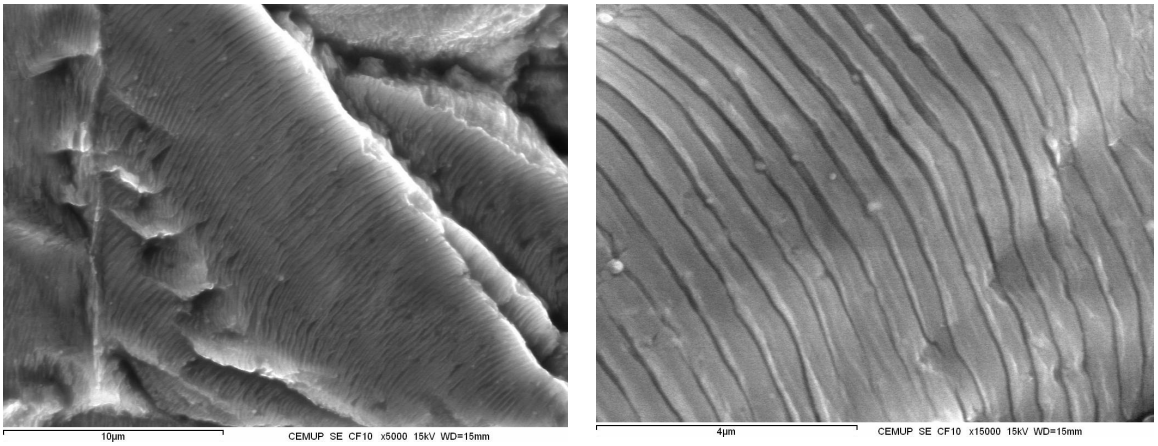


a) AA6082-T6 fractograph 4, crack length of 0,503*mm*

b) AA6082-T6 fractograph 19 crack length of 3,974*mm*

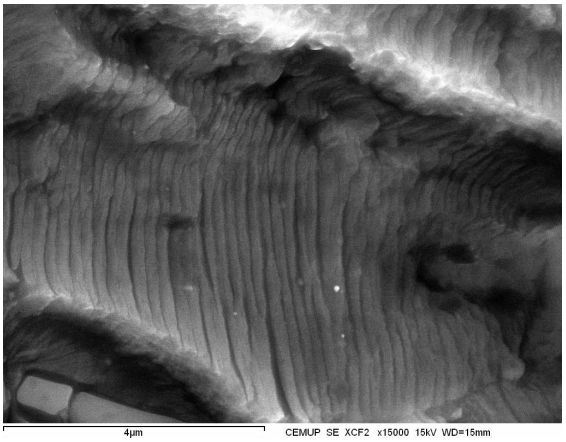


c) AA6061-T6 fractograph 6, crack length of $0{,}377mm$

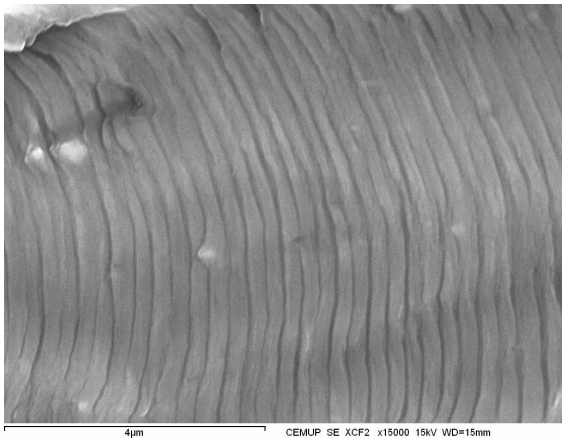


d) AA6061-T6 fractograph 18, crack length of $3{,}322mm$

**Figure 200 - Fatigue striations for different crack lengths.**

Figure 201 and Figure 202 present the striation spacing *vs.* crack length. The crack growth can be fitted using an exponential approximation, with reasonable correlation. As an approximation, the fatigue striation spacing can be interpreted as crack growth rate da/dN.

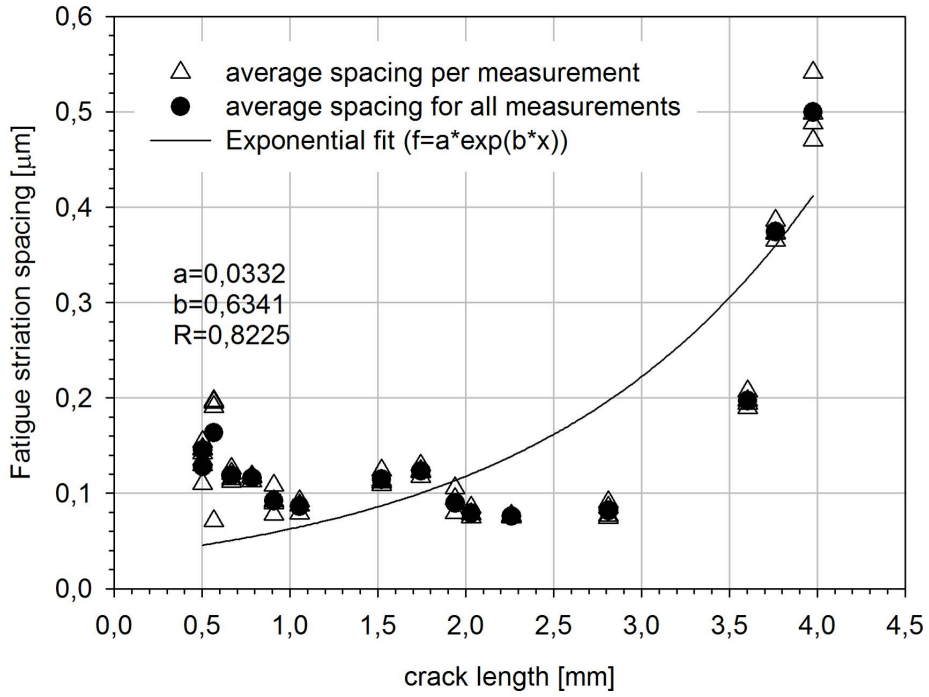


**Figure 201 - Fatigue striation spacing *vs.* crack length for specimen of AA6082-T6.**

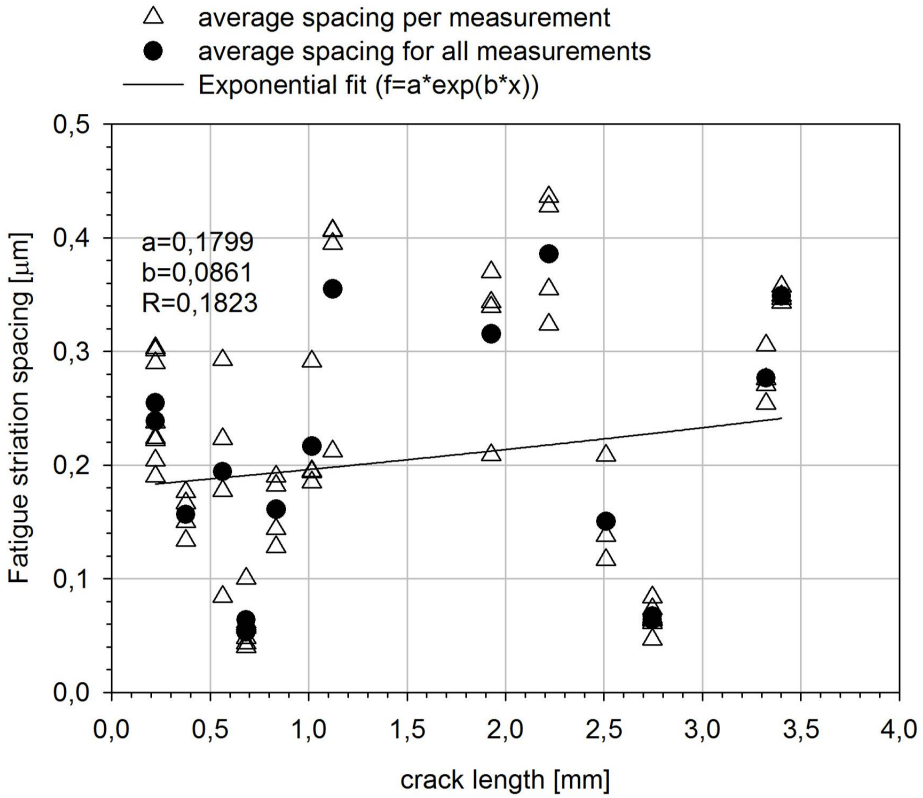


**Figure 202 - Fatigue striation spacing *vs.* crack length for specimen of AA6061-T6.**

*4.3.7.2 MIG welded specimens, striations spacing*

Two MIG butt welded specimens in the as-welded configuration were analyzed after fatigue testing (R=0,1). The specimen of aluminium 6082-T6 was fatigue tested at a maximum stress of 60% of the yield stress (106,1*MPa*), and the specimen of aluminium 6061-T6 was tested at a maximum stress of 70% of the yield stress (109,4*MPa*). The aluminium 6082-T6 specimen presented a fatigue life of 46645 cycles and the 6061-T6 specimen had a fatigue life of 28476 cycles. In the MIG welded specimens fatigue cracks appeared at the end of the weld seam, near the V notch effect due to the extra material deposited by the melted feed wire.

A low magnification of both fatigue cracks are presented in Figure 203. In this figure, besides the fatigue crack growth area which presents a darker colour are also identified the several sites were measurements of fatigue striations spacing were measured. For the aluminium 6082-T6 the fatigue area has 24,8$mm^2$ and a crack length of 12,56$mm$. For the aluminium 6061-T6 the fatigue area has 22,4$mm^2$ and a crack length of 12,50$mm$.

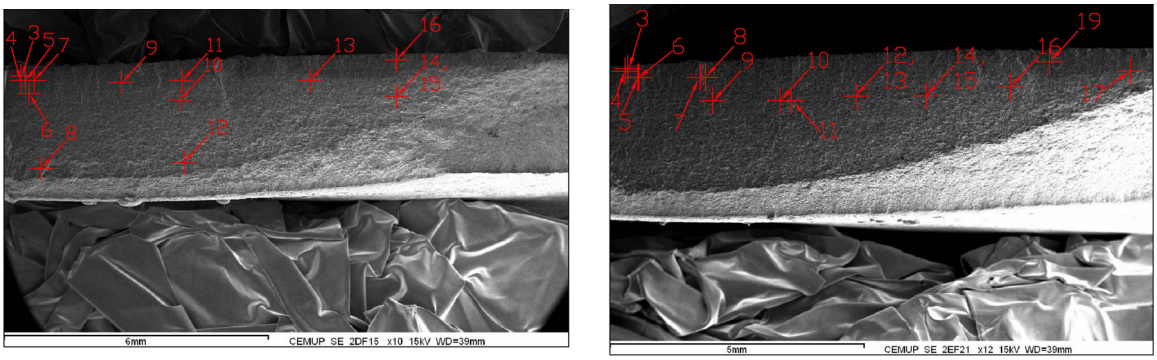


a) MIG AA6082-T6 b) MIG AA6061-T6

**Figure 203 - Fatigue crack of MIG welded specimens, striation measurements sites.**

In the aluminium 6082-T6 MIG welded specimen the striations identification process was very hard to carry out. The fatigue crack surface presented a heterogenic structure with different structures randomly dispersed. Figure 204 shows SEM images of fatigue striations at two crack lengths for the aluminium 6082-T6 MIG welded specimen.

For example in fractograph 9 presented in Figure 204 besides the larger striations at the top of the fractograph a finer type of striations are identified. This leads induces that the coarser striations are of a second order that contain several finer striations.

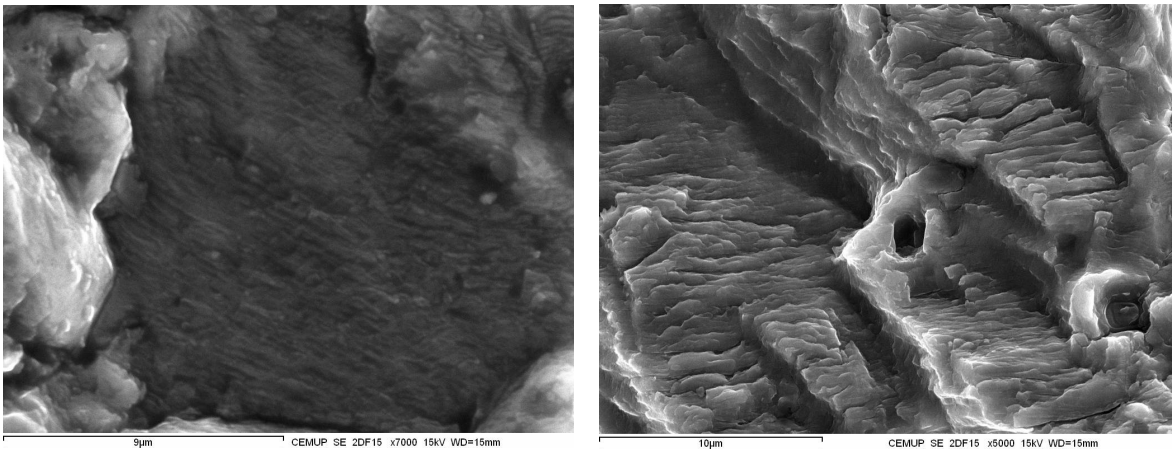


a) fractograph 4, crack length of 0,361$mm$ b) fractograph 9 crack length of 2,582$mm$

**Figure 204 - Fatigue striations for two crack lengths, AA6082-T6 MIG welded specimen.**

Figure 205 presents two examples of features identified in the SEM analysis of the aluminium 6082-T6 MIG welded specimen. Fatigue cracks initiated and have propagated not at the centre of the weld but at the end of the deposited material. This area was subjected to high temperatures during welding. This high temperature lead to the appearance of disperse micropores (diameter with less than 4$\mu m$), as identified in fractograph 3. The fractograph 10 obtained with a small magnification shows macro fatigue crack propagation striations near the specimen outside surface.

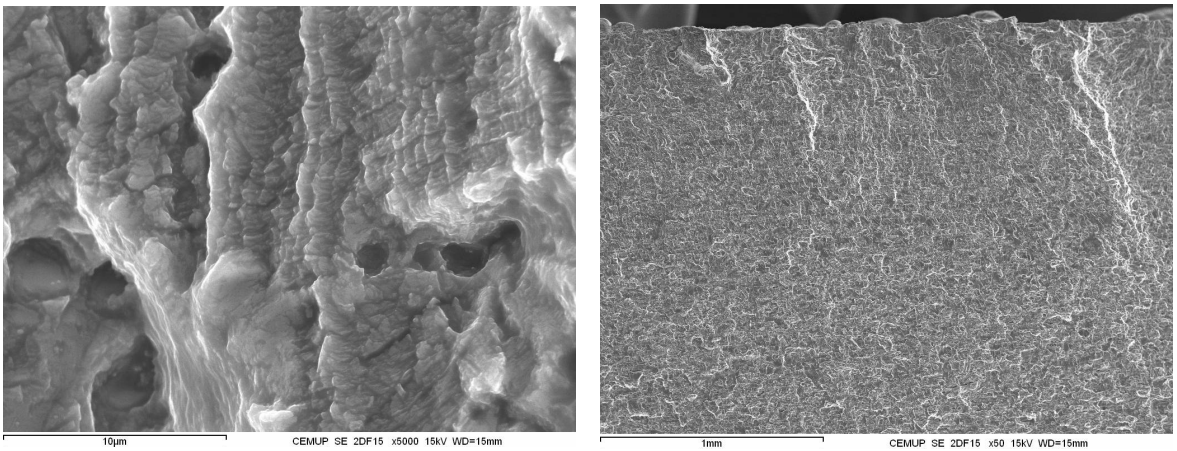


a) fractograph 3, crack length of 0,316$mm$ b) fractograph 10, crack length of 3,954$mm$

**Figure 205 - SEM analysis of the AA6082-T6 MIG welded specimen.**

Figure 206 shows SEM images of fatigue striations at two crack lengths for the aluminium 6061-T6 MIG welded specimen.

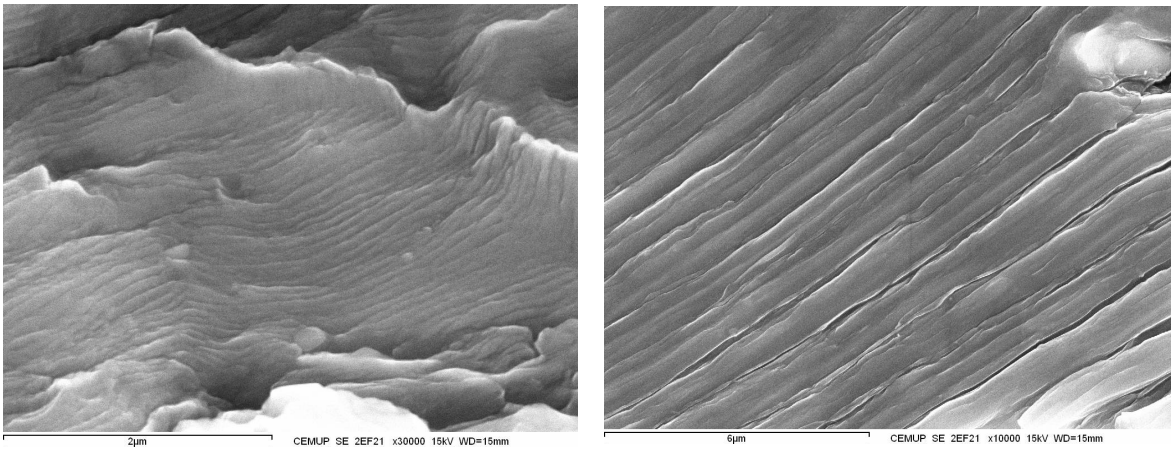


a) fractograph 8, crack length of 1,893$mm$ b) fractograph 17 crack length of 10,250$mm$

**Figure 206 - Fatigue striations for two crack lengths, AA6061-T6 MIG welded specimen.**

In this specimen the striations identification process was easier than in the aluminium 6082-T6 MIG specimen. Nevertheless the fatigue crack surface was a heterogenic structure with several different structures dispersed randomly. For example, in fractograph 8 presented in Figure 206 fine striations are identified in an irregular structure. In fractograph 17, almost at the end of the fatigue crack are, coarse striations are found.

Figure 207 presents two examples of features identified in the SEM analysis of the aluminium 6061-T6 MIG welded specimen. In fractograph 6, besides some fatigue striations, some gaps in the material continuity are identified. These gaps were probably formed in the heating and cooling during welding leading to the appearance of internal cracks. These gaps are micro-cracks that can be signs of small hot cracks. Hot cracks can be formed in AlMgSi fusion welds when the low melting MgSi eutectic in the grain boundaries remains liquid during weld solidification and subsequent material shrinkage [90]. Heat treatable aluminium alloys are sensitive to hot short cracking, which results from HAZ liquidation

during welding [174]. This specimen presents no less micropores than the aluminium 6082-T6 MIG specimen. In fractograph 12 striations with a V shape orientation were found. The image shows the random distributions that can be found in striations if the fatigue crack is observed with high magnifications. In this case, the two orientations found are probably due to an internal gap formed during the cooling process.

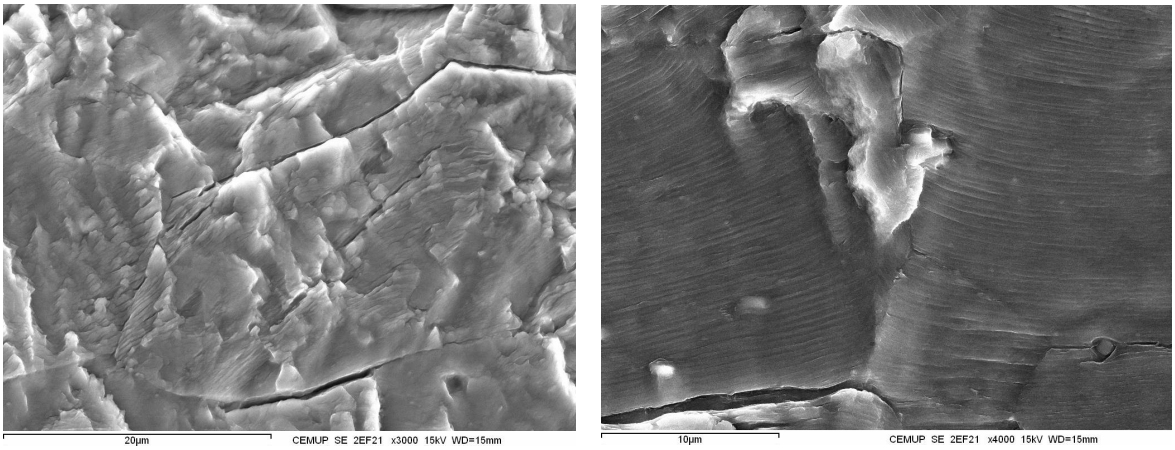


a) fractograph 6, crack length of 0,611$mm$ b) fractograph 12, crack length of 4,886$mm$

**Figure 207 - SEM analysis of the AA6061-T6 MIG welded specimen.**

Figure 208 and Figure 209 present the striation spacing versus crack length for the aluminium 6082-T6 and 6061-T6 MIG welded specimens.

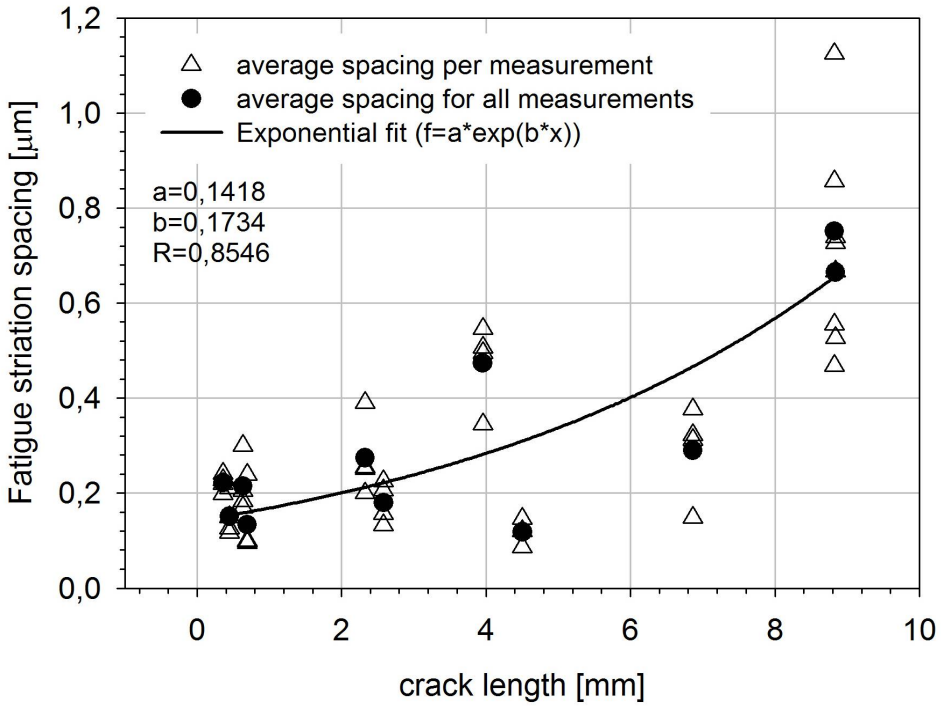


**Figure 208 - Fatigue striation spacing *vs.* crack length AA6082-T6 MIG welded specimen.**

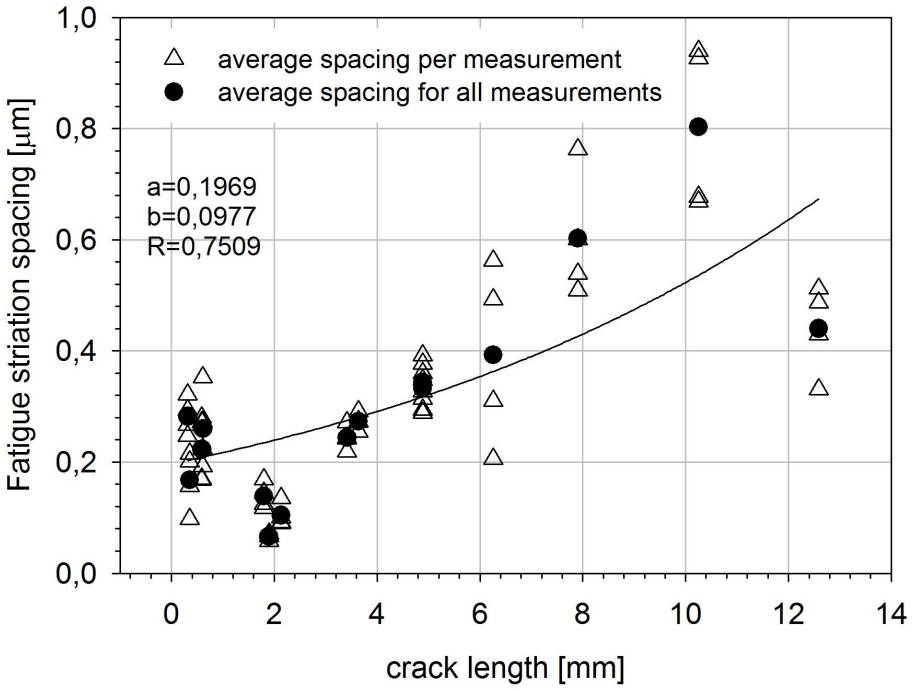


**Figure 209 - Fatigue striation spacing *vs.* crack length AA6061-T6 MIG welded specimen.**

In the fractured surface of the MIG welded 6082-T6 specimen and the MIG welded 6061-T6 specimen it is possible to identify to distinct zones, Figure 210. In both fractographs a layer near the external surface presents a darker colour. Nevertheless this difference is not so easy to identify in the aluminium 6061-T6 specimen. In order to understand this difference a chemical composition analysis was carried out.

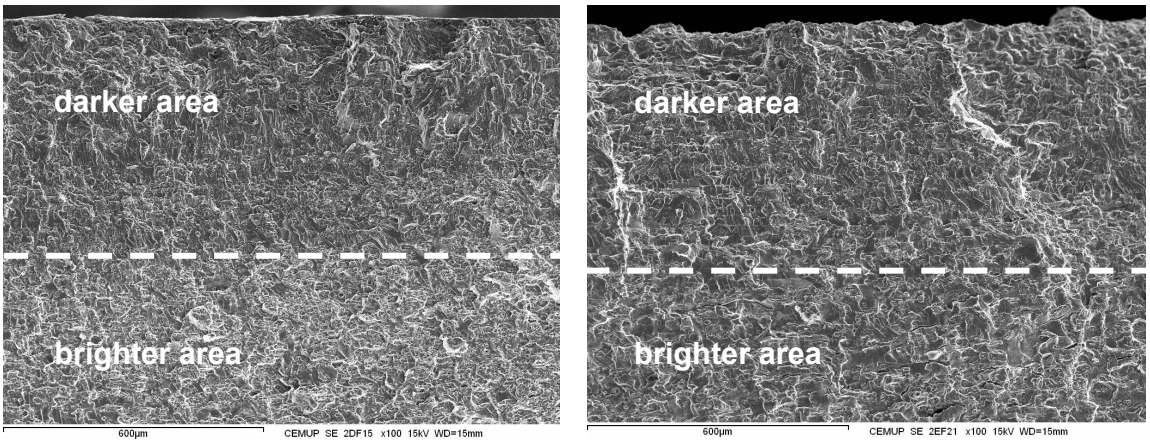


a) fractograph 14, fracture surface of the MIG welded 6082-T6

b) fractograph 19, fracture surface of the MIG welded 6061-T6

**Figure 210 – Fractured surface of the MIG welded specimens.**

Analysing both areas by means of Energy Dispersive Spectrometer (EDS) the chemical composition found for the MIG welded 6082-T6 and for the MIG 6061-T6 are presented in Table 35 and Table 36.

Besides the EDS, the chemical composition was determined before welding by spectrometry using a SPECTROLAB M7. This analysis was carried out at the chemical laboratory of CETECOFF INEGI.

**Table 35 - Chemical composition of the of the MIG welded 6082-T6 [%]**

| Element | EDS analysis, fractograph 14 darker area | EDS analysis, fractograph 14 brighter area | SPECTR OLAB M7 | Supplier 6082-T6 | Supplier Autrod18.15 (filler wire) |
|---|---|---|---|---|---|
| Mg | 0,71 | 1,56 | 0,69 | 0,6-1,2 | 5 |
| Al | 96,87 | 94,71 | 97,4 | remaining | remaining |
| Si | 1,16 | 2,21 | 0,91 | 0,7-1,3 | <0,25 |
| Mn | 0,71 | 0,97 | 0,56 | 0,4-1 | <0,2 |
| Fe | 0,55 | 0,55 | 0,23 | 0,5 | <0,4 |
| Cu | - | - | 0,062 | 0,1 | - |
| Cr | - | - | 0,035 | 0,25 | - |
| Zn | - | - | 0,098 | 0,2 | - |
| Ti | - | - | 0,019 | 0,1 | - |

In the MIG welded aluminium 6082-T6 specimen a good agreement between the Spectrolab M7 and the supplier data was found. When analysing both areas of fractograph 14 by EDS some differences were found between the layer near the surface and the inside surface. These differences are mainly in the percentage of % Al which decreases in the inside surface and the percentage of Si is lower in the outside surface.

**Table 36 - Chemical composition of the of the MIG welded 6061-T6 [%]**

| Element | EDS analysis, fractograph 19 darker area | EDS analysis, fractograph 19 brighter area | SPECTR OLAB M7 | Supplier 6061-T6 | Supplier Autrod18.15 (filler wire) |
|---|---|---|---|---|---|
| Mg | 0,90 | 0,82 | 0,84 | 0,9 | 5 |
| Al | 98,21 | 98,24 | 97,7 | remaining | remaining |
| Si | 0,49 | 0,60 | 0,54 | 0,59-0,62 | <0,25 |
| Mn | 0,06 | 0,00 | 0,01 | 0,01 | <0,2 |
| Fe | 0,34 | 0,33 | 0,40 | 0,5 | <0,4 |
| Cu | - | - | 0,24 | 0,24-0,26 | - |
| Cr | - | - | 0,18 | 0,18-0,19 | - |
| Zn | - | - | 0,006 | 0,01-0,02 | - |
| Ti | - | - | 0,031 | 0,02-0,03 | - |

In the MIG welded aluminium 6061-T6 specimen a good agreement between the Spectrolab M7 and the supplier data was also found. When analysing both areas of fractograph 19 by EDS only residual differences were found between the layer near the surface and the inside surface. These minor differences are reflected in a not so pronounce contrast between the outside and inside surface.

*4.3.7.3 FS welded specimens, striations spacing*

The specimens were fatigue tested at a maximum stress of 70% of their yield stress (98,4*MPa* for the aluminium 6082-T6 and 111,1*MPa* for the aluminium 6061-T6). The 6082-T6 specimen presented a fatigue life of 258827 cycles and the 6061-T6 specimen had a fatigue life of 173499 cycles.
A low magnification of both fatigue cracks are presented in Figure 211. In this figure are identified the several sites where fractographs were acquired. For the aluminium 6082-T6 the fatigue area has 20,4$mm^2$ and a crack length of 10,29$mm$. For the aluminium 6061-T6 the fatigue area has 24,8$mm^2$ and a crack length of 12,50$mm$.

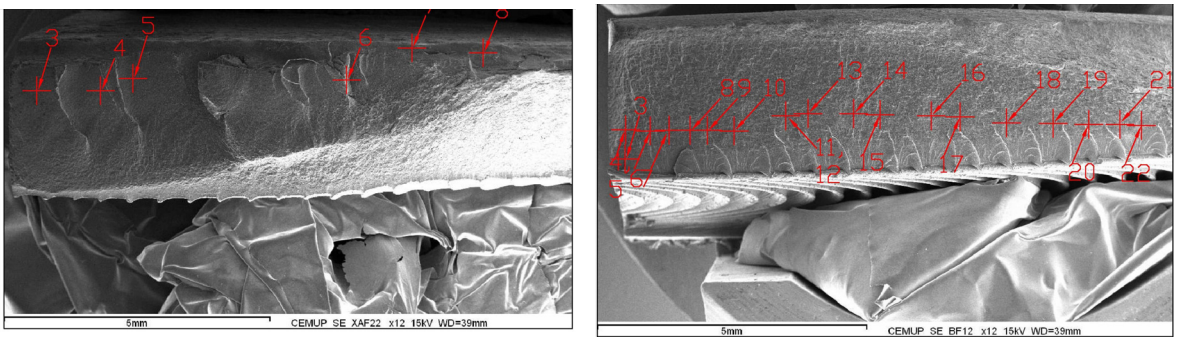


a) FS welded AA6082-T6 b) FS welded AA6061-T6

**Figure 211 - Fatigue crack of FS welded specimens, striation measurements sites.**

For the aluminium 6082-T6 friction stir welded, the fractograph presented in Figure 212 shows the fatigue crack initiation site (left upper corner). In this fractograph a layer near the weld root indicates that lack of penetration occurred during the welding process. This features promoted the crack initiation at the middle of the weld, at the weld root.

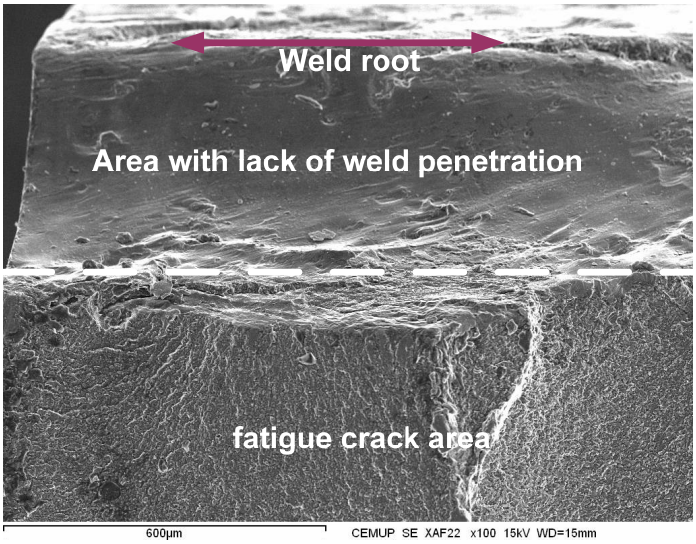


**Figure 212 - Fatigue crack initiation site, AA6082-T6 FS welded specimen.**

The friction stir welded aluminium 6082-T6 specimen has an irregular structure in its entire fracture surface preventing the identification of measurable striations. As an example fractograph 3, Figure 213, shows a fractograph of an initial crack propagation site with an irregular area Nevertheless in some fractographs faded striations can be identified, fractograph 6 presented in Figure 213.

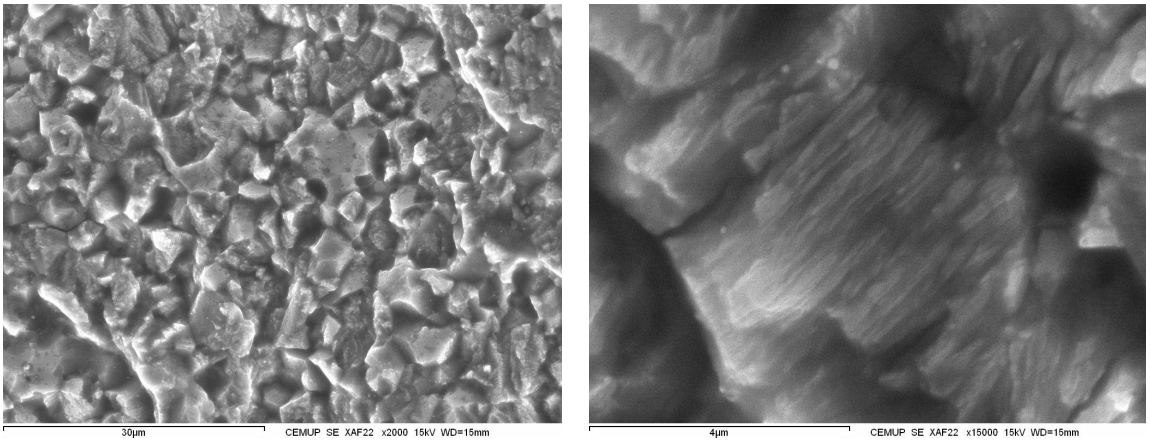


a) fractograph 3 b) fractograph 6

**Figure 213 - Fatigue crack structure and striations, AA6082-T6 FS welded specimen.**

For the aluminium 6061-T6 friction stir welded the fatigue crack propagated near the shoulder edge, Figure 211b). Despite the heterogeneity found in the fractured surface the striations measurement process was feasible. In fractograph 5 presented in Figure 214 several striations sets with different orientations are identified. In fractograph 21, almost at the end of the fatigue crack, are found coarser striations.

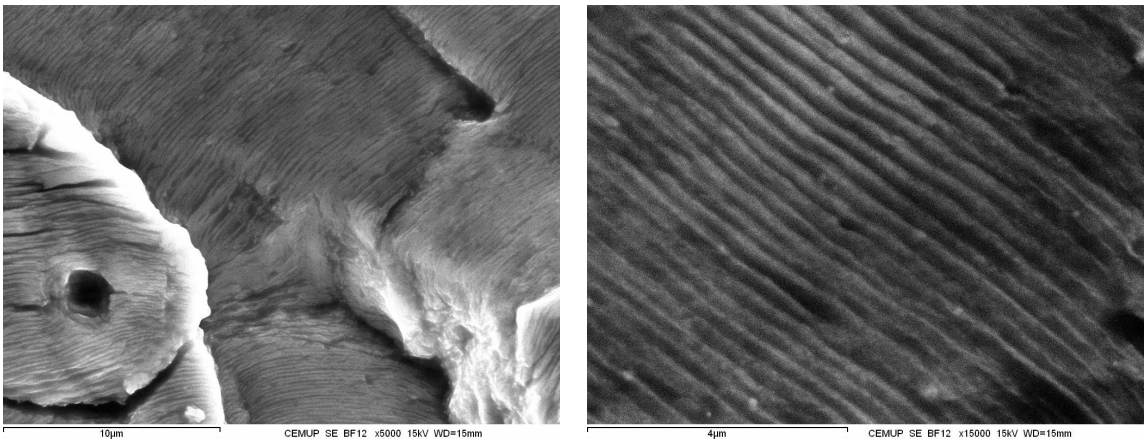


a) fractograph 5, crack length of 0,877$mm$ b) fractograph 21 crack length of 9,544$mm$

**Figure 214 - Fatigue striations for two crack lengths, AA6061-T6 MIG welded specimen.**

Figure 215 presents the striation spacing versus crack length for the aluminium 6061-T6 friction stir welded specimen.

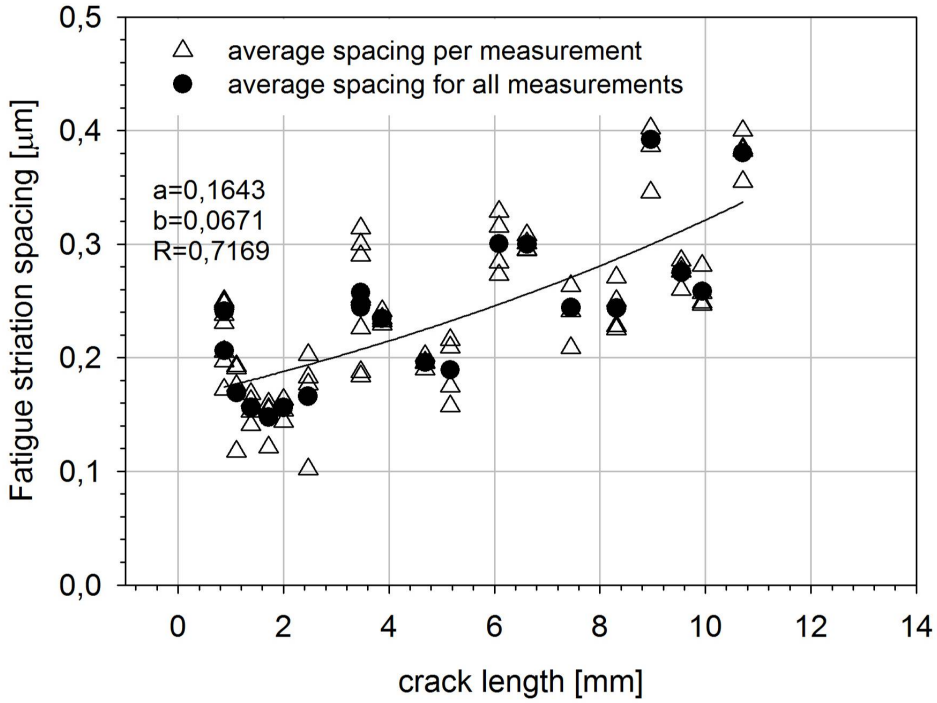


**Figure 215 - Fatigue striation spacing *vs.* crack length AA6061- T6 FS welded specimen.**

### *4.3.8 Concluding remarks*

Sound welds have been obtained using MIG, LBW and FSW for 3*mm* plate thickness of two aluminium alloys 6082-T6 and 6061-T6. Tensile testing of the weld joints and base material produced adequate tensile strength values.
Yield and rupture stress of friction stir welded and MIG welded specimens are lower than for base material. All welding processes lead to a decrease of the material mechanical properties, more pronounced in the MIG specimens. Detailed hardness examination revealed lower hardness values in the MIG welded specimens.
When compared with the friction stir welds and MIG welds, the laser beam welds presented the smaller area (width) affected by the welding process.
The friction stir welded 6061-T6 specimens presented lower lives than the friction stir 6082-T6 specimens when tested at stresses lower than 130*MPa*. Fatigue scatter is somewhat higher in the MIG welded specimens. Its fatigue lives are lower than friction stir welded specimen. The MIG welded 6061-T6 specimens presented higher fatigue lives than the MIG 6082-T6 specimens.
An increase of the crack propagation resistance, i.e. lower crack propagation rates, was verified for the welded material in comparison with the HAZ or even the base material.
The general microstructure was in good agreement with previous published researches. In friction stir welding the nugget has recrystallized grains smaller than the base material. A SEM analysis of fatigue striation measurements was performed for fatigue specimens of both welding processes and fatigue crack growth rate can be estimated using these measurements.

## 4.4 Conclusions

As a result of the work presented in this Chapter, the following conclusions may be reached:

- The influence of the FSW process on the fatigue life of the aluminium alloy 6063-T6 notched specimens was studied, and it was concluded that:
    - Hardness drastically decreases in the thermo-mechanically affected zone; the average hardness of the nugget zone is significantly lower than the base alloy;
    - Yield stress and rupture stress of friction stir welded specimens have lower values than un-welded specimens;
    - Welded notched specimens presented longer fatigue lives than similar geometry un-welded;
    - As a result of the fatigue specimens finite element analysis it was found that for all remote stress levels the notch stress concentration effect is more pronounced in the un-welded specimens, due to an earlier plastification of the area surrounding the notch in the welded specimens. It was verified that for stress levels below the friction stir welded material yield stress, elastic and plastic strain are of the same order of magnitude;
    - In the SEM examination features as welding defects were identified; nevertheless good fatigue properties were obtained.

- A study on friction stir butt welded plates of single material 6082-T6 and 6061-T6 were produced, and dissimilar joints of both alloys were also performed. It was found that:
    - The friction stir welded aluminium 6082-T6 material revealed lower yield and ultimate stresses, and the dissimilar joints displayed intermediate properties;
    - The hardness profile of the dissimilar joint presents the lowest values of all joints in the aluminium 6082-T6 alloy plate side where rupture occurred. Nevertheless in the nugget all three joints present similar values;
    - In the microstructure analysis of the dissimilar joint the mixture of the two alloys is easily identified by the different etching response of both alloys;
    - Residual stress profile was measured by a destructive process and compressive values were found in the plate weld surface. Maximum residual stress values reached 91,7$MPa$ at the root surface.

- When studying sound welds obtained using MIG, LBW and FSW for 3$mm$ plate thickness of two aluminium alloys 6082-T6 and 6061-T6 it was revealed that:
    - Tensile testing of the weld joints and base material produced adequate tensile strength values. Yield and rupture stress of friction stir welded and MIG welded specimens are lower than for base material;

- All welding processes lead to a decrease of the material mechanical properties, more pronounced in the MIG specimens. Detailed hardness examination revealed lower hardness values in the MIG welded specimens. When compared with the friction stir welds and MIG welds, the laser beam welds presented the smaller area (width) affected by the welding process;
- An increase of the fatigue crack propagation resistance, i.e. lower crack propagation rates, was verified for the welded material in comparison with the HAZ or even the base material;
- In friction stir welding the nugget has recrystallized grains smaller than the base material.

# Chapter 5

# Stress intensity factor calculation using 3D finite element models

Three-dimensional studies of the stress field ahead of a crack tip reveal a through the thickness variation that is systematically studied in this Chapter for the case of a centre cracked plate.
To study crack growth and to evaluate remaining life prediction of stiffened panels, rigorous numerical analysis have to be performed to compute stress intensity factors. In the literature there is still a lack of stress intensity factor solutions for the emerging integrally stiffened cracked panels. A study on three-dimensional stress intensity factor solutions for a cracked stiffened plate using the Finite Element Method is presented in this Chapter.

The work of Section 5.1 was presented at the 13th International Conference of Fracture Mechanics, Bacău, Romania, November 1–3, 2007: P M G P Moreira, Ş D Pastramă, P M S T de Castro, Three-dimensional stress field and stress intensity factor calibration for a central cracked plate.

The work of Section 5.2 was presented at the International Conference on Structural Analysis of Advanced Materials - ICSAM 2007, Patras, Greece, September 2-6, 2007: P M G P Moreira, S D Pastrama, P M S T de Castro, Three-dimensional stress intensity factor calibration for a stiffened cracked plate.

# 5. Stress intensity factor calculation using 3D finite element models

Stress intensity factor (SIF) values are essential ingredients of fatigue crack growth analyses. Notwithstanding the vast literature dedicated to SIF calculations, there remains a need for evaluating three-dimensional effects and, in particular, to compare two- and three-dimensional solutions. The purpose of this Chapter is to contribute to the understanding of the three-dimensional (3D) behaviour of cracked structures using the Finite Element Method (FEM) and as case studies a plate with a central crack and a cracked stiffened plate were analysed.

When studying a centre cracked plate, for the comparison of the three-dimensional solutions, further to reference solutions given by the literature, two-dimensional (2D) FEM and Dual Boundary Element Method (DBEM) [175] analyses were performed.

The J integral technique was used in the finite element method. Further to the J integral, the DBEM results were also obtained using the singularity subtraction technique (SST) [176].

The J integral is a contour integral, originally defined assuming non-linear elastic behaviour, introduced by Eshelby [177] and Rice [178]. The use of J integral in three-dimensional analysis to calculate the stress intensity factor has an advantage that neither plane stress nor plane strain need to be assumed. The J integral is widely accepted as a fracture mechanics parameter for both linear and non-linear material response. It is related to the energy release associated with crack growth and is also a measure of the intensity of deformation at a notch or crack tip, especially for non-linear materials. If the material response is linear, the J integral can be related to the stress intensity factors. ABAQUS provides a procedure for evaluating the $J$ integral based on the virtual crack extension/domain integral methods [147]. This parameter avoids the difficulties of the characterization of the stress field near the crack tip using local parameters such as the Crack Opening Displacement (COD), because its value is independent of the chosen contour $\Gamma$ surrounding the crack tip, Figure 216. The analytical definition of $J$ integral is given by the relationship

$$J = \int_{\Gamma} w \cdot dy - \overline{T} \frac{\partial \vec{u}}{\partial x} \partial s \qquad \textbf{(16)}$$

where $w$ is the strain energy density in points of the contour, $\overline{T}$ is the traction vector, $\vec{u}$ is the displacement and $ds$ the element of the contour $\Gamma$.

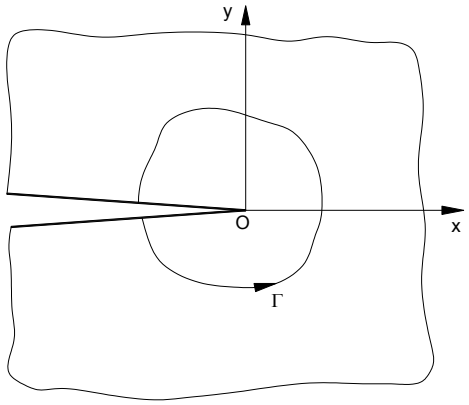


**Figure 216 - Contour used for the determination of J integral.**

For the calculation of the $J$ integral in a two-dimensional analysis using ABAQUS, the domain is described through rings of elements around the crack tip. Different contours (domains) are created. The first contour consists of the elements linked directly to the nodes of the crack tip. The following contour consists of a ring of elements in contact with the first. Each subsequent contour is defined by the next ring of elements. Even with coarse meshes it is possible to obtain precise values of $J$ integral, [178].

The stress intensity factors $K_I$, $K_{II}$ and $K_{III}$ are used in linear elastic fracture mechanics to characterize the local crack tip stress and displacement fields. They are related to the energy release rate (the $J$ integral) through

$$J = \frac{1}{8\pi} K^T \cdot B^{-1} \cdot K \qquad \textbf{(17)}$$

where $K=[K_I, K_{II}, K_{III}]^T$ are the stress intensity factors in mode I, II and III, and $B$ is called the pre-logarithmic energy factor matrix. For homogeneous, isotropic materials $B$ is diagonal, and the above equation simplifies to

$$J = \frac{1}{\overline{E}} \left( K_I^2 + K_{II}^2 \right) + \frac{1}{2G} K_{III}^2 \qquad \textbf{(18)}$$

where $\overline{E} = E$ for plane stress and $\overline{E} = E \Big/ \left(1 - \nu^2\right)$ for plane strain, axisymmetry, and three dimensions, [147].

According to the ABAQUS manual [147], stress intensity factor values obtained near the free surface should be neglected due to difficulties of $J$ integral calculation in this area. A solution to this issue is to refine the mesh near the

surface. In the three-dimensional analyses the stress intensity factor values obtained using only nodes in the outside surface of the plate were not taken into account.

When comparing a three-dimensional analysis with a two-dimensional one, attention should be given to the type of problem that is analysed: plane strain or plane stress. When a thin plate is loaded parallel to the plane of the plate and the load is distributed uniformly over the thickness the stress components $\sigma_z$, $\tau_{xz}$ and $\tau_{yz}$ are assumed to be zero, [179]. When the thickness of the body is very large, it is assumed that a plane strain state is present. In this case, $\gamma_{yz}$, $\gamma_{xz}$ and $\varepsilon_z$ are zero.

The singularity subtraction technique used in dual boundary element method uses a particular solution representing the singular field around the crack tip of a semi-infinite crack. Such a singular field is defined as the first term of the Williams eigenexpansion.

One point in front of the crack tip is considered in this technique, implemented in dual boundary element method in the post-processing phase [176]. The normal and shear stresses, denoted in Figure 217 as $t_I = \sigma$ and $t_{II} = \tau$ respectively, are calculated in an internal point at a distance $\varepsilon$ as close as possible to the crack tip.

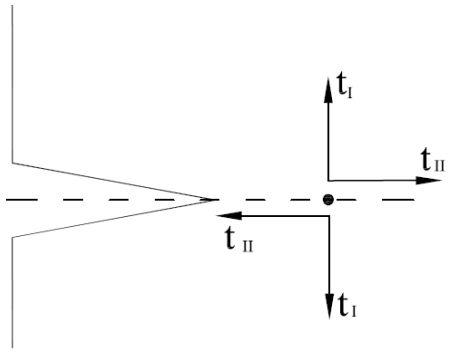


**Figure 217 - Tractions at a point.**

The stress intensity factors $K_I$ and $K_{II}$ are determined from equations (19),

$$K_I = t_I \sqrt{2\pi r} \qquad \textbf{(19)}$$
$$K_{II} = t_{II} \sqrt{2\pi r}$$

As shown in Figure 218, $s_p$ is a numerical approximation of the stress at an internal point placed at a distance $\in$ ahead of the crack tip.

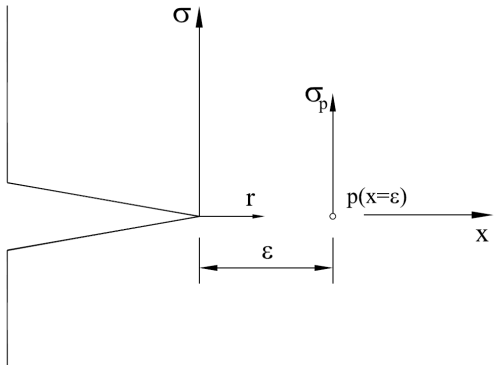


**Figure 218 - Stress $\sigma_p$ in a point p at a distance $\varepsilon$ of the crack tip.**

In equations (19), one must use a value of the distance $r$ for which that stress exists. Notice that $\epsilon$ and $r$ can have independent values, since they represent different approximations. The calibration of $r$ was carried out taking into account several reference cases with known values of stress intensity factors. In a previous work by de Matos *et al.* [176] the values which gave good results for a large variety of tested cases, were found to be $\epsilon = 0{,}0075 \cdot l_e$ and $r = 0{,}0011 \cdot l_e$, where $l_e$ is the length of the boundary element closest to the crack tip.

### 5.1 Plate with a central crack

The numerical investigations of cracked structures include both two-dimensional and three-dimensional analyses. The two-dimensional ones are simpler and, in most cases, have a reasonable degree of accuracy.
Since the state of deformation near the crack tip is always three-dimensional, as it was shown since the early work of Kassar *et al.* [180], three-dimensional analysis of cracked structures has been used extensively in the last years, in order to produce more accurate numerical solutions for the stress and strain fields around the crack tip.
The plate-like structures having different types of cracks were analyzed by many researchers. The first analysis of a plate of finite thickness containing a through crack was made by Hartranft *et al.* [181, 182] who obtained the stress distribution close to the crack front and made an attempt to determine the stress intensity factor distribution along the thickness. Further, other researchers have drawn their attention to this problem, with focus on the crack tip singularity and the stress behaviour in the boundary layers, at the intersection of the crack front with the free surface of the plate, see for example [183-185].
Three-dimensional analyses of thin cracked plates were presented by Nakamura *et al.* [186] and Shivakumar *et al.* [187], who performed refined three-dimensional finite element analyses in order to obtain stress distributions and stress intensity factor values. A detailed three-dimensional analysis was presented by Kwon *et al.* [188] who investigated the stress field near the crack tip, the degree of plane strain and the crack tip singularity.

In two-dimensional structural analyses, plane strain is commonly assumed where deformation is highly constrained, and plane stress is used for thin plates.

However, the state of deformation near the crack tip is always three-dimensional, and the use of two-dimensional Linear Elastic Fracture Mechanics (LEFM) should be examined.
In the this section, the effects of specimen geometry and mesh refinement on the stress intensity factor values through the thickness of centre cracked plates are presented. Whenever possible, these results are compared with stress intensity factor solutions found in the literature and/or with results from two-dimensional finite element method and two-dimensional dual boundary element method analyses. The drop of the stress intensity factor values at the intersection of the crack front with the free surface of the plate is discussed and the plane strain behaviour near the crack front and the variation of the opening stress (*i.e.* the stress in the load direction, $\sigma_y$) are also investigated.
The three-dimensional stress intensity factor results are presented in two different ways. In a first study, results for coordinates along the thickness are presented; each coordinate represents a layer of nodes. In the second study, using the three results of stress intensity factor for each element, and according to Figure 219 and equation (20), an average value of stress intensity factor is calculated. For the two-dimensional dual boundary element method analyses, stress intensity factors obtained using the J integral technique and the SST are presented.

$$K_{average} = \frac{K_A + 4K_B + K_C}{6} \qquad \textbf{(20)}$$

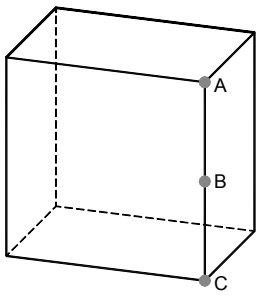


**Figure 219 - Average SIF for an element (crack front is line $\overline{AC}$ ).**

The several geometric configurations of a centre cracked plate are defined according to Figure 220. Note that the axis origin is defined at the middle thickness plane. The elastic constants $\nu$ = 0,3 and E = $21 \cdot 10^4$ *MPa*, were considered for all studied plates.

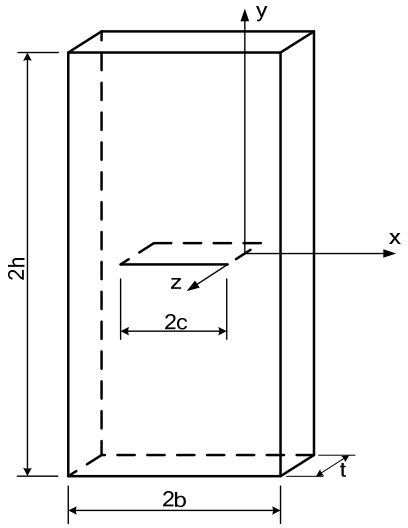


**Figure 220 - Plate with a central crack.**

Three different ratios of $h/b$ and $c/b$ were studied, as listed in Table 37. Also, in case 1 and case 3 different values of the ratio $t/c$ were analysed. Last column of Table 37 presents for each case the reference solutions that were used for comparison.

**Table 37 - The studied geometries of the plate**

| | $h/b$ | $c/b$ | $t/c$ | Reference value available in the literature |
|---|---|---|---|---|
| Case 1 | 0,5 | 0,5 | 0,5 | 3D FEM; 2D FEM and DBEM; literature |
| | | | 0,25 | 2D FEM and DBEM; literature |
| | | | 1 | |
| Case 2 | 2 | 1/3 | 1/5 | 2D FEM and DBEM; literature |
| Case 3 | 0,875 | 0,5 | 3 | 3D FEM; 2D FEM and DBEM; literature |
| | | | 0,75 | 2D FEM and DBEM; literature |
| | | | 1,5 | |
| | | | 6 | |

These geometries were selected because they were also analyzed by Newman *et al.* [189] and Atluri *et al.* [190]. These authors attempted to calculate numerically the stress intensity factor through the thickness without the assumption of plane strain or plane stress at the crack tip.
In the analysis of case 3, three-dimensional characteristics were discussed by investigating stress fields near the crack front and the degree of plane strain. The strain energy release rate and the stress intensity factor obtained from the three-dimensional analysis were compared with those from the two-dimensional analysis to study the validity of the two-dimensional LEFM in cracked plates.

### *5.1.1 Case 1 - Plate with a central crack h/b=0,5, c/b=0,5*

According to Tada *et al.* [191] the stress intensity factor for this case is 1,9145 (non-dimensional $K/\left(\sigma\sqrt{\pi c}\right)$).

For each plate thickness, a three-dimensional finite element analysis was carried out. Also, for this configuration, two-dimensional finite element and dual boundary element analyses were performed. For the two-dimensional dual boundary element analysis, stress intensity factors obtained using the J integral technique and the SST are presented.

Table 38 shows results of stress intensity factor obtained in the two-dimensional analyses using the dual boundary element method and the finite element method. For the two-dimensional finite element analysis, 6840 CPE8 elements (eight nodded isoparametric quadrilateral elements) were used, while for the dual boundary element analysis the mesh contained only 60 elements.

**Table 38 - 2D results, FEM and DBEM**

| Tada [191] | FEM (J integral) | | DBEM (J integral) | | DBEM (SST) | |
|---|---|---|---|---|---|---|
| | solution | Difference % | solution | Difference [%] | solution | Difference [%] |
| 1,9145 | 1,9651 | 2,64 | 1,9884 | 3,86 | 1,9480 | 1,75 |

The three-dimensional stress intensity factor, results are presented in two different ways. In the first study, results for 7 coordinates along the thickness are presented, each coordinate corresponding to a node. In the second study, using the three results of stress intensity factor for each element, and according to Figure 219 and equation (20), an average value of stress intensity factor is calculated. The stress intensity factor value is presented non-dimensionally according to (21).

$$K/\left(\sigma\sqrt{\pi c}\right) \quad \textbf{(21)}$$

To obtain the stress intensity factor for the three-dimensional analysis, a mesh with 19440 elements and another with 67200 elements were used in all cases. Only half of the plate was modelled. In the first mesh, 6 elements were used along the thickness and in the second mesh 16 elements were used along the thickness. The plates were modelled with 20-nodes brick isoparametric elements (C3D20); these elements use quadratic interpolation and are called quadratic elements or second-order elements.

#### *5.1.1.1 Plate with a central crack h/b=0,5, c/b=0,5 and t/c=0,5*

In this case a centre crack tension specimen, Figure 220, with h/b=0,5, c/b=0,5 and t/c=0,5 was analyzed. Newman *et al.* present in [189] stress intensity factors solutions for the same geometry. The geometry was defined with the values presented in Table 39.

**Table 39 - Geometry, [units of length]**

| 2b | 2h | t | 2c |
|---|---|---|---|
| 60 | 30 | 7,5 | 30 |

Figure 221 presents a detail of the less refined mesh showing the $\sigma_y$ stress distribution in the load direction when a remote stress of 100 units is applied.

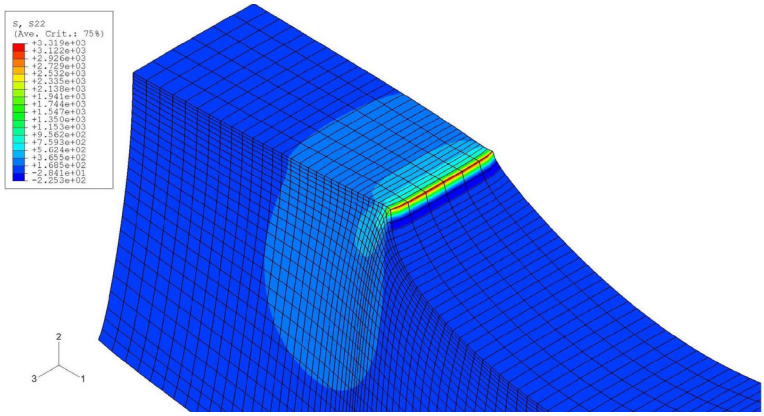

**Figure 221 - 3D 19440 elements $\sigma_y$ mesh detail (1/4 of the plate is represented).**

Table 40 and Table 41 show the values of non-dimensional stress intensity factor along the thickness for the different meshes used. Difference [%] relates finite element three-dimensional results with the results found in the literature, and it is defined as,

$$Difference[\%] = \frac{result - reference\,value}{reference\,value} \times 100 \qquad \textbf{(22)}$$

**Table 40 - Non-dimensional 3D FEM SIF along the thickness, 19440 elements mesh**

| Node layer | z/t | $K/\left(\sigma\sqrt{\pi c}\right)$ | Tada [191] | Difference [%] |
|---|---|---|---|---|
| 1 (free surface) | 0,5000 | 1,8297 | 1,9145 | -4,432 |
| 2 | 0,4167 | 2,0059 | | 4,775 |
| 3 | 0,3333 | 2,0613 | | 7,667 |
| 4 | 0,2500 | 2,0700 | | 8,123 |
| 5 | 0,1667 | 2,0817 | | 8,732 |
| 6 | 0,0833 | 2,0831 | | 8,808 |
| 7 (half thickness) | 0,0000 | 2,0846 | | 8,884 |

**Table 41 - Non-dimensional 3D FEM SIF along the thickness, 67200 elements mesh**

| Node layer | z/t | $K/\left(\sigma\sqrt{\pi c}\right)$ | Tada [191] | Difference [%] |
|---|---|---|---|---|
| 1 (free surface) | 0,5000 | 1,7189 | 1,9145 | -10,215 |
| 3 | 0,4375 | 1,9986 | | 4,395 |
| 5 | 0,3750 | 2,0423 | | 6,677 |
| 7 | 0,3125 | 2,0613 | | 7,667 |
| 9 | 0,2500 | 2,0729 | | 8,275 |
| 11 | 0,1875 | 2,0788 | | 8,427 |
| 13 | 0,1250 | 2,0831 | | 8,656 |
| 15 | 0,0625 | 2,0846 | | 8,809 |
| 17 (half thickness) | 0,0000 | 2,0846 | | 8,884 |

A comparative plot of the percent differences between Tada [191] and three-dimensional finite element as a function of z/t for both meshes is presented in Figure 222. In this case the use of a more refined mesh is useless; the difference with respect to the reference solution is similar for both meshes.

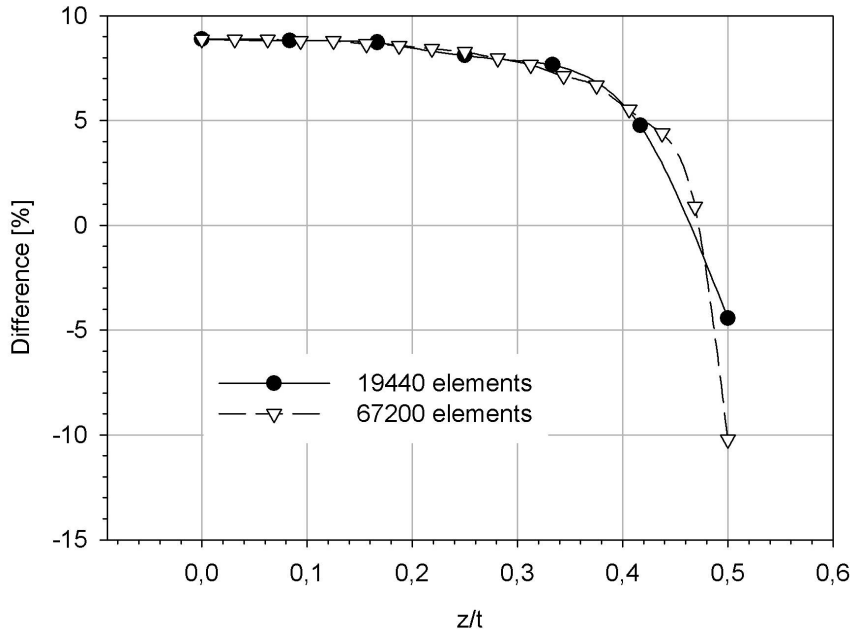


**Figure 222 - Comparative plot of the % differences between Tada [191] and FEM as a function of the coordinate z/t for both meshes.**

Figure 223 shows the values of non-dimensional stress intensity factor along the thickness for the different meshes used. Three-dimensional reference solutions were found in Newman *et al.* [189], including Atluri *et al.* [190] results.

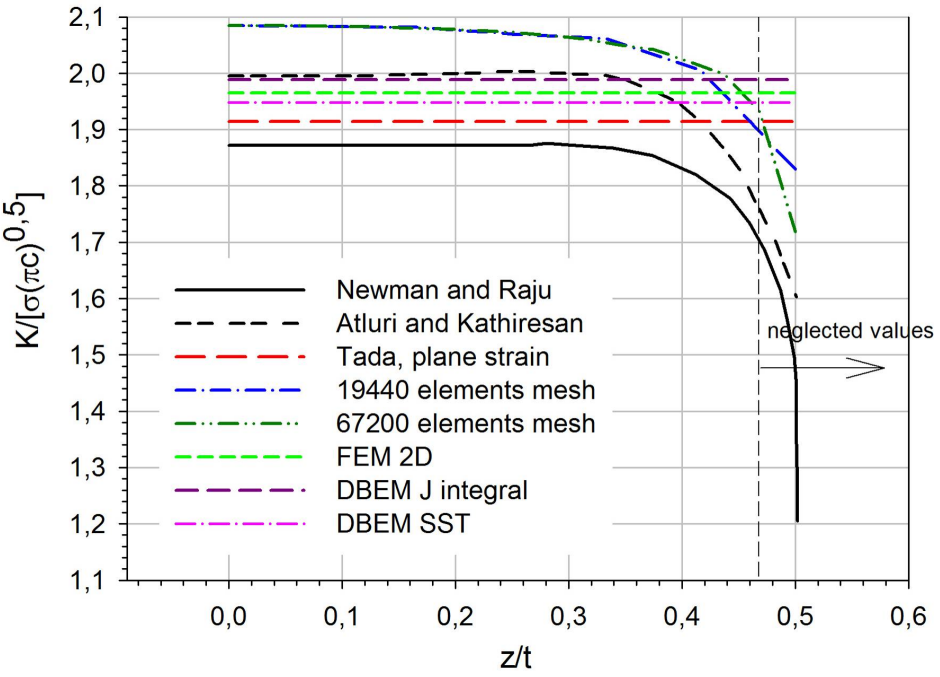


**Figure 223 - Non-dimensional SIF along thickness.**

Table 42 presents values of non-dimensional stress intensity factor in each element along the thickness at a crack tip for the 19440 elements mesh. Layer 1 contains elements on the surface; since the external nodes layer is averaged with the other two subsequent layers of nodes, the stress intensity factor were not disregarded. Stress intensity factors obtained using the three-dimensional finite element analyses are compared with Tada [191] and dual boundary element SST results. Dual boundary element results present the best agreement with finite element three-dimensional results.

**Table 42 - 3D FEM $K/\left(\sigma\sqrt{\pi c}\right)$, 19440 elements mesh**

| Element layer | FEM 3D | Tada [191] | | DBEM SST | |
|---|---|---|---|---|---|
| | | solution | Difference [%] | solution | Difference [%] |
| 1<br>free surface | 1,9858 | 1,9145 | 3,723 | 1,9884 | -0,132 |
| 2 | 2,0705 | | 8,148 | | 4,129 |
| 3<br>half thickness | 2,0831 | | 8,808 | | 4,764 |

*5.1.1.2 Plate with a central crack h/b=0,5, c/b=0,5 and t/c=0,25*

In this case a centre crack tension specimen with h/b=0,5, c/b=0,5 and t/c=0,25 was analyzed. A three-dimensional stress intensity factor solution for this geometry could not be found in the literature. The geometry was defined with the values presented in Table 43.

**Table 43 - Geometry, [units of length]**

| 2b | 2h | t | 2c |
|---|---|---|---|
| 60 | 30 | 3,75 | 30 |

Table 44 and Table 45 show the values of non-dimensional stress intensity factor along the thickness for the different meshes used.

A comparative plot of the percent differences between Tada [191] and finite element as a function of z/t for both meshes is presented in Figure 224.

**Table 44 - Non-dimensional 3D FEM SIF along thickness, 19440 elements mesh**

| Node layer | z/t | $K/\left(\sigma\sqrt{\pi c}\right)$ | Tada [191] | Difference [%] |
|---|---|---|---|---|
| 1 (free surface) | 0,5000 | 1,8122 | 1,9145 | -5,345 |
| 2 | 0,4167 | 2,0074 | | 4,851 |
| 3 | 0,3333 | 2,0642 | | 7,819 |
| 4 | 0,2500 | 2,0744 | | 8,351 |
| 5 | 0,1667 | 2,0875 | | 9,036 |
| 6 | 0,0833 | 2,0890 | | 9,112 |
| 7 (half thickness) | 0,0000 | 2,0919 | | 9,264 |

**Table 45 - Non-dimensional 3D FEM SIF along thickness, 67200 elements mesh**

| Node layer | z/t | $K/\left(\sigma\sqrt{\pi c}\right)$ | Tada [191] | Difference [%] |
|---|---|---|---|---|
| 1 (free surface) | 0,5000 | 1,6884 | 1,9145 | -11,812 |
| 3 | 0,4375 | 1,9957 | | 4,243 |
| 5 | 0,3750 | 2,0453 | | 6,830 |
| 7 | 0,3125 | 2,0642 | | 7,819 |
| 9 | 0,2500 | 2,0773 | | 8,504 |
| 11 | 0,1875 | 2,0846 | | 8,656 |
| 13 | 0,1250 | 2,0890 | | 8,960 |
| 15 | 0,0625 | 2,0904 | | 9,188 |
| 17 (half thickness) | 0,0000 | 2,0919 | | 9,264 |

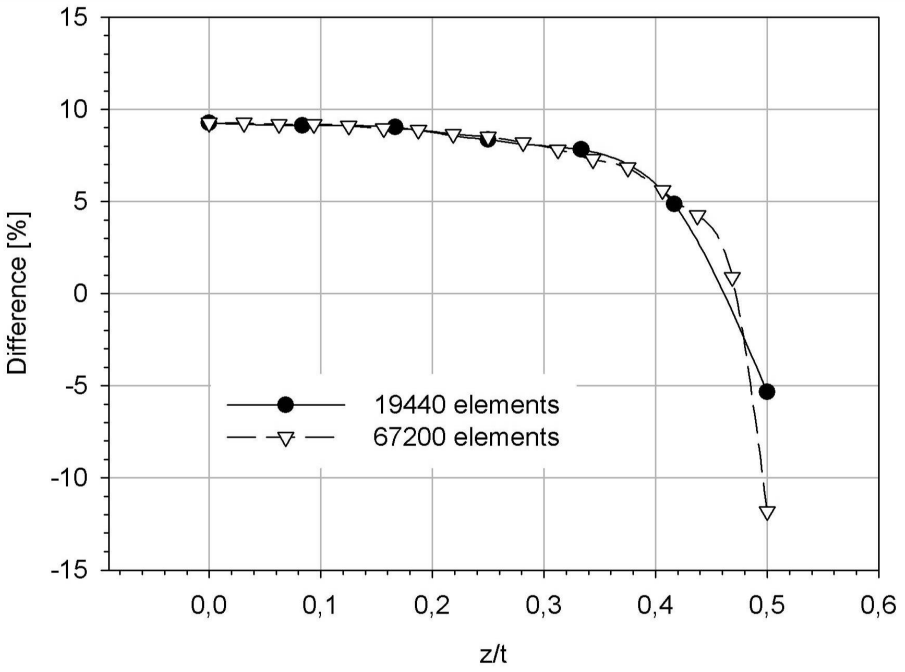


**Figure 224 - Comparative plot of the % differences between Tada [191] and FEM as a function of z/t for both meshes.**

Figure 225 shows the values of non-dimensional stress intensity factor along the thickness for the different meshes used, dual boundary element J integral and SST analysis, and finite element two-dimensional analysis.

Table 46 presents values of non-dimensional stress intensity factor in each element along the thickness at the crack tip for the 19440 elements mesh. Since the external nodes layer is averaged with the other two subsequent layers of nodes, the stress intensity factor were not disregarded. Stress intensity factors obtained using the three-dimensional finite element analyses are compared with Tada [191] and dual boundary element SST results. Again, dual boundary element results show a good agreement with finite element three-dimensional results.

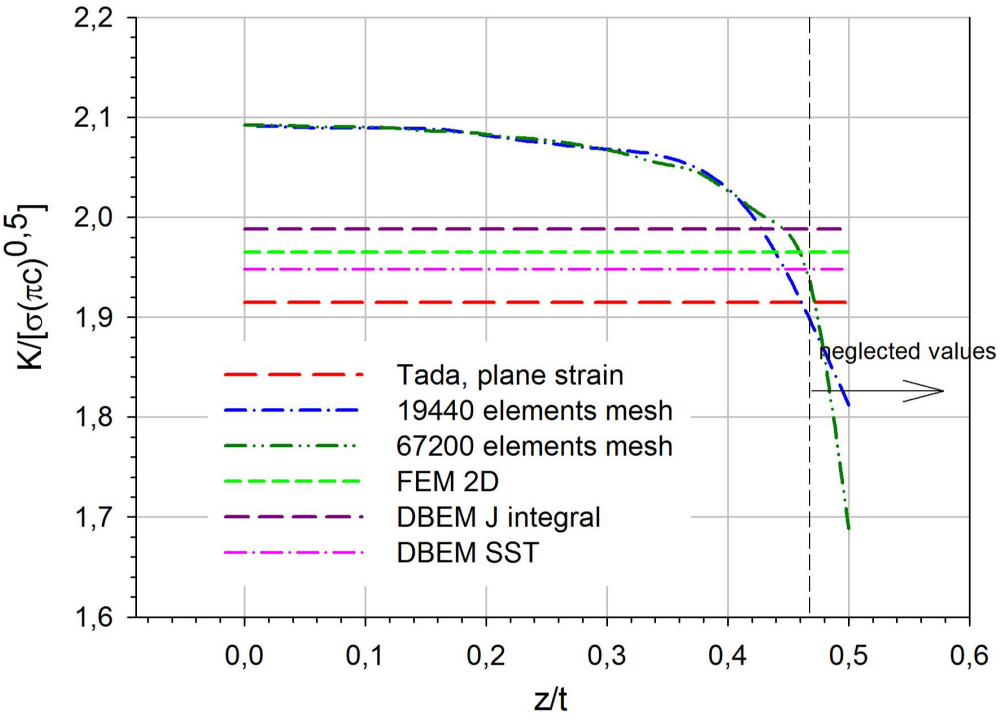


**Figure 225 - Non-dimensional SIF along thickness.**

**Table 46 - 3D FEM $K/\left(\sigma\sqrt{\pi c}\right)$, 19440 elements mesh**

| Element layer | FEM 3D | Tada [191] | | DBEM SST | |
|---|---|---|---|---|---|
| | | ref value | Difference [%] | solution | Difference [%] |
| 1<br>free surface | 1,9843 | 1,9145 | 3,646 | 1,9884 | -0,206 |
| 2 | 2,0749 | | 8,377 | | 4,349 |
| 3<br>half thickness | 2,0892 | | 9,125 | | 5,069 |

*5.1.1.3 Plate with a central crack h/b=0,5, c/b=0,5 and t/c=1*

In this case a centre crack tension specimen with h/b=0,5, c/b=0,5 and t/c=1 was analyzed. A three-dimensional stress intensity factor solution for this geometry could not be found in the literature. The geometry was defined with the values presented in Table 47.

**Table 47 - Geometry, [units of length]**

| 2b | 2h | t | 2c |
|---|---|---|---|
| 60 | 30 | 15 | 30 |

Figure 226 presents a detail of the less refined mesh showing the stress $\sigma_y$ distribution in the load direction when a remote stress of 100 units is applied.

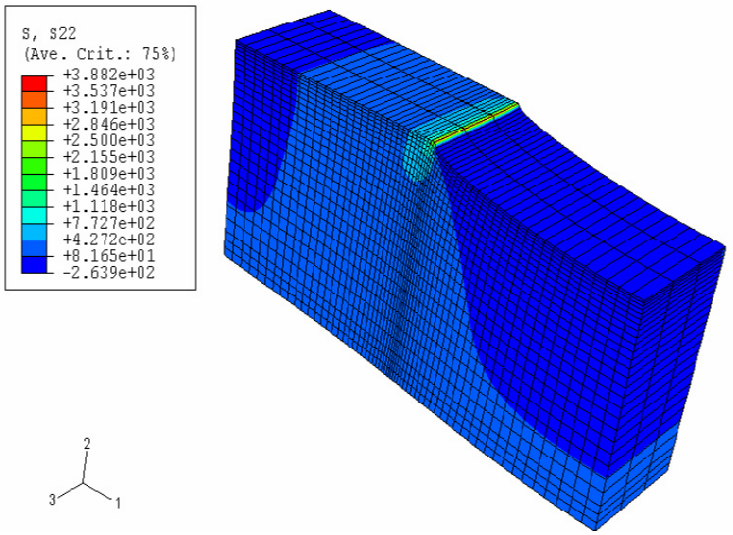


**Figure 226 - 3D 19440 elements $\sigma_y$ (S22) mesh detail (1/8 of the plate is represented).**

Table 48 and Table 49 show the values of non-dimensional stress intensity factor along the thickness for the different meshes used.

**Table 48 - Non-dimensional 3D FEM SIF along thickness, 19440 elements mesh**

| Node layer | z/t | $K/\left(\sigma\sqrt{\pi c}\right)$ | Tada [191] | Difference [%] |
|---|---|---|---|---|
| 1 (free surface) | 0,5000 | 1,8500 | 1,9145 | -3,367 |
| 2 | 0,4167 | 2,0074 | | 4,851 |
| 3 | 0,3333 | 2,0554 | | 7,362 |
| 4 | 0,2500 | 2,0554 | | 7,362 |
| 5 | 0,1667 | 2,0627 | | 7,743 |
| 6 | 0,0833 | 2,0613 | | 7,667 |
| 7 (half thickness) | 0,0000 | 2,0613 | | 7,667 |

**Table 49 - Non-dimensional 3D FEM SIF along thickness, 67200 elements mesh**

| Node layer | z/t | $K/\left(\sigma\sqrt{\pi c}\right)$ | Tada [191] | Difference [%] |
|---|---|---|---|---|
| 1 (free surface) | 0,5000 | 1,7510 | 1,9145 | -8,541 |
| 3 | 0,4375 | 2,0074 | | 4,851 |
| 5 | 0,3750 | 2,0394 | | 6,525 |
| 7 | 0,3125 | 2,0525 | | 7,210 |
| 9 | 0,2500 | 2,0584 | | 7,514 |
| 11 | 0,1875 | 2,0598 | | 7,590 |
| 13 | 0,1250 | 2,0613 | | 7,667 |
| 15 | 0,0625 | 2,0627 | | 7,743 |
| 17 (half thickness) | 0,0000 | 2,0627 | | 7,743 |

A comparative plot of the percent differences between Tada [191] and finite element as a function of z/t for both meshes is presented in Figure 227.

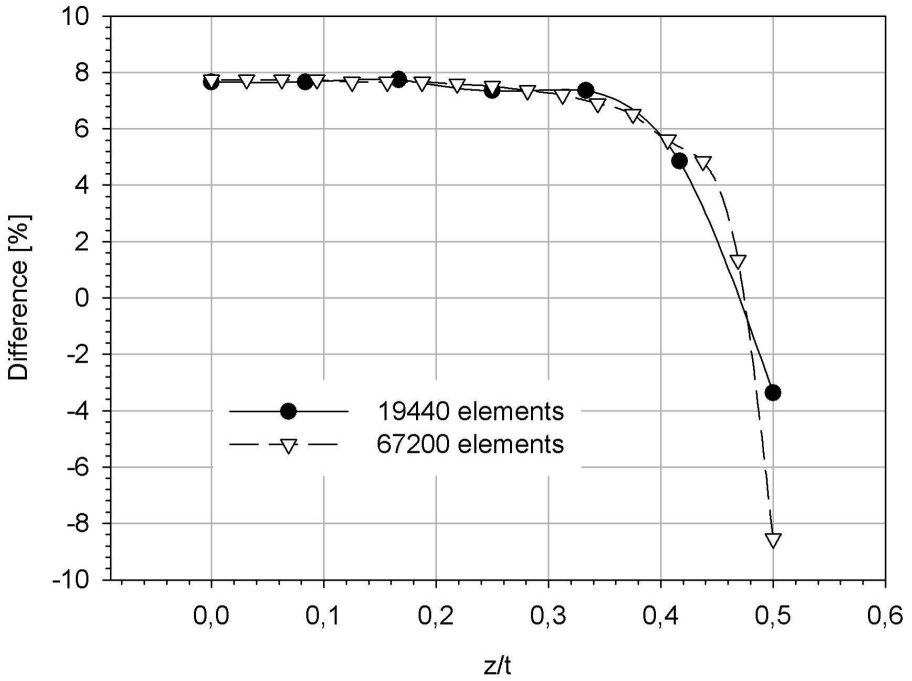


**Figure 227 - Comparative plot of the % differences between Tada [191] and FEM as a function of z/t for both meshes.**

Figure 228 shows the values of non-dimensional stress intensity factor along the thickness for the different meshes used, dual boundary element J integral and SST analysis and finite element two-dimensional analysis.

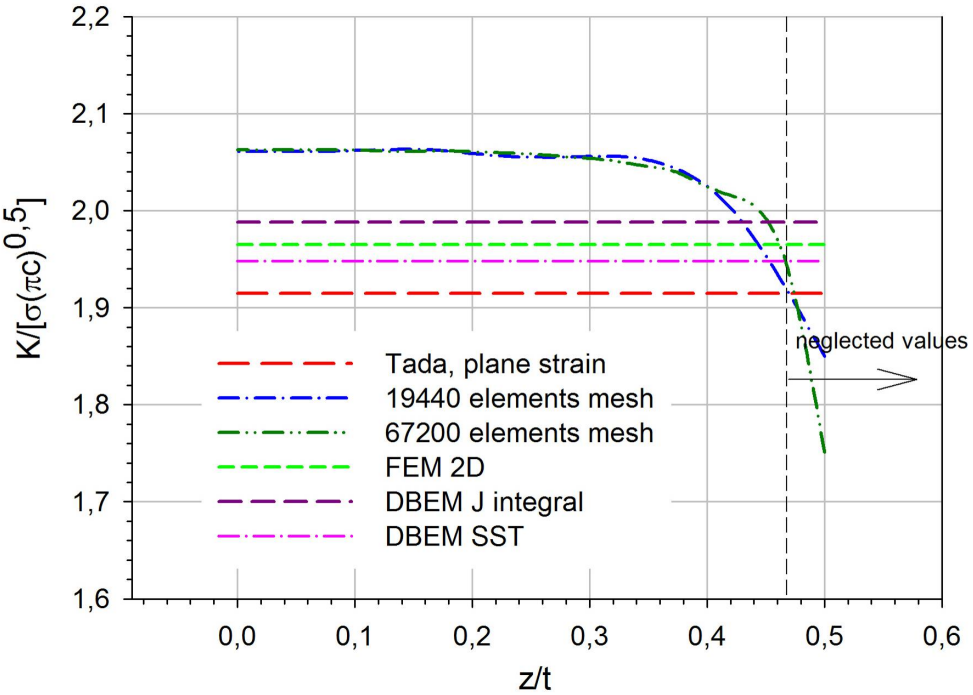


**Figure 228 - Non-dimensional SIF along thickness.**

Table 50 presents values of non-dimensional stress intensity factor in each element along the thickness at a crack tip for the 19440 elements mesh. Layer 1

contains elements on the surface; since the external nodes layer is averaged with the other two subsequent layers of nodes, the stress intensity factor were not disregarded. Stress intensity factors obtained using the three-dimensional FEM analyses are compared with Tada [191] and DBEM SST results. DBEM results show a good agreement with FEM three-dimensional results.

**Table 50 - 3D FEM $K/\left(\sigma\sqrt{\pi c}\right)$, 19440 elements mesh**

| Element layer | FEM 3D | Tada [191] | | DBEM SST | |
|---|---|---|---|---|---|
| | | ref value | Difference [%] | solution | Difference [%] |
| 1<br>free surface | 1,9892 | 1,9145 | 3,90 | 1,9884 | 0,04 |
| 2 | 2,0567 | | 7,43 | | 3,43 |
| 3<br>half thickness | 2,0615 | | 7,68 | | 3,68 |

*5.1.1.4 Discussion of results*

A comparison between the three-dimensional stress intensity factor results obtained for the several plate thickness and the two-dimensional reference results is presented in Figure 229. The difference between each three-dimensional FEM stress intensity factor result and the two-dimensional DBEM J integral result is presented in Figure 230.

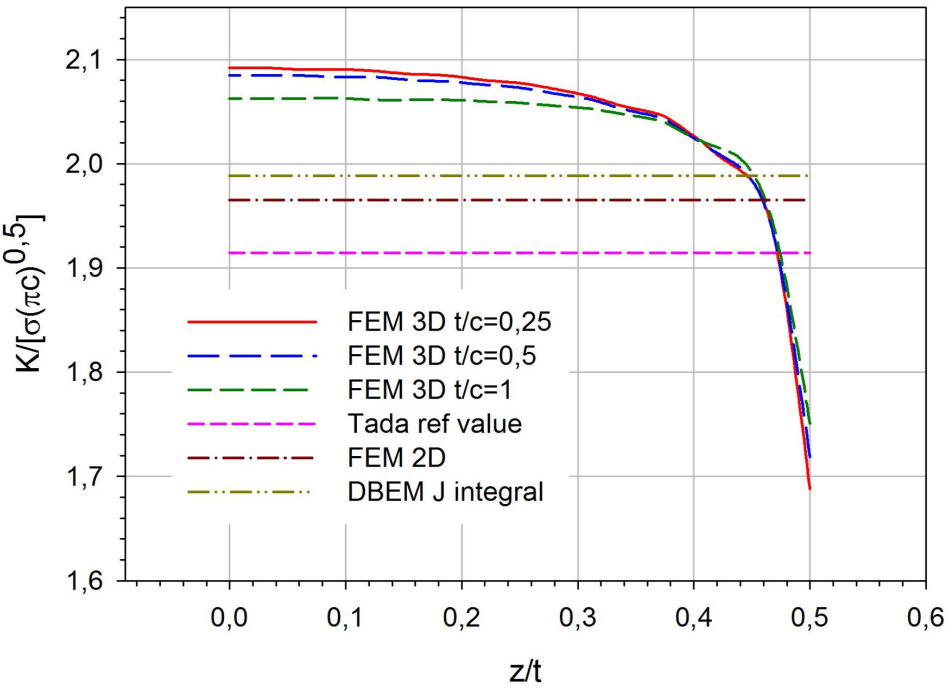


**Figure 229 - Non-dimensional SIF for each studied plate thickness.**

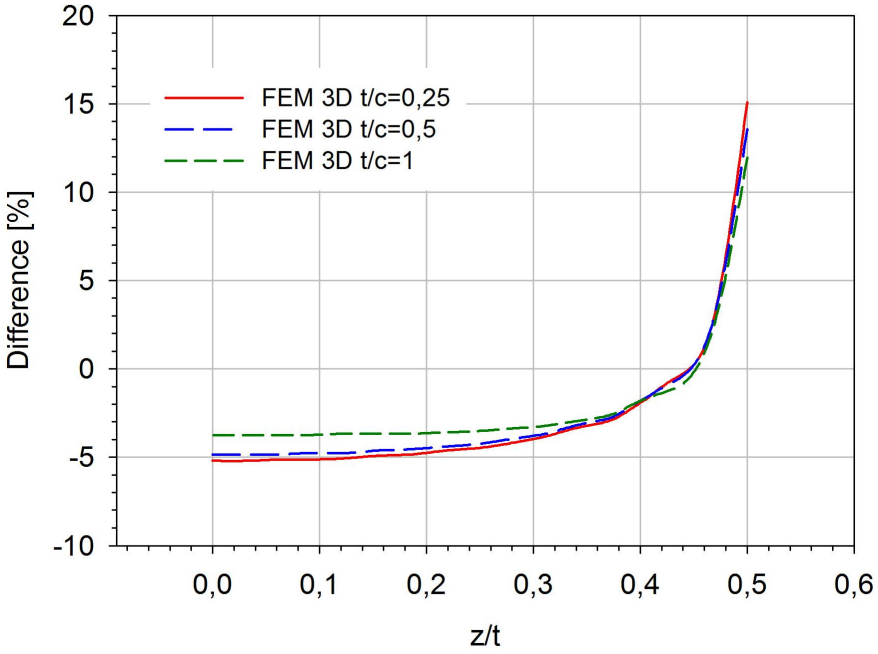


**Figure 230 - Difference between the 3D FEM SIF for each plate thickness and the 2D DBEM J integral result.**

### *5.1.2 Case 2 - Plate with a central crack h/b=2, c/b=1/3 and t/c=1/5*

In this case a cracked plate with h/b=2, c/b=1/3 and t/c=1/5 was analyzed. This geometry can be considered to be a thin plate, plane stress analysis. According to Tada [191] the stress intensity factor $K/\left(\sigma\sqrt{\pi c}\right)$ (non-dimensional) for this case is 1,0724. The geometry was defined with the dimensions presented in Table 51.

**Table 51- Geometry, [units of length]**

| 2b | 2h | t | 2c |
|---|---|---|---|
| 60 | 120 | 2 | 20 |

A detailed two-dimensional finite element analysis of stress intensity factor solutions for this geometry was reported in [192]. The mesh used in this previous work is presented in Figure 231.
Table 52 presents stress intensity factor solution obtained in [192] as a function of the number of elements used to model a quarter of the plate. ABAQUS was also used in this study. In this table, *qnq* stands for quarter node point technique.

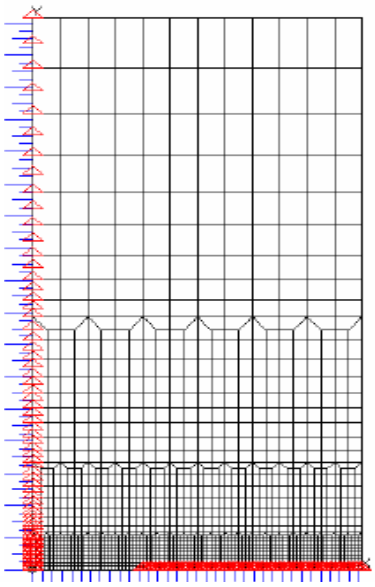

**Figure 231 - Detail of a 2D mesh used in [192]. Because of symmetry, only ¼ of the plate was modelled.**

**Table 52 - Non-dimensional SIF obtained in the 2D analysis [192]**

| Mesh type | Elements | $K/\left(\sigma\sqrt{\pi c}\right)$ | Tada [191] | Difference [%] |
|---|---|---|---|---|
| very coarse | 300 | 1,0658 | 1,9145 | -0,61 |
| coarse | 600 | 1,0677 | | -0,43 |
| refined | 1704 | 1,0720 | | 1,07 |
| refined and qnp | 1704 | 1,0734 | | 0,09 |

In the present work, three different analyses were performed: three-dimensional finite element, two-dimensional finite element and two-dimensional dual boundary element. To obtain the stress intensity factor in the three-dimensional analysis, two meshes with different number of elements were used, one with 27000 elements and another with 36480 elements. Only half of the plate was modelled with 20-nodes brick isoparametric elements (C3D20). In the coarse mesh, 3 elements were used along the thickness while in the other mesh 8 elements were placed along the thickness.

For the two-dimensional finite element method analysis 7800 CPE8 elements were used, and for the dual boundary element method analysis only 60 elements were used.

Figure 232 presents a detail of the 2700 elements mesh representing the von Mises stress distribution when a remote stress of 120 units is applied.

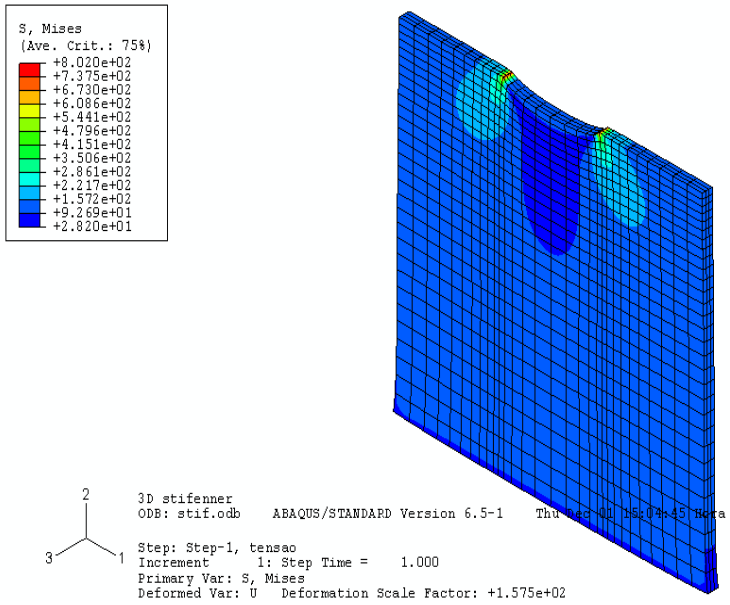


**Figure 232 - 3D mesh detail, von Mises stress for 120 units of remote stress.**

Table 53 and Table 54 show the values of non-dimensional K along the thickness for both three-dimensional meshes.

**Table 53 - Non-dimensional 3D FEM SIF along thickness, 2700 elements mesh**

| Nodes layer | z/t | $K/\left(\sigma\sqrt{\pi c}\right)$ | Tada [191] | Difference [%] |
|---|---|---|---|---|
| 1 (free surface) | 0,5000 | 0,9663 | 1,0724 | 11,95 |
| 2 | 0,3333 | 1,1311 | | -6,61 |
| 3 | 0,1667 | 1,1334 | | -6,86 |
| 4 (half thickness) | 0,0000 | 1,1424 | | -7,88 |

**Table 54 - Non-dimensional 3D FEM SIF along thickness, 36480 elements mesh**

| Nodes layer | z/t | $K/\left(\sigma\sqrt{\pi c}\right)$ | Tada [191] | Difference [%] |
|---|---|---|---|---|
| 1 (free surface) | 0,5000 | 0,8883 | 1,0724 | 20,72 |
| 2 | 0,4375 | 1,1090 | | -4,12 |
| 3 | 0,3750 | 1,1023 | | -3,36 |
| 4 | 0,3125 | 1,1331 | | -6,83 |
| 5 | 0,2500 | 1,1426 | | -7,90 |
| 6 | 0,1875 | 1,1430 | | -7,95 |
| 7 | 0,1250 | 1,1457 | | -8,25 |
| 8 | 0,0625 | 1,1467 | | -8,37 |
| 9 (half thickness) | 0,0000 | 1,1472 | | -8,42 |

Table 55 shows results of stress intensity factor obtained in the two-dimensional analysis using the dual boundary element and the finite element methods.

**Table 55 - 2D results, FEM and DBEM**

| Tada [191] | FEM (J integral) | | DBEM (J integral) | | DBEM (SST) | |
|---|---|---|---|---|---|---|
| | solution | Difference % | solution | Difference [%] | solution | Difference [%] |
| 1,0724 | 1,0730 | -0,06 | 1,0787 | -0,58 | 1,0544 | 1,68 |

Figure 233 shows the values of non-dimensional stress intensity factor along the thickness for the different meshes and analyses carried out.

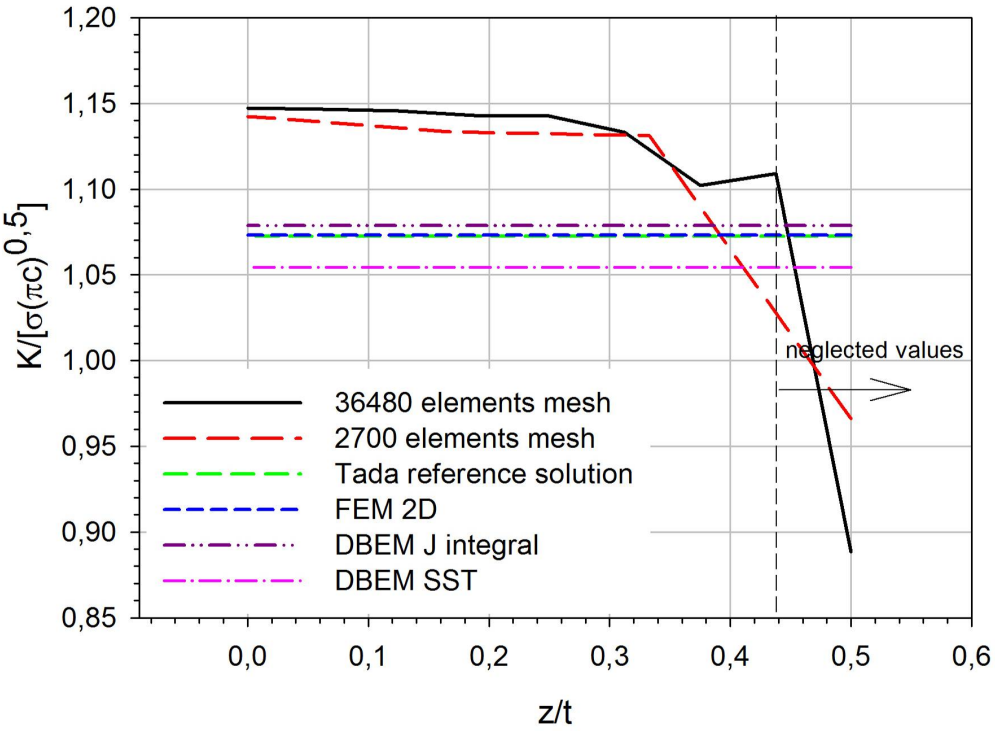


**Figure 233 - Non-dimensional SIF along thickness.**

Table 56 and Table 57 present the values of non-dimensional three-dimensional finite element method stress intensity factor in the elements of each mesh. In the 2700 elements mesh, the elements layer 1 lay on the surface (since the external nodes layer is averaged with the other two subsequent layers of nodes the stress intensity factor were not disregarded), and element 2 is the elements layer in the middle of the plate. For the 36480 elements mesh, elements layer 1 is the surface layer.

**Table 56 - 3D FEM $K/\left(\sigma\sqrt{\pi c}\right)$, 2700 elements mesh**

| Elements layer | $K/\left(\sigma\sqrt{\pi c}\right)$ | Tada [191] | Difference (%) |
|---|---|---|---|
| 1 (free surface) | 1,1040 | 1,0724 | -2,95 |
| 2 (half thickness) | 1,1394 | | 6,25 |

**Table 57 - 3D FEM $K/\left(\sigma\sqrt{\pi c}\right)$, 36480 elements mesh**

| Elements layer | $K/\left(\sigma\sqrt{\pi c}\right)$ | Tada [191] | Difference (%) |
|---|---|---|---|
| 1 (free surface) | 1,0711 | 1,0724 | 0,12 |
| 2 | 1,1296 | | 5,33 |
| 3 | 1,1434 | | 6,62 |
| 4 (half thickness) | 1,1466 | | 6,92 |

A comparative plot of the percent differences between Tada [191] and finite element results as a function of the coordinate z/t for both meshes is presented in Figure 234.

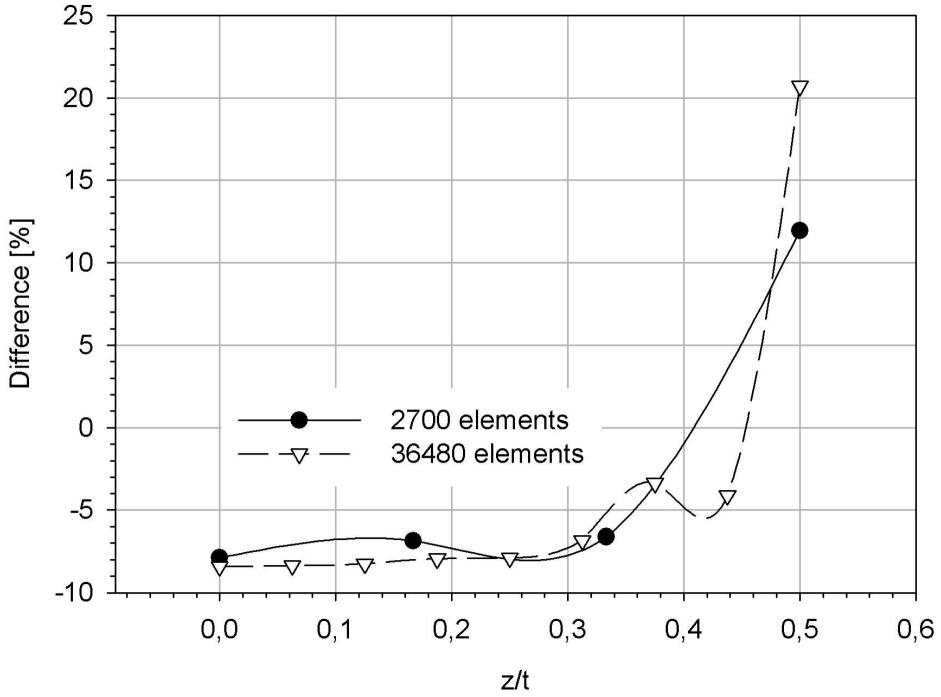


**Figure 234 - Comparative plot of the % differences between Tada [191] and FEM as a function of the coordinate z/t for both meshes.**

### *5.1.3 Case 3 - Plate with a central crack h/b=0,875, c/b=0,5*

According to Tada *et al.* [191], the stress intensity factor for this case is 1,4220 (non-dimensional $K/\left(\sigma\sqrt{\pi c}\right)$). For this configuration two-dimensional FEM and DBEM analyses were performed. For the two-dimensional DBEM analysis, stress intensity factors obtained using the J integral technique and the SST are presented. Table 58 shows results of stress intensity factor obtained in the two-dimensional analysis using the DBEM and the FEM.

**Table 58 - 2D results, FEM and DBEM**

| Tada [191] | FEM (J integral) | | DBEM (J integral) | | DBEM (SST) | |
|---|---|---|---|---|---|---|
| | solution | Difference % | solution | Difference [%] | solution | Difference [%] |
| 1,4220 | 1,4223 | 0,02 | 1,4350 | 0,92 | 1,4001 | -1,54 |

Also, for each thickness configuration a three-dimensional FEM analysis was carried out. To obtain the stress intensity factor for the three-dimensional analysis, a mesh with 51072 elements and another with 67200 elements were used; the same number of elements were used along the plate thickness but with different refinements in the plate surface. Only half of the plate was modelled using 12 elements along the its thickness. To model the plate, 20-nodes brick isoparametric elements (C3D20) were used. For the two-dimensional FEM analysis, 8760 CPE8 elements were used, while the DBEM analysis was performed with a mesh of only 60 elements. The stress intensity factor value is presented non-dimensionally according to equation (21).

*5.1.3.1 Plate with a central crack h/b=0,875, c/b=0,5 and t/c=3*

In this case, a centre crack tension specimen with h/b=0,875, c/b=0,5 and t/c=3 was analyzed. Three-dimensional stress intensity factors solutions were found in the literature for this configuration, [189]. The geometry was defined with the values presented in Table 59.

**Table 59 - Geometry, [units of length]**

| 2b | 2h | t | 2c |
|---|---|---|---|
| 60 | 52,5 | 45 | 30 |

Since the plate can be considered as thick, a plane strain state is expected to be found in the middle plane and a plane stress state is expected near the external surface. Table 60 shows the values of non-dimensional stress intensity factor along the thickness for the different meshes used.

Figure 235 shows the values of non-dimensional stress intensity factor along the thickness for the different meshes used.

**Table 60 - Non-dimensional 3D FEM SIF along thickness**

| Node layer | z/t | $K/\left(\sigma\sqrt{\pi c}\right)$ | | Tada [191] | Difference [%] | |
|---|---|---|---|---|---|---|
| | | 51072 elem mesh | 67200 elem mesh | | 51072 elem mesh | 67200 elem mesh |
| 1 free surface | 0,5000 | 1,3909 | 1,3804 | 1,4220 | -2,188 | -2,926 |
| 3 | 0,4583 | 1,5252 | 1,5237 | | 7,257 | 7,155 |
| 5 | 0,4167 | 1,5165 | 1,5194 | | 6,643 | 6,847 |
| 7 | 0,3750 | 1,5004 | 1,5077 | | 5,516 | 6,028 |
| 9 | 0,3333 | 1,4844 | 1,4931 | | 4,389 | 5,004 |
| 11 | 0,2917 | 1,4698 | 1,4800 | | 3,364 | 4,082 |
| 13 | 0,2500 | 1,4582 | 1,4684 | | 2,545 | 3,262 |
| 15 | 0,2083 | 1,4473 | 1,4582 | | 1,777 | 2,545 |
| 17 | 0,1667 | 1,4391 | 1,4487 | | 1,203 | 1,879 |
| 19 | 0,1250 | 1,4328 | 1,4413 | | 0,762 | 1,357 |
| 21 | 0,0833 | 1,4283 | 1,4353 | | 0,445 | 0,937 |
| 23 | 0,0417 | 1,4257 | 1,4308 | | 0,260 | 0,619 |
| 25 half thickness | 0,0000 | 1,4248 | 1,4276 | | 0,199 | 0,394 |

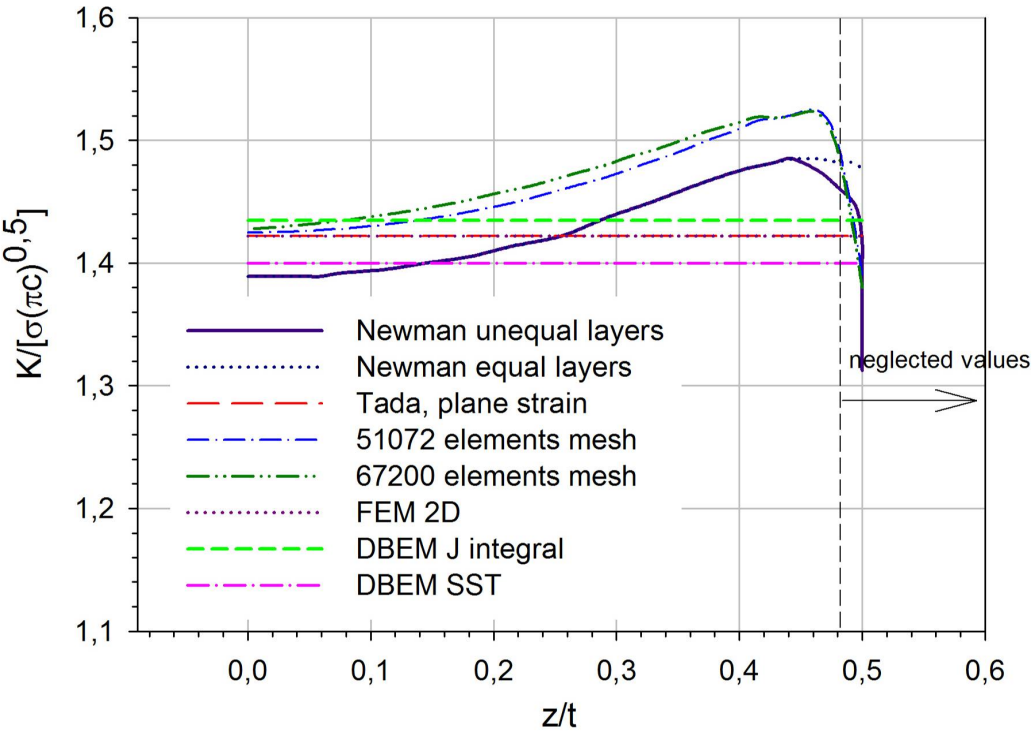


**Figure 235 - Non-dimensional SIF along thickness.**

In this figure, when z/t equals zero, we are at the middle of the plate and three-dimensional stress intensity factor are similar to the reference values, plane strain (middle plane).

Table 61 presents values of non-dimensional stress intensity factor in each element along the thickness at the crack tip for the mesh with 51072 elements. Although layer 1 is on the surface, since the result for the external nodes layer is averaged with those for the other two subsequent layers, the stress intensity factor were not disregarded.

**Table 61 - 3D FEM $K/\left(\sigma\sqrt{\pi c}\right)$, 51072 elements mesh**

| Element layer | FEM 3D | Tada [191] | Difference [%] |
|---|---|---|---|
| 1 (free surface) | 1,4863 | 1,422 | -4,522 |
| 2 | 1,5199 | | -6,882 |
| 3 | 1,5080 | | -6,045 |
| 4 | 1,4919 | | -4,918 |
| 5 | 1,4771 | | -3,877 |
| 6 | 1,4640 | | -2,955 |
| 7 | 1,4525 | | -2,144 |
| 8 | 1,4431 | | -1,483 |
| 9 | 1,4358 | | -0,972 |
| 10 | 1,4305 | | -0,600 |
| 11 | 1,4270 | | -0,353 |
| 12 (half thickness) | 1,4253 | | -0,230 |

A comparative plot of the % differences between Tada [191] and FEM as a function of z/t for both meshes is presented in Figure 236.

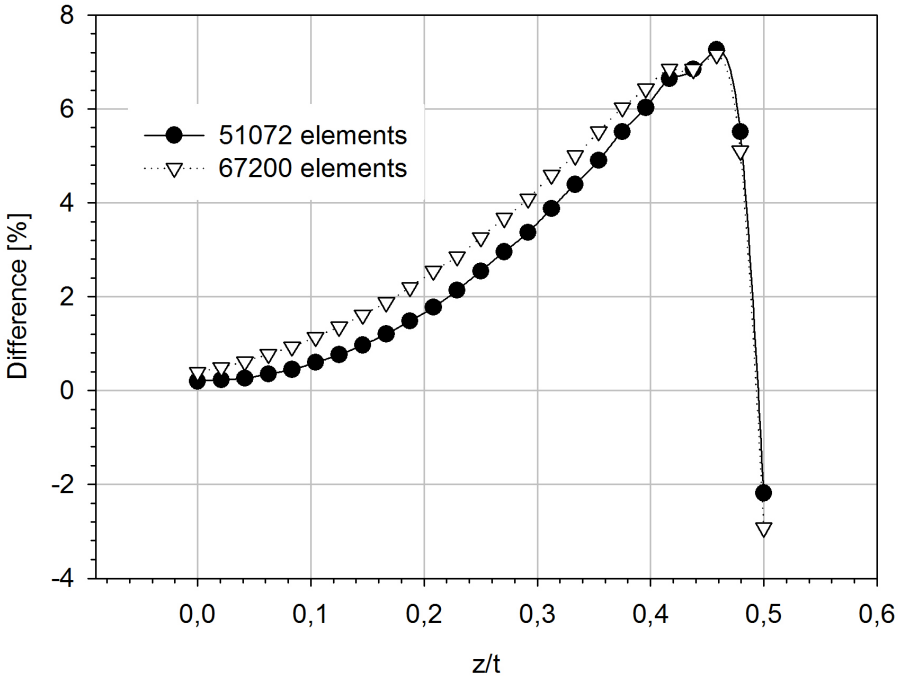


**Figure 236 - Comparative plot of the % differences between Tada [191] and FEM as a function of z/t for both meshes.**

Lower difference values were found for the more refined mesh, but they are small in both cases.

*5.1.3.2 Plate with a central crack h/b=0,875, c/b=0,5 and t/c=1,5*

In this case, a centre crack tension specimen with h/b=0,875, c/b=0,5 and t/c=1,5 was analyzed. Three-dimensional stress intensity factors solutions were not found in the literature for this configuration. The geometry was defined with the values presented in Table 62.

**Table 62 - Geometry, [units of length]**

| 2b | 2h | t | 2c |
|---|---|---|---|
| 60 | 52,5 | 22,5 | 30 |

Table 63 shows the values of non-dimensional stress intensity factor along the thickness for the different meshes used.

**Table 63 - Non-dimensional 3D FEM SIF along thickness**

| Node layer | z/t | $K/\left(\sigma\sqrt{\pi c}\right)$ | | Tada [191] | Difference [%] | |
|---|---|---|---|---|---|---|
| | | 51072 elem mesh | 67200 elem mesh | | 51072 elem mesh | 67200 elem mesh |
| 1 free surface | 0,5000 | 1,2896 | 1,2781 | 1,4220 | -9,308 | -10,117 |
| 3 | 0,4583 | 1,4655 | 1,4596 | | 3,057 | 2,647 |
| 5 | 0,4167 | 1,4830 | 1,4800 | | 4,286 | 4,082 |
| 7 | 0,3750 | 1,4873 | 1,4859 | | 4,594 | 4,491 |
| 9 | 0,3333 | 1,4888 | 1,4888 | | 4,696 | 4,696 |
| 11 | 0,2917 | 1,4873 | 1,4888 | | 4,594 | 4,696 |
| 13 | 0,2500 | 1,4844 | 1,4873 | | 4,389 | 4,594 |
| 15 | 0,2083 | 1,4815 | 1,4844 | | 4,184 | 4,389 |
| 17 | 0,1667 | 1,4800 | 1,4830 | | 4,082 | 4,286 |
| 19 | 0,1250 | 1,4786 | 1,4800 | | 3,979 | 4,082 |
| 21 | 0,0833 | 1,4771 | 1,4786 | | 3,877 | 3,979 |
| 23 | 0,0417 | 1,4757 | 1,4771 | | 3,774 | 3,877 |
| 25 half thickness | 0,0000 | 1,4757 | 1,4771 | | 3,774 | 3,877 |

Figure 237 shows the values of non-dimensional stress intensity factor along the thickness for the different meshes used.

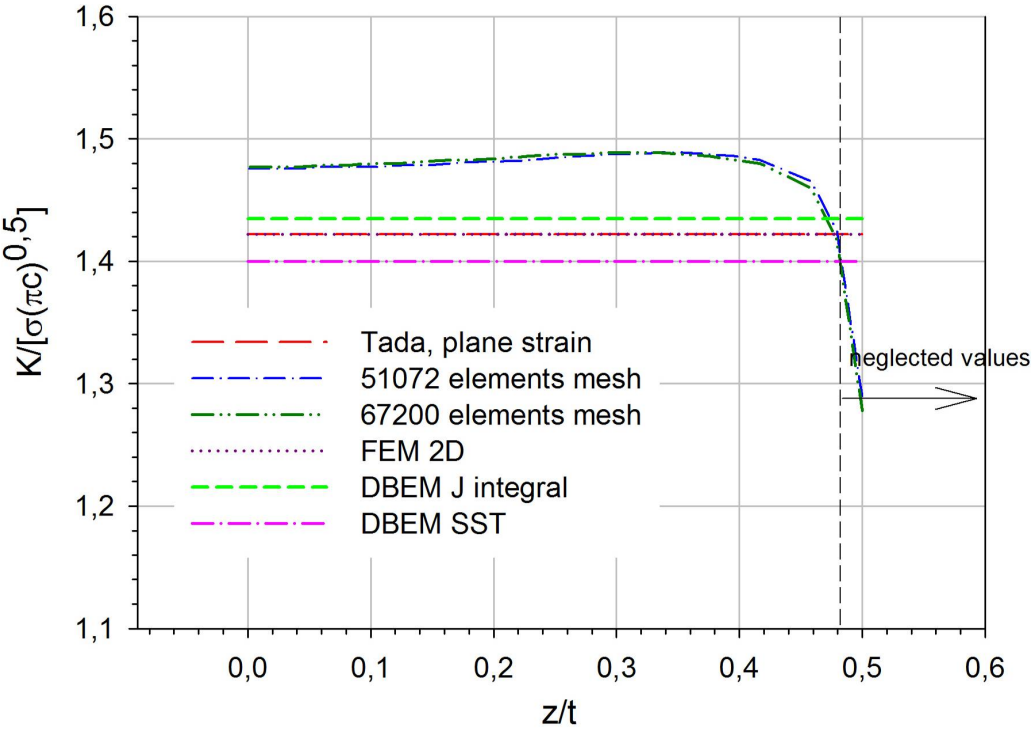


**Figure 237 - Non-dimensional SIF along thickness.**

Table 64 presents values of non-dimensional stress intensity factor in each element along the thickness at the crack tip for the mesh with 51072 elements. Although layer 1 is on the surface, since the result for the external nodes layer is averaged with those for the other two subsequent layers, the stress intensity factor were not disregarded for this comparison.

**Table 64 - 3D FEM $K/\left(\sigma\sqrt{\pi c}\right)$, 51072 elements mesh**

| Element layer | FEM 3D | Tada [191] | Difference [%] |
|---|---|---|---|
| 1 (free surface) | 1,4095 | 1,422 | 0,882 |
| 2 | 1,4742 | | -3,672 |
| 3 | 1,4856 | | -4,474 |
| 4 | 1,4885 | | -4,679 |
| 5 | 1,4876 | | -4,611 |
| 6 | 1,4859 | | -4,491 |
| 7 | 1,4830 | | -4,286 |
| 8 | 1,4813 | | -4,167 |
| 9 | 1,4788 | | -3,996 |
| 10 | 1,4774 | | -3,894 |
| 11 | 1,4769 | | -3,860 |
| 12 (half thickness) | 1,4757 | | -3,774 |

A comparative plot of the percent differences between Tada [191] and FEM as a function of z/t for both meshes is presented in Figure 238. In this case the use of both meshes lead to similar results.

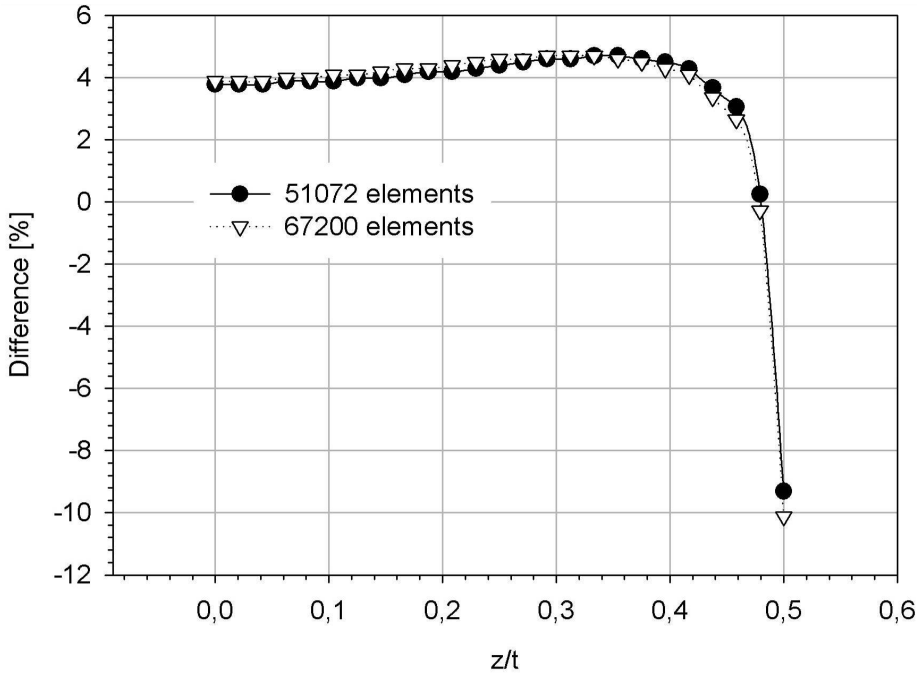


**Figure 238 - Comparative plot of the % differences between Tada [191] and FEM as a function of z/t for both meshes.**

*5.1.3.3 Plate with a central crack h/b=0,875, c/b=0,5 and t/c=6*

In this case centre crack tension specimen with $h/b = 0{,}875$, $c/b = 0{,}5$, and $t/c = 6$ was analyzed. Three-dimensional stress intensity factors solutions were not found in the literature for this configuration. The geometry was defined with the values presented in Table 65.

**Table 65 - Geometry, [units of length]**

| 2b | 2h | t | 2c |
|---|---|---|---|
| 60 | 52,5 | 90 | 30 |

Table 66 and Figure 239 show the values of non-dimensional stress intensity factor along the thickness for the different meshes used.

**Table 66 - Non-dimensional 3D FEM SIF along thickness**

| Node layer | z/t | $K/\left(\sigma\sqrt{\pi c}\right)$ | | Tada [191] | Difference [%] | |
|---|---|---|---|---|---|---|
| | | 51072 elem mesh | 67200 elem mesh | | 51072 elem mesh | 67200 elem mesh |
| 1 (free surface) | 0,5000 | 1,4830 | 1,4728 | 1,4220 | 4,286 | 3,569 |
| 3 | 0,4583 | 1,5558 | 1,5602 | | 9,409 | 9,716 |
| 5 | 0,4167 | 1,5121 | 1,5237 | | 6,335 | 7,155 |
| 7 | 0,3750 | 1,4786 | 1,4917 | | 3,979 | 4,901 |
| 9 | 0,3333 | 1,4527 | 1,4669 | | 2,156 | 3,160 |
| 11 | 0,2917 | 1,4344 | 1,4470 | | 0,875 | 1,756 |
| 13 | 0,2500 | 1,4216 | 1,4324 | | -0,026 | 0,732 |
| 15 | 0,2083 | 1,4130 | 1,4218 | | -0,631 | -0,016 |
| 17 | 0,1667 | 1,4073 | 1,4142 | | -1,030 | -0,549 |
| 19 | 0,1250 | 1,4037 | 1,4088 | | -1,287 | -0,928 |
| 21 | 0,0833 | 1,4017 | 1,4052 | | -1,430 | -1,184 |
| 23 | 0,0417 | 1,4005 | 1,4028 | | -1,512 | -1,348 |
| 25 (half thickness) | 0,0000 | 1,4001 | 1,4014 | | -1,543 | -1,450 |

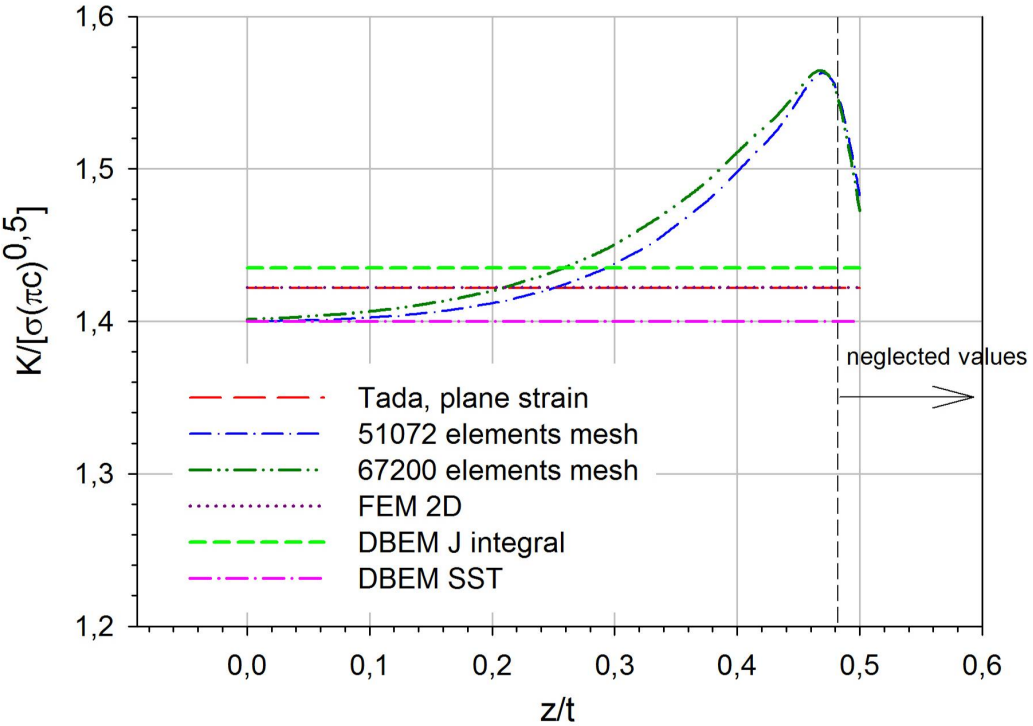


**Figure 239 - Non-dimensional SIF along thickness.**

Table 67 presents values of non-dimensional stress intensity factor in each element along the thickness at a crack tip for the mesh with 51072 elements. Although layer 1 is on the surface, since the result for the external nodes layer is averaged with those for the other two subsequent layers, the stress intensity factor were not disregarded.

**Table 67 - 3D FEM $K/\left(\sigma\sqrt{\pi c}\right)$, 51072 elements mesh**

| Element layer | FEM 3D | Tada [191] | Difference [%] |
|---|---|---|---|
| 1 (free surface) | 1,5436 | 1,422 | -8,555 |
| 2 | 1,5320 | | -7,735 |
| 3 | 1,4948 | | -5,123 |
| 4 | 1,4655 | | -3,060 |
| 5 | 1,4433 | | -1,498 |
| 6 | 1,4278 | | -0,411 |
| 7 | 1,4172 | | 0,339 |
| 8 | 1,4101 | | 0,834 |
| 9 | 1,4055 | | 1,162 |
| 10 | 1,4027 | | 1,358 |
| 11 | 1,4010 | | 1,478 |
| 12 (half thickness) | 1,4002 | | 1,531 |

A comparative plot of the percent differences between Tada [191] and finite element method as a function of z/t for both meshes is presented in Figure 240. A better accuracy for the more refined mesh can be noticed but the differences are small.

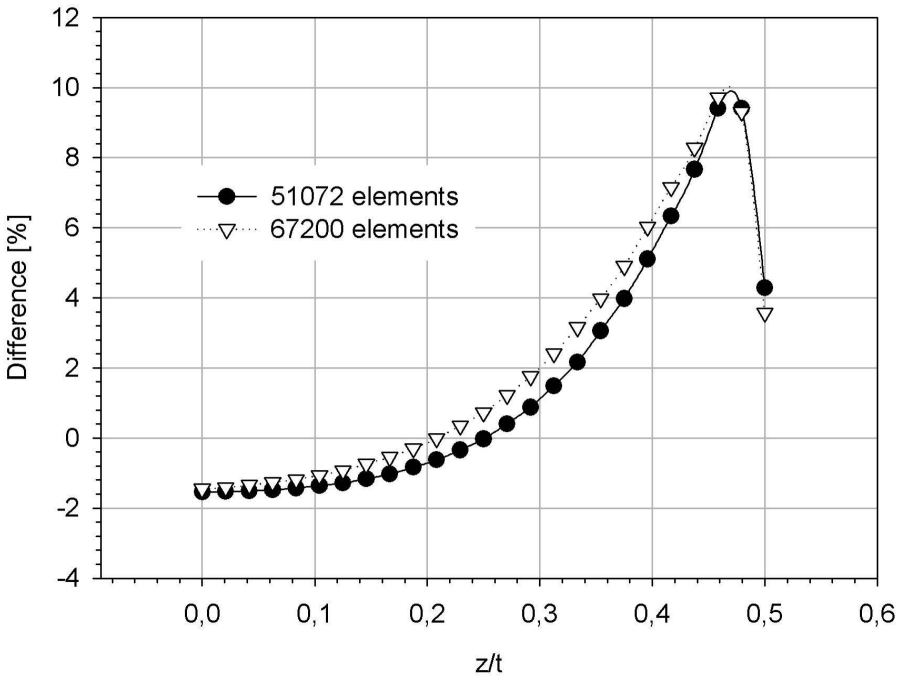


**Figure 240 - Comparative plot of the % differences between Tada [191] and FEM as a function of z/t for both meshes.**

*5.1.3.4 Plate with a central crack h/b=0,875, c/b=0,5 and t/c=0,75*

In this case, a centre crack tension specimen with h/b=0,875, c/b=0,5 and t/c=0,75 was analyzed. Three-dimensional stress intensity factors solutions were not found in the literature. The geometry was defined with the values presented in Table 68.

**Table 68 - Geometry, [units of length]**

| 2b | 2h | t | 2c |
|---|---|---|---|
| 60 | 52,5 | 11,25 | 30 |

For this analysis only the refined mesh was used. Table 69 and Figure 241 show the values of non-dimensional stress intensity factor along the thickness.

**Table 69 - Non-dimensional 3D FEM SIF along thickness (67200 elements mesh)**

| Node layer | z/t | $K/\left(\sigma\sqrt{\pi c}\right)$ | Tada [191] | Difference [%] |
|---|---|---|---|---|
| 1 free surface | 1,2200 | 0,5000 | 1,4220 | -2,926 |
| 3 | 1,4321 | 0,4643 | | 7,155 |
| 5 | 1,4713 | 0,4107 | | 6,847 |
| 7 | 1,4771 | 0,3929 | | 6,028 |
| 9 | 1,4888 | 0,3393 | | 5,004 |
| 11 | 1,4931 | 0,3036 | | 4,082 |
| 13 | 1,4975 | 0,2500 | | 3,262 |
| 15 | 1,4990 | 0,1964 | | 2,545 |
| 17 | 1,4990 | 0,1429 | | 1,879 |
| 19 | 1,5004 | 0,0893 | | 1,357 |
| 21 | 1,5004 | 0,0714 | | 0,937 |
| 23 | 1,5004 | 0,0179 | | 0,619 |
| 25 half thickness | 1,5004 | 0,0000 | | 0,394 |

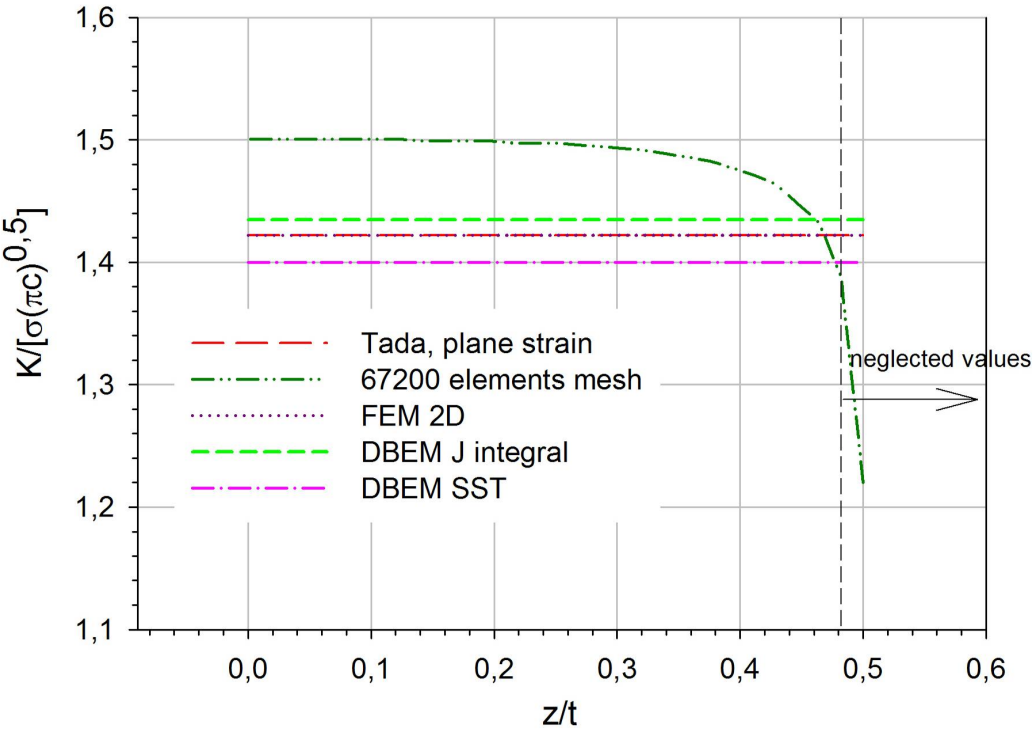


**Figure 241 - Non-dimensional SIF along thickness.**

*5.1.3.5 Discussion of results*

A comparison between the three-dimensional stress intensity factors obtained for each plate thickness with the two-dimensional reference results is presented in Figure 242. The percent difference between each three-dimensional finite element result, and the J integral result obtained with the two-dimensional dual boundary element is presented in Figure 243. When t<c the three-dimensional stress intensity factors at the mid plane are higher than the two-dimensional stress intensity factors. For thick or very thick plates the three- and two-dimensional stress intensity factors are similar at the mid plane. Similar trends are also reported in [188].

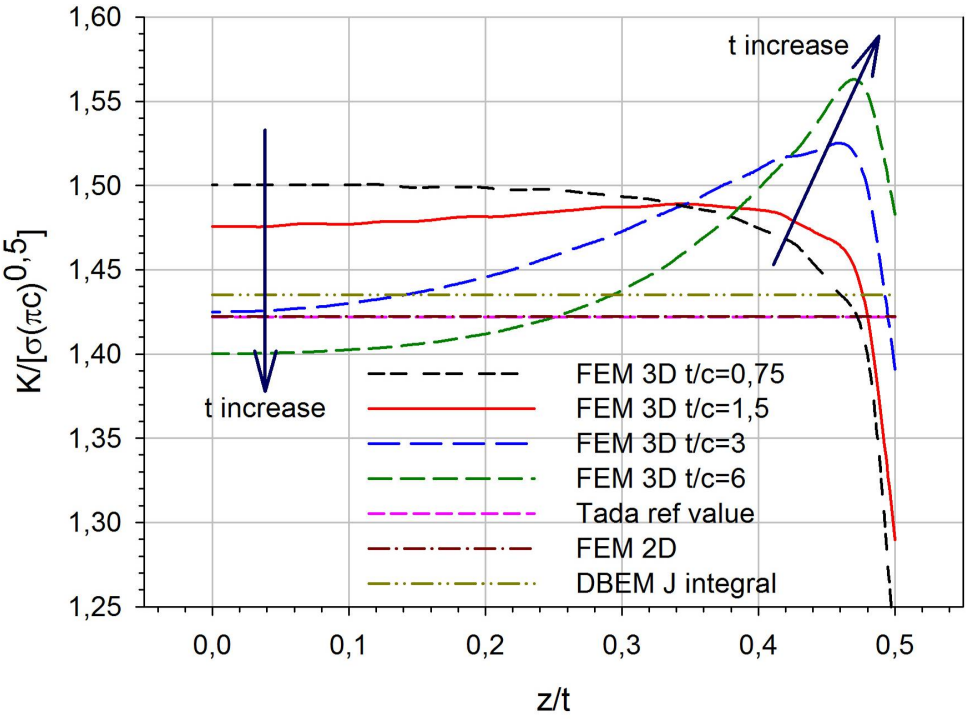


**Figure 242 - Non dimensional SIF for each studied plate thickness.**

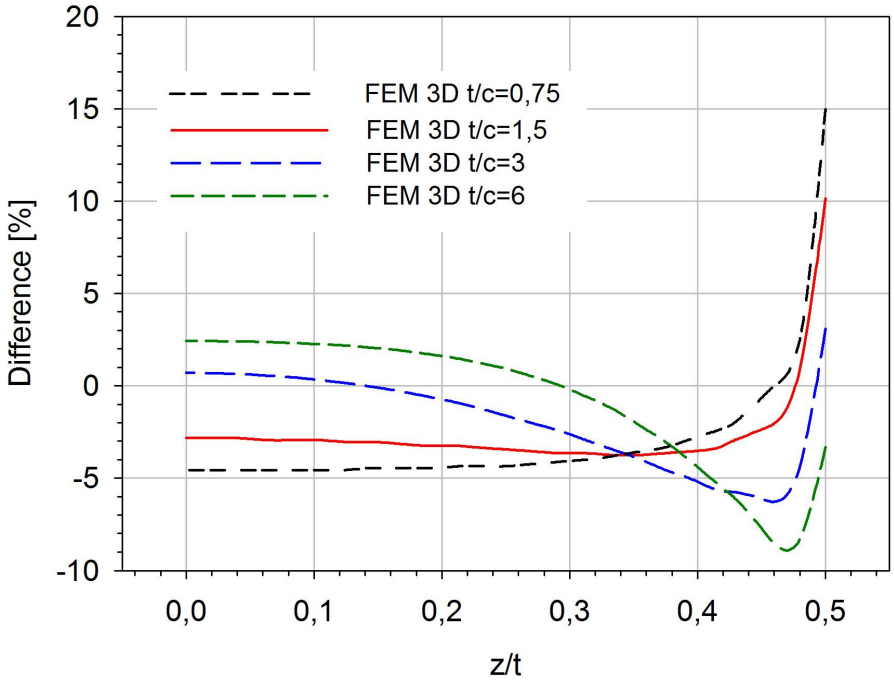


**Figure 243 - Difference between 3D FEM results for each studied thickness and 2D DBEM J integral result.**

Kwon *et al.* [188] have proposed a method, equation (23), to obtain approximate three-dimensional stress intensity factors from two-dimensional solutions.

$$\frac{K_{3D}}{K_{2D}} = \sqrt{\frac{1}{1-\nu^2}} \tag{23}$$

This equation was proposed taking into account that the stress state at the mid-plane of the plate approaches plane strain, as shown above. For t ≤ c, Kwon *et al.* [188] showed that the three-dimensional energy release rate can be approximated with the two-dimensional plane stress one. Considering the well known relationships between the energy release rate G and the stress intensity factor K:

$$G_{2D} = \frac{K_{2D}^2}{E} \quad for\ \ plane\ stress$$
$$G_{3D} = \frac{K_{3D}^2\left(1-\nu^2\right)}{E} \quad for\ \ plane\ strain \tag{24}$$

equation (23) results from equalizing the two expression of the energy release rate.

A comparison of the $K_{3D}$ estimated using equation (23) and the $K_{3D}$ calculated in the finite element analysis is presented in Table 70. In this study it was verified that this technique, equation (23), is accurate only for thin plates, t<1,5c. For this comparison the DBEM J integral solution was used as the reference value.

**Table 70 - Difference [%] between the estimated $K_{3D}$ and the FEM calculated $K_{3D}$ at the plate mid thickness**

| Difference [%] | t/c=0,75 | t/c=1,5 | t/c=3 | t/c=6 |
|---|---|---|---|---|
| approximate $K_{3D}$ from reference $K_{2D}$ | -0,26 | 1,81 | 5,10 | 6,84 |

*5.1.3.6 Characteristics of the three-dimensional stress fields*

The stress field near the crack front is three-dimensional. However, the deformation field very close to the crack front is almost in a state of plane strain, while away from the crack front it approaches a state of plane stress. Between these two states, the deformation is three-dimensional.

The results that yielded from the finite element analyses were used to characterize the stress field near the crack front, to determine the stress intensity factor variation along the thickness, and to prove the variation of the stress state in the vicinity of the crack. The three-dimensional region in the cracked plate is often characterized using a parameter  which measures the variation of the constraint factor (the degree of plane strain, equation (25)) with respect to the thickness direction, [186].

$$D_{p\varepsilon} = \frac{\sigma_{zz}}{\nu\left(\sigma_{xx} + \sigma_{yy}\right)} \quad \textbf{(25)}$$

The degree of plane strain is shown for all configurations near the crack front in Figure 244 and Figure 245. The plane strain condition seemed to be invalid near the plate free surface, which raises the question about the validity of using the plane strain condition along the crack front for calculating K from near tip displacements.
The degree of plane strain is zero for a state of plane stress, and it is unity where plane strain occurs. The plots clearly show that plane strain behaviour occurs at and near the middle of the plate, where a degree of plane strain of almost 1,00 was obtained. As the distance from the crack front increases, the degree of plane strain tends to smaller values, showing three-dimensional near the crack front and then plane stress behaviour.

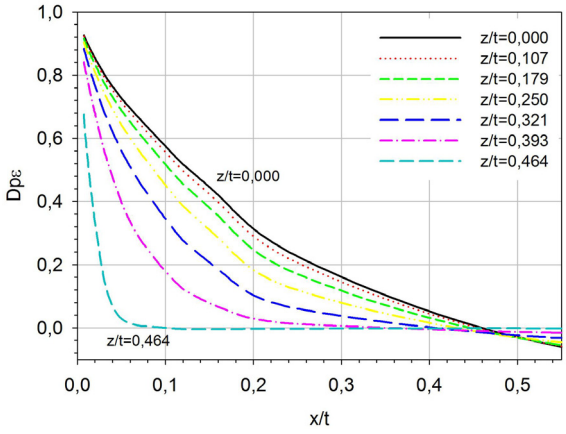


a) t/c=0,75

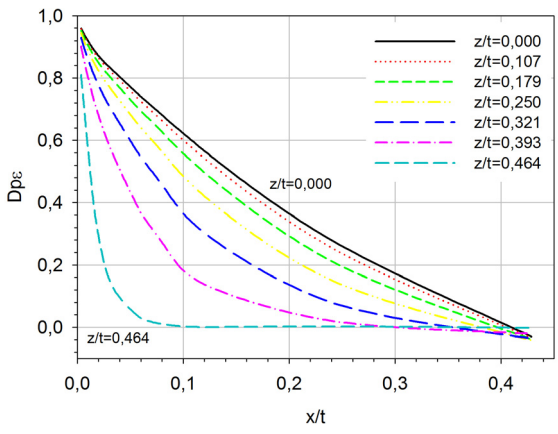


b) t/c=1,5

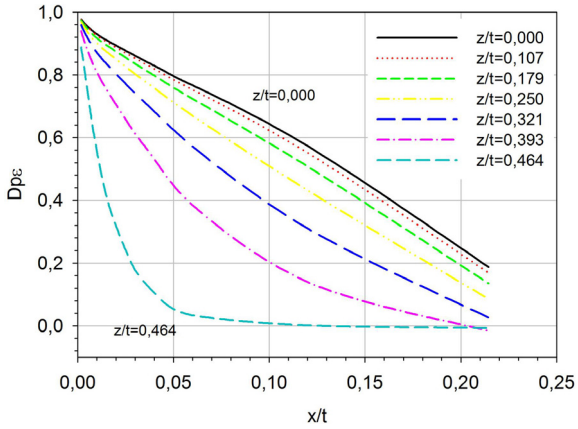


c) t/c=3

**Figure 244 - Degree of plane strain in the x direction.**

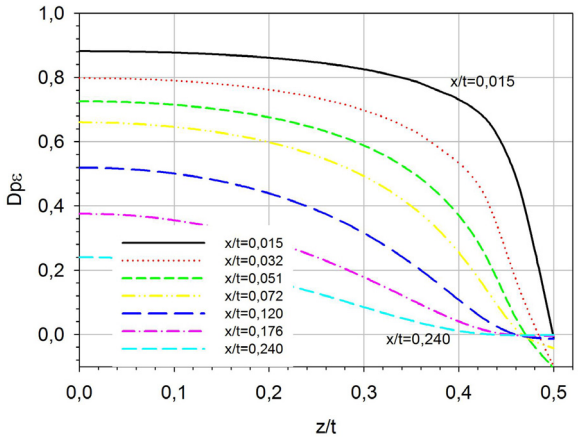


a) t/c=0,75

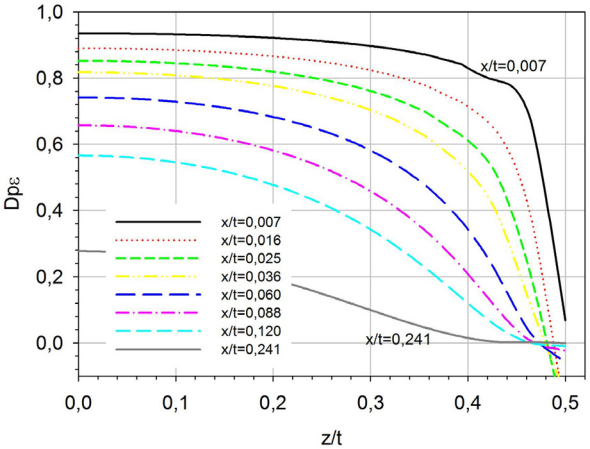


b) t/c=1,5

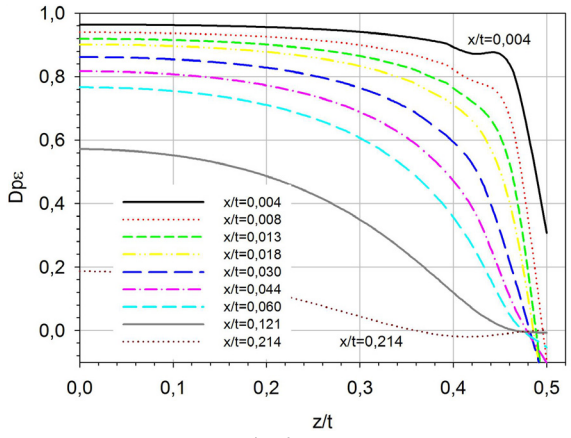


c) t/c=3

**Figure 245 - Degree of plane strain in the z direction for different x location.**

Based on the degree of plane strain plots, it was observed that the size of the plane strain zone, δ, depends on the plate thickness. The size of the plane strain zone is defined as the value of x/t when $D_{p\varepsilon}$ becomes zero, Figure 244. As presented in Table 71, for t<c the plane strain behaviour is present on almost half of the thickness, as shown also in [186, 188]. The ratio δ/t of the size of the plane strain zone decreases as the thickness of the plate increases.

**Table 71 - Size of the plane strain zone**

| | t/c=0,75 | t/c=1,5 | t/c=3 |
|---|---|---|---|
| δ/t | 0,46 | 0,4 | 0,26 |

A detailed stress analysis was carried out in the vicinity of the crack front, in order to emphasize the characteristics of the three-dimensional stress field. The non dimensional stresses in the y and z direction are plotted in Figure 246 and Figure 247.
Due to the fact that, in Mode I, the crack propagation is determined by the stress perpendicular to the crack, namely $\sigma_y$, this stress component was dealt with in the analysis. A decrease of the stress $\sigma_y$ values with the distance from the crack front, which is normal due to the strong stress concentration effect near the crack, is noticed. As the distance from the crack front increases, the values of the stress tend to the remote stress.

The plots in Figure 246 and Figure 247 represent the variation of the opening stress $\sigma_y$ and the stress in the thickness direction $\sigma_z$ with the distance from the crack tip, at different z/t values. The considered stress was made non dimensional in a form specific to the series expansion of Williams [193]. In this representation, the Mode I opening stress ahead of the crack tip can be written as:

$$\sigma_y = \frac{K}{\sqrt{2\pi x}} + A_0\sqrt{x} + A_1\sqrt{x^3} + \ldots \qquad \textbf{(26)}$$

where the first term on the right hand represents the singular stress having the well-known $x^{-1/2}$ singularity; the second, third and the other higher order terms

are non-singular. This means they vanish for x → 0. Multiplying both sides by $\sqrt{2\pi x}$ , one obtains:

$$\sigma_y \sqrt{2\pi x} = K + A_0 x + A_1 x^2 + \ldots \quad \textbf{(27)}$$

For x → 0, the equation above becomes:

$$\sigma_y \sqrt{2\pi x}\Big|_{x\to 0} = K \quad \textbf{(28)}$$

It is clear that in the vicinity of the crack tip (for very small values of x) the first term is dominant while the others are negligible. As the distance from the crack tip increases, the other terms have an important influence and the one-term stress field approach is not valid anymore. This tendency is illustrated in Figure 246, where one can notice a decreasing tendency up to a certain value of x/t then, the non-dimensional values of the stress begin to increase, due to the influence of the second and higher order terms.

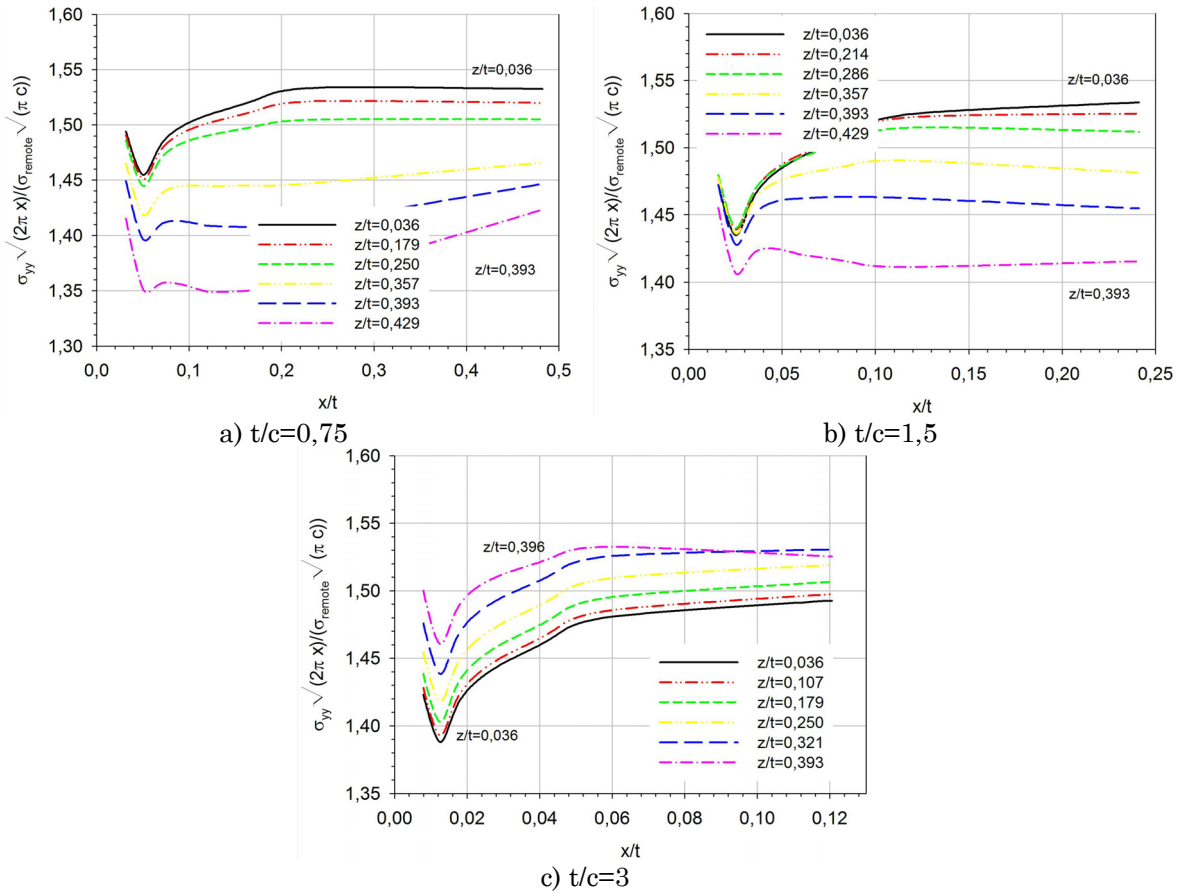


a) t/c=0,75 b) t/c=1,5

c) t/c=3

**Figure 246 - Stress distribution in the y direction near the crack front.**

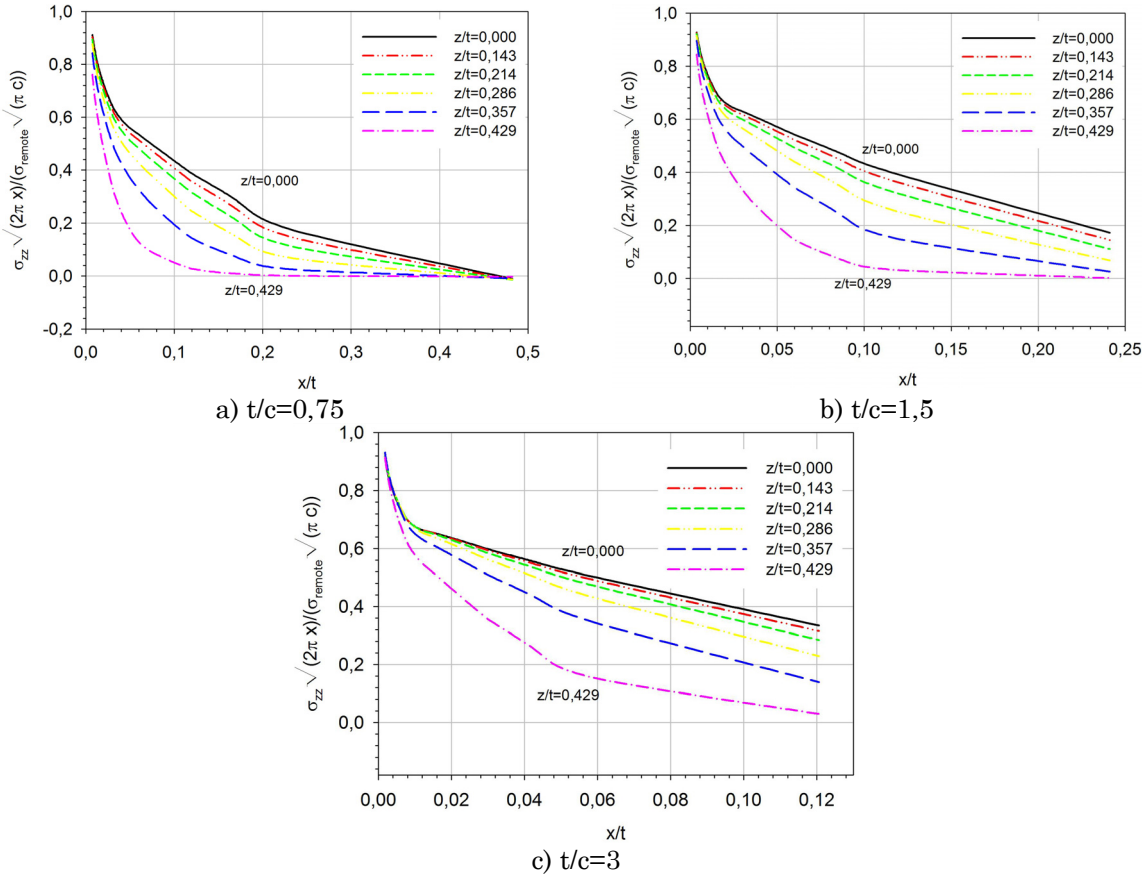


a) t/c=0,75 b) t/c=1,5

c) t/c=3

**Figure 247 - Stress distribution in the z direction near the crack front.**

### *5.1.4 Concluding remarks*

As a contribution to the understanding of 3D effects, detailed three-dimensional finite element analyses of cracked plates were conducted in order to characterize the near-tip stress field and to determine the variation of the stress intensity factor through the thickness of the plate. A very refined finite element model was built having 24 elements along half the thickness in order to obtain a smooth distribution of the stress intensity factor. The stress intensity factor results for each of the three layers of node on each element were averaged following a simple rule. The obtained results were compared both with those in the literature and with the values obtained following a two-dimensional finite element analysis and dual boundary element analysis.

In the finite element and dual boundary element analyses, the J integral technique is used to obtain the stress intensity factor solutions. In a two-dimensional numerical simulation, despite carrying out a plane strain analysis or a plane stress analysis, leading to different strain and stress results, $K_I$ solutions are independent of the type of analysis.

In a three-dimensional analysis, stress intensity factor has different values through the thickness. So, a two-dimensional stress intensity factor analysis is

only an approximation of the exact solution since there is no difference on plane stress or plane strain stress intensity factor solutions for linear elastic fracture mechanics.

Values of stress intensity factor obtained by Newman and Atluri are lower than those obtained in the three-dimensional finite element method analyses. A parametric study was carried out in order to assess the influence of mesh refinement in the final solution. The study showed also that from a certain level of refinement, subsequent refinement of the mesh does not lead to a significant improvement of the results. It was found that when using coarse meshes a good agreement between the present three-dimensional analysis and the Newman solution was found. Nevertheless it should be reminded that the three-dimensional references solutions [189] were obtained with finite element meshes created in the middle 1970's when computational resources were quite low.

The stress intensity factor varies over the thickness and drops to zero at the plate surface. A boundary layer exists near the plate free surface and its size is a function of thickness/crack length ratio. The best agreement with the reference values was obtained for the middle layer.

The opening stress remains almost constant through the thickness except near the free surface where an important decrease can be noticed in the vicinity of the crack front. This behaviour is not noticed far from the crack front, where the opening stress is constant and tends to the applied remote stress.

The plane strain behaviour near the middle of the plate was demonstrated by calculating the degree of plane strain. It was shown also that the degree of plane strain tends to smaller values when the distance from the crack front increases. Plane strain behaviour occurs at and near the middle of the plate, where a degree of plane strain near unity was obtained. As the distance from the crack front increases, the degree of plane strain tends to smaller values, showing thus three-dimensional and then plane stress behaviour.

## 5.2 Finite element analysis of a stiffened cracked plate

The main purpose of this analysis is to model the tensile behaviour of a cracked stiffened panel in order to identify special features of that behaviour, in particular as concerns bending effects. For this purpose, the stress intensity factor for as example of stiffened cracked plate subjected to remote uniform traction was calculated. A crack symmetrically crossing a stiffener is considered. The case of an unbroken stiffener and the case of a broken stiffener are studied. In this analysis it was not used any type of anti-bending or anti-buckling device.

The crack crosses the left stiffener, being symmetric with respect to this stiffener, as it can be seen in the cross view presented in Figure 248. The left crack tip is identified as crack tip A and right crack tip as crack tip B. The plate height is $700mm$.

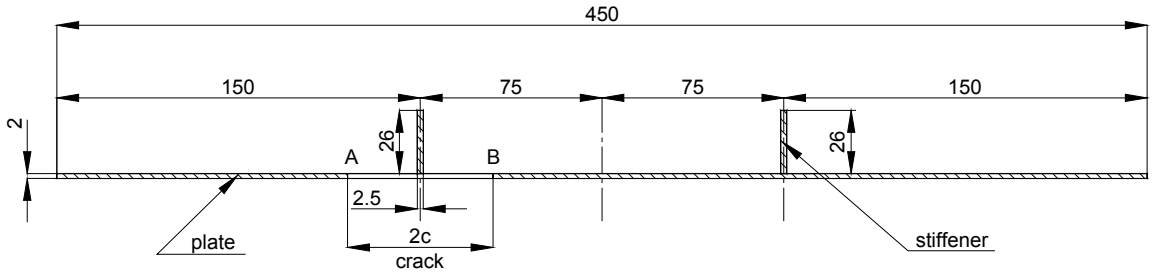


**Figure 248 - Cross section through the stiffened plate with a crack crossing a stiffener.**

### *5.2.1 Mesh*

In order to model the plate, 20 nodes brick isoparametric elements (C3D20) were used. For the case of an unbroken stiffener, two meshes were tested with 3 elements along the thickness but with a different total number of elements: a mesh with 21356 elements and another mesh with 57759 elements. A supplementary analysis using a mesh with 129651 elements (585863 nodes) was carried out. This mesh uses 7 elements along the plate thickness. No anti-bending device was used in the numerical modelling.
For the case of a broken stiffener, the analysis was carried out using a mesh with 129651 elements (585863 nodes). In this case, the same 7 elements along the plate thickness were used as for the case of an unbroken stiffener mesh.
A detail of the coarser mesh, for the case of an unbroken stiffener, is presented in Figure 249. In all studies, due to the symmetry only half of the plate was modelled.

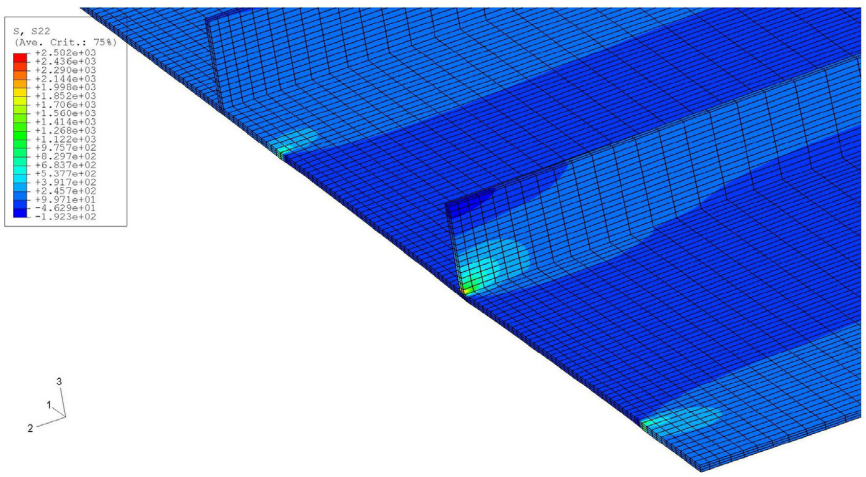

**Figure 249 - Deformed mesh detail in the less refined mesh for 2c=195*mm,* case of an unbroken stiffener.**

### *5.2.2 SIF evaluation for the case of an unbroken stiffener*

*5.2.2.1 Results of SIFs using 3 elements along the plate thickness*

A parametric study of 7 crack lengths was carried out, 2c = 32,50, 65,00, 97,50, 130,00, 162,50, 195,00 and 227,00$mm$. The J integral technique was used in ABAQUS to calculate the values of the stress intensity factor along the plate thickness.
The results for the case of unbroken stiffener obtained with the compounding technique [194], are presented in Table 72.

**Table 72 - Unbroken stiffener, non-dimensional SIF compounding results [194]**

| c | 3c/W | $K/\sigma\sqrt{\pi c}$ | |
|---|---|---|---|
| | | Tip A | Tip B |
| 16,25 | 0,108 | 0,665 | 0,665 |
| 32,50 | 0,217 | 0,69 | 0,689 |
| 48,75 | 0,325 | 0,716 | 0,712 |
| 65,00 | 0,433 | 0,739 | 0,727 |
| 81,25 | 0,542 | 0,765 | 0,737 |
| 97,50 | 0,65 | 0,806 | 0,748 |
| 113,75 | 0,758 | 0,871 | 0,751 |
| 130,00 | 0,867 | 1,018 | 0,743 |

The non-dimensional stress intensity factor values obtained using the finite element method with the 21356 elements mesh for crack tips A and B along the thickness are presented in Figure 250 as a function of the crack length. The non smooth stress intensity factor distribution obtained with the finite element method is due to lack of sufficient mesh refinement.

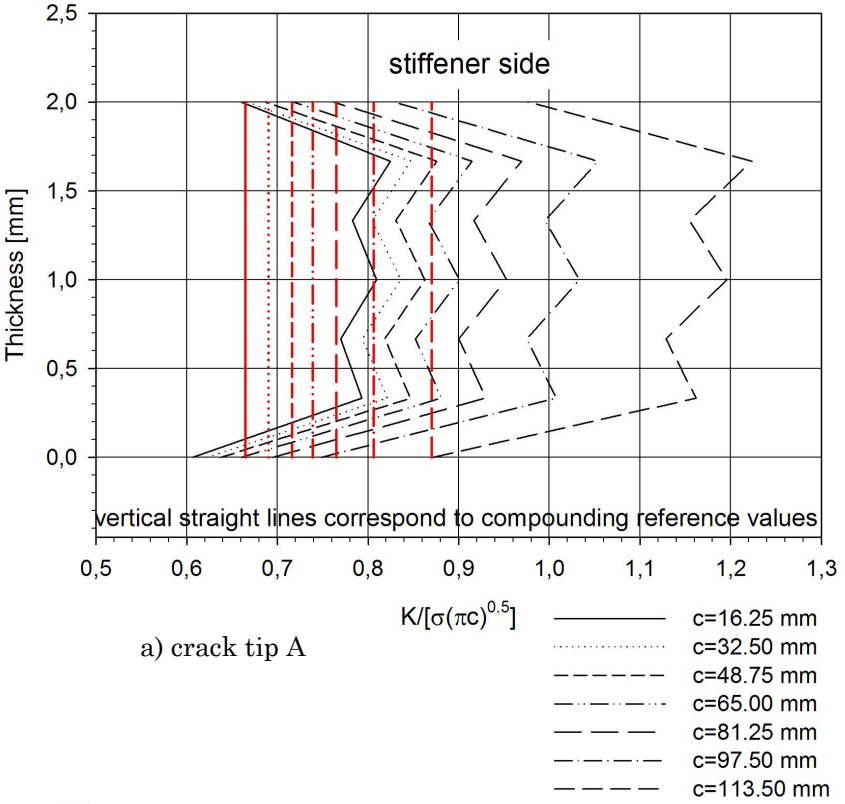


a) crack tip A

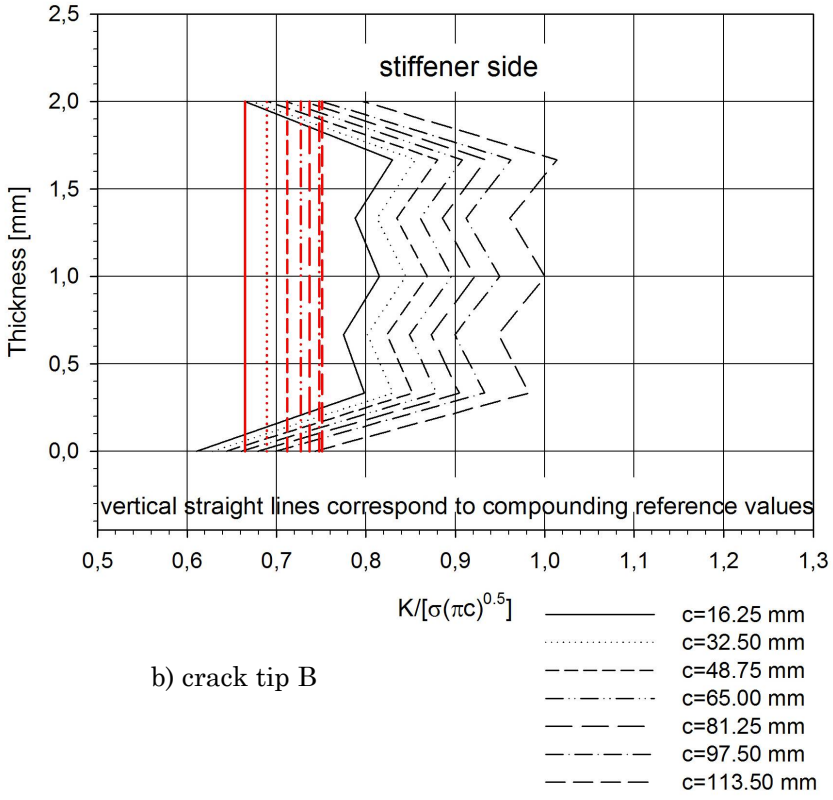


b) crack tip B

**Figure 250 - SIF along the thickness for several crack lengths, crack tip A and crack tip B obtained with the 21356 elements mesh, unbroken stiffener.**

The non-dimensional stress intensity factor values obtained with the 57759 elements mesh for crack tips A and B along the thickness as a function of the crack length are presented in Figure 251.

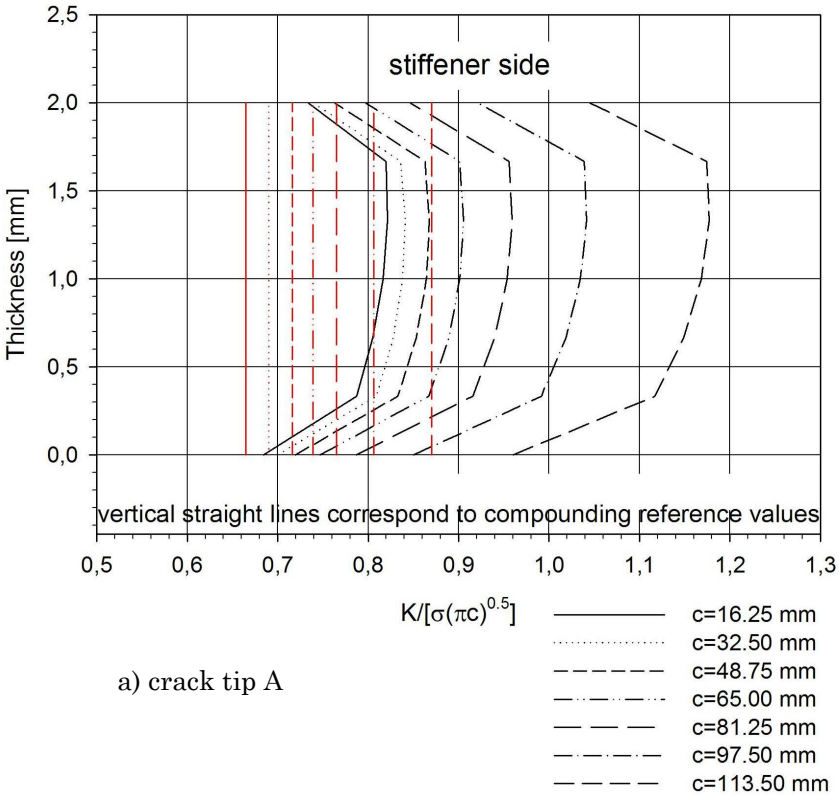


a) crack tip A

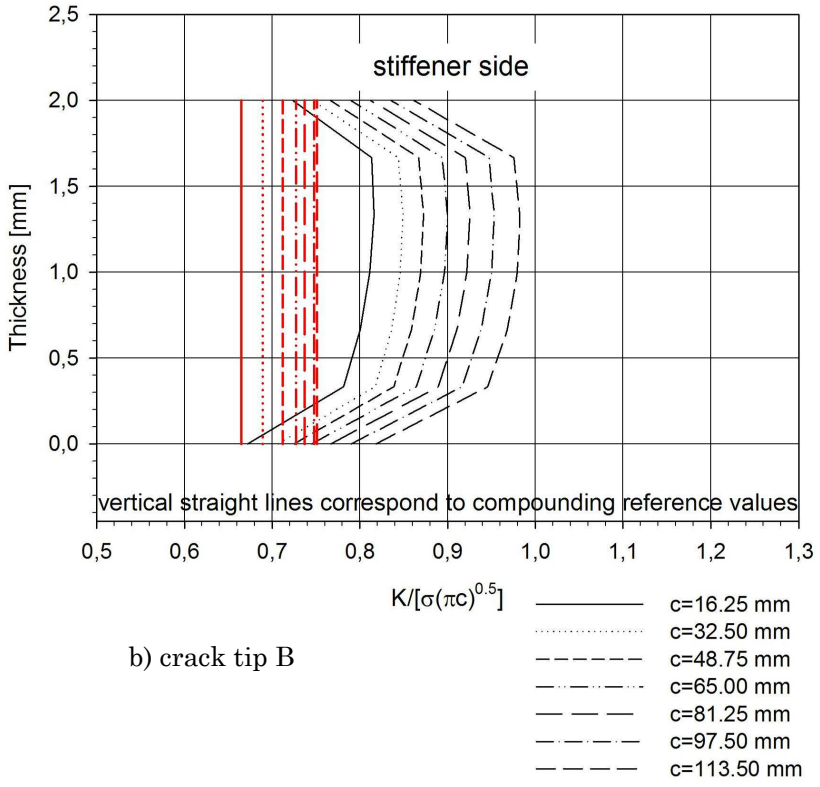


b) crack tip B

**Figure 251 - SIF along the thickness for several crack lengths, crack tip A and crack tip B obtained with the 57759 elements mesh, unbroken stiffener.**

Table 73 presents the average $K/\sigma\sqrt{\pi c}$ for crack tip A and crack tip B. In this table, *stiff elem* is the element layer at the stiffener side, *middle elem* is the element layer at the middle of the plate and *back elem* is the element layer at the opposite side of the stiffener. These results were obtained with the 21356 elements mesh.

**Table 73 - Average $K/\sigma\sqrt{\pi c}$ for crack tip A and crack tip B, unbroken stiffener**

| | crack tip A [average $K/\sigma\sqrt{\pi c}$] | | | crack tip B [average $K/\sigma\sqrt{\pi c}$] | | |
|---|---|---|---|---|---|---|
| c [$mm$] | stiff elem | middle elem | back elem | stiff elem | middle elem | back elem |
| 16,25 | 0,758 | 0,799 | 0,790 | 0,763 | 0,804 | 0,795 |
| 32,50 | 0,784 | 0,824 | 0,810 | 0,792 | 0,832 | 0,818 |
| 48,75 | 0,807 | 0,850 | 0,837 | 0,813 | 0,855 | 0,841 |
| 65,00 | 0,840 | 0,887 | 0,874 | 0,838 | 0,882 | 0,867 |
| 81,25 | 0,886 | 0,938 | 0,926 | 0,862 | 0,908 | 0,892 |
| 97,50 | 0,959 | 1,017 | 1,006 | 0,888 | 0,935 | 0,918 |
| 113,5 | 1,108 | 1,178 | 1,171 | 0,937 | 0,985 | 0,969 |

A comparative plot of results for the unbroken stiffener obtained by finite element method and the compounding technique is presented in Figure 252.

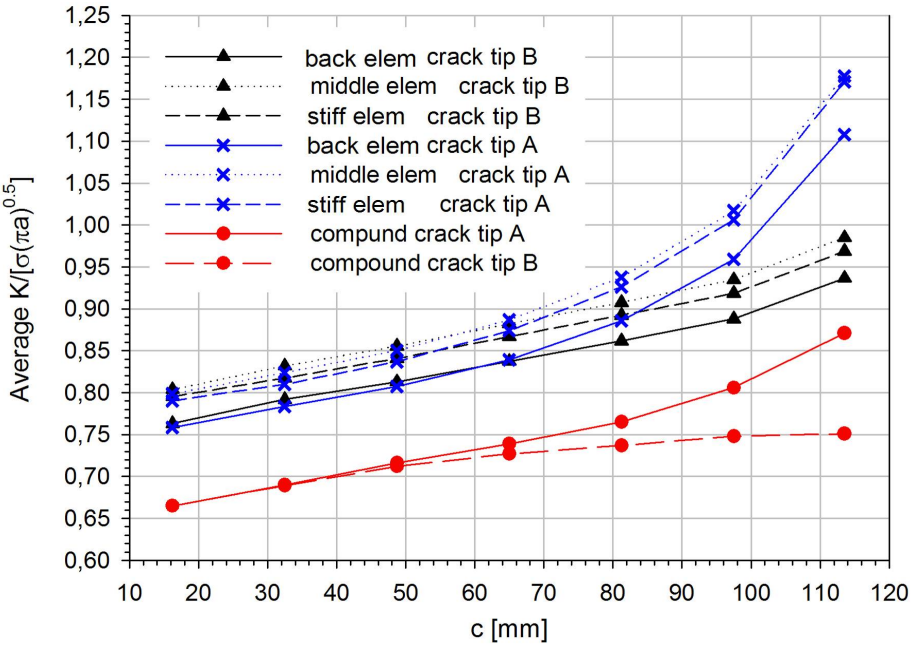


**Figure 252 - Non-dimensional SIF for the crack crossing an unbroken stiffener, compound and 21356 elements mesh results.**

*5.2.2.2 Results of SIFs using 7 elements along the plate thickness*

According to the considerations presented in the previous section, stress intensity factor results obtained only on nodes that lay on the plate surface should be

disregarded, and a higher number of elements through the thickness are necessary in order to accurately calculate stress intensity factors.
A study using a mesh with 129651 elements with a total of 585863 nodes was carried out. In this study, the plate was modelled with 7 elements along the thickness. A detail of the mesh and the order of layers along the thickness are presented in Figure 253.

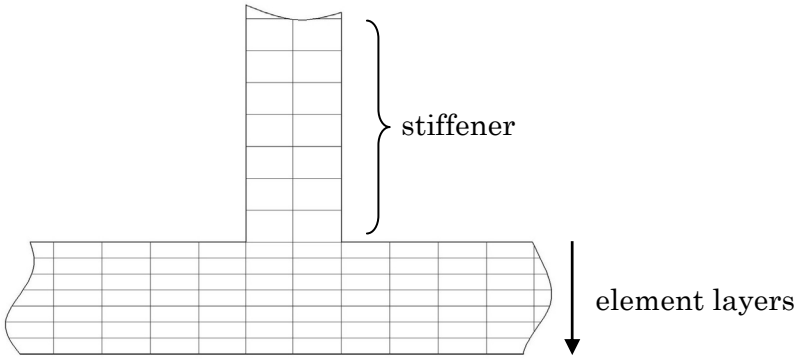


**Figure 253 - Mesh detail and element layer through thickness order.**

A comparison between the obtained stress intensity factors and the values given by the compounding technique [194] is presented in Table 74 and Table 75, and Figure 254 and Figure 255. The average stress intensity factors obtained according to equation (20) are compared.

**Table 74 - Average $K/\sigma\sqrt{\pi c}$ for crack tip A, unbroken stiffener**

| | crack tip A [average $K/\sigma\sqrt{\pi c}$] | | | | | | | |
|---|---|---|---|---|---|---|---|---|
| | stiff elem layer | middle elem layers | | | | | back elem layer | Compound results |
| c [$mm$] | 1 | 2 | 3 | | 5 | 6 | 7 | |
| 16,25 | 0,778 | 0,823 | 0,824 | 0,665 | 0,808 | 0,812 | 0,717 | 0,665 |
| 32,50 | 0,801 | 0,850 | 0,853 | 0,689 | 0,842 | 0,848 | 0,745 | 0,69 |
| 48,75 | 0,819 | 0,870 | 0,872 | 0,712 | 0,860 | 0,865 | 0,759 | 0,716 |
| 65,00 | 0,856 | 0,908 | 0,910 | 0,727 | 0,895 | 0,901 | 0,788 | 0,739 |
| 81,25 | 0,908 | 0,962 | 0,964 | 0,737 | 0,946 | 0,951 | 0,832 | 0,765 |
| 97,50 | 0,987 | 1,045 | 1,047 | 0,748 | 1,026 | 1,030 | 0,900 | 0,806 |
| 113,5 | 1,117 | 1,182 | 1,183 | 0,751 | 1,158 | 1,164 | 1,012 | 0,870 |

**Table 75 - Average $K/\sigma\sqrt{\pi c}$ for crack tip B, unbroken stiffener**

| | crack tip B [average $K/\sigma\sqrt{\pi c}$] | | | | | | | |
|---|---|---|---|---|---|---|---|---|
| | stiff elem layer | middle elem layers | | | | | back elem layer | Compounding result |
| c [$mm$] | 1 | 2 | 3 | 4 | 5 | 6 | 7 | |
| 16,25 | 0,783 | 0,828 | 0,829 | 0,817 | 0,813 | 0,817 | 0,721 | 0,665 |
| 32,50 | 0,793 | 0,843 | 0,845 | 0,836 | 0,834 | 0,840 | 0,737 | 0,689 |
| 48,75 | 0,823 | 0,873 | 0,877 | 0,868 | 0,865 | 0,871 | 0,764 | 0,712 |
| 65,00 | 0,847 | 0,901 | 0,904 | 0,894 | 0,891 | 0,898 | 0,786 | 0,727 |
| 81,25 | 0,872 | 0,927 | 0,930 | 0,920 | 0,917 | 0,923 | 0,809 | 0,737 |
| 97,50 | 0,897 | 0,954 | 0,957 | 0,948 | 0,945 | 0,951 | 0,834 | 0,748 |
| 113,50 | 0,924 | 0,983 | 0,987 | 0,977 | 0,975 | 0,984 | 0,861 | 0,751 |

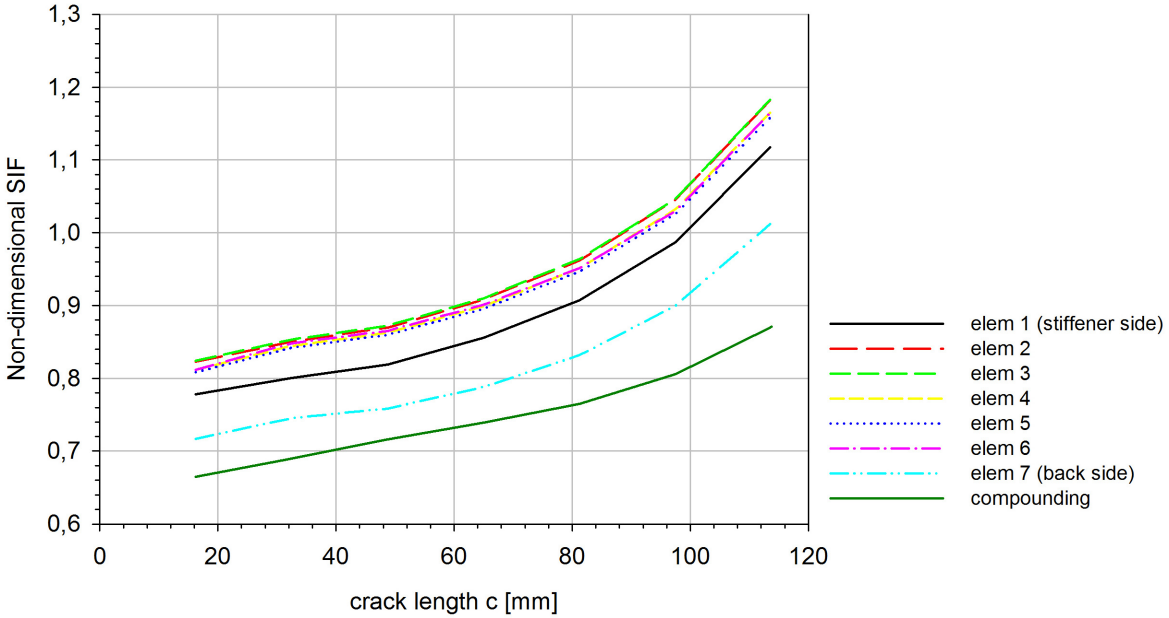


**Figure 254 - Results of SIFs for crack tip A for several crack lengths using the compounding technique and the FEM (results for each layer of elements), unbroken stiffener.**

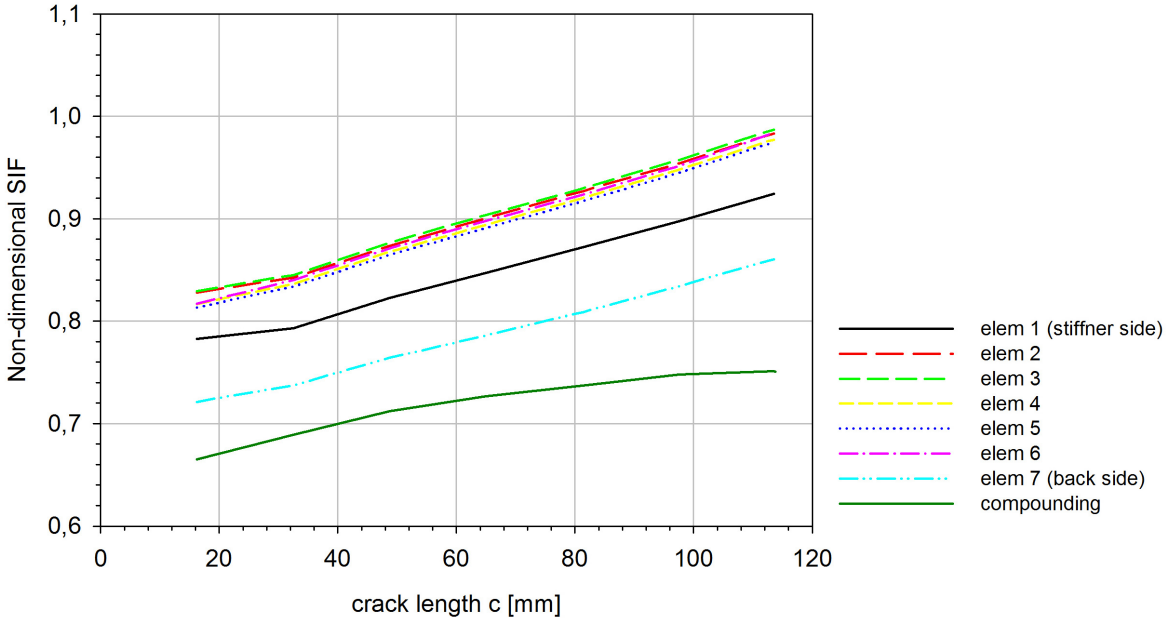


**Figure 255 - Results of SIFs for crack tip B for several crack lengths using the compounding technique and the FEM (results for each layer of elements), unbroken stiffener.**

The element layer 7, laying on the opposite side to the stiffener, has the best agreement with the compounding results. This is also the layer that has lower stress intensity factor values for both crack tips at all cracks lengths. The differences between the results obtained for this layer of elements and the compounding ones are presented in Table 76. The finite element method results were considered as reference values.

**Table 76 - Difference between SIFs of FEM of elements layer 7 and the compounding results, unbroken stiffener**

| c [$mm$] | Crack Tip A | | | Crack Tip B | | |
|---|---|---|---|---|---|---|
| | FEM back element layer | Compound technique | difference [%] | FEM back element layer | Compounding technique | difference [%] |
| 16,25 | 0,717 | 0,665 | 7,25 | 0,721 | 0,665 | 7,77 |
| 32,50 | 0,745 | 0,69 | 7,38 | 0,737 | 0,689 | 6,51 |
| 48,75 | 0,759 | 0,716 | 5,67 | 0,764 | 0,712 | 6,81 |
| 65,00 | 0,788 | 0,739 | 6,22 | 0,786 | 0,727 | 7,51 |
| 81,25 | 0,832 | 0,765 | 8,05 | 0,809 | 0,737 | 8,90 |
| 97,50 | 0,900 | 0,806 | 10,44 | 0,834 | 0,748 | 10,31 |
| 113,5 | 1,012 | 0,87 | 14,03 | 0,861 | 0,751 | 12,78 |

### *5.2.3 SIF evaluation for the case of a broken stiffener*

A study using a mesh with 129651 elements and 585863 nodes was carried out. In this study the plate was modelled with 7 elements along the thickness. A detail of the mesh and the order of layers along the thickness are presented in Figure 253. Again, a parametric study for 7 crack lengths was carried out, 2c = 32,50, 65,00, 97,50, 130,00, 162,50, 195,00 and 227,00*mm*. The J integral technique was used in ABAQUS to calculate the values of the stress intensity factor along the plate thickness.
The results for the case of broken stiffener obtained with the compounding technique are presented in Table 77.

**Table 77- Broken stiffener, non-dimensional SIF compounding results [194]**

| c | 3c/W | $K/\sigma\sqrt{\pi c}$ | |
|---|---|---|---|
| | | Tip A | Tip B |
| 16,25 | 0,108 | 1,476 | 1,480 |
| 32,50 | 0,217 | 1,269 | 1,274 |
| 48,75 | 0,325 | 1,222 | 1,223 |
| 65,00 | 0,433 | 1,231 | 1,220 |
| 81,25 | 0,542 | 1,271 | 1,245 |
| 97,50 | 0,650 | | 1,317 |
| 113,75 | 0,758 | | |
| 130,00 | 0,867 | | |

The non-dimensional stress intensity factor values obtained with the 129651 elements mesh for crack tips A and B along the thickness are presented in Figure 256 as a function of the crack length.

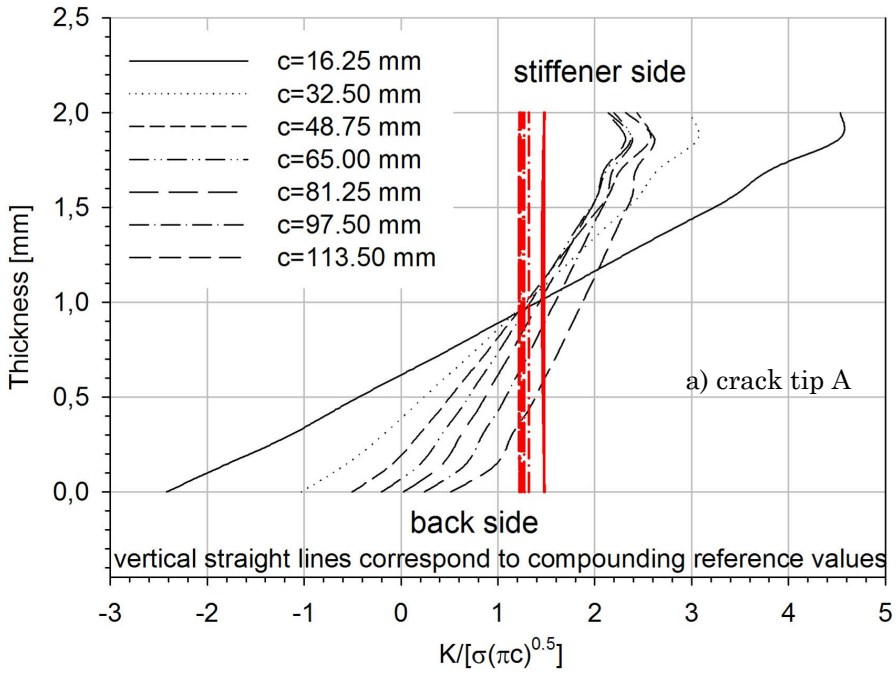

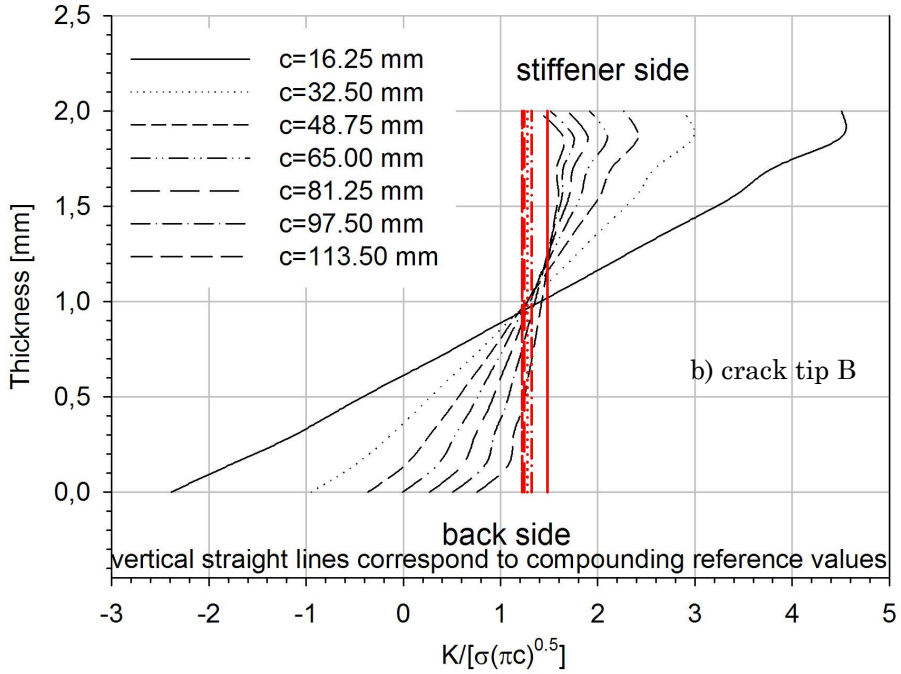


**Figure 256 - SIF along the thickness for several crack lengths for a broken stiffener, crack tip A and crack tip B obtained with the 129651 elements mesh.**

A comparison between the stress intensity factors obtained and the values given by the compounding technique is presented in Table 78 and Table 79, and Figure 257 and Figure 258. The average stress intensity factors obtained according to equation (20) are compared.

**Table 78 - Average $K/\sigma\sqrt{\pi c}$ for crack tip A, broken stiffener**

| | crack tip A [average $K/\sigma\sqrt{\pi c}$] | | | | | | | |
|---|---|---|---|---|---|---|---|---|
| | stiff elem layer | middle elem layers | | | | | back elem layer | Compounding results |
| c [$mm$] | 1 | 2 | 3 | 4 | 5 | 6 | 7 | |
| 16,25 | 4,412 | 3,452 | 2,438 | 1,405 | 0,365 | -0,686 | -1,810 | 1,448 |
| 32,50 | 2,985 | 2,463 | 1,887 | 1,296 | 0,699 | 0,088 | -0,589 | 1,276 |
| 48,75 | 2,504 | 2,141 | 1,723 | 1,290 | 0,850 | 0,397 | -0,121 | 1,220 |
| 65,00 | 2,306 | 2,026 | 1,689 | 1,335 | 0,975 | 0,601 | 0,161 | 1,256 |
| 81,25 | 2,251 | 2,024 | 1,735 | 1,428 | 1,114 | 0,785 | 0,387 | 1,350 |
| 97,50 | 2,317 | 2,128 | 1,868 | 1,590 | 1,304 | 1,001 | 0,620 | |
| 113,50 | 2,540 | 2,381 | 2,139 | 1,876 | 1,602 | 1,308 | 0,927 | |

**Table 79 - Average $K/\sigma\sqrt{\pi c}$ for crack tip B, broken stiffener**

| | crack tip B [average $K/\sigma\sqrt{\pi c}$] | | | | | | | |
|---|---|---|---|---|---|---|---|---|
| | stiff elem layer | middle elem layers | | | | | back elem layer | Compounding results |
| c [$mm$] | 1 | 2 | 3 | 4 | 5 | 6 | 7 | |
| 16,25 | 4,392 | 3,440 | 2,434 | 1,410 | 0,378 | -0,665 | -1,780 | 1,480 |
| 32,50 | 2,905 | 2,408 | 1,859 | 1,293 | 0,721 | 0,136 | -0,515 | 1,274 |
| 48,75 | 2,348 | 2,029 | 1,657 | 1,269 | 0,875 | 0,467 | -0,002 | 1,223 |
| 65,00 | 2,040 | 1,828 | 1,561 | 1,279 | 0,990 | 0,688 | 0,322 | 1,220 |
| 81,25 | 1,840 | 1,706 | 1,515 | 1,307 | 1,093 | 0,865 | 0,574 | 1,245 |
| 97,50 | 1,698 | 1,630 | 1,500 | 1,354 | 1,202 | 1,035 | 0,803 | 1,317 |
| 113,50 | 1,596 | 1,587 | 1,514 | 1,425 | 1,328 | 1,215 | 1,036 | |

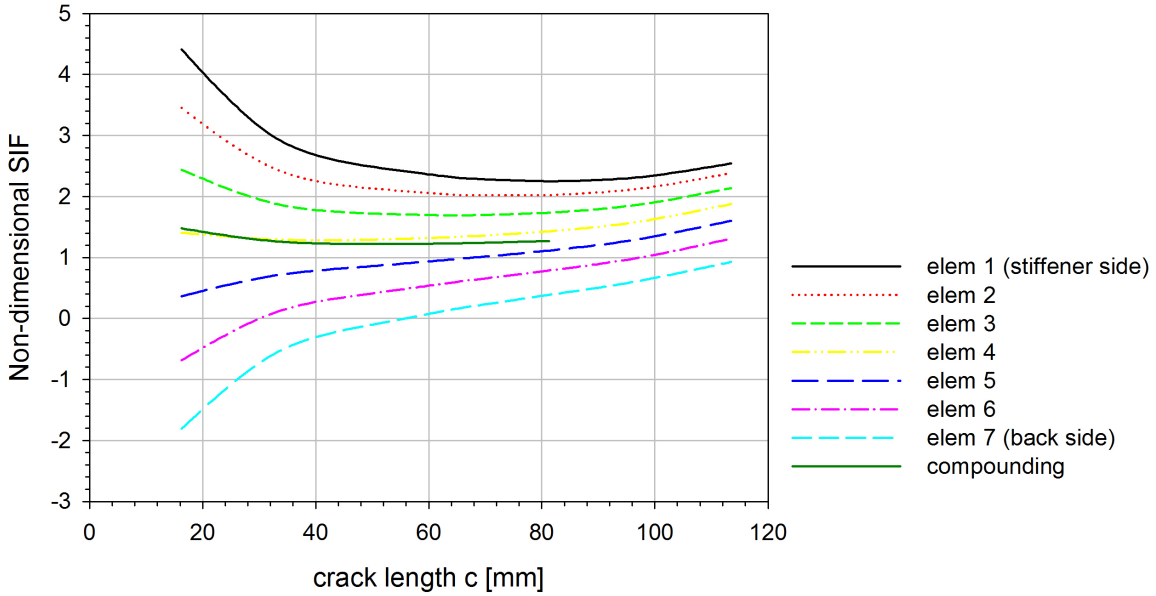


**Figure 257 - Results of SIFs for crack tip A for several crack lengths using the compounding technique and the FEM (results for each layer of elements), broken stiffener.**

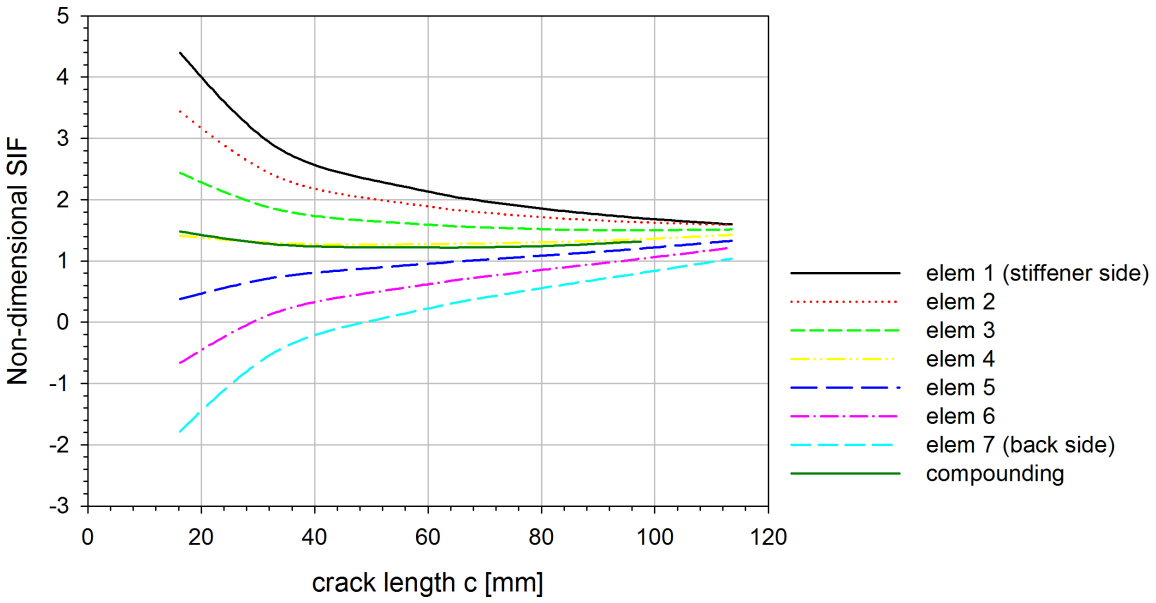


**Figure 258 - Results of SIFs for crack tip B for several crack lengths using the compounding technique and the FEM (results for each layer of elements), broken stiffener.**

The negative values of stress intensity factor are due to the negative $\sigma_y$ stress values that exist in the top layer as presented in Figure 259.

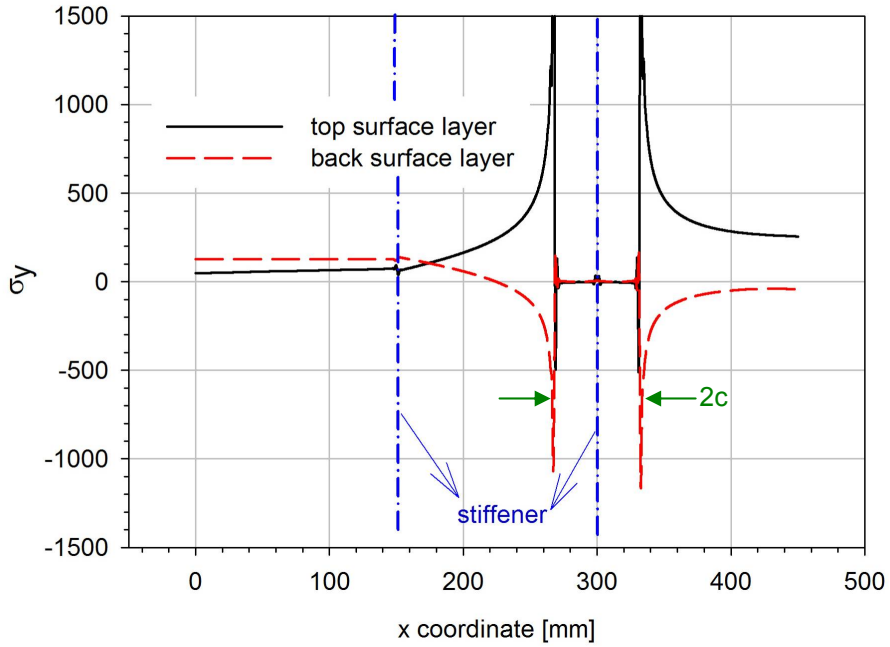


**Figure 259 - Stress $\sigma_y$ in the stiffener side (top layer) and in the opposite side (back layer) for c=32,5*mm*.**

The element layer 4 has the best agreement with the compounding results. The differences between this layer of elements results and the compounding ones are presented in Table 80. The finite element method results were considered as reference values.

**Table 80 - Difference between FEM SIFs of elements layer 4 and the compounding results, broken stiffener**

| c [$mm$] | Crack Tip A | | | Crack Tip B | | |
|---|---|---|---|---|---|---|
| | FEM element 4 layer | Compounding technique | difference [%] | FEM element 4 layer | Compounding technique | difference [%] |
| 16,25 | 1,405 | 1,448 | -3,06 | 1,410 | 1,48 | -4,95 |
| 32,50 | 1,296 | 1,276 | 1,56 | 1,293 | 1,274 | 1,49 |
| 48,75 | 1,290 | 1,220 | 5,42 | 1,269 | 1,223 | 3,64 |
| 65,00 | 1,335 | 1,256 | 5,95 | 1,279 | 1,22 | 4,60 |
| 81,25 | 1,428 | 1,350 | 5,46 | 1,307 | 1,245 | 4,76 |
| 97,50 | 1,590 | | | 1,354 | 1,317 | 2,76 |
| 113,50 | 1,876 | | | 1,425 | | |

For the case of broken stiffener, two-dimensional finite element calculations were also undertaken in order to make a supplementary check of the three-dimensional finite element accuracy. In this case, a two-dimensional analysis with six nodded triangular elements of different thickness (2$mm$ for the plate and 28$mm$ for the stiffener) was employed. Singular elements were used to model the crack tip. The $\sigma_y$ stress distribution and the finite element mesh for the case c=32,5$mm$ is shown in Figure 260. This mesh had 23825 elements and 47920 nodes. Similar meshes were used for the other crack lengths. A comparison between the three-dimensional finite element and two-dimensional finite element analyses is presented in Table 81 (three-dimensional results were taken as reference).

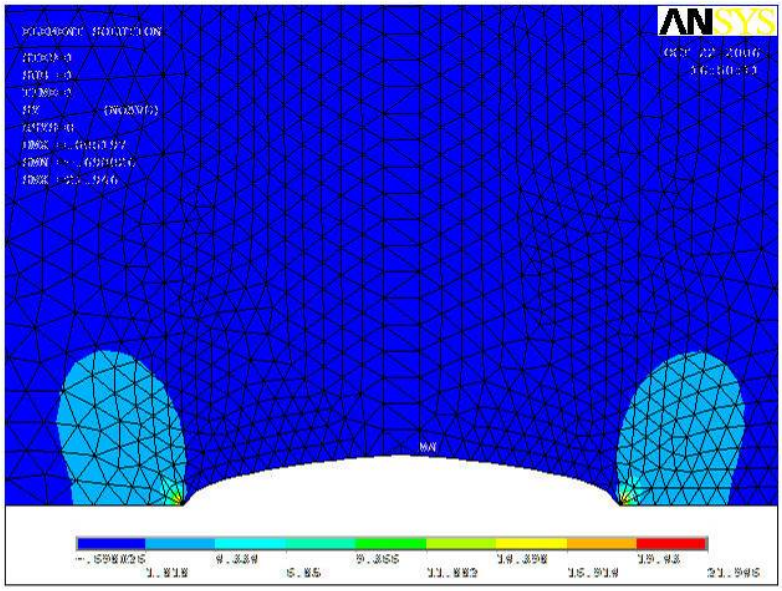


**Figure 260 - Stress $\sigma_y$ and FEM mesh for the 2D analysis of plate with broken stiffener (c=32,5$mm$)**

**Table 81 - Comparison between 3D and 2D FEM results, case of broken stiffener**

| c | 3c/W (a/b) | Tip A | | | Tip B | | |
|---|---|---|---|---|---|---|---|
| | | 3D FEM layer 4 | 2D FEM | Diff. [%] | 3D FEM layer 4 | 2D FEM | Diff. [%] |
| 16,25 | 0,108 | 1,405 | 1,448 | -3,06 | 1,410 | 1,444 | -2,41 |
| 32,50 | 0,217 | 1,296 | 1,276 | 1,54 | 1,293 | 1,265 | 2,17 |
| 48,75 | 0,325 | 1,290 | 1,220 | 5,43 | 1,269 | 1,208 | 4,81 |
| 65,00 | 0,433 | 1,335 | 1,256 | 5,92 | 1,279 | 1,204 | 5,86 |
| 81,25 | 0,542 | 1,428 | 1,350 | 5,46 | 1,307 | 1,244 | 4,82 |
| 97,50 | 0,65 | 1,590 | | - | 1,354 | 1,285 | 5,10 |

### *5.2.4 Concluding remarks*

A very refined three-dimensional finite element analysis was performed in order to calibrate the stress intensity factors for a symmetrically stiffened plate subjected to uniform tensile stress. Cracks that could develop in such a structure were assessed by considering the case of a crack that crosses one of the stiffeners in two possible scenarios:

*i.* the stiffener crossed by the crack is broken, and
*ii.* the stiffener is unbroken.

Several conclusions can be drawn from this work:

- the three-dimensional finite element method shows that the stress intensity factor varies through the thickness, even in this case of a very thin plate;

- the results that are in best agreement with those obtained with the compounding technique are those from the layer opposite to the stiffener;

- a non smooth stress intensity factor distribution through the thickness is obtained with the finite element method in the case of a coarser mesh due to lack of sufficient mesh refinement;

- the result obtained justifies the non-straight crack front of advancing fatigue cracks in stiffened panels subjected to cyclic loading.

Since such structures are often use in aeronautical industry, where fatigue phenomena are often present, the results obtained can be used in a subsequent fatigue analysis based on crack growth.

## 5.3 Conclusions

In this Chapter three-dimensional stress intensity factor solutions for a plate with a central crack and for a cracked stiffened plate were obtained using the Finite Element Method.
As a summary the following conclusions could be reached:

- In a three-dimensional analysis, stress intensity factor has different values through the thickness. So, a two-dimensional stress intensity factor analysis is only an approximation of the exact solution;
- It was verified that when a certain level of refinement is reached, subsequent refinement of the mesh does not lead to a significant improvement of the results;
- The stress intensity factor varies over the thickness and at the plate surface the singularity $r^{-1/2}$ no longer applies. A boundary layer exists near the plate free surface and its size is a function of thickness/crack length ratio;
- For the centre cracked plate, the $\sigma_y$ opening stress remains almost constant through the thickness except near the free surface where an important decrease can be noticed in the vicinity of the crack front;
- Also for the centre cracked plate, it was verified that the plane strain behaviour near the middle of the plate was demonstrated by calculating the degree of plane strain. It was shown also that the degree of plane strain tends to smaller values when the distance from the crack front increases;
- For a stiffened cracked panel, a non smooth stress intensity factor distribution through the thickness is obtained which the result obtained justifies the non-straight crack front of advancing fatigue cracks in stiffened panels subjected to cyclic loading.

# Chapter 6

# Stiffened cracked panel (DaToN specimen)

Chapter six aims to contribute to fundamental knowledge and assessment tools for the damage tolerance of integrally stiffened structures, which are produced by means of Laser Beam Welding, Friction Stir Welding and High Machining. After presenting the Finite Element Method analysis of the stiffened panel used, a testing programme including fatigue crack growth of High Speed Machining, Laser Beam Welding, and Friction Stir Welding stiffened panels is described. This testing programme was complemented by a Scanning Electron Microscopy analysis of the fractured specimens.

The work of Chapter 6 is the object of several working documents, currently under discussion within the DaToN European Union project.

# 6. Stiffened cracked panel (DaToN specimen)

An aircraft fuselage structure includes, among other parts, the external skin and longitudinal stiffeners. Investigations on the strength and behaviour of aluminium alloy stiffened sheet specimens used in aircraft construction have been carried out for several decades. Stiffeners improve the strength and stability of the structure and provide a means of slowing down or arresting the growth of cracks in a panel. Most commonly stiffeners are connected to the skin by means of fasteners. Riveted stiffeners remain intact as a crack propagates under them, providing an alternative path for the panel load to pass. The continuous need for low cost and the emergence of new technologies has brought interest for large integral metallic structures for aircraft applications. Studies show that in a integral monolithic stiffened panel a crack propagates simultaneously in the stiffener and in the skin, and into the stiffener and break it.

This Chapter is a contribution to the European DaToN project. Its aim is to provide knowledge and assessment tools for the damage tolerance of integrally stiffened structures, which are produced by means of three modern production methods: Laser Beam Welding, Friction Stir Welding and High Speed Machining. There is an urgent pressure from the manufacturing side in the aerospace industry to apply these advanced structural concepts, since they promise considerable cost and production time benefits. In addition, a smaller number of fatigue and corrosion critical locations are produced. The main drawback of integrally stiffened structures is the damage tolerance behaviour. Such an integrally stiffened design behaves totally different from the differential designs, which are usually created by using riveted stiffeners. The prime problem is the crack arresting capability of the stiffeners both in fatigue crack growth as well as in residual strength. Fatigue and damage tolerance is therefore one of the main drivers in innovative aerospace structural designs as well as one of the main concerns on the safety of aging aircraft.

The first task in this study was the finite element method analysis of the stiffened panel geometry that was defined by the project guide lines. A test programme which included fatigue crack growth rate of High Speed Machining, Laser Beam Welding, and Friction Stir Welding stiffened panels was performed. This test programme was complemented by a scanning electron microscopy analysis of the fractured specimens.

## 6.1 Finite element analysis of DaToN specimen

The geometry of the specimen to be studied in the experimental component of the DaToN project [195] is presented in Figure 261. The complexity of the specimen geometry makes it necessary to perform a three-dimensional (3D) stress analysis. For that purpose the finite element method (FEM) code ABAQUS was used [168].

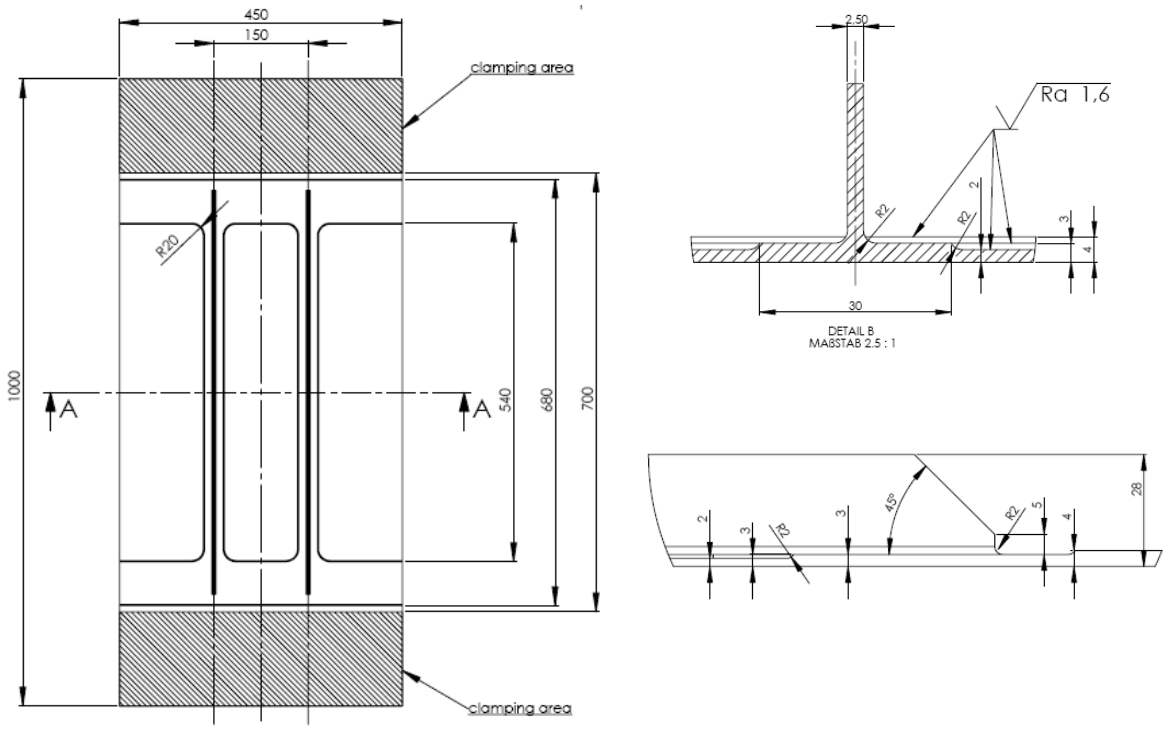


**Figure 261 - Specimen geometry of specimens to be used in the experimental component of the DaToN project, [195].**

The cross section identifying the centre of gravity in the stiffened specimen middle plane is shown in Figure 262. The centre of gravity is located $2{,}76mm$ above the specimen front face. In all the analyses carried out the load was applied aligned with the centre of gravity.

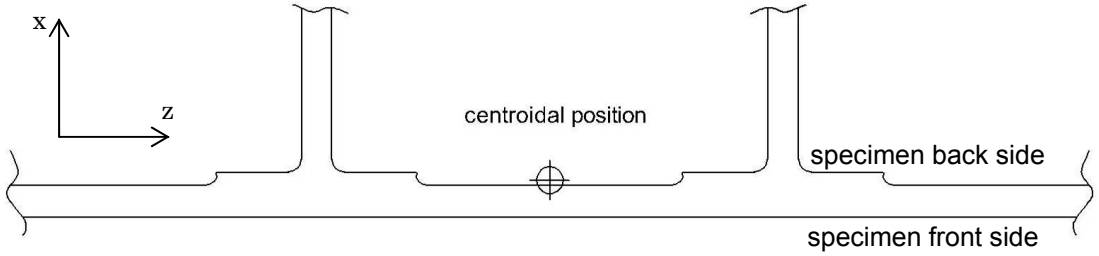


**Figure 262 - Schematic representation of the specimen middle plane cross section identifying the centre of gravity (section A-A of Figure 261).**

The remote load chosen for all analyses corresponds to a $100MPa$ uniformly distributed nominal stress.

Three different situations were analysed: stiffened panel without and with a central crack, and stiffened panel with a central crack and an anti-bending device.
In the following analyses x (and 1) is the coordinate axis in the thickness direction, y (and 2) is the coordinate axis in the loading (longitudinal) direction, and z (and 3) is the coordinate axis in the transversal direction. The specimen side containing the stiffeners will be named back side, whereas the opposite side will be named front side.

### *6.1.1 Specimen geometry*

#### *6.1.1.1 Mesh*

8-nodes brick elements (C3D8) and 6-nodes brick elements (C3D6) were used to model the specimen. These elements use linear interpolation in each direction and are often called linear elements or first-order elements. A total of 60083 elements were used to model half of the stiffened panel. The mesh used is shown in Figure 263.

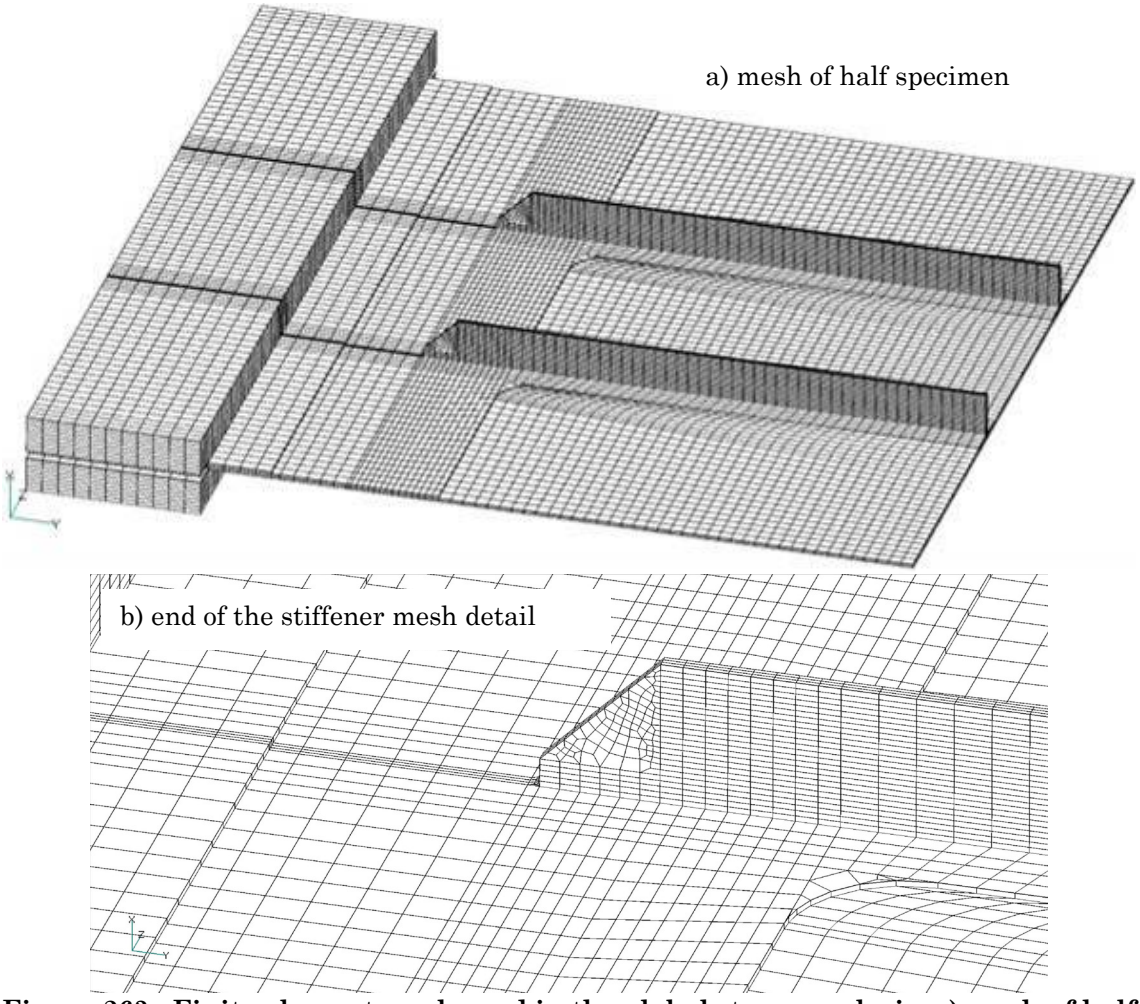


**Figure 263 - Finite element mesh used in the global stress analysis: a) mesh of half specimen; b) end of the stiffener, mesh detail.**

*6.1.1.2 Remotely loaded un-cracked stiffened plate*

Figure 264 shows the stress in the load direction, $\sigma_y$ throughout the stiffened panel. The deformed three-dimensional FEM model is shown in Figure 265. In this figure, displacements were enlarged (deformation scale factor of 20) in post-processing of the FEM analysis.

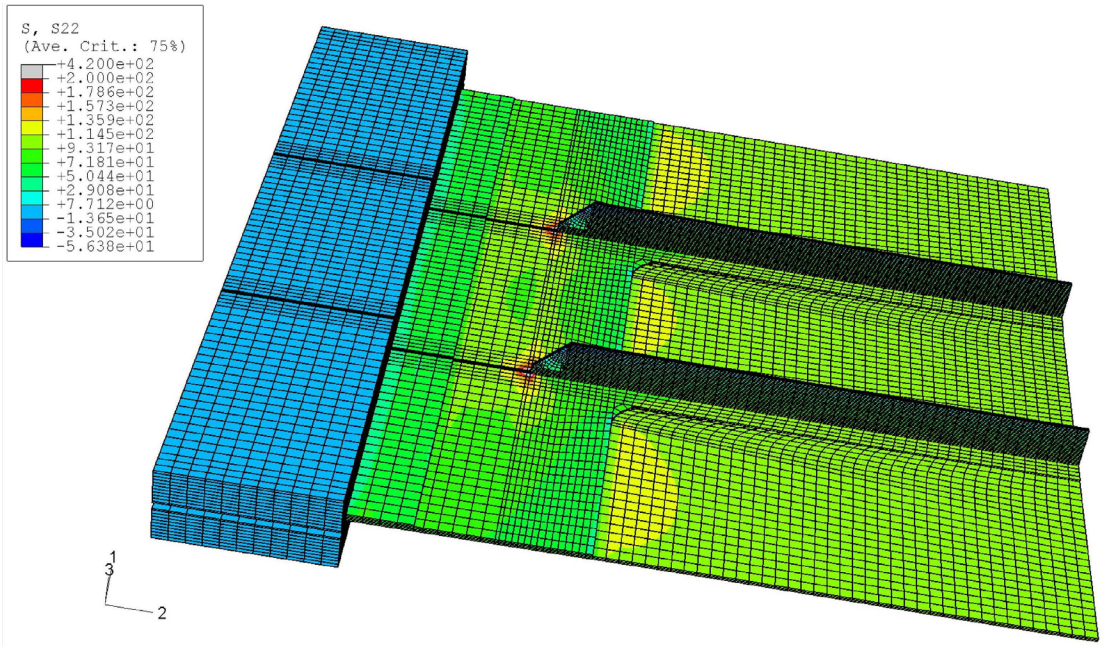


**Figure 264 - Stress distribution on the stiffened plate, stress in the load direction.**

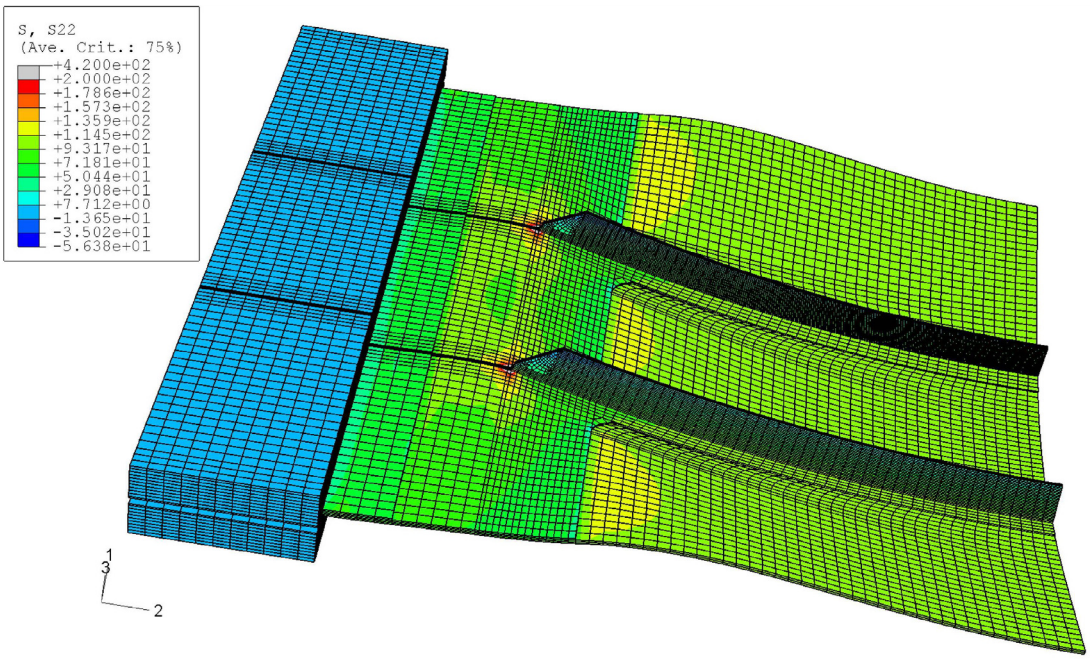


**Figure 265 - Deformed model (deformation scale factor of 20) and stress distribution on the stiffened plate, stress in the load direction.**

A detail of the $\sigma_y$ stress distribution in the specimen middle cross section is presented in Figure 266. The stress values are higher in the plate and decrease through the stiffener moving away from the plate, as indicated by the arrow. The evolution of $\sigma_y$ stress values along the nodes that lay on the arrow is presented in Figure 267. The higher and lower $\sigma_y$ stress values along this line are 112,2$MPa$ and 17,5$MPa$ respectively.

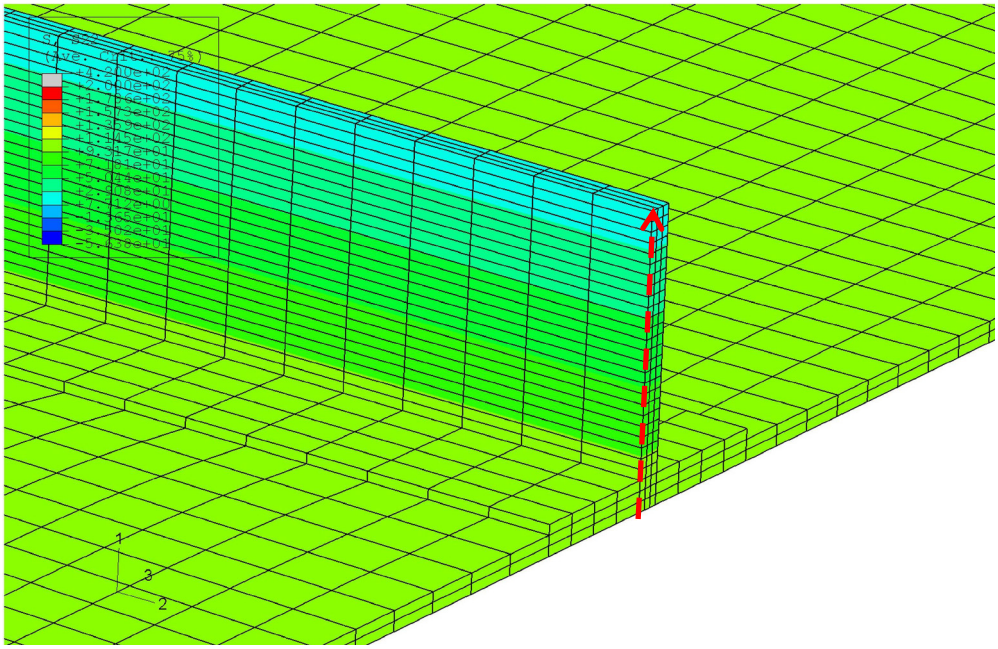

**Figure 266 - Detail of specimen middle cross section.**

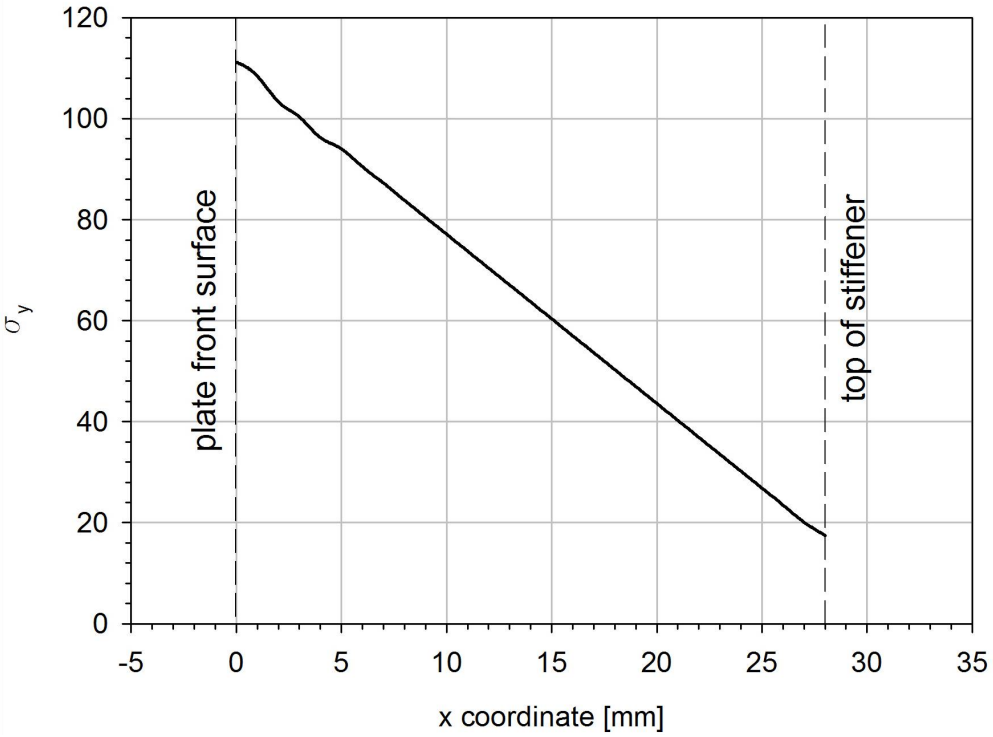


**Figure 267 - Stress distribution along the nodes that lay on the arrow shown in Figure 266.**

The stress distribution in the specimen middle cross section is presented in Figure 268. The $\sigma_y$ stress distribution and displacements in the x direction were analysed along the nodes on the plate side containing the stiffeners, and on the opposite plate side, along the direction of the arrow plotted in this figure.

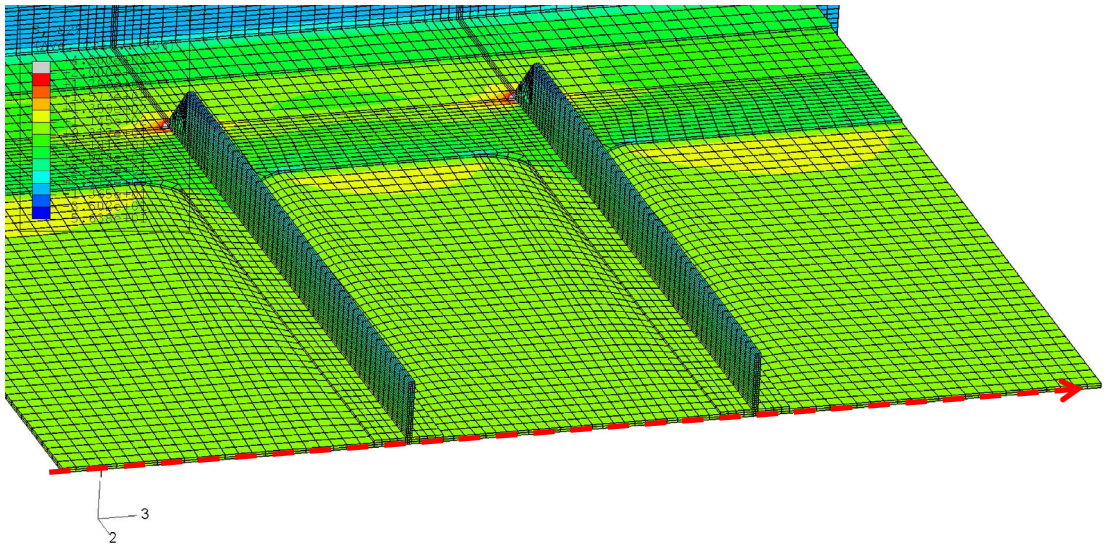


**Figure 268 - Specimen middle cross section.**

The $\sigma_y$ stress distributions in the specimen middle cross section in the back and front layer nodes (*i.e.* plate side containing the stiffeners, and opposite side) are presented in Figure 269. The stress values are higher in the plate side opposite to the stiffeners, and lower in the stiffeners side. Also higher stress values are found in the centre of the plate. In the plate stiffener side the maximum stress value is $104{,}9MPa$ and the lower value is $97{,}9MPa$. In the plate side opposite to the stiffener the maximum stress value is $111{,}5MPa$ and the lower value is $108{,}4MPa$.

The displacement in the x direction in the specimen middle cross section in the front and back layer nodes is presented in Figure 270. For both layers the displacement is similar. For the remote load applied it was found that the maximum displacement is $2{,}77mm$. The maximum displacement occurs at the middle of the plate.

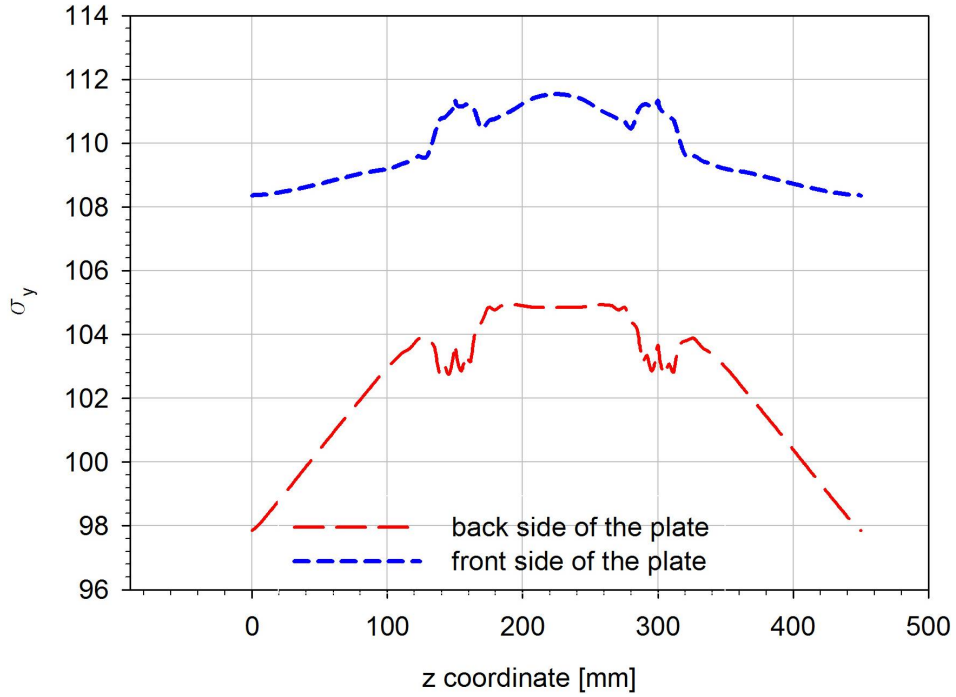


**Figure 269 - $\sigma_y$ distribution in the specimen middle cross section in the front and back layer nodes.**

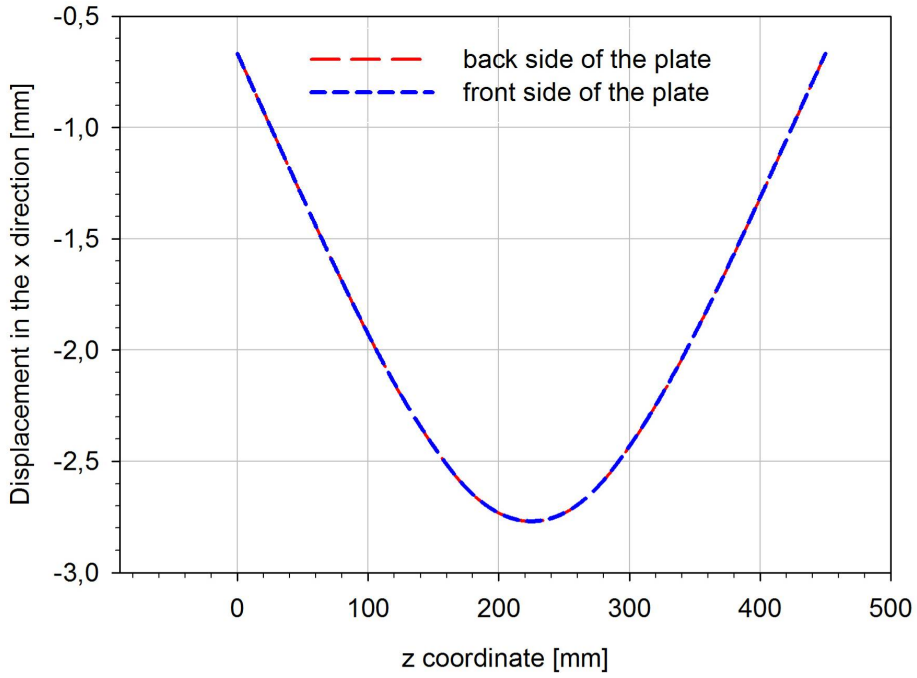


**Figure 270 - Displacement x in the specimen middle cross section in the front and back layer nodes**

The $\sigma_y$ stress distribution along the specimen longitudinal direction is presented in Figure 271. In this figure three lines - a), b) and c) – are marked. The $\sigma_y$ stress and displacements in the x direction were determined along these lines. Results presented for lines b) and c) were obtained in the plate side opposite to the stiffeners (front side).

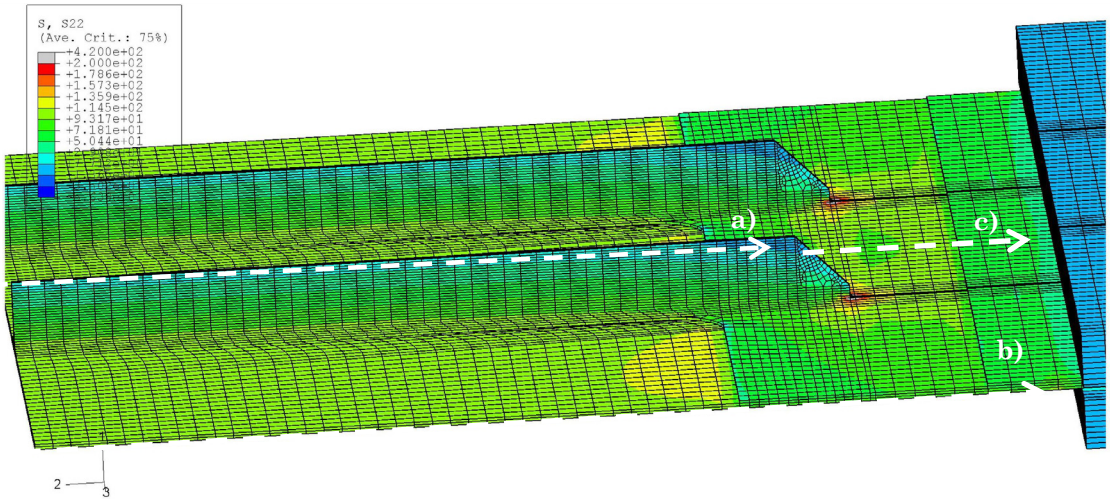


**Figure 271 - $\sigma_y$ distribution along the specimen longitudinal direction.**

Figure 272 presents the $\sigma_y$ stress distribution through the specimen longitudinal direction along three lines: a) stiffener top surface; b) plate's lateral layer; c) plate's centre layer. The higher stress values are found in the centre of the plate, but they are of the same magnitude as those found in the side layer. Stress values on the stiffener top surface are near 18*MPa*, except in the stiffener end where some low compressive values are found.

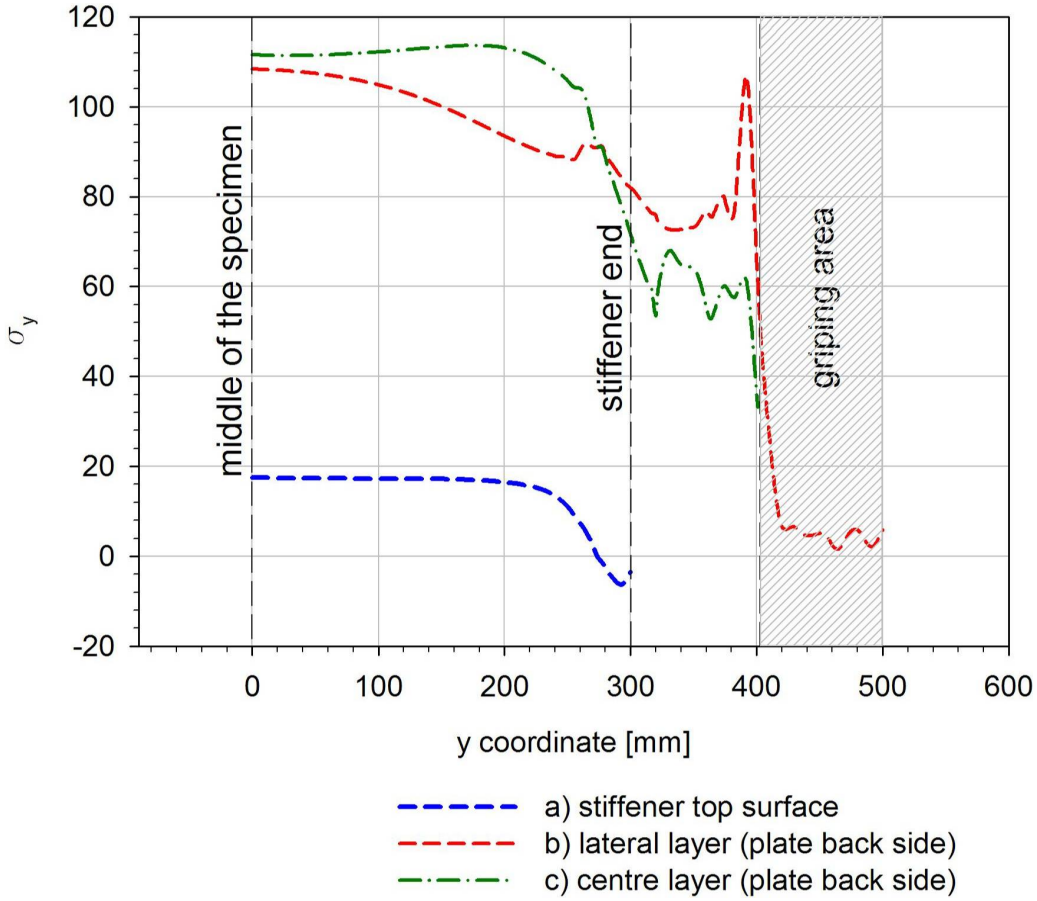


**Figure 272 - $\sigma_y$ distribution through the specimen longitudinal direction in three lines: a) stiffener top surface; b) plate's lateral layer; c) plate's centre layer.**

The displacement in the x direction along the three lines in the loading direction a) stiffener top surface; b) plate's lateral layer; c) plate's centre layer, is presented in Figure 273. The maximum displacements are found in the middle cross section at the middle of the plate. It was found that in the lateral layer the displacements start with negative values and progress to positive values before becoming zero in the grip area.

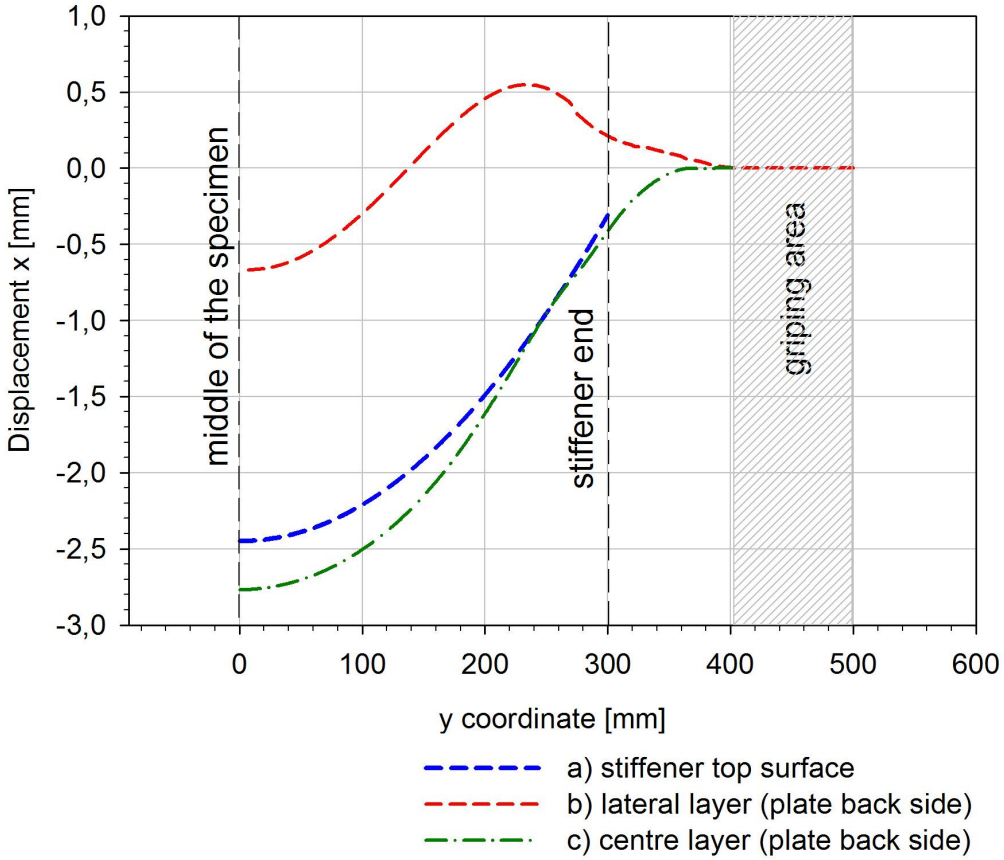


**Figure 273 - Displacement in the x direction through the specimen longitudinal direction in three lines: a) stiffener top surface; b) plate's lateral layer; c) plate's centre layer.**

The stress concentration effect found in the end of the stiffener concordance radius is presented in Figure 274. The maximum $\sigma_y$ stress value found is $420MPa$. Comparing with the $\sigma_y$ value in the specimen mid point (approximately $110MPa$) a stress concentration factor of 3,8 is found.

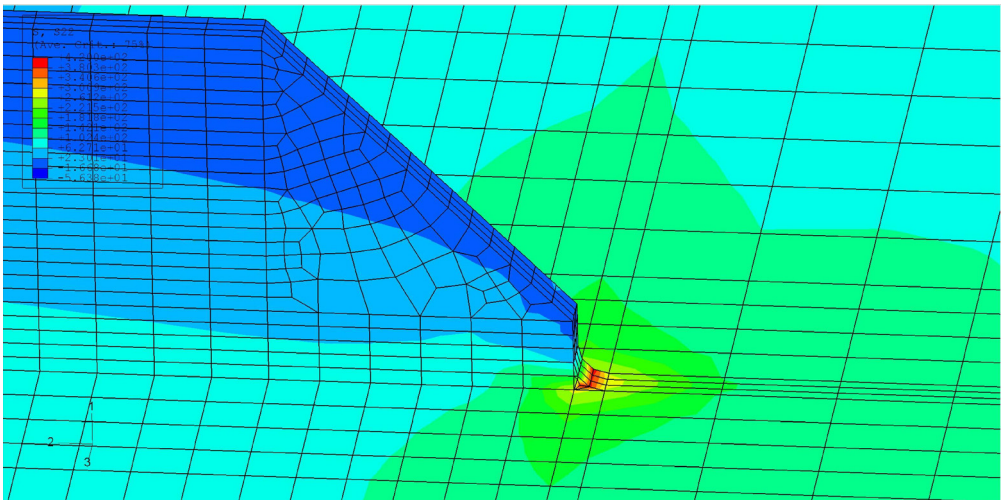

**Figure 274 - Stress concentration factor at the end of the stiffener.**

Regions where compressive stresses were found are presented in Figure 275. The most extensive area is at the end of the stiffeners, but the values found are near zero. This fact was promoted by the decrease of the plate thickness at the end of the stiffener (it decreased from $4mm$, in the preliminary specimen geometry, to $3mm$ in the current geometry).

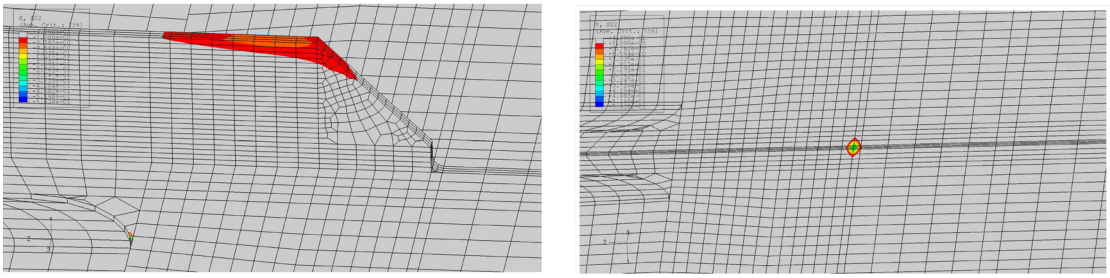

**Figure 275 - Identification of zones with compressive stresses**

*6.1.1.3 Remotely loaded cracked stiffened plate*

A crack with length 2a=55,39$mm$ was modelled in the centre of the specimen shown in Figure 261. The distribution of $\sigma_y$ stress (load direction) throughout the stiffened plate, and the deformed three-dimensional FEM model, are shown in Figure 276. In this figure displacements were enlarged (deformation scale factor of 20) in post-processing of the FEM analysis.

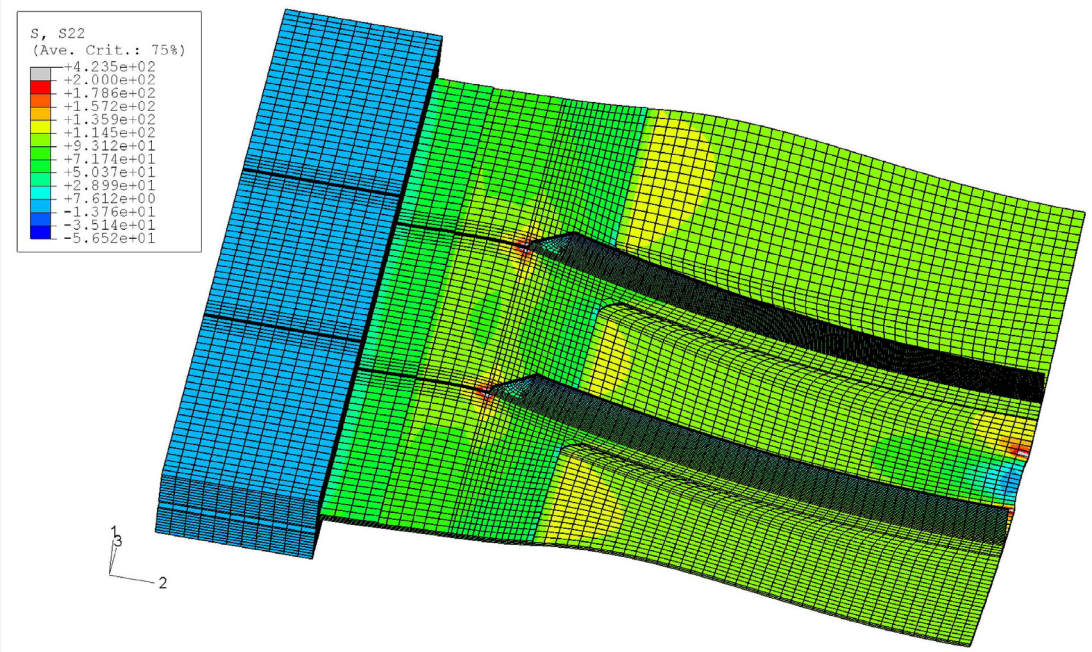


**Figure 276 - Stress $\sigma_y$ distribution and deformed model of a stiffened panel with a crack (deformation scale factor of 20), stress in the load direction.**

The detail of $\sigma_y$ stress distribution in the specimen middle cross section is presented in Figure 277. The evolution of $\sigma_y$ stress along the nodes that lay on the arrow a) is presented in Figure 278. The introduction of a crack in the stiffened panel leads to an increase of the stress values in the plate and a decrease at the top of the stiffener.

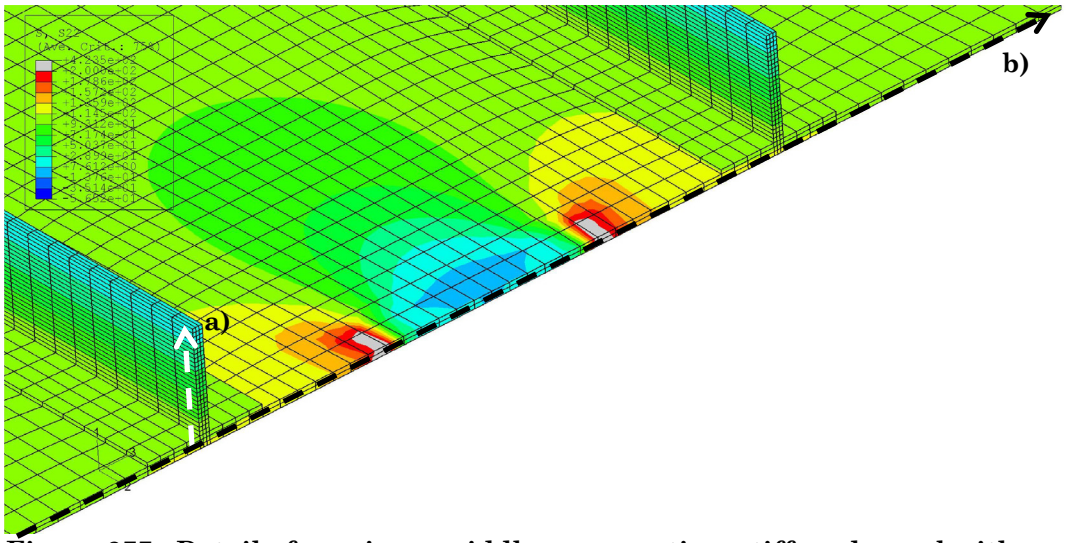


**Figure 277 - Detail of specimen middle cross section, stiffened panel with a crack.**

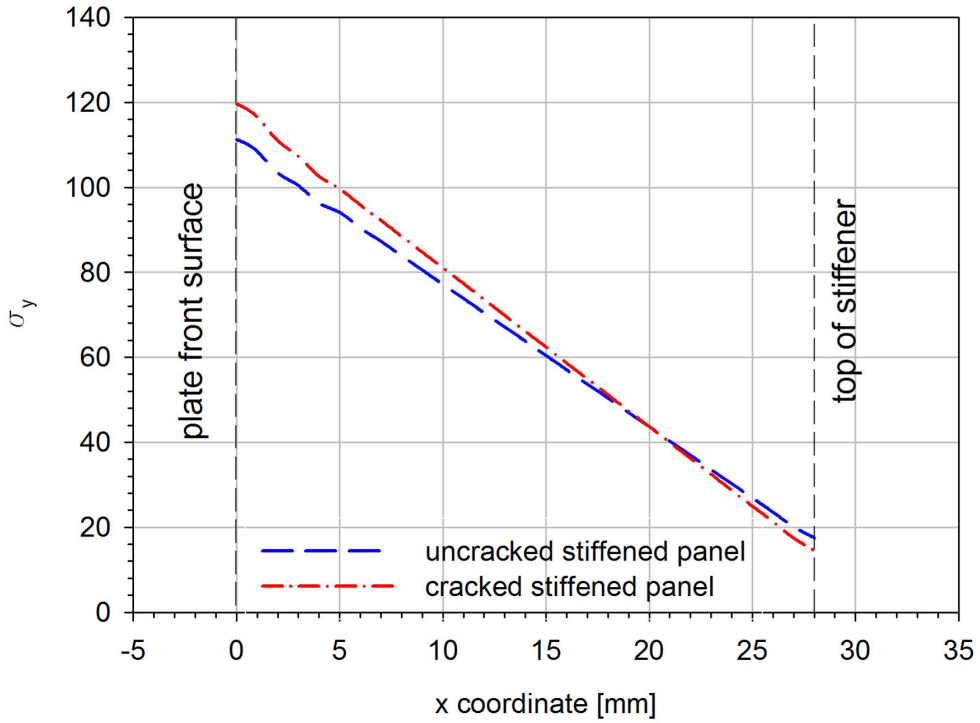


**Figure 278 - Stress distribution along the nodes that lay on the arrow a) presented in Figure 277. Stiffened panel with a crack.**

The $\sigma_y$ stress distribution and displacements in the x direction were analysed along the nodes on the side of the plate containing the stiffeners and on the opposite side, in the direction of the arrow b) plotted in Figure 277.
The $\sigma_y$ stress distribution in the specimen middle cross section, with and without a crack, in the front and back layers (*i.e.*, side containing the stiffener, and opposite side) is presented in Figure 279. In the lateral areas $\sigma_y$ stress is similar in the panel with and without a crack. It is also possible to identify the change in the stress distribution due to the crack.

The displacement in the x direction in the specimen middle cross section, with and without a crack, in the front layer nodes is presented in Figure 280. The maximum displacement value found in the cracked panel is $2{,}95mm$, and occurs at the middle of the panel. In the case of an un-cracked panel the displacement was $2{,}77mm$.

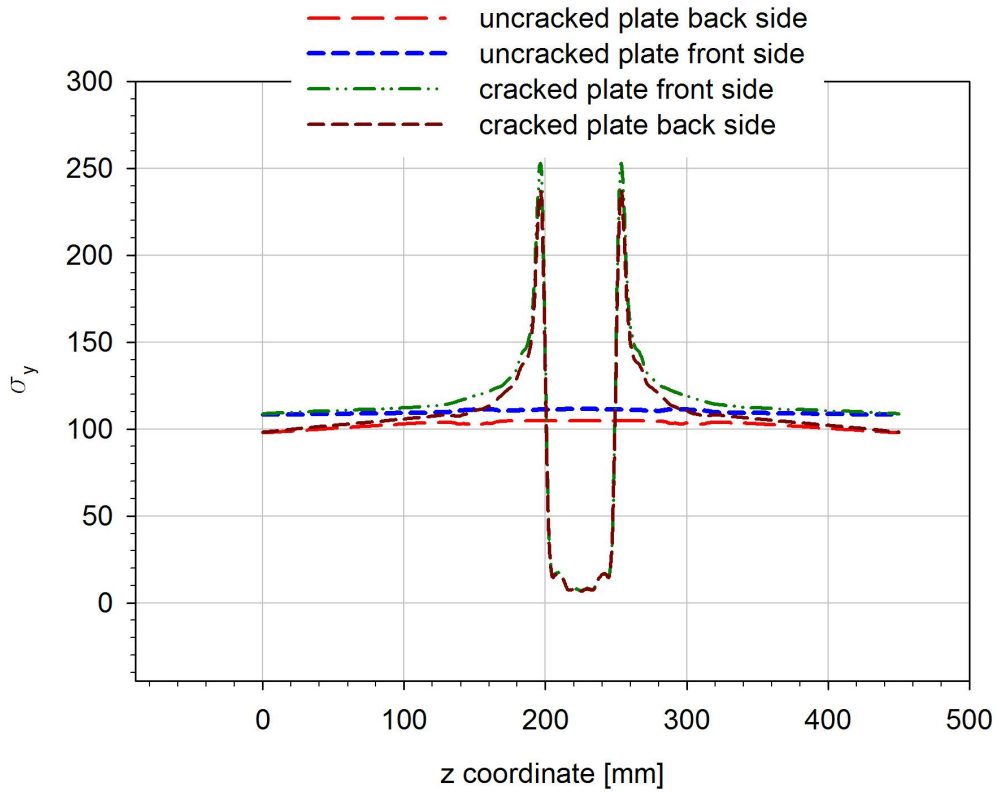


**Figure 279 - $\sigma_y$ distribution in the specimen middle cross section in the front and back layer nodes.**

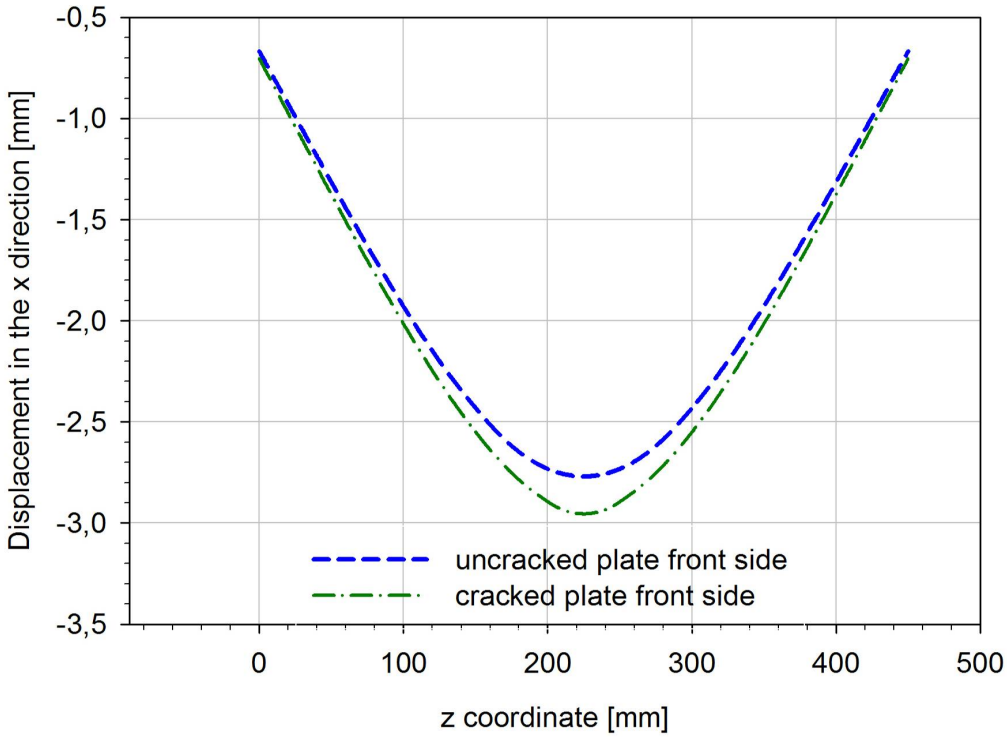


**Figure 280 - Displacement x in the specimen middle cross section, with and without a crack, in the front layer nodes.**

The $\sigma_y$ stress distribution along the specimen longitudinal direction for a stiffened panel with a crack is similar to the study presented in Figure 271. In this figure three lines - a), b) and c) - are identified where $\sigma_y$ stress and displacements in the x direction are analysed. Results presented for lines b) and c) were obtained in the side opposite to the stiffeners (front side).
The $\sigma_y$ stress distribution throughout the specimen longitudinal direction in the stiffener top surface a), panel lateral surface b) and panel longitudinal central line c) (as presented in Figure 271) is presented in Figure 281. Due to the presence of a crack there is a decrease of the $\sigma_y$ stress value in the stiffener near the crack, but in the remaining stiffener $\sigma_y$ stress has similar values as in the un-cracked panel. In the case of the cracked panel, $\sigma_y$ stress is similar to the un-cracked panel, except in the middle plane near the crack face where $\sigma_y$ has zero or very low values as expected.

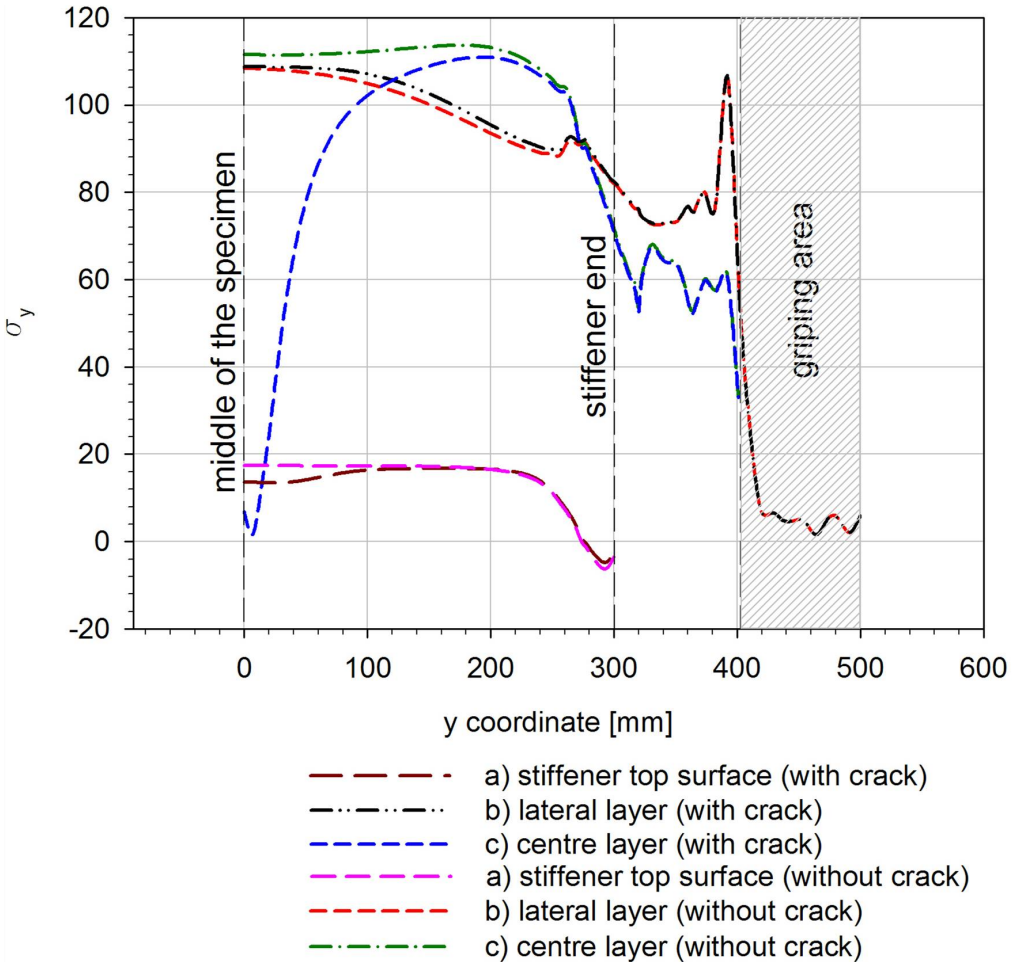


**Figure 281 - $\sigma_y$ distribution through the specimen longitudinal direction in stiffener top surface a), lateral surface b) and centre layer c), as presented in Figure 271. Stiffened panel with and without a crack.**

The displacements in the x direction for a stiffened panel along lines a), b) and c) are presented in Figure 282. Results presented for lines b) and c) were obtained in the side opposite to the stiffener (front side). Differences for the cracked and un-cracked plates are small.

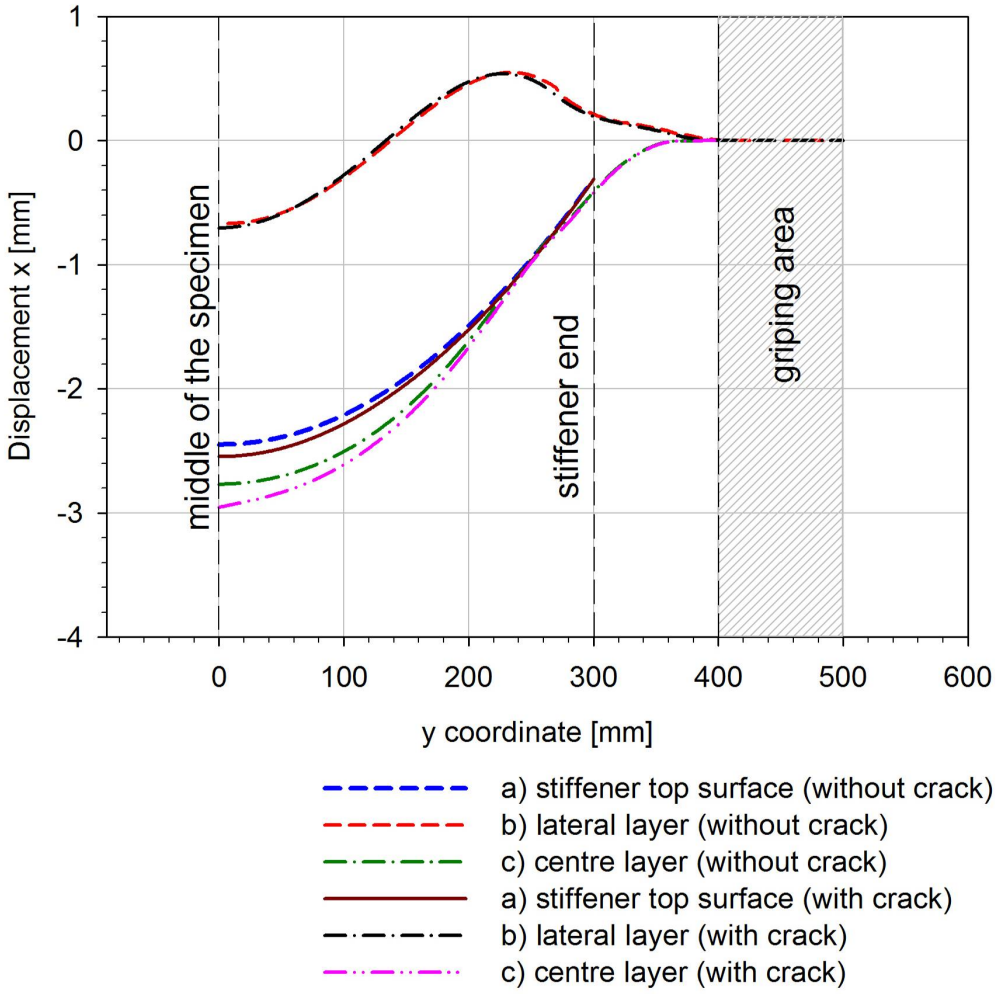


**Figure 282 - Displacement in the x direction through the specimen principal dimension in three lines: a) stiffener top surface; b) plate's lateral layer; c) plate's centre layer. Stiffened panel with and without a crack.**

As far as the stress concentration effect at the end of the stiffeners is concerned, the maximum $\sigma_y$ stress value found in the cracked stiffened plate is $423{,}5MPa$, whereas in the case of the un-cracked panel it was $420MPa$. So, the presence of a crack with length $2a=55{,}39mm$ has a negligible effect in the value of the stress concentration factor.

### *6.1.1.4 Remotely loaded cracked stiffened plate with an anti-bending device*

A crack with length $2a=55{,}39mm$ and an anti-bending device were modelled in the specimen. The $\sigma_y$ stress distribution in the load direction throughout the stiffened plate, and the deformed three-dimensional FEM model, are shown in Figure 283. In this figure displacements were enlarged (deformation scale factor of 20) in post-processing of the FEM analysis. The anti-bending device constrained the plate's front surface preventing movement in the negative x direction.

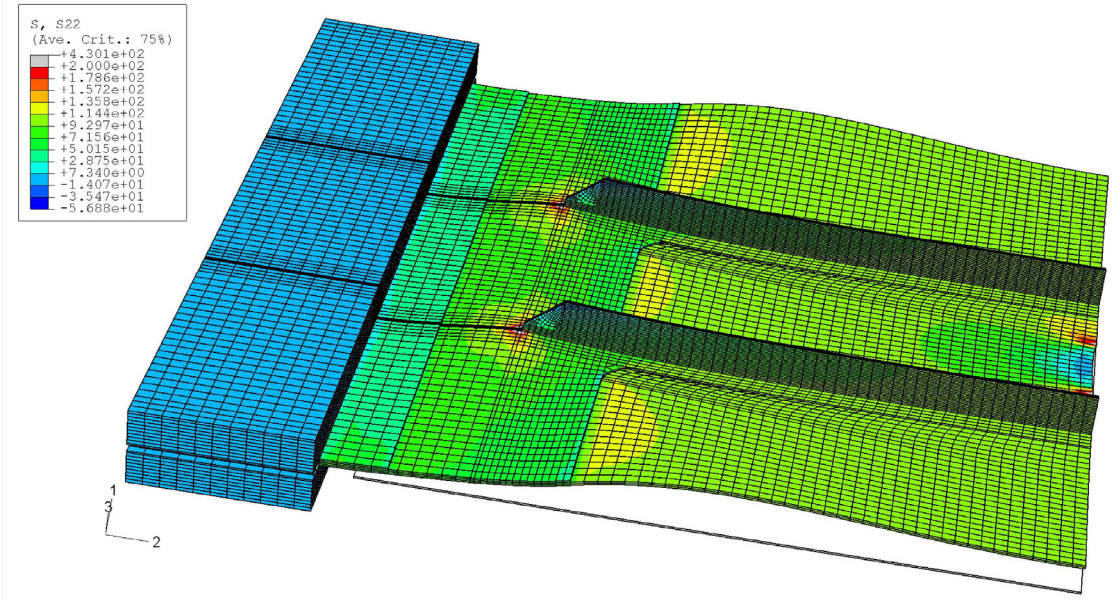


**Figure 283 - Stress $\sigma_y$ distribution and deformed model (deformation scale factor of 20). Model with a crack and an anti-bending device.**

The detail of stress distribution in the specimen middle cross section is presented in Figure 284. The $\sigma_y$ stress evolution along the nodes that lay on the arrow a) is presented in Figure 285. With the anti-bending device stress $\sigma_y$ is almost constant through the line a). The stiffener has higher $\sigma_y$ stress values than without the anti-bending device.

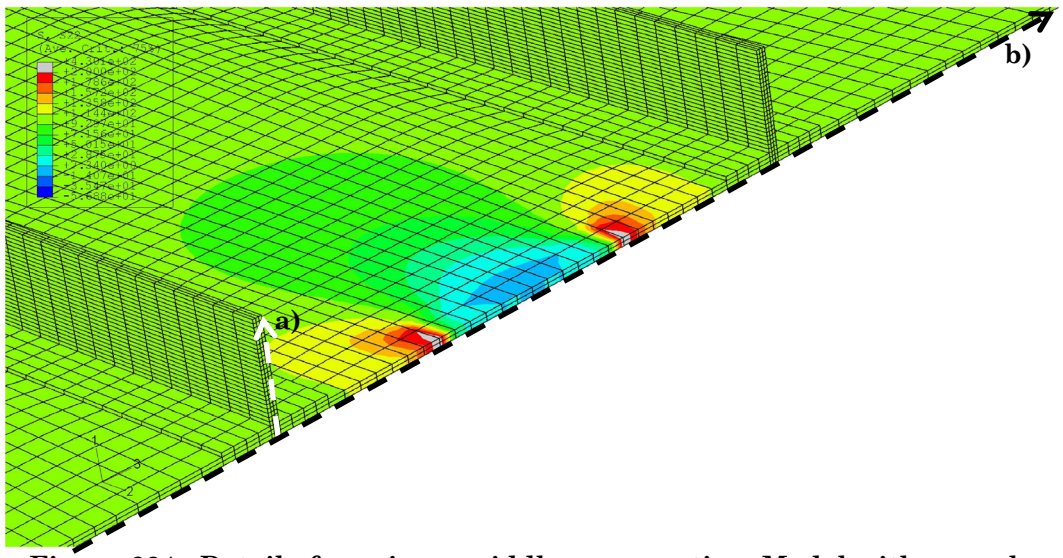


**Figure 284 - Detail of specimen middle cross section. Model with a crack and an anti-bending device.**

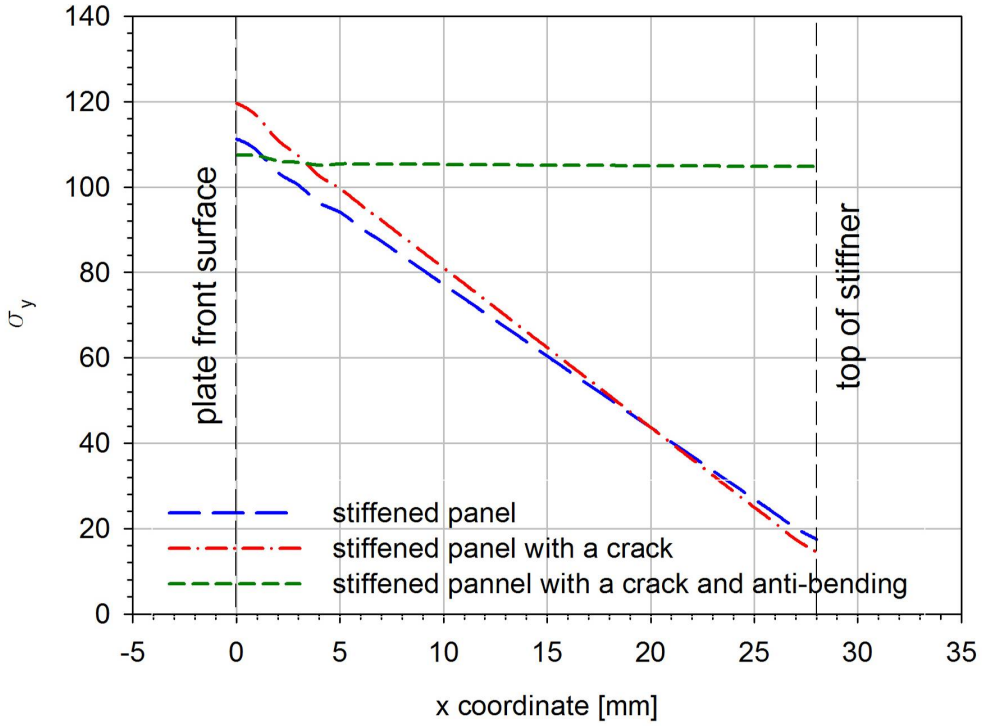


**Figure 285 - Stress distribution along the nodes that lay on the arrow a) presented in Figure 284.**

The $\sigma_y$ stress distribution and the displacements in the x direction in the specimen middle cross section were analysed along the nodes on the stiffener plate side and on the opposite side, in the direction of the arrow b). The $\sigma_y$ stress distribution in the cracked specimen middle cross section, with and without the use of an anti-bending device, in the front and back layer nodes is presented in Figure 286. Stress values with an anti-bending device are slightly lower than without this device.

Figure 287 shows displacement x for the cases: un-cracked and cracked panel, always without anti-bending device, and cracked panel with anti-bending device. The displacements constrained by the anti-bending device presented in this figure show that the specimen central area is in contact with the anti-bending device and the external lateral areas bend in the x positive direction, and do not contact that device.

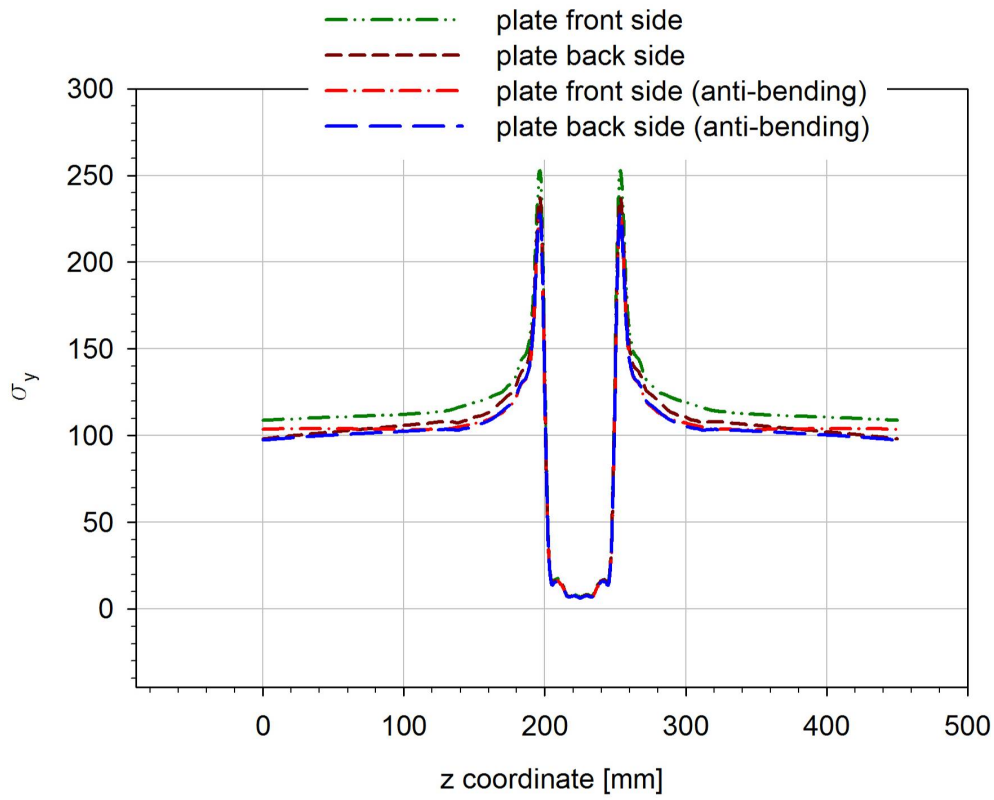


**Figure 286 - $\sigma_y$ distribution in the specimen middle cross section in the front and back layer nodes. Stiffened cracked panel, with and without an anti-bending device.**

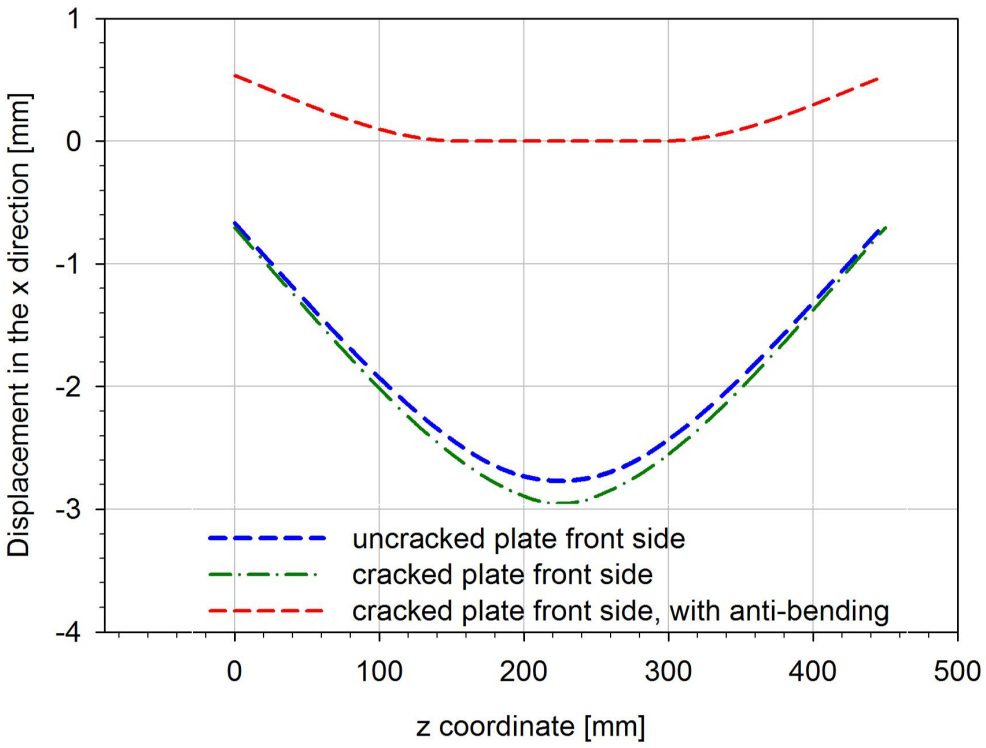


**Figure 287 - Displacement x in the specimen middle cross section, with and without a crack, in the front layer nodes.**

The $\sigma_y$ stress distribution along the specimen longitudinal direction is presented in Figure 288. This analysis was carried out using an anti-bending device on a cracked panel. Three lines - a), b) and c) - where $\sigma_y$ stress and x direction displacements were analysed are identified in this figure. Results presented for lines b) and c) were obtained in the plate side opposite to the stiffeners (front side).

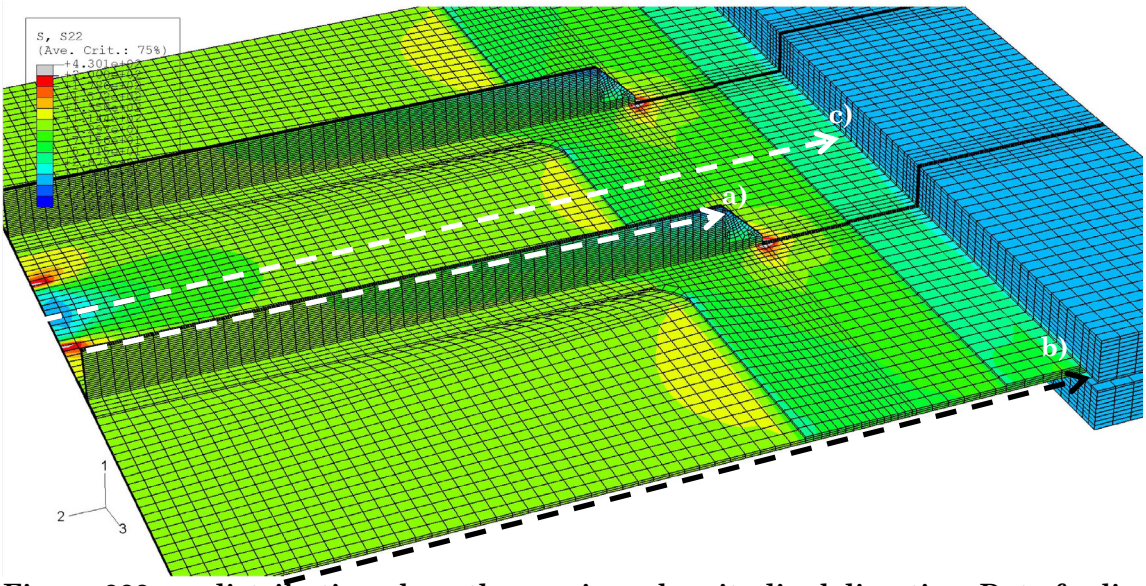


**Figure 288 - $\sigma_y$ distribution along the specimen longitudinal direction. Data for lines b) and c) corresponds to the plate front side. Model with a crack and an anti-bending device.**

The $\sigma_y$ stress distribution through the specimen longitudinal direction along three lines: a) stiffener top surface; b) plate's lateral layer; and c) plate's central longitudinal axis is presented in Figure 289. Cracked panels with and without an anti-bending device were analysed.

It is possible to identify the difference in stress distribution due to the use of the anti-bending device. The stiffener top surface has higher values near the specimen middle cross section. But, as in the case of a panel without an anti-bending device, at the end of the stiffener compressive low values are found. Along lines b) and c) the use of an anti-bending device does not alter substantially the stress distributions; nevertheless, lower values are found when using the anti-bending device.

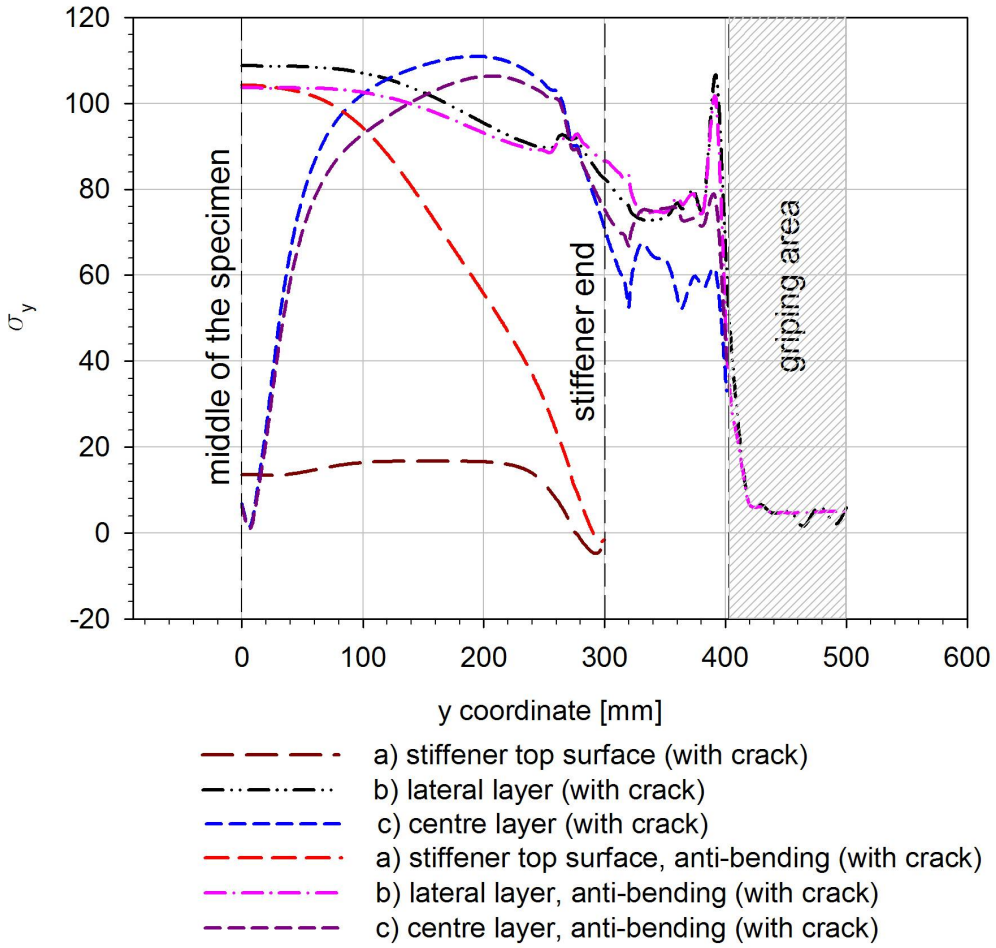


**Figure 289 - $\sigma_y$ distribution through the specimen longitudinal direction in three lines: a) stiffener top surface; b) plate's lateral layer; c) plate's centre layer.**

The x direction displacements along the specimen longitudinal direction in lines a), b) and c) are presented in Figure 290. Results for lines b) and c) were obtained in the side opposite to the stiffener (front side). A cracked panel with and without anti-bending device was studied. Using the anti-bending device, displacements are zero along most of the specimen length, for lines a) and c). When the anti-bending device is not used the displacements in line c) acquires negative maximum values of the order of $3mm$. In line b), when using an anti-bending device the displacement presents positive values; without the anti-bending device, x displacements present negative values near the specimen middle section and evolves to positive values closer to the grips.

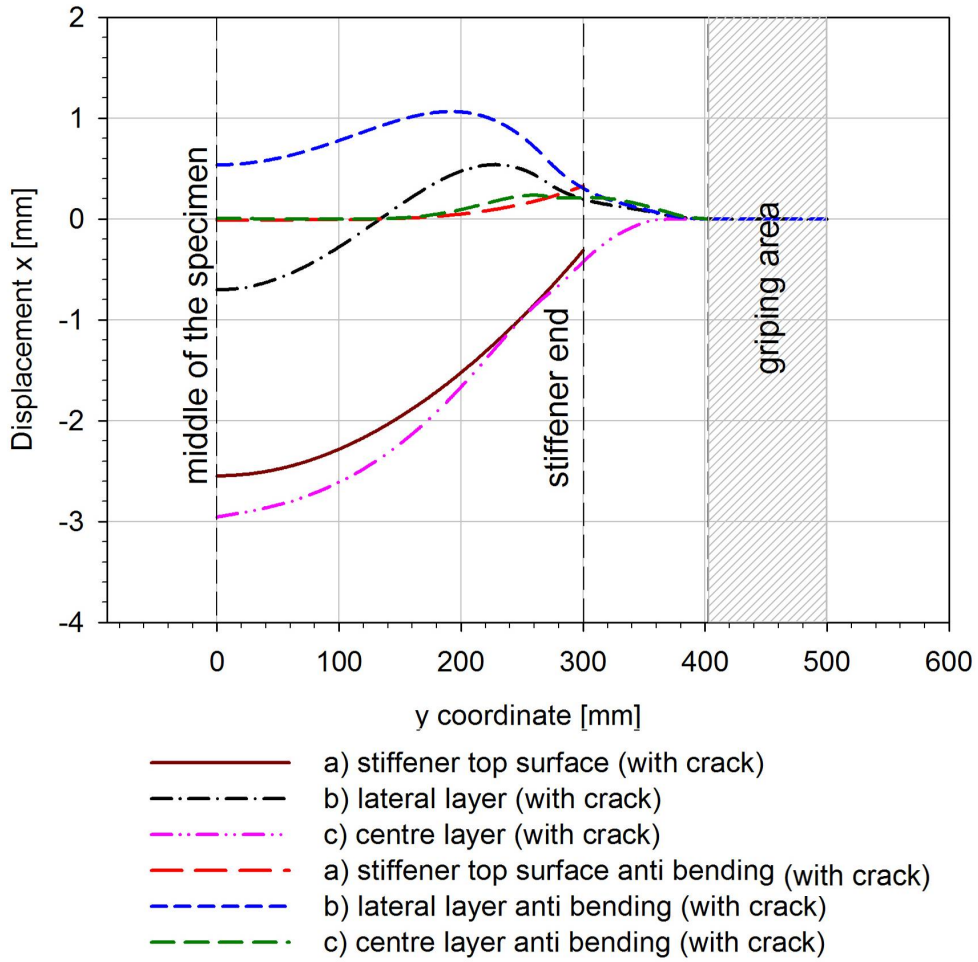


**Figure 290 - Displacement in the x direction through the specimen longitudinal direction in three lines: a) stiffener top surface; b) plate's lateral layer; c) plate's centre layer. Stiffened panel with a crack and an anti-bending device.**

When using an anti-bending device, the stress concentration effect found at the end of stiffener concordance radius is presented in Figure 291. The maximum $\sigma_y$ stress value found is 430,1*MPa*. Comparing with the values found at the stiffener plate (approximately 110*MPa*) a stress concentration factor of 3,9 is found.

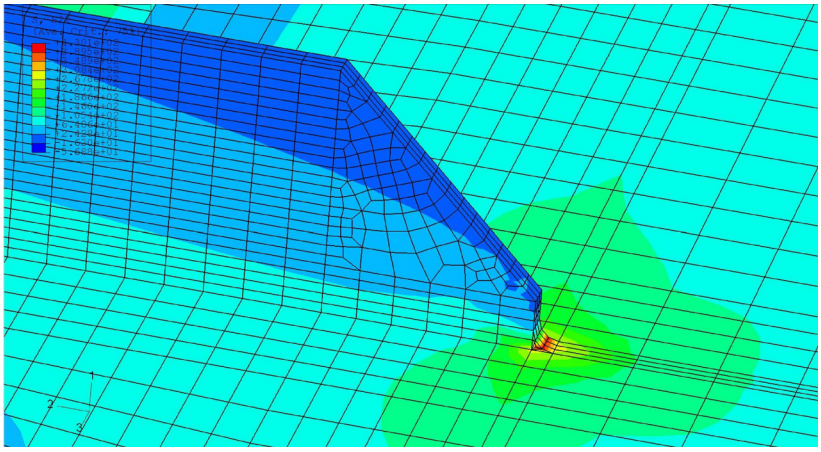

**Figure 291 - Stress concentration factor at the end of the stiffener in the presence of an anti-bending device.**

Regions with compressive stresses are presented in Figure 292. Compressive stresses in a panel with and without an anti-bending device are found in the same sites. The values found in both analyses are near zero.

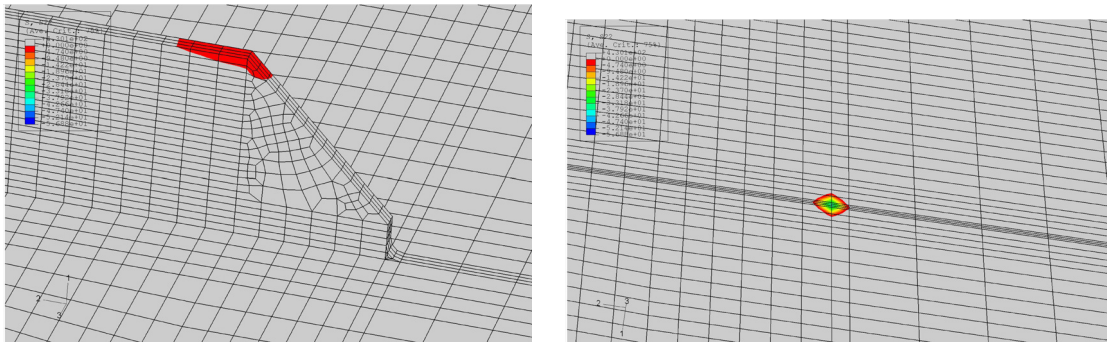

**Figure 292 - Identification of zones with compressive stresses**

### *6.1.2 Preliminary specimen geometry*

The preliminary geometry of specimen to be considered for the experimental component of the DaToN project [195] is presented in Figure 293. This preliminary geometry is compared with the current geometry, already presented in the previous section.

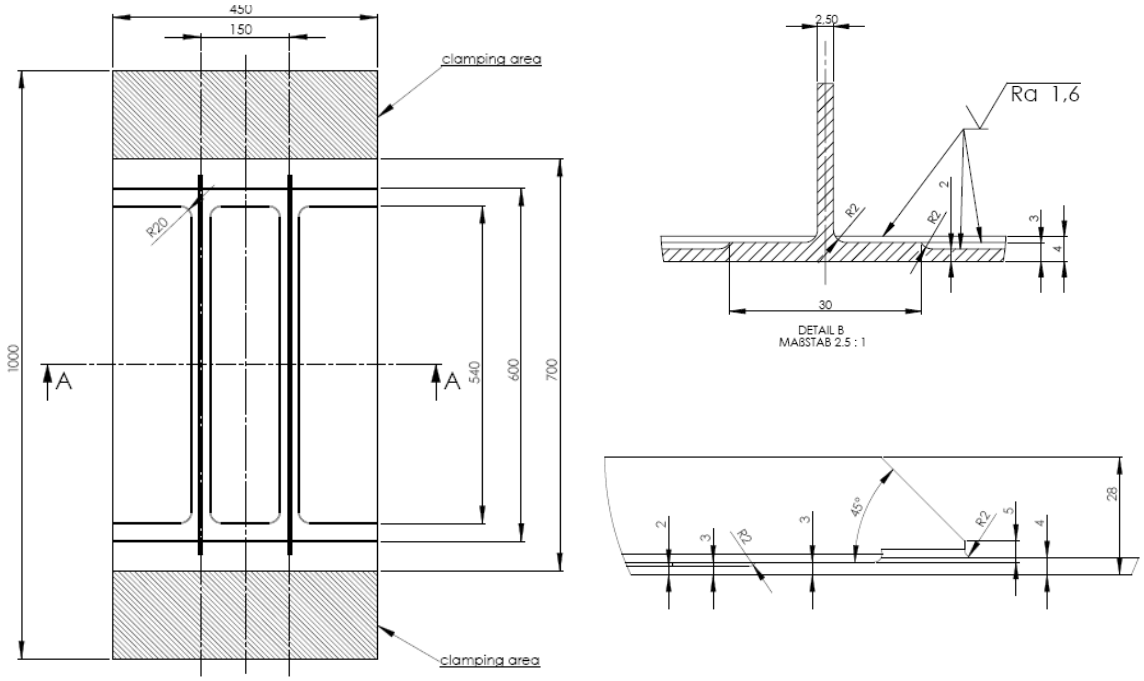


**Figure 293 - Preliminary specimen geometry of specimens proposed for use in the experimental component of the DaToN project [195].**

For this discarded geometry configuration only the case of stiffened un-cracked panel was analysed. 8-nodes brick elements (C3D8) and 6-nodes brick elements (C3D6) were used to model the specimen. A total of 67780 elements were used to model half of the stiffened panel.

Figure 294 shows the stress (in the load direction), throughout the deformed stiffened panel. In this figure, displacements were enlarged (deformation scale factor of 20) in post-processing of the FEM analysis.

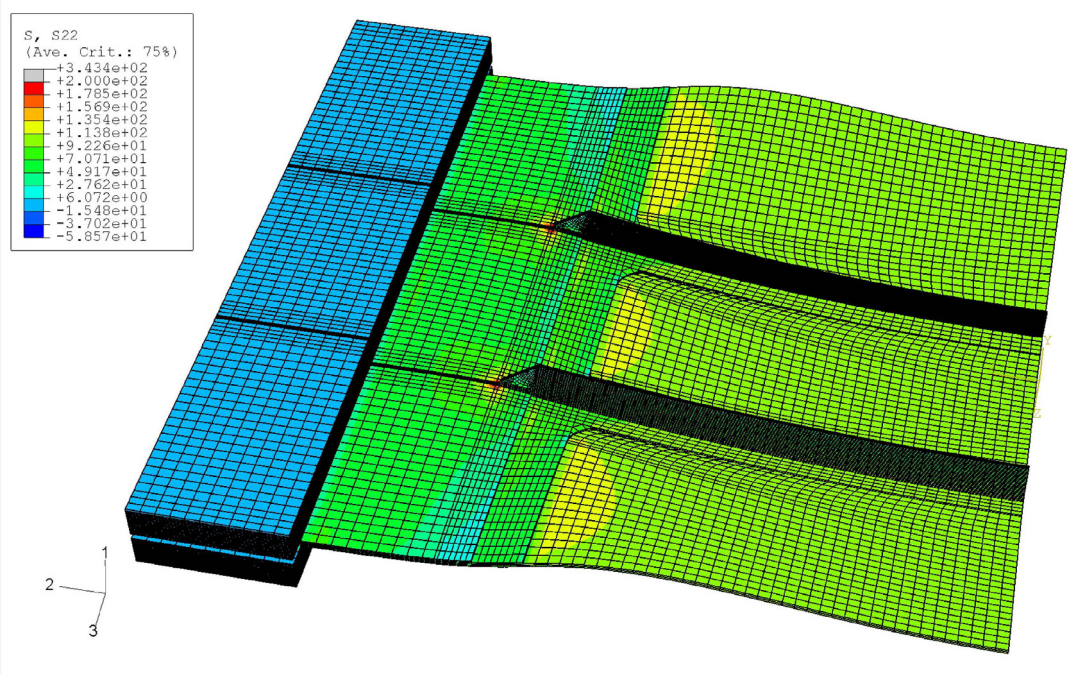


**Figure 294 - Stress distribution on the stiffened plate preliminary geometry (deformation scale factor of 20), stress in the load direction.**

The detail of stress distribution in the specimen middle cross section is presented in Figure 295.

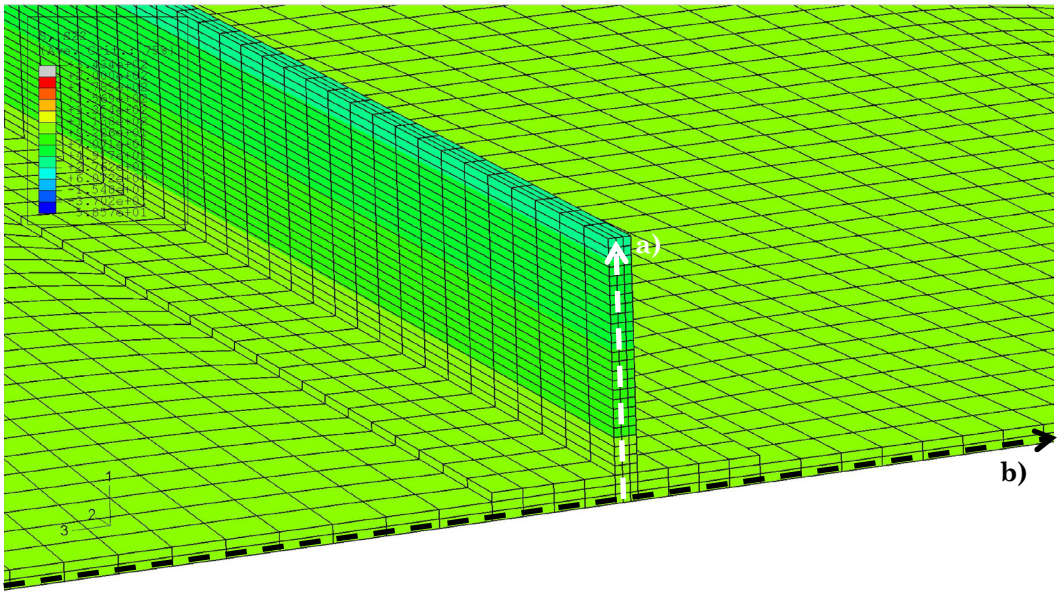


**Figure 295 - Detail of preliminary geometry specimen middle cross section, $\sigma_y$ stress distribution.**

The evolution of $\sigma_y$ stress along the nodes that lay on the arrow a) is presented in Figure 296. The $\sigma_y$ stress values are higher in the plate and decrease through the stiffener moving away from the plate, as indicated by the arrow. When analysing the preliminary geometry, higher stress values are found in the stiffener, suggesting that this geometry is more effective in using the stiffeners to transfer the load.

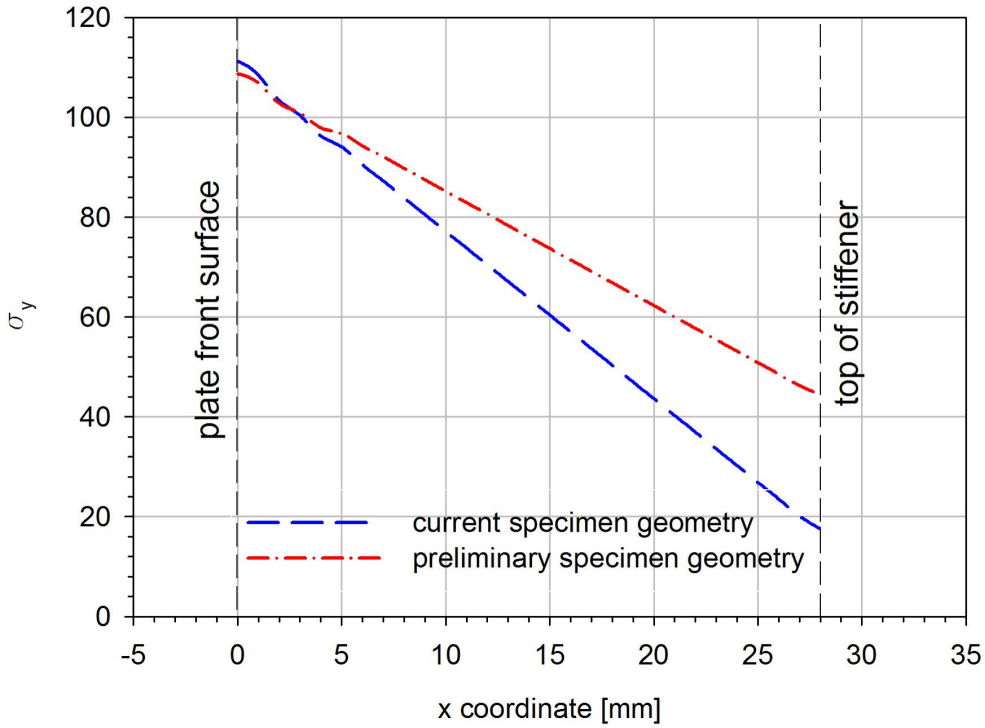


**Figure 296 - Stress distribution along the nodes that lay on the arrow presented in Figure 295.**

The $\sigma_y$ stress distribution and displacements in the x direction were analysed along the nodes on the back plate side (containing stiffeners) and on the opposite side, in the direction of the arrow b) plotted in the Figure 295.
The $\sigma_y$ stress distribution in the specimen middle cross section in the front and back layer nodes is presented in Figure 297, comparing the preliminary and current geometries. Results of stresses obtained with the preliminary specimen geometry are always lower, and they have the same distribution as the results obtained for the current specimen geometry.

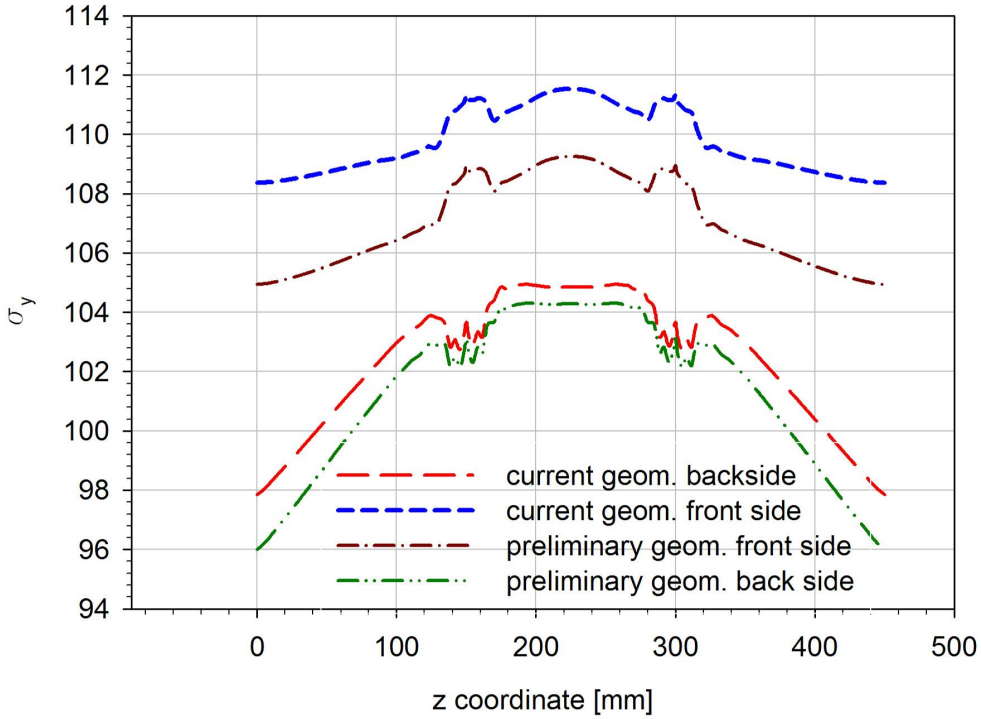


**Figure 297 - $\sigma_y$ distribution in the specimen middle cross section in the front and back layer nodes.**

The displacement in the x direction in the specimen middle cross section in the front and back layer nodes is presented in Figure 298. In the case of the current specimen geometry, for the remote load applied it was found that the maximum displacement is $2{,}77mm$. For the case of the preliminary geometry the maximum displacement obtained is $2{,}07mm$. The maximum displacement occurs at the middle of the plate.

The $\sigma_y$ stress distribution along the longitudinal direction is presented in Figure 299. Three lines - a), b) and c) - where $\sigma_y$ stress and displacements in the x direction are analysed are identified in this figure. Results presented for lines b) and c) were obtained in the side of the plate opposite to the stiffeners (front side).

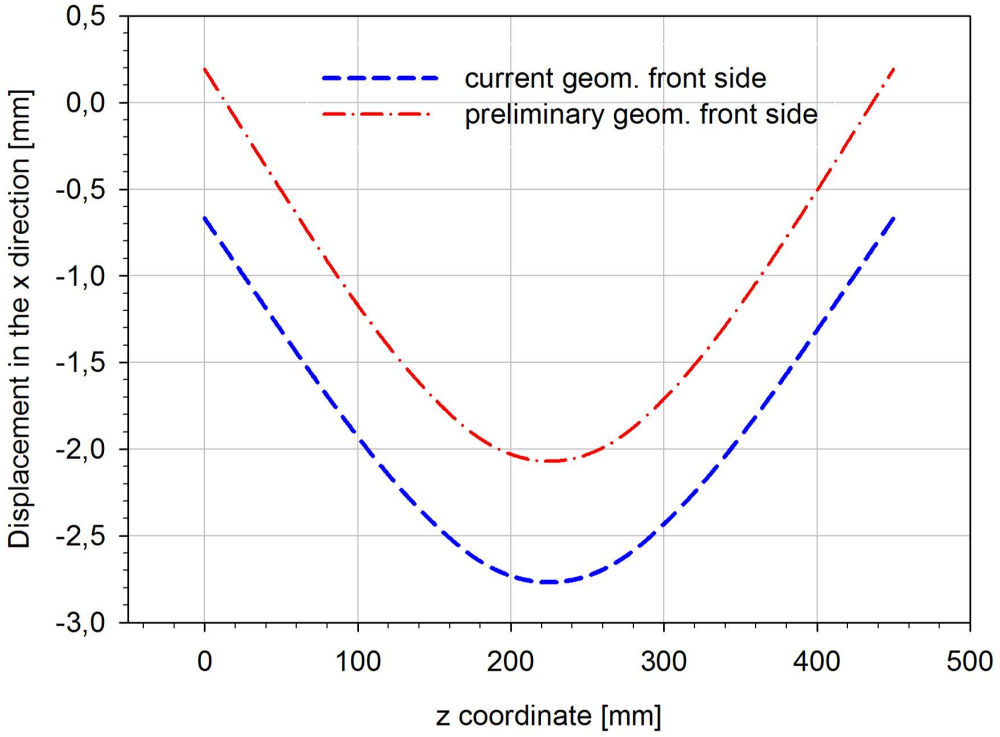


**Figure 298 - Displacement x in the specimen middle cross section in the front and back layer nodes.**

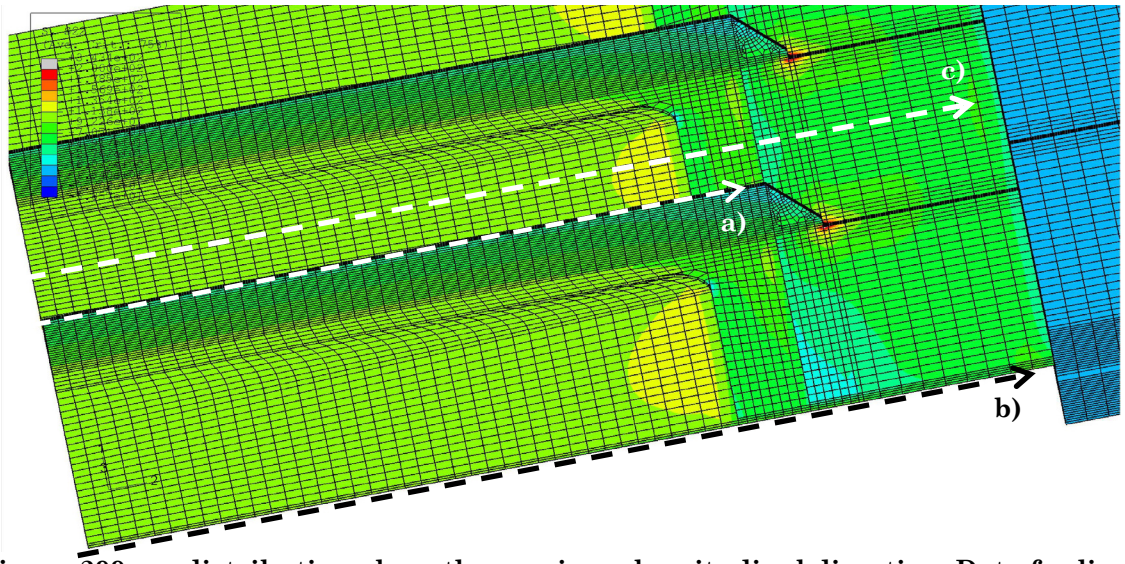


**Figure 299 - $\sigma_y$ distribution along the specimen longitudinal direction. Data for lines b) and c) was obtained in the front side.**

The $\sigma_y$ stresses through the specimen longitudinal direction along three lines: a) stiffener top surface; b) plate's lateral layer; c) plate's centre layer are presented in Figure 300. In line a), top of the stiffener surface, specimen with the preliminary geometry had higher stress values. Lines b) and c) presented similar stress distributions but stresses in the preliminary geometry are lower.

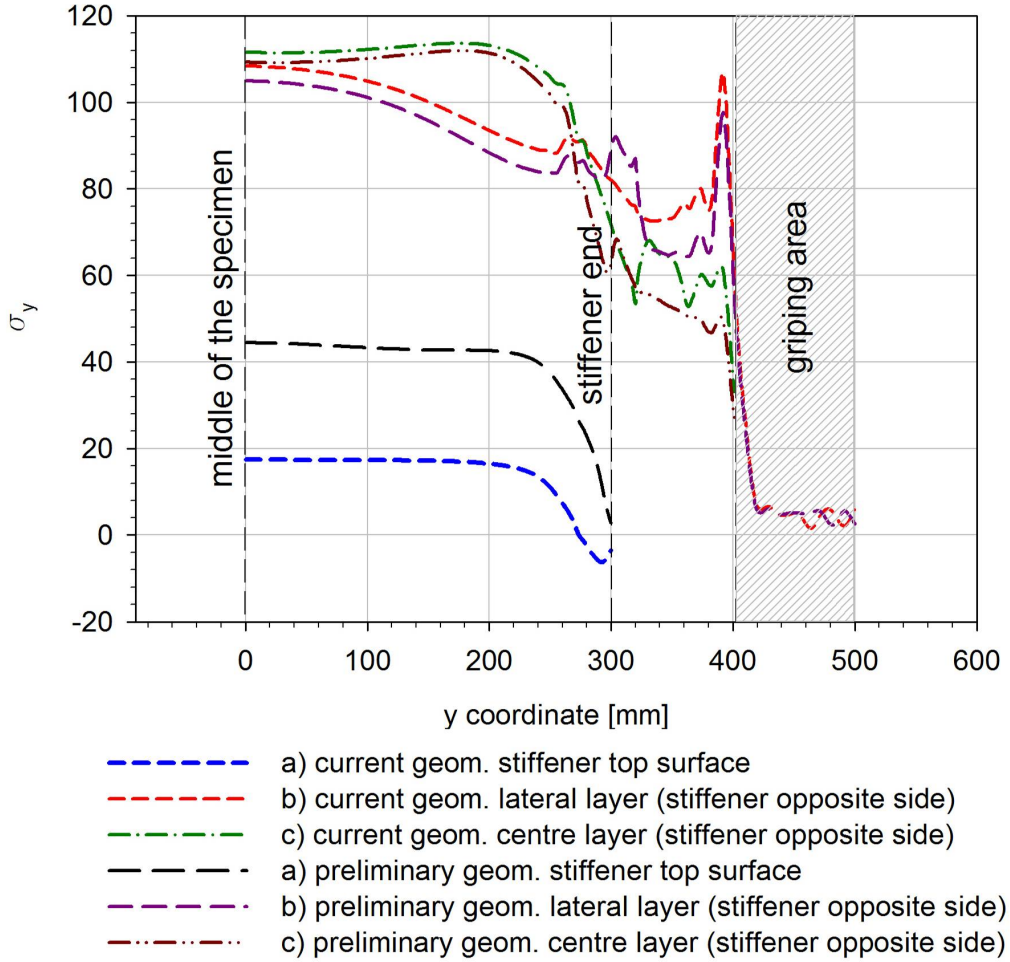


**Figure 300 - $\sigma_y$ distribution through the preliminary and current specimen geometry principal dimension in three lines: a) stiffener top surface; b) plate's lateral layer; c) plate's centre layer.**

Figure 301 presents the x displacement for nodes along three lines: a) stiffener top surface; b) plate's lateral layer; c) plate's centre layer. In lines a) and c) the preliminary specimen geometry resulted in lower negative displacements. For line b) the displacements in the preliminary specimen geometry are always positive, but for the current geometry the displacements start with negative values and at the middle length they become positive. The preliminary specimen geometry has a maximum displacement of 2,07$mm$ and the current geometry has a maximum value of 2,77$mm$.

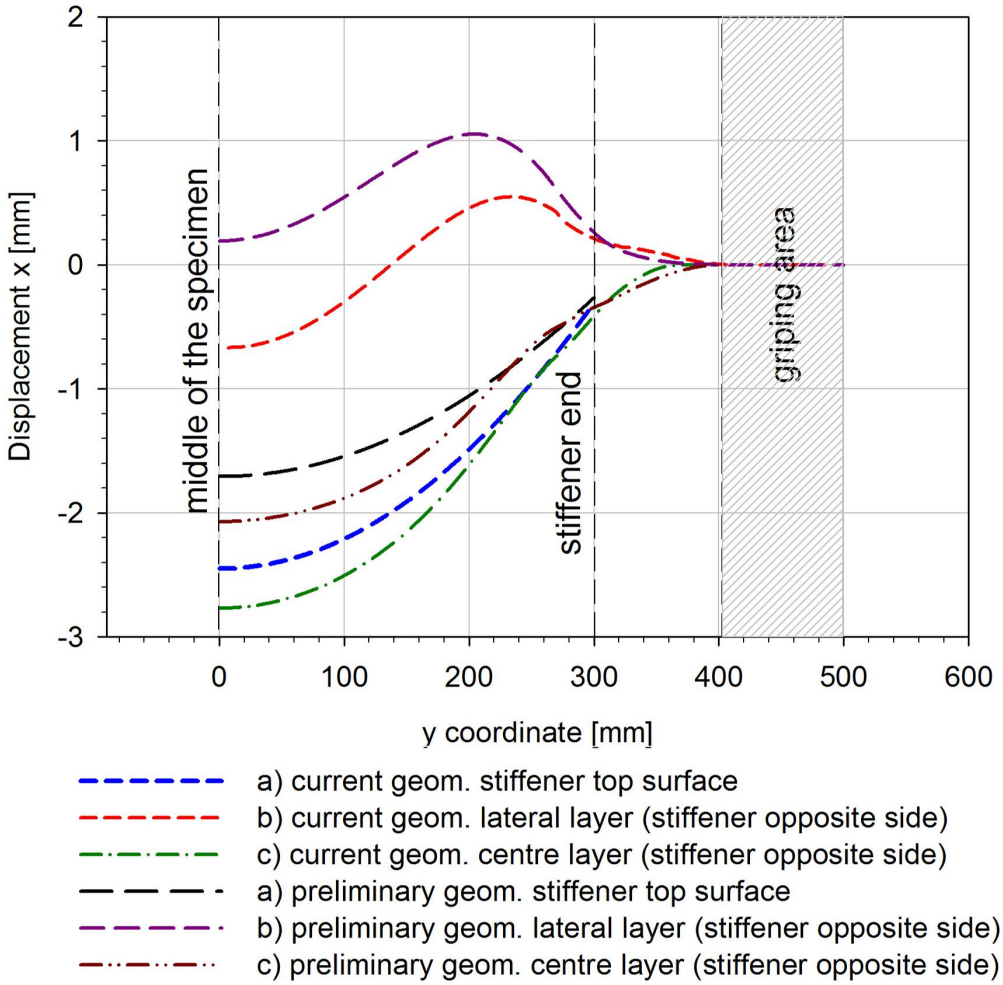


**Figure 301 - Displacement in the x direction through the preliminary and current specimen geometry longitudinal direction along three lines: a) stiffener top surface; b) plate's lateral layer; c) plate's centre layer.**

In the case of the preliminary specimen geometry, the stress concentration effect found in the end of stiffener concordance radius is presented in Figure 302. The maximum $\sigma_y$ stress value found is 343,4*MPa*. Comparing with the values found in the centre of the specimen (approximately 104*MPa*) a stress concentration factor of 3,3 is found. The stress concentration factor found for the current specimen geometry is 3,8.

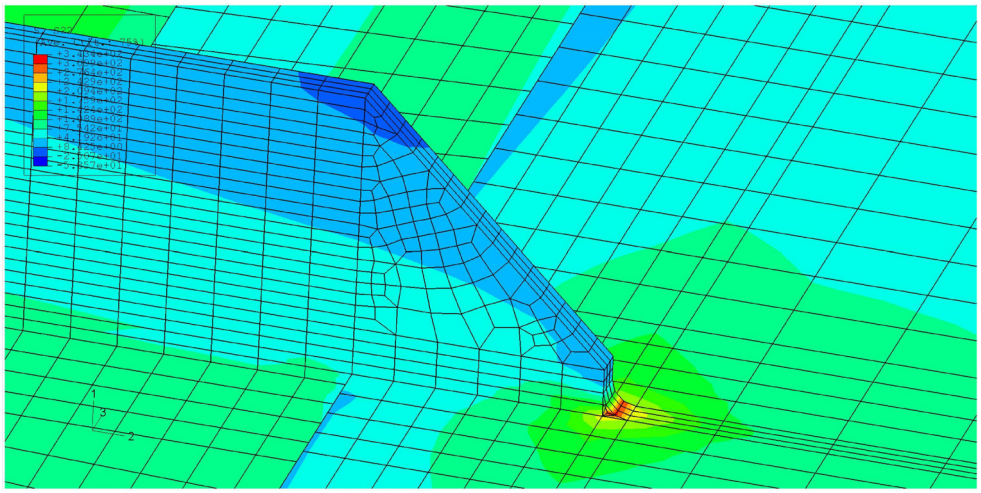

**Figure 302 - Stress concentration factor at the end of the stiffener.**

The site in the top side of the stiffeners previously identified as an area with compressive stresses (see Figure 275 and Figure 292) is no longer in compression in the preliminary specimen geometry, as shown in Figure 303. Compressive stresses only occurred in the front surface under the stiffener end in both the preliminary and current geometries.

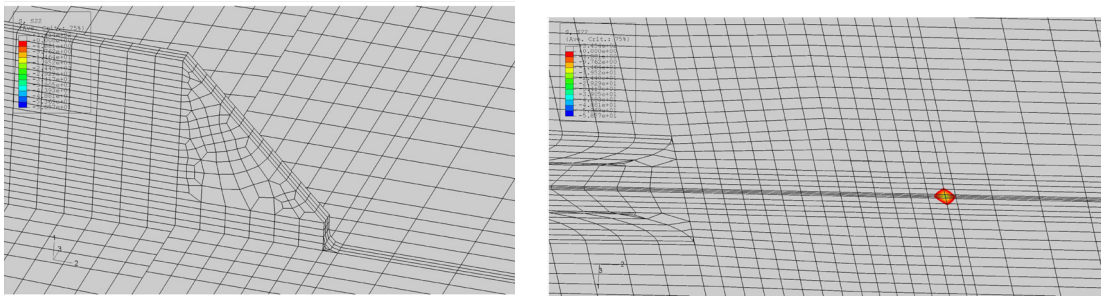

**Figure 303 - Identification of zones with compressive stresses in the preliminary specimen geometry.**

### *6.1.3 Concluding remarks*

For the load specified, corresponding to 100*MPa* nominal stress in the specimen's cross section, the displacement of the centre of the panel in the direction perpendicular to its plane was found to be of the order of 3*mm* if no anti-bending device is used. In this situation the stiffeners are subjected to longitudinal stresses that decrease when moving away from the panel, and reach a low positive value in the top of the stiffeners.
Using the anti-bending device the stress in the stiffeners cross section is approximately uniform, and of the same order of magnitude as $\sigma_y$ in the plate.
In the case of the preliminary geometry, the centre of the specimen presented a lower displacement in the direction perpendicular to its plane (approximately 25% lower than for the final geometry), and a lower value of stress concentration factor created by the stiffeners (approximately 13% lower than for the final geometry).

### 6.2 DaToN stiffened panels fatigue life; experimental measurements

Fatigue tests of two stiffener specimens (Figure 261) manufactured by three different processes were carried out, HSM (High Speed Machining), LBW (Laser Beam Welding) and FSW (Friction Stir Welding). The stiffened panels were manufactured using the AA6056, a modified variant of the AA6013, which is considered a promising airframe candidate for processing by fusion laser beam welding and solid-state friction stir welding. The AA6056 is a Al-Mg-Si-Cu alloy that can be heat treated to different strength levels by precipitation hardening and has a good corrosion resistance. A total of ten specimens were tested:

- two HSM AA6056-T651 panels:
  - HSM AA6056-T651, maximum stress of 80*MPa* with R=0,1 (specimen HSM01);
  - HSM AA6056-T651, maximum stress of 110*MPa* with R=0,5 (specimen HSM02);

- six LBW AA6056 panels:
  - LBW1 6056 PWHT–T6, maximum stress of 80*MPa* with R=0,1 (specimen LBW03);
  - LBW1 6056 PWHT–T6, maximum stress of 110*MPa* with R=0,5 (specimen LBW04);
  - LBW2 6056 PWHT–T6, maximum stress of 80*MPa* with R=0,1 (specimen LBW05);
  - LBW2 6056 PWHT–T6, maximum stress of 110*MPa* with R=0,5 (specimen LBW06);
  - LBW2 6056-T6 as-welded, maximum stress of 80*MPa* with R=0,1 (specimen LBW07);
  - LBW2 6056-T6 as-welded, maximum stress of 110*MPa* with R=0,5 (specimen LBW08);

- two FSW AA6056-T651 panels:
  - FSW 6056-T6 as-welded, maximum stress of 80*MPa* with R=0,1 (specimen FSW09);
  - FSW 6056-T6 as-welded, maximum stress of 110*MPa* with R=0,5 (specimen FSW10).

Measurements of crack length in all specimens were performed according to the scheme presented in Figure 304. It should be emphasised that the specimen front side is the plate side without the stiffeners and the back side is the side containing the stiffeners.

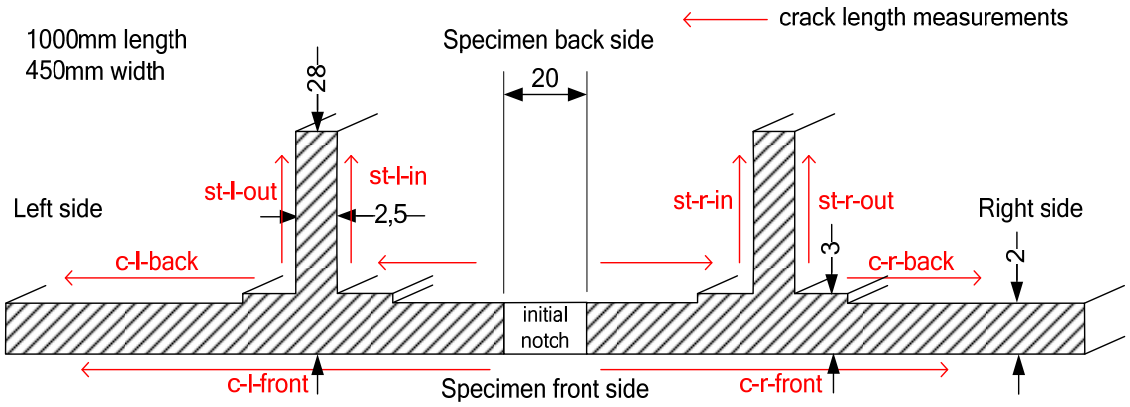


**Figure 304 - Fatigue crack measurement scheme.**

### *6.2.1 Base material tensile and crack growth tests*

In order to understand and validate the DaToN panels fatigue crack growth test results, a characterization of tensile properties and Paris law constants for the relevant materials (aluminium alloys 6056-T651 and 6056-T6) was carried out.

Two types of 6056 DaToN panels were tested in the fatigue crack growth of stiffened panels programme. In the first type, HSM panels, the panels were obtained by high speed machining of 30$mm$ thick plate. In the second type, LBW and FSW panels, the panels were fabricated from thin plates with the stiffeners attached by welding. The different thicknesses of the original material may imply different mechanical properties, and for this reason tensile and CT specimens were machined from the 4$mm$ thick part of HSM, LBW and FSW 6056 DaToN stiffened panels.

Tensile tests of base material specimens extracted from each type of DaToN panels were performed. The 2$mm$ thick specimens' configuration used was in accordance to [144], Figure 305.

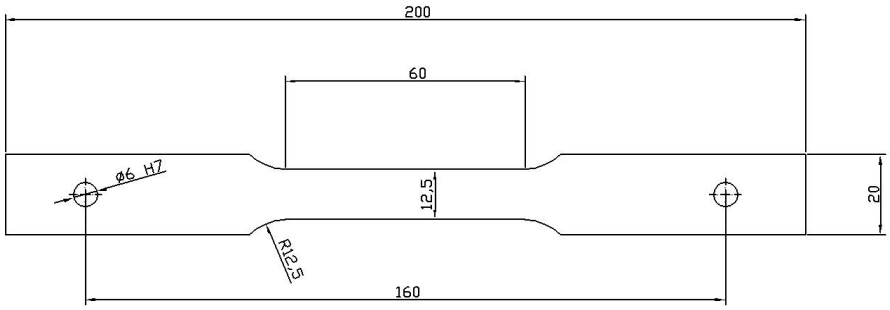


**Figure 305 - Tensile test specimen geometry.**

Tensile tests were performed at 1$mm/min$ and strain was acquired with a 25$mm$ gage. Table 82 summarises the results obtained and the stress/strain plot is presented in Figure 306. It was found that the HSM base material specimens, machined from a 30$mm$ thick plate, presented higher rupture and yield stress

than the base material extracted from the LBW and FSW panels that were machined from a 5*mm* thick plate. Also, according to Alcan results, the LBW base material presented lower mechanical properties than expected.

**Table 82 - Tensile test results of DaToN specimens base material**

| | $\sigma_{rupt}$ [*MPa*] | $\sigma_{yield}$ [*MPa*] | Elongation [%] | E [*GPa*] |
|---|---|---|---|---|
| HSM 6056-T651 | 381,3 | 357,5 | 9,0 | 70,8 |
| LBW 6056 PWHT-T6 | 346,9 | 335,3 | 11,6 | 67,0 |
| LBW 6056-T6 as-welded | 350,3 | 341,3 | 11,1 | 72,4 |
| FSW 6056 PWHT-T6 | 352,2 | 341,3 | 10,3 | 69,7 |
| | | | | |
| Alcan data 6056-T6 | 370 | 358 | | |
| Alcan data 6056-T4 | 320 | 190 | | |

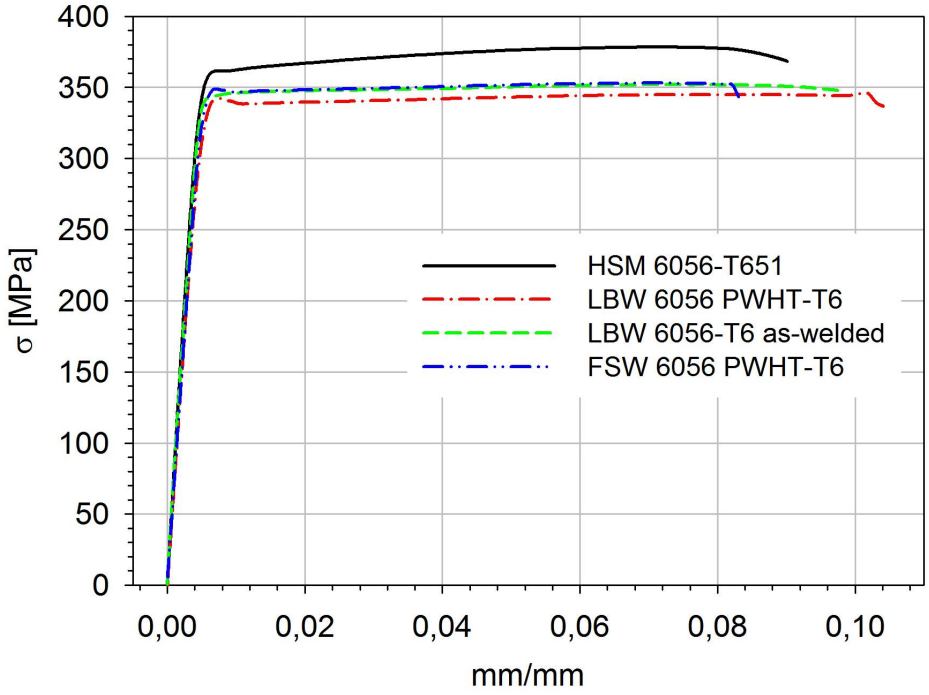


**Figure 306 - Stress/strain plot of base material tensile tests.**

Fatigue crack propagation behaviour of the alloy 6056 in the conditions used for the HSM, LBW and FSW panels was investigated at two different R values (R=0,1 and R=0,5). The HSM DaToN panels were machined from material obtained from the surface layer of a 30*mm* thick plate in the T651 condition, and the LBW and FSW panels were obtained from a 5*mm* thick sheet in the T6 condition. The CT specimens in these two conditions presented a different crack surface appearance which may be related to the difference found in the da/dN *vs.* ΔK results, Figure 307.

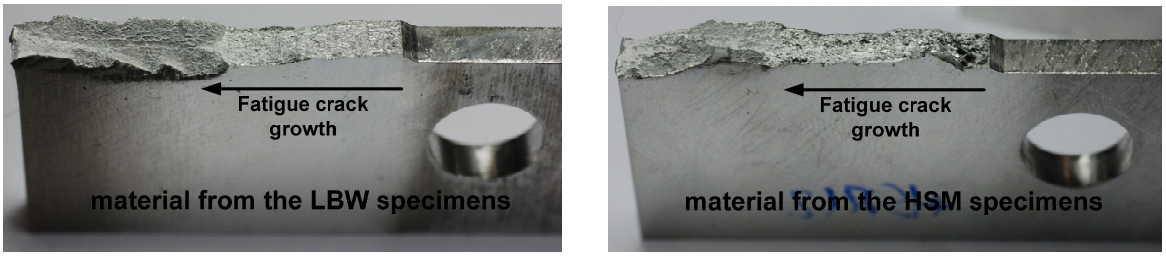


**Figure 307 - Fracture surface of CT specimens.**

The fracture surface of the HSM CT specimens presents a roughness and heterogeneity not found in the LBW CT specimens. This may be due to the fact that HSM panels and their CT specimens are machined from very thick material (30*mm* thick) by high speed machining, and the skin of the panels, from where the CT specimens were machined, corresponds to one of the surface layers of the thick material. Possibly the material in the interior of the thick plate presents a more homogeneous structure, although this was not investigated.
This situation does not occur with the LBW specimens, which are machined from thinner material, and possibly this is reflected in the more homogeneous features displayed by their fracture surfaces.

Values in the Paris regime ($10^{-5}$<da/dN<$10^{-3}$ *mm/cycle*) were obtained using CT specimens of 4*mm* thickness with the crack growing in the same direction as in the stiffened panels. The CT specimens dimensions are presented in Figure 308 and follow the ASTM E647 standard [173]. Fatigue testing was carried out on a servo-hydraulic MTS321.31 machine using a 5*kN* load cell at a frequency of 20*Hz* in laboratory air. Crack length was optically measured at both specimen surfaces with a resolution of 0,01*mm*. The fatigue crack propagation behaviour for the AA6056 material in both conditions and tested at both R values is shown in Figure 309.

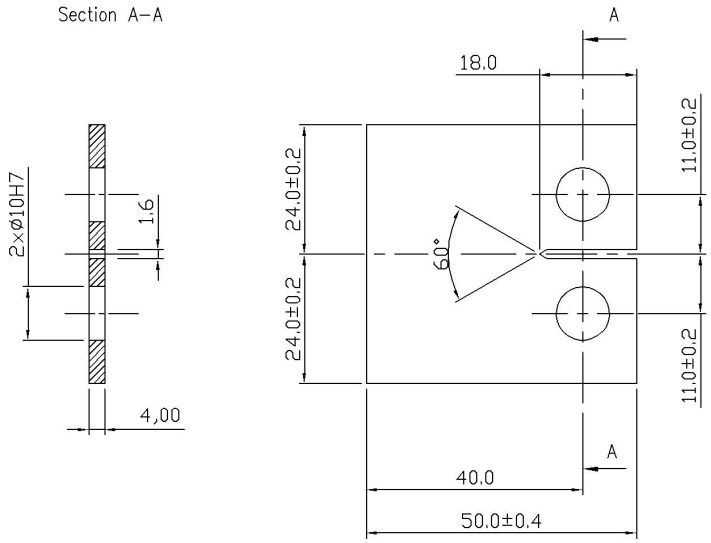


**Figure 308 - Compact tension (CT) specimen (dimensions in *mm*).**

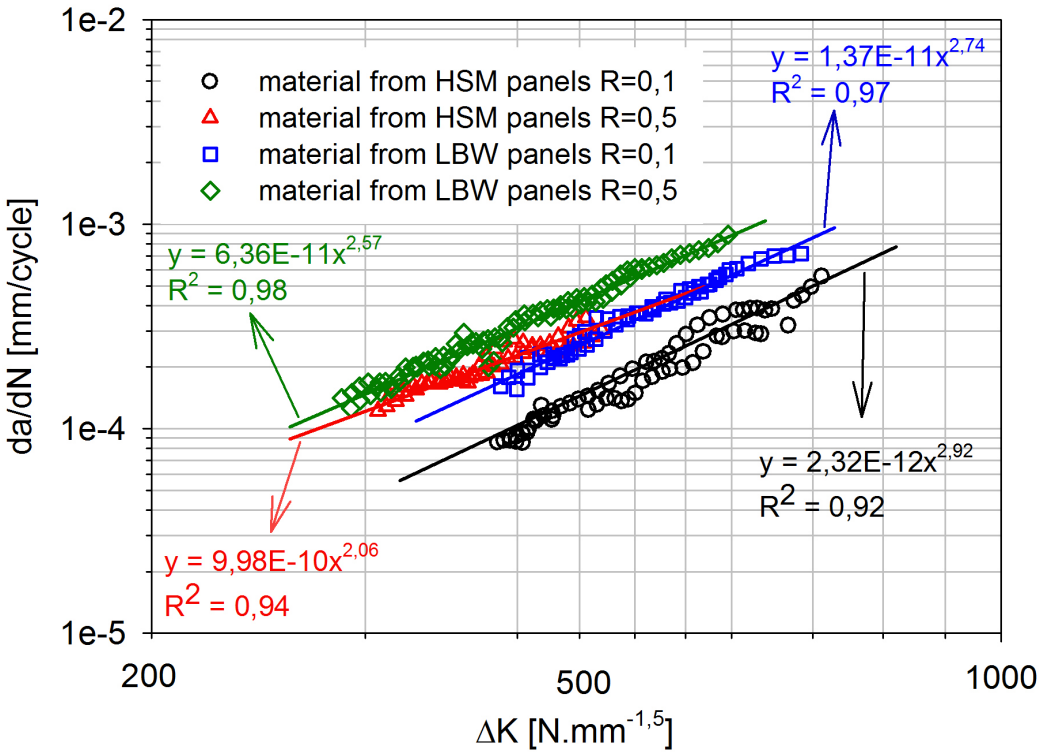


**Figure 309 - Crack propagation data obtained with CT specimens from the HSM AA6056-T651 and from the LBW AA6056-T6 panels.**

The results obtained are in accordance with the values found by Vaidya *et al.* [196] testing AA6056-T6 specimens with a thickness of $4mm$. The results could be successfully fitted with a power law with their coefficients C and m being the parameters of the Paris law[1],

$$\frac{da}{dN} = C \cdot \Delta K^{m} \tag{29}$$

where da/dN is the fatigue crack growth rate, ΔK is the stress intensity factor ($\Delta K = K_{max} - K_{min}$), and C and m are material constants dependant upon environment, frequency, temperature and stress ratio among other factors.

The parameters C and m obtained for each type of material are presented in Table 83.

**Table 83 - C and m Paris law parameters for the AA6056 material from the HSM and LBW panels**

| $\left[\frac{N \cdot mm^{-1,5}}{mm/cycle}\right]$ | material from the HSM panel AA6056-T651 | | material from the LBW panel AA6056-T6 | |
|---|---|---|---|---|
| | R=0,1 | R=0,5 | R=0,1 | R=0,5 |
| C | 2,32E-12 | 9,98E-10 | 1,37E-11 | 6,36E-11 |
| m | 2,92 | 2,06 | 2,74 | 2,57 |

It was verified that for both material conditions the specimens with R=0,5 presented a higher crack growth rate for the same ΔK value, as expected. Also,

when tested at the same R value the specimens extracted from the LBW panels have higher crack growth rate then those extracted from HSM panels.

### *6.2.2 High Speed Machining AA6056 panels*

Two stiffened High Speed Machining panels of aluminium 6056-T651 were fatigue tested at two different stress levels. The first panel was tested at a maximum stress of 80*MPa* with R=0,1 (specimen HSM01) and the second panel was tested at a maximum stress of 110*MPa* with R=0,5 (specimen HSM02). The stress distributing for static and fatigue loading was recorded and the crack growth rate was also measured. An initial central full depth notch (crack) with 20*mm* length and 0,2*mm* width was created by electro-discharge machining.

#### *6.2.2.1 Stress distribution for different static remote loads*

Two panels containing a central crack (notch) of 20*mm* length were instrumented and loaded at five incremental loads to acquire the stress distribution in specific sites of the specimen. The strain gages were distributed in the specimen according to the scheme presented in Figure 310:
- two couples (C1, C5, C6 and C7), on both faces of the panel, bonded on the skin at the centre of each bay (spaced 225*mm* in horizontal direction), on the horizontal symmetry plane;
- another couple (C3 and C8), placed on the longitudinal axis of the panel, 200*mm* above the horizontal symmetry plane;
- two couples (C2, C4, C7 and C9), placed in correspondence of a stringer, with a strain gauge bonded on top of the stringer and the other one on the skin.

In the first specimen were used ten strain gages (C1 to C10) and in the second specimen five strain gages (C2, C3, C7, C8 and C9).

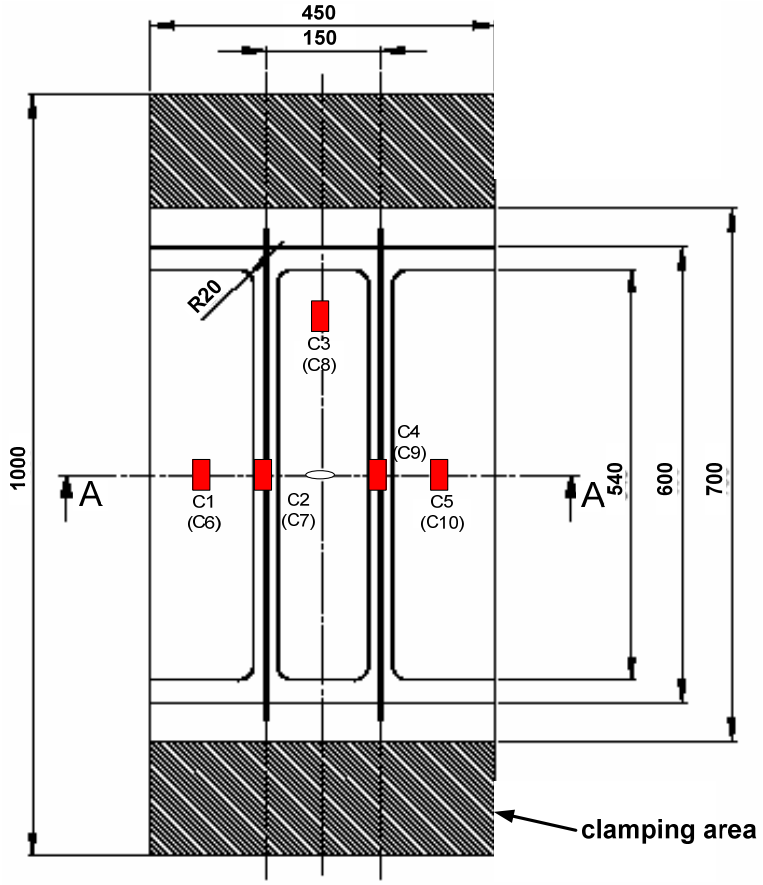


**Figure 310 - DaToN panel strain gages location (front gages in brackets, see Figure 304).**

Results for both specimens are presented in Table 84. The stress distribution along the specimen for all the applied remote loads can be analysed in Figure 311 and Figure 312 for specimens HSM01 and HSM02, respectively. An accurate symmetry of load distribution along the specimen width was identified. At the specimen horizontal middle line, the stiffener top surface has the lower values of stresses. A value of 70*GPa* was used for the Young modulus in order to convert strain to stress.

**Table 84 - Strain gages measurements function of the remote stress applied [*MPa*]**

| Remote stress | HSM01 | | | | | | | | | | HSM02 | | | | |
|---|---|---|---|---|---|---|---|---|---|---|---|---|---|---|---|
| | C1 | C2 | C3 | C4 | C5 | C6 | C7 | C8 | C9 | C10 | C2 | C3 | C7 | C8 | C9 |
| 20 | 18,5 | 11,0 | 19,4 | 11,6 | 17,9 | 20,1 | 20,3 | 22,1 | 20,0 | 19,9 | 9,7 | 19,5 | 20,9 | 22,4 | 20,7 |
| 40 | 37,6 | 24,5 | 39,4 | 25,3 | 36,8 | 39,6 | 40,1 | 43,8 | 39,9 | 39,6 | 23,6 | 39,6 | 41,0 | 44,1 | 40,9 |
| 60 | 56,8 | 40,3 | 59,6 | 41,1 | 55,8 | 59,0 | 59,7 | 64,9 | 59,5 | 59,2 | 39,4 | 59,6 | 60,8 | 65,2 | 60,8 |
| 80 | 76,0 | 57,6 | 79,9 | 58,3 | 75,0 | 78,3 | 79,1 | 85,8 | 78,9 | 78,6 | 56,6 | 79,8 | 80,4 | 86,0 | 80,4 |
| 100 | 95,2 | 76,0 | 100,3 | 76,6 | 94,2 | 97,7 | 98,4 | 106,5 | 98,3 | 98,0 | 74,8 | 100,0 | 100,0 | 106,8 | 100,0 |

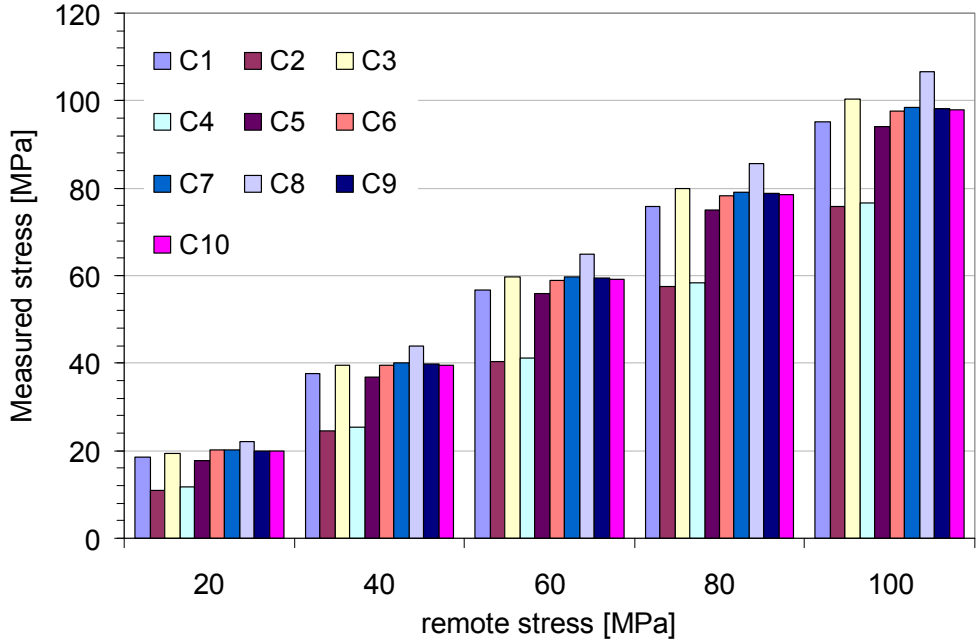


**Figure 311 - Stress distribution for different applied remote stress, specimen HSM01.**

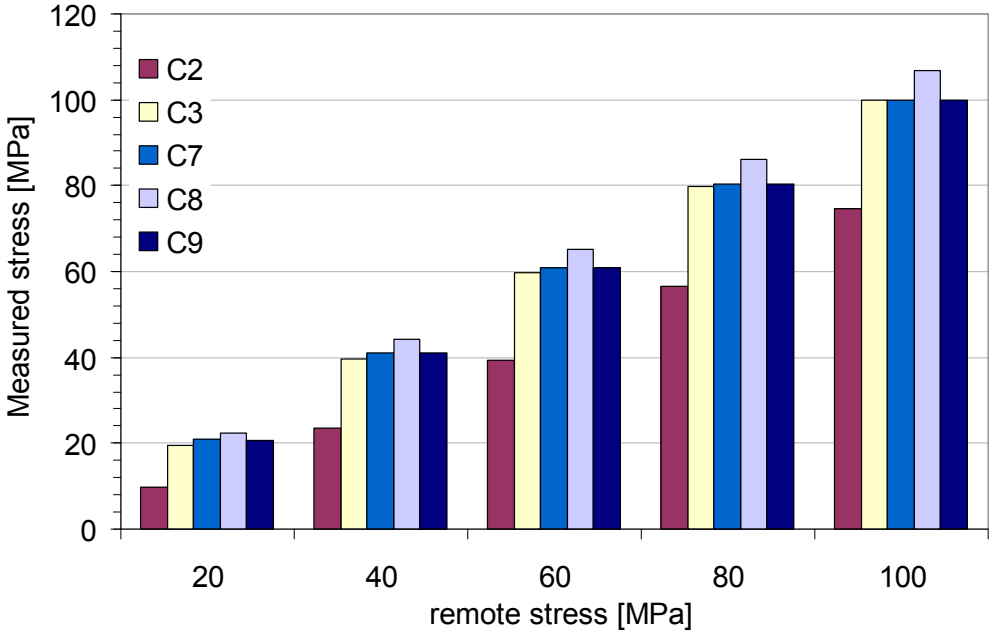


**Figure 312 - Stress distribution for different applied remote stress, specimen HSM02.**

*6.2.2.2 Stress distribution during the fatigue tests*

Fatigue crack propagation tests were carried out and strain was measured in order to understand the different load transfer stages. The first panel was tested at a maximum stress of 80*MPa* with R=0,1 and the second panel was tested at a maximum stress of 110*MPa* with R=0,5

*6.2.2.2.1 Fatigue crack growth test $\sigma_{max}$=80MPa, R=0,1 (HSM01 specimen)*

The strain gages values were measured in periodic stops of the fatigue test at the average fatigue load (44*MPa*, 47,98*kN*). The stress distribution on the stiffened panel along the fatigue test is presented in Figure 313.
Taking into account that C2 and C4 corresponds to gages at the top of the stiffener and C7 and C9 to gages at the same width but placed in the plate front side it is easily identified that when the crack is near and reaches the stiffener most of the load is transmitted to the plate front side.

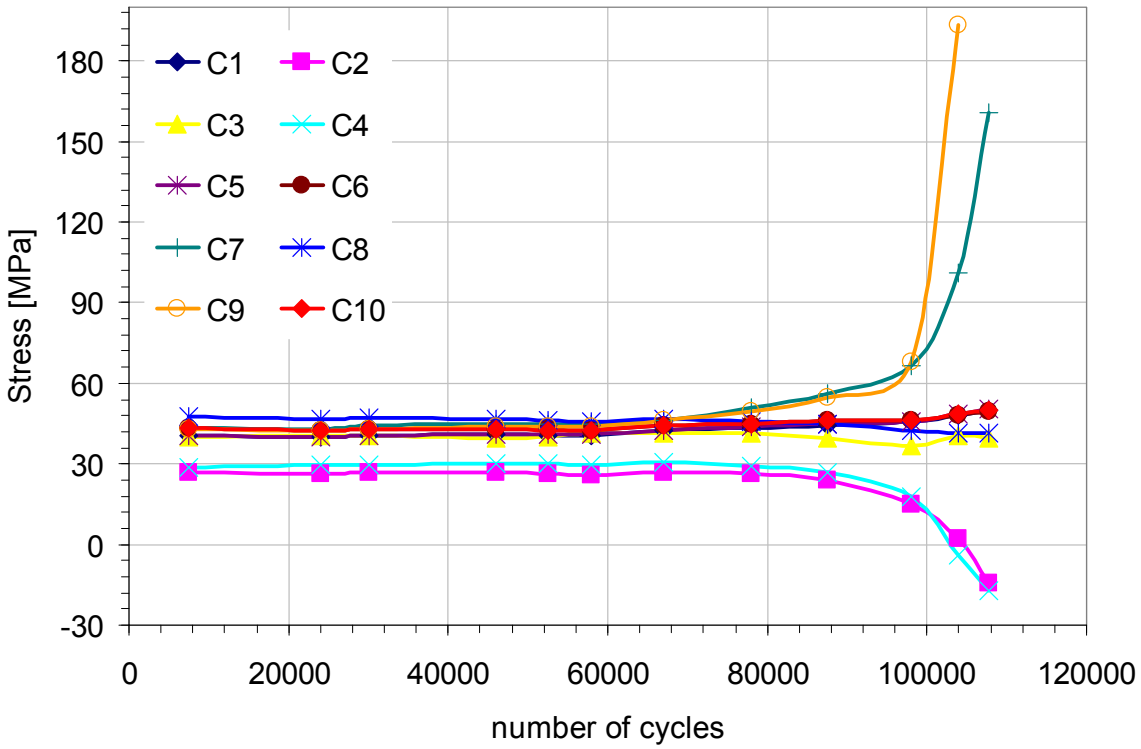


**Figure 313 - Stress distribution during the fatigue crack growth test, HSM01.**

*6.2.2.2.2 Fatigue crack growth test $\sigma_{max}$=110MPa, R=0,5 (HSM02 specimen)*

The strain gages values were measured in periodic stops of the fatigue test at the maximum fatigue load (119,95*kN*). The stress distribution on the stiffened panel during the fatigue test is presented in Figure 314. Again, when the crack grows through the stiffener most of the load is carried out by the plate front side.

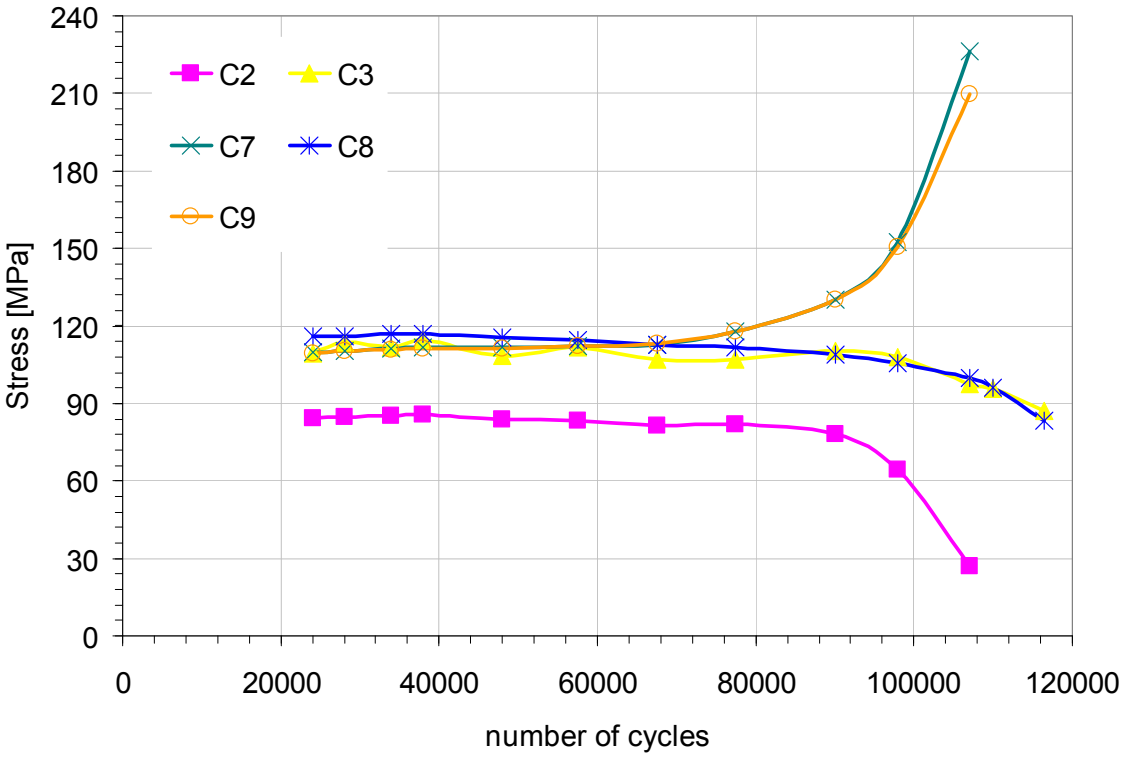


**Figure 314 - Stress distribution during the fatigue crack growth test, HSM02.**

*6.2.2.3 Fatigue crack growth analysis*

Fatigue crack propagation tests were carried out and crack length was measured at periodic stops of the fatigue test. The cracks were measured when the specimen was loaded with the average fatigue load, 47,98*kN*, in the first test, and at the maximum load 89,96*kN*, in the second test. The first panel was tested at a maximum stress of 80*MPa* with R=0,1 and the second panel was tested at a maximum stress of 110*MPa* with R=0,5.

*6.2.2.3.1 Fatigue crack growth test $\sigma_{max}$=80MPa, R=0,1 specimen HSM01*

Specimen HSM01, tested at a maximum stress of 80*MP*a and R=0,1, had a fatigue life of 113784 cycles. The fatigue crack growth in the stiffened panel during the fatigue test is presented in Figure 315. The first fatigue crack was only detected at 15000 cycles. The crack started to growth through the stiffener at 109800 cycles, 96,5% of the total fatigue life. The crack in the left stiffener bifurcated at nearly 113000 cycles.

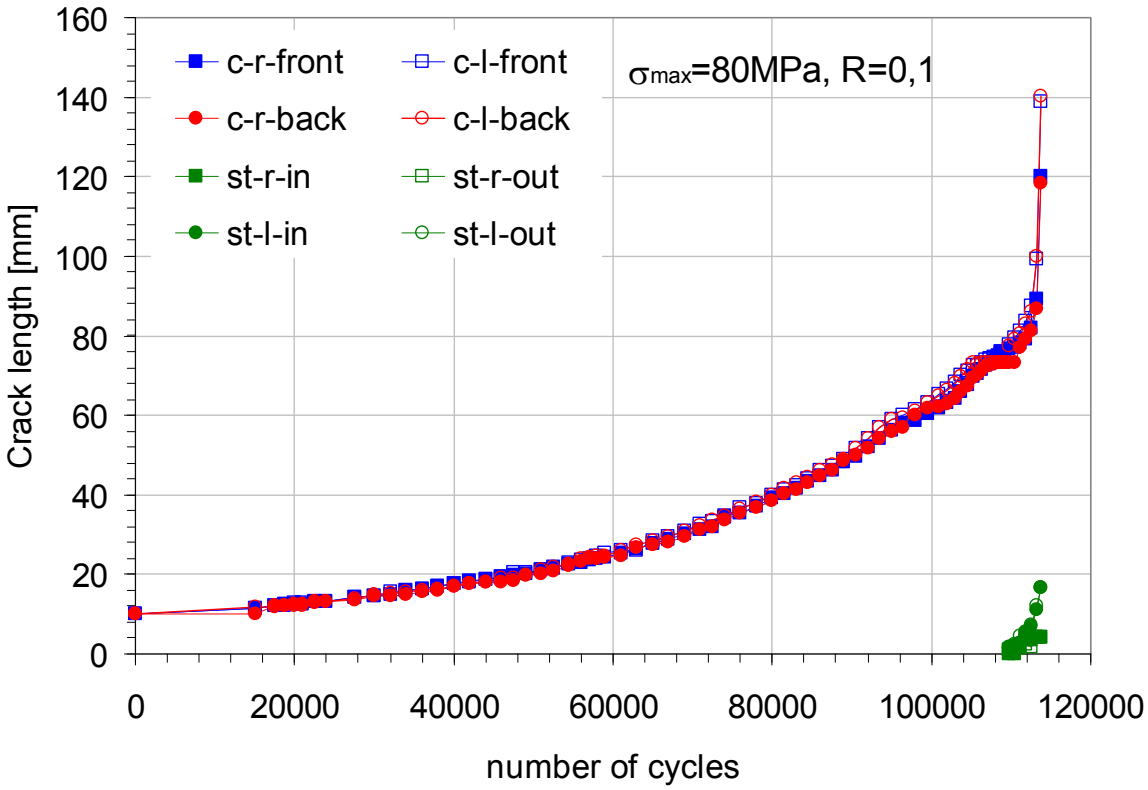


**Figure 315 - Fatigue crack growth test, specimen HSM01.**

*6.2.2.3.2 Fatigue crack growth test $\sigma_{max}$=110MPa, R=0,5 specimen HSM02*

This specimen, tested at a maximum stress of 110*MPa* and R=0,5, had a fatigue life of 117744 cycles. The fatigue crack growth in the stiffened panel during the fatigue test is presented in Figure 316.
The first fatigue crack was first detected at 7500 cycles. The crack started to grow through the stiffener at 113000 cycles, 96,0% of the total fatigue life. After 115000 cycles the fatigue crack in both stiffeners bifurcated and started to propagate parallel to the panel along the stiffener.

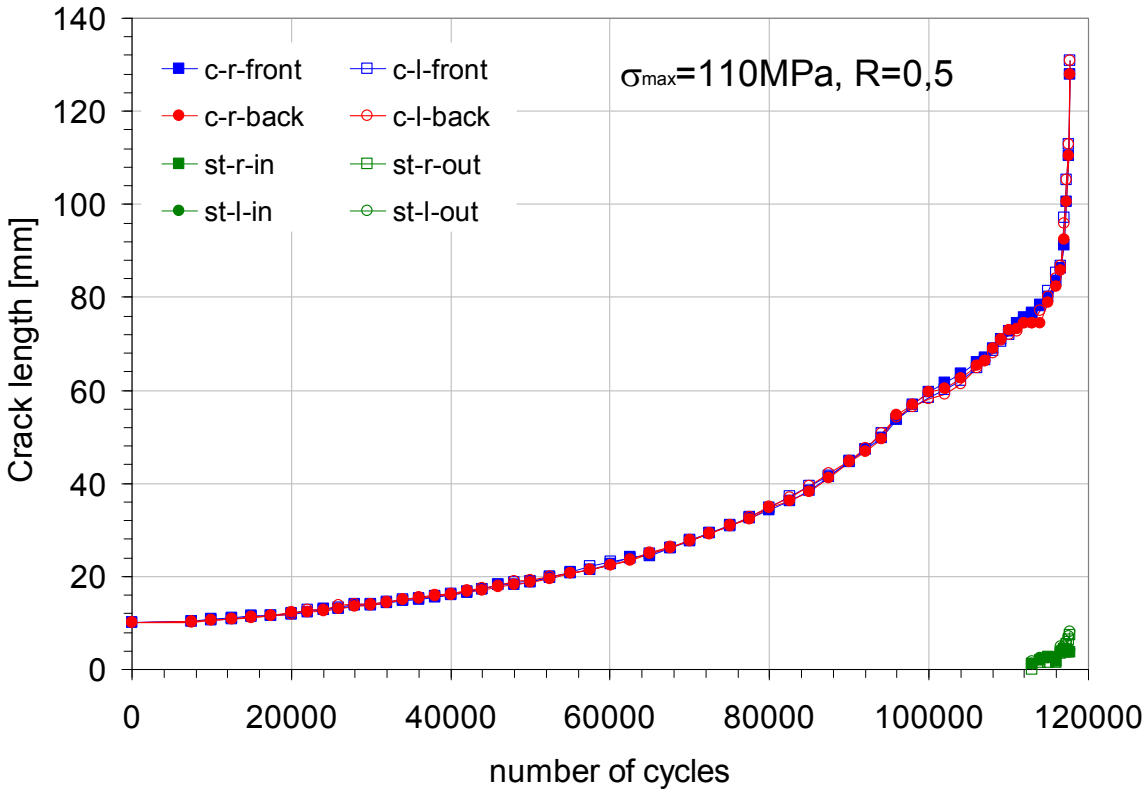


**Figure 316 - Fatigue crack growth test, specimen HSM02.**

*6.2.2.4 Photographic report of the HSM specimens fatigue tests*

During the tests a photographic data base was created in order to record their particular features. The complete test setup for specimens HSM01 and HSM02 is presented in Figure 317. It is possible to identify the grip system, the instrumented specimen, and the measuring travelling microscopes. Specimen HSM01 was photographed without a fatigue crack and specimen HSM02 presents a fatigue crack which is near the stiffeners root.

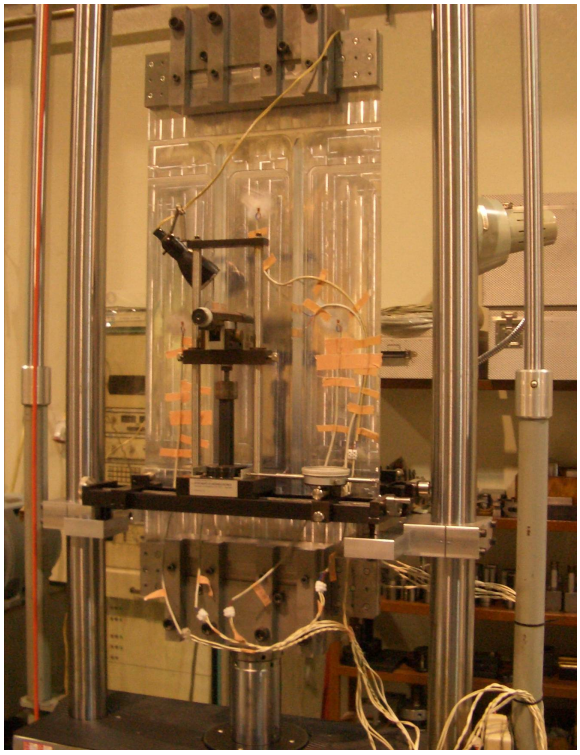

a) specimen HSM01

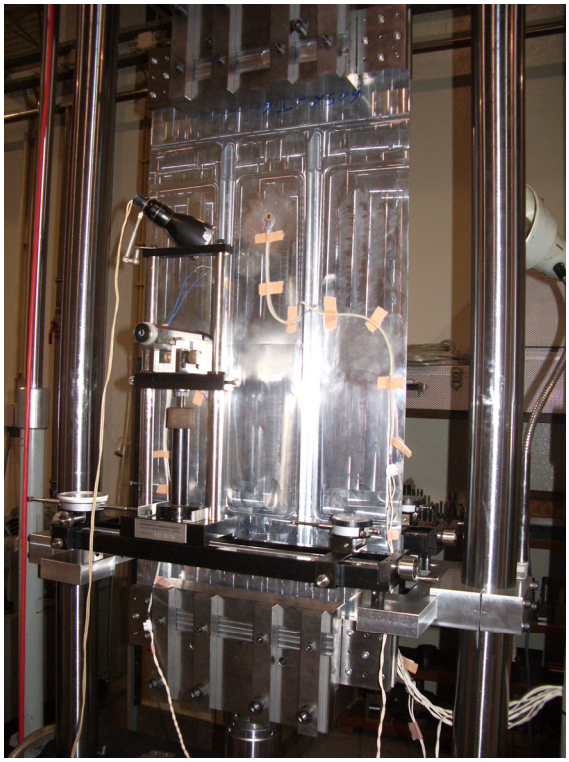

b) specimen HSM02

**Figure 317 - Test setup.**

Two different stages of the crack propagating in the front and back surface of specimen HSM01 are presented in Figure 318. In Figure 319a) the bifurcation of the crack at the left side stiffener is presented. The fatigue crack propagation at the right stiffener is presented in Figure 319b).

a) specimen back side.

b) specimen front side

**Figure 318 - Crack propagating in specimen HSM01.**

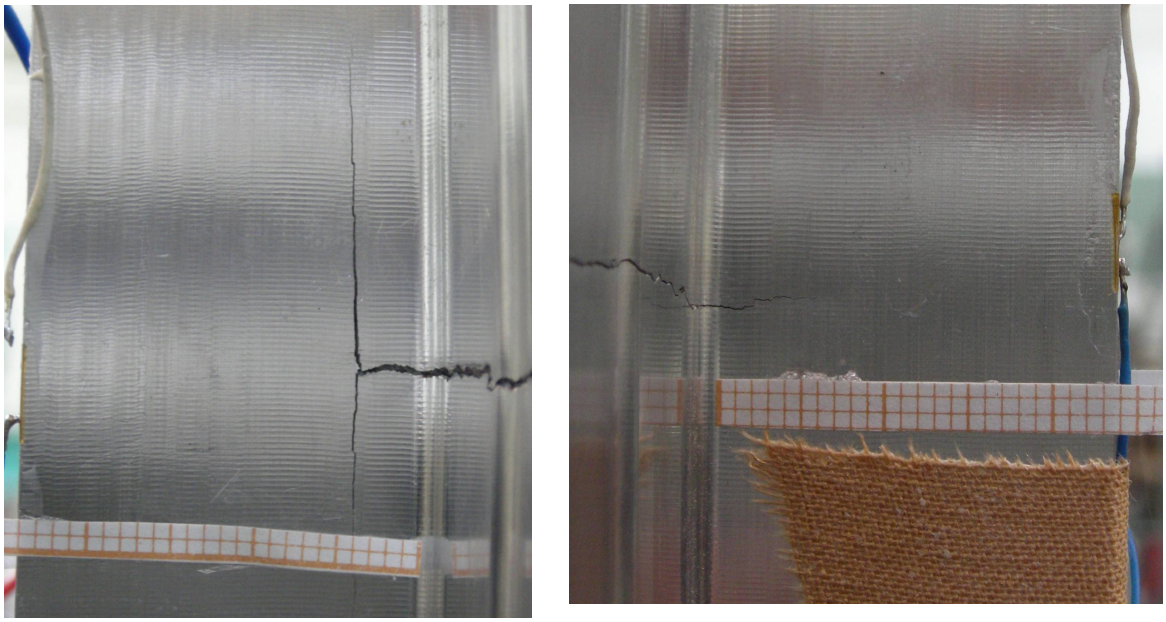

a) crack in the left stiffener b) crack in the right stiffener

**Figure 319 - Cracks at the stiffeners (113700 cycles), specimen HSM01.**

The fatigue crack bifurcation in the left and right stiffeners of specimen HSM02 is presented in Figure 320. In the right stiffener the bifurcation occurred for a shorter crack length than in the left stiffener.

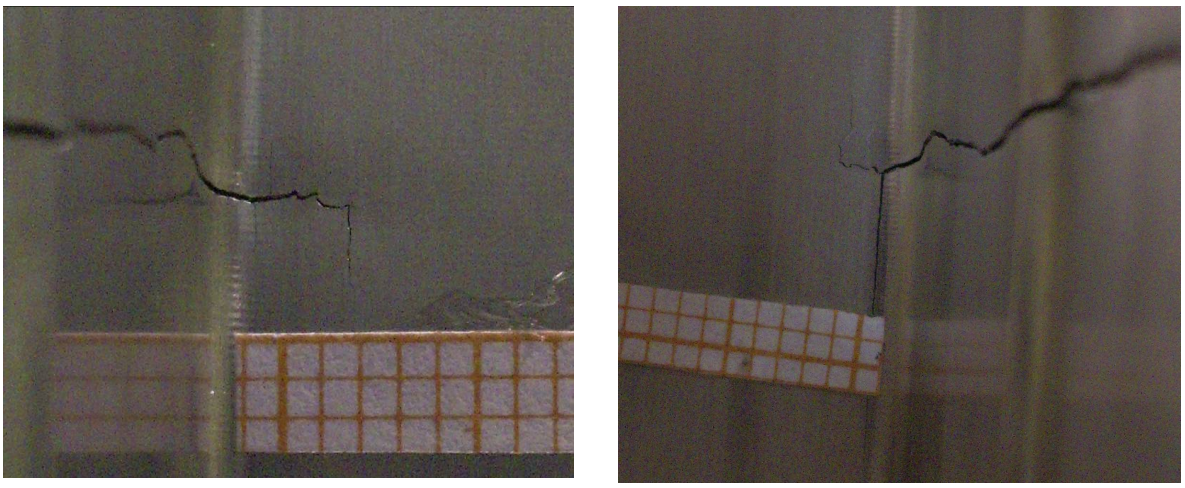

a) crack in the left stiffener, 160000 cycles b) crack in the right stiffener, 160500 cycles

**Figure 320 - Crack in the stiffeners, specimen HSM02.**

A detail of the fatigue crack surface in a stiffener of specimen HSM01 is presented in Figure 321. A rough surface in the entire fractured area was found.

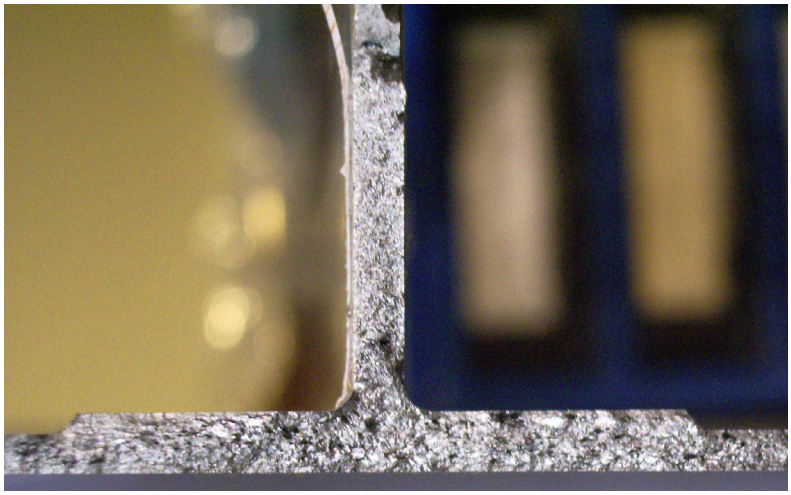

**Figure 321 - Fatigue crack surface for HSM01.**

### *6.2.3 Laser Beam Welded AA6056 2-stiffener panels*

Six laser beam welded panels of aluminium 6056 were fatigue tested. Half of the panels were tested at a maximum stress of 80$MPa$ with R=0,1 and the remaining at 110$MPa$ R=0,5. Panels with two different heat treatment conditions were tested:

i- after the welding procedure panels were submitted to an aging treatment T6 (PWHT) which corresponds to 4$h$ at 190°$C$. The machining of the panels has performed on T4 tempered 5$mm$ thickness sheet;

ii- another set of panels were previously heat treated to the condition T6 and than tested (as-welded).

Two different welding configurations were analyzed (LBW1 and LBW2), as presented in Figure 322. The main difference between LBW1 and LBW2 is the position of the weld bead. In the LBW1 configuration the weldment is at the junction of the skin with the blade (T-joint); in the LBW2 configuration the weldment is at the lower part of the stringer web (butt-joint), 1$mm$ above the skin.

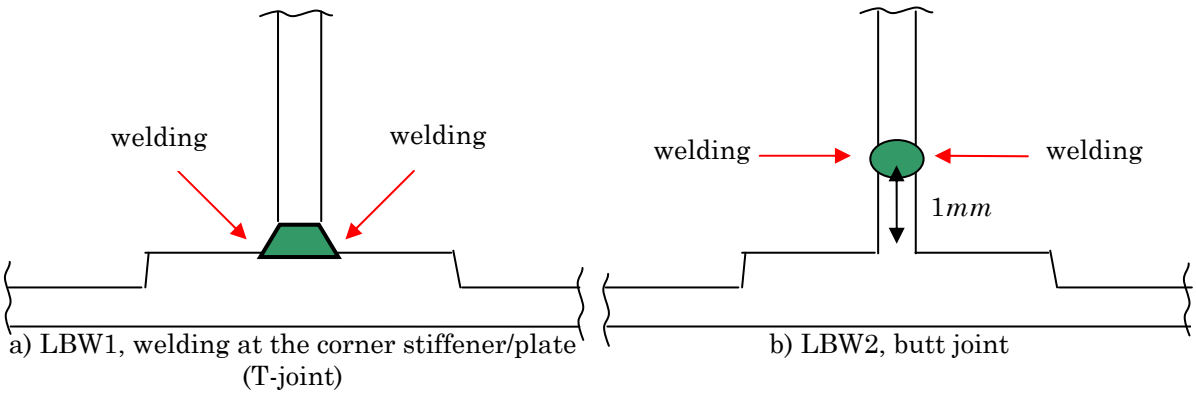


**Figure 322 - Welding configurations for the LBW specimens.**

The stress distributing for static and fatigue loading was recorded and the crack growth rate was also measured. An initial central through notch with 20*mm* length and 0,2*mm* width was created by electro-discharging.

### *6.2.3.1 Stress distribution for different static remote loads for specimen*

Panels with a central notch of 20*mm* length were instrumented and loaded at five incremental loads to acquire the stress distribution in different sites of the specimen. The strain gages were distributed in the specimen according to the scheme presented in Figure 310.

#### *6.2.3.1.1 LBW1 6056 PWHT-T6 specimen (LBW03 specimen)*

In this specimen were used four strain gages (C3, C4, C8 and C9), as presented in Figure 310. These strain gages correspond to the specimen vertical middle line, to the top of the left stiffener and its correspondent opposite specimen surface. The results obtained are presented in Table 85 and Figure 323.

**Table 85 - Strain gages measurements function of the remote stress applied, specimen LBW03 [*MPa*]**

| Remote stress | C3 | C4 | C8 | C9 |
|---|---|---|---|---|
| 20 | 21,5 | 52,6 | 23,4 | 17,4 |
| 40 | 41,8 | 84,0 | 45,0 | 35,9 |
| 60 | 62,2 | 110,6 | 66,0 | 54,8 |
| 80 | 82,7 | 135,2 | 86,8 | 74,1 |
| 100 | 103,5 | 159,0 | 107,6 | 93,5 |

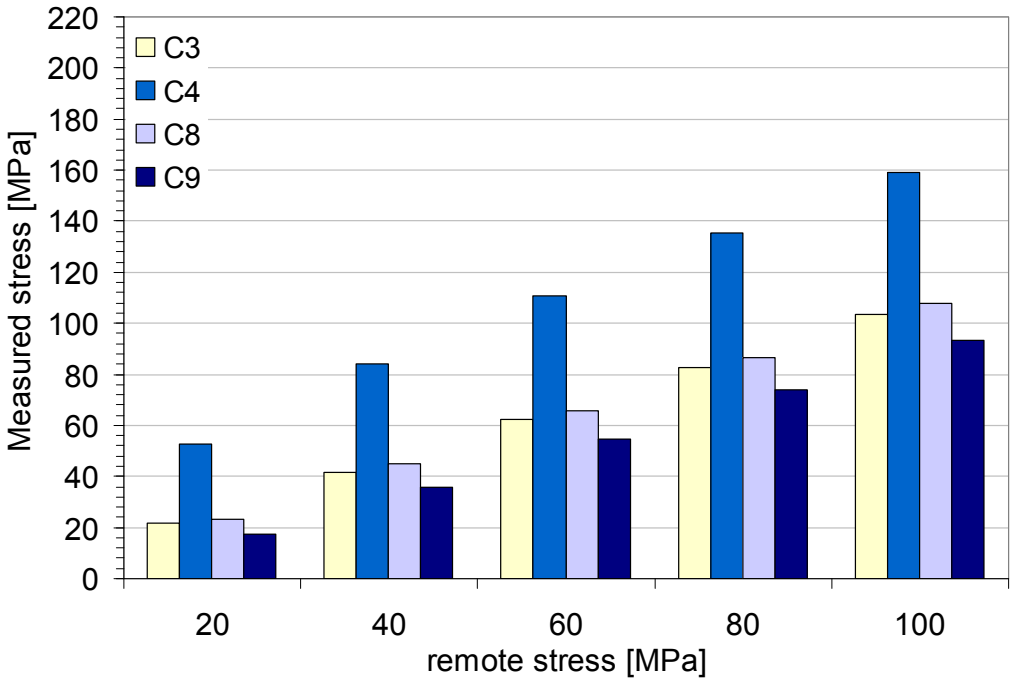


**Figure 323 - Stress distribution for different remote stress, specimen LBW03.**

For all remote loads, the strain gage situated at the top of the stiffener (C4) measured the higher stress and at the same site but in the plate front surface (C9) measured the lower value.

*6.2.3.1.2 LBW1 6056 PWHT-T6 specimen (LBW04 specimen)*

In this specimen six strain gages (C2, C3, C4, C7, C8 and C9) were used, as presented in Figure 310. These strain gages correspond to the specimen vertical middle line, and to the top of the left and right stiffeners in the plate back side and in its opposite side of the specimen. The results obtained are presented in Table 86 and Figure 324.

**Table 86 - Strain gages measurements function of the remote stress applied, specimen LBW04 [*MPa*]**

| Remote stress | C2 | C3 | C4 | C7 | C8 | C9 |
|---|---|---|---|---|---|---|
| 20 | 16,2 | 21,4 | 67,6 | 22,6 | 25,0 | 17,6 |
| 40 | 39,6 | 41,3 | 99,9 | 42,1 | 47,0 | 35,8 |
| 60 | 61,9 | 61,4 | 126,6 | 61,5 | 68,2 | 55,0 |
| 80 | 83,2 | 81,8 | 151,1 | 80,9 | 89,0 | 74,1 |
| 100 | 103,5 | 102,3 | 174,7 | 100,4 | 109,9 | 93,4 |

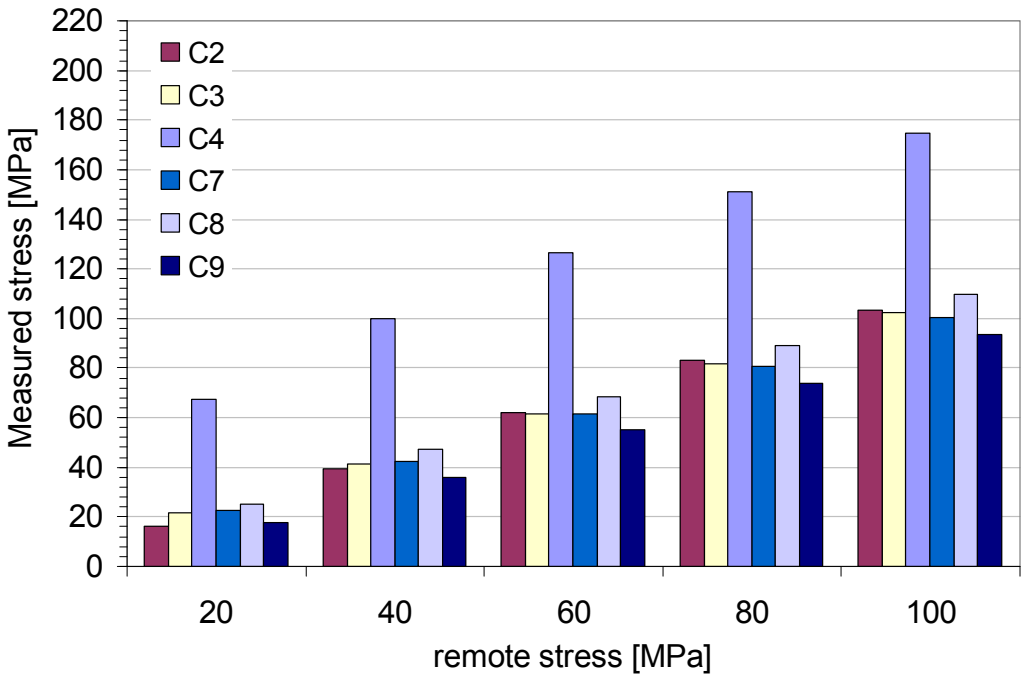


**Figure 324 - Stress distribution for different remote stress, specimen LBW04.**

*6.2.3.1.3 LBW2 6056 PWHT-T6 specimen (LBW05 specimen)*

In this specimen six strain gages (C2, C3, C4, C7, C8 and C9) were used, as presented in Figure 310. The results obtained are presented in Table 87 and Figure 325.

**Table 87 - Strain gages measurements function of the remote stress applied, specimen LBW05 [*MPa*]**

| Remote stress | C2 | C3 | C4 | C7 | C8 | C9 |
|---|---|---|---|---|---|---|
| 20 | 70,6 | 23,5 | 58,3 | 17,2 | 21,9 | 17,0 |
| 40 | 110,5 | 43,9 | 95,1 | 34,4 | 41,9 | 34,3 |
| 60 | 141,1 | 64,1 | 125,0 | 52,6 | 61,6 | 52,3 |
| 80 | 168,1 | 84,2 | 152,0 | 71,2 | 81,3 | 70,7 |
| 100 | 193,2 | 104,5 | 177,2 | 90,1 | 101,0 | 89,3 |

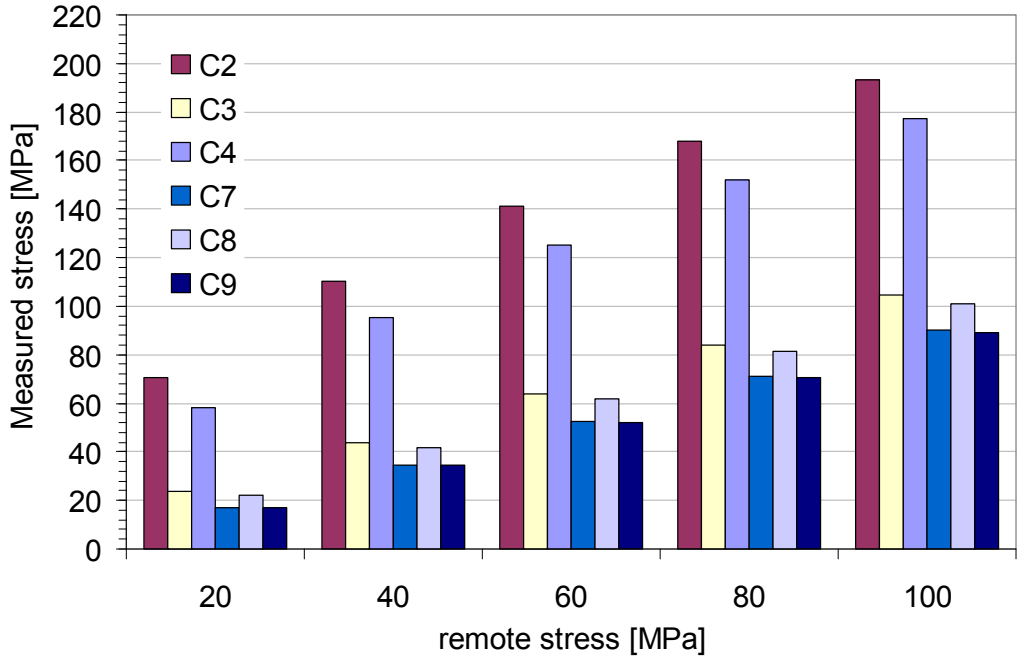


**Figure 325 - Stress distribution for different remote stress, specimen LBW05.**

Strain gages C2 and C4 represent the top of both stiffeners. They present the higher stress values. The lower values occur in the specimen front side in the stiffeners sites.

*6.2.3.1.4 LBW2 6056 PWHT-T6 specimen (LBW06 specimen)*

In this specimen were used six strain gages (C2, C3, C4, C7, C8 and C9), as presented in Figure 310. The results obtained are presented in Table 88 and Figure 326.

**Table 88 - Strain gages measurements function of the remote stress applied, specimen LBW06 [*MPa*]**

| Remote stress | C2 | C3 | C4 | C7 | C8 | C9 |
|---|---|---|---|---|---|---|
| 20 | 67,4 | 20,2 | 61,4 | 15,9 | 21,7 | 16,4 |
| 40 | 109,1 | 40,2 | 99,5 | 33,4 | 42,2 | 34,3 |
| 60 | 140,7 | 60,1 | 130,2 | 51,5 | 62,2 | 52,6 |
| 80 | 168,3 | 80,0 | 157,8 | 70,0 | 82,1 | 71,3 |
| 100 | 194,0 | 100,1 | 183,8 | 88,8 | 102,0 | 90,2 |

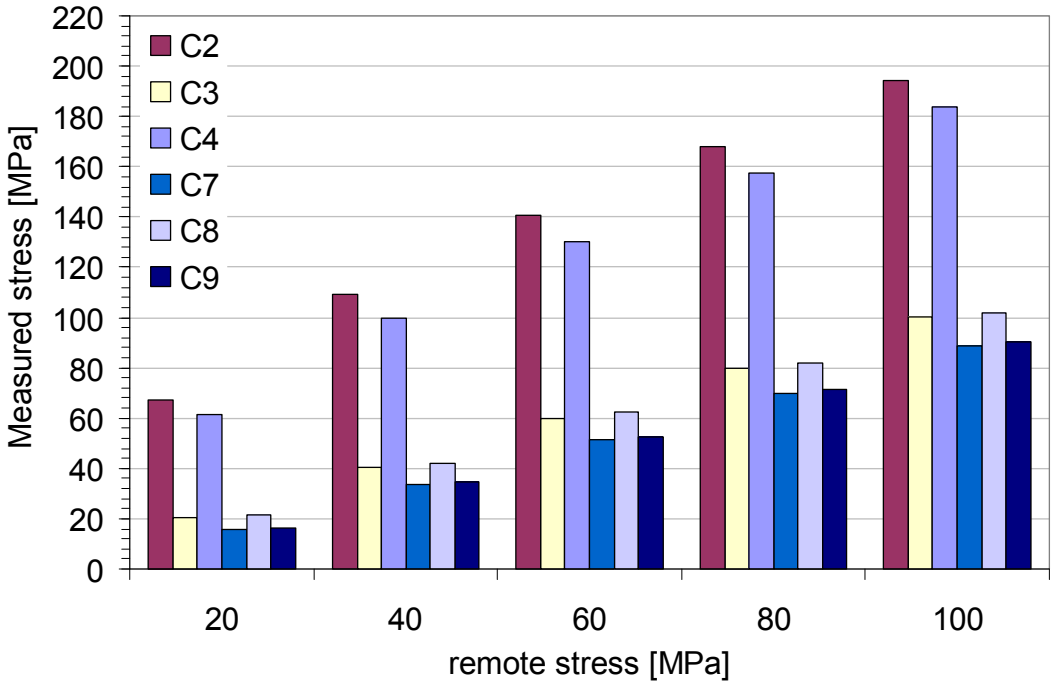


**Figure 326 - Stress distribution for different remote stress, specimen LBW06.**

This specimen presented a stress profile similar to the profile found in the LBW05 specimen.

*6.2.3.1.5 LBW2 6056-T6 as-welded specimen (LBW07 specimen)*

In this specimen were used six strain gages (C2, C3, C4, C7, C8 and C9), as presented in Figure 310. The results obtained are presented in Table 89 and Figure 327.

**Table 89 - Strain gages measurements function of the remote stress applied, specimen LBW07 [*MPa*]**

| Remote stress | C2 | C3 | C4 | C7 | C8 | C9 |
|---|---|---|---|---|---|---|
| 20 | 64,0 | 25,2 | 73,1 | 12,8 | 20,0 | 13,7 |
| 40 | 103,7 | 45,9 | 116,4 | 30,5 | 40,6 | 31,7 |
| 60 | 135,1 | 66,3 | 148,3 | 48,3 | 60,2 | 49,6 |
| 80 | 162,8 | 86,2 | 176,0 | 66,6 | 79,9 | 68,0 |
| 100 | 188,9 | 106,4 | 201,8 | 85,1 | 99,5 | 86,7 |

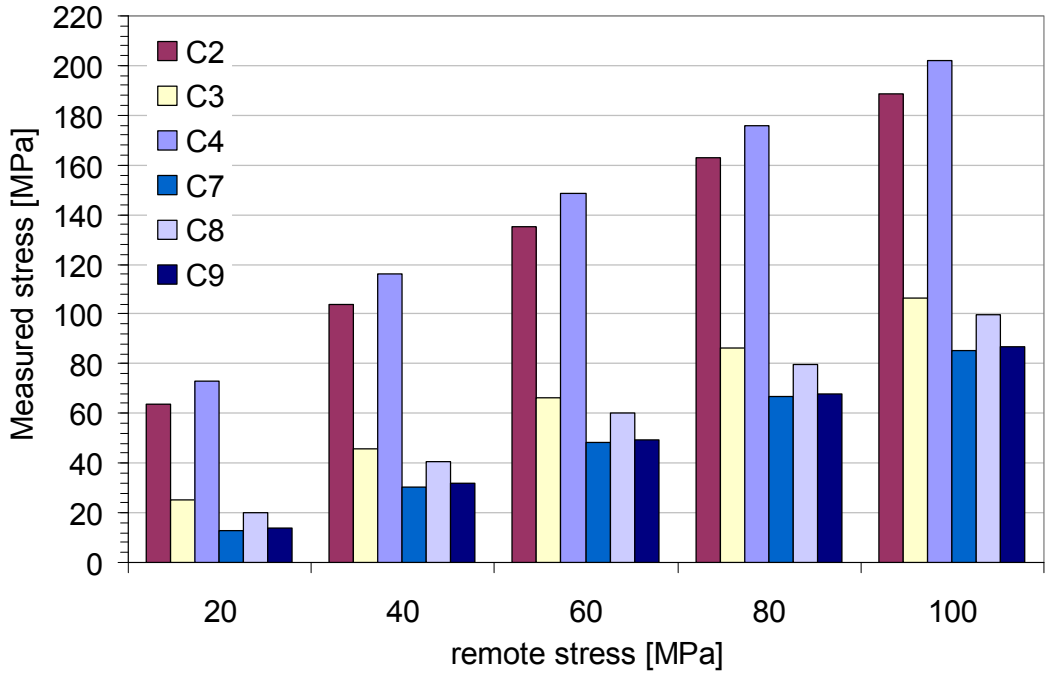


**Figure 327 - Stress distribution for different remote stress, specimen LBW07.**

Strain gages C2 and C4, which represent the top of both stiffeners, present the higher stress values being the lowers values in the specimen front side in the stiffeners sites.

*6.2.3.1.6 LBW2 6056-T6 as-welded specimen (LBW08 specimen)*

In this specimen were used six strain gages (C2, C3, C4, C7, C8 and C9), as presented in Figure 310. The results obtained are presented in Table 90 and Figure 328.

**Table 90 - Strain gages measurements function of the remote stress applied, specimen LBW08 [*MPa*]**

| Remote stress | C2 | C3 | C4 | C7 | C8 | C9 |
|---|---|---|---|---|---|---|
| 20 | 66,2 | 21,6 | 76,2 | 15,3 | 20,9 | 14,8 |
| 40 | 107,3 | 41,7 | 122,1 | 32,2 | 40,8 | 31,4 |
| 60 | 140,1 | 61,5 | 157,1 | 50,0 | 60,3 | 49,0 |
| 80 | 169,1 | 81,5 | 187,5 | 68,2 | 80,0 | 67,1 |
| 100 | 196,0 | 101,7 | 215,5 | 86,8 | 99,7 | 85,5 |

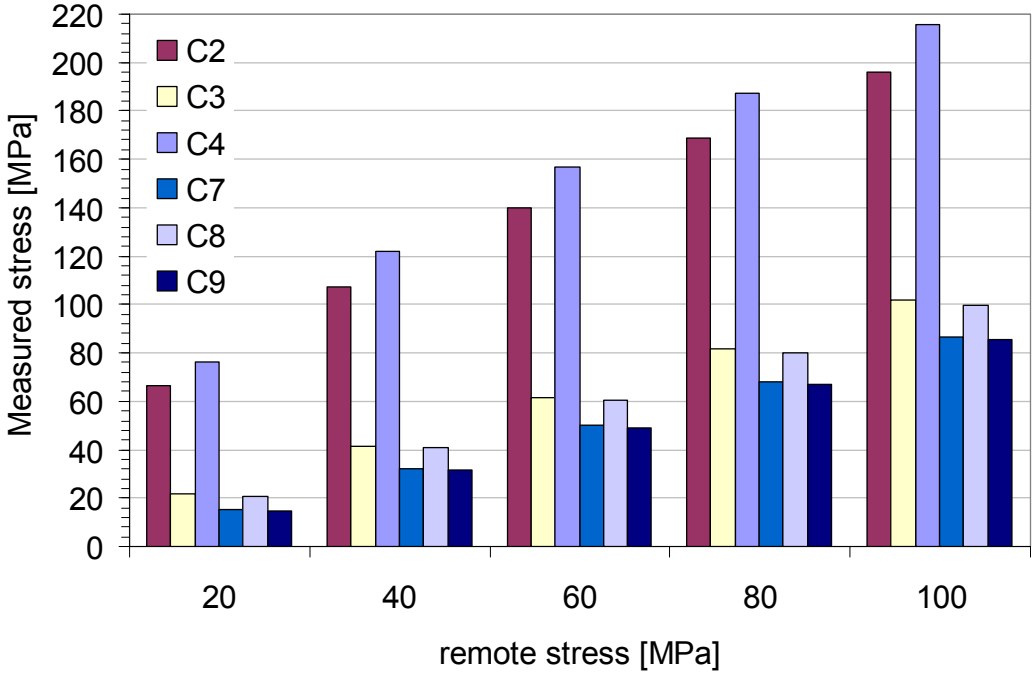


**Figure 328 - Stress distribution for different remote stress, specimen LBW08.**

Strain gages C2 and C4, which represent the top of both stiffeners, present the higher stress values being the lowers values in the specimen front side in the stiffeners sites.

*6.2.3.1.7 Comparison of static loading (specimens tested at R=0,1)*

The comparison of the static loading measurements on HSM (R=0,1) and LBW specimens tested with R=0,1 is presented in Figure 329. The results are presented as a function of the panel width and measurements were performed at a remote load of 100*MPa*. For the HSM specimen the back and the front strain gages present almost symmetrical values for all measurement locations being the front strain gages the ones that have higher stress values. For each type of LBW specimens (LBW1, LBW2 PWHT and LBW2 as-welded) the load at the top of the stiffeners presented higher values than in the HSM specimen. This difference is due to the specimen distortion introduced by the welding process. At the stiffeners location, but in the panel front surface, the stress is lower in the LBW's specimens than in HSM specimens. At the central strain gage all specimens presented similar stress values, which are near the remote stress.

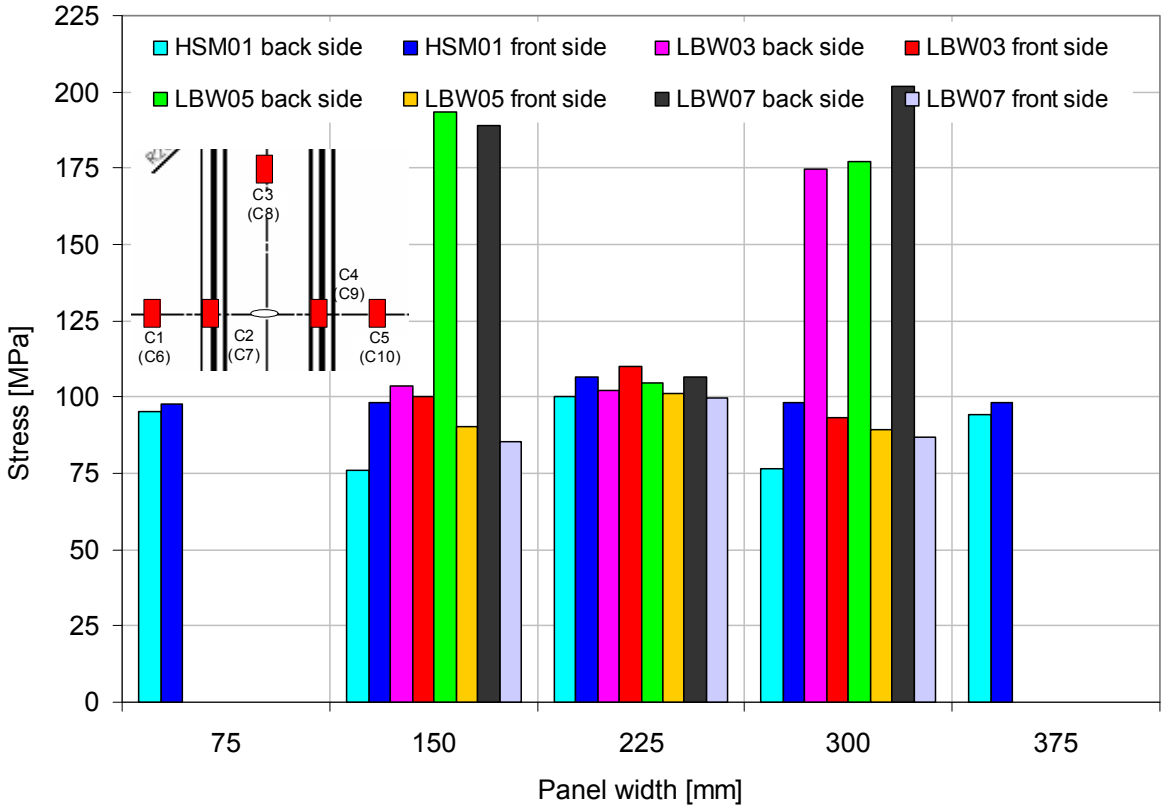


**Figure 329 - Comparison of static loading of HSM and LBW specimens.**

*6.2.3.2 Fatigue crack growth test LBW1 6056 PWHT-T6 $\sigma_{max}$=80MPa R=0,1 (LBW03)*

A stiffened panel in the LBW1 configuration was fatigue tested at a maximum remote stress of 80*MPa* with R=0,1. This panel was welded in the aluminium 6056-T4 temper and a post welding heat treatment was done do achieve the T6 temper. Fatigue crack propagation tests were carried out and crack length was measured at periodic stops of the fatigue test.

*6.2.3.2.1 Weldments details*

When analysing the LBW03 specimen, tested at R=0,1, some problems were detected at the end and beginning of the weldments. At the weldment initial site (Figure 330 a) and b)) it was verified that the stiffener was not welded in its total length creating a notch. Also, in the weldment ending site (Figure 330 c) and d)) un-melted filler wire was present also creating a stress concentration effect. These features make the specimen prone to secondary cracks. In order to minimize the effect of these defects the stiffeners ends were manually polished. The polishement procedure was performed in such a way that minimum geometrical changes were introduced. The final result of this polishement procedure is presented in Figure 331.

a) side view of the weldment initial site

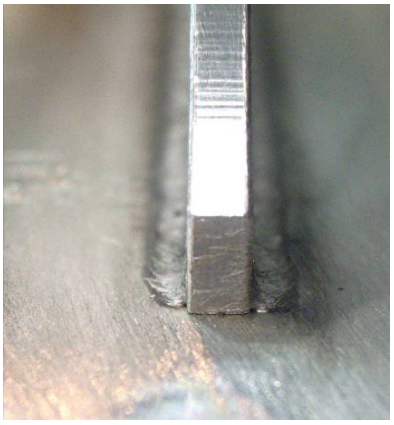

b) front view of the weldment initial site

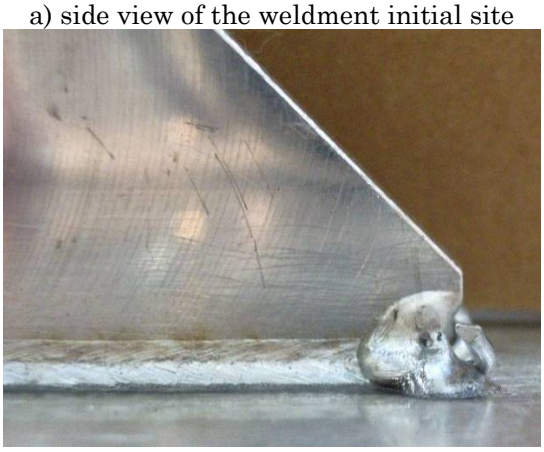

c) side view of the weldment ending site

d) front view of the weldment ending site

**Figure 330 - Details of beginning and end site of weldments.**

**Figure 331 - Visual detail of a polished stiffener end.**

*6.2.3.2.2 Secondary cracks*

At 17500 cycles secondary cracks were identified at the stiffeners run-out. These cracks appeared at a firsts instance in both stiffeners at the end of the weldment. An example of one of these cracks is presented in Figure 332.

**Figure 332 - Secondary crack at 17500 cycles.**

As a solution for secondary cracks arrest, aluminium patches were adhesively bonded at 17500 cycles to the plate in the opposite side of the stiffeners. A detail of these patches is presented in Figure 333.

**Figure 333 - Patches used to control the fatigue crack growth of secondary cracks.**

The patches delayed the secondary crack growth for 40000 cycles but, since the secondary cracks had already a considerable size (at 18000 cycles), they did not sustain their growth. A schematic representation of all secondary cracks at 100000 cycles is presented in Figure 334. The down left side crack and the up right side crack which correspond to the weldment end sites presented the longer cracks.

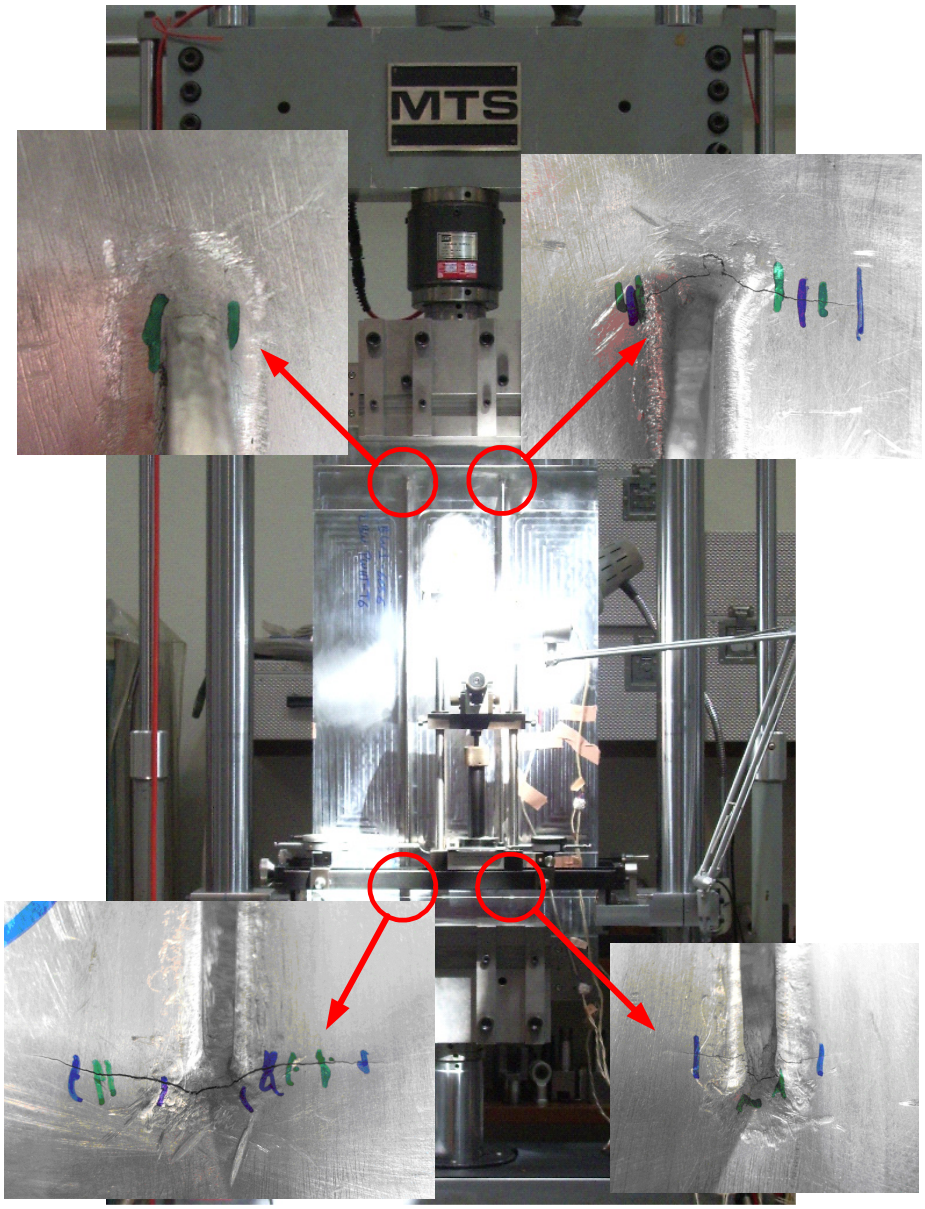


**Figure 334 - Secondary cracks in all stiffeners ends at 100000 cycles.**

A detailed secondary crack length versus number of cycle's analysis is presented in Figure 335 and Figure 336. It can be seen the effect of the patches, which were able to decrease the fatigue crack growth rate until 50000 cycles.

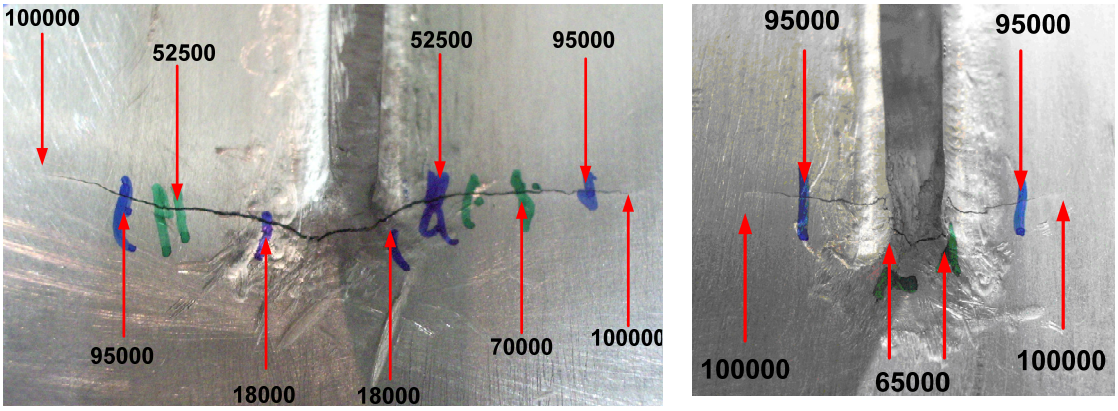


a) down left side crack b) down right side crack

**Figure 335 - Down side cracks function of the number of cycles.**

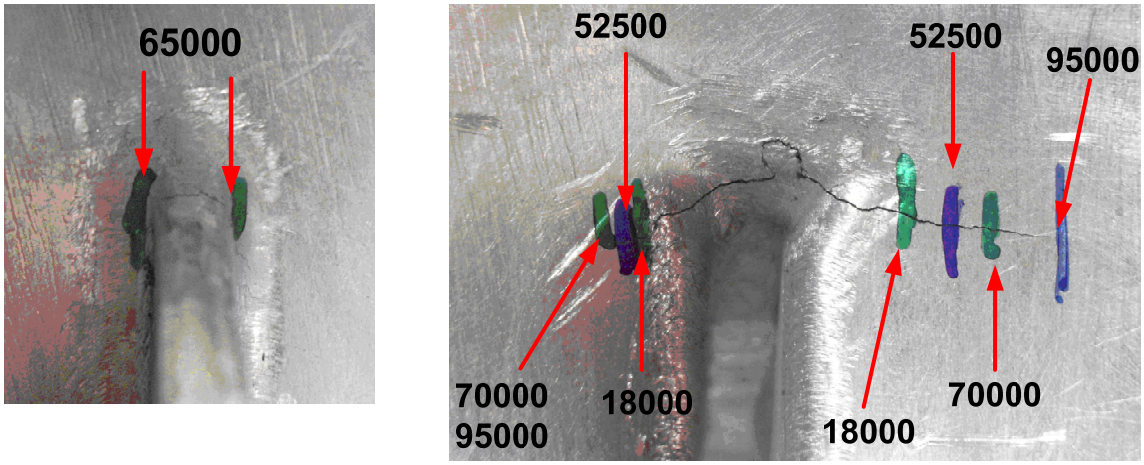


a) up left side crack b) up right side crack

**Figure 336 - Up side cracks function of the number of cycles.**

In order to complete the test a through hole was drilled at all secondary crack tips and a blind rivet was introduced. This solution, presented in Figure 337, was able to stop the crack and the test was successfully carried out until the final rupture by the central crack.

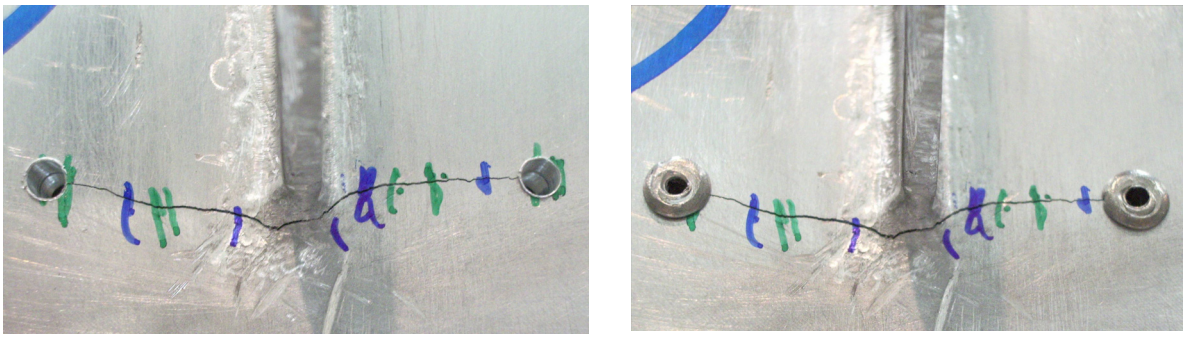

a) hole drilled at the crack tip (3$mm$ diameter) b) rivet crack tip

**Figure 337 - Riveting procedure in the down left side crack.**

*6.2.3.2.3 Stress distribution during the fatigue crack growth test*

Fatigue crack propagation tests were carried out and strain was measured in order to understand the different load transfer stages.
The strain gages values were measured in periodic stops of the fatigue test at the maximum fatigue load (95,96*kN*). The stress distribution on the stiffened panel along the fatigue test is presented in Figure 338. C4 represent the strain gage at the top of the stiffener and shows that as the crack size increases the load transferred in the stiffener increases. Also, the difference between the stress in C3 and C8 decreased during the test.

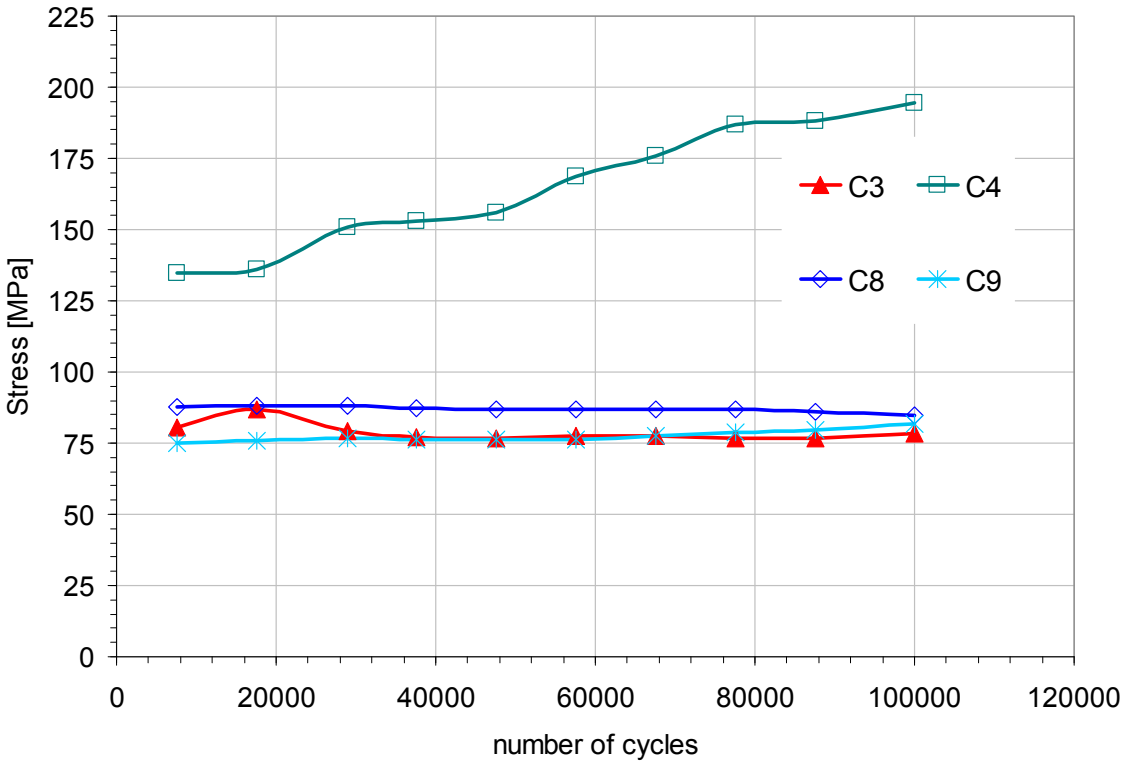


**Figure 338 - Stress distribution during the fatigue crack growth test, LBW1 6056 PWHT-T6 $\sigma_{max}$=80*MPa* R=0,1.**

*6.2.3.2.4 a-N results*

The LBW1 6056 PWHT-T6 specimen, tested at a maximum stress of 80*MPa* with R=0,1, had a fatigue life of 153874 cycles. The fatigue crack growth in the stiffened panel during the fatigue test is presented in Figure 339. The crack started to grow through the stiffener at 151879 cycles, which corresponds to 98,7% of the total fatigue life.

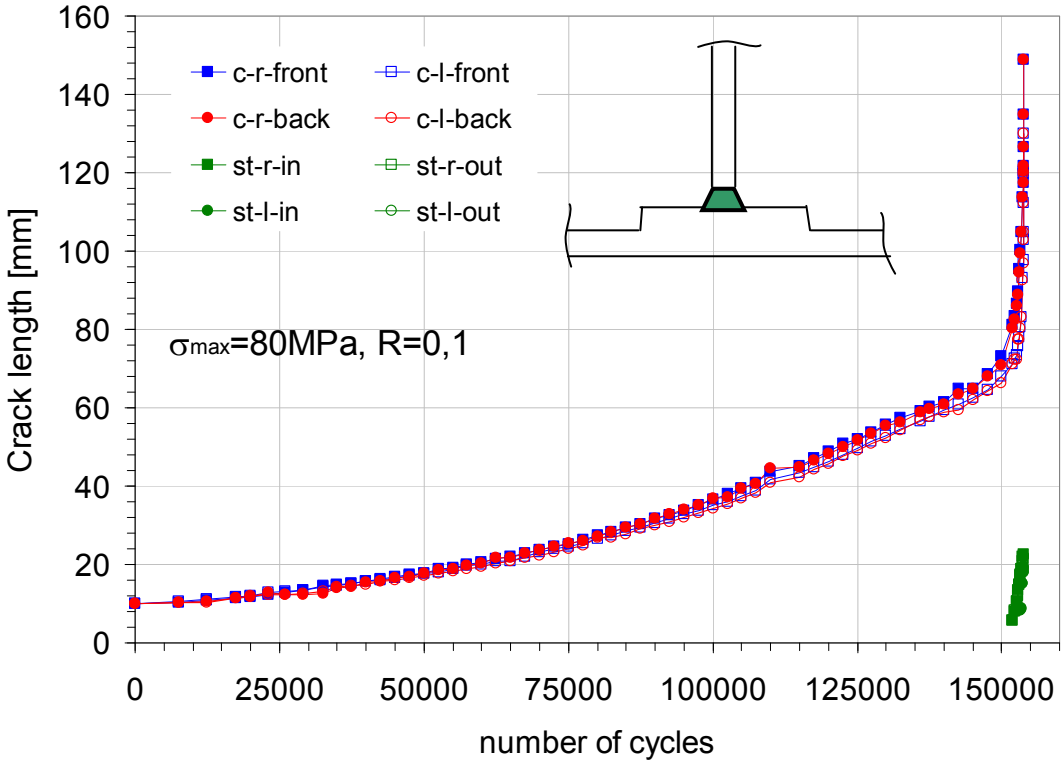


**Figure 339 - Fatigue crack growth test, LBW1 6056 PWHT-T6 $\sigma_{max}$=80*MPa* R=0,1.**

*6.2.3.3 Fatigue crack growth test LBW1 6056 PWHT-T6 $\sigma_{max}$=110MPa R=0,5 (LBW04)*

A stiffened panel in the LBW1 configuration was fatigue tested at a maximum remote stress of 110*MPa* with R=0,5. This panel was welded in the aluminium 6056-T4 temper and a post welding heat treatment was done do achieve the T6 temper. Fatigue crack propagation tests were carried out and crack length was measured at periodic stops of the fatigue test.

*6.2.3.3.1 Stress distribution during the fatigue crack growth test*

Fatigue crack propagation tests were carried out and strain was measured in order to understand the different load transfer stages.
The strain gages values were measured in periodic stops of the fatigue test at the maximum fatigue load (119,95*kN*). The stress distribution on the stiffened panel along the fatigue test is presented in Figure 340. In this specimen a high increase in the load transfer by the specimen front surface, in the stiffeners location, was verified as the crack reaches the stiffeners.

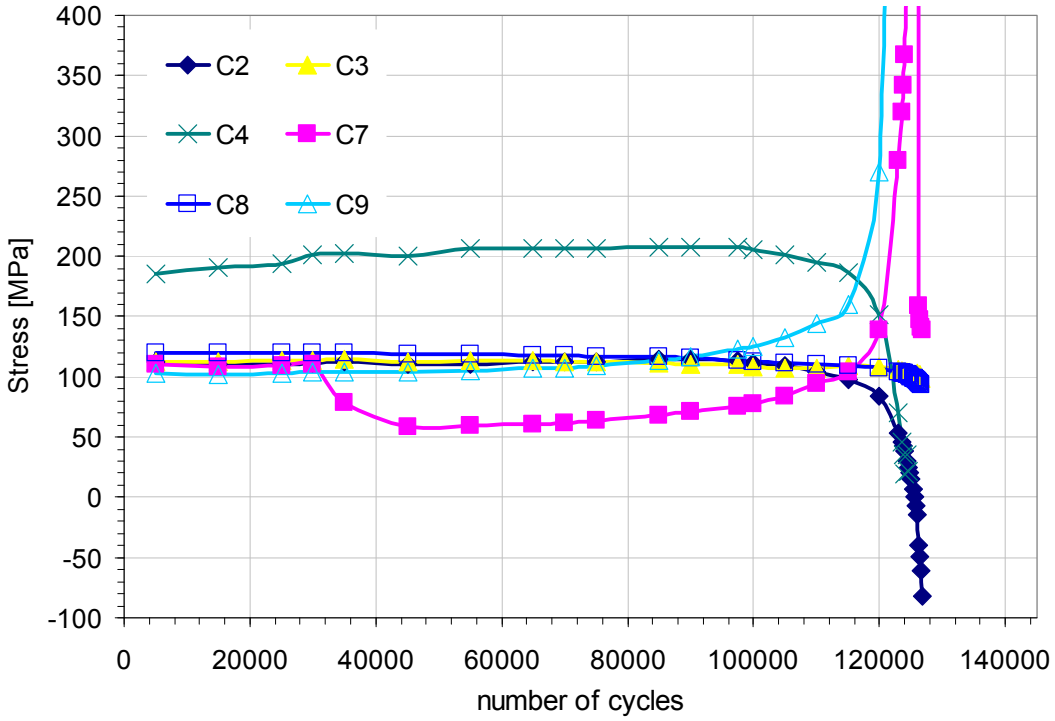


**Figure 340 - Stress distribution during the fatigue crack growth test, LBW1 6056 PWHT-T6 $\sigma_{max}$=110*MPa* R=0,5.**

*6.2.3.3.2 a-N results*

The LBW1 6056 PWHT-T6 specimen, tested at a maximum stress of 110*MPa* with R=0,5, had a fatigue life of 128279 cycles. The fatigue crack growth in the stiffened panel during the fatigue test is presented in Figure 341. The crack started to grow through the stiffener at 123500 cycles, which corresponds to 96,3% of the total fatigue life.

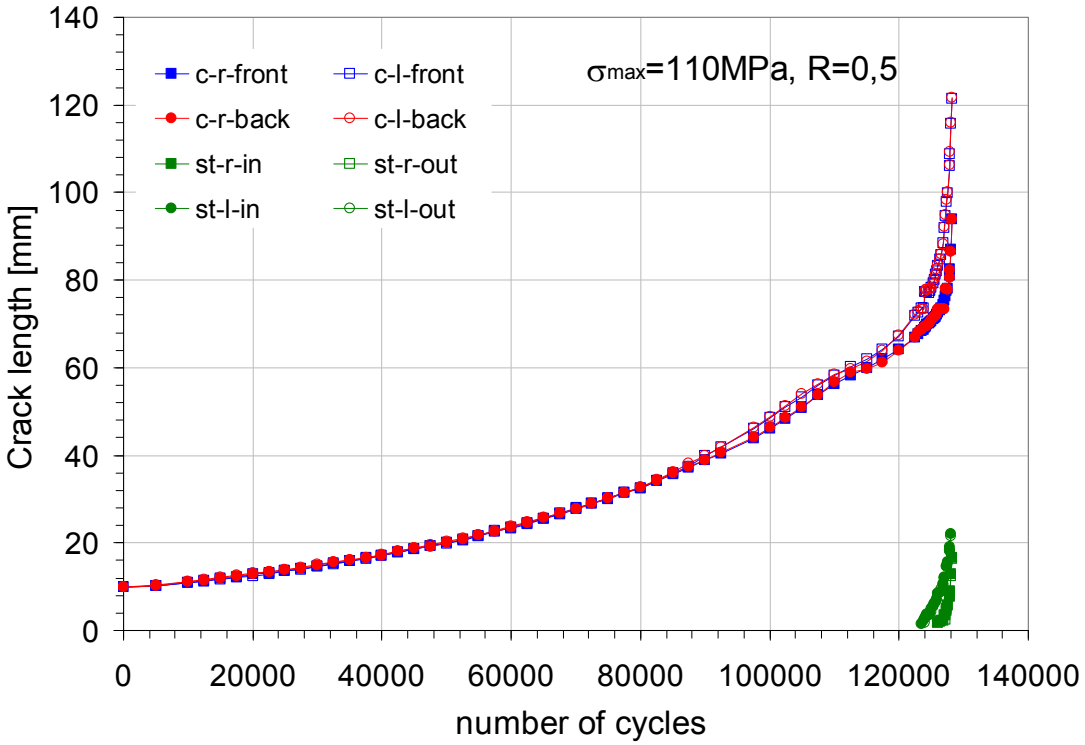


**Figure 341 - Fatigue crack growth test, LBW1 6056 PWHT-T6 $\sigma_{max}$=110*MPa* R=0,5.**

*6.2.3.4 Fatigue crack growth test LBW2 6056 PWHT-T6 $\sigma_{max}$=80MPa R=0,1 (LBW05)*

A stiffened panel in the LBW2 configuration was fatigue tested at a maximum remote stress of 80*MPa* with R=0,1. This panel was welded in the aluminium 6056-T4 temper and a post welding heat treatment was done to achieve the T6 temper.
Fatigue crack propagation tests were carried out and crack length was measured at periodic stops of the fatigue test.

*6.2.3.4.1 Weldment details*

Despite this specimen being welded in a butt joint configuration, similar defects were present at the end and beginning of the weldment. Again, these defects were eliminated prior to testing, but instead of only removing the defected part a smoothed angle (30º) was machined. This smoothing was performed in two procedures, first the material was removed by a milling procedure, and finally the surface was smoothed by hand polishing, see Figure 342.

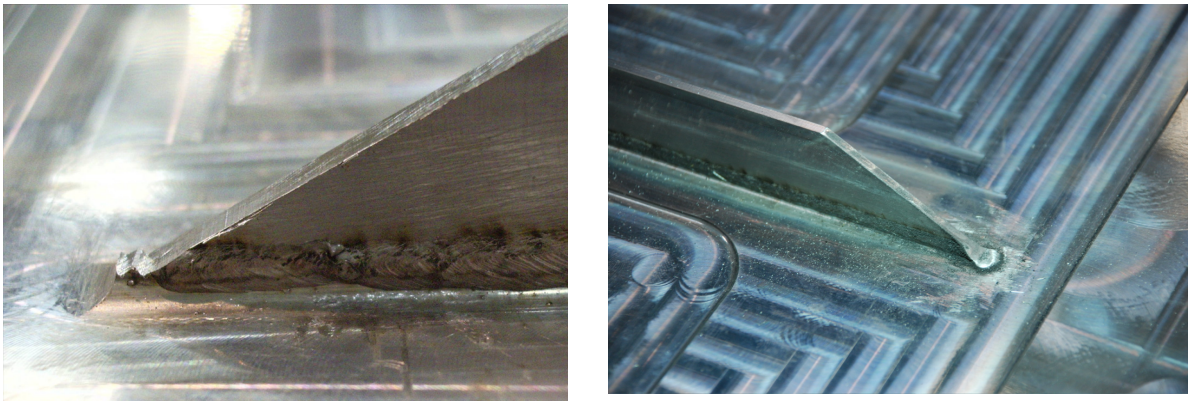

a) stiffener after the milling procedure b) stiffener after the hand polishing procedure

**Figure 342 - Stiffener ends smoothing procedures.**

*6.2.3.4.2 Secondary cracks*

Before the tests, in this specimen besides the smoothing procedure, two patches, one in each side were placed in the skin opposite to the stiffeners, as presented in Figure 343.

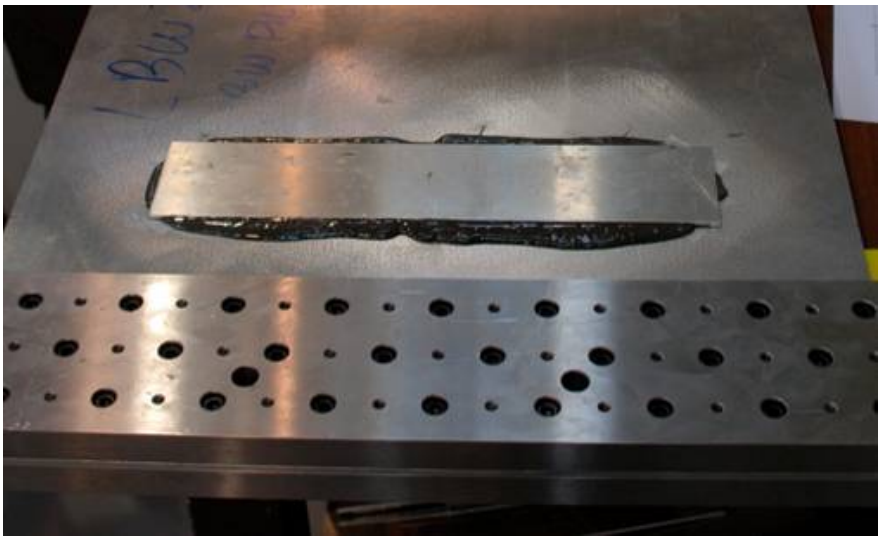

**Figure 343 - Patch comprehending both stiffeners.**

Despite this effort, secondary cracks appeared in the stiffeners at 60000 cycles. The patch was not working at its full capability, because problems with the adhesive hardening occurred. At 105000 cycles, rivets had to be placed at the crack tips which appeared at the weldment run-outs, Figure 344.

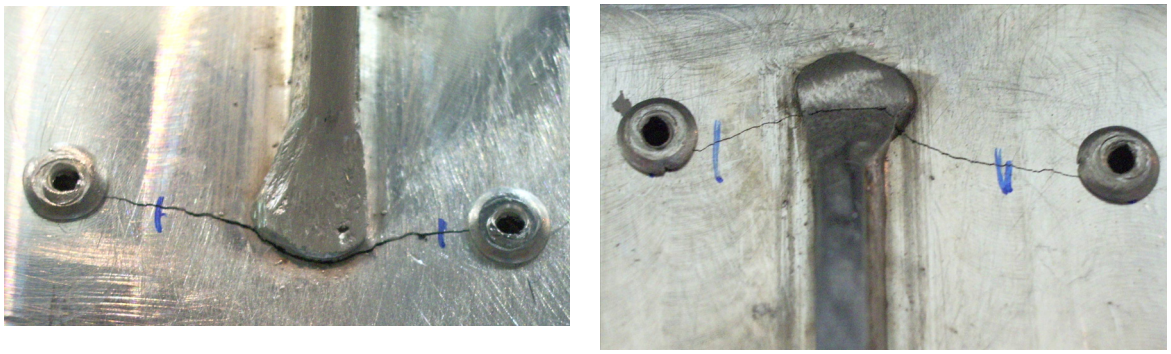

**Figure 344 - Riveting process of the LBW2 6056 PWHT-T6 $\sigma_{max}$=80*MPa* R=0,1 at 105000 cycles.**

Besides the secondary cracks perpendicular to the stiffener, a longitudinal crack appeared at the beginning of a weldment. This crack was identified just before 60000 cycles and grew during the test. A detail of this crack is presented in Figure 345.

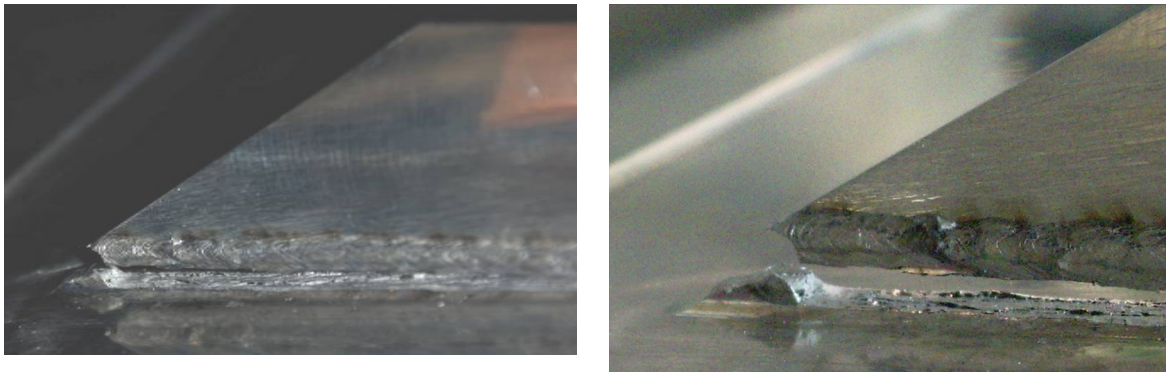

**Figure 345 - Longitudinal crack.**

*6.2.3.4.3 Stress distribution during the fatigue crack growth test*

Fatigue crack propagation tests were carried out and strain was measured in order to understand the different load transfer stages.
The strain gages values were measured in periodic stops of the fatigue test at the maximum fatigue load (95,96*kN*). The stress distribution on the stiffened panel along the fatigue test is presented in Figure 346.
The strain gage C4 represents the stiffener in which a longitudinal crack appeared (see Figure 345). As the crack advances the load transfer in this stiffener decreases, and consequently increases in the opposite stiffener. Despite this difference, between the maximum stress at the top of both stiffeners, the fatigue crack grew symmetrically.

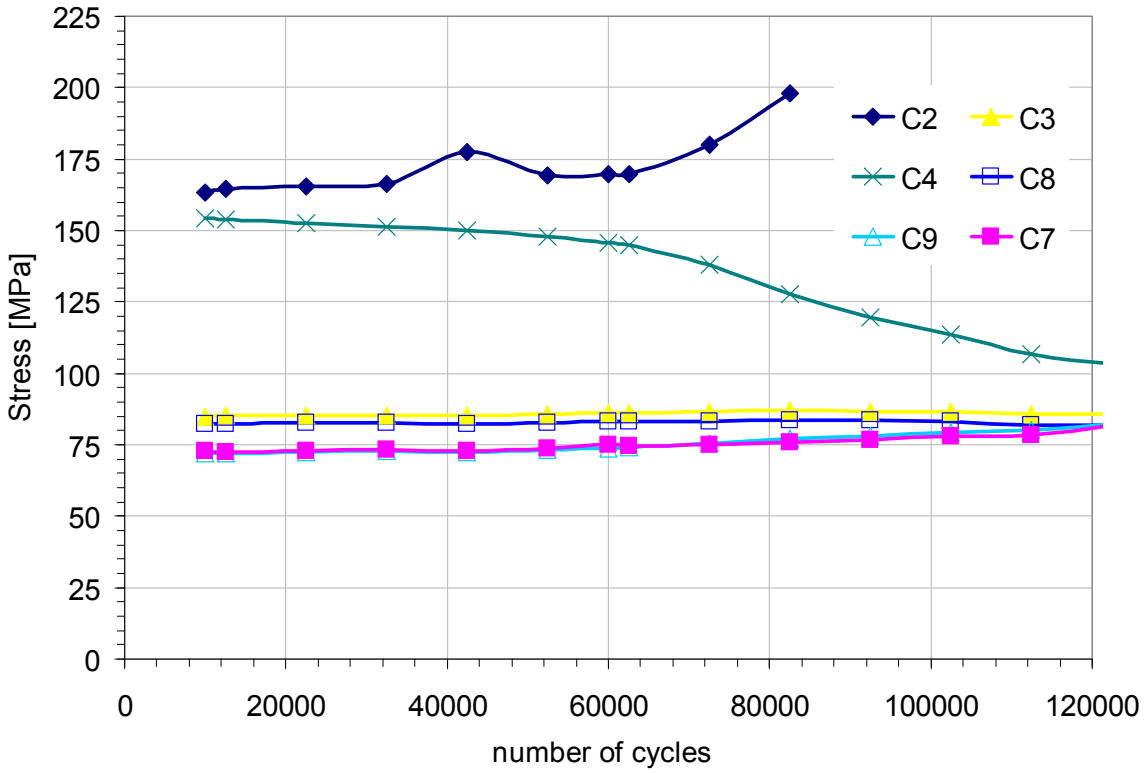


**Figure 346 - Stress distribution during the fatigue crack growth test, LBW2 6056 PWHT-T6 $\sigma_{max}$=80*MPa* R=0,1.**

*6.2.3.4.4 a-N results*

The LBW2 6056 PWHT-T6 specimen, tested at a maximum stress of 80*MPa* with R=0,1, had a fatigue life of 178864 cycles. The fatigue crack growth in the stiffened panel during the fatigue test is presented in Figure 347. The crack started to grow through the stiffener at 176500 cycles, 98,8% of the total fatigue life. This LBW2 specimen presented a 16% higher life than the LBW1 specimen tested with the same parameters.

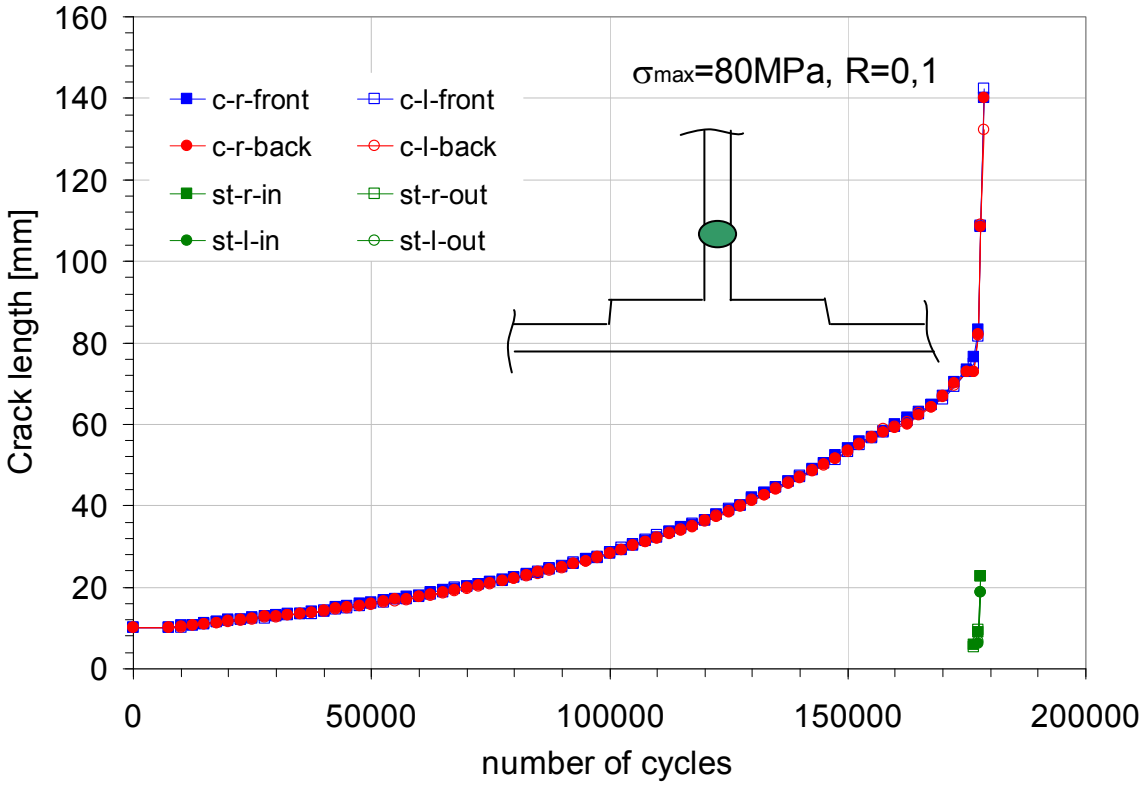


**Figure 347 - Fatigue crack growth test, LBW2 6056 PWHT-T6 $\sigma_{max}$=80*MPa* R=0,1.**

*6.2.3.4.5 Results comparison*

A comparison between the fatigue crack lengths versus the number of cycles for the LBW1 6056 PWHT-T6 and the LBW2 6056 PWHT-T6 specimen tested at R=0,1 is presented in Figure 348. It was found, that for the same material and tested with the same parameters, the LBW1 specimen presented a lower fatigue life. For comparison, an initial fatigue crack of 24*mm* was considered in order to eliminate the influence of different EDM notches.

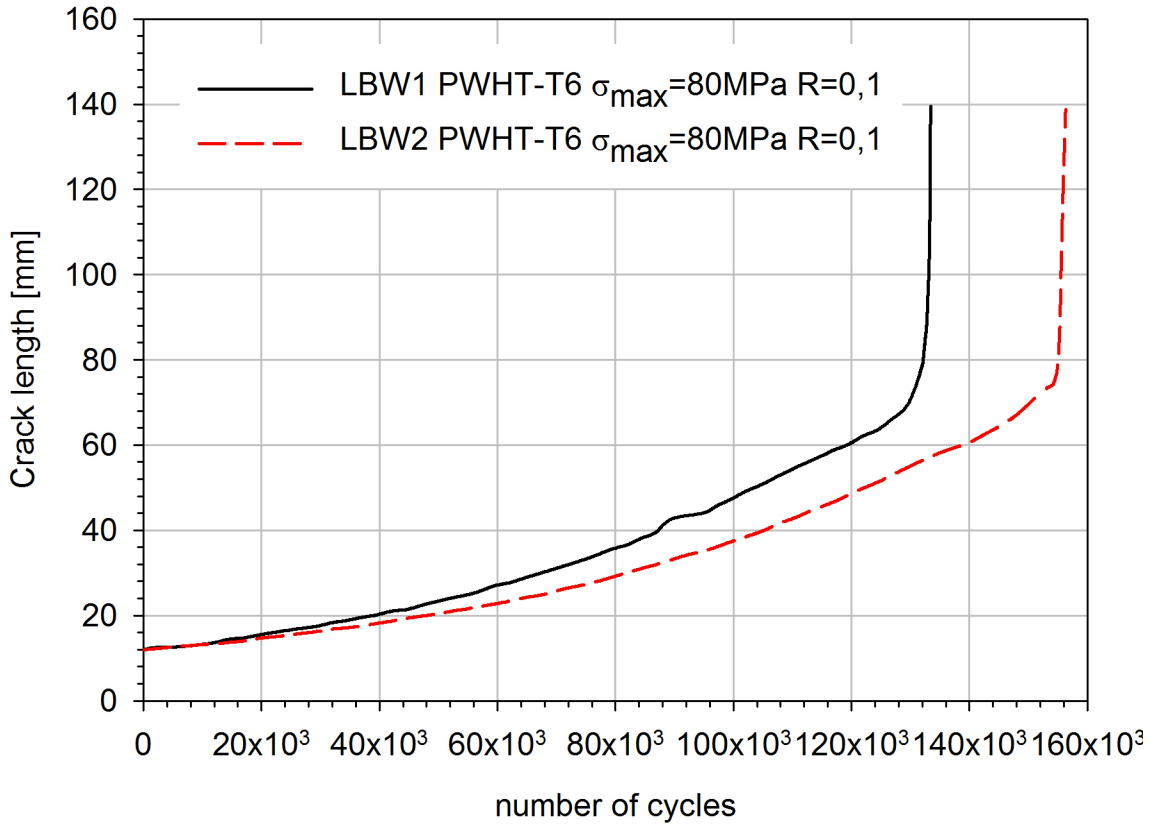


**Figure 348 - Comparison of a-N LBW1 6056 PWHT-T6 *vs.* LBW2 6056 PWHT-T6, R=0,1.**

*6.2.3.5 Fatigue crack growth test LBW2 6056 PWHT-T6 $\sigma_{max}$=110MPa R=0,5 (LBW06)*

A stiffened panel in the LBW2 configuration was fatigue tested at a maximum remote stress of 110*MPa* with R=0,5. This panel was welded in the aluminium 6056-T4 temper and a post welding heat treatment was done do achieve the T6 temper. Fatigue crack propagation tests were carried out and crack length was measured at periodic stops of the fatigue test.

*6.2.3.5.1 Stress distribution during the fatigue crack growth test*

Fatigue crack propagation tests were carried out and strain was measured in order to understand the different load transfer stages.
The strain gages values were measured in periodic stops of the fatigue test at the maximum fatigue load (119,95*kN*). The stress distribution on the stiffened panel along the fatigue test is presented in Figure 349.
The specimen distortion is patented in the different load transfer of both stiffeners, C2 and C4, as the crack grows.

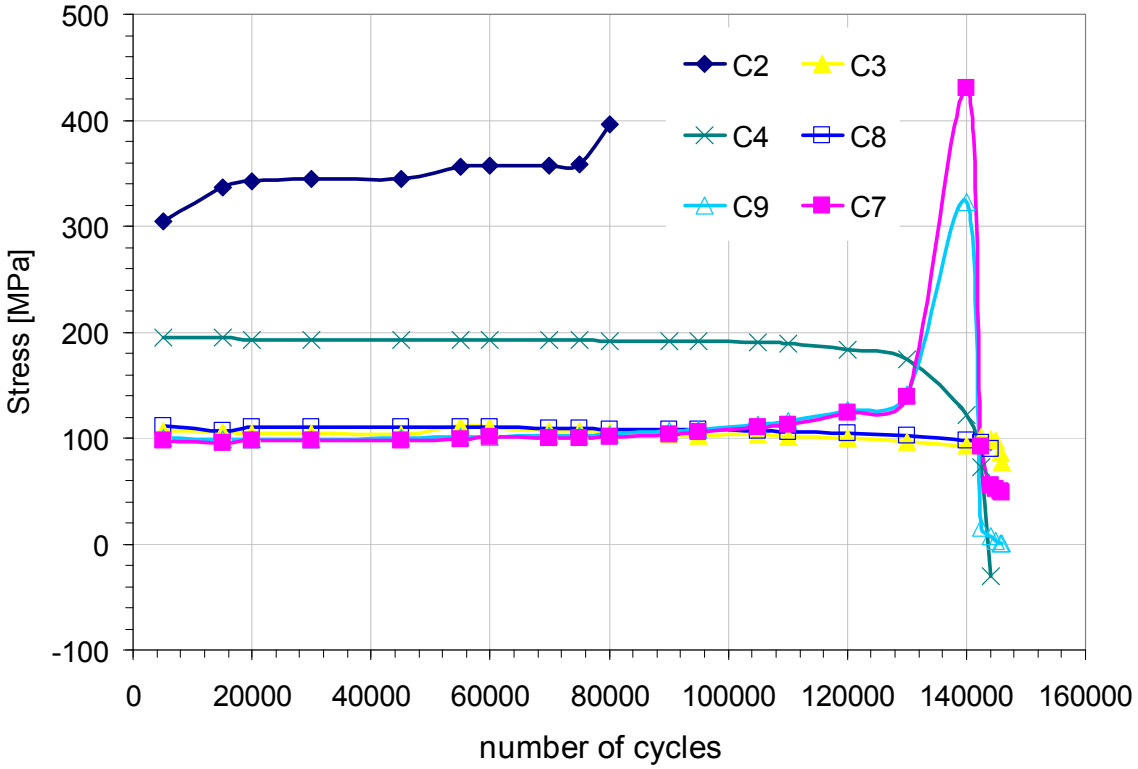


**Figure 349 - Stress distribution during the fatigue crack growth test, LBW2 6056 PWHT-T6 $\sigma_{max}$=110*MPa* R=0,5.**

*6.2.3.5.2 a-N results*

The LBW2 6056 PWHT-T6 specimen, tested at a maximum stress of 110*MPa* with R=0,5, had a fatigue life of 146239 cycles. The fatigue crack growth in the stiffened panel during the fatigue test is presented in Figure 350. The crack started to grow through the stiffener at 142500 cycles, 97,4% of the total fatigue life.

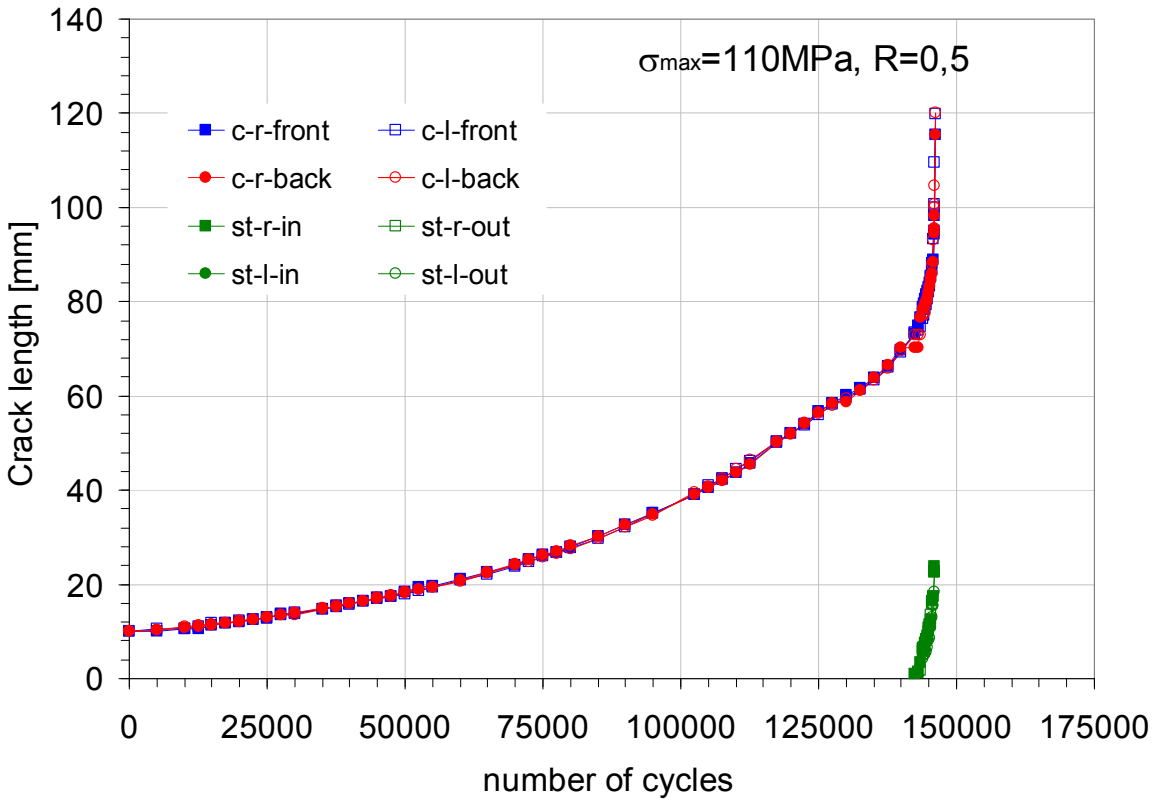


**Figure 350 - Fatigue crack growth test, LBW2 6056 PWHT-T6 $\sigma_{max}$=110*MPa* R=0,5.**

*6.2.3.6 Fatigue crack growth test LBW2 6056-T6 as-welded $\sigma_{max}$=80MPa R=0,1 (LBW07)*

A stiffened panel in the LBW2 configuration was fatigue tested at a maximum remote stress of 80MPa with R=0,1. This panel was fabricated in aluminium 6056-T6 and tested, after welding, in the as-welded configuration. Fatigue crack propagation tests were carried out and crack length was measured at periodic stops of the fatigue test.

*6.2.3.6.1 Weldments details*

Defects were also identified at the end and beginning of the weldments. Again these defects were eliminated prior to testing, but instead of only removing the defected material a smoothed angle (30º) was machined. As in the previous specimen, this smoothing was performed in two procedures. First a rough procedure of material removal by a milling machine, and finally the surface was smoothed by hand polishing. The material milling procedure is presented in Figure 351. A detail of a stiffener after hand polishing is presented in Figure 352.

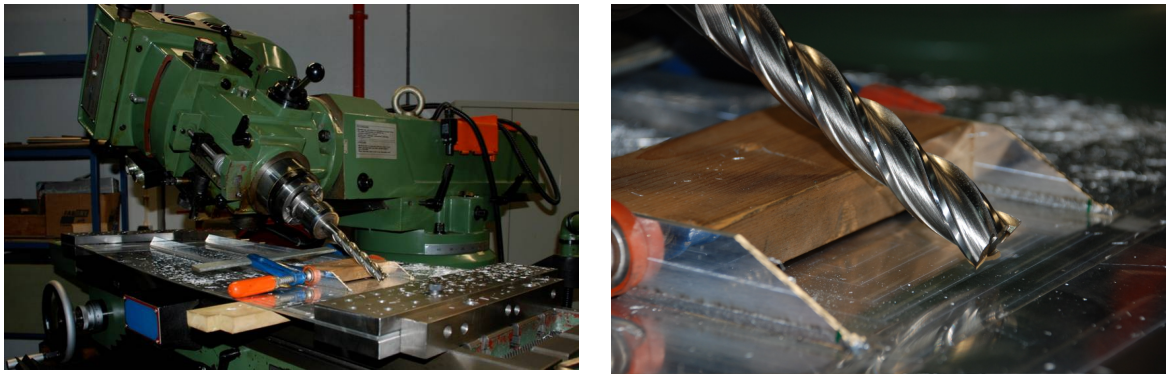

a) milling procedure b) detail of the milling procedure

**Figure 351 - Stiffener smoothing procedures.**

**Figure 352 - Stiffener after hand polishing.**

As in the LBW1 6056 PWHT-T6 R=0,1 specimen, square patches were place at the opposite side of each stiffener end.

*6.2.3.6.2 Test details*

During the fatigue test, short secondary cracks appeared in the weldments at the end of the stiffeners. These cracks appeared at 85000 cycles and 107500 cycles but riveting was not necessary since the patch was an effective crack stopper. The patching procedure was successful and no riveting procedure was needed to end the test. In Figure 353b) is presented the fractured specimen at the end of the test; besides the fatigue crack the patches can be identified near the gripping area. A photograph of a patch detail is presented in Figure 354.

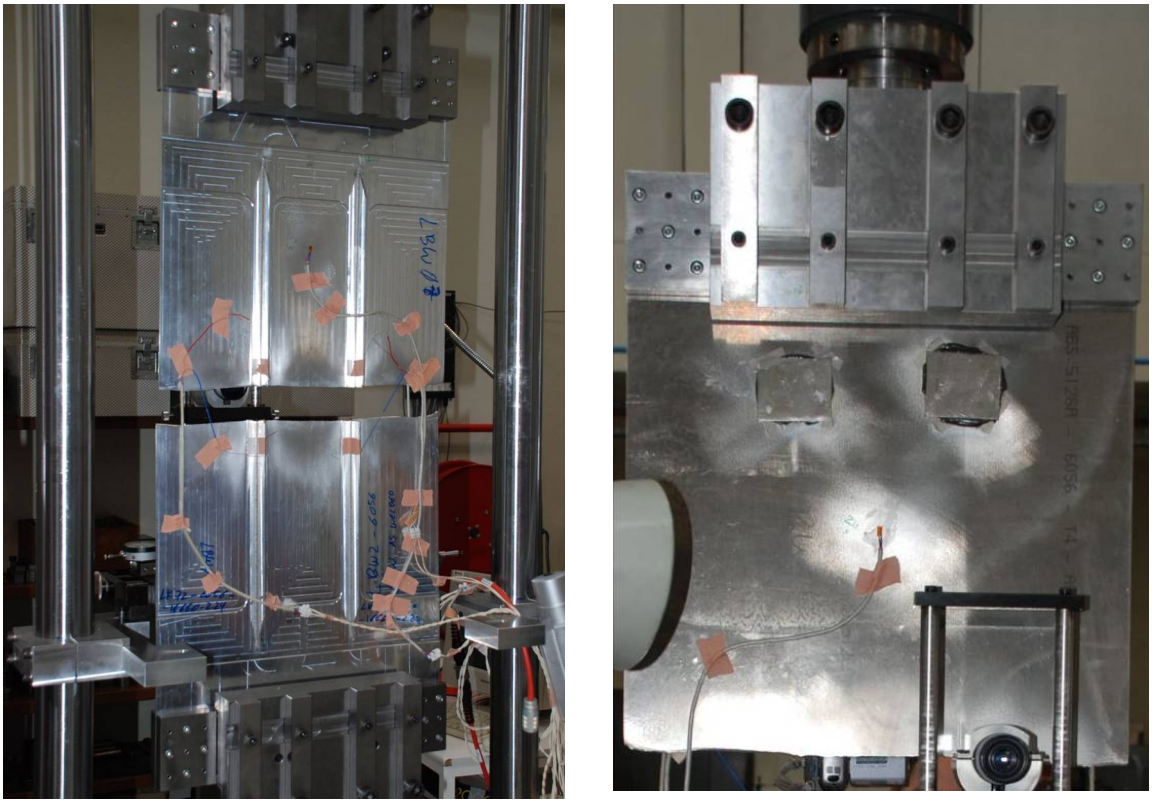

a) back side b) front side

**Figure 353 - Fatigue cracked specimen.**

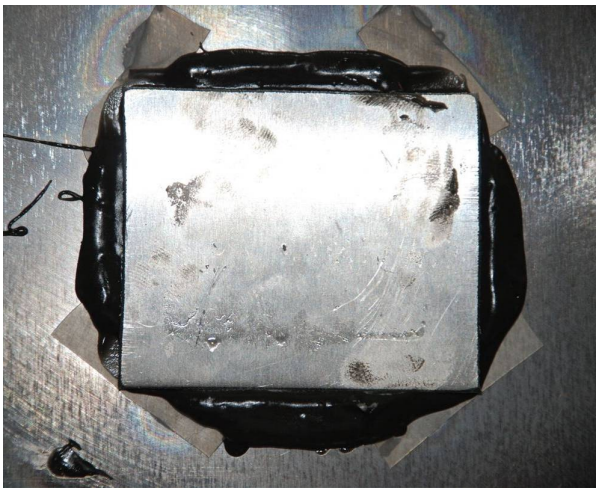

**Figure 354 - Detail of an adhesive patch.**

A detail of the crack just crossing through the stiffeners is presented in Figure 355. Also, the photographic history of a crack breaking a stiffener is presented in Figure 356.

The fatigue crack has propagated at the specimen middle line, as can be seen in Figure 357. In this figure the strain gage placed in the plate front side, just opposite to the stiffener, was broken at its middle line by the fatigue crack. Also a short deviation in the crack path is seen before reaching the stiffener; after breaking the stiffener the path is dependent upon the crack location in the other stiffener.

**Figure 355 - Fatigue crack just outside the stiffeners.**

**Figure 356 - Fatigue crack propagating at the stiffener.**

**Figure 357 - Fatigue crack crossing the strain gage opposite to the stiffener.**

*6.2.3.6.2 Stress distribution during the fatigue crack growth test*

Fatigue crack propagation tests were carried out and strain was measured in order to understand the different load transfer stages.
The strain gages values were measured in periodic stops of the fatigue test at the maximum fatigue load (95,96$kN$). The stress distribution on the stiffened panel during the fatigue test is presented in Figure 358.

The strain gage C4, which was placed at the right side stiffener, worked until 10000 cycles and the strain gage at the left side stiffener worked until 80000 cycles. Nevertheless, as the crack grows C2 shows the increase in stress at the stiffener. Gages C7 and C9 also present the load increase in the stiffener as a function of the crack size. When the fatigue crack is almost with its maximum size, C3 and C8 which are placed at the specimen half width, show a decrease in stress because the load is now being transferred by the remaining connected section

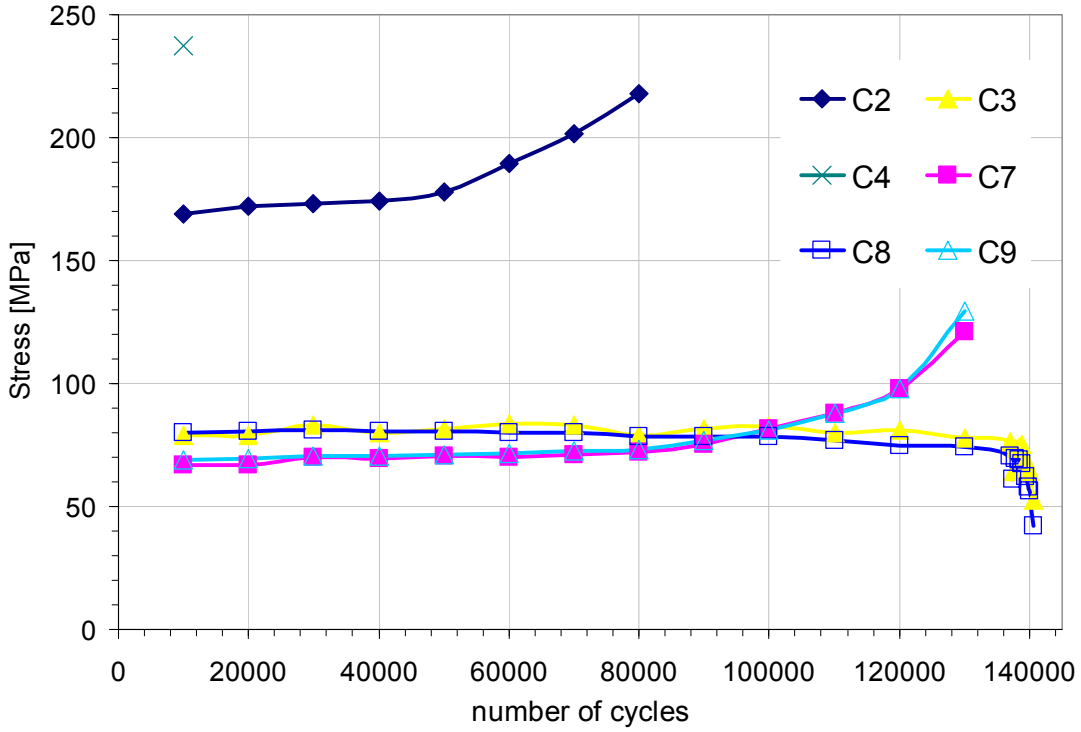


**Figure 358 - Stress distribution during the fatigue crack growth test, LBW2 6056 as-welded $\sigma_{max}$=80*MPa* R=0,1.**

*6.2.3.6.4 a-N results*

The LBW2 6056-T6 as-welded specimen, tested at a maximum stress of 80*MPa* with R=0,1, had a fatigue life of 140747 cycles. The fatigue crack growth in the stiffened panel is presented in Figure 359. The crack started to grow through the stiffener at 137100 cycles, 97,4% of the total fatigue life.

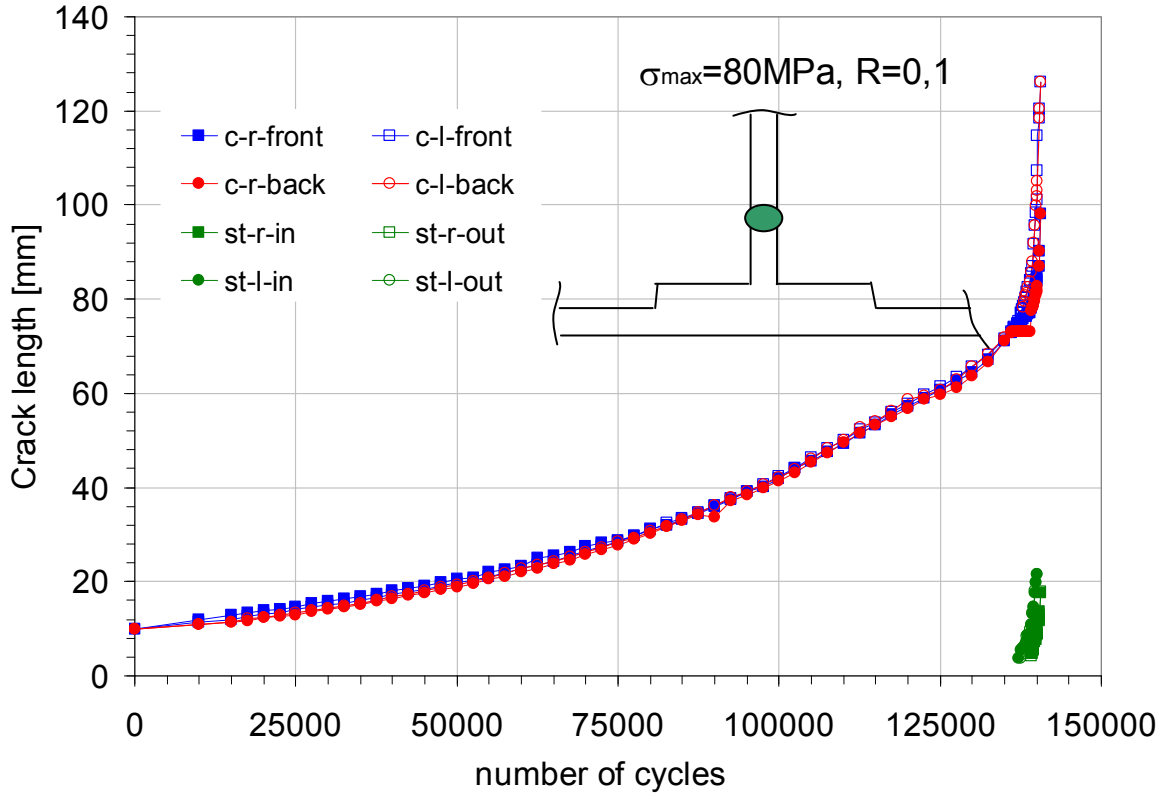


**Figure 359 - Fatigue crack growth test, LBW2 6056-T6 as-welded $\sigma_{max}$=80*MPa* R=0,1.**

*6.2.3.6.5 Results comparison*

A comparison between the fatigue crack lengths versus the number of cycles for the LBW1 6056 PWHT-T6 specimen, LBW2 6056 PWHT-T6 specimen and LBW2 6056-T6 as-welded specimen tested at R=0,1 is presented in Figure 360. It was found, that the LBW2 as-welded specimen presented the lower fatigue live when tested with the same parameters. For comparison, an initial fatigue crack of 24*mm* was considered in order to eliminate the influence of different EDM notches.

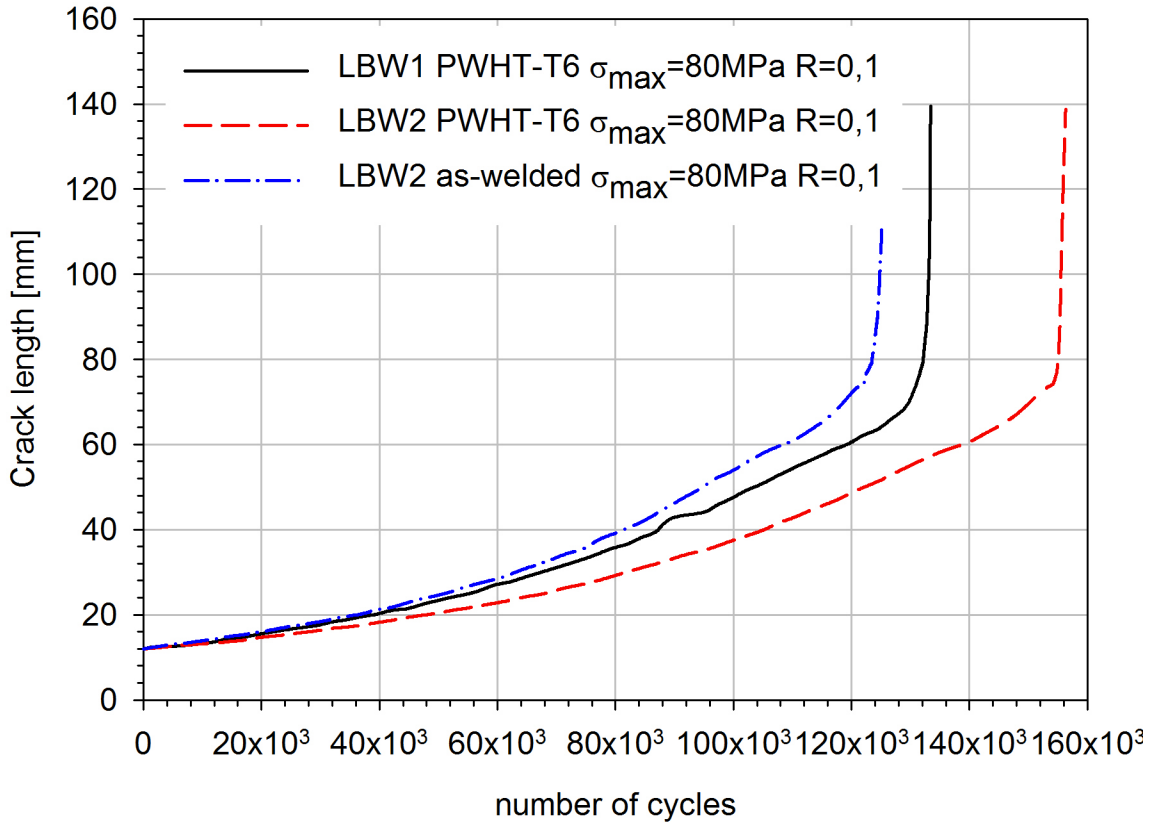


**Figure 360 - Comparison of a-N LBW1 6056 PWHT-T6/LBW2 6056 PWHT-T6/LBW2 6056-T6 as-welded, R=0,1.**

*6.2.3.7 Fatigue crack growth test LBW2 6056-T6 as-welded $\sigma_{max}$=110MPa R=0,5 (LBW08)*

A stiffened panel in the LBW2 configuration was fatigue tested at a maximum remote stress of 110*MPa* with R=0,5. This panel was fabricated in aluminium 6056-T6 and tested, after welding, in the as-welded configuration. Fatigue crack propagation tests were carried out and crack length was measured at periodic stops of the fatigue test.

*6.2.3.7.1 Weldments details*

Defects at the end and beginning of the weldment were identified. Again these defects were eliminated prior to testing but instead of only removing the defected material a smoothed angle (30º) was machined. Finally the surface was smoothed by hand polishing. Square patches were place at the opposite side of each stiffener end.

*6.2.3.7.2 Test details*

Smoothing the stiffeners (Figure 361) and the patching procedure were beneficial and no secondary cracks were observed during the entire test.

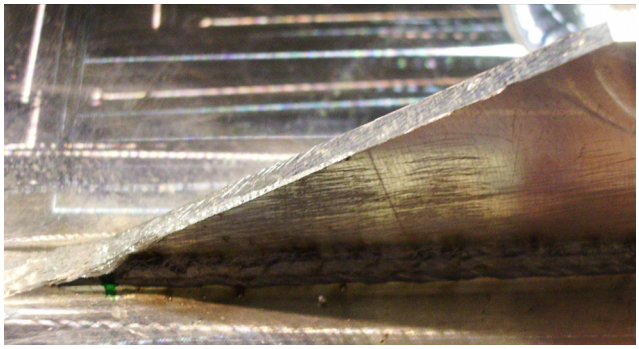

**Figure 361 - Smoothed stiffener.**

The fatigue crack has propagated at the specimen horizontal middle line as can be seen in Figure 362.

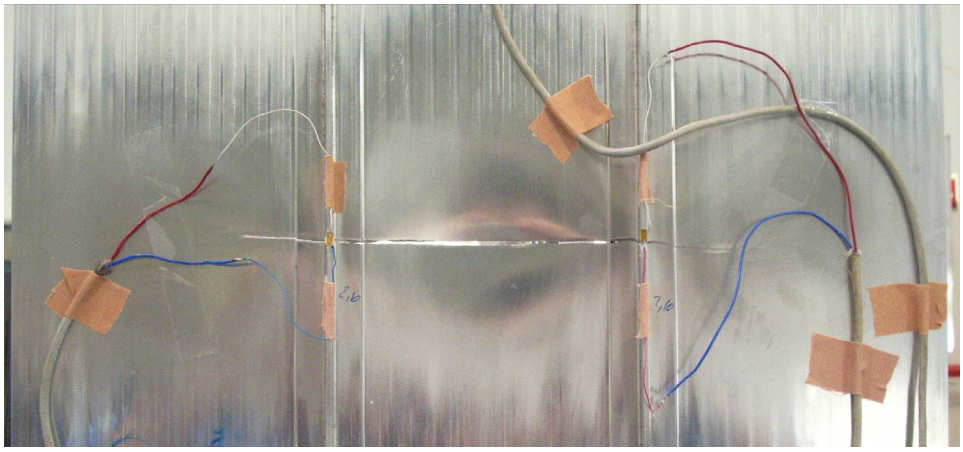

**Figure 362 - Fatigue crack just outside the stiffeners.**

*6.2.3.7.3 Stress distribution during the fatigue crack growth test*

Fatigue crack propagation tests were carried out and strain was measured in order to understand the different load transfer stages.
The strain gages values were measured in periodic stops of the fatigue test at the maximum fatigue load ($119{,}95kN$). The stress distribution on the stiffened panel during the fatigue test is presented in Figure 363.
All strain gages survived the entire test. Near 100000 cycles cracks were at $45mm$ from the stiffeners; it corresponded to the moment where the load increased at the stiffeners top side and decreased in the plate front side in the stiffeners location. This increase was more pronounced when the crack was at $10mm$ from the stiffeners. It continued to increase until the stiffeners were broken. At the specimen vertical middle plane, the crack remained almost constant during the test.

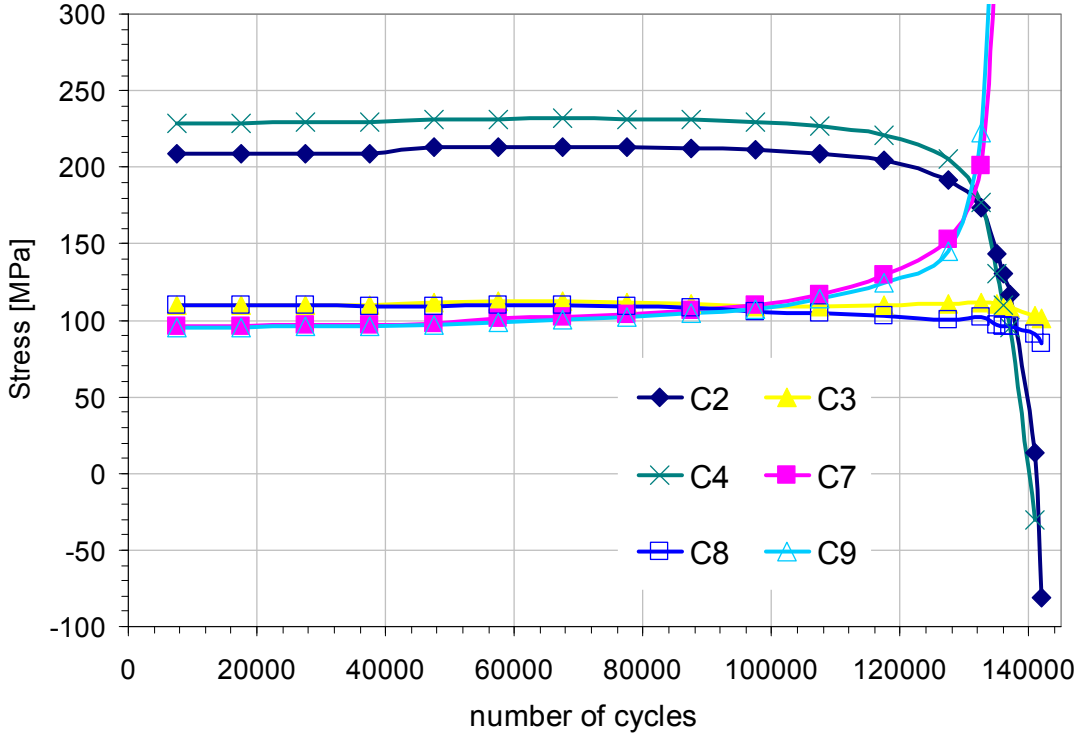


**Figure 363 - Stress distribution during the fatigue crack growth test, LBW2 6056 as-welded $\sigma_{max}$=110*MPa* R=0,5.**

*6.2.3.7.4 a-N results*

The LBW2 6056-T6 as-welded specimen, tested at a maximum stress of 110*MPa* with R=0,5, had a fatigue life of 143059 cycles. The fatigue crack growth is presented in Figure 364. The crack started to grow through the stiffener near 140000 cycles, 97,9% of the total fatigue life.

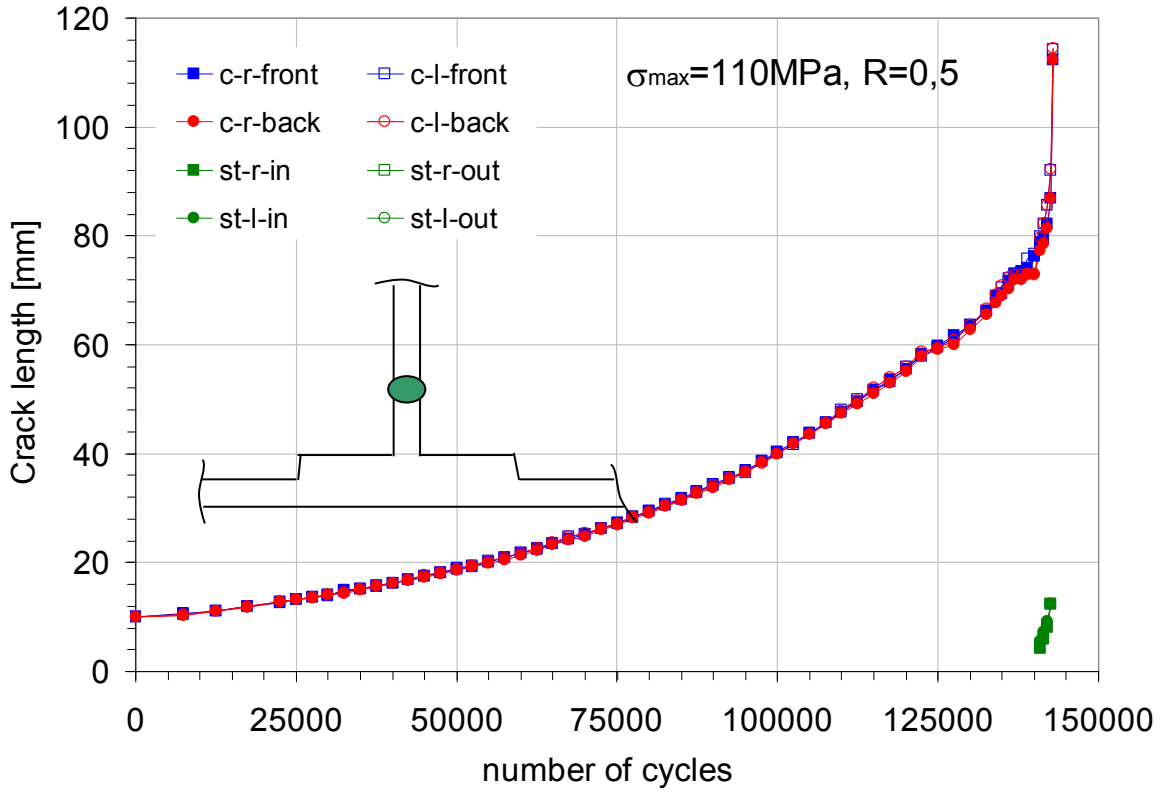


**Figure 364 - Fatigue crack growth test, LBW2 6056-T6 as-welded $\sigma_{max}$=110*MPa* R=0,5.**

### *6.2.4 Friction Stir Welding AA6056 2-stiffener panels*

Two stiffened friction stir welded panels of aluminium 6056 PWHT-T6 were fatigue tested: i) at a maximum stress of 80*MPa* with R=0,1; ii) and at a maximum stress of 110*MPa* with R=0,5. Panels were welded in the T4 condition, and after welding were tempered to achieve the T6 condition. The stress distributing for static and fatigue loading was recorded and the crack growth rate was also measured. An initial central notch with a length of 20*mm* and a width of 0,2*mm* was created by electro-discharging.
The geometry of the FSW panels was slightly different from the previous panels. The panels arrived at our laboratory with a total length of 700*mm*; the clamp device area was, by an error, cut off by the job shopper of EADS Corporate Research Center Ottobrunn, who supplied these panels. The new geometry is presented in Figure 365a). To solve this situation, steel extensions were manufactured. These clamping extensions consist of 3*mm* thick mild steel cover sheets with 3*mm* interlayer, Figure 365b). Since the behaviour during testing might differ from the previous tested panels (HSM and LBW) the strain gage measurements must be compared.

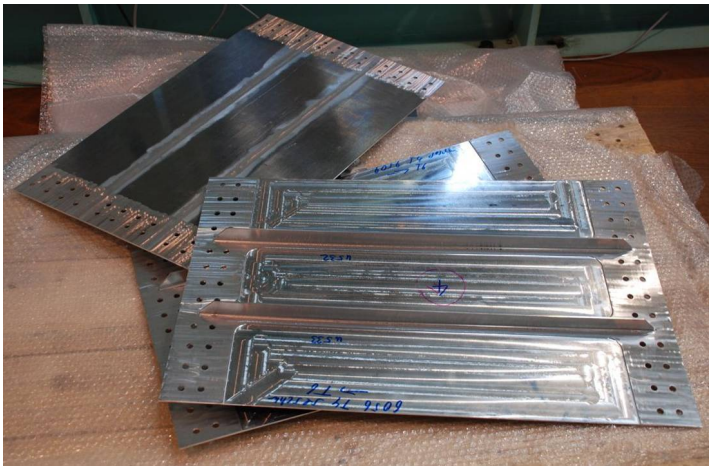

a) FSW panels geometry

b) manufactured clamping extensions

**Figure 365 - FSW panels geometry and correspondent clamping extensions.**

These panels presented the highest distortion when compared with the HSM and LBW panels as presented in Figure 366.

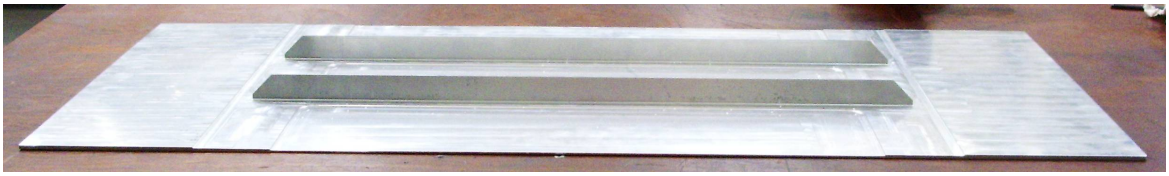

a) HSM panel (almost flat)

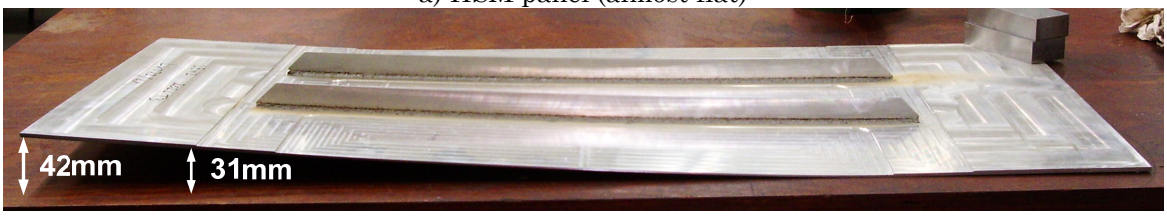


b) LBW panel

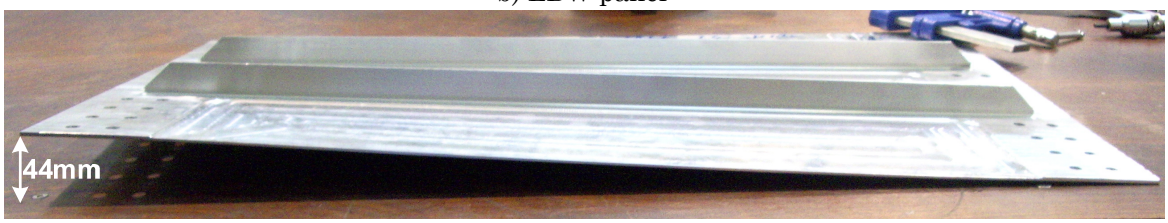


c) FSW panel

**Figure 366 - Distortion detail of the HSM, LBW and FSW panels.**

The grip assemblage used on the FSW specimens is presented in Figure 367.

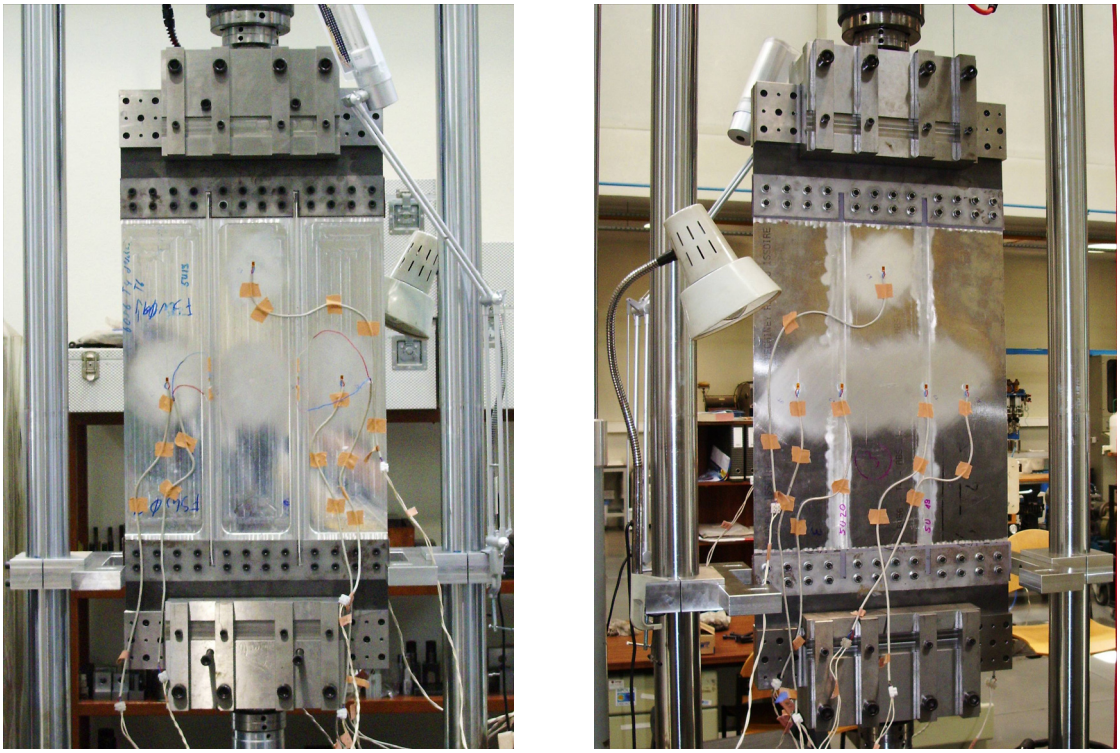

a) stiffeners side b) side opposite to the stiffeners

**Figure 367 - Testing machine FSW panel assemblage.**

The steel extensions assembled in the specimen are presented in Figure 368. Also in this figure is presented a detail of the specimen and the extensions assembled in the machine grip system.

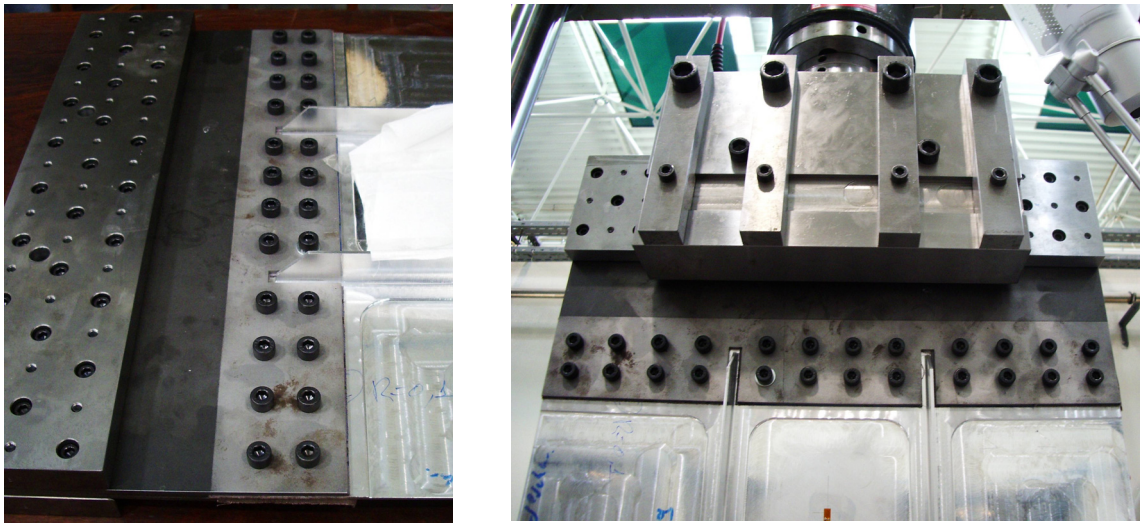

a) extensions detail b) specimen in the test machine

**Figure 368 - Details of specimen and extension assemblage.**

A detail of the strain gages used in specimen FSW09 (ten strain gages) are presented in Figure 369.

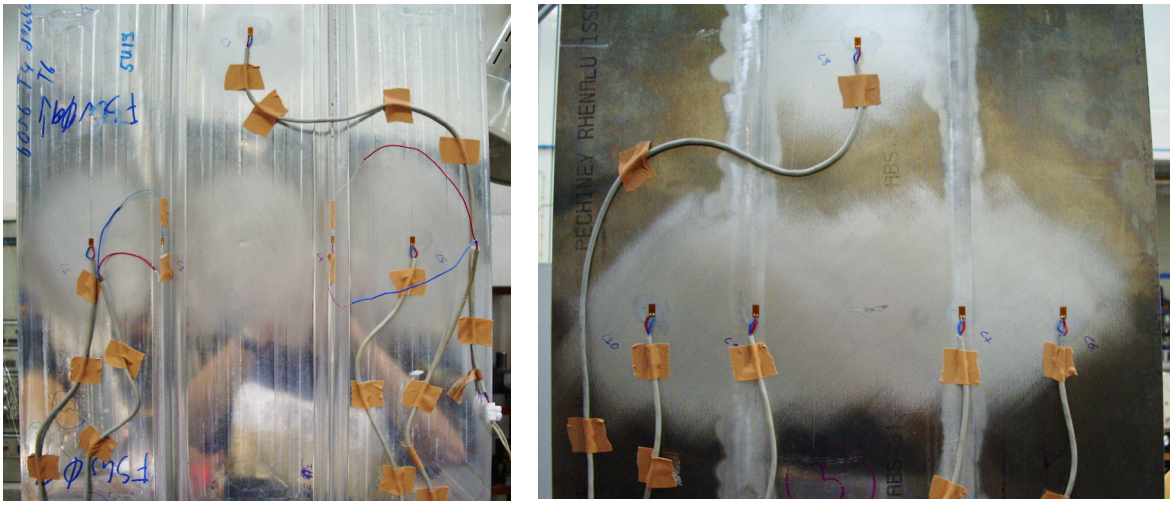

a) stiffener side b) side opposite to the stiffeners

**Figure 369 - Detail of specimen FSW09 instrumentation.**

*6.2.4.1 Stress distribution for different static remote loads*

Panels with a central crack (notch) of 20*mm* length were instrumented and loaded at five incremental loads to acquire the stress distribution in different sites of the specimen. The strain gages were distributed in the specimen according to the scheme presented in Figure 310.

*6.2.4.1.1 FSW 6056 PWHT-T6 specimen (FSW09 specimen)*

In this specimen were used 10 strain gages (C1 to C10), as presented in Figure 310. The results obtained are presented in Table 91 and Figure 370.

**Table 91 - Strain gages measurements function of the remote stress applied, specimen FSW09 6056 PWHT-T6 [*MPa*]**

| Remote stress | C1 | C2 | C3 | C4 | C5 | C6 | C7 | C8 | C9 | C10 |
|---|---|---|---|---|---|---|---|---|---|---|
| 20 | 25,6 | 41,2 | 24,9 | 51,2 | 28,1 | 4,5 | 19,7 | 22,5 | 20,8 | -0,5 |
| 40 | 43,7 | 68,3 | 44,2 | 84,2 | 48,4 | 22,3 | 38,3 | 43,1 | 38,9 | 14,0 |
| 60 | 62,3 | 93,2 | 63,6 | 111,2 | 67,3 | 41,0 | 56,9 | 63,4 | 57,4 | 31,8 |
| 80 | 80,9 | 117,2 | 82,8 | 136,4 | 86,0 | 59,8 | 75,6 | 83,5 | 76,0 | 50,1 |
| 100 | 99,8 | 140,5 | 102,3 | 160,7 | 104,8 | 78,8 | 94,6 | 103,6 | 94,9 | 68,6 |

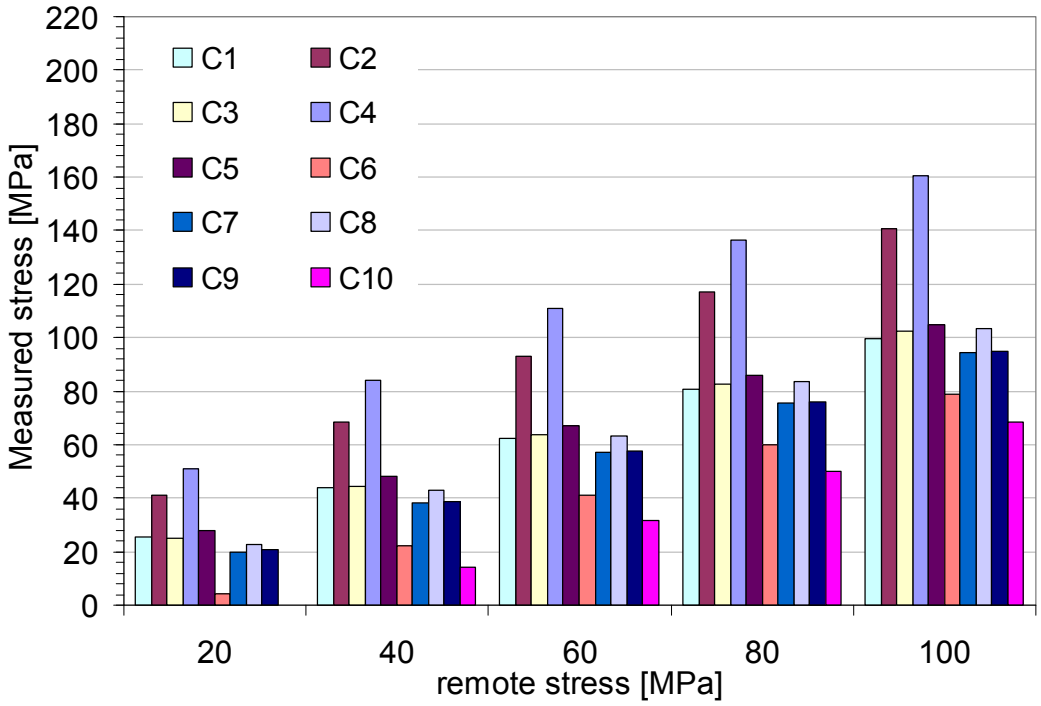


**Figure 370 - Stress distribution for different remote stress, specimen FSW09.**

For all remote loads the strain gage situated at the top of the stiffener (C4) measured the higher stress.

*6.2.4.1.2 FSW 6056 PWHT-T6 specimen (FSW10 specimen)*

In this specimen were used six strain gages (C2, C3, C4, C7, C8 and C9), as presented in Figure 310. The results obtained are presented in Table 92 and Figure 371.

**Table 92 - Strain gages measurements function of the remote stress applied, specimen FSW10 6056-T6 [*MPa*]**

| Remote stress | C2 | C3 | C4 | C7 | C8 | C9 |
|---|---|---|---|---|---|---|
| 20 | 35,8 | 23,7 | 50,8 | 19,3 | 22,2 | 20,0 |
| 40 | 60,1 | 43,1 | 82,5 | 37,9 | 43,1 | 38,4 |
| 60 | 83,3 | 62,4 | 108,9 | 56,7 | 63,6 | 56,9 |
| 80 | 105,7 | 81,6 | 133,9 | 75,6 | 84,1 | 75,7 |
| 100 | 127,8 | 101,7 | 158,1 | 94,5 | 104,4 | 94,5 |

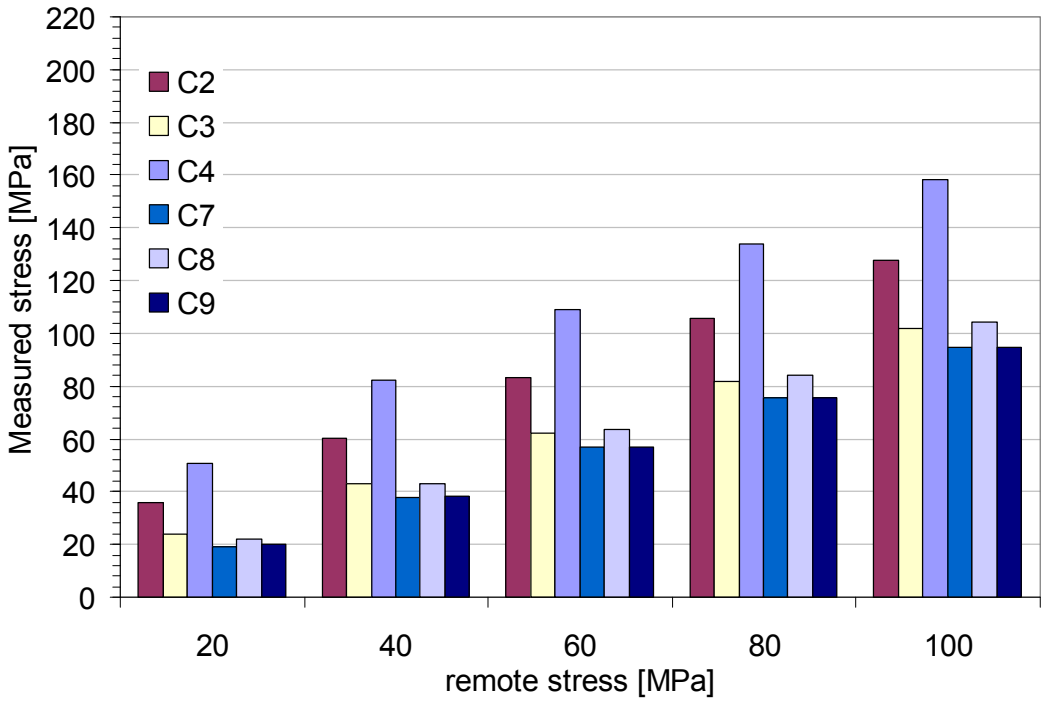


**Figure 371 - Stress distribution for different remote stress, specimen FSW10.**

*6.2.4.1.3 Comparison of static loading (specimens tested at R=0,1)*

The comparison of the static loading measured stresses for the HSM, LBW and FSW specimens is presented in Figure 372. The results are presented as a function of the panel width and at measurements performed for a remote stress of 100*MPa*. It was found that, despite the new clamping extensions, the load distribution on the FSW panel is similar to the one found in the LBW specimens.

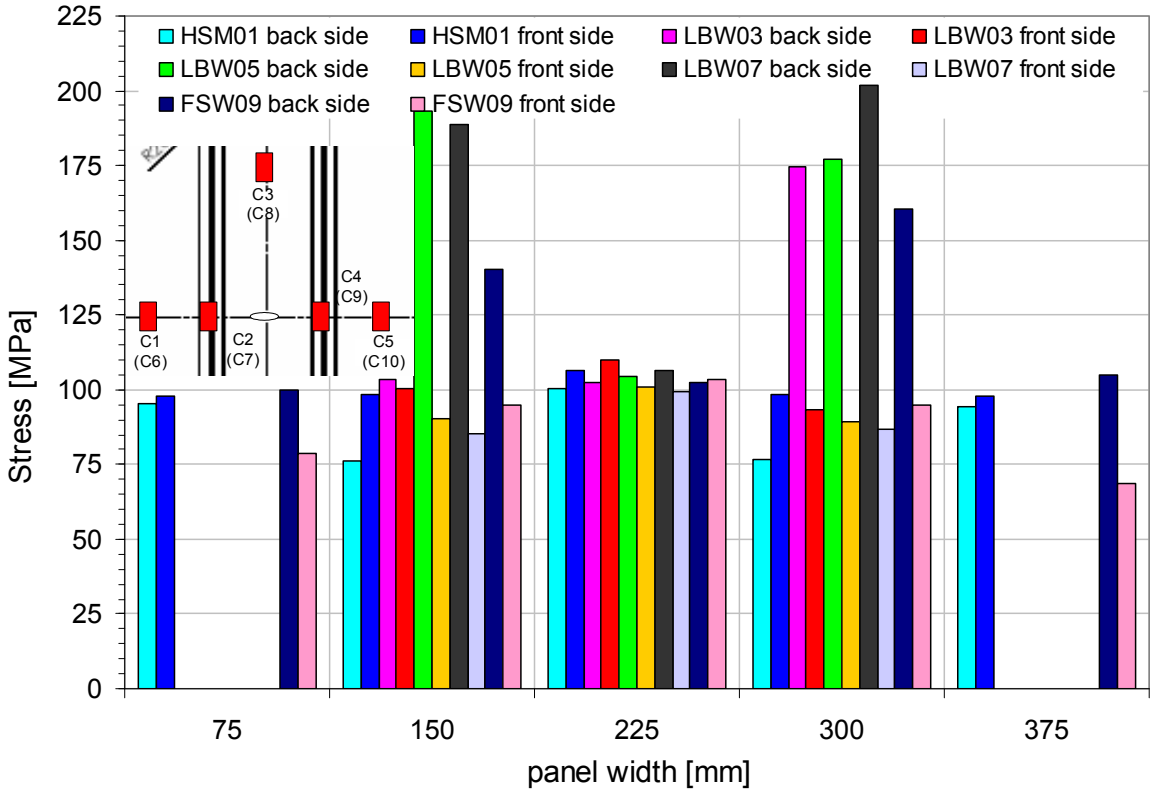


**Figure 372 - Comparison of static loading of HSM, LBW and FSW specimens.**

*6.2.4.2 Fatigue crack growth test FSW 6056 PWHT-T6 $\sigma_{max}$=80MPa R=0,1 (FSW09)*

A stiffened panel was fatigue tested at a maximum remote stress of 80*MPa* with R=0,1. Fatigue crack propagation tests were carried out and crack length was measured at periodic stops of the fatigue test.

*6.2.4.2.1 Test details*

In this specimen no secondary crack appeared throughout the test. The new grip system, with the steel extensions, protected the stiffeners' run-outs transition to the plate. A detail of the transition between the stiffener run-out to the plate is presented in Figure 373a). Since the specimen pocketing was machined after welding there are no discontinuities in the weldment. Figure 373a) shows a detail of the surface where the shoulder contacted the plate.

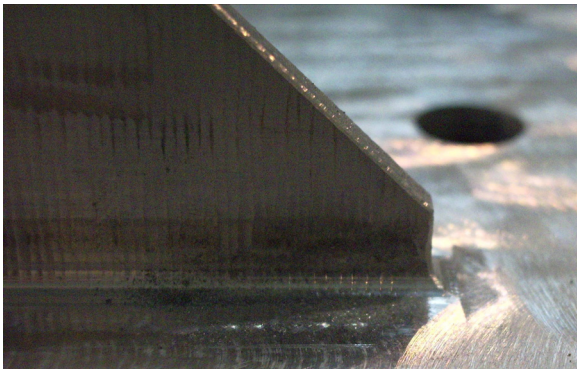

a) stiffener run-out

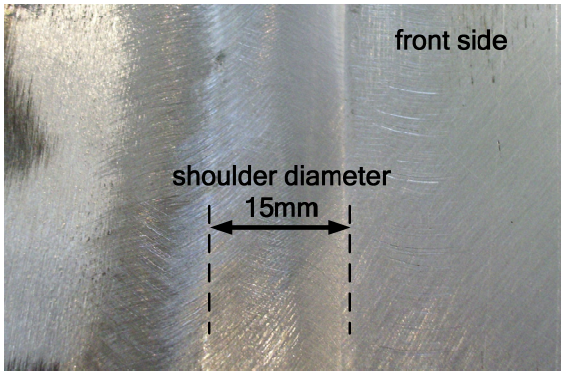


b) plate top surface after welding

**Figure 373 - Fatigue FSW specimen detail.**

The crack grew symmetrically during the test as shown in Figure 374a). At this stage, approximately 135000 cycles, the crack was crossing the stiffener in the front surface, presented in detail in Figure 374b).

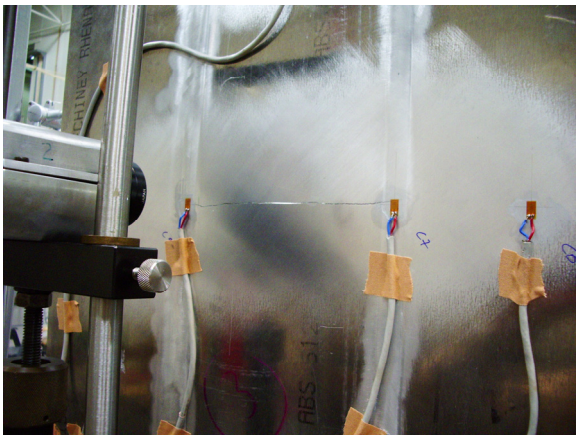

a) specimen front surface at 135000 cycles

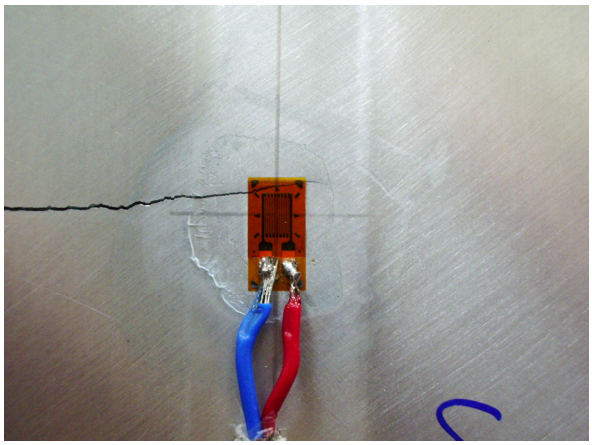

b) crack crossing a strain gage

**Figure 374 - Fatigue crack, specimen front surface at approximately 135000 cycles.**

Different stages of a crack developing in a stiffener are presented in Figure 375.

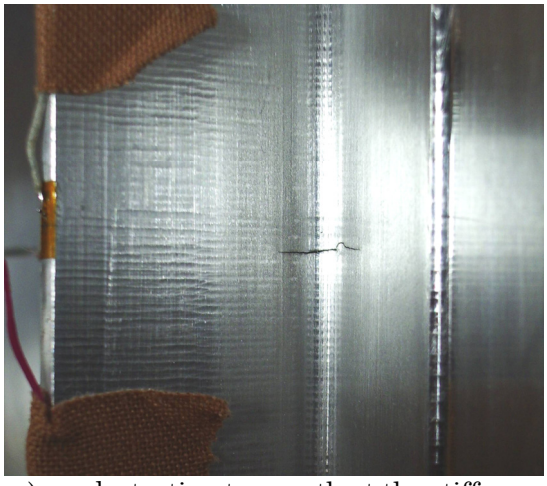

a) crack starting to growth at the stiffener outside surface

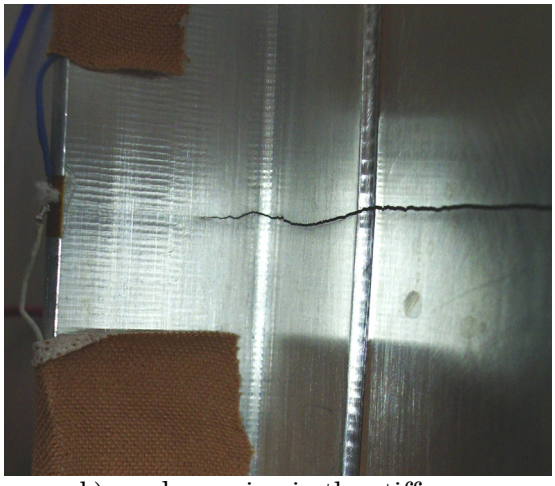

b) crack growing in the stiffener

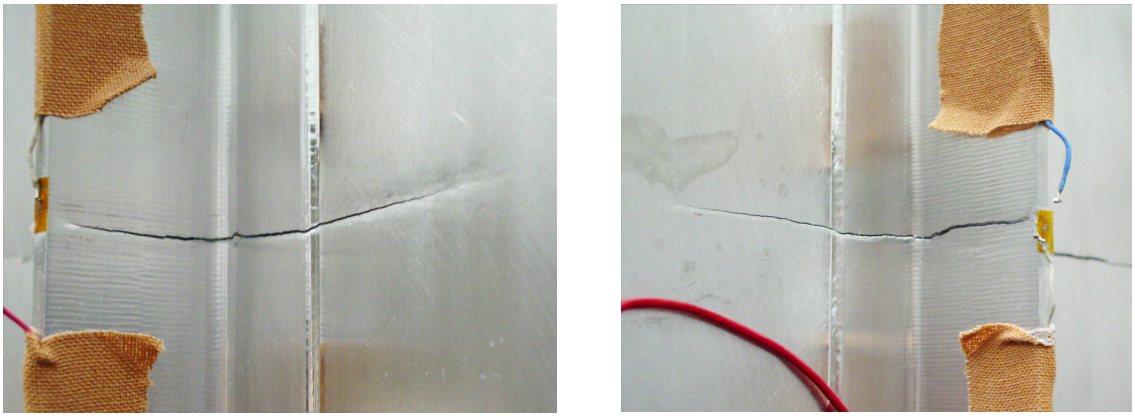

c) crack arriving at the top of the stiffener d) crack crossing the stiffener

**Figure 375 - Crack growing in a FSW specimen.**

The specimen back surface, after the fatigue crack break the stiffener, is presented in Figure 376a). The stiffeners were broken at 141200 cycles and after 200 cycles more the specimen was also broken, Figure 376b).

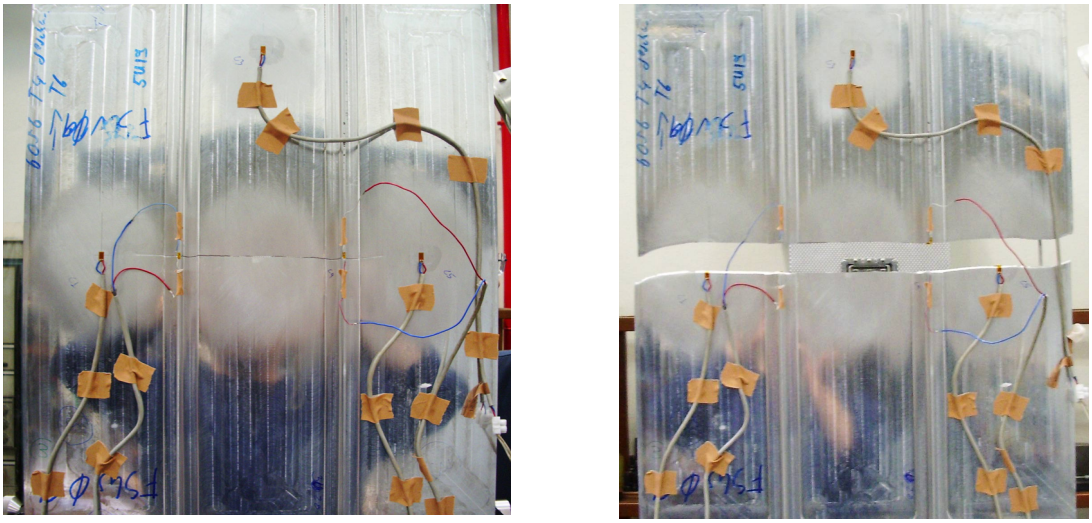

a) after breaking the stiffeners b) after breaking the specimen

**Figure 376 - Cracked specimen back surface.**

A detail of the crack surface weldment area (T-joint) is presented in Figure 377. By the visual analysis of the surface texture it is easily identified the area affected by the welding process.

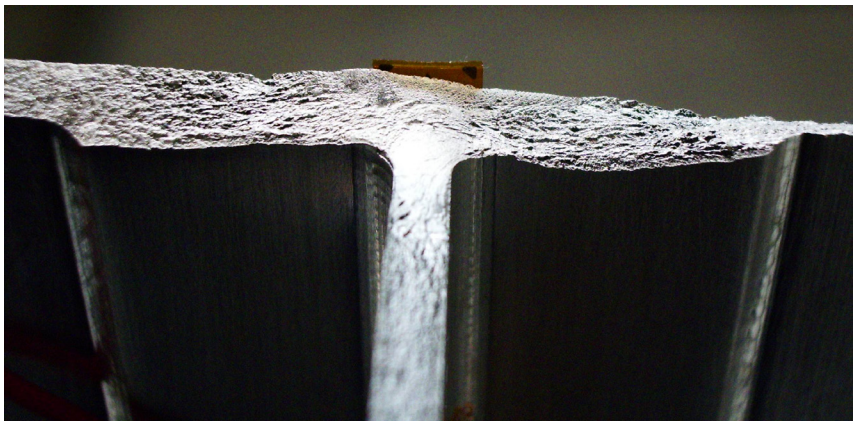

**Figure 377 - FSW T-joint crack surface detail.**

*6.2.4.2.2 Stress distribution during the fatigue crack growth test*

Fatigue crack propagation tests were carried out and strain was measured in order to understand the different load transfer stages.
The strain gages values were measured in periodic stops of the fatigue test at the maximum fatigue load (95,96$kN$). The stress distribution on the stiffened panel during the fatigue test is presented in Figure 378.
At approximately 123000 cycles cracks were at 21$mm$ from the stiffeners and at the stiffeners the load increased in its top side and decreased in the plate front side in the stiffeners location. At the specimen vertical middle plane the load remained almost constant until the stiffeners were fractured.

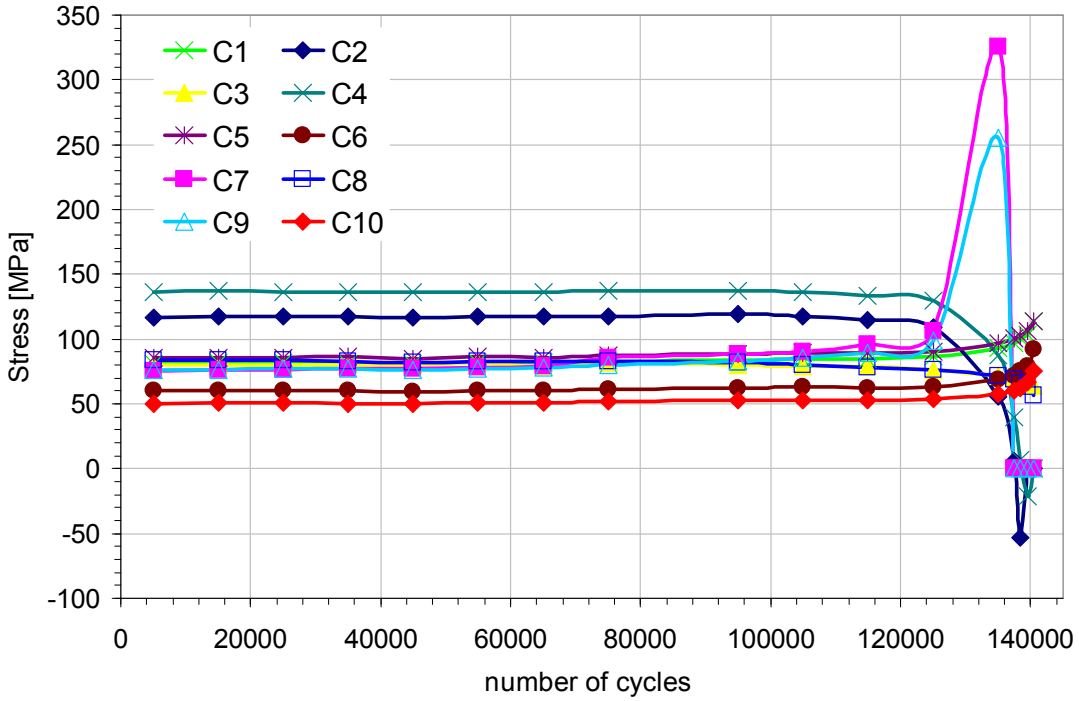


**Figure 378 - Stress distribution during the fatigue crack growth test, FSW 6056 PWHT-T6 $\sigma_{max}$=80$MPa$ R=0,1.**

*6.2.4.2.3 a-N results*

The FSW 6056 PWHT-T6 specimen, tested at a maximum stress of 80*MPa* with R=0,1, had a fatigue life of 141400 cycles. The fatigue crack growth in the stiffened panel during the fatigue test is presented in Figure 379. The crack started to grow through the stiffener near 135000 cycles, 95,6% of the total fatigue life.

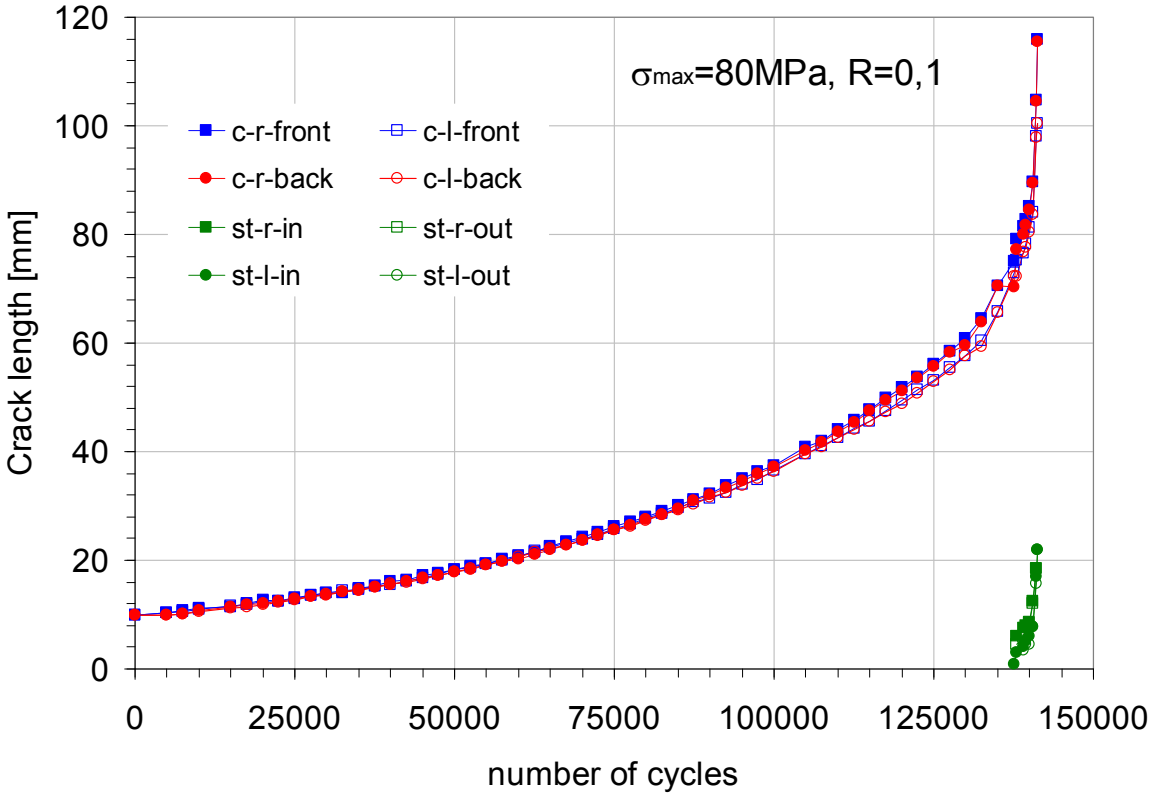


**Figure 379 - Fatigue crack growth test, FSW 6056 PWHT-T6 $\sigma_{max}$=80*MPa* R=0,1.**

*6.2.4.3 Fatigue crack growth test FSW 6056 PWHT-T6 $\sigma_{max}$=110MPa R=0,5 (FSW10)*

A stiffened panel was fatigue tested at a maximum remote stress of 110*MPa* with R=0,5. Fatigue crack propagation tests were carried out and crack length was measured at periodic stops of the fatigue test.

*6.2.4.3.1 Test details*

Again, in this specimen no secondary crack appeared throughout the test. The specimen assembled with the steel extensions is presented in Figure 380.

**Figure 380 - FSW10 specimen.**

A detail of the specimen assembled in the test machine is presented in Figure 381.

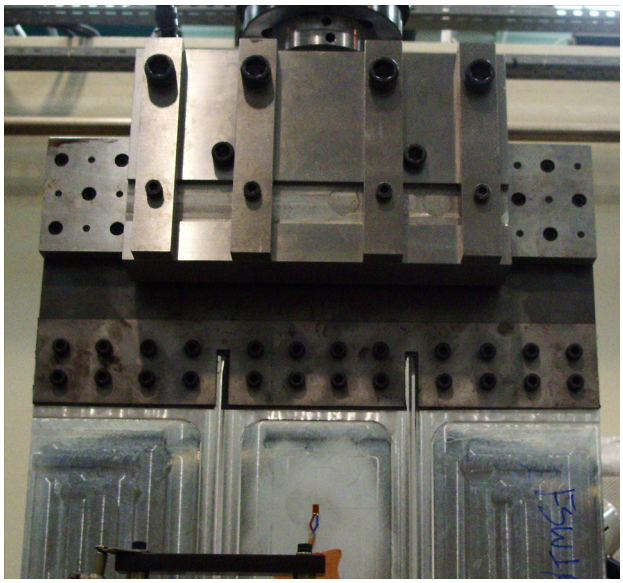

a) view of the side of the panel that contains the stiffeners

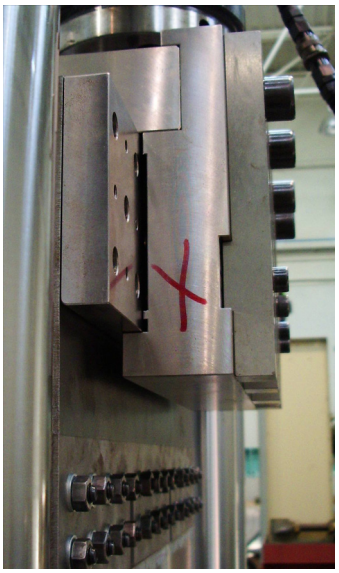

b) plate top surface after welding

**Figure 381 - Grip system details.**

The crack grew symmetrically during the test. A detail of the crack reaching the zone affected by heat during welding (TMAZ) is presented in Figure 382. It was observed that the crack changes its growing path in this area.

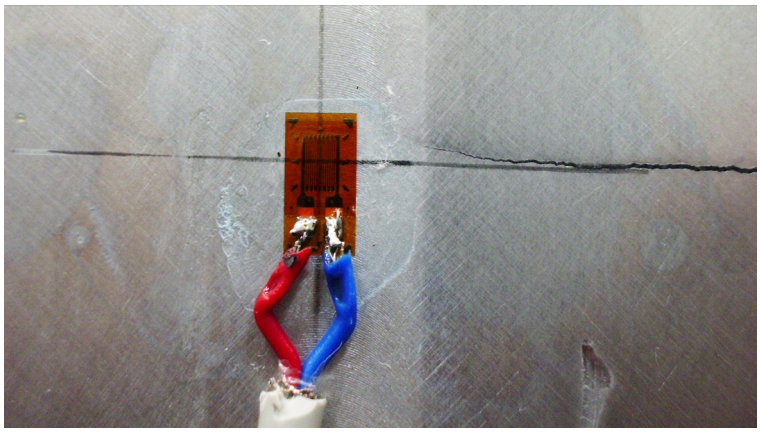

**Figure 382 - Crack reaching the TMAZ.**

A detailed, step by step, presentation of a crack crossing a stiffener is presented in Figure 383.

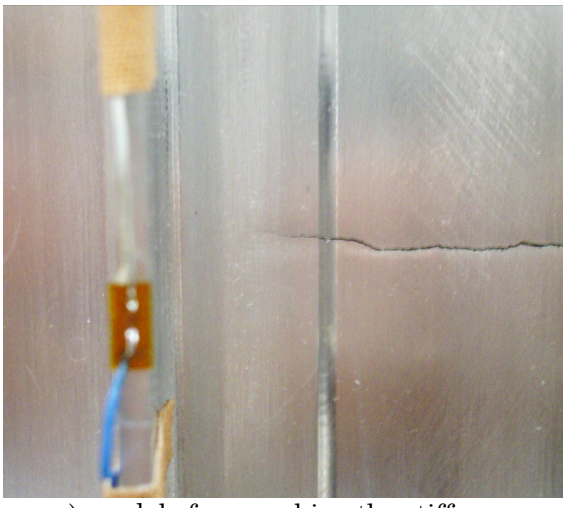

a) crack before reaching the stiffener

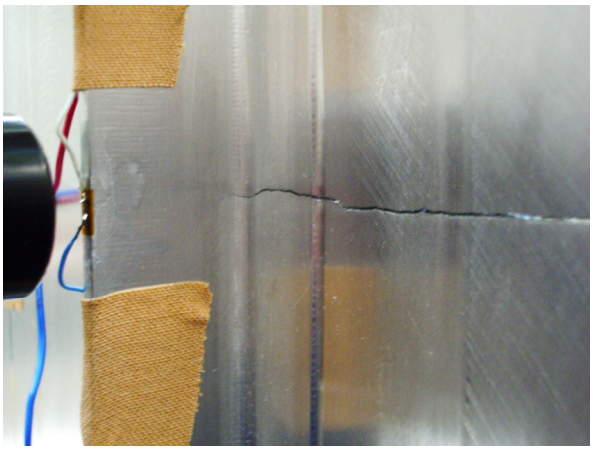

b) crack starting to grow in the stiffener

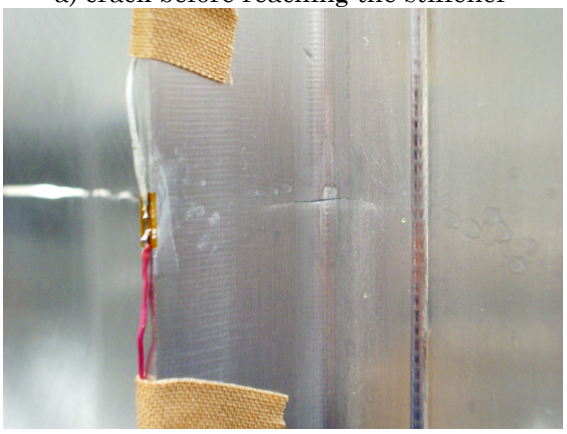

c) crack crossing the stiffener root

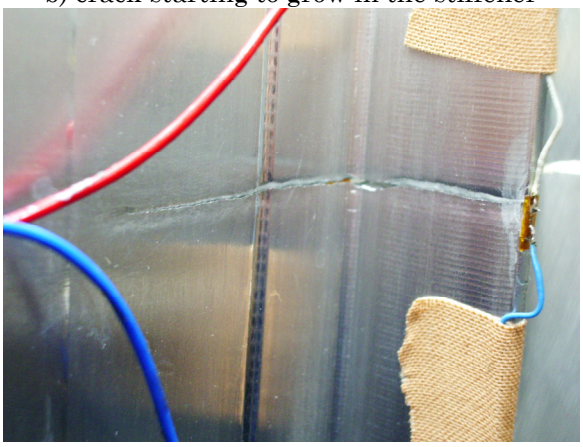

d) broken stiffener

**Figure 383 - Fatigue crack crossing a stiffener, different stages.**

The fatigue crack surface near the central notch and in a broken stiffener root is presented in Figure 384.

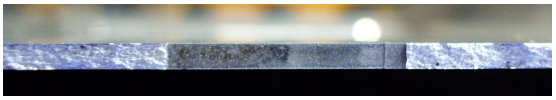

a) EDM central notch

b) root of a broken stiffener

**Figure 384 - Fatigue crack details, central notch and root of broken stiffener.**

*6.2.4.3.2 Stress distribution during the fatigue crack growth test*

Fatigue crack propagation tests were carried out and strain was measured in order to understand the different load transfer stages.
The strain gages values were measured in periodic stops of the fatigue test at the maximum fatigue load (119,95*kN*). The stress distribution on the stiffened panel during the fatigue test is presented in Figure 385.

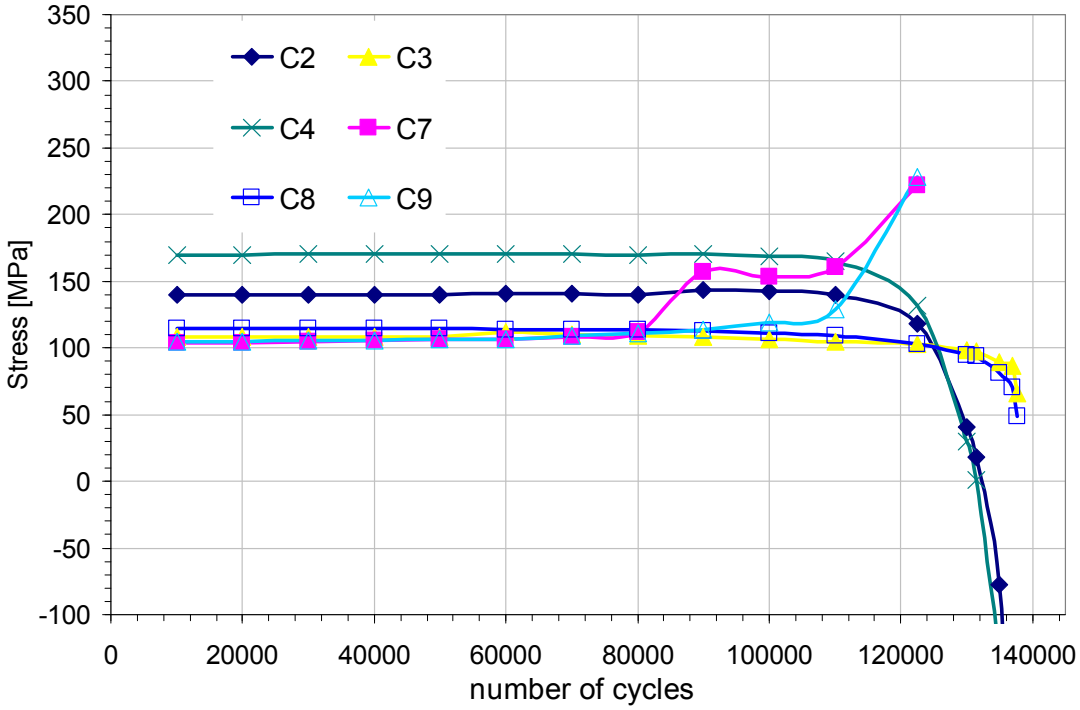


**Figure 385 - Stress distribution during the fatigue crack growth test, FSW10 6056 PWHT-T6 $\sigma_{max}$=110*MPa* R=0,5.**

*6.2.3.3.3 a-N results*

The FSW 6056 PWHT-T6 specimen, tested at a maximum stress of 110*MPa* with R=0,5, had a fatigue life of 137930 cycles. The fatigue crack growth in the stiffened panel during the fatigue test is presented in Figure 386. The crack started to grow through the stiffener near 133000 cycles, 96,4% of the total fatigue life.

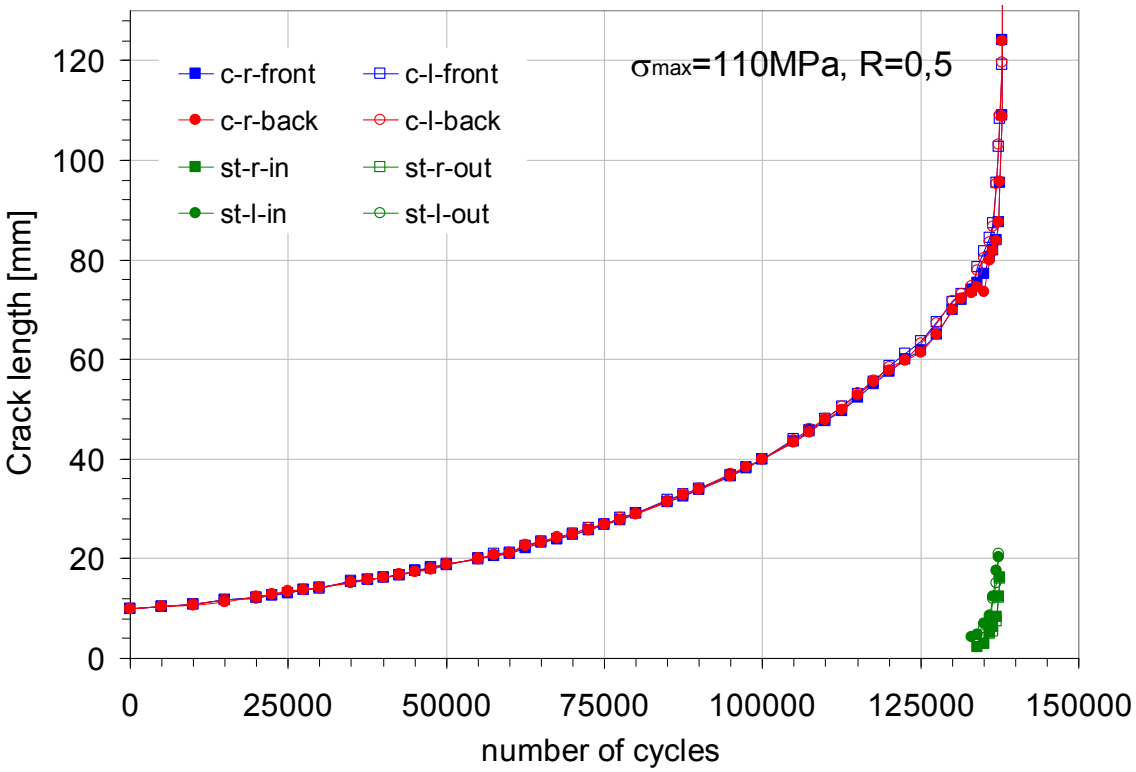


**Figure 386 - Fatigue crack growth test, FSW 6056 PWHT-T6 as-welded $\sigma_{max}$=110*MPa* R=0,5.**

### *6.2.5 Results discussion*

The crack length measurements at the stiffeners location was somehow difficult to execute. A solution was found using a photographic camera which permitted crack growth reconstitution. In all specimens the crack grew symmetrically at both sides, as shown by the plots of the crack size at both sides and both surfaces of the stiffener. This feature validates the geometry of the grip system developed for these tests.

An analysis of the residual stress field presented in each type of specimen was performed by X-ray diffraction methods in the University of Coimbra. Unfortunately, as mentioned in the study presented in Chapter 3, this technique was found not suitable for such material. As an example of the results obtained, Figure 387 presents the residual stress profile in the surface opposite to the stiffeners for a LBW2 PWHT-T6 specimen. The data points measured present a large scatter, and the distribution presents no discernible trend.

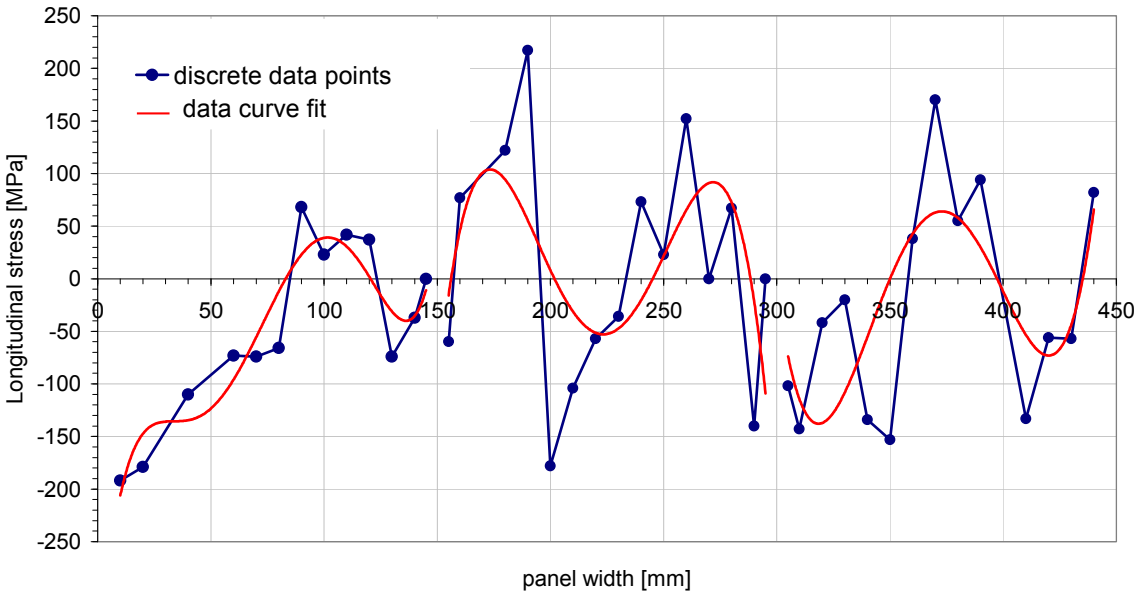


**Figure 387 - Residual stress profile in the surface opposite to the stiffeners for a LBW2 PWHT-T6 specimen (stiffeners located at 150*mm* and 300*mm*).**

A comparison of the specimens tested with R=0,1 and R=0,5 (HSM, LBW1 PWHT-T6, LBW2 (as-welded and PWHT-T6) and FSW PWHT-T6) are presented in Figure 388 and Figure 389, respectively. For both values of R, the HSM specimen presented the lower fatigue lives. At the opposite, the PWHT-T6 specimens tested in the LBW2 configuration (butt joint) presented the higher fatigue lives for both R ratios.

The FSW specimen tested at R=0,1 presented a fatigue life similar to the LBW2 as-welded specimen. For R=0,5 the FSW specimen performed higher than the LBW1 PWHT-T6 specimen and lower than the LBW2 as-welded specimen.

In all specimens tested it was found that the crack arrest feature (decrease of crack growth rate) introduced by the stiffener was not significative, probably due to the low width of these specimens. Nevertheless when the stiffeners is fractured the remaining life of the specimen is marginal.

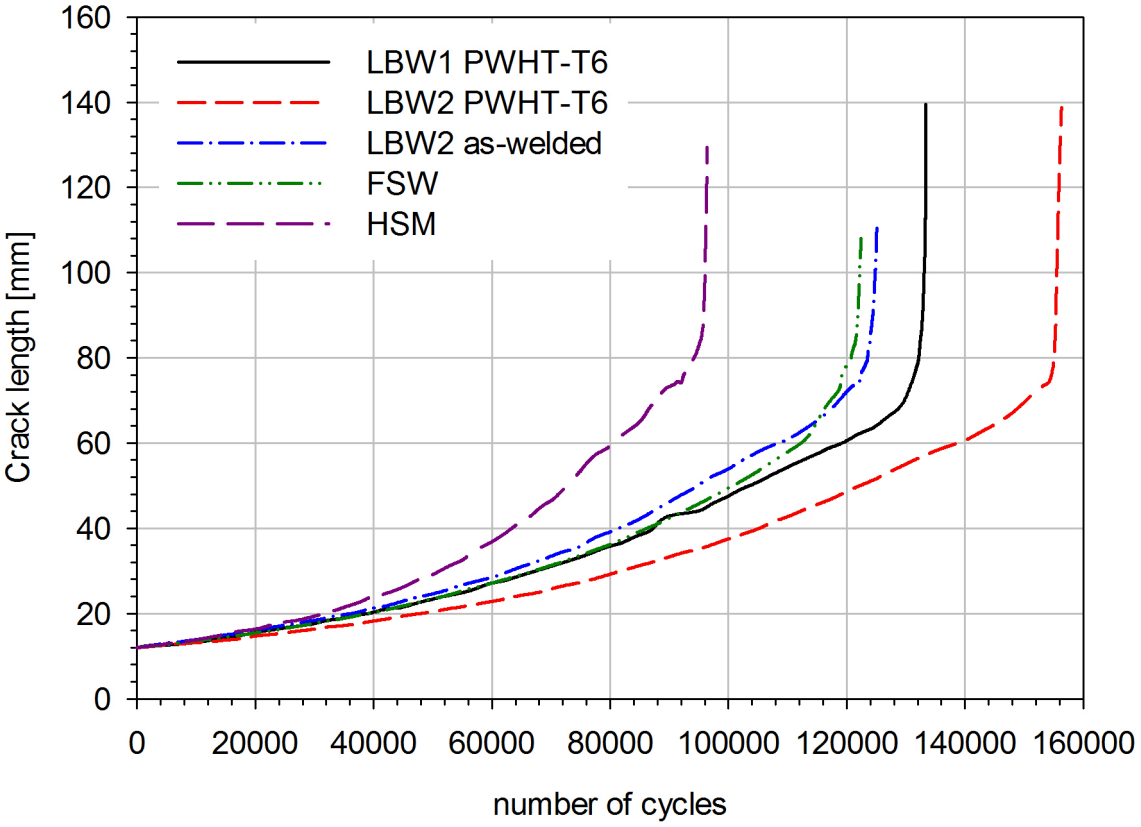


**Figure 388 - Comparison of a-N for all specimens tested at R=0,1.**

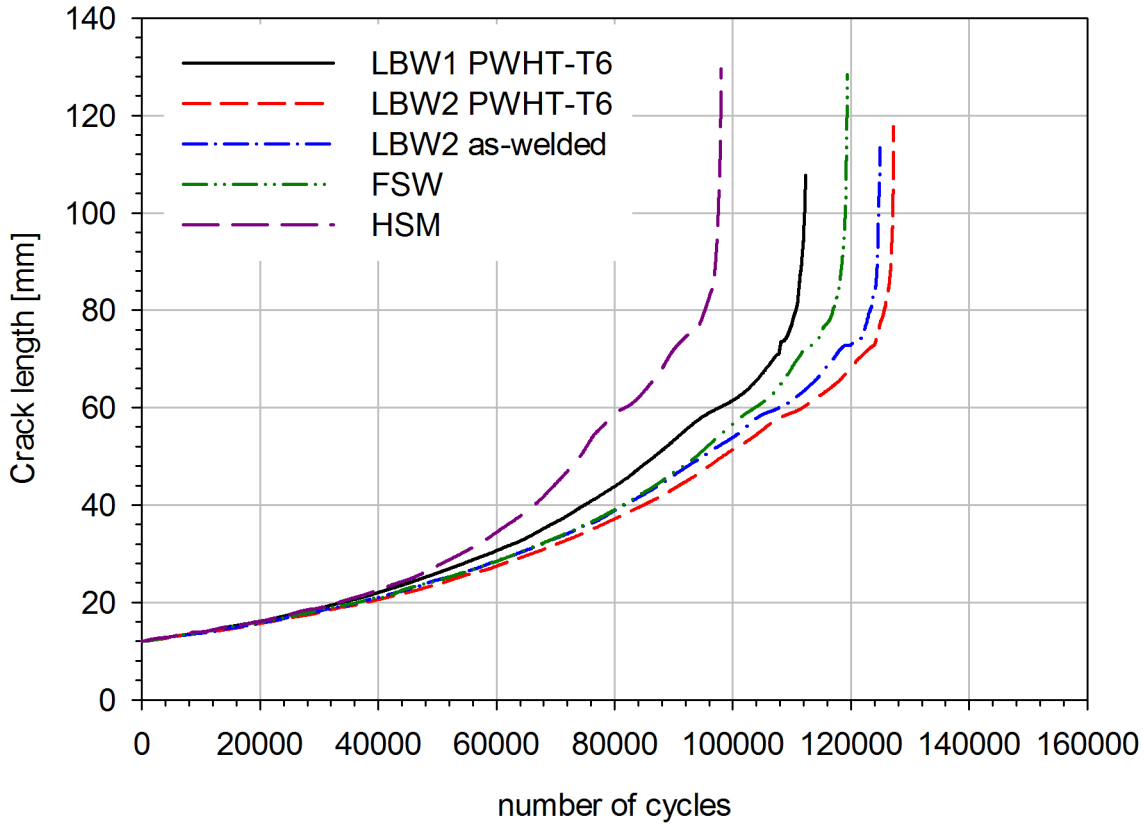


**Figure 389 - Comparison of a-N for all specimens tested at R=0,5.**

In a test of a multi-stiffener panel performed by AIRBUS [197] it was verified that there was a marked slow-down of crack growth rate as the crack reaches the stiffeners. But on the tests of the two stiffeners panels this phenomenon was not identified. This difference can be attributed to the relatively light stiffeners used in the DaToN panels when compared with the AIRBUS panel. These observations emphasise the need for further research studying the behaviour of stiffened panels with other ratios of stiffener to skin cross sections. Also, the number of stiffeners per panel, and the location of the initial crack (between stiffeners, or broken stiffeners) should be considered.

### *6.2.6 Crack growth prediction*

The stress intensity factor calibration of the DaToN stiffened panel geometry was obtained using the VCCT (virtual crack closure technique) in conjunction with the finite element model presented in Figure 263. The non-dimensional SIF as a function of the crack length is presented in Figure 390, where the local decrease of the SIF value in the stiffener region is identified.

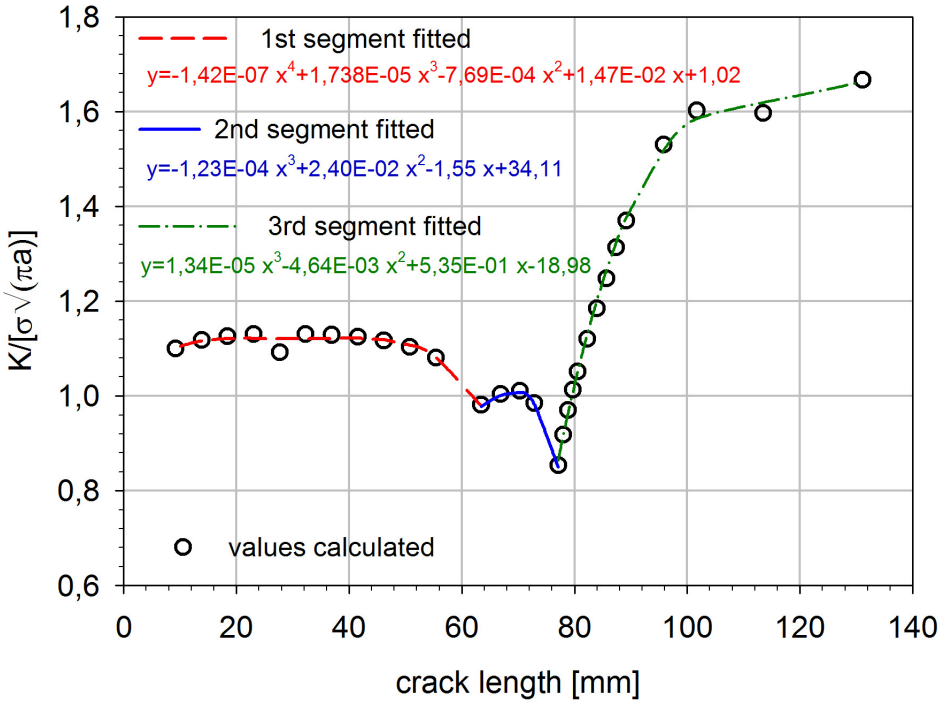


**Figure 390 - Stress intensity factor calibration for the DaToN panels' geometry.**

Using an algorithm in MAPLE that integrates the Paris law equation and takes into account the stress intensity factor curve fit presented in Figure 390, the number of cycles as a function of crack length was calculated, Figure 391. The SIF distribution of Figure 390 corresponds to the maximum value for each crack length. A more detailed analysis taking into account SIF variation along the thickness, as presented in Chapter 5, was not pursued, since the present approximation proved acceptable, and further improvement in modelling depends firstly in residual stresses. The results of this modelling exercise were compared

with the experimental measurements of the two HSM panels. The panels were tested at $\sigma_{max}$=80*MPa* R=0,1 and $\sigma_{max}$=110*MPa* R=0,5. The Paris law parameters used, see Table 93, were already presented in section 6.2.1.

**Table 93 - C and m Paris law parameters for the AA6056 material from the HSM panels**

| $\left[\frac{N \cdot mm^{-1,5}}{mm / cycle}\right]$ | material from the HSM panel AA6056-T651 | |
|---|---|---|
| | R=0,1 | R=0,5 |
| C | 2,32E-12 | 9,98E-10 |
| m | 2,92 | 2,06 |

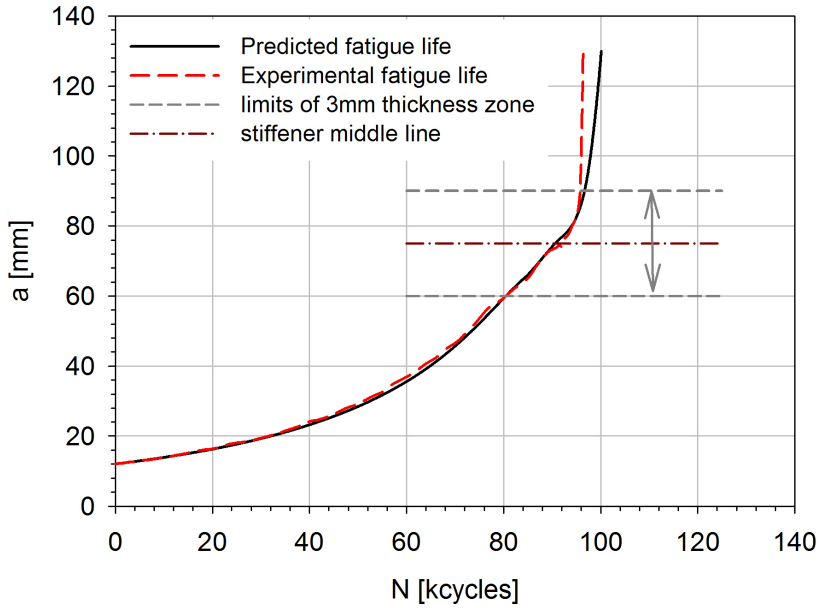


a) HSM panel tested with $\sigma_{max}$=80*MPa* and R=0,1

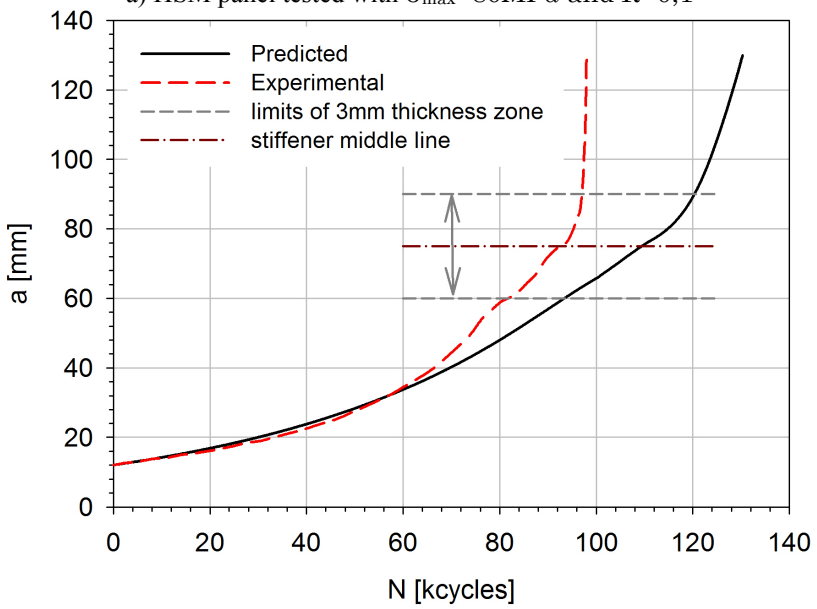


b) HSM panel tested $\sigma_{max}$=110*MPa* and R=0,5

**Figure 391 - Comparison between predicted and experimental fatigue life for HSM panels.**

For both test levels a good agreement between the predicted fatigue life and the experimental measurements was found. For the case of R=0,5 the predicted fatigue life was found to be slightly higher than the experimental measurements at a crack length a=60$mm$, and approximately 30% higher when critical crack length was reached. This difference can be due to the complex test setup used for experimental tests and to the simplified numerical model. It is to be noted that a difference of 20% in fatigue life is of the order of the scatter found when testing similar DaToN panels under similar loading conditions, [198].

Finally the crack growth in the modelled stiffened panels was compared with crack growth in unstiffened panels in two different cases, Figure 392. Figure 392. In a first case a panel without stiffeners with cross section α identical to the DaToN stiffened panel cross section area was used. So, in this case the remote stress applied in the stiffened and in the unstiffened panels is identical. The remote load transmitted by the stiffened or by the unstiffened panel is the same.
In the second case, an unstiffened panel with cross section area α' and thickness of 2$mm$ was considered. So despite being subjected to the same remote load, the panels are subjected to different stress levels, equation (30).

$$\sigma_{unstiffened\ panel} = \frac{\sigma_{stiffened\ panel} \cdot \alpha}{\alpha'} \quad (30)$$

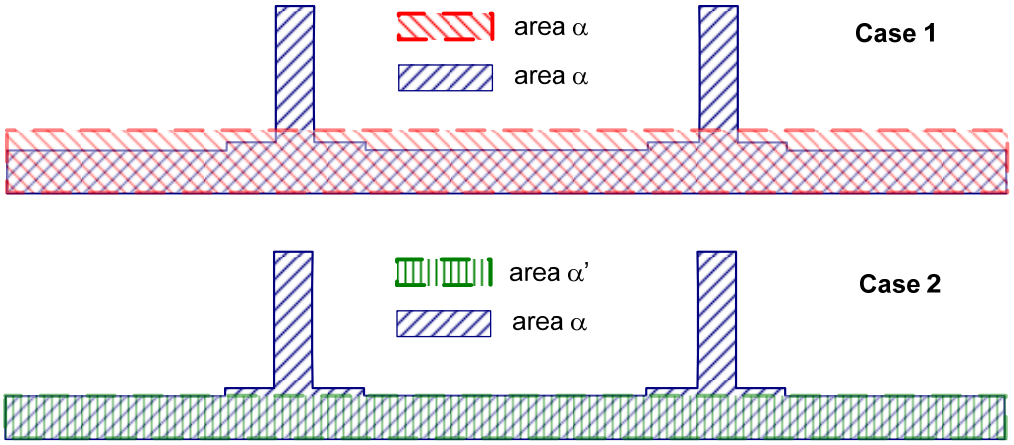


**Figure 392 - Unstiffened and stiffened panel areas for fatigue life comparison.**

The results are presented in Figure 393, where the benefits of using stiffeners in delaying crack growth are clearly displayed, see case 2. In this case, when using a panel without stiffeners with the thickness of the panel skin, there is a decrease of 25% for R=0,1, and 20% for R=0,5.
This figure also shows the unrealistic case of the unstiffened panel with uniform thickness subjected to the same remote stress, case 1; in this case the life of the unstiffened panel is predicted as greater than the life of the stiffened structure. In this case there is an increase of 30% for R=0,1, and 20% for R=0,5.

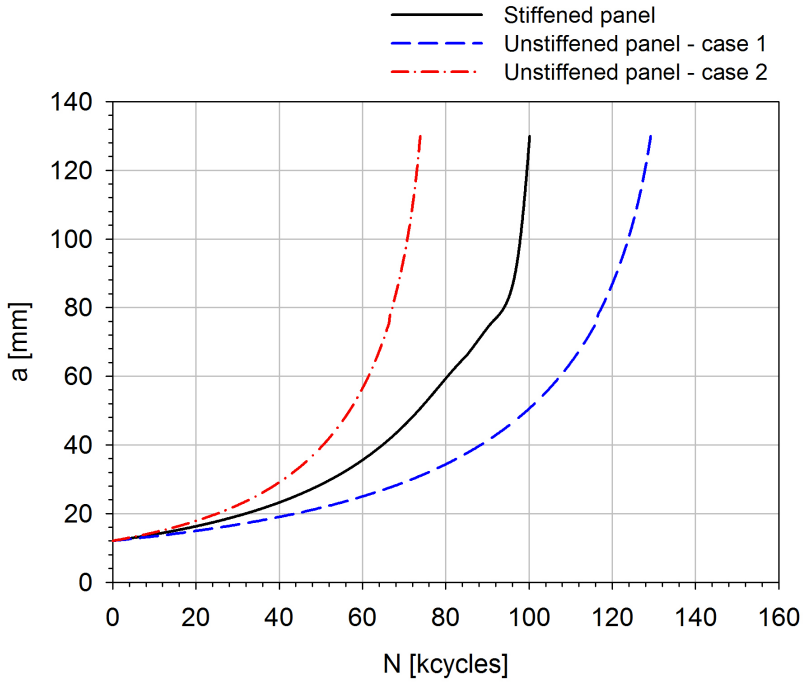


a) crack growth for panels with and without stiffeners with R=0,1

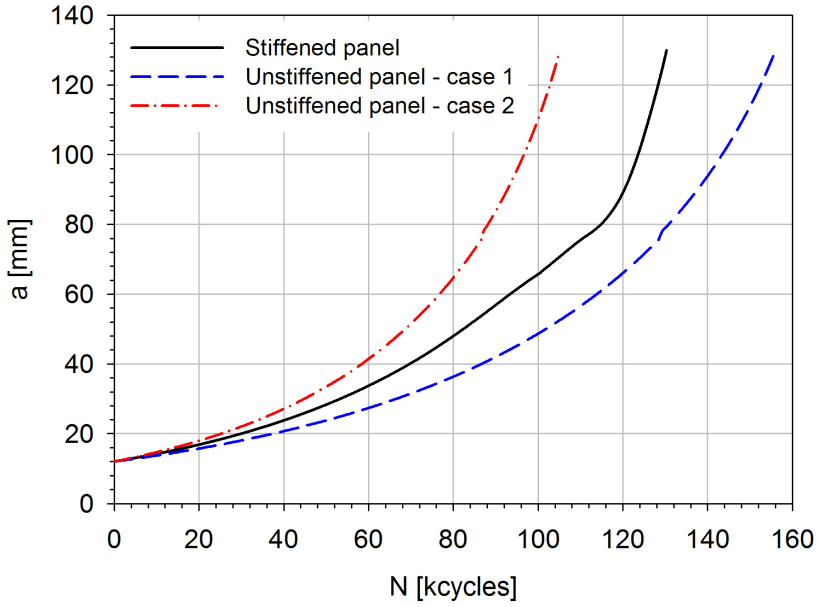


b) crack growth for panels with and without stiffeners with R=0,5

**Figure 393 - Crack growth for panels with and without stiffeners.**

The Figure 394 shows the a=f(N) behaviour of a laser beam welded DaToN stiffened panel of the type LBW1 PWHT-T6, plotted together with the predicted a=f(N) behaviour for this base material.

It is evident that a substantial difference between prediction and test data is found, approximately 32% in fatigue life. This difference may be even higher for other specimens, but in all cases predicted life is lower than the experimental results. This may be due to the fact that the prediction assumes a geometrically flat panel geometry, and does not consider any residual stress effects.

A contribution to explain the slower crack growth observed in the LBW welded stiffened panels may consist in the crack growth retardation caused by the

compressive residual stress field in the region between the stiffeners. Lanciotti *et al.* showed in [199] that in the region between the stiffeners a compressive stress of the order of -20 to -30*MPa* is present, and this may delay crack propagation. Of course, near the stiffeners large positive residual stresses were also identified [199], and this accelerates crack propagation. However when the crack tip is close to the stiffeners, fatigue life is almost finished and this acceleration is likely to have little influence in the overall fatigue life.
Obviously the welded specimens were supplied with an important distortion not taken into account in the numerical model. Further more, attempts to measure residuals stress fields of welded DaToN panels using X-ray technique proved to be unsuccessful. Because of these two reasons, a more sophisticated numerical modelling would be required in order to obtain a better agreement with experimental results.

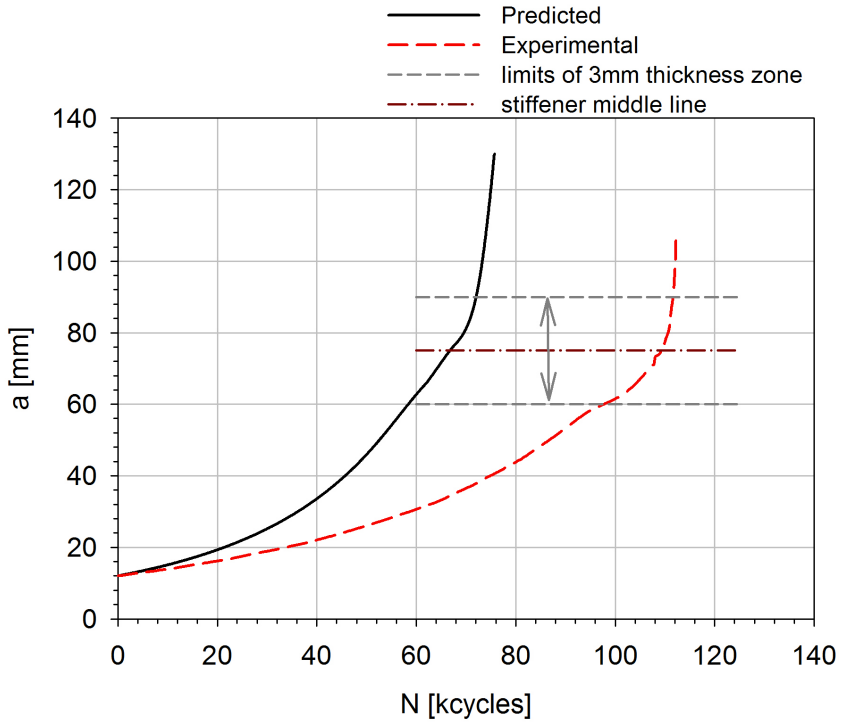


**Figure 394 - Comparison between the predicted and the experimental fatigue life of a LBW1 PWHT-T6 panel.**

### *6.2.7 Concluding remarks*

Mechanically fastened panels are desirable in terms of fail-safety criterion since the stringers are effective crack stoppers. However, whereas riveted stiffeners continue to limit crack growth after the crack propagates past the stiffener, the effect of a welded or integral stiffener is quite different, since the crack may propagate directly into an integral stiffener and completely break it, e.g. [18, 200-202].

The stress intensity factor calibration of the DaToN stiffened panel geometry was obtained using the VCCT technique in conjunction with a finite element model.

The resulting stress intensity factor solutions for both skin and stiffener, used with the Paris law, gave adequate predictions of experimental crack propagation behaviour in HSM DaToN panels. Although the surface layers of these HSM panels may present machining residual stresses, these are not expected to be significant along most of the thickness. The relatively low state of residual stress of HSM panels is qualitatively confirmed by the almost precisely flat geometry of the HSM machined panels, as documented in Figure 366.

Welded panels presented longer lives up to rupture, implying that during most of their fatigue testing the crack growth rates were smaller than with HSM panels. This somewhat unexpected result – fatigue lives of welded components longer than fatigue lives of monolithic machined similar components – is certainly associated to the residual stress fields existing in the welded panels, and also to the location of the initial artificial defect, placed in the skin precisely in the middle distance between the two stiffeners.

The welded panel specimens were supplied to the author, by EADS CRC France in the case of LBW, and by EADS CRC Germany in the case of FSW, with important distortion, documented in Figure 366, not taken into account in the numerical model. Furthermore, attempts to measure residuals stress fields of welded DaToN panels using X-ray technique proved to be unsuccessful. Although it is known that a wide range of scatter in the residual stress measurements in essentially similar panels is typically found, as reminded for example in [200], the measurements at the University of Coimbra did not give a sufficiently clear result of residual stress distribution usable with confidence for modelling purposes.

As also stated in [200], welded stiffeners affect skin crack growth in a unique way because of residual stresses. In the vicinity of the stiffeners, welding is expected to create predominantly tensile residual stresses that may be of the order of the material yield stress, whereas lower-level compressive stress will occur in the skin between the stiffeners. Therefore, such a schematic residual stress distribution will increase crack growth rates near the stiffeners, and decrease crack growth rate between them. A contribution to explain the slower crack growth observed in the LBW welded stiffened panels may therefore consist in the crack growth retardation caused by the compressive residual stress field in the region between the stiffeners. Of course the reverse trend is expected when the crack tip finds the high positive residual stresses close to the stiffeners. There, the crack growth rate is expected to accelerate. However, for the DaToN two-stiffener panels, when the crack tip is close to the stiffeners, fatigue life is almost finished and this acceleration is likely to have little influence in the overall fatigue life.

If the starting artificial crack was located in a region of positive residual stress - skin under a stiffener - the reverse effect should be expected and a lower fatigue life would result from accelerated crack growth.

The complex testing of the DaToN panels raised a question concerning the choice of their geometry. It was found that, with these two-stiffener HSM and welded

panels, the crack growth rate when the crack tip reaches the stiffener is already very large, implying that there is almost no noticeable crack slowing down effect of the stiffeners. However, a clear crack slowing down effect was found when testing panels in a separate and previous AIRBUS programme [203, 204]. It should be noticed that the stiffener cross section versus skin cross section area ratio was higher for the AIRBUS panels than for the DaToN panels. As suggested in [205], a systematic study of this ratio should be carried out in order to identify its optimum value. Also, the shape of stiffener cross section is likely to influence the fatigue behaviour, and a related research effort is already documented in [201], continuing the exploration of fail-safety design options for integral/welded stringer panels.

A more sophisticated numerical modelling would be required in order to obtain a better agreement of the DaToN test data and the numerical model, a suggestion that is made for future work, which, unlike the present one focused on experiments, should focus modelling.

### 6.3 SEM analysis

Two HSM, two LBW and one FSW panels were analysed by scanning electron microscopy (SEM) at Centro de Materiais da Universidade do Porto (CEMUP). To carry out the analysis different zones (samples) were chosen from the panel fractured surface.
With the SEM analysis striations measurements throughout the fractured surface, and particular features as weld defects were characterized. Measurements of fatigue striations were performed considering the middle specimen as the measurement origin and several values were obtained through the crack length. To obtain results of fatigue striation spacing “s” for a given point (coordinate value), in the corresponding screen image four measurements of the number of striations in a perpendicular line to their orientation are carried out. The average value of these measurements is the result in the correspondent coordinate.

In order to identify differences in the welding procedures, before the SEM analysis a macrographic analysis of all type of welded specimens was performed, Figure 395. The welding configurations LBW1 and LBW2 are easily identified comparing the specimen LBW03 with specimens LBW05 and LBW09. The TMAZ is also identified in the FSW09 specimen.

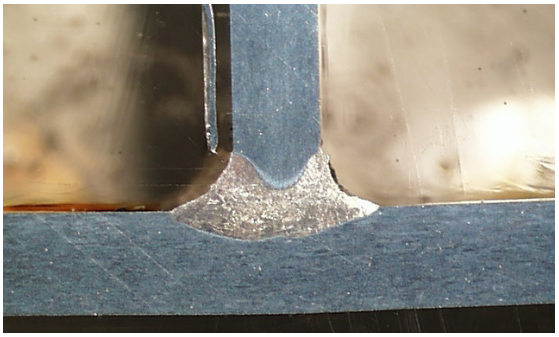

a) specimen LBW03 (LBW1 configuration)

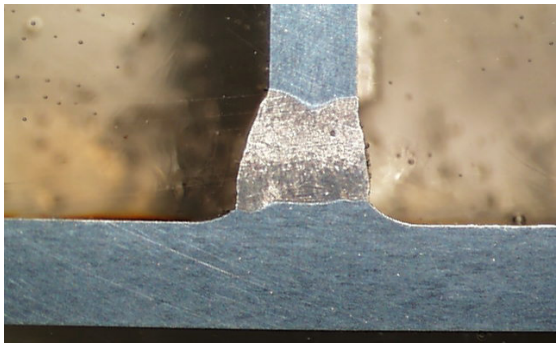

b) specimen LBW05 (PWHT-T6)

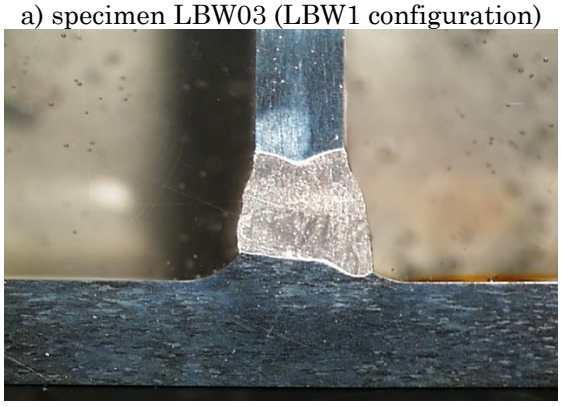

c) specimen LBW07 (as-welded)

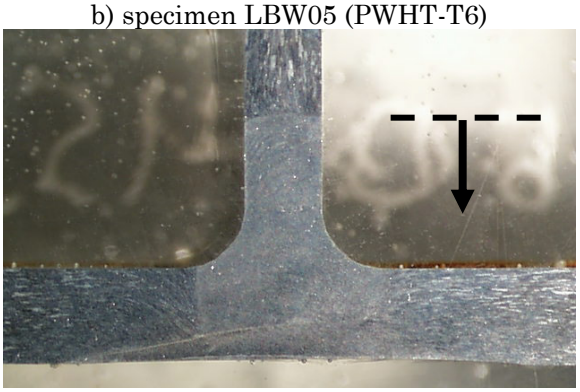

d) specimen FSW09

**Figure 395 - Macrographs of welded specimens.**

### *6.3.1 HSM 6056-T6 R=0,5 specimen (HSM02)*

The HSM 6056 PWHT-T6 tested at R=0,5 was analyzed by SEM. Four samples, as presented in Figure 396, were analysed: samples A, B, C and D. Sample A includes the fatigue crack initiation and sample C includes de stiffener.

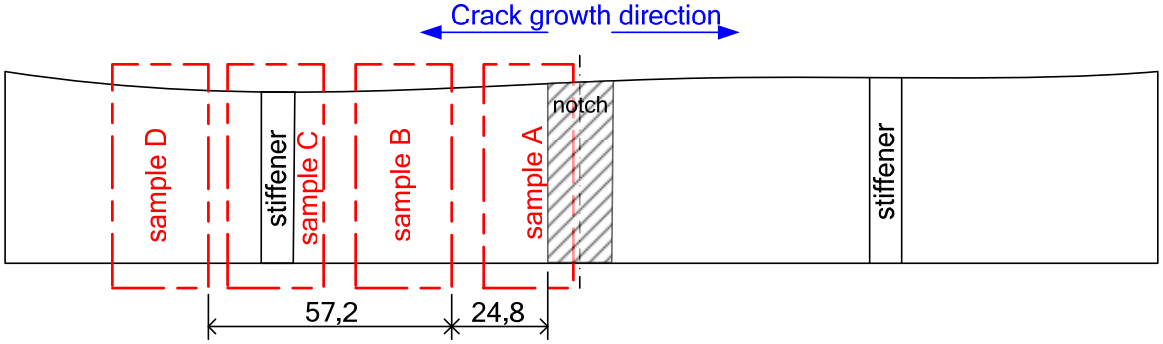


**Figure 396 - Sample location for SEM analysis of the HSM 6056 PWHT-T6 R=0,5 specimen.**

*6.3.1.1 Fracture surface features*

Figure 397 corresponds to the initial fatigue crack location, sample A. In this figure at the left side is identified the initial notch created by electro discharge machining (EDM) and at the right side the initial steps of the fatigue crack.

Figure 398 presents, in the same ample, a fissure crossing a length longer than $400\mu m$.

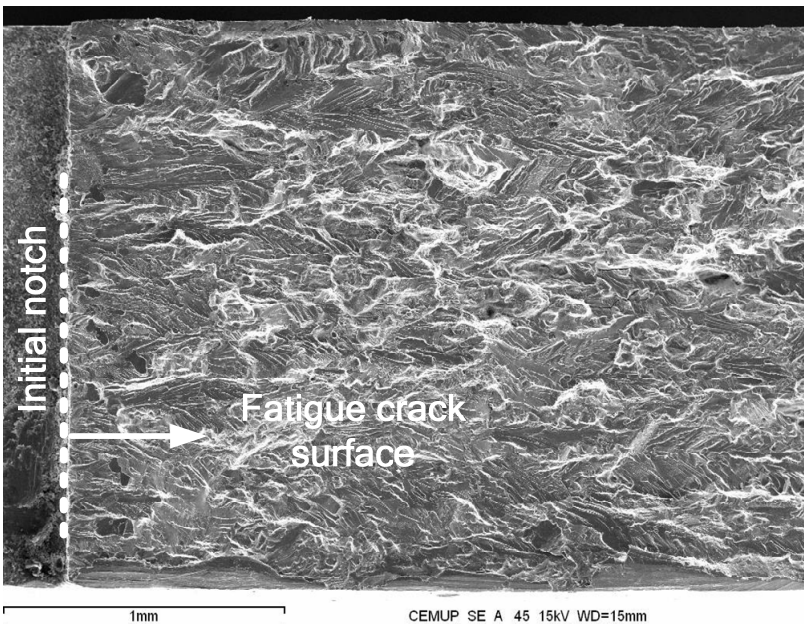


**Figure 397 - Initial site of the fatigue crack.**

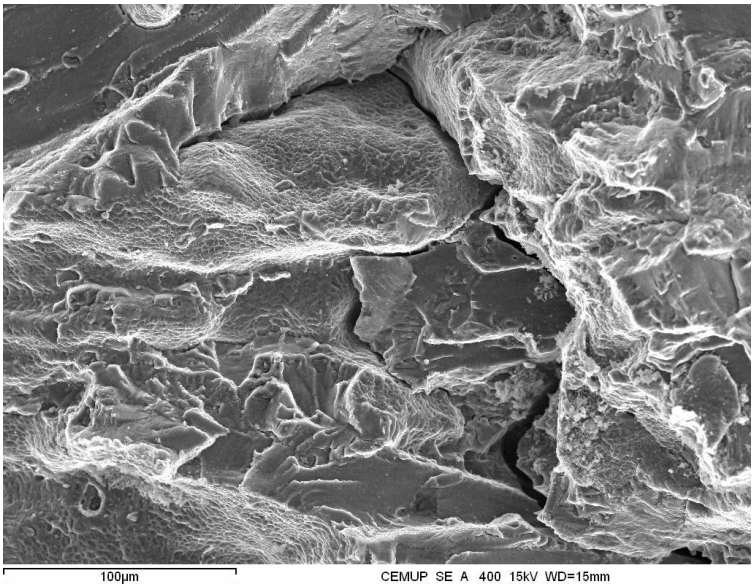


**Figure 398 - Fissure in sample A.**

In sample B using the back scattered electron detector Manganese particles were identified dispersed in the matrix (white particles) as presented in Figure 399.

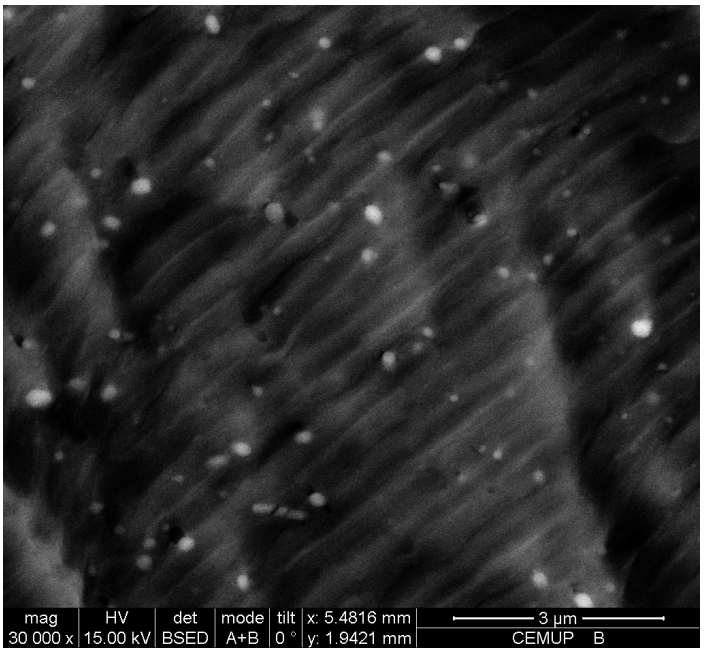


**Figure 399 - Sample B fractograph showing Manganese particles as light particles (back scatted electron detector).**

Analyzing sample C some particular features were also found. In Figure 400a) some dispersed particles and pores were observed in the fractured surface. A mesh of separate areas of striations with different orientations is presented in Figure 400b).

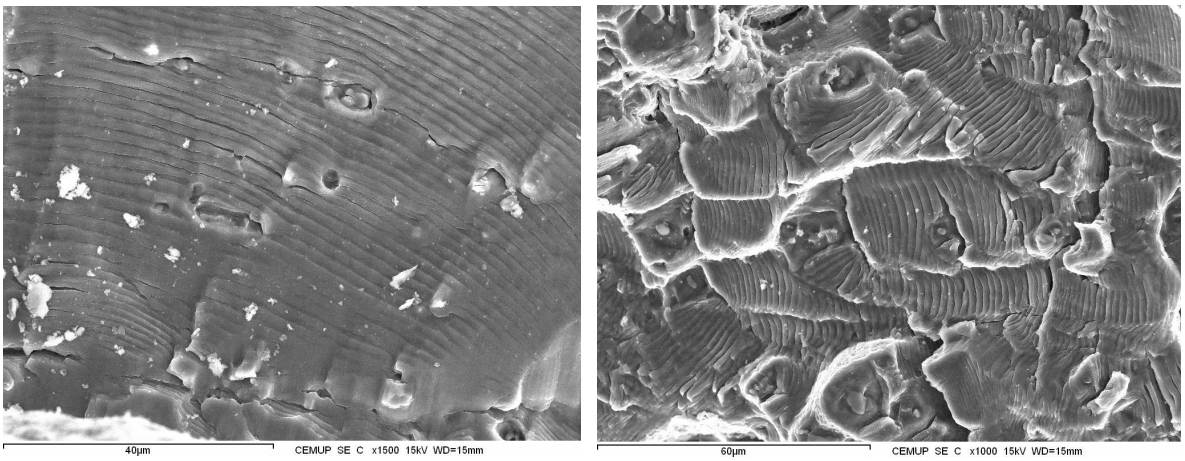


a) dispersed inclusions

b) mesh of striations with different orientation

**Figure 400 - Sample C, features before reaching the stiffener.**

Just above the stiffener a fissure was found, presented in Figure 401a). Also the stiffener surface presented large cracks crossing the stiffener, Figure 401b).

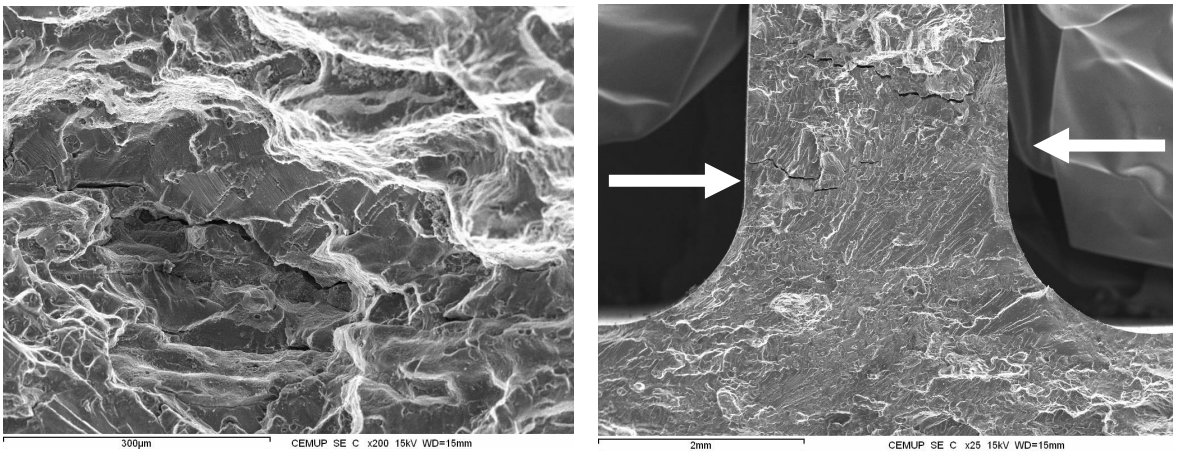


a) fissure in the stiffener area b) stiffener fracture surface detail

**Figure 401 - Sample C features near the stiffener.**

Some pores were observed along the fatigue crack. A $4\mu m$ pore is presented in Figure 402a). Figure 402b) presents a site after the stiffener where a transition to a ductile fracture surface occurred.

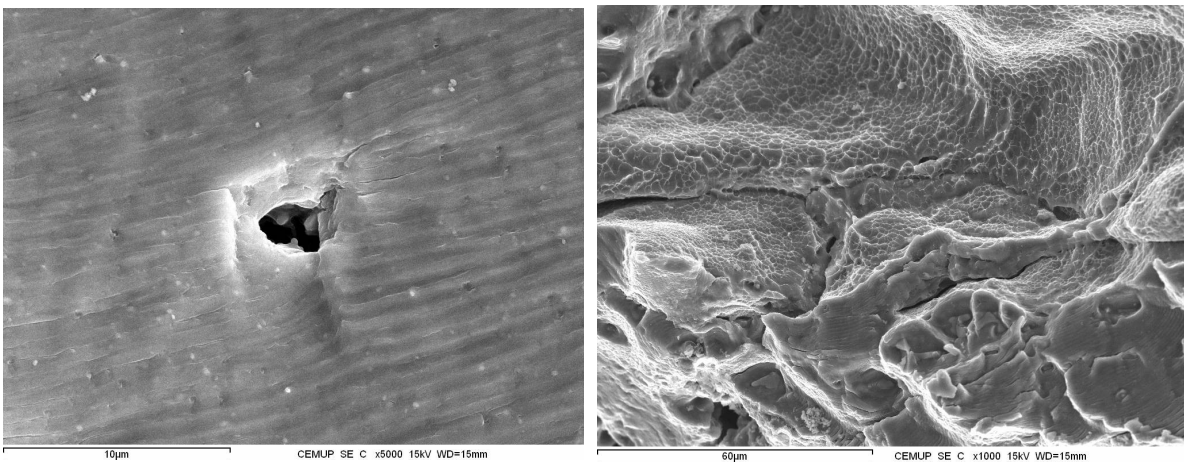


a) pore b) transition to a ductile fracture surface

**Figure 402 - Features observed after the stiffener.**

In this HSM specimen, the crack has propagated along the stiffener in the direction of the applied remote load. This surface, crack along the stiffener, was analyzed and a fractograph is presented in Figure 403. The surface presents a rough finishing indication of a material plane containing some impurities.

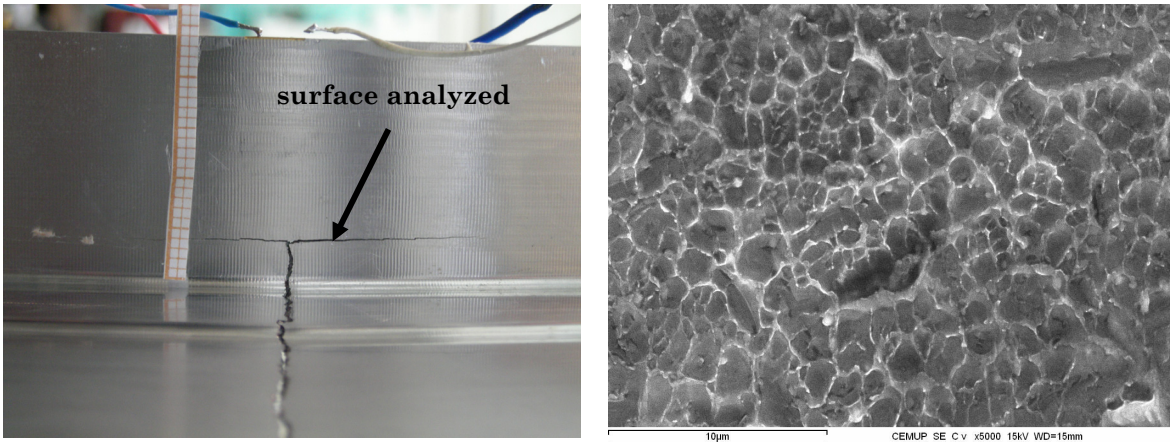


**Figure 403 - Crack surface along the stiffener (load direction)**

Sample D corresponds to an area which is characterized mainly by a ductile fracture process. In this sample a heterogenic surface indicating a high plastic deformation which also contains some pores and internal cracks (fissures) were identified, presented in Figure 404.

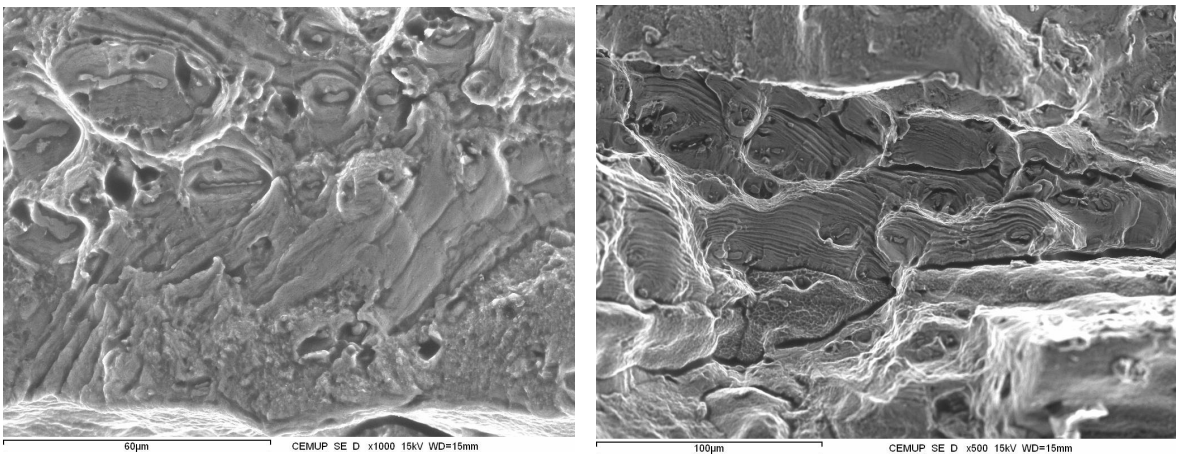


a) dispersed pores in sample D

b) striations with different orientations separated by fissures

**Figure 404 - Sample D fractographs.**

*6.3.1.2 Fatigue striations*

Fatigue striations measurements were performed in samples A, B, C and D, fractographs were acquired near the middle thickness plane. From sample A were analyzed 30 fractographs, from sample B 32 fractographs, from sample C 58 fractographs and from sample D 8 fractographs. Examples of fractographs analyzed in samples A and B are presented in Figure 405. The first fractograph shows striations at $9mm$ from the initial notch and the second fractograph shows striations at $14mm$ from the initial notch. Between these two locations the striations approximately double their spacing.

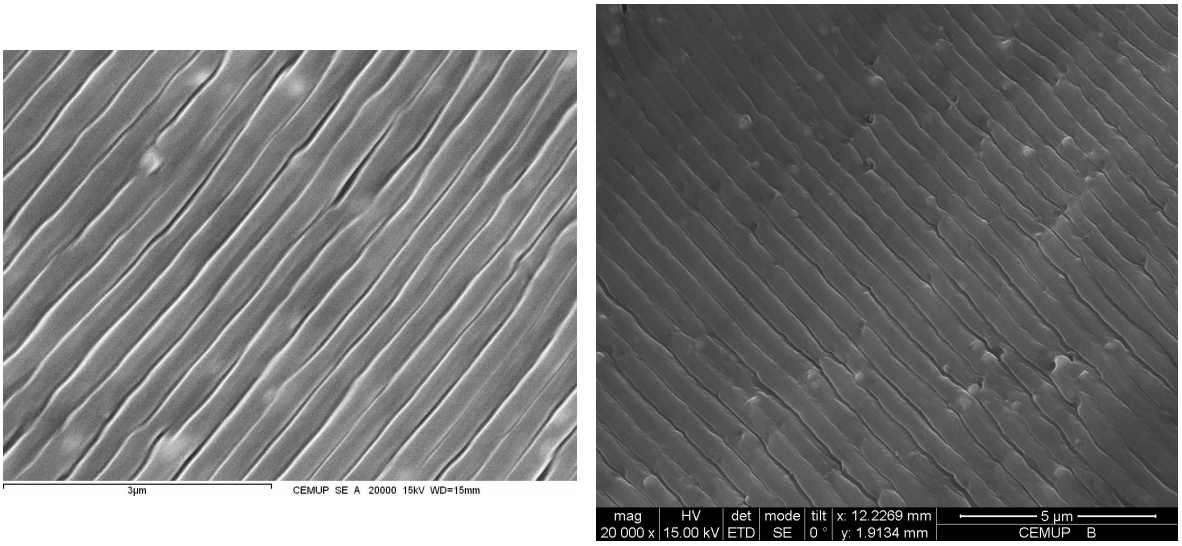


a) fractograph 18 of sample A, x=19,82$mm$, y=0,67$mm$, s=0,29$\mu m$

b) fractograph 6 of sample B, x=34,10$mm$, y=1,01$mm$, s=0,52$\mu m$

**Figure 405 - Fractographs showing striations in sample C.**

A fractograph showing the stiffener root and the crack growth direction is presented in Figure 406.

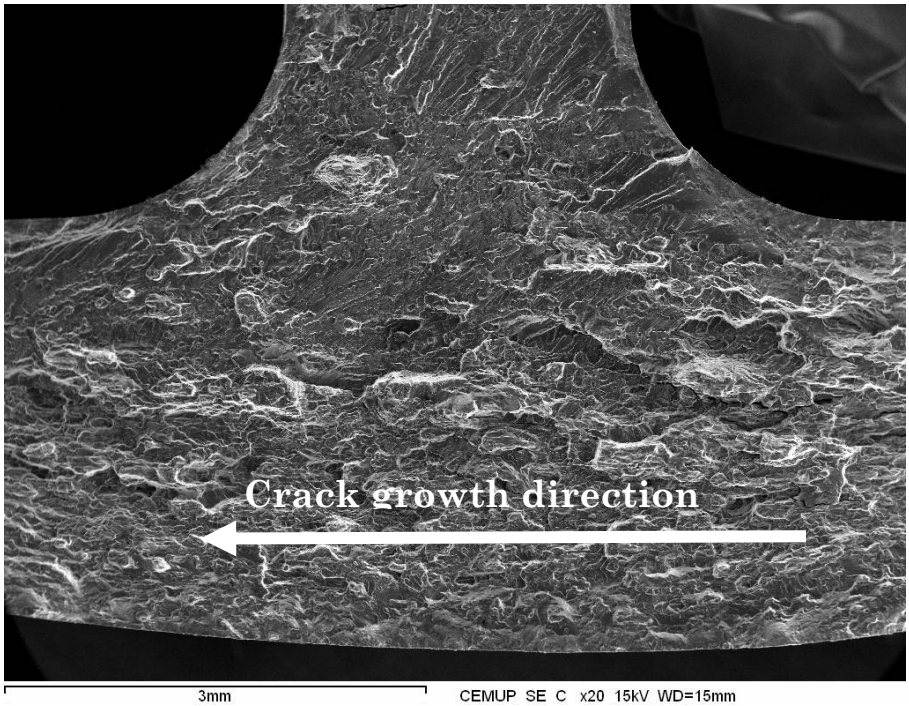


**Figure 406 - Fractograph showing the stiffener root.**

In Figure 400b) a mesh of different type of striations are presented. Analyzing two of these areas, striations with different spacing were found as presented in Figure 407. This fractographs are located at approximately 4$\mu m$ from the stiffener. This example shows that the crack as some scatter in its growth and a comprehensive analysis should be performed to obtain the final curve.

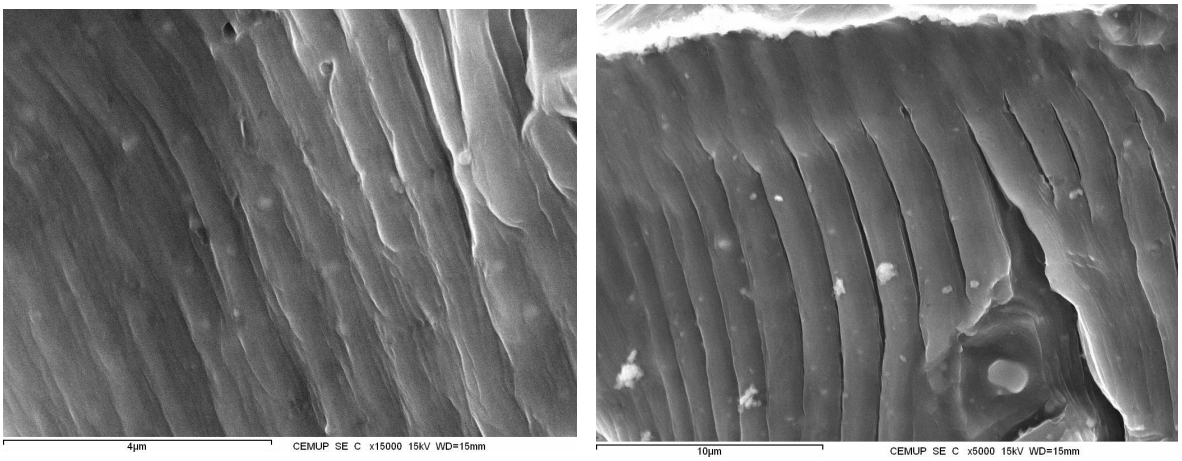


a) fractograph 21 of sample C, x=69,48$mm$, y=2,07$mm$, s=0,60$\mu m$

b) fractograph 22 of sample C, x=69,47$mm$, y=2,03$mm$, s=1,38$\mu m$

**Figure 407 - Fractographs showing striations before the stiffener.**

In Figure 408, fractograph 40 shows striations at the stiffener and fractograph 54 shows striations 10$mm$ after the stiffener. The increase in crack growth rate is easily identified by the increase in striations spacing.

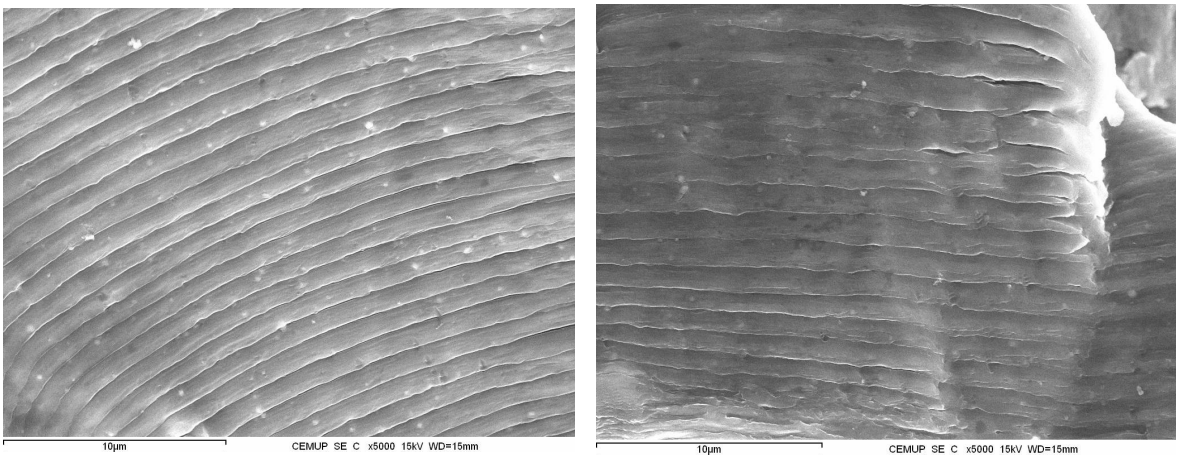


a) fractograph 40 of sample C, x=74,99$mm$, y=4,49$mm$, s=0,92$\mu m$

b) fractograph 54 of sample C, x=85,67$mm$, y=1,73$mm$, s=1,14$\mu m$

**Figure 408 - Fractographs showing striations in and after the stiffener.**

The final results of fatigue striations spacing measurements along the stiffener and along the specimen base plate are presented in Figure 409 and Figure 410. Each plot was fitted by an exponential equation. In Figure 409, sample A, B, C and D fit together to give the history of striation spacing along the base plate as the crack grows. In Figure 410, due to the nature of the fracture surface observed in the stiffener, only the first 5$mm$ could be analyzed.

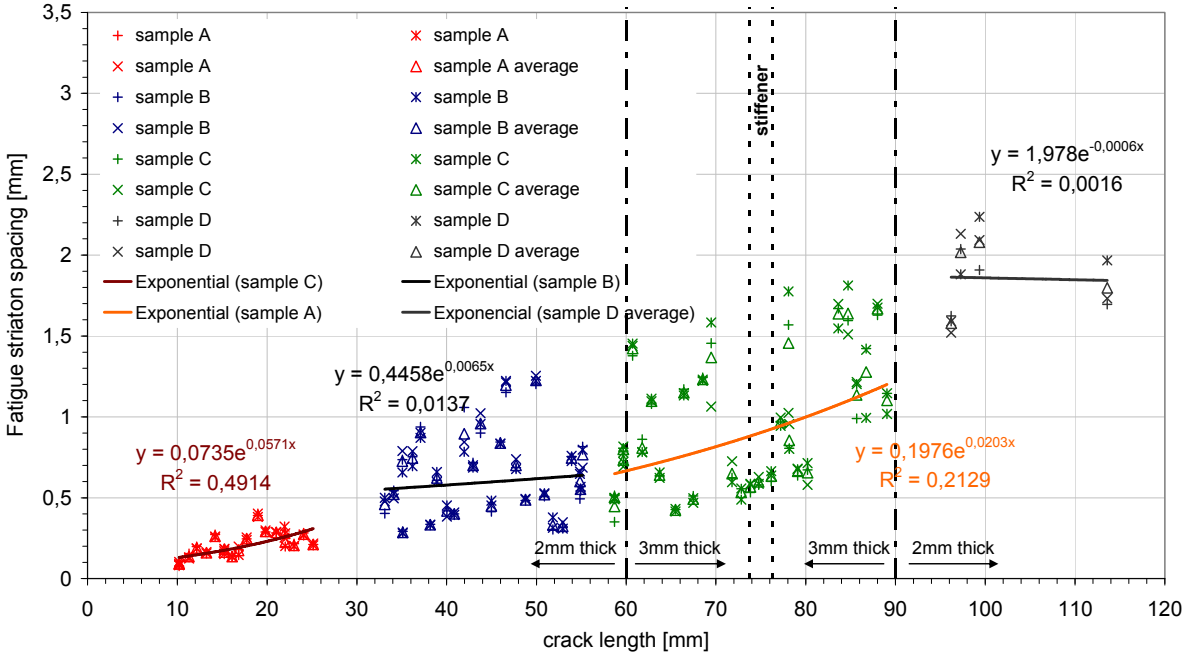


**Figure 409 - Fatigue striation spacing along the base plate.**

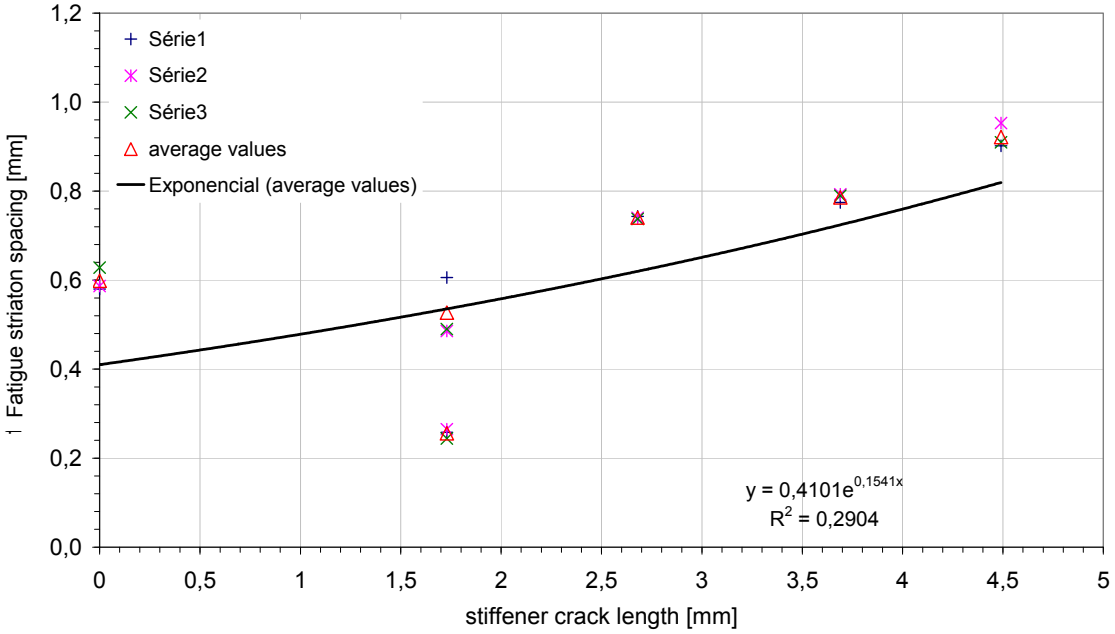


**Figure 410 - Fatigue striation spacing along the stiffener.**

### *6.3.2 HSM 6056-T6 R=0,1 specimen (HSM01)*

The HSM 6056 PWHT-T6 tested at R=0,1 was analyzed by SEM. Two samples, as presented in Figure 411, were analysed: samples A and C. Sample A includes the fatigue crack initiation and sample C includes the stiffener.

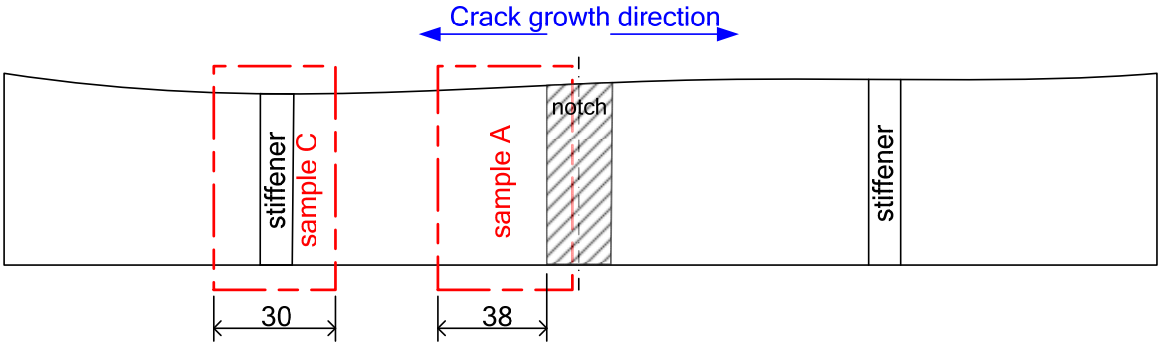


**Figure 411 - Sample location for SEM analysis of the HSM 6056 PWHT-T6 R=0,1 specimen.**

*6.3.2.1 Fracture surface features*

Figure 412 presents, in ample A, some fissures in the fracture surface.

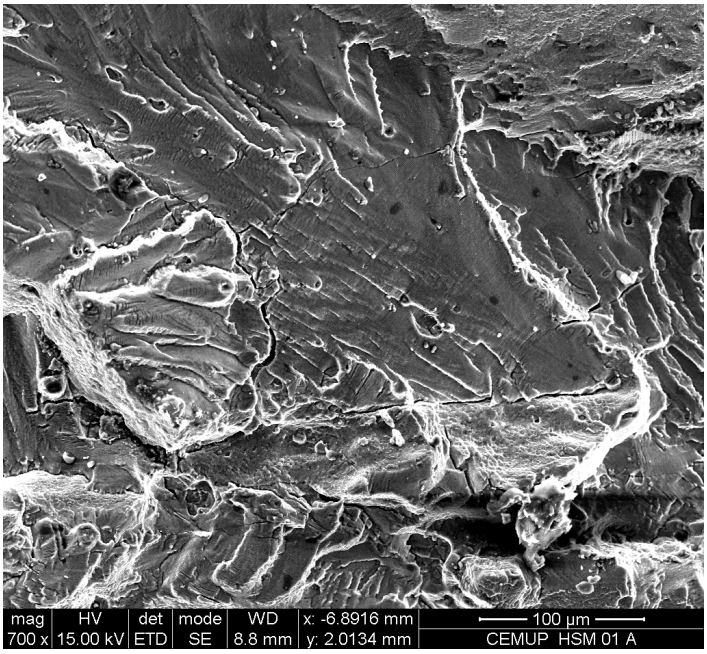


**Figure 412 - Fissure in sample A.**

Analyzing sample C some features were also found and are similar to the ones presented for the other HSM specimen. Some pores were observed along the fatigue crack, Figure 413a). Figure 413b) presents a site after the stiffener where a transition to a ductile fracture surface occurred, see Figure 403.

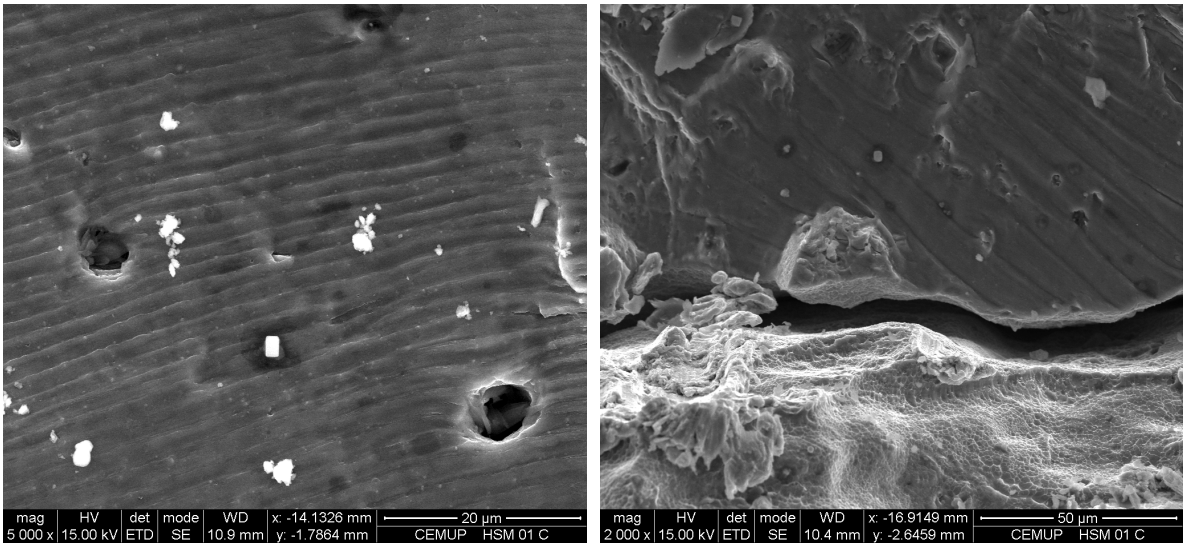


a) pores b) transition to a ductile fracture surface

**Figure 413 - Features observed after the stiffener.**

In this HSM specimen, the crack also propagated along the stiffener in the direction of the applied remote load.

*6.3.2.2 Fatigue striations*

Fatigue striations measurements were performed in samples A and C; fractographs were acquired near the middle thickness plane. From sample A were analyzed 32 fractographs and from sample C 42 fractographs.

The final results of fatigue striations spacing measurements along the stiffener and along the specimen base plate are presented in Figure 414 and Figure 415; each plot was fitted by an exponential equation. In Figure 414, sample A and C were plotted together to give the history of striation spacing along the base plate as the crack grows.

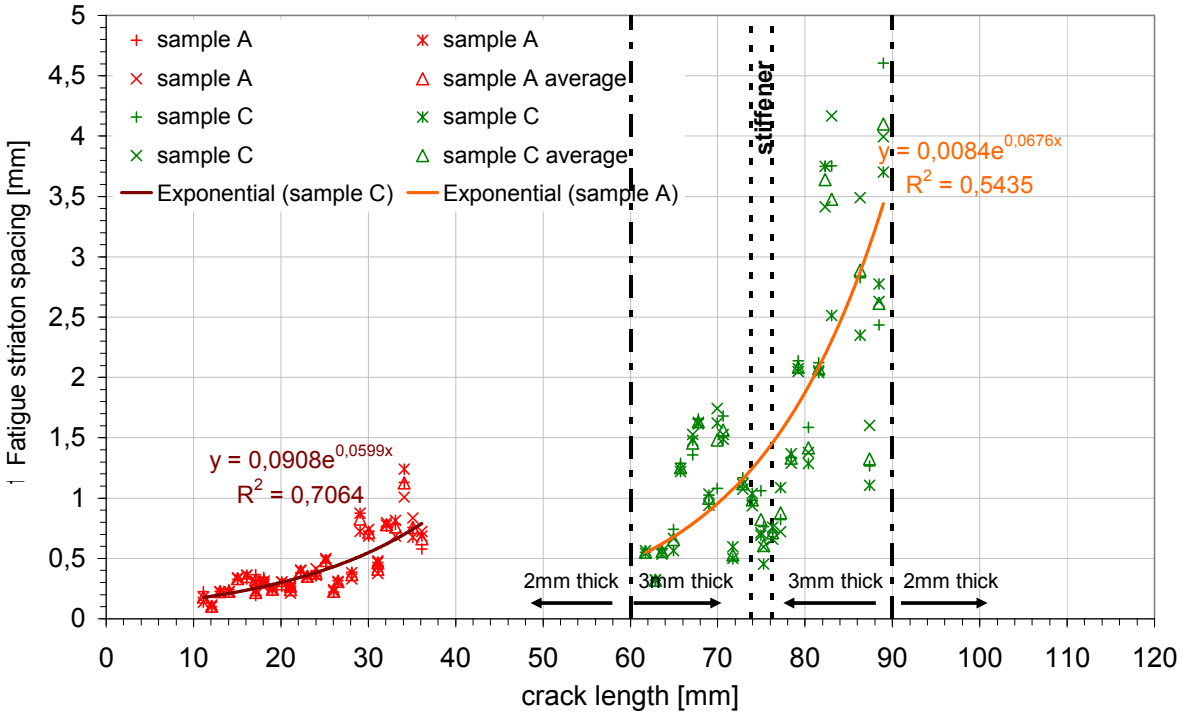


**Figure 414 - Fatigue striation spacing along the base plate.**

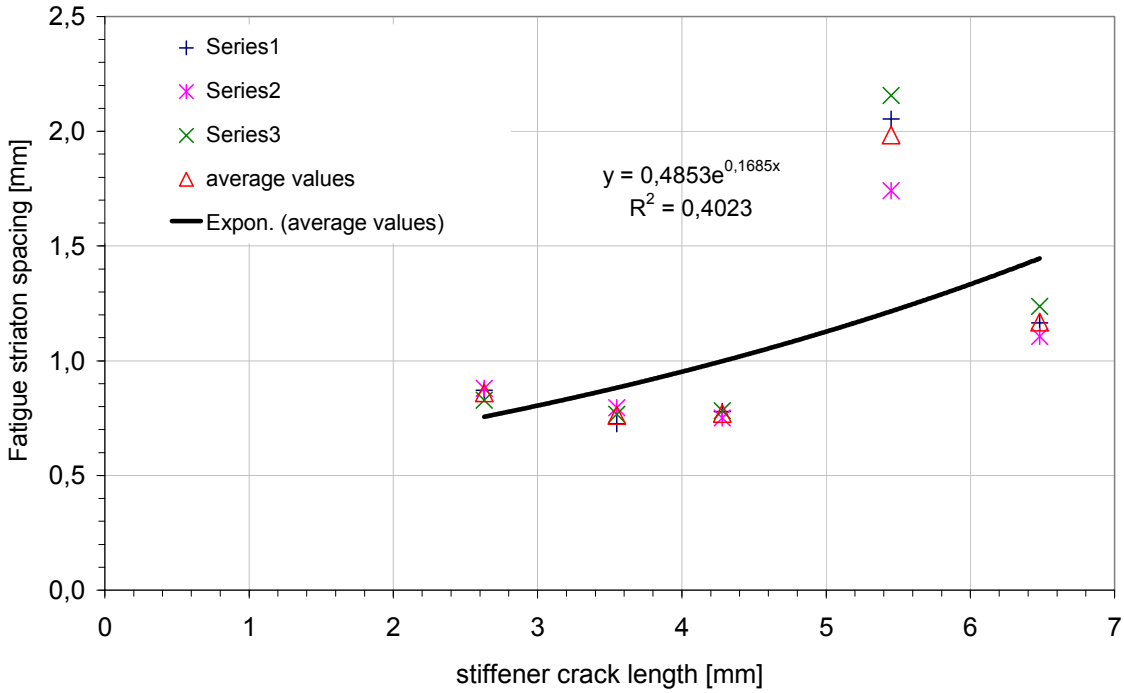


**Figure 415 - Fatigue striation spacing along the stiffener.**

### *6.3.3 LBW1 6056 PWHT-T6 R=0,1 specimen (LBW03)*

The first LBW specimen to be analysed was the LBW1 6056 PWHT-T6 tested at R=0,1. Four samples, as presented in Figure 416, were analysed: samples A, B, C

and D. Sample C includes the fatigue crack initiation, and sample A includes the stiffener. In sample D was not possible to identify fatigue striations.

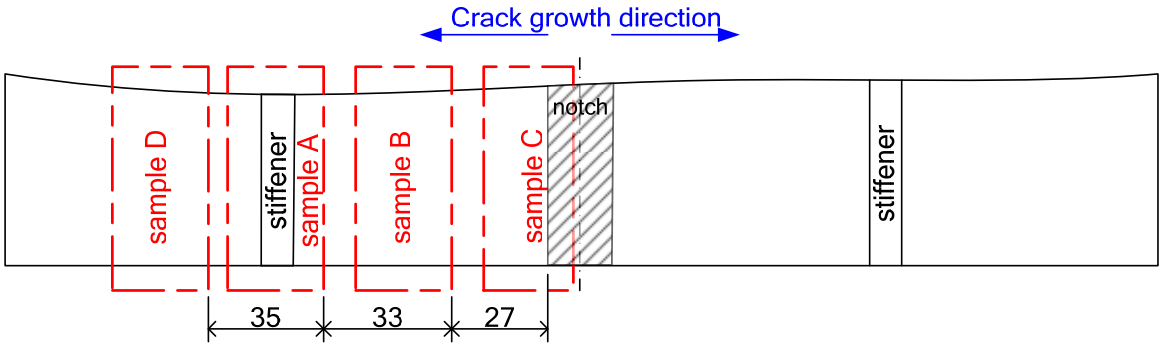


**Figure 416 - Sample location for SEM analysis of the LBW1 6056 PWHT-T6 R=0,1 specimen.**

*6.3.3.1 Fracture surface features*

Figure 417 corresponds to the initial fatigue crack location, sample C. In this figure, at the right side is seen the initial notch created by electro discharge machining and at the left side the initial fatigue crack. Pores were found in some sites of the fatigue crack as demonstrated in Figure 418. This figure shows a fractograph at 3*mm* from the initial notch.

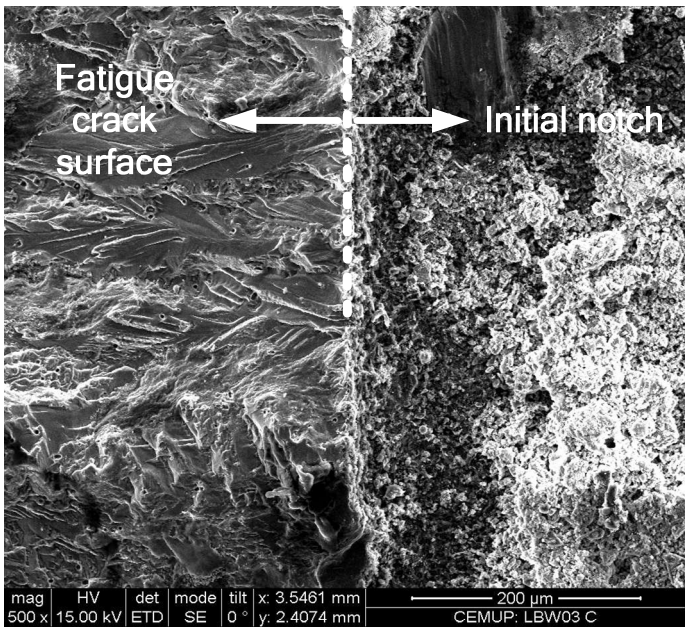


**Figure 417 - Initial site of the fatigue crack.**

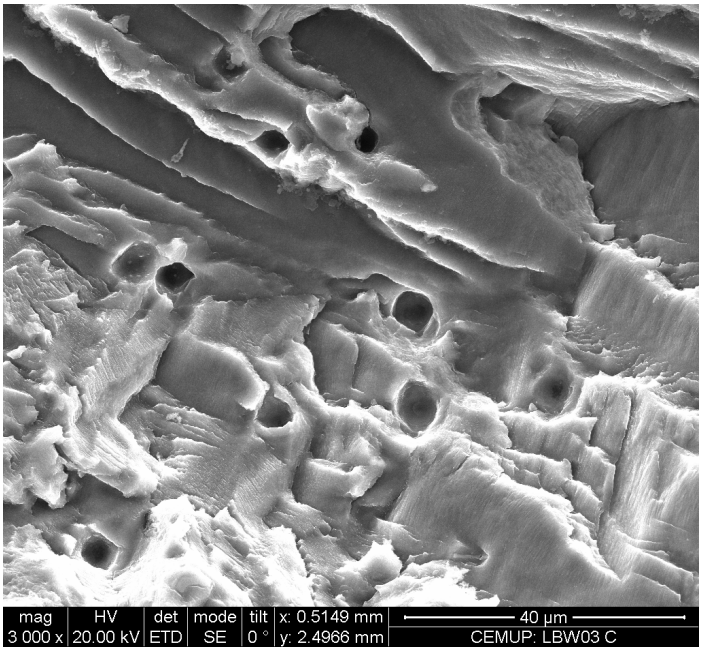


**Figure 418 - Pores disperse along the fatigue crack.**

Another example of pores dispersed in a surface containing different striations sets, sample B, is presented in Figure 419. This fractograph was acquired at approximately 32*mm* from the initial notch.

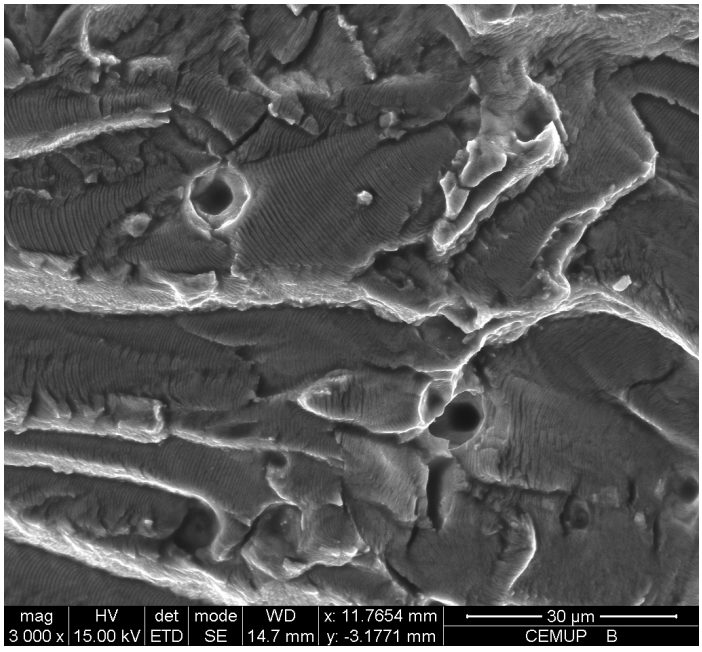


**Figure 419 - Sample B fractograph showing different striations sets and some pores.**

Sample A contains the stiffener root where the weld was performed. The T joint macrograph is presented in Figure 420a). At the centre of the weld, pores with a maximum diameter of 0,24*mm,* were identified. These pores seem to be coincident with the laser maximum penetration depth from each side of the T-joint. A detail of these pores is presented in Figure 420b).

Magnifying the transition line which separates the melted and un-melted material a new macrograph, Figure 421a) was obtained. In this area cracks were identified out of the weld bead. This zone, just outside of the weld bead, was heated during welding and these cracks were probably formed during the cooling process. A detail of this crack, with an approximate length of 220$\mu m$, is presented in Figure 421 b).

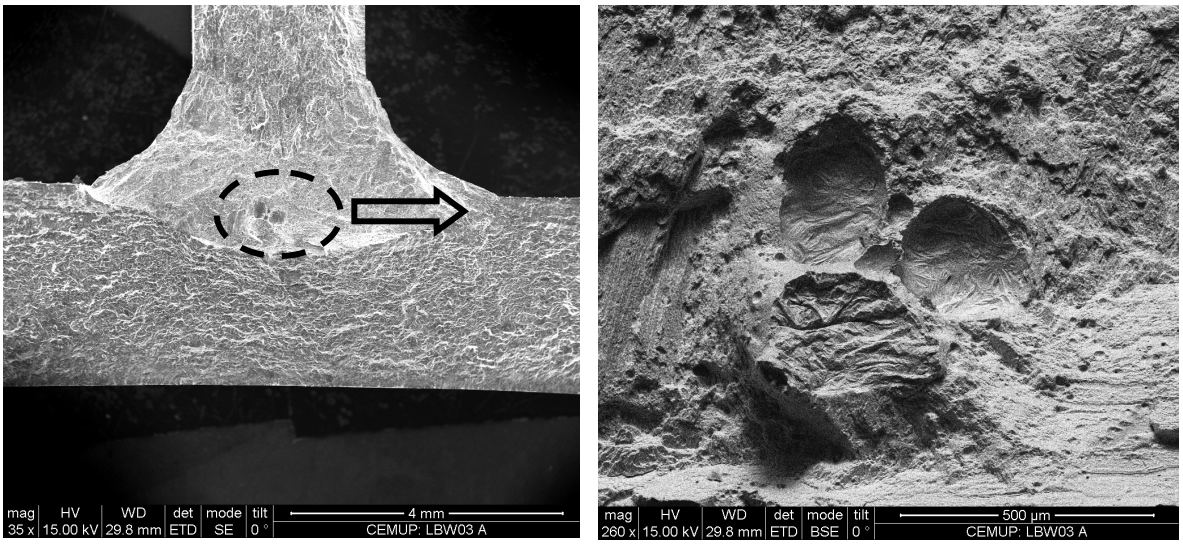


a) T-joint macrograph b) Detail of pores at the weld centre

**Figure 420 - T-joint LBW1 PWHT-T6 R=0,1.**

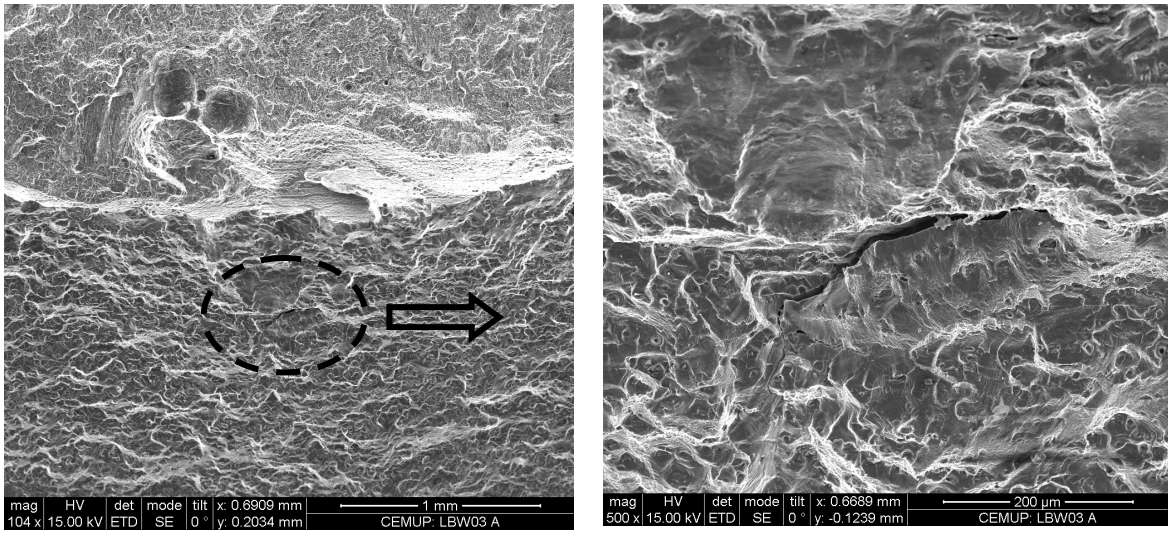


a) macrograph b) detail of the crack

**Figure 421 - Cracks just outside the weld bead.**

A macrograph of the transition line between the melted an un-melted material is presented in Figure 422a). In this figure are also identified small pores just under the line of the weld bead. Through this transition zone are also identified cracks that separate the two zones (marked with the dash dot ellipse). In Figure 422 are shown the different striations spacing at both sides of the line which divides the melted and un-melted material.

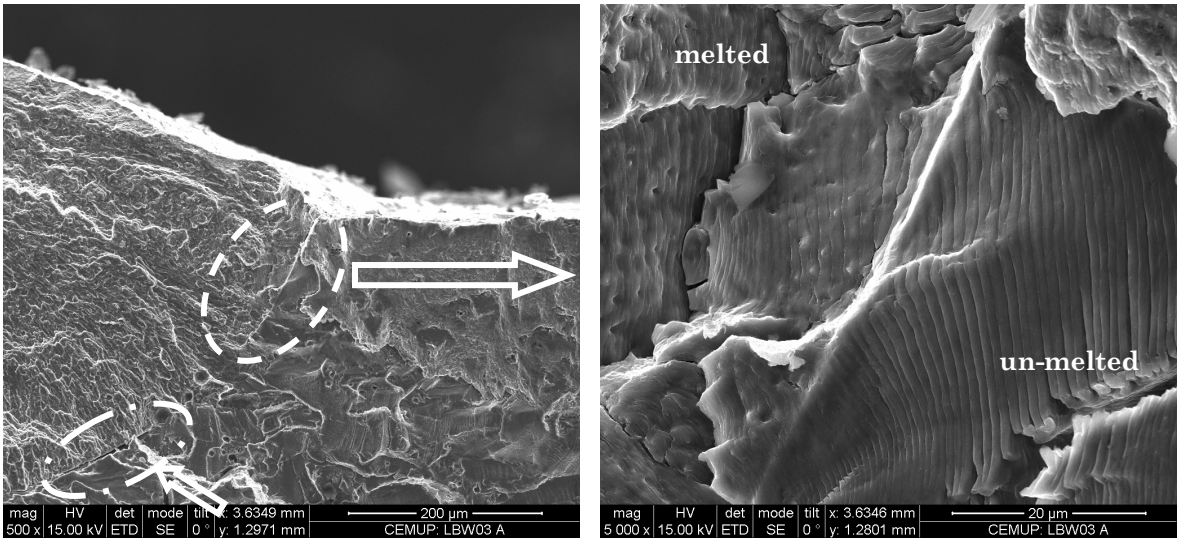


a) macrograph b) striations at both side of the transition line

**Figure 422 - Striations at both sides of the weld line (weld bead and parent material).**

The stiffener root is analyzed in Figure 423. It is verified that the weld had full penetration. There is a transition line, which separates areas with different brightness due to the melting process and to the added filler wire which caused zones with a different chemical composition. It is again observed cracks around the limits of the heat affected zone and pores dispersed in the stiffener root. In the area above the transition line it was not possible to identify fatigue striations.

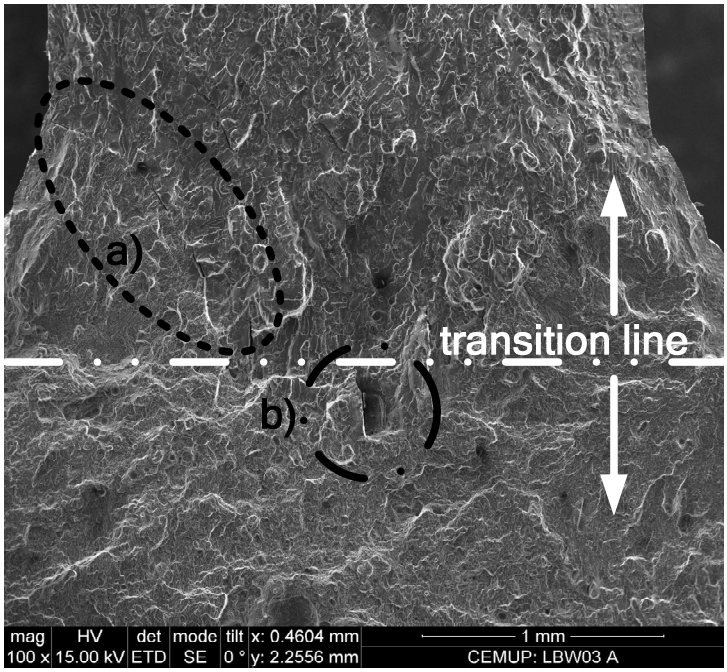

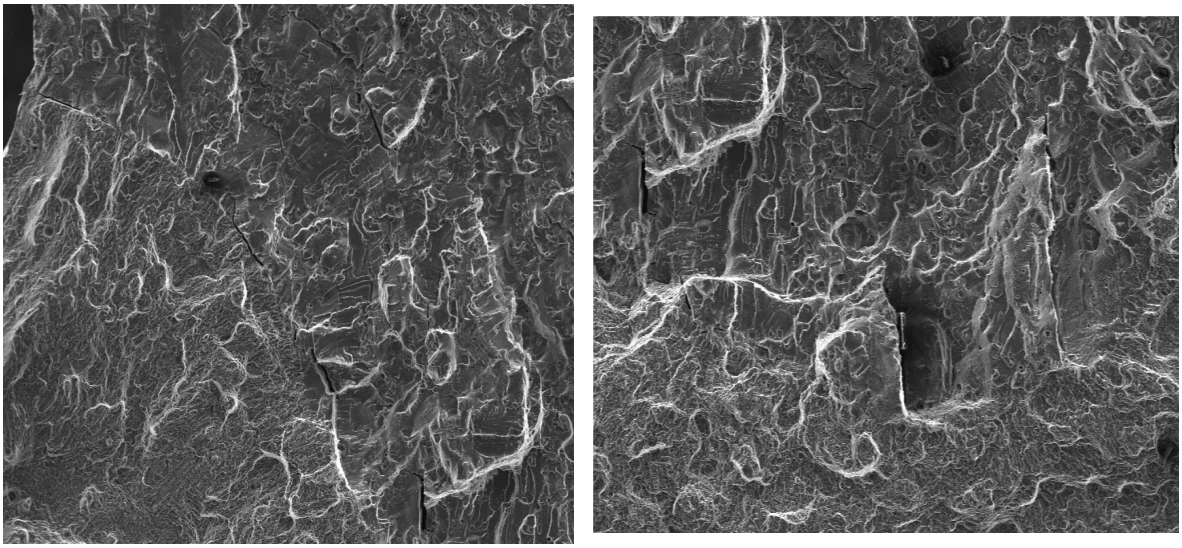

a) fracture lines in the weld bead b) pores detail

**Figure 423 - Stiffener root analysis.**

Sample D corresponds to an area which is characterized mainly by a ductile fracture process. In this sample a heterogenic surface, indicating high plastic deformations which contain pores and internal horizontal cracks (fissures), is identified as presented in Figure 424. Figure 425 shows the specimen whole thickness and pores which are represented by the darker dispersed areas. A magnification of a pore and a fissure are presented in Figure 426 a) and b), respectively.

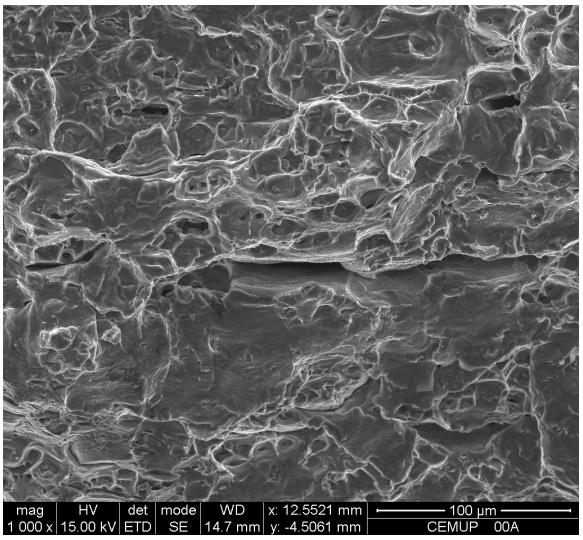


**Figure 424 - Sample D ductile fracture surface.**

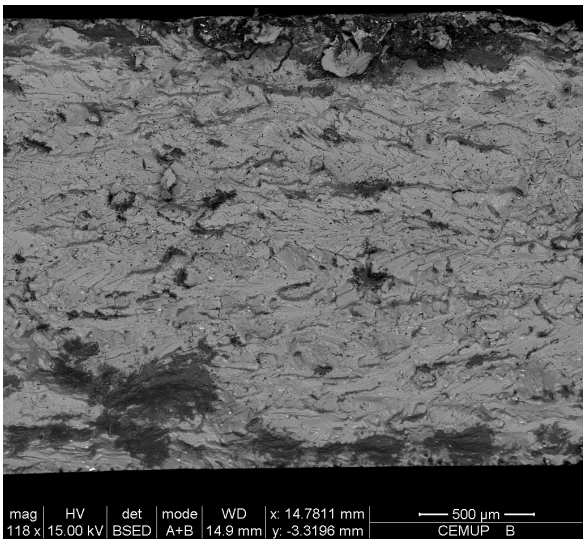


**Figure 425 - Pores identification.**

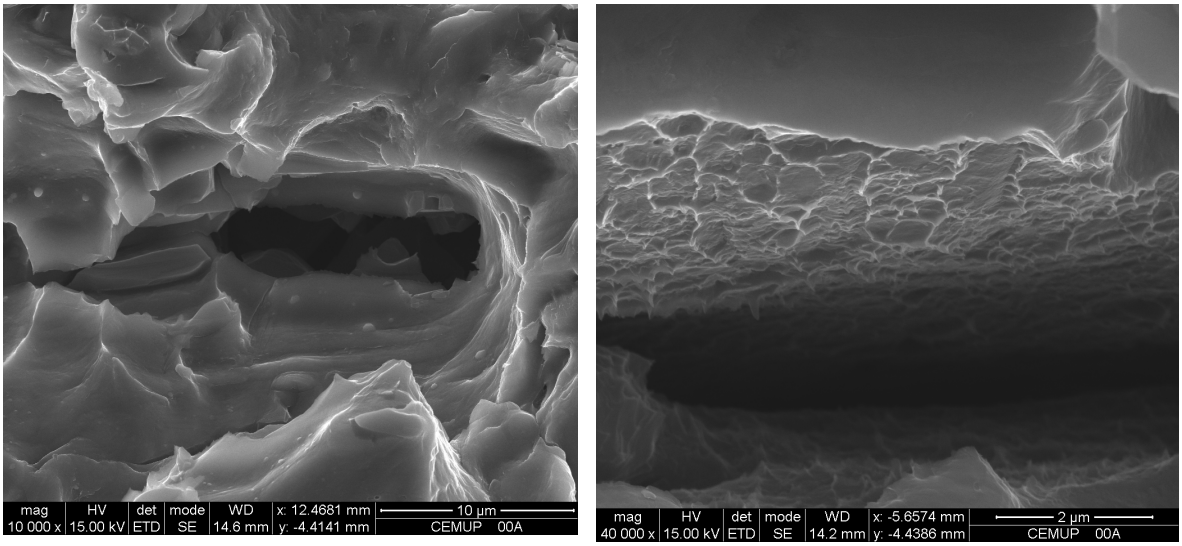


a) detail of a pore b) magnification of an horizontal fissure

**Figure 426 - Sample D fracture surface particular features.**

*6.3.3.2 Fatigue striations*

Fatigue striations measurements were performed in samples A, B and C. From sample A were analyzed 41 fractographs, from sample B 38 fractographs and from sample C 21 fractographs. Two examples of fractographs analyzed in sample C are presented in Figure 427. Fractographs were acquired at approximately the middle thickness plane. The first fractograph shows striations at $3mm$ from the initial notch and the second fractograph shows striations at $14mm$; the striations double their spacing.

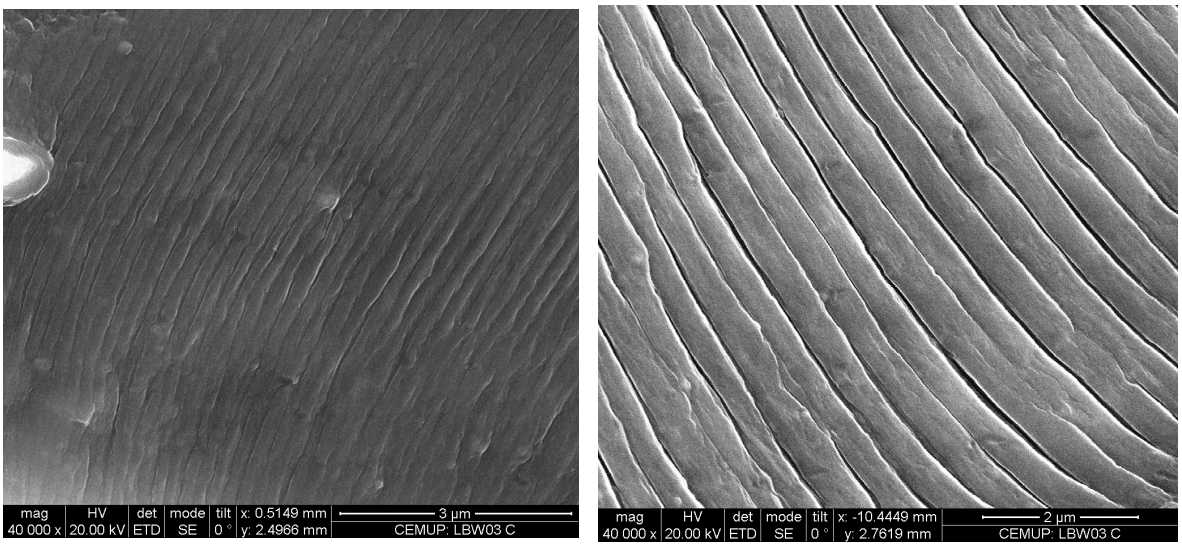


a) fractograph 6 of sample C, x=13,03$mm$, y=1,09$mm$, s=0,19$\mu m$ b) fractograph 20 of sample C, x=24,00$mm$, y=1,35$mm$, s=0,42$\mu m$

**Figure 427 - Fractographs showing striations in sample C.**

As an example of measurements performed in the stiffener, Figure 428 shows sites where fractographs were acquired. Along the base plate fractographs were acquired near the middle thickness plane.

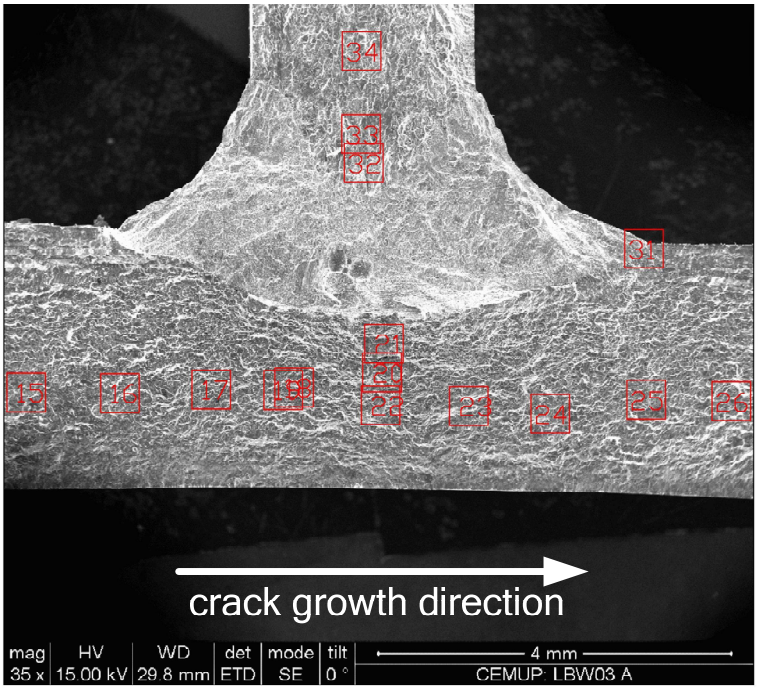


**Figure 428 - Fractographs sites near the stiffener root.**

Examples of fatigue striations before, under and after the stiffener are presented in Figure 429 a), b) and c). Comparing these fractographs it is possible to identify the increase in striation spacing before and after the stiffener. Also, striations throughout the stiffener are presented. in Figure 429 d)

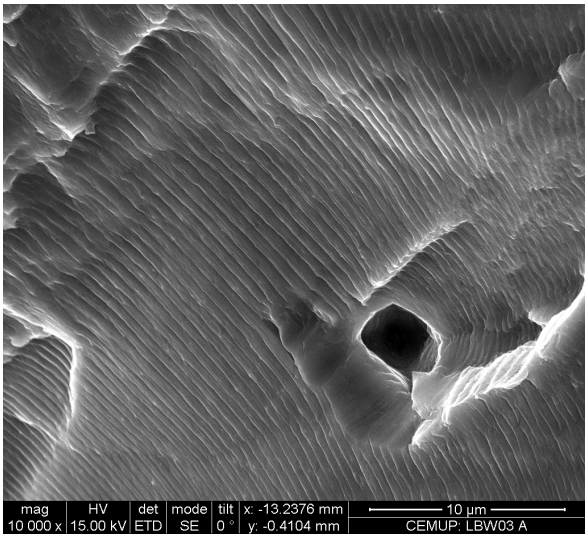


a) fractograph 15 of sample A, x=71,18$mm$, y=1,36$mm$, s=0,99$\mu m$

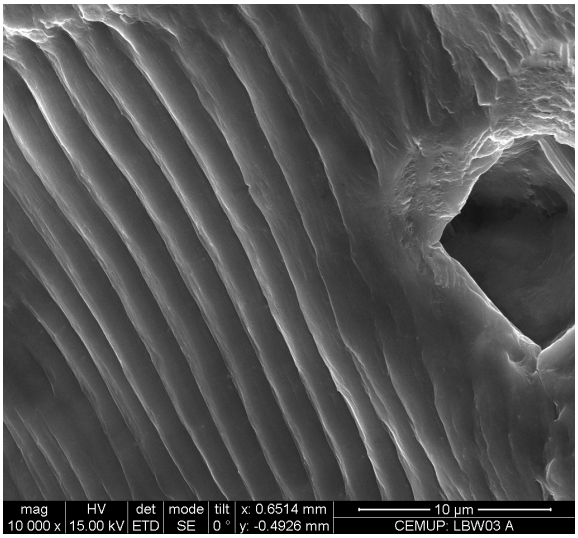


b) fractograph 22 of sample A, x=75,19$mm$, y=1,21mm, s=1,53$\mu m$

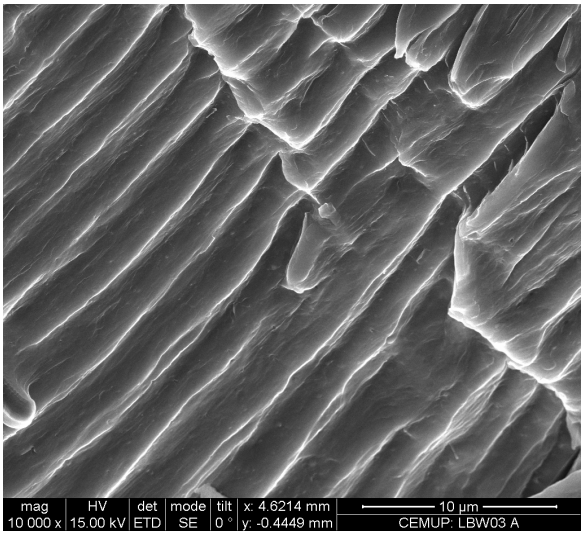


c) fractograph 26 of sample A, x=79,16$mm$, y=1,26$mm$, s=2,30$\mu m$

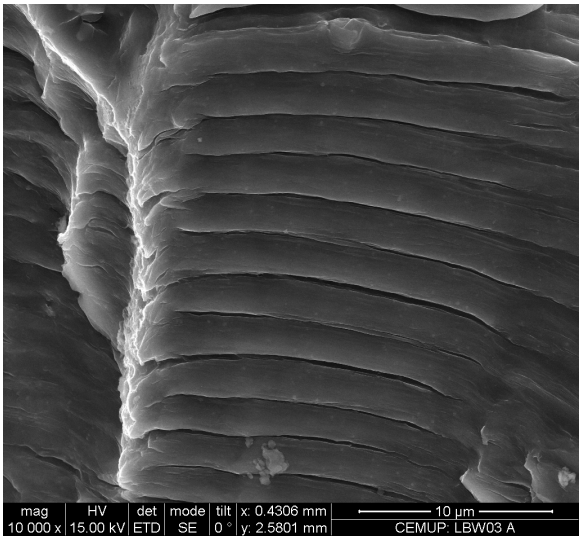


d) fractograph 33 of sample A, x=75,03$mm$, y=4,28$mm$, s=1,86$\mu m$

**Figure 429 - Fractographs showing striations in different positions around the stiffener.**

The final results of fatigue striations spacing measurements in the stiffener and in the specimen base plate are presented in Figure 430 and Figure 431. In Figure 430, despite some scatter, it is possible to see the increase in fatigue striation spacing throughout the stiffener length. In Figure 431, sample A, B and C fit together to give the history of striation spacing along the base plate. The striation spacing in the stiffener has values of the same magnitude of the ones found in base plate after the stiffener.

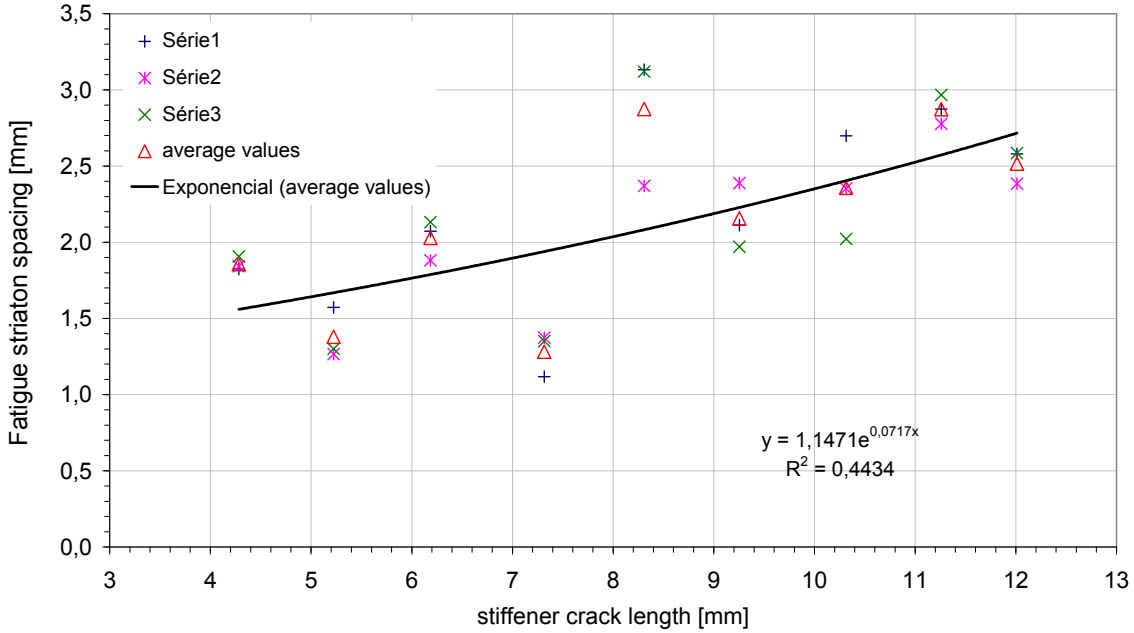


**Figure 430 - Fatigue striation spacing in the stiffener.**

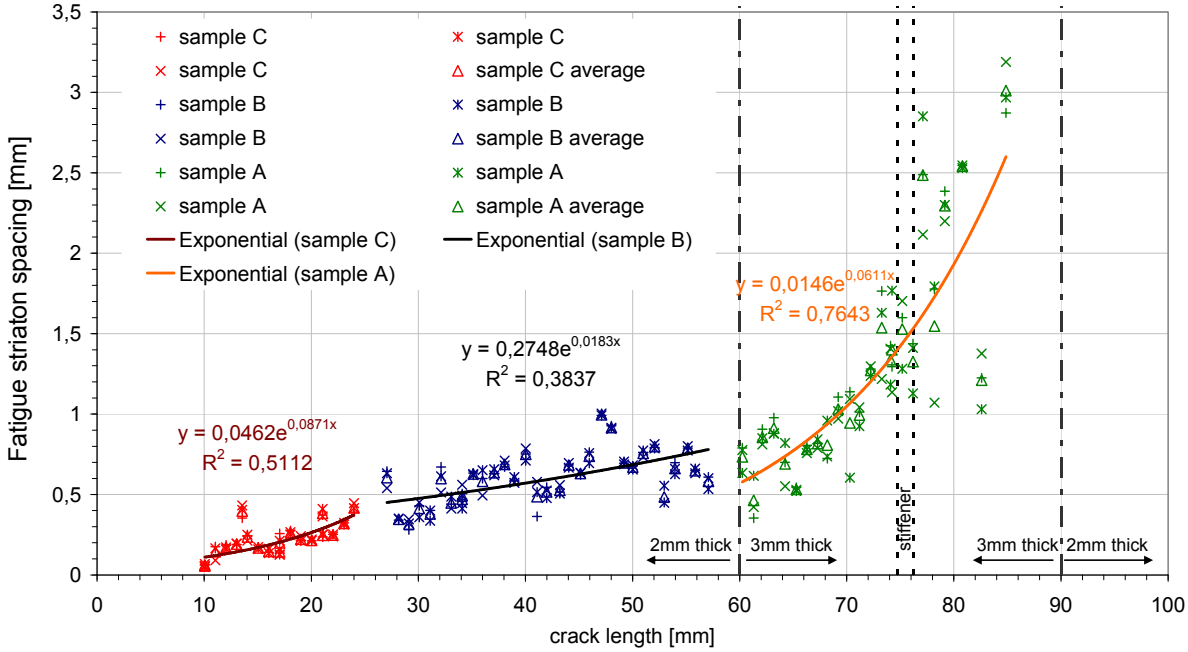


**Figure 431 - Fatigue striation spacing in the specimen base plate.**

### *6.3.4 LBW2 6056-T6 as-welded R=0,1 specimen (LBW07)*

The LBW2 6056-T6 as-welded specimen tested at R=0,1 was analyzed by SEM. Four samples, as presented in Figure 432, were analysed: samples A, B, D and E. Sample A includes the fatigue crack initiation and sample D includes the stiffener.

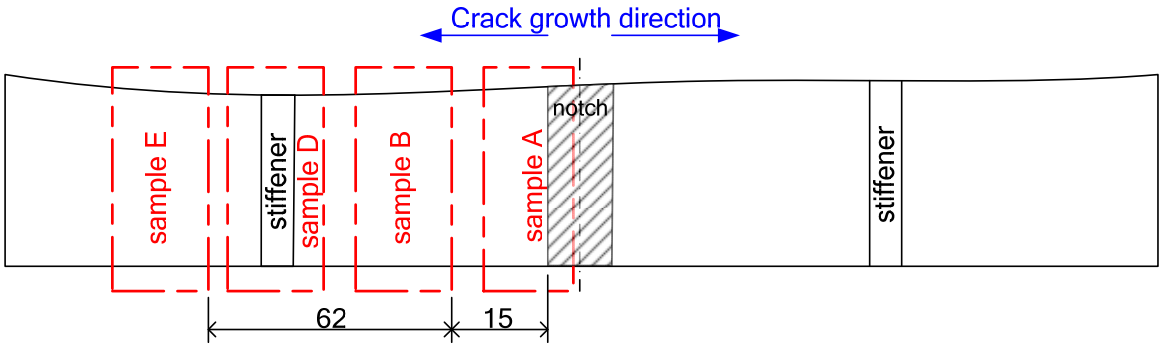


**Figure 432 - Sample location for SEM analysis of the LBW2 6056-T6 as-welded R=0,1 specimen.**

#### *6.3.4.1 Fracture surface features*

Figure 433 corresponds to the initial fatigue crack location, sample A. In this figure, at the left side, is seen the initial notch created by electro discharge machining and at the right side the initial fatigue crack. Dispersed pores were found in the fatigue crack area as demonstrated in Figure 434, which shows a fractograph at 7*mm* from the initial notch.

Figure 435 presents the fatigue crack surface of sample B where pores were identified.

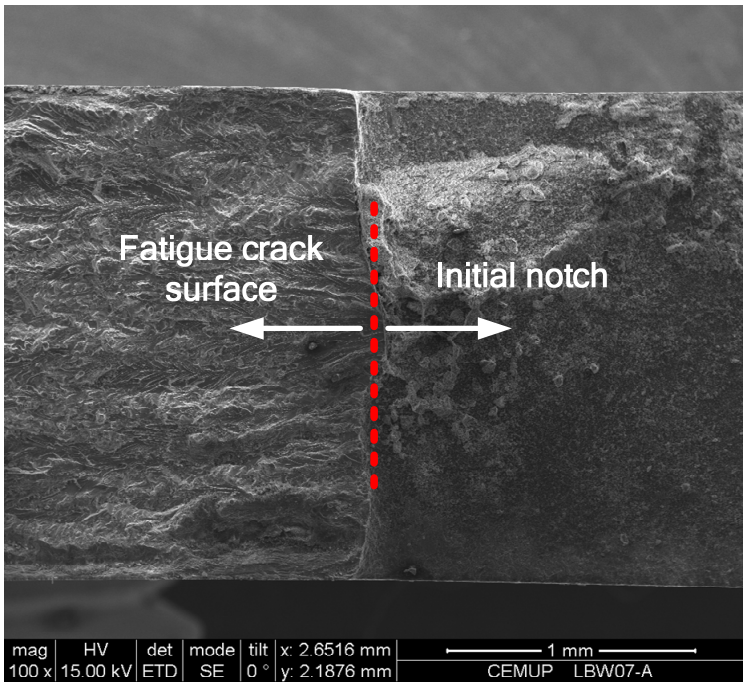


**Figure 433 - Initial site of the fatigue crack.**

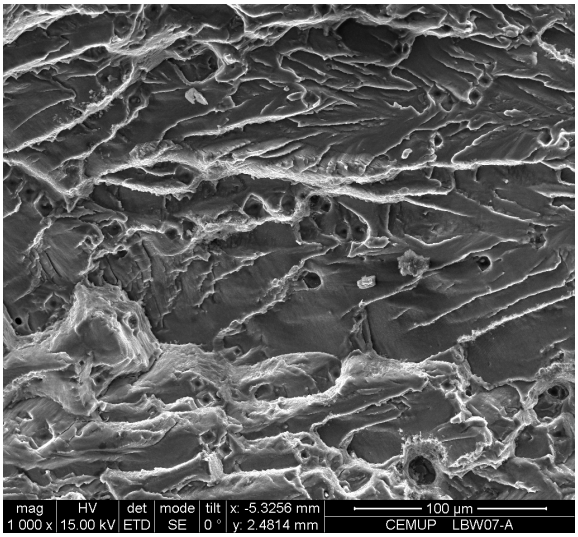


**Figure 434 - Pores disperse along the fatigue crack.**

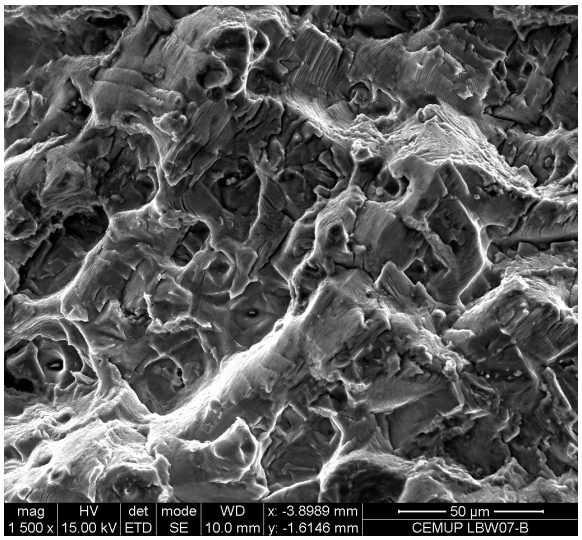


**Figure 435 - Sample B, fatigue crack surface.**

Sample D contains the laser beam welded stiffener. The T-joint macrograph is presented in Figure 436. This specimen was welded in the LBW2 configuration, butt joint.

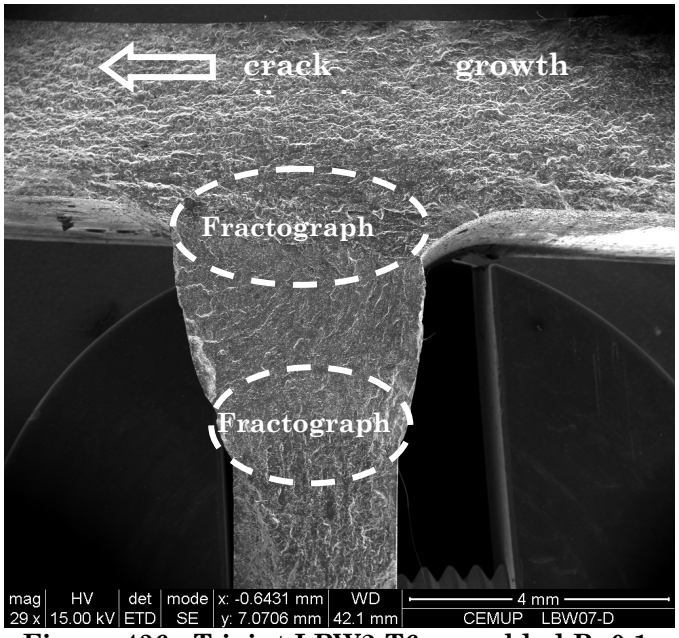


**Figure 436 - T-joint LBW2-T6 as-welded R=0,1.**

Figure 437a), fractograph 18, shows the configuration of the fatigue crack surface just after the stiffener. The transition between the stiffener and the base plate is presented in Figure 437b). A fissure along the transition between the two surfaces was identified.

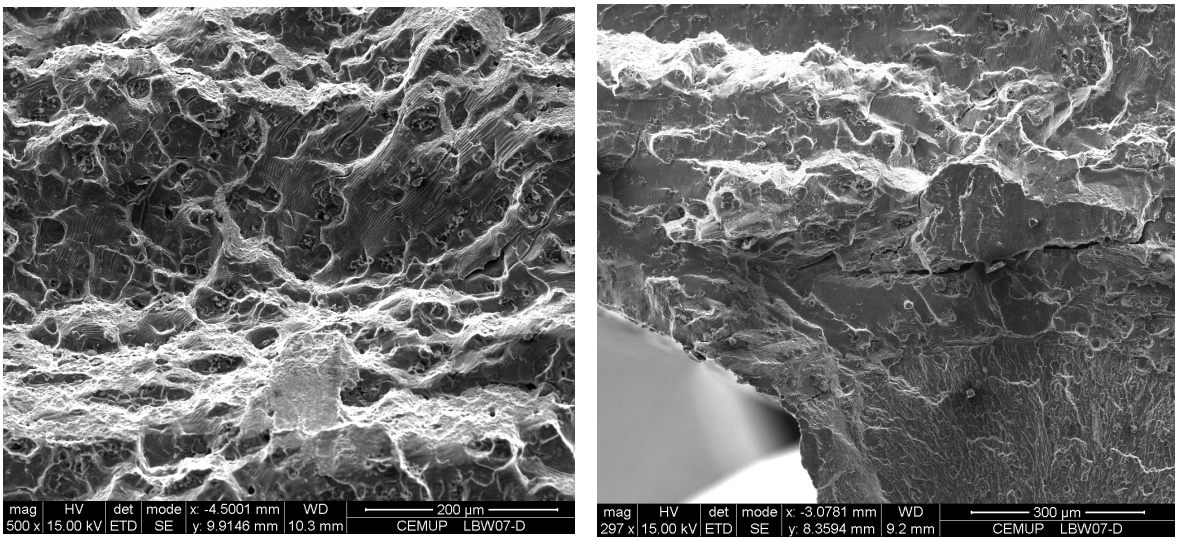


a) fractograph 18 b) fractograph 30

**Figure 437 - Details of the stiffened area.**

The analysis of the two weld bead limits was analysed using fractographs 27 and 29, Figure 438a) and Figure 439a) respectively. Fractograph 27 corresponds to the weld bead limit located near the specimen plate. Fissures were found in this limit of the weld bead. A detail of these features and some pores located in the area of fractograph 27 are presented in Figure 438b).

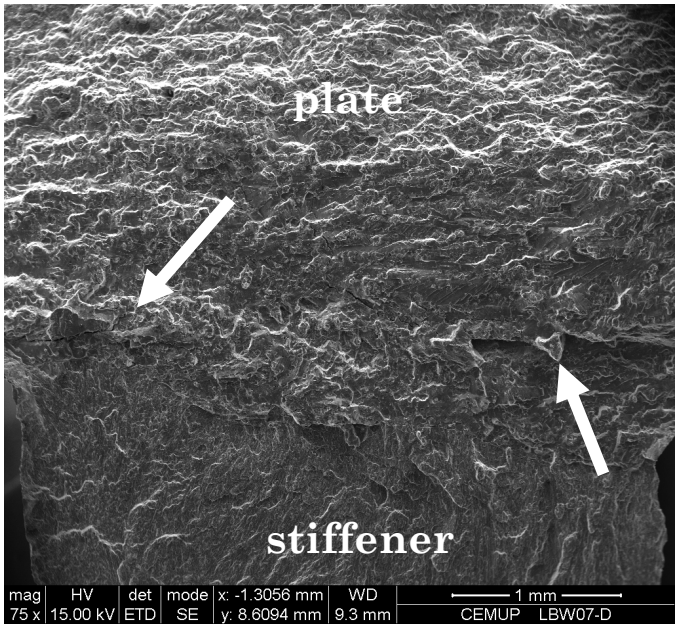


a) fractograph 27

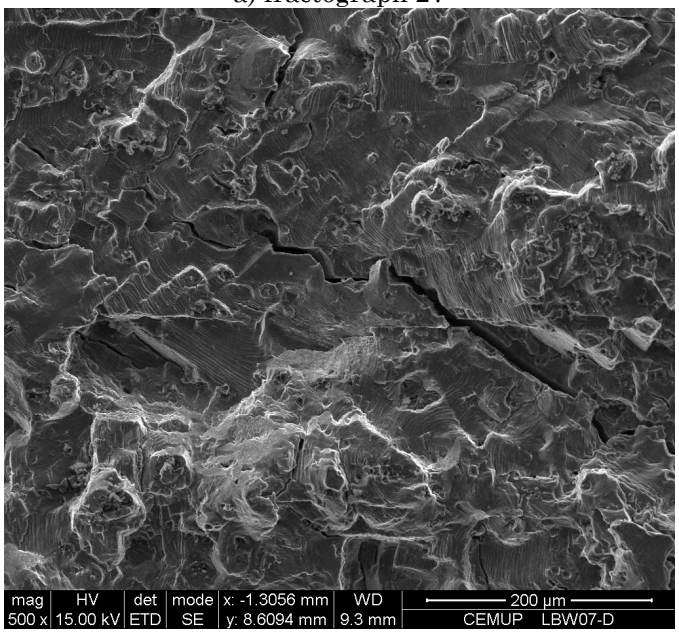


b) fractograph 28

**Figure 438 - Weld bead limit near the specimen plate.**

Figure 439a) shows the other weld bead limit, located only at the stiffener. In this site no fissures or cracks were identified. A detail of this weld bead limit is presented in Figure 439b) where the transition from the melted material to the un-melted material is easily identified.

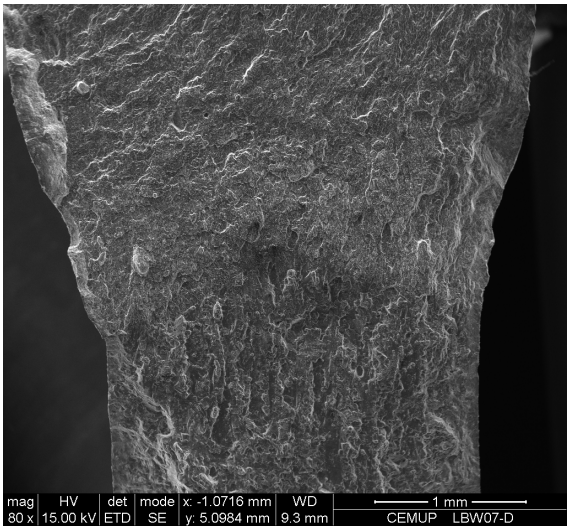


a) fractograph 29

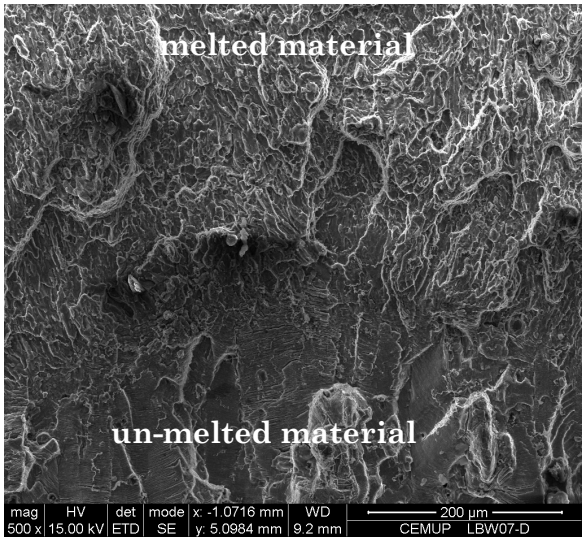


b) fractograph 30

**Figure 439 - Weld bead limit located at the stiffener.**

In sample E, located at 82*mm* from the specimen middle line, it was not possible to identify measurable striations. As an example, fractograph 12 shows this fatigue crack surface, Figure 440.

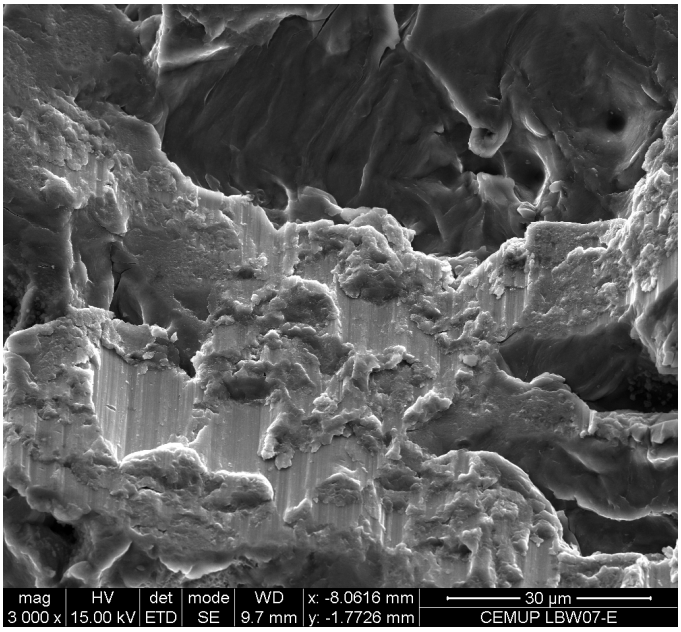


**Figure 440 - Sample E fracture surface, fractograph 12.**

*6.3.4.2 Fatigue striations*

Fatigue striations measurements were performed in samples A, B and D. From sample A were analyzed 18 fractographs, from sample B 34 fractographs and from sample D 40 fractographs. An example of fractographs analyzed in sample A and B are presented in Figure 441. Fractographs were acquired near the middle

thickness plane. The first fractograph shows striations at 19$mm$ from the initial notch and the second fractograph shows striations at 32$mm$.

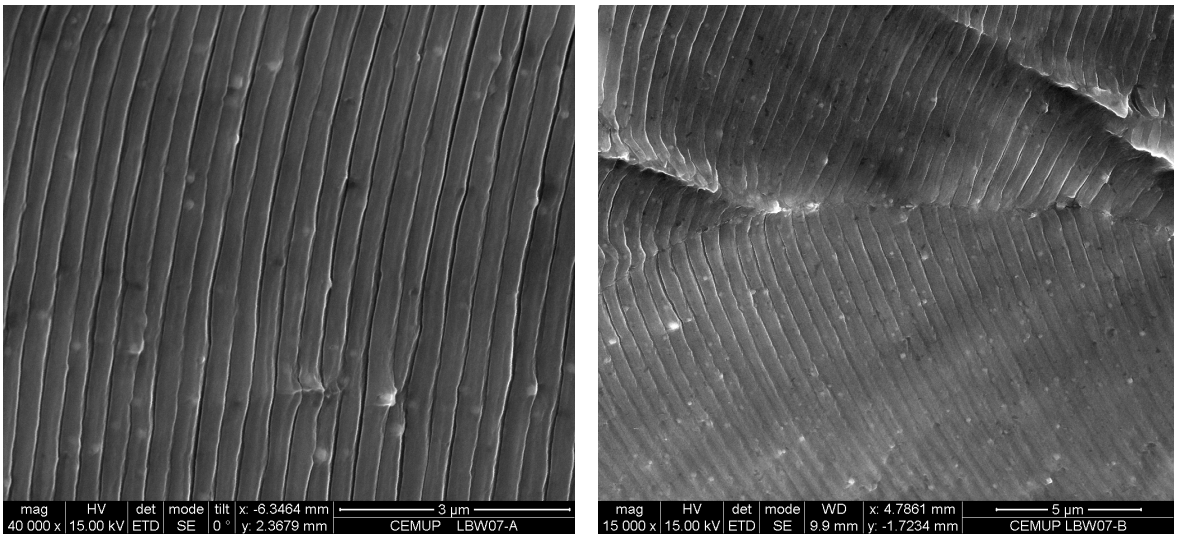


a) fractograph 13 of sample A, x=19,00$mm$, y=1,18$mm$, s=0,29$\mu m$

b) fractograph 9 of sample B, x=32,66$mm$, y=0,83$mm$, s=0,51$\mu m$

**Figure 441 - Fractographs showing striations in samples A and B.**

Examples of fatigue striations before, under and after the stiffener are presented in Figure 442 a) and b). Comparing these fractographs it is possible to identify the increase in striation spacing before and after the stiffener.

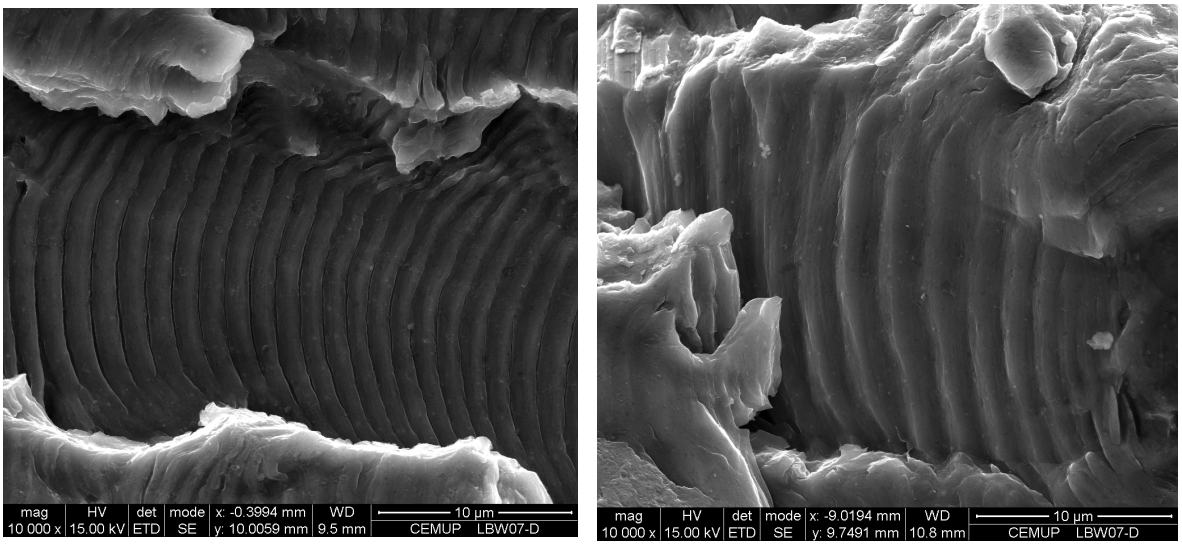


a) fractograph 12 of sample A, x=74,40$mm$, y=1,62$mm$, s=1,21$\mu m$

b) fractograph 24 of sample A, x=83,01$mm$, y=1,36$mm$, s=1,79$\mu m$

**Figure 442 - Fractographs showing striations in different positions around the stiffener.**

The final results of fatigue striations spacing measurements along the stiffener and along the specimen base plate are presented in Figure 443 and Figure 444. Each plot was successfully fitted by an exponential equation. In Figure 443 it is possible to identify the increase in fatigue striation spacing throughout the

stiffener length. Samples A, B and D fit together to give the history of striation spacing along the base plate as the crack grows, Figure 444,.

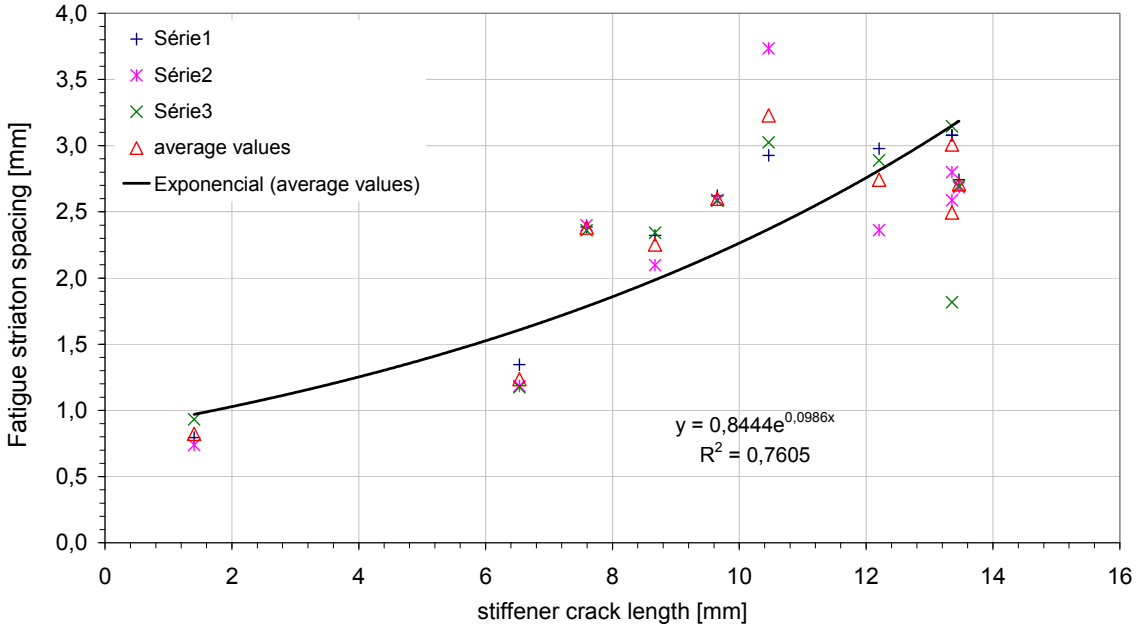


**Figure 443 - Fatigue striation spacing along the stiffener.**

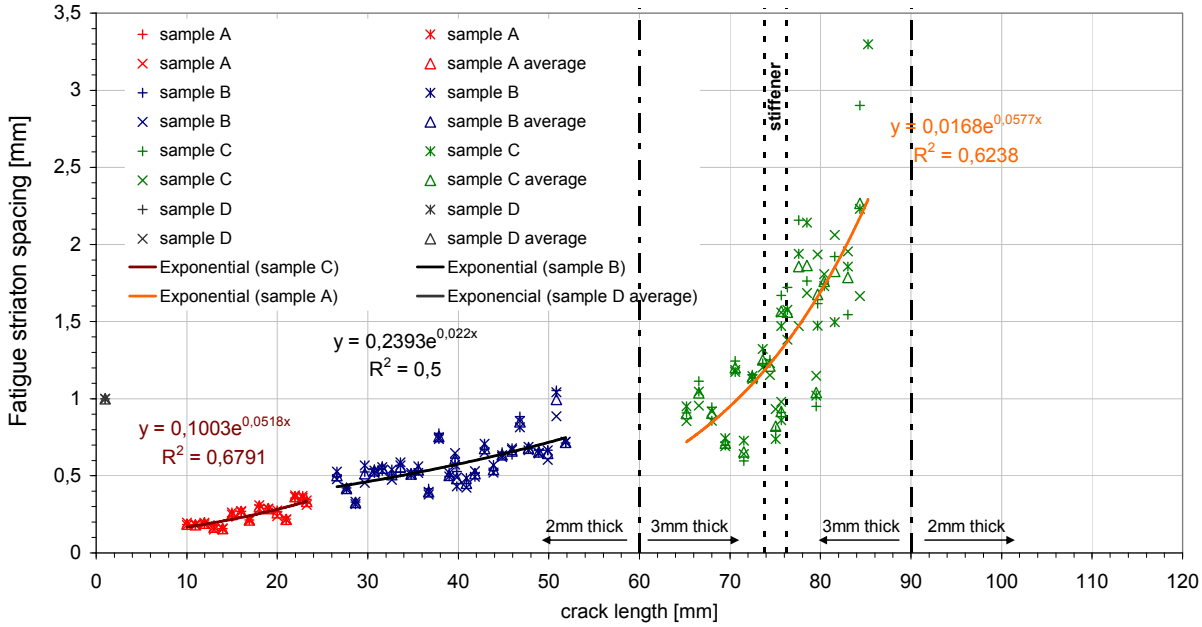


**Figure 444 - Fatigue striation spacing along the specimen base plate.**

### *6.3.5 FSW 6056-T4 PWHT-T6 R=0,1 specimen (FSW09)*

The FSW 6056-T4 PWHT-T6 specimen tested at R=0,1 was analyzed by SEM. Four samples, as presented in Figure 445, were analysed: samples A, B, C and D.

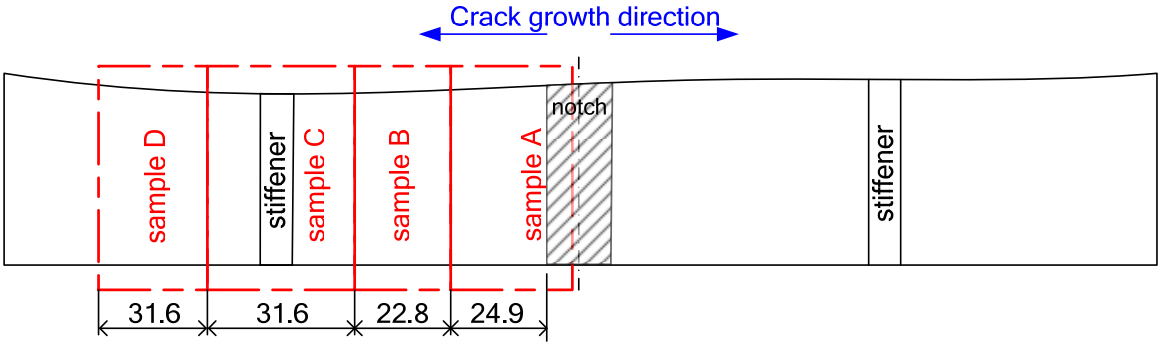


**Figure 445 - Sample location for SEM analysis of the FSW 6056 PWHT-T6 R=0,1 specimen.**

*6.3.5.1 Fracture surface features*

Figure 446 corresponds to the initial fatigue crack location, sample A.

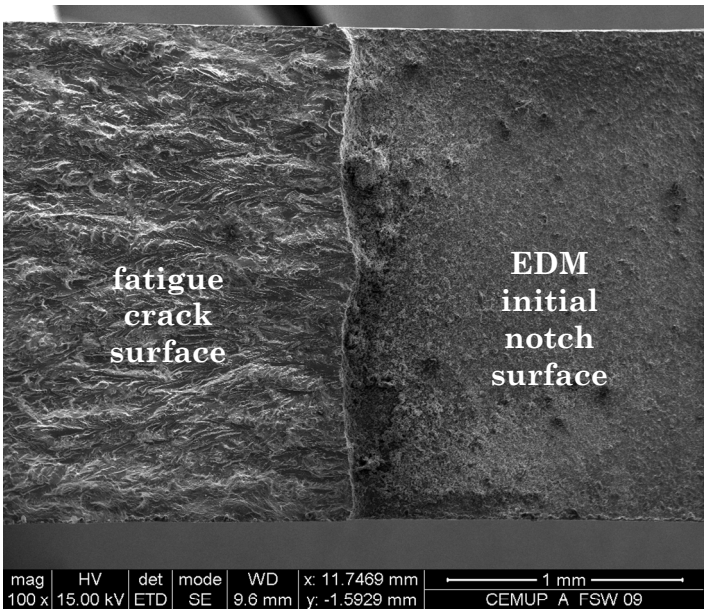


**Figure 446 - Initial site of the fatigue crack, sample A.**

Sample C contains the friction stir welded stiffener. The T-joint macrograph is presented in Figure 447.

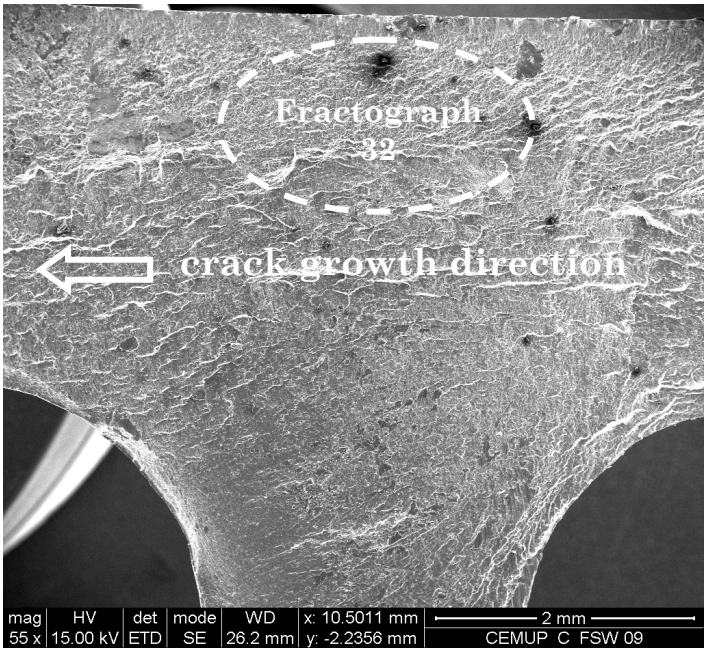


**Figure 447 - T-joint FSW 6056 PWHT-T6 R=0,1.**

Figure 448a), fractograph 32, shows the configuration of the fatigue crack surface above the surface where the shoulder is supported during welding. This zone corresponds to the TMAZ, a zone where the material was stirred by the movement of the pin and the shoulder. A detail of this surface is presented in Figure 448b) (fractograph 33) where a rough surface is identified.

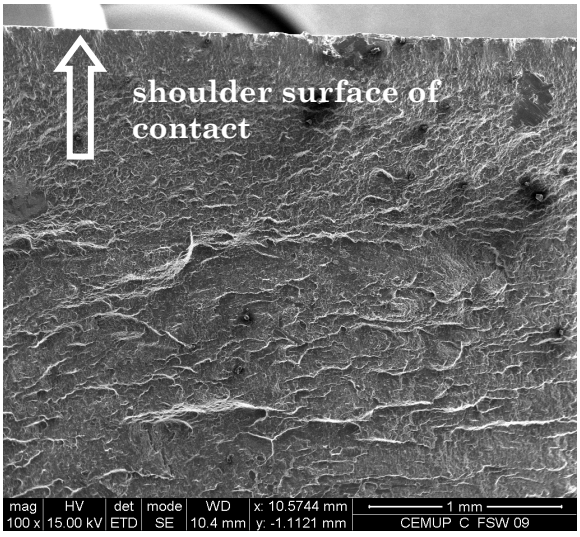


a) fractograph 32

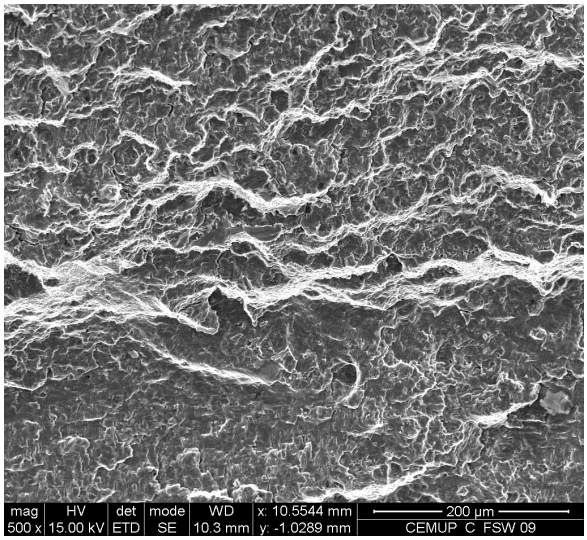


b) fractograph 33

**Figure 448 - Details of the stiffened area, TMAZ.**

The fracture surface outside the thermomechanically affected zone, before the crack reach the stiffener, is presented in Figure 449, fractograph 34. Comparing this fractograph and the one presented in Figure 448b), it is seen that outside the weld affected area the fracture shows a more regular structure. This difference

was reflected in the striation identification process; it was harder to perform the analysis under the shoulder limits.

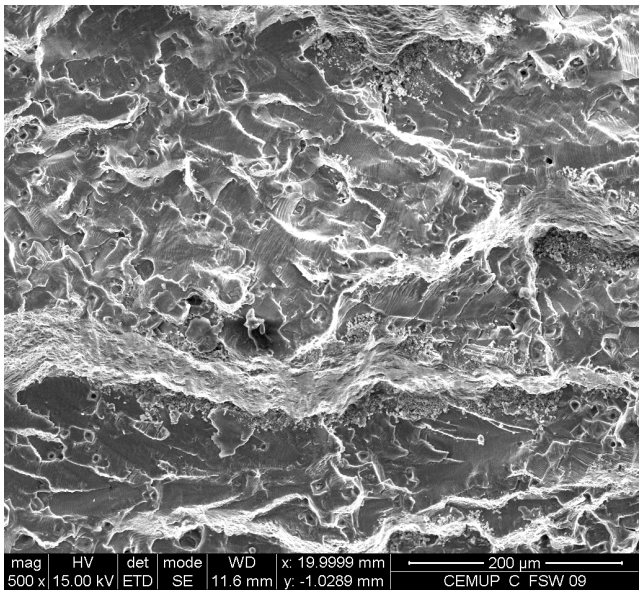


**Figure 449 - Fracture surface outside the TMAZ, fractograph 34.**

Figure 450 shows the surface of the transition to the stiffener. In this figure is clearly identified a zone which is expected to correspond to the limit of the thermomechanically affected zone. In this zone inside the stiffener, which should be related to the pin height, a change in the fracture surface occurs. Also, this limit indicates where striation could be identified. The different areas are presented in detail in Figure 451. The upper zone of the fractograph shows a heterogenic area where striation were of difficult identification. In the lower zone of the fractograph measurable striations were identified.

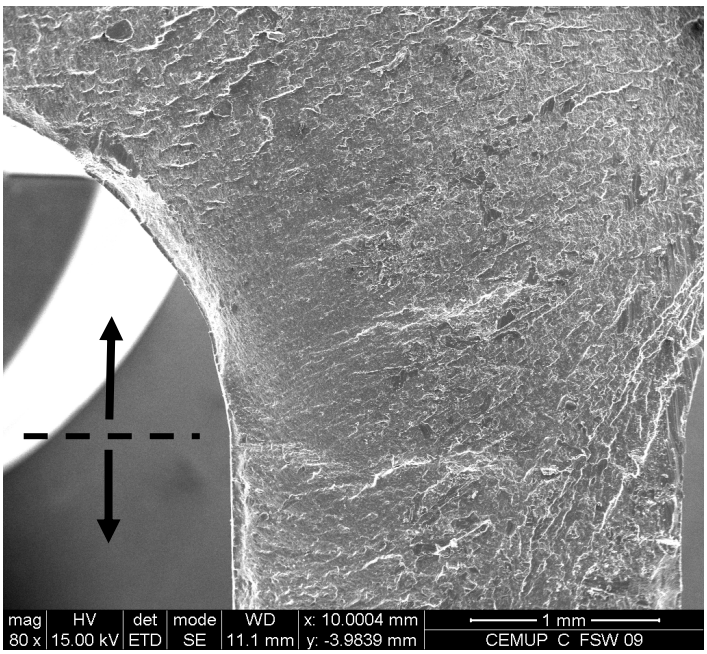


**Figure 450 - Stiffener surface, fractograph 35.**

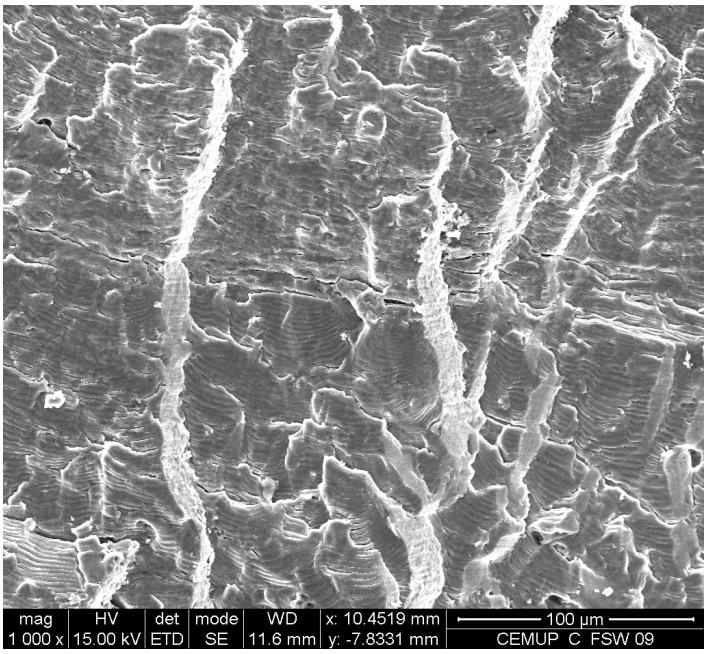


**Figure 451 - Stiffener surface detail, fractograph 40.**

*6.3.5.2 Fatigue striations*

Fatigue striations measurements were performed in samples A, B and C. From sample A were analyzed 19 fractographs, from sample B 24 fractographs and from sample C 48 fractographs. Examples of fractographs analyzed in sample A are presented in Figure 452. Fractographs were acquired near the middle thickness plane.

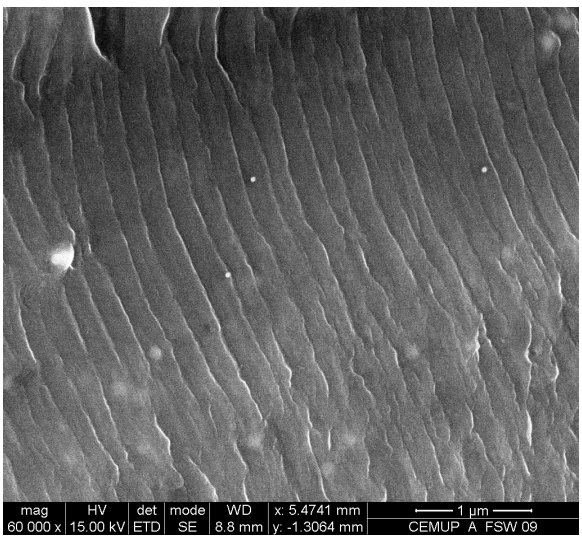


a) fractograph 7 of sample A, x=16,28$mm$, y=1,29$mm$, s=0,20$\mu m$

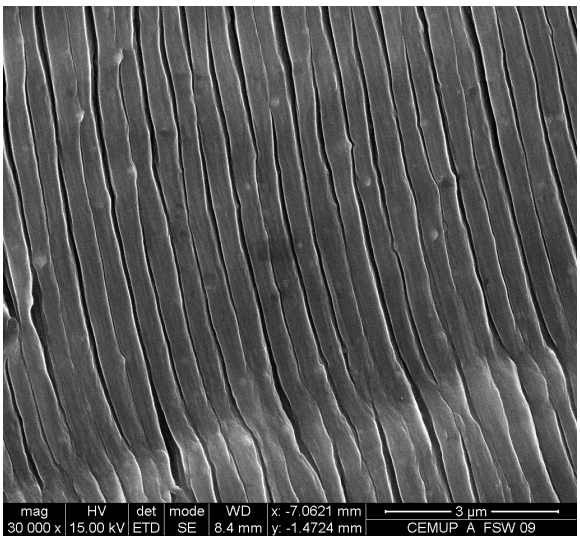


b) fractograph 9 of sample A, x=28,81$mm$, y=1,12$mm$, s=0,40$\mu m$

**Figure 452 - Fractographs showing striations in sample A.**

Examples of fatigue striations before and after the stiffener are presented in Figure 453. Comparing these fractographs it is possible to identify the increase in striation spacing before and after the stiffener.

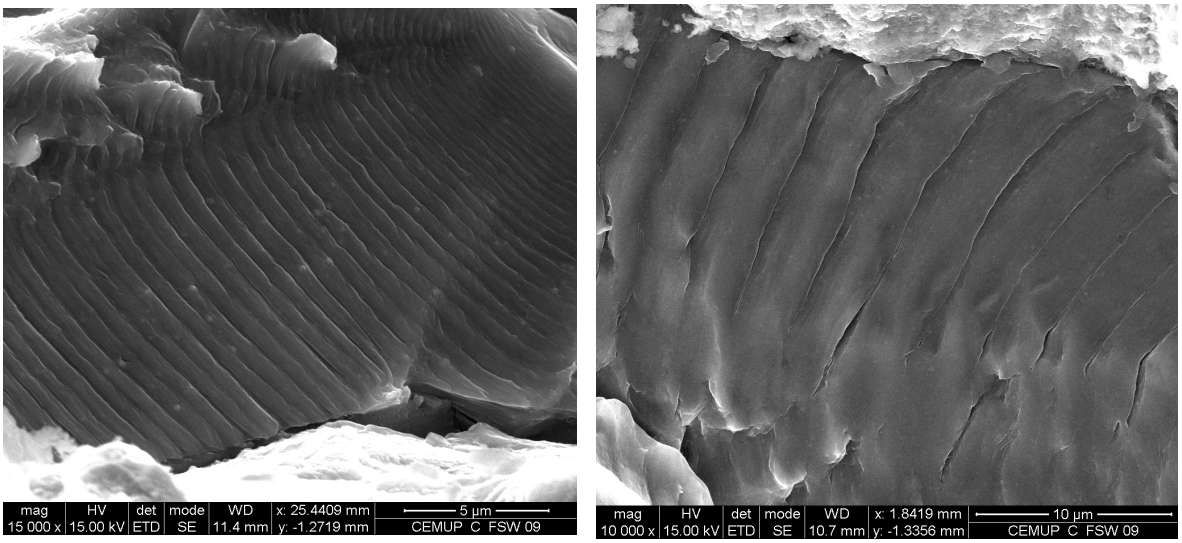


a) fractograph 2 of sample C, x=60,22$mm$, y=0,84m$m$, s=0,54$\mu m$

b) fractograph 27 of sample C, x=83,82$mm$, y=0,77$mm$, s=2,80$\mu m$

**Figure 453 - Fractographs showing striations on the skin before (fractograph 2) and after (fractograph 27) the stiffener.**

The striation measurement process was difficult to be carried out in the zone affected by the welding process. The configuration of striations that were found in this area is presented in Figure 454.

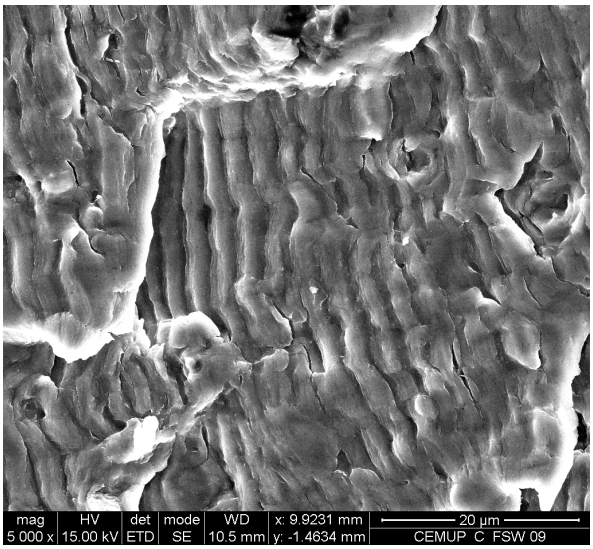


**Figure 454 - Fractograph showing striations in the weld affected area, x=75,74 y=0,65, s=2,11µm.**

In the stiffener different type of striations were found before and after the weld affected zone, as presented in Figure 455. Fractograph 38 presents the weld affected area and fractograph 43 was acquired outside the weld affected area.

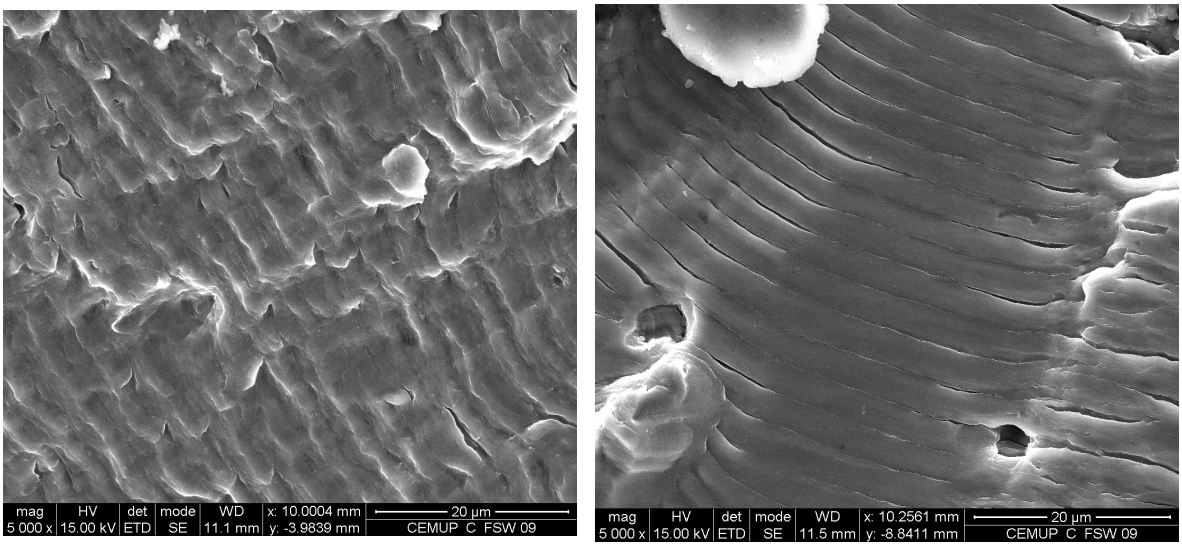


a) fractograph 38 of sample C, x=75,36$mm$, y=5,73$mm$, s=2,88$\mu m$

b) fractograph 43 of sample C, x=75,41$mm$, y=8,73$mm$, s=2,96$\mu m$

**Figure 455 - Fractographs showing striations before (fractograph 38) and after (fractograph 43) the weld affected zone in the stiffener.**

The final results of fatigue striations spacing measurements along the stiffener and the specimen base plate are presented in Figure 456 and Figure 457.

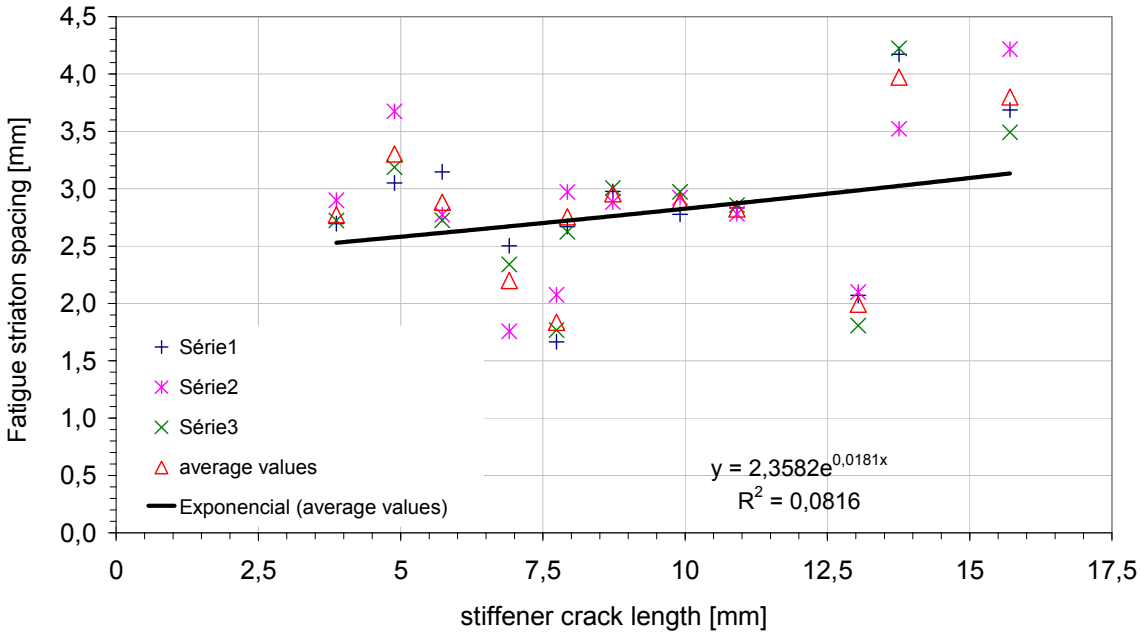


**Figure 456 - Fatigue striation spacing along the stiffener.**

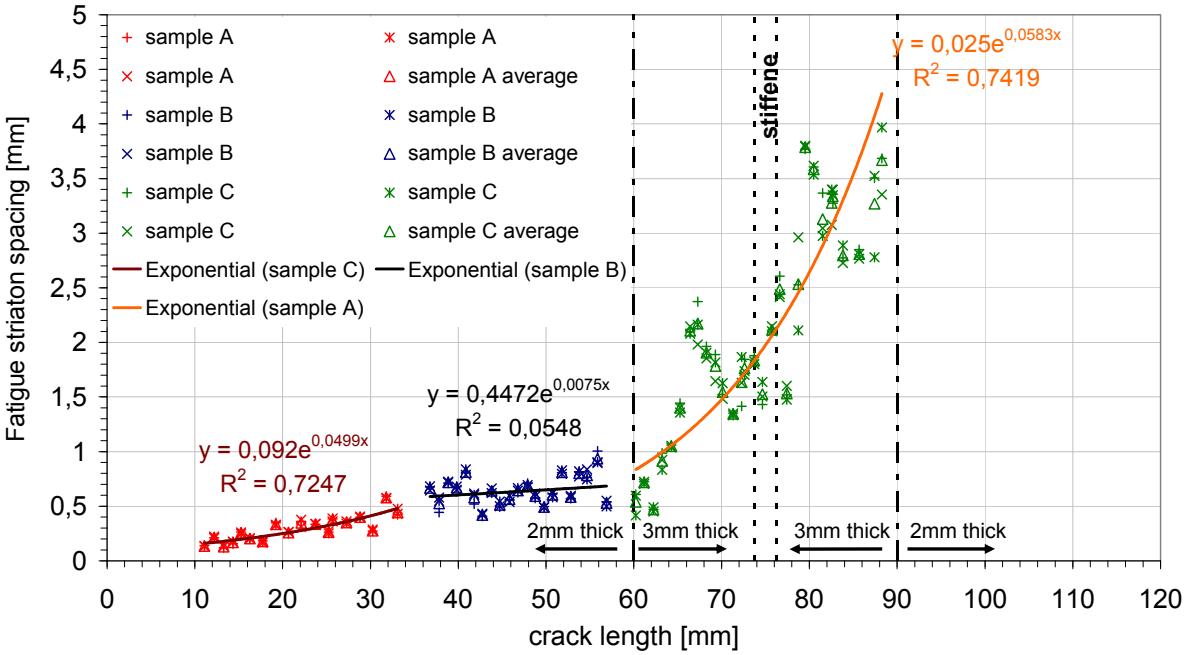


**Figure 457 - Fatigue striation spacing along the specimen base plate.**

### *6.3.6 Concluding remarks*

Two HSM, two LBW and one FSW panels were analysed by scanning electron microscopy. Striations measurements were carried out throughout the fractured surface, and particular features as weld defects were characterized. Measurements of fatigue striations were performed considering the middle specimen as the measurement origin and several values were obtained through the crack length. The fatigue crack growth rate can be estimated using these measurements.

In the HSM panels internal fissures and some pores were observed along the fatigue crack. In this type of specimens the surface presents a rough finishing and some impurities are also present.

In the LBW panels, at the centre of the weld, pores with a maximum diameter of approximately 0,24$mm$ were identified. These pores seem to be coincident with the laser maximum penetration depth from each side of the T-joint. In the transition area between the melted and un-melted material cracks out of the weld bead were identified. This zone, just outside of the weld bead, was heated during welding and these cracks were probably formed during the cooling process.
In these specimens it was verified that the weld had full penetration. In the area above the transition line it was not possible to identify fatigue striations.

In the FSW panels it is verified that outside the weld affected area the fracture shows a more regular structure than in the weld affected area. This difference was reflected in the striation identification process; it was harder to perform the

analysis under the shoulder limits. In the thermomechanically affected zone, inside the stiffener, a change in the fracture surface occurs.

### 6.4 Conclusions

Mechanically fastened panels are desirable in terms of fail-safety criterion since the stringers are effective crack stoppers. However, whereas riveted stiffeners continue to limit crack growth after the crack propagates past the stiffener, the effect of a welded or integral stiffener is quite different, since the crack may propagate directly into an integral stiffener and completely break it.

As a result of this work:

- The stress intensity factor calibration of the DaToN stiffened panel geometry was obtained using the VCCT technique in conjunction with a finite element model. The resulting stress intensity factor solutions for both skin and stiffener, used with the Paris law, gave adequate predictions of experimental crack propagation behaviour in HSM DaToN panels.

- When fatigue testing the DaToN stiffened panels it was found that, although when cracks approach the stiffeners the stress intensity factor decreases, there is no clear slowing down of the crack propagation.
- A systematic study of the stiffener cross section versus skin cross section area ratio should be carried out in order to identify its optimum value, since the slowing down effect of the stiffeners evident in previous AIRBUS work was not displayed in the present tests, and a major difference between both specimens concerns precisely that ratio.
- Welded panels presented longer lives up to rupture, implying that during most of their fatigue testing the crack growth rates were smaller than with HSM panels. This somewhat unexpected result is certainly associated to the residual stress fields existing in the welded panels, and also to the location of the initial artificial defect, placed in the skin precisely in the middle distance between the two stiffeners.
- The X-ray measurements at the University of Coimbra did not give a sufficiently clear result of residual stress distribution usable with confidence for modelling purposes.

- In the HSM panels internal fissures and some pores were observed along the fatigue crack. In this type of specimens the surface presents a rough finishing and some impurities are also present.
- In the LBW panels, at the centre of the weld, pores with a maximum diameter of approximately $0{,}24mm$ were identified. These pores seem to be coincident with the laser maximum penetration depth from each side of the

T-joint. In the transition area between the melted and un-melted material cracks out of the weld bead were identified. In these specimens it was verified that the weld had full penetration.

- In the FSW panels it is verified that outside the weld affected area the fracture shows a more regular structure than in the weld affected area. This difference was reflected in the striation identification process; it was harder to perform the analysis under the shoulder limits. In the thermomechanically affected zone, inside the stiffener, a change in the fracture surface occurs.

# Chapter 7

# Conclusions and future work

The seventh Chapter of this thesis presents the major achievements and suggestions for future and complementary work.

# 7. Conclusions and future work

## 7.1 Conclusions

In order to allow the industry to use novel manufacturing techniques as Laser Beam Welding and Friction Stir Welding, which promise high efficiency but still lack dedicated research, this thesis aims to contribute to the assessment of the mechanical behaviour of joints manufactured using such new tools. These techniques lead to a type of structure which is close to an integral structural design. This design offers benefits, *e.g.* from the cost point of view, but quite some concerns from the damage tolerance behaviour, crucial point in the application of the new techniques, which today limit their application. In this study a contribution to fundamental knowledge and assessment for damage tolerance of modern structures manufactured using novel techniques as laser beam welded and friction stir welded was provided.

Since heat generation is a fundamental aspect of any welding technique, an effective temperature measurement procedure that could be applied to any welding process was developed. As a basis for the development of an accurate temperature measurement procedure an aggressive and well known welding method was used, Gas Metal Arc Welding. A technique using fibre Bragg grating sensors was introduced and developed. Three different temperature acquisition systems during GMAW welding were analysed: thermocouples, thermography and fibre Bragg grating sensors. Weldments were deposited on 500×300$mm$ and 10$mm$ thick aluminium alloy 6082-T6 plates. When analysing the use of thermocouples for temperature measurements during MIG welding it was found that the best results were achieved with the 0,08$mm$ diameter thermocouples with their junction covered by thin cyanoacrylate glue clad to insulate electrically the thermocouples from the plate. In this set of tests a comparison between maximum temperatures in each point acquired with thermography and thermocouples showed a good agreement between both techniques. Also, FBG sensors protected with cyanoacrylate glue, with stripes of aluminium foil covering each sensor, and a silicon based compound were able to maintain integrity of measurement at a distance of 15$mm$ in the perpendicular direction to the weld line. With the silicon based compound this distance could reach 10$mm$. The results obtained suggest the possibility to use this new type of sensors to acquire

temperature values in the aggressive conditions found in the arc weld side of the plate. Temperature profiles were also measured in plates welded by three different welding techniques: MIG, LBW and FSW. Despite the differences in the boundary constraints the MIG welding presented the higher temperature profile, and the FSW and LBW present lower and similar temperatures.

Residual stresses are locked-in stresses which exist in a structural part without the application of any service or other external loads. Residual stresses are created due to mechanically induced plasticity or by thermal effect which arise from a production process as welding. For MIG welded plates a quantitative estimation of such residual stresses field was performed. A comparative study of several residual stress measuring techniques - sectioning, hole drilling and X-ray diffraction techniques - was performed. Measurements with the hole drilling technique acquired at $0{,}3mm$ depth are in agreement with the values obtained using the sectioning method. It was verified that the sectioning method does not give the residual stress values just at the surface, but it gives an average measurement of a thin layer of material. The X-ray diffraction revealed to be a procedure not easily applied in welded aluminium plates, because high scatter was found making it difficult the evaluation of the true residual stress profile. When comparing the results obtained in this work with measurements obtained with the contour method previously reported, it was found that outside the weldment area, the results obtained with all methods are in good agreement. It was also verified that the stress profile measured with the contour method at half the plate depth is in between of results obtained with the sectioning method for each plate surface.

The study of the mechanical behaviour of Friction Stir Welded and Laser Beam Welded butt joints was presented in three different parts.
Since friction stir welded components can include notches in the weldment due to design constraints, in a first study the effect of notches on friction stir weldments was investigated. This study quantifies the influence of the FSW process on the fatigue life of the aluminium alloy 6063-T6 notched specimens. Base materials and welded specimens were fatigue tested under load control at several stress levels. It was found that hardness drastically decreases in the thermo-mechanically affected zone and the yield stress and rupture stress of friction stir welded specimens presented lower values than un-welded specimens. The most important observation in this work consisted of the longer fatigue lives of welded specimens, for all stress levels, even at the maximum stress level used, above the friction stir welded specimens yield stress. As a result of a finite element analysis of the fatigue specimens it was found that that for all remote stress levels the notch stress concentration effect is more intense in the un-welded specimens, due to an earlier plastification of the area surrounding the notch. A scanning electron microscopy analysis was performed and welding defects were identified but during testing it was observed that they did not influence the joint mechanical behaviour
In the second study an experimental characterization and computational modelling analysis of dissimilar friction stir welded butt joints performed between aluminium alloys 6061-T6 and 6082-T6 was carried out. The friction stir welded

aluminium 6082-T6 material revealed lower yield and ultimate stresses, and the dissimilar joints displayed intermediate properties. Also, the hardness profile of the dissimilar joint presents the lowest values of all joints in the aluminium 6082-T6 alloy plate side where rupture occurred. Nevertheless in the nugget all three joints present similar values. In the microstructure analysis of the dissimilar joint the mixture of the two alloys was easily identified by the different etching response of both alloys. Bending tests, not yet reported on the literature in this context, were performed using a finite element model of the bending test that successfully simulated the tests carried out, up to approximately maximum load. Residual stress profile was measured by a destructive process and compressive values were found in the plate weld surface. Maximum residual stress values occurred at the root surface.
In the third study, using the aluminium alloys 6061-T6 and 6082-T6, the fatigue behaviour of both base materials and joints made using a traditional process, Metal Inert Gas welding, and two novel processes, Laser Beam and Friction Stir Welding, was carried out. All welding processes lead to a decrease of the material mechanical properties, more pronounced in the MIG specimens. Also, detailed hardness examination revealed lower hardness values in the MIG welded specimens. The study carried out revealed that when compared with the friction stir welds and MIG welds, the laser beam welds presented the smaller area affected by the welding process. In fatigue tests the friction stir welded 6061-T6 specimens presented lower lives than the friction stir 6082-T6 specimens when tested at stresses lower than 130*MPa*. The MIG welded specimens fatigue lives were lower than friction stir welded specimen. The LBW specimens were the ones that performed better in the fatigue tests. In the fatigue crack growth propagation tests it was verified that an increase of the crack propagation resistance occurs when a crack propagates in the welded material.

The numerical investigations of cracked structures feature both two- and three-dimensional analyses. In two-dimensional structural analyses, plane strain is commonly assumed where deformation is highly constrained, and plane stress is used for thin plates.
As a contribution to the understanding of three-dimensional effects, the influence of specimen geometry and mesh refinement on the stress intensity factor values through the thickness of centre cracked plates were analysed. Detailed three-dimensional finite element analyses of cracked plates were conducted in order to characterize the near-tip stress field and to determine the variation of the stress intensity factor through the thickness of the plate. It was verified that the stress intensity factor varies over the thickness and present lower values in a layer of material very close to the surface. A boundary layer exists near the plate free surface and its size is a function of thickness/crack length ratio. The best agreement with the reference two-dimensional values was obtained for the middle layer. The stress $\sigma_y$ remains almost constant through the thickness except near the free surface where an important decrease can be noticed in the vicinity of the crack front. This behaviour is not noticed far from the crack front, where the opening stress is constant and tends to the applied remote stress. The plane strain behaviour near the middle of the plate was demonstrated by calculating the degree of plane strain. It was also shown that the degree of plane strain tends

to smaller values when the distance from the crack front increases. Plane strain behaviour occurs at and near the middle of the plate, where a degree of plane strain near unity was obtained.
A very refined three-dimensional finite element analysis was performed in order to calibrate the stress intensity factors for a symmetrically stiffened plate subjected to uniform tensile stress. Cracks that could develop in such a structure were assessed by considering the case of a crack that crosses one of the stiffeners in two possible scenarios: *i.* the stiffener crossed by the crack is unbroken; and *ii.* the stiffener is broken. Three-dimensional finite element method shows that the stress intensity factor varies through the thickness, even in this case of a very thin plate. When compared with the compounding technique, the results that are in best agreement with those obtained with the finite element analysis are those from the layer opposite to the stiffener. The three-dimensional stress intensity factor variation through the thickness justifies the non-straight crack front of advancing fatigue cracks in fatigue cracks in stiffened panels subjected to cyclic loading.

An aircraft fuselage structure includes, among other parts, the external skin and longitudinal stiffeners. The continuous need for low cost and the emergence of new technologies has brought interest for large integral metallic structures for aircraft applications. Stiffeners improve the strength and stability of the structure and provide a mean of slowing down or arresting the growth of cracks in a panel. But in the case of an integral stiffener, a crack propagates simultaneously in the stiffener and in the skin. So, in order to provide knowledge about such structures, the strength and behaviour of integral aluminium alloy stiffened sheet specimens used in aircraft construction was imvestigated. These stiffened structures were manufactured with High Speed Machining, Laser Beam Welding and Friction Stir Welding.
The first task in this study was the finite element method analysis of the stiffened panel geometry. The specimen behaviour under load when using or not using an anti-bending device was studied. (This study lead to a decision that the anti-bending device would not be used for the sake of comparability of tests conducted by the DaToN project partners. Indeed, if no anti-bending device is used, the testing procedures throughout the laboratories involved could be more easily homogenised)
An extensive test programme which included fatigue crack growth rate of the different type of stiffened panels was performed. This test programme was complemented by a scanning electron microscopy analysis of the fractured specimens.
It was verified that in all specimens the crack grew symmetrically at both sides of and both surfaces of the stiffener. This feature validates the geometry of the grip system developed for these tests. When attempting to measure the residual stress profile that the X-ray diffraction method, it was found that this method is unsuitable for these specimens.
After testing it was found that for both load conditions (different R ratios and maximum load) the HSM specimen presented the lower fatigue lives. The PWHT-T6 specimens tested in the LBW2 configuration (butt joint) presented the higher fatigue lives for both R ratios. The FSW specimen tested at R=0,1 presented a

fatigue life similar to the LBW2 as-welded specimen. For R=0,5 the FSW specimen performed higher than the LBW1 PWHT-T6 specimen and lower than the LBW2 as-welded specimen.
In all specimens tested it was found that although there is a decrease of the stress intensity factor value close to the stiffener, the decrease of crack growth rate introduced by the stiffener was not significative, probably due to the low width of these specimens, and when the stiffeners are fractured the remaining life of the specimen is marginal.

### 7.2 Suggestions for future work

The work presented in this thesis should be used as a starting point in order to perform further studies on some topics. For example, the residual stress measurement procedures and analyses presented in Chapter three should be applied to friction stir welded specimens. Besides the knowledge of the residual stress distribution created by that welding technique, the fatigue crack growth behaviour in the different welded zones could be more clearly understood.

The temperature measurements presented in Chapter two shows a comparison between the heat generated during the different welding processes: metal inert gas, laser beam and friction stir welding. With this data and the residual stress measurements presented in Chapter three, a numerical modelling technique of a welding process will be validated. In the near future, this model can be used to predict the temperature and residual stress fields when using different constraints and welding parameters.

In Chapter four an analysis of the fatigue striation spacing *vs.* crack length was presented. The results obtained will be analysed in order to relate the striation spacing to the real fatigue crack growth rate for each type of welded structure. Afterwards, this procedure can be applied to the stiffened welded panels. Furthermore, a comparison of striation spacing and experimentally measured da/dN in stiffened panels should be carried out.

For the analysis of DaToN welded stiffened panels, an attempt to measure the residual stress field using other techniques should be carried out. Using more reliable residual stress measurements together with a more sophisticated numerical model the fatigue life prediction of welded panels could be performed. This sophisticated model should be developed taking into account the analysis presented in Chapter five, where a detailed characterization of the 3D stress intensity factor evolution through the thickness is presented, as well as a reliable residual stress field evaluation.

A systematic study of the stiffener cross section versus skin cross section area ratio should be carried out in order to identify its optimum value, since the slowing down effect of the stiffeners evident in previous AIRBUS work was not displayed in the present tests, and a major difference between both specimens concerns precisely that ratio.

# References


1. P. Paris, P. Gomez, and W. Anderson, *A rational analytic theory of fatigue.* The Trend in Engineering, 1961. 13(1): p. 9-14.
2. J. Paik, S. van der Veen, A. Duran, and M. Collette, *Ultimate compressive strength design methods of aluminum welded stiffened panel structures for aerospace, marine and land-based applications: A benchmark study.* Thin-Walled Structures, 2005. 43(10): p. 1550-1566.
3. P. Wen, M. Aliabadi, and A. Young, *Fracture mechanics analysis of curved stiffened panels using BEM.* International Journal of Solids and Structures, 2003. 40(1): p. 219-236.
4. A. Murthy, G. Palani, and N. Iyer, *Remaining life prediction of cracked stiffened panels under constant and variable amplitude loading.* International Journal of Fatigue, 2007. 29(6): p. 1125-1139.
5. P. de Castro, P. de Matos, P. Moreira, and L. da Silva, *An overview on fatigue analysis of structural details: Open hole, single rivet lap-joint, and lap-joint panel.* Materials Science and Engineering A, 2007. 468-470: p. 144-157.
6. R. Pettit, J. Wang, and C. Toh, *Validated feasibility study of integrally stiffened metallic fuselage panels for reducing manufacturing costs*, in *NASA / CR-2000-209342*. 2000.
7. N. Salgado and M. Aliabadi, *The application of the dual boundary element method to the analysis of cracked stiffened panels.* Engineering Fracture Mechanics, 1996. 54(1): p. 91-105.
8. B. Seshadri, J. Newman, and D. Dawicke, *Residual strength analyses of stiffened and unstiffened panels - Part II: wide panels.* Engineering Fracture Mechanics, 2003. 70(3-4): p. 509-524.
9. A. Murphy, M. Price, C. Lynch, and A. Gibson, *The computational post-buckling analysis of fuselage stiffened panels loaded in shear.* Thin-Walled Structures, 2005. 43(9): p. 1455-1474.
10. H. Wagner, *Structures of thin sheet metal, their design and construction*, in *Technical note 490 - National Advisory Committee for Aeronautics*. 1928.
11. M. Holt, *Tests of aluminium alloy stiffened sheet specimens cut from an airplane wing*, in *Technical note 883 - National Advisory Committee for Aeronautics*. 1943.
12. A. Aalberg, M. Langseth, and P. Larsen, *Stiffened aluminium panels subjected to axial compression.* Thin-Walled Structures, 2001. 39(10): p. 861-885.
13. E. Hoffman, R. Harley, J. Wagner, D. Jegley, R. Pecquet, C. Blum, and W. Arbegast, *Compression buckling behavior of large-scale friction stir welded and riveted 2090-T83 A1-Li alloy skin-stiffener panels*, in *NASA/TM-2002-211770*. 2002.
14. H. Mahmoud and R. Dexter, *Propagation rate of large cracks in stiffened panels under tension loading.* Marine Structures, 2005. 18(3): p. 265-288.
15. S. Mellings, J. Baynham, R. Adey, and T. Curtin, *Durability prediction using automatic crack growth simulation in stiffened panel structures*, in http://www.beasy.com/. 2002.

16. J. Sanders, *Effect of a stringer on the stress concentration due to a crack in a thin sheet*, in *NASA TR R-13*. 1959.
17. D. Rooke and D. Cartwright, *Compendium of Stress Intensity Factors*. 1976, London HMSO.
18. R. Dexter, P. Pilarski, and H. Mahmoud, *Analysis of crack propagation in welded stiffened panels*. International Journal of Fatigue, 2003. 25(9-11): p. 1169-1174.
19. H. Vlieger, *The residual strength characteristics of stiffened panels containing fatigue cracks*. Engineering Fracture Mechanics, 1973. 5(2): p. 447-470.
20. M. Ratwani and D. Wilhem, *Influence of biaxial loading on analysis of cracked stiffened panels*. Engineering Fracture Mechanics, 1979. 11(3): p. 585-593.
21. S. Shkarayev and E. Mover, *Edge cracks in stiffened plates*. Engineering Fracture Mechanics, 1987. 27(2): p. 127-134.
22. M. Utukuri and D. Cartwright, *Stress intensity factors for a crack near finite boundaries in multiply stiffened sheets*. Theoretical and Applied Fracture Mechanics, 1991. 15(3): p. 257-266.
23. Gene Mathers, *The welding of aluminium and its alloys [electronic resource]*. Welding of aluminum and its alloys. 2002, Boca Raton, Fla.: CRC Press.
24. G. Verhaeghe and P. Hilton. *Achieving low-porosity laser welds in aerospace aluminium alloy*. in *Aerospace Manufacturing Technology Conference (AMTC)*. 2003. Montreal, Canada.
25. W. Thomas, E. Nicholas, J. Needham, M. Murch, P. Temple-Smith, and C. Dawes, *Patent - Friction stir butt welding*, International Patent No. PCT/GB92/02203, Editor. 1995: GB Patent No. 9125978.8 (1991), US Patent No. 5.460.317.
26. E. Nicholas and S. Kallee. *Friction Stir Welding - a decade on*. in *IIW Asian Pacific International Congress*. 2000. Sydney.
27. Eclipse Aviation, http://www.eclipseaviation.com. 2005.
28. Joining Technologies LLC, http://www.joinintech.com. Services: Laser Beam. 2004.
29. E. Schubert, M. Klassen, I. Zerner, C. Walz, and G. Sepold, *Light-weight structures produced by laser beam joining for future applications in automobile and aerospace industry*. Journal of Materials Processing Technology, 2001. 115(1): p. 2-8.
30. J. Ion, *Laser beam welding of wrought aluminium alloys*. Science and Technology of Welding and Joining, 2000. 5(5): p. 265-276.
31. Alabama Specialty Products Inc, http://www.alspi.com, in *Alabama Laser*. 2005.
32. J. Onoro and C. Ranninger, *Fatigue behaviour of laser welds of high-strength low-alloy steels*. Journal of Materials Processing Technology, 1997. 68(1): p. 68-70.
33. M. Frewin and D. Scott, *Finite element model of pulsed laser welding*. Welding Journal, 1999. 78(1): p. 15S-22S.
34. K. Behler, J. Berkmanns, A. Ehrhardt, and W. Frohn, *Laser beam welding of low weight materials and structures*. Materials & Design, 1997. 18(4-6): p. 261-267.
35. G. Bruggemann, A. Mahrle, and T. Benziger, *Comparison of experimental determined and numerical simulated temperature fields for quality assurance at laser beam welding of steels and aluminium alloyings*. NDT & E International, 2000. 33(7): p. 453-463.

36. S. Wang, M. Wei, and L. Tsay, *Tensile properties of LBW welds in Ti-6Al-4V alloy at evaluated temperatures below 450 degrees C.* Materials Letters, 2003. 57(12): p. 1815-1823.
37. C. Carmignani, R. Mares, and G. Toselli, *Transient finite element analysis of deep penetration laser welding process in a singlepass butt-welded thick steel plate.* Computer Methods in Applied Mechanics and Engineering, 1999. 179(3-4): p. 197-214.
38. S. Fawzi and R. Arif, *Influence of electrical field on pulsed laser beam welding of stainless steel (304).* Turkish Journal of Physics, 1999. 23(6): p. 959-968.
39. X. Zhang, W. Chen, E. Ashida, and F. Matsuda, *Relationship between weld quality and optical emissions in underwater Nd:YAG laser welding.* Optics and Lasers in Engineering, 2004. 41(5): p. 717-730.
40. Z. Li, S. Gobbi, I. Norris, S. Zolotovsky, and K. Richter, *Laser welding techniques for titanium alloy sheet.* Journal of Materials Processing Technology, 1997. 65(1-3): p. 203-208.
41. L. Quintino, P. Vilaça, R. Rodrigues, and L. Bordalo, *Laser beam welding of automobile hinges.* Welding Journal, 2001. 80(11): p. 261S-267S.
42. R. Mueller and W. Duley. *Application of a capacitive autofocus system to laser welding*. in *International Congress on Applications of Lasers & Electro-Optics* 1998. Orlando, USA.
43. D. Hand, M. Fox, F. Haran, C. Peters, S. Morgan, M. McLean, W. Steen, and J. Jones, *Optical focus control system for laser welding and direct casting.* Optics and Lasers in Engineering, 2000. 34(4-6): p. 415-427.
44. A. Costa, L. Quintino, and M. Greitmann, *Laser beam welding hard metals to steel.* Journal of Materials Processing Technology, 2003. 141(2): p. 163-173.
45. R. Braun, C. Donne, and G. Staniek, *Laser beam welding and friction stir welding of 6013-T6 aluminium alloy sheet.* Materialwissenschaft Und Werkstofftechnik, 2000. 31(12): p. 1017-1026.
46. A. Haboudou, P. Peyre, A. Vannes, and G. Peix, *Reduction of porosity content generated during Nd: YAG laser welding of A356 and AA5083 aluminium alloys.* Materials Science and Engineering A-Structural Materials Properties Microstructure and Processing, 2003. 363(1-2): p. 40-52.
47. H. Zhao and I. DebRoy, *Pore formation during laser beam welding of die-cast magnesium alloy AM60B - Mechanism and remedy.* Welding Journal, 2001. 80(8): p. 204S-210S.
48. A. Wu, G. Zou, J. Ren, H. Zhang, G. Wang, X. Liu, and M. Xie, *Microstructures and mechanical properties of Ti-24Al-17Nb laser beam welding joints.* Intermetallics, 2002. 10(7): p. 647-652.
49. F. Caiazzo, F. Curcio, G. Daurelio, and F. Minutolo, *Ti6A14V sheets lap and butt joints carried out by CO2 laser: mechanical and morphological characterization.* Journal of Materials Processing Technology, 2004. 149(1-3): p. 546-552.
50. N. Heo, T. Nagasaka, T. Muroga, A. Nishimura, K. Shinozaki, and N. Takeshita, *Metallurgical and mechanical properties of laser weldment for low activation V-4Cr-4Ti alloy.* Fusion Engineering and Design, 2002. 61-2: p. 749-755.
51. P. Negre, D. Steglich, W. Brocks, and M. Kocak, *Numerical simulation of crack extension in aluminium welds.* Computational Materials Science, 2003. 28(3-4): p. 723-731.

52. C. Liu, D. Northwood, and S. Bhole, *Tensile fracture behavior in CO2 laser beam welds of 7075-T6 aluminum alloy*. Materials & Design, 2004. 25(7): p. 573-577.
53. M. Eibl, C. Sonsino, H. Kaufmann, and G. Zhang, *Fatigue assessment of laser welded thin sheet aluminium*. International Journal of Fatigue, 2003. 25(8): p. 719-731.
54. P. Wang, *Fracture Mechanics parameter for the fatigue resistance of laser welds*. International Journal of Fatigue, 1995. 17(1): p. 25-34.
55. U. Draugelates, B. Bouaifi, and S. Steinborn. *Simulation of laser beam welding of magnesium alloys*. in *First International Conference on Magnesium Science & Technology*. 1998. Jerusalem, Israel.
56. V. Dattoma, M. de Giorgi, and R. Nobile, *Numerical evaluation of residual stress relaxation by cyclic load*. Journal of Strain Analysis, 2004. 39(6): p. 663-672.
57. H. Du, L. Hu, J. Liu, and X. Hu, *A study on the metal flow in full penetration laser beam welding for titanium alloy*. Computational Materials Science, 2004. 29(4): p. 419-427.
58. W. Chang and S. Na, *A study on the prediction of the laser weld shape with varying heat source equations and the thermal distortion of a small structure in micro-joining*. Journal of Materials Processing Technology, 2002. 120(1-3): p. 208-214.
59. A. Mahrle and J. Schmidt, *The influence of fluid flow phenomena on the laser beam welding process*. International Journal of Heat and Fluid Flow, 2002. 23(3): p. 288-297.
60. S. Kallee, E. Nicholas, and W. Thomas. *Friction Stir Welding - invention, innovations and applications*. in *INALCO 2001 - 8th International Conference on Joints in Aluminium*. March 2001. Munich, Germany.
61. D. Harris and A. Norman. *Properties of frictions stir welded joints: A review of the literature*. in *EUROSTIR*. 2003. Progress report presented at the 6th PSG Meeting.
62. T. Lienert, W. Stellwag Jr., and L. Lehman. *Comparison of heat inputs: friction stir welding vs. arc welding*. in *AWS 2002 Professional Program & Poster Session*. 2002.
63. T. Lienert, W. Stellwag, B. Grimmett, and R. Warke, *Friction stir welding studies on mild steel - Process results, microstructures, and mechanical properties are reported*. Welding Journal, 2003. 82(1): p. 1S-9S.
64. T. Lienert, W. Tang, J. Hogeboom, and L. Kvidahl. *Friction stir welding of DH-36 steel*. in *AWS 2003 Professional Program & Poster Session*. 2003.
65. R. John, K. Jata, and K. Sadananda, *Residual stress effects on near-threshold fatigue crack growth in friction stir welds in aerospace alloys*. International Journal of Fatigue, 2003. 25(9-11): p. 939-948.
66. M. Zah and D. Eireiner, *Friction stir welding using NC milling machines*. Welding and Cutting 3. 4: p. 220-223.
67. W. Thomas and R. Dolby. *Friction stir welding developments*. in *6th International Conference on Trends in Welding Research*. April 2002. Georgia, USA.
68. S. Kallee and D. Nicholas. *Friction and forge welding processes for the automotive industry*. in *International Body Engineering*. September 1999. Detroit, USA.

69. M. Hansen, *Mechanical Engineering Design - A Cooler Weld, http://www.eclipseaviation.com*, in *Eclipse Aviation*. 2003.
70. J. Ogando, *New jet will stir up aircraft assembly - http://www.designnews.com/article/CA155041.html*. Design News. 2001.
71. NASA - Marshall Space Flight Center News. *Space Shuttle Technology Summary - Friction Stir Welding*. 2001 [cited.
72. T. Dickerson, Q. Shi, and H. Shercliff. *Heat fow into friction stir welding tools*. in *4th International Symposium on Friction Stir Welding*. May 2003. Park City, Utah, USA.
73. T. Seidel and A. Reynolds, *Material flow in friction stir welding: Experiment and fluid mechanics based process model*. http://www.engr.sc.edu/research/fsw/research/process/mflow.html
74. T. Dickerson, H. Shercliff, and H. Schmidt. *A weld marker technique for flow visualization in friction stir welding*. in *4th International Symposium on Friction Stir Welding*. May 2003. Park City, Utah, USA.
75. A. Guerra, C. Schmidt, J. McClure, L. Murr, and A. Nunes, *Flow patterns during friction stir welding*. Materials Characterization, 2002. 49(2): p. 95-101.
76. P. Threadgill, *Friction stir welds in aluminium alloys - Preliminary microstructural assessment*, in *TWI Bulletin*. 1997. p. 37, (3).
77. TWI website: http://twi.co.uk/. *Friction stir welding - Superior Weld Quality*. [cited.
78. L. Svensson, L. Karlsson, H. Larsson, B. Karlsson, M. Fazzini, and J. Karlsson, *Microstructure and mechanical properties of friction stir welded aluminium alloys with special reference to AA 5083 and AA 6082*. Science and Technology of Welding & Joining, 2000. 5(5): p. 285-296(12).
79. G. Oertelt, S. Babu, S. David, and E. Kenik, *Effect of thermal cycling on friction stir welds of 2195 aluminum alloy*. Welding Journal, 2001. 80(3): p. 71S-79S.
80. K. Jata and S. Semiatin, *Continuous dynamic recrystallization during friction stir welding of high strength aluminum alloys*. Scripta Materialia, 2000. 43(8): p. 743-749.
81. C. Rhodes, M. Mahoney, W. Bingel, R. Spurling, and C. Bampton, *Effects of friction stir welding on microstructure of 7075 aluminum*. Scripta Materialia, 1997. 36(1): p. 69-75.
82. S. Benavides, Y. Li, L. Murr, D. Brown, and J. McClure, *Low-temperature friction-stir welding of 2024 aluminum*. Scripta Materialia, 1999. 41(8): p. 809-815.
83. M. Sutton, B. Yang, A. Reynolds, and R. Taylor, *Microstructural studies of friction stir welds in 2024-T3 aluminum*. Materials Science and Engineering A-Structural Materials Properties Microstructure and Processing, 2002. 323(1-2): p. 160-166.
84. G. Liu, L. Murr, C. Niou, J. McClure, and F. Vega, *Microstructural aspects of the friction-stir welding of 6061-T6 aluminum*. Scripta Materialia, 1997. 37(3): p. 355-361.
85. O. Flores, C. Kennedy, L. E. Murr, D. Brown, S. Pappu, B. Nowak, and J. McClure, *Microstructural issues in a friction-stir-welded aluminium alloy*. Scripta Materialia, 1998. 38(5): p. 703-708.
86. B. Yang, J. Yan, M. Sutton, and A. Reynolds, *Banded microstructure in AA2024-T351 and AA2524-T351 aluminum friction stir welds - Part I.*

*Metallurgical studies*. Materials Science and Engineering A-Structural Materials Properties Microstructure and Processing, 2004. 364(1-2): p. 55-65.
87. C. Chen, R. Kovacevic, and D. Jandgric, *Wavelet transform analysis of acoustic emission in monitoring friction stir welding of 6061 aluminum*. International Jounal of Machine Tools & Manufacture, 2003. 43(13): p. 1383-1390.
88. R. Leal and A. Loureiro, *Defects formation in friction stir welding of aluminium alloys*. Advanced Materials Forum II, 2004. 455-456: p. 299-302.
89. Y. Sato, Y. Kurihara, S. Park, H. Kokawa, and N. Tsuji, *Friction stir welding of ultrafine grained Al alloy 1100 produced by accumulative roll-bonding*. Scripta Materialia, 2004. 50(1): p. 57-60.
90. M. Ericsson and R. Sandstrom, *Influence of welding speed on the fatigue of friction stir welds, and comparison with MIG and TIG*. International Journal of Fatigue, 2003. 25(12): p. 1379-1387.
91. C. Donne, E. Lima, J. Wegener, A. Pyzalla, and T. Buslaps. *Investigations on residual stresses in friction stir welds*. in *3rd International Symposium on Friction Stir Welding*. September 2001. Kobe, Japan.
92. P. Staron, M. Kocak, and S. Williams, *Residual stresses in friction stir welded Al sheets*. Applied Physiscs A - Materials Science & Processing, 2002. 74: p. S1161-S1162.
93. T. Dickerson and J. Przydatek, *Fatigue of friction stir welds in aluminium alloys that contain root flaws*. International Journal of Fatigue, 2003. 25(12): p. 1399-1409.
94. H. Liu, H. Fujii, M. Maeda, and K. Nogi, *Tensile properties and fracture locations of friction-stir-welded joints of 2017-T351 aluminum alloy*. Journal of Materials Processing Technology, 2003. 142(3): p. 692-696.
95. A. Davenport, R. Ambat, M. Jariyaboon, P. Morgan, D. Price, A. Wecott, and S. Williams, *Corrosion of friction stir welds in high strength aluminium allys*. The Journal of Corrosion Science and Engineering, 2003. 6: p. preprint paper 15.
96. P. Prevey, D. Hornbach, P. Mason, and M. Mahoney. *Improving corrosion fatigue performance of AA2219 friction stir welds with low plasticity burnishing*. in *International Surface Engineering Conference*. 2002. Columbus, OH.
97. P. Prevey and M. Mahoney. *Improved fatigue performance of friction stir welds with low plasticity burnishing: residual stress design and fatigue performance assessment*. in *7th International Conference on Thermomechanical Processing of Steels*. July 2003. Madrid, Spain.
98. A. Lanciotti and C. Polese. *Resistanza a fatica e caratteristiche di damage tolerance di giunzioni friction stir welding nella lega alluminio-litio 2195-T8*. in *Giornata di Studio: Friction Stir Welding Day*. 2004. Torino.
99. G. Bussu and P. Irving, *The role of residual stress and heat affected zone properties on fatigue crack propagation in friction stir welded 2024-T351 aluminium joints*. International Journal of Fatigue, 2003. 25(1): p. 77-88.
100. M. Sutton, A. Reynolds, B. Yang, and R. Taylor, *Mode I fracture and microstructure for 2024-T3 friction stir welds*. Materials Science and Engineering A-Structural Materials Properties Microstructure and Processing, 2003. 354(1-2): p. 6-16.
101. M. Sutton, A. Reynolds, B. Yang, and R. Taylor, *Mixed mode I/II fracture of 2024-T3 friction stir welds*. Engineering Fracture Mechanics, 2003. 70(15): p. 2215-2234.

102. C. Chen and R. Kovacevic, *Finite element modeling of friction stir welding - thermal and thermomechanical analysis*. International Journal of Machine Tools & Manufacture, 2003. 43(13): p. 1319-1326.
103. P. Ulysse, *Three-dimensional modeling of the friction stir-welding process*. International Journal of Machine Tools & Manufacture, 2002. 42(14): p. 1549-1557.
104. M. Song and R. Kovacevic, *Thermal modeling of friction stir welding in a moving coordinate system and its validation*. International Journal of Machine Tools & Manufacture, 2003. 43(6): p. 605-615.
105. X. Zhu and Y. Chao, *Numerical simulation of transient temperature and residual stresses in friction stir welding of 304L stainless steel*. Journal of Materials Processing Technology, 2004. 146(2): p. 263-272.
106. P. Vilaça, L. Quintino, and J. dos Santos, *iSTIR - Analytical thermal model for friction stir welding*. Journal of Materials Processing Technology, 2005. 169(3): p. 452-465.
107. Air Products PLC, *Welder's Handbook, For Gas Shielded Arc Welding, Oxy Fuel Cutting & Plasma Cutting*. 3rd ed. 1999 Air Products PLC.
108. M. Wahab, M. Painter, and M. Davies, *The prediction of the temperature distribution and weld pool geometry in the gas metal arc welding process*. Journal of Materials Processing Technology, 1998. 77(1-3): p. 233-239.
109. C. Meola and G. Carlomagno, *Recent advances in the use of infrared thermography*. Measurement Science & Technology, 2004. 15(9): p. R27-R58.
110. D. Camilleri, P. Mollicone, and T. Gray, *Alternative simulation techniques for distortion of thin plate due to fillet-welded stiffeners*. Modelling and Simulation in Materials Science and Engineering, 2006. 14(8): p. 1307-1327.
111. J. Doong, C. Wu, and J. Hwang, *Infrared temperature sensing of laser-welding*. International Journal of Machine Tools & Manufacture, 1991. 31(4): p. 607-616.
112. ESAB Filler Materials, *ESAB Welding Handbook - Filler materials for manual and automatic welding*. 5th ed.
113. S. Kasap, *Thermoelectric effects in metals: thermocouples*. Materials and Devices Website for Scientists and Engineers. (http://kasap3.usask.ca/), ed. Special Custom Published e-Booklet. 1990-2001.
114. Labfacility, *The temperature handbook*. Temperature & process technology. 2004, Middlesex, UK: Labfacility Ltd.
115. Analog Devices, *Monolithic Thermocouple Amplifiers with Cold Junction Compensation*. Data sheet, Rev. c, C731g-0-11/99, USA.
116. ESDU 02006, *Temperature measurement: Techniques*. May 2002.
117. D. Camilleri, T. Gray, and T. Comlekci, *Use of thermography to calibrate fusion welding procedures in virtual fabrication applications*, in *InfraMation 2004: Proceedings of the infrared camera applications international conference held by Infrared Training Center and FLIR Systems, Inc.* 2004: Las Vegas, Nevada, USA.
118. K. Hill, B. Malo, F. Bilodeau, D. Johnson, and J. Albert, *Bragg gratings fabricated in monomode photosensitive optical-fiber by UV exposure through a phase mask*. Applied Physics Letters, 1993. 63(3): p. 424-424.
119. J. Suarez, B. Remartinez, J. Menendez, A. Guemes, and F. Molleda, *Optical fibre sensors for monitoring of welding residual stresses*. Journal of Materials Processing Technology, 2003. 143: p. 316-320.

120. P. Withers and H. Bhadeshia, *Overview - Residual stress part 2 - Nature and origins*. Materials Science and Technology, 2001. 17(4): p. 366-375.
121. P. Venkitakrishnan, J. Philip, and R. Krishnamurthy, *An assessment of stresses in thin walled welded tubes through hole drilling and sectioning methods*. Journal of Materials Processing Technology, 2007. 185(1-3): p. 228-232.
122. J. Allen, N. Bailey, J. Harrison, R. Leggatt, A. Parlane, E Procter, and G. Saunders, *Residual stresses and their effects*, ed. TWI. 1981.
123. C. Walker, McKelvie, and J. Hyzer, *An analysis of residual stress patterns resulting from hole expansion in an infinite plate, a thick cylinder, and an asymmetric lug*. Optics and Lasers in Engineering, 1997. 27(1): p. 75-87.
124. R. Galatolo and A. Lanciotti, *Fatigue crack propagation in residual stress fields of welded plates*. International Journal of Fatigue, 1997. 19(1): p. 43-49.
125. J. Mathar, *Determination of initial stresses by measuring the deformation around drilled holes*. ASME Transactions, 1934. 56(4): p. 249-254.
126. ASTM E837, *Standard Test Method for Determining Residual Stresses by the Hole drilling Strain-Gauge Method*. 2001.
127. Vishay Measurements Group, *Measurement of residual stresses by the hole-drilling strain gage method*, in *Technical Note TN-503-5*. 1993.
128. P. Grant and J. Lord, *An evaluation of four hole drilling analysis Techniques with respect to non-uniform residual stress fields*. Measurement Note MATC(MN)31.
129. G. Schajer, *Applications of finite element calculations to residual stress measurements*. Journal of Engineering Materials and Technology, 1981. 103: p. 157-163.
130. A. Nikulari, J. Lu, and J. Flavenot, *Measurement of residual-stress distribution by the incremental hole-drilling method*. Experimental Mechanics, 1985. 25(2): p. 175-185.
131. G. Schajer, *Measurement of non-uniform residual stresses using the hole drilling method*. Journal of Engineering Materials and Technology, 1988. 110(4): p. Part I: pp.338-343, Part II: pp.3445-349.
132. ASTM E837, *Determining Residual Stresses by the Hole-Drilling Strain-Gage Method*. distributed at the Residual Stress Summit 2007, ORNL, USA, draft for discussion up to October 22, 2007.
133. V. Hauk, *Structural and residual stress analysis by X-ray diffraction on polymeric materials and composites*. Materialwissenschaft Und Werkstofftechnik, 1999. 30(7): p. 377-384.
134. G. Schajer, *H-Drill software*. V 3.01, ed. Vishay Measurements Group.
135. V. Richter-Trummer, S. Tavares, P. Moreira, and P. de Castro. *Residual stress measurement using the contour and the sectioning methods: Application to MIG and FSW joints*. in *3rd Residual Stress Summit* 2007 ORNL, USA (cd of proceedings available from SEM-Society for Experimental Mechanics).
136. V. Richter-Trummer, *Residual stress measurement using the contour and the sectioning methods: application to MIG and FSW joints*, in *Final Project, Licenciatura em Engenharia Mecânica*. 2007, Faculdade de Engenharia da Universidade do Porto: Porto.
137. M. Prime, *Cross-sectional mapping of residual stresses by measuring the surface contour after a cut*. Journal of Engineering Materials and Technology-Transactions of the ASME, 2001. 123(2): p. 162-168.

138. W. Thomas, E. Nicholas, J. Needham, M. Murch, P. Templesmith, and C. Dawes, *Improvements Relating to Friction Welding*, TWI, Editor. 1992.
139. ESDU 81031, *Fatigue crack propagation rates and threshold stress intensity factor ranges for aluminium alloy plate, extruded bar and forgings*. 1998.
140. *Metallic materials and elements for aerospace vehicle structures [electronic resource]*. Military handbook MIL-HDBK-5H. 2003, Norwich, N.Y.
141. Automation Creations MatWeb.com, *http://www.matls.com*, Blacksburg.
142. ASM, *ASM Handbook: Metallography and microstructures*. Vol. 9. 1995, ASM, Materials, Park, OH.
143. A. Scialpi, L. de Filippis, and P. Cavaliere, *Influence of shoulder geometry on microstructure and mechanical properties of friction stir welded 6082 aluminium alloy*. Materials & Design, 2007. 28(4): p. 1124-1129.
144. ASTM E8–03, *Standard Test Methods for Tension Testing of Metallic Materials*. 2004.
145. R. Mishra and Z. Ma, *Friction stir welding and processing*. Materials Science & Engineering R-Reports, 2005. 50(1-2): p. 1-78.
146. G. Biallas, C. Donne, and C. Juriçic, *Monotonic and cyclic strength of friction stir welded aluminium joints*. Advances in Mechanical Behaviour, Plasticity and Damage, 2000. 1: p. 115-120.
147. Hibbitt, Karlson, and Sorensen, *ABAQUS, Fracture Mechanics (course notes)*. 1991.
148. R. Hertzberg, *Deformation and fracture mechanics of engineering materials*. 4th ed ed. 1996, New York: John Wiley.
149. M. Sharp, G. Nordmark, and C. Menzemer, *Fatigue design of aluminium components and structures*. 1996, New York McGraw-Hill. 353.
150. S. Suresh, *Fatigue of materials*. 1998, Cambridge; New York: Cambridge University Press.
151. A. Ribeiro and A. Fernandes, *Modelos numéricos de análise de danos da fadiga de juntas soldadas*. Anales de Mecanica de la Fracture, 1996. 13: p. 114-118.
152. N. Dowling, *Mechanical behavior of materials: Engineering methods for deformation, fracture, and fatigue*. 2nd ed. 1998, Upper Saddle River, NJ Prentice Hall.
153. SAE, *Fatigue Design Handbook*. Vol. 4. 1968, Two Pennsylvania Plaza, New York: Society of Automotive Engineers, Inc.
154. K. Lee and J. Song, *Estimation methods for strain-life fatigue properties from hardness*. International Journal of Fatigue, 2006. 28(4): p. 386-400.
155. ASTM, *Standard Hardness Conversion Tables for Metal*, in *Annual Book of ASTM STD E140-97*. 2000: USA. p. 1-21.
156. W. Lee, Y. Yeon, and S. Jung, *The joint properties of dissimilar formed Al alloys by friction stir welding according to the fixed location of materials*. Scripta Materialia, 2003. 49(5): p. 423-428.
157. W. Lee, Y. Yeon, and S. Jung, *The mechanical properties related to the dominant microstructure in the weld zone of dissimilar formed Al alloy joints by friction stir welding*. Journal of Materials Science, 2003. 38(20): p. 4183-4191.
158. P. Srinivasan, W. Dietzel, R. Zettler, J. dos Santos, and V. Sivan, *Stress corrosion cracking susceptibility of friction stir welded AA7075-AA6056 dissimilar joint*. Materials Science and Engineering A, 2005. 392(1-2): p. 292-300.

159. P. Cavaliere, R. Nobile, F. Panella, and A. Squillace, *Mechanical and microstructural behaviour of 2024-7075 aluminium alloy sheets joined by friction stir welding.* International Journal of Machine Tools and Manufacture, 2006. 46(6): p. 588-594.
160. A. Scialpi, M. de Giorgi, L. de Filippis, R. Nobile, and F. Panella, *Mechanical analysis of ultra-thin FSW joined sheets with dissimilar and similar materials.* Materials & Design, 2007(In Press, Accepted Manuscript).
161. H. Zhang, Z. Zhang, and J. Chen, *The finite element simulation of the friction stir welding process.* Materials Science and Engineering A-Structural Materials Properties Microstructure and Processing, 2005. 403(1-2): p. 340-348.
162. L. Fratini and B. Zuccarello, *An analysis of through-thickness residual stresses in aluminium FSW butt joints.* International Journal of Machine Tools and Manufacture, 2006. 46(6): p. 611-619.
163. A. Steuwer, M. Peel, and P. Withers, *Dissimilar friction stir welds in AA5083-AA6082: The effect of process parameters on residual stress.* Materials Science and Engineering a-Structural Materials Properties Microstructure and Processing, 2006. 441(1-2): p. 187-196.
164. Ø. Grong, *Metallurgical modelling of welding*. 2nd edition ed. Materials Modelling Series, ed. The Institute of Materials. 1997, London.
165. W. Woo, H. Choo, D. Brown, S. Vogel, P. Liaw, and Z. Feng, *Texture analysis of a friction stir processed 6061-T6 aluminum alloy using neutron diffraction.* Acta Materialia, 2006. 54(15): p. 3871-3882.
166. ASME. Boiler and Pressure Vessel Committee, *ASME boiler and pressure vessel code Qualification standard for welding and brazin procedures, welders, brazers, and welding and brazing operators*. 2004, New York: ASME.
167. Portugal. Instituto Português da Qualidade, *Ensaios destrutivos em soldadura de materiais metálicos Ensaio de dobragem NP EN 910 1999*. 1999, Caparica: Instituto Português da Qualidade. 25.
168. Hibbitt, Karlsson, and Sorenson, *ABAQUS Users Manual*. 2006.
169. ESAB AB. *ESAB Welding Handbook - Filler Materials for Manual and Automatic Welding*. 2003. Goteborg Sweden.
170. S. Hong, S. Kim, C. Lee, and S. Kim, *Fatigue crack propagation behavior of friction stir welded Al-Mg-Si alloy.* Scripta Materialia, 2006. 55(11): p. 1007-1010.
171. J. Weston, I. Jones, and E. Wallach, *Laser welding of aluminium alloys using different laser sources*, in *CISFFEL 6 - International Conference on Laser and Power Beam Welding*. 1998: Toulon, France.
172. ASTM E466, *Constant Amplitude Axial Fatigue Tests of Metallic Materials*.
173. ASTM E647-05, *Standard Test Method for Measurement of Fatigue Crack Growth Rates*. 2007.
174. J. Davis, *Aluminum and aluminum alloys*. ASM Specialty Handbook. 1993, Materials Park, OH: ASM International. 784 p.
175. A. Portela and M. Aliabadi, *Crack growth analysis using boundary elements*. 1993: Computational Mechanics Publications Southampton UK and Boston USA.
176. P. de Matos, P. Moreira, A. Portela, and P. de Castro, *Dual boundary element analysis of cracked plates: post-processing implementation of the singularity subtraction technique.* Computers & Structures, 2004. 82(17-19): p. 1443-1449.

177. J. Eshelby, *The continuum theory of lattice defects*. Solid State Physics-Advances in Research and Applications, 1956. 3: p. 79-144.
178. J. Rice, *Mathematical analysis in the mechanics of fracture*, in *Fracture, an Advanced Treatise*. 1968: New York. p. 191-308.
179. S. Timoshenko and J. Goodier, *Theory of Elasticity*. 3rd ed. 1970, Tokio: McGraw-Hill Kogakusha. 567.
180. M. Kassir and G. Sih, *Three dimensional stress distribution around an elliptical crack under arbitrary loadings*. Transactions of ASME, Journal of Applied Mechanics, 1966. 33: p. 601-611.
181. R. Hartranft and G. Sih, *The use of eigenfunction expansions in the general solution of three dimensional crack problems*. Journal of Mathematics and Mechanics, 1969. 19: p. 123-138.
182. R. Hartranft and G. Sih, *An approximate three dimensional theory of plates with application to crack problems*. International Journal of Engineering Science, 1970. 8: p. 711-729.
183. J. Benthem, *State of stress at the vertex of a quarter infinite crack in the half space*. International Journal of Solids and Structures, 1977. 13: p. 479-492.
184. A. Bloom and B. Andersson, *On the semi-elliptical surface crack problem: Detailed numerical solutions for complete elastic stress fields*. Surface-Crack Growth: Models, Experiments and Structures, ASTM STP 1060 (W.G. Reuter et al., Eds.), Philadelphia, American Society for Testing and Materials, 1990: p. 77-98.
185. W. Zhu, *Singular stress fields of three diemnsional crack*. Engineering Fracture Mechanics, 1990. 36: p. 239-244.
186. T. Nakamura and D. Parks, *Three-dimensional stress field near the crack front of a thin elastic plate*. Journal of Applied Mechanics, 1988. 55: p. 805-813.
187. K. Shivakumar and I. Raju, *Treatment of singularities in cracked bodies*. International Journal of Fracture, 1990. 45: p. 159-178.
188. S. Kwon and C. Sun, *Characteristics of three-dimensional stress fields in plates with a though-the-thickness crack*. International Journal of Fracture, 2000. 104: p. 291-315.
189. I. Raju and J. Newman, *Three dimensional finite-element analysis of finite-thickness fracture specimens, TN-D-8414, NASA Center for AeroSpace Information (CASI)*. 1977.
190. S. Atluri and K. Kathiresan. *An assumed displacement hybrid finite element model for three-dimensional linear-fracture-mechanics analysis*. in *12th Annual Meeting of the Society of Engineering Science*. 1975.
191. H. Tada, P. Paris, and G. Irwin, *The stress analysis of cracks handbook*. 3rd ed ed. 2000, New York, London: ASME Press Professional Engineering Publishing. XX, 677.
192. P. de Matos, P. Moreira, and P. de Castro. *Stress intensity factor determination using the finite element method*. in *8th Portuguese Conference on Fracture*. 2002. Vila Real, Portugal.
193. M. Williams, *On the stress distribution at the base of a stationary crack*. Journal of Applied Mechanics, 1957. 24: p. 109-114.
194. S. Pastramă, S. Tavares, P. Moreira, and P. de Castro. *Compounded stress intensity factors: introduction to the method and the case of cracked stiffened plates*. in *10th Portuguese Conference on Fracture*. 2006. Guimarães, Portugal.
195. DaToN, *Innovative Fatigue and Damage Tolerance Methods for the Application of New Structural Concepts*. Strengthening the competitiveness,

Specific Targeted Research Project. 2004: A Proposal for the 6th European Framework Program.
196. W. Vaidya, K. Angamuthu, and M. Kocak. *Effect of load ratio and temper on fatigue crack propagation behaviour of Al-Alloys 6056*. in *8th International Fatigue Congress - FATIGUE 2002*. 2002. Stockholm, Sweden.
197. AIRBUS, *Test Report 1: Damage Tolerant Investigations on Integral Shells (Crack Propagation test)*, compiled by AIRBUS for use on EC DATON project only, Editor. 2005.
198. University of Pisa, *WP3: Manufacturing and testing, Status at month 30*. DaToN project, meeting at Brno, slides presentation, 15-16 October 2007.
199. A. Lanciotti, L. Lazzeri, and C. Polese, *Pisa contribution to WP3*. DaToN project Porto meeting, slides presentation, 17-18 April 2007.
200. R. Dexter and P. Pilarski, *Crack propagation in welded stiffened panels*. Journal of Constructional Steel Research, 2002. 58(5-8): p. 1081-1102.
201. L. Llopart, B. Kurz, C. Wellhausen, M. Anglada, K. Drechsler, and K. Wolf, *Investigation of fatigue crack growth and crack turning on integral stiffened structures under mode I loading*. Engineering Fracture Mechanics, 2006. 73(15): p. 2139-2152.
202. L. Edwards, M. Fitzpatrick, P. Irving, I. Sinclair, X. Zhang, and D. Yapp, *An integrated approach to the determination and consequences of residual stress on the fatigue performance of welded aircraft structures*. Journal of ASTM International, 2006. 3(2): p. 1-17.
203. R. Franke, B. Brenner, V. Ulbricht, and W. Zink. *Moderne werkstoffe und testmethoden in flugzeugbau*. in *Tagungsband zum 6. Chemnitzer Symposium Fugetechnik/Schweisstechnik*. 2004. Technische Universitat Chemnitz.
204. S. Tavares, P. Moreira, V. Richter-Trummer, and P. de Castro, *Fatigue crack growth in AIRBUS test panels with seven stiffeners and a central crack, DaToN - WD4 - WP2 - 1.0 / IDMEC*. 2006 (revised version '1.1' Feb 2007).
205. A. Brot and Y. Peleg-Wolfin. *The damage-tolerance behaviour of integrally stiffened metallic structures*. in *48th Israel Annual Conference on Aerospace Sciences*. 2008.

# Appendix A

# Temperature field in GMAW, LBW and FSW; measurements details

# Appendix A - Temperature field in GMAW, LBW and FSW; measurement details

This appendix seeks to record experimental data acquired during the temperature field measurements of MIG, FSW and LBW processes. The experimental details already presented in Section 2.2 of Chapter two are not repeated here. Therefore, this appendix is not intended to be read as an independet separate text, but instead should be consulted when reading Section 2.2 in order to obtain aditional experimental data. In particular, references to thermocouples numbers and locations are all identified in the main text (Section 2.2).

### MIG welding – temperature profiles

#### *Aluminium 6061-T6*

In the first and second temperature acquisition the thermocouples were placed in the side of the plate opposite to the weldments, Figure 458 a) and b) respectively. In the first acquisition thermocouple 5 was not considered and in the fourth acquisition thermocouple 13 was not considered.

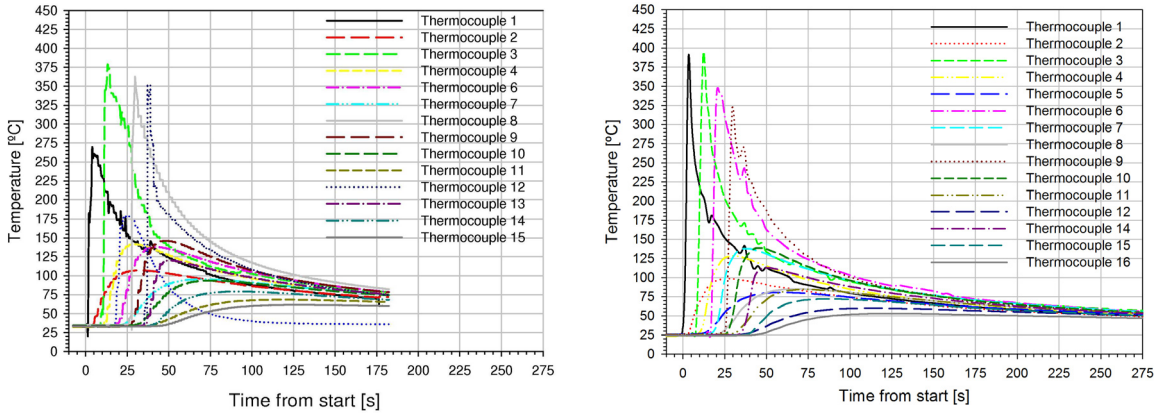


a) deposition 1 b) deposition 2

**Figure 458 - Temperature distribution the plate back surface.**

In order to get a spatial understanding of the temperature distributions, a comparative plot of the 5 lines and 4 columns of thermocouples temperature profiles are presented. The temperature distributions in column 1, 2, 3 and 4 are

presented in Figure 459. Column 1 represents the thermocouples nearest to the weld line, positioned at $5mm$ from the weld line and separated by $100mm$ from each other. As the welding advances in the plate, at the same distance from the weld line, thermocouples acquire higher temperatures. This trend is identified comparing the maximum temperatures of thermocouples 1, 3, 6 and 9.

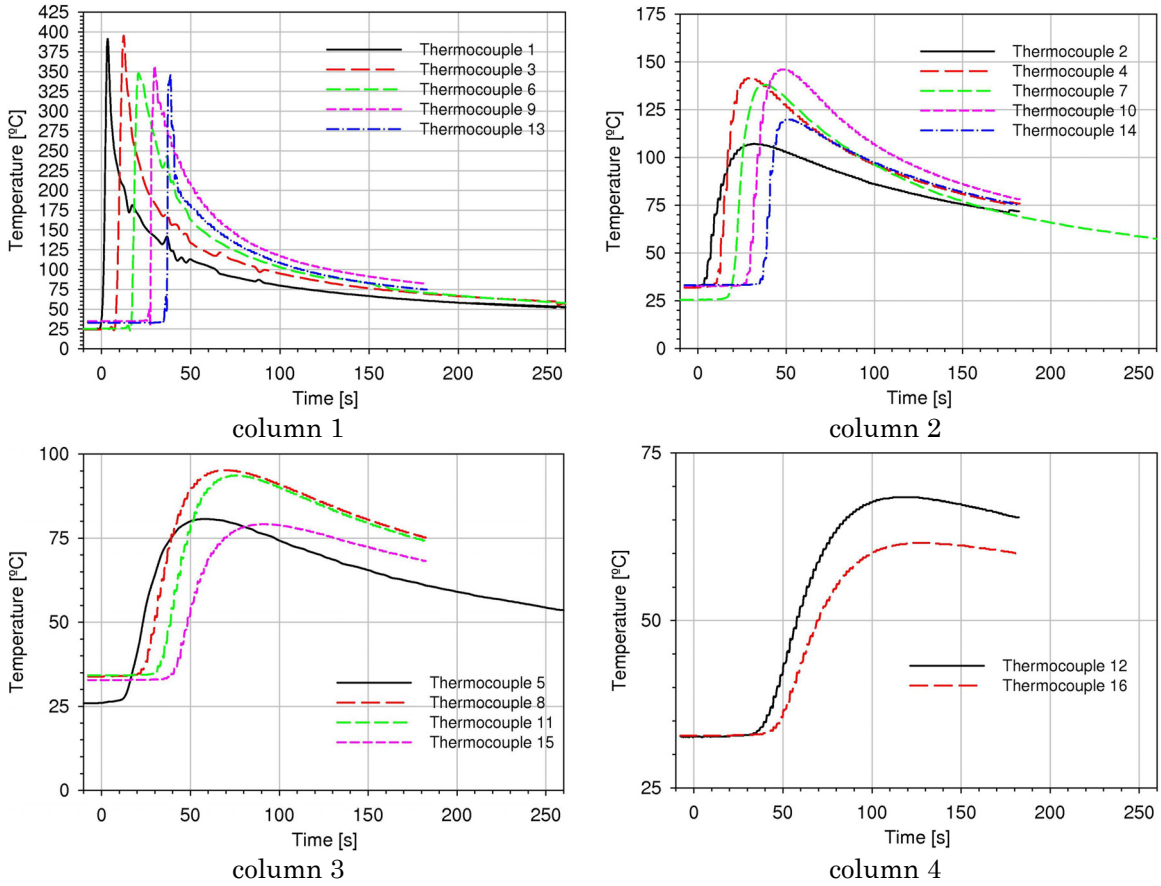


**Figure 459 - Temperature profiles in thermocouples placed parallel to the weld line.**

The temperature distribution in lines 1, 2, 3, 4 and 5 are presented in Figure 460. These lines represent the perpendicular direction to the weld line and are placed $100mm$ between each other.

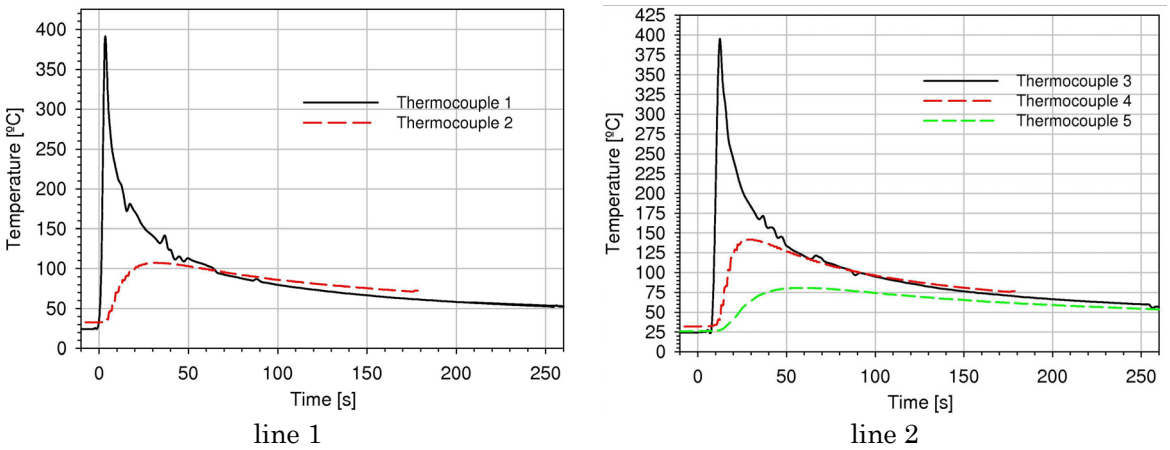

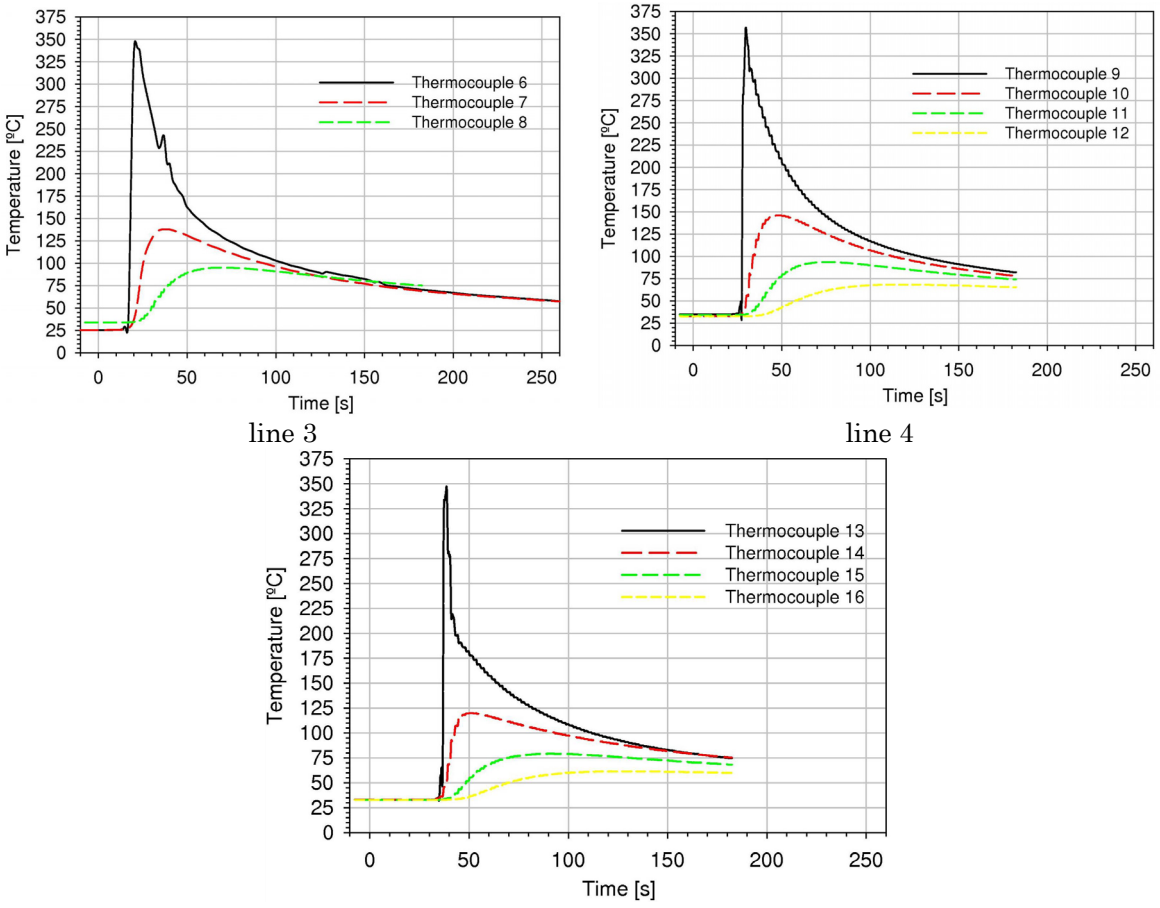


**Figure 460 - Temperature profiles in thermocouples placed perpendicular to the weld line.**

A spatial picture of the temperature distribution along the plate top surface is given by a plot of the 5 lines and 4 columns of temperature profiles obtained using thermocouples. The temperature distributions in column 1, 2, 3 and 4 are presented in Figure 461. They are positioned at 15$mm$ from the weld line and separated by 100$mm$ from each other.

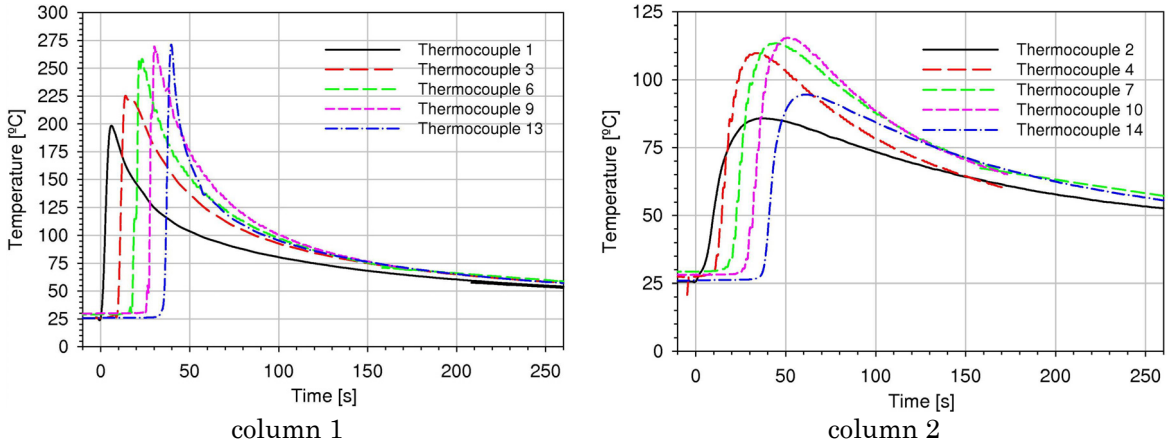

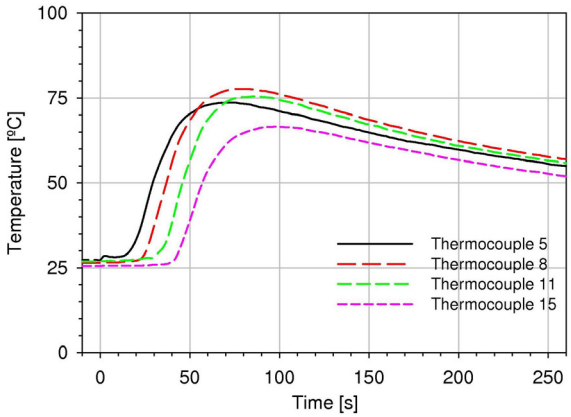


column 3

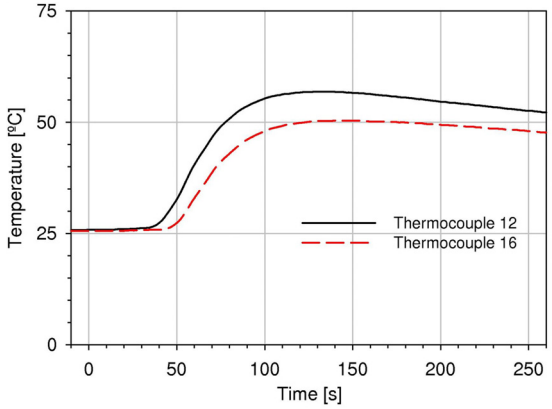


column 4

**Figure 461 - Temperature profiles in thermocouples placed parallel to the weld line in the top surface.**

The temperature distributions in lines 1, 2, 3, 4 and 5 are presented in Figure 462. A temperature decrease in the perpendicular direction to the weld line is present in all plots, as expected.

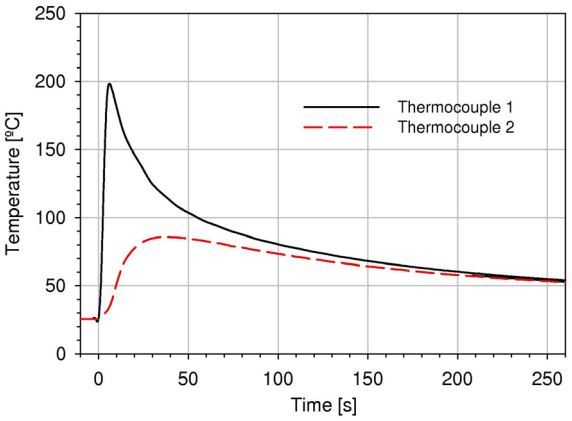


line 1

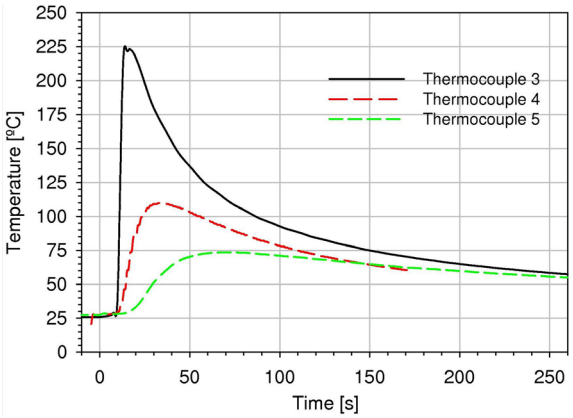


line 2

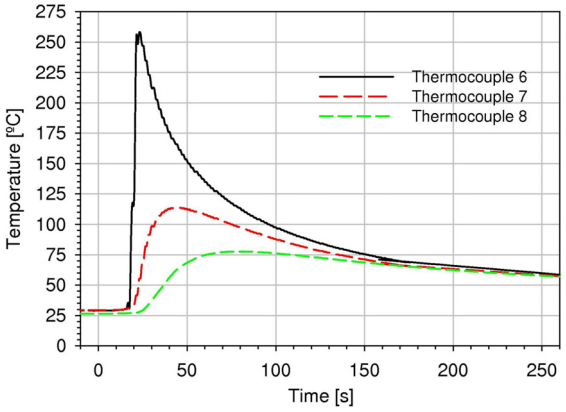


line 3

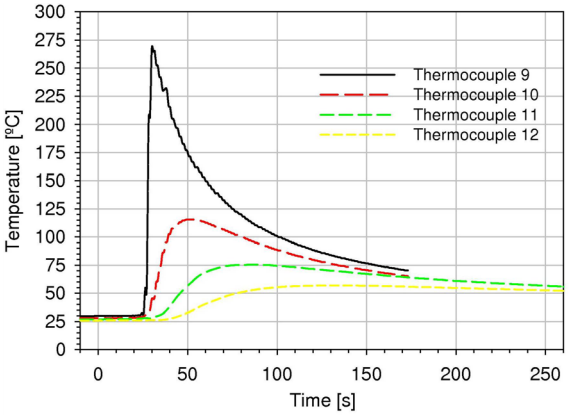


line 4

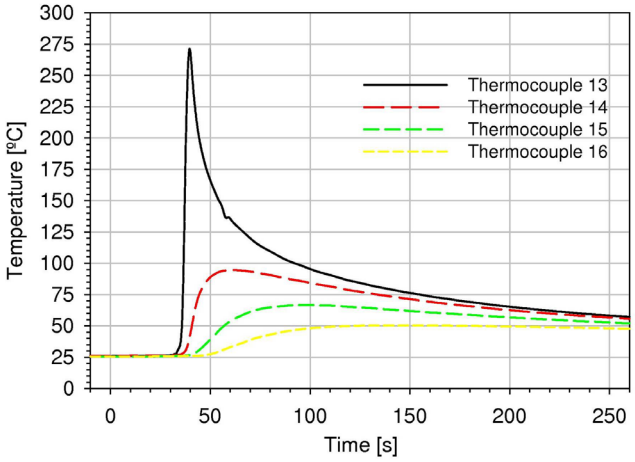


line 5

**Figure 462 - Temperature profiles in thermocouples placed perpendicular to the weld line in the plate top surface.**

## FSW welding – temperature profiles

Temperatures acquired at a frequency of 14,7*Hz*, during tests 1 and 2 are presented in Figure 462 a) and b), respectively.

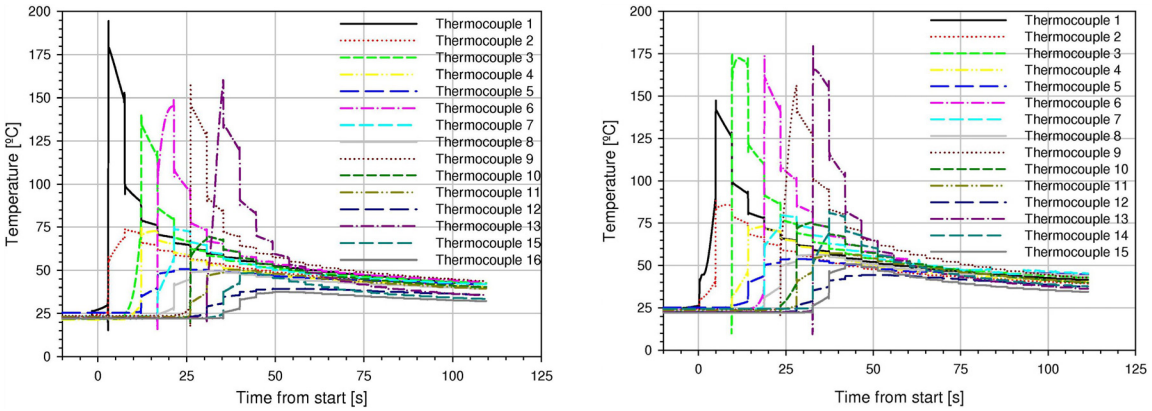


a) deposition 1 b) deposition 2.

**Figure 463 - Temperature distribution in welding deposition 1.**

In order to understand the temperature distribution along the plate a comparative plot of the 5 lines and 4 columns of thermocouples temperature profiles are presented. The temperature distributions in column 1, 2, 3 and 4 are presented in Figure 464. Column 1 represents the thermocouples nearest to the weld line. They are positioned at 10*mm* from the weld line and separated by 100*mm* from each other. As the welding advances in the plate, at the same distance from the weld line, thermocouples acquire higher temperatures. This trend is identified comparing the maximum temperatures of thermocouples 1, 3, 6 and 9.

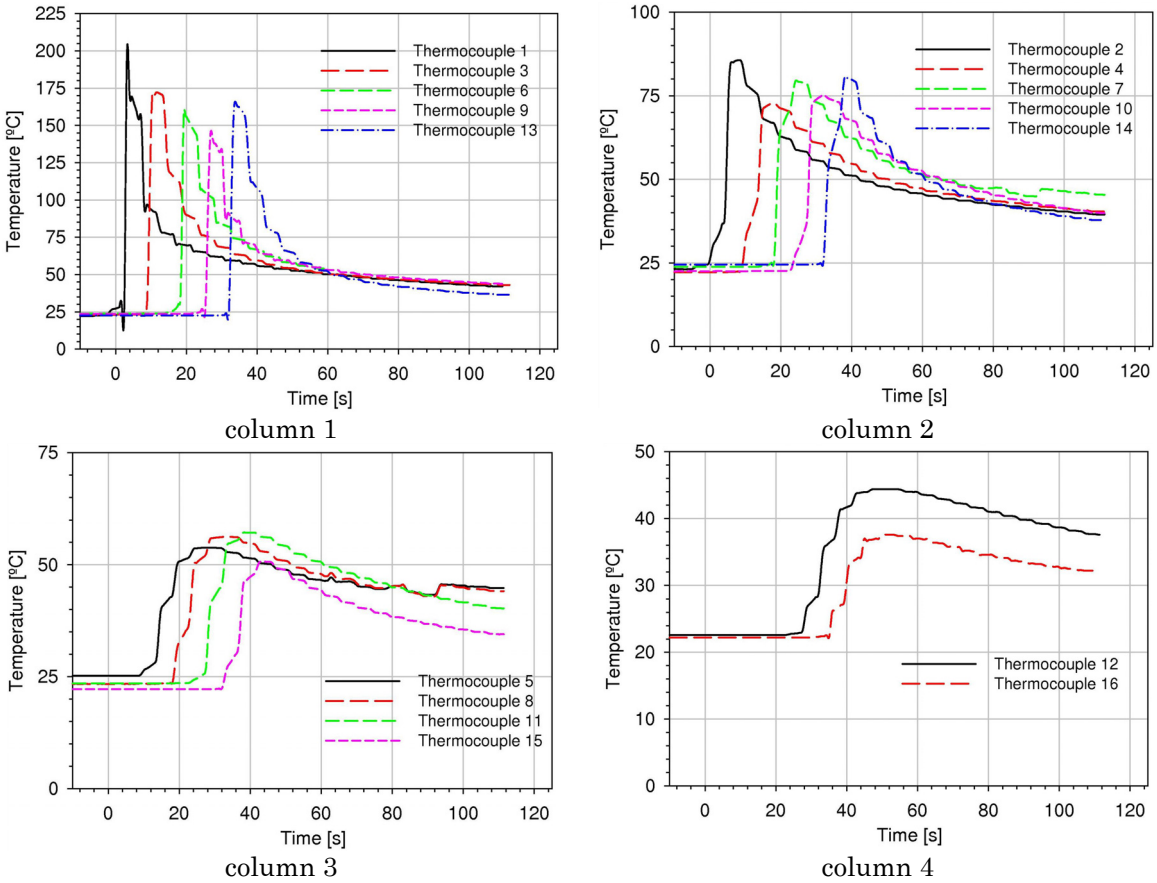


**Figure 464 - Temperature profiles in thermocouples placed parallel to the weld line.**

The temperature distributions in lines 1, 2, 3, 4 and 5 are presented in Figure 465. These lines represent the perpendicular direction to the weld line and are placed 100$mm$ between each other.

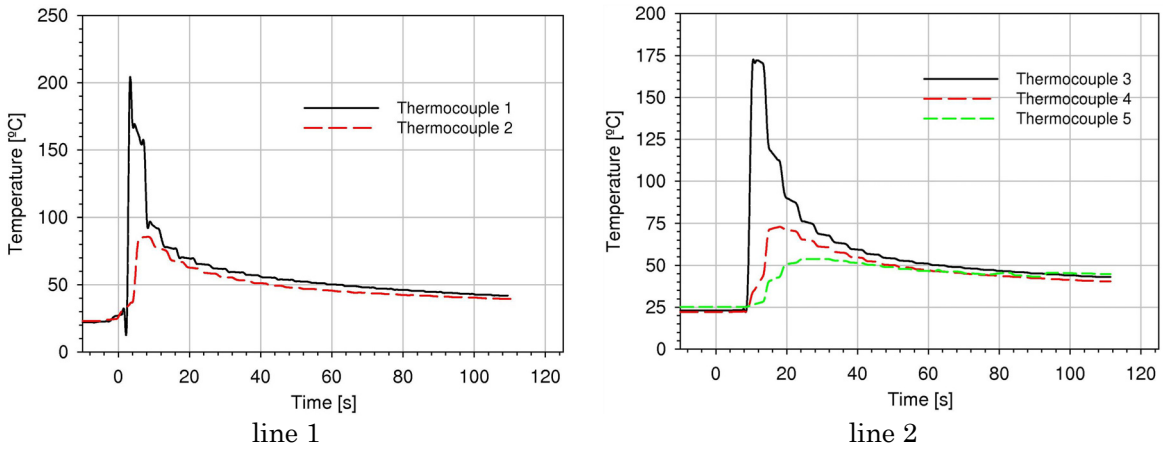

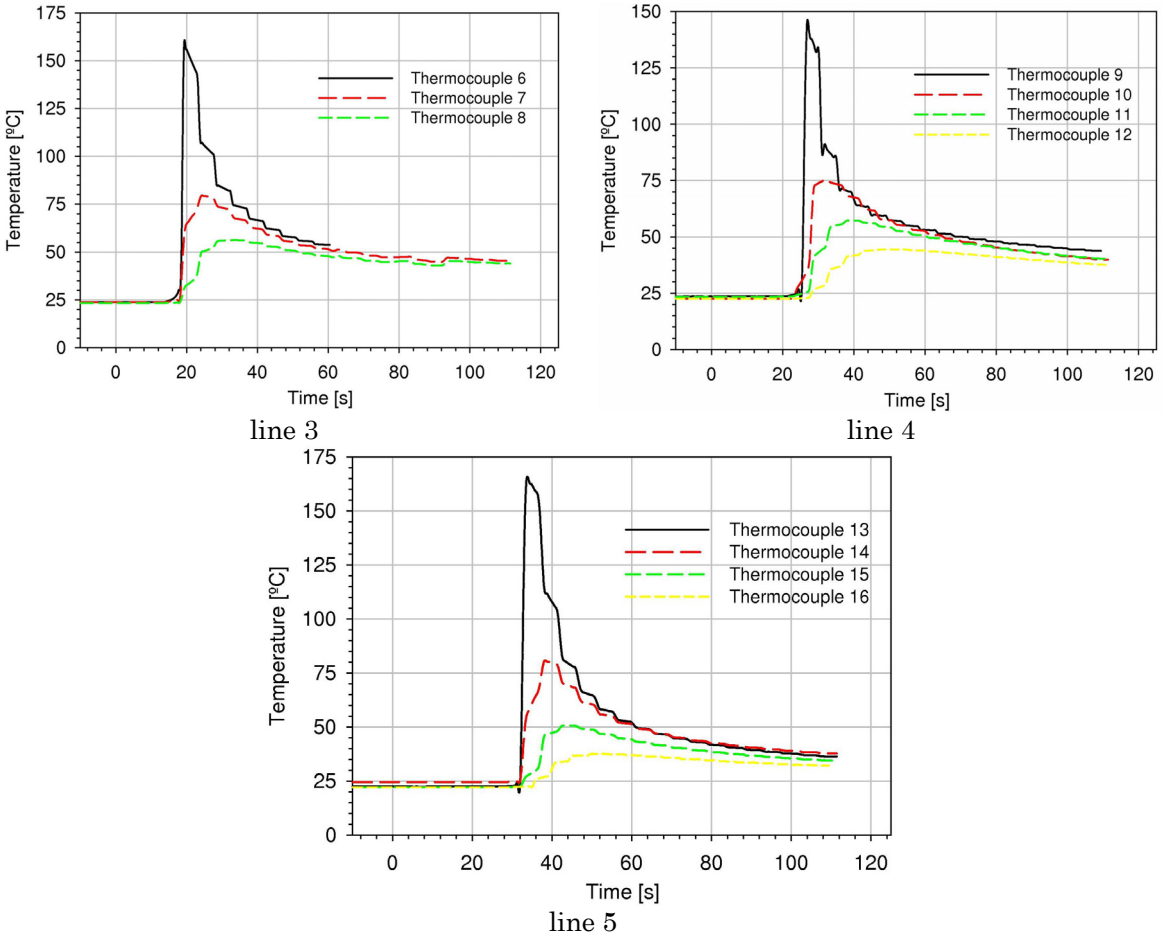


**Figure 465 - Temperature profiles in thermocouples placed perpendicular to the weld line.**

## LBW welding – temperature profiles

### *Aluminium 6082-T6*

In order to understand the temperature distribution along the plate a comparative plot of the 5 lines and 4 columns of thermocouples temperature profiles are presented. The temperature distributions in column 1, 2, 3 and 4 are presented in Figure 466. Column 1 represents the thermocouples nearest to the weld line. They are positioned at $5mm$ from the weld line and separated by $100mm$ from each other. As the welding advances in the plate, at the same distance from the weld line, thermocouples acquire higher temperatures. This trend is identified comparing the maximum temperatures of thermocouples 1, 3 and 6.

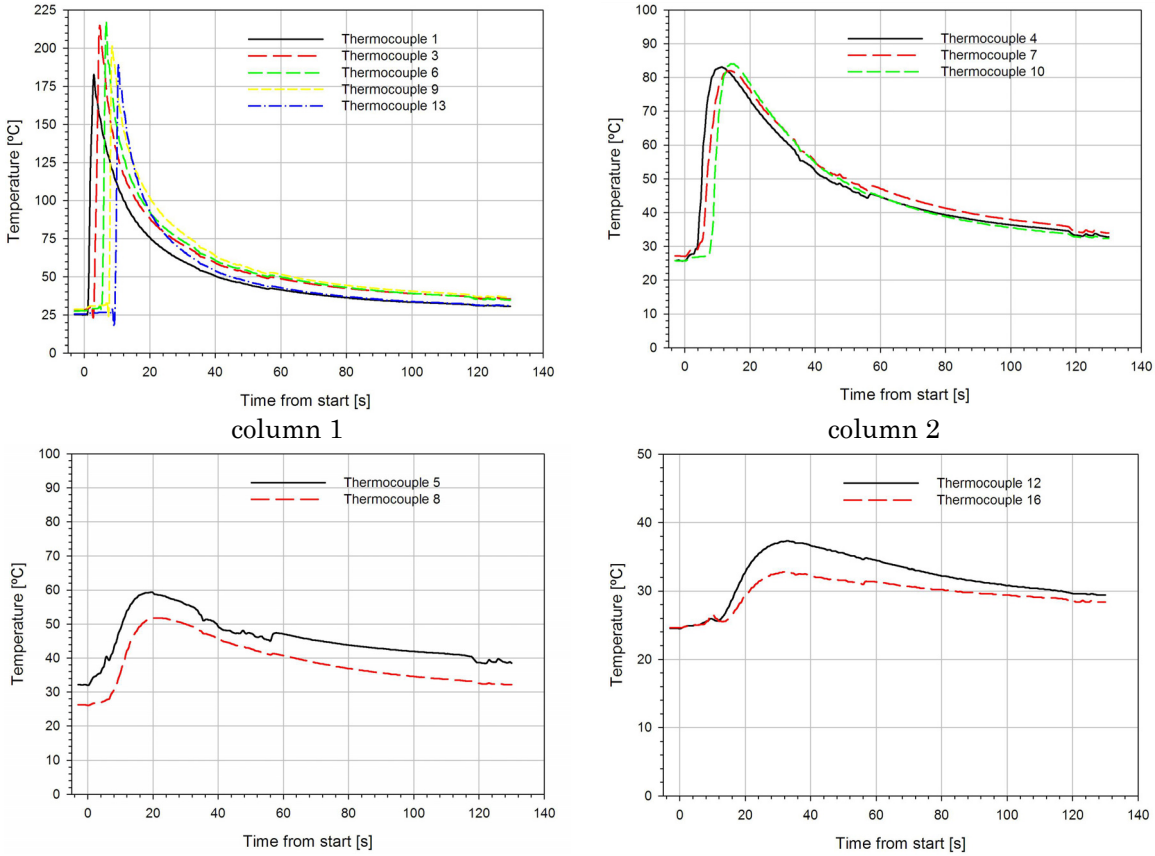


**Figure 466 - Temperature profiles in thermocouples placed parallel to the weld line.**

The temperature distributions in lines 1, 2, 3, 4 and 5 are presented in Figure 467. These lines represent the perpendicular direction to the weld line and are placed $100mm$ between each other. As expected, a temperature decrease is observed in the perpendicular direction to the weld line.

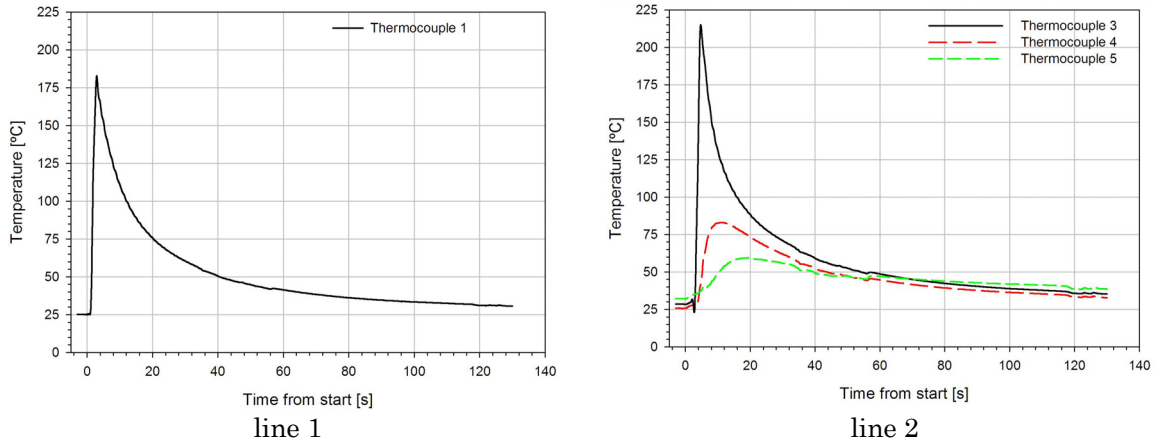

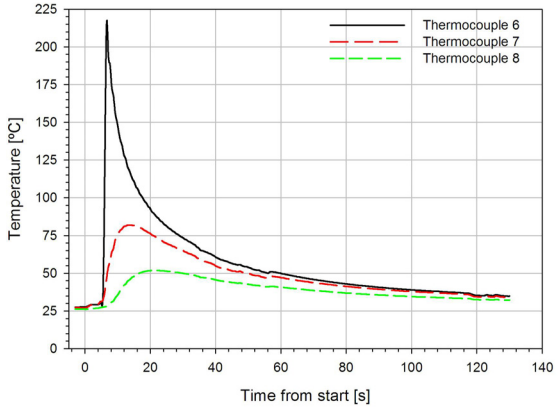


line 3

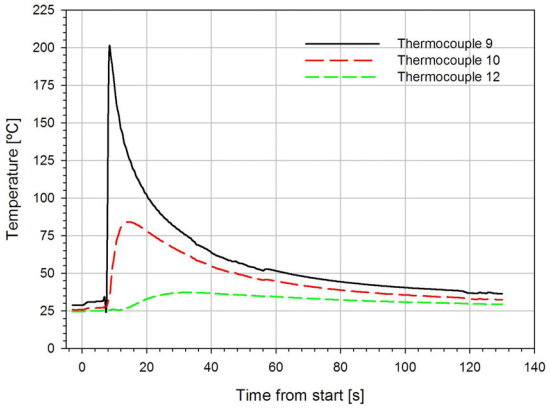


line 4

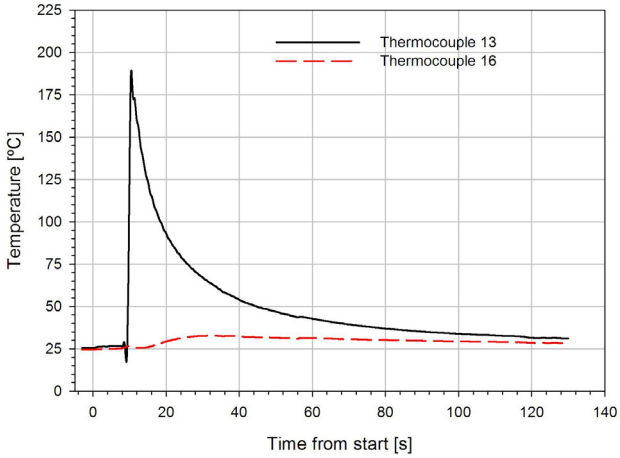


line 5

**Figure 467 - Temperature profiles in thermocouples placed perpendicular to the weld line.**

### *Aluminium 6061-T6*

In order to understand the temperature distributions along the plate a comparative plot of the 5 lines and 4 columns of thermocouples temperature profiles are presented. The temperature distributions in column 1, 2, 3 and 4 are presented in Figure 468.

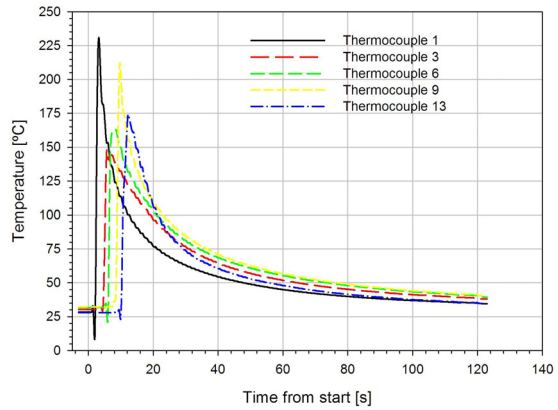


column 1

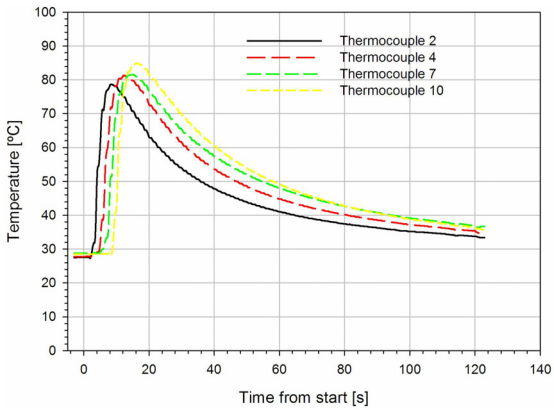


column 2

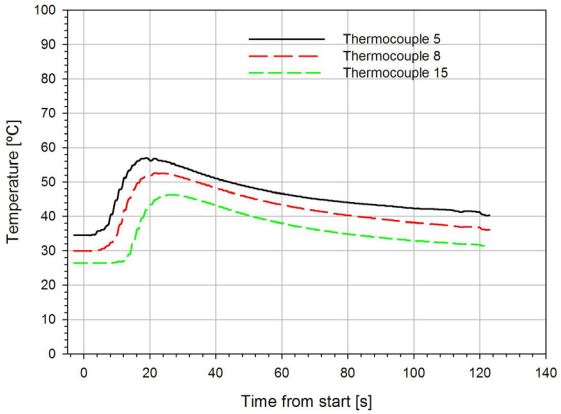


column 3

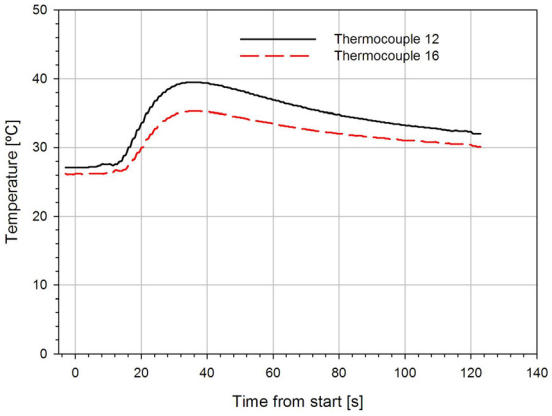


column 4

**Figure 468 - Temperature profiles in thermocouples placed parallel to the weld line.**

The temperature distributions in lines 1, 2, 3, 4 and 5 are presented in Figure 469. Again, a temperature decrease is observed in the perpendicular direction to the weld line.

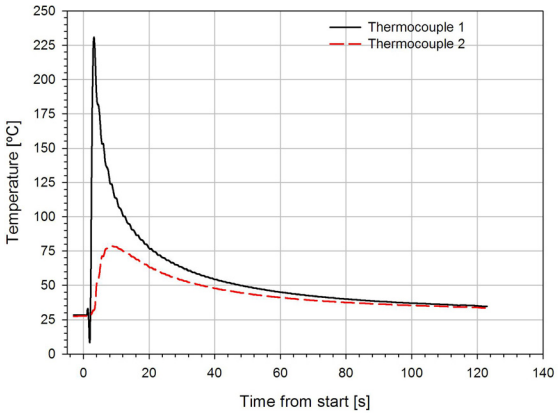


line 1

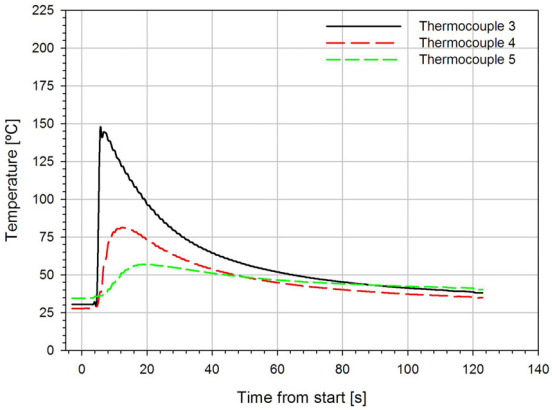


line 2

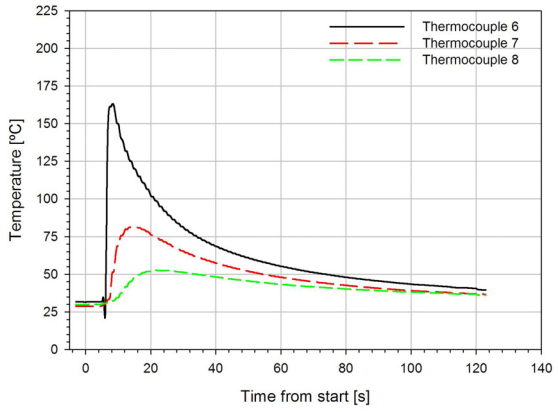


line 3

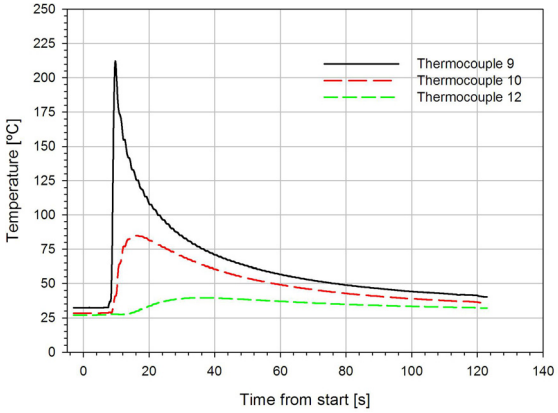


line 4

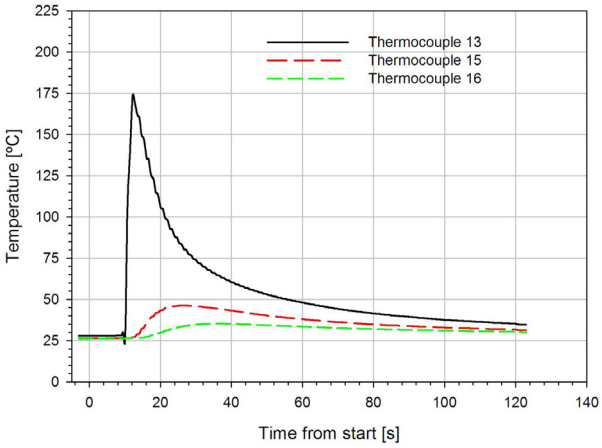


line 5

**Figure 469 - Temperature profiles in thermocouples placed perpendicular to the weld line.**